



Titre: Enhancement of Mesh-free Particle Methods for Highly Dynamic
Free-Surface and Granular Flows

Auteur: Mojtaba Jandaghian
Author:

Date: 2022

Type: Mémoire ou thèse / Dissertation or Thesis

Référence: Jandaghian, M. (2022). Enhancement of Mesh-free Particle Methods for Highly
Dynamic Free-Surface and Granular Flows [Ph.D. thesis, Polytechnique Montréal].
Citation: PolyPublie. <https://publications.polymtl.ca/10243/>

 **Document en libre accès dans PolyPublie**
Open Access document in PolyPublie

URL de PolyPublie: <https://publications.polymtl.ca/10243/>
PolyPublie URL:

**Directeurs de
recherche:** Ahmad Shakibaeinia
Advisors:

Programme: Génie civil
Program:

POLYTECHNIQUE MONTRÉAL

affiliée à l'Université de Montréal

Enhancement of mesh-free particle methods for highly dynamic free-surface and granular flows

MOJTABA JANDAGHIAN

Département des génies civil, géologique et des mines

Thèse présentée en vue de l'obtention du diplôme de *Philosophiæ Doctor*
Génie Civil

Mars 2022

POLYTECHNIQUE MONTRÉAL

affiliée à l'Université de Montréal

Cette thèse intitulée :

Enhancement of mesh-free particle methods for highly dynamic free-surface and granular flows

présentée par **Mojtaba JANDAGHIAN**

en vue de l'obtention du diplôme de *Philosophiæ Doctor*

a été dûment acceptée par le jury d'examen constitué de :

Tew-Fik MAHDI, président

Ahmad SHAKIBAEINIA, membre et directeur de recherche

Elmira HASSANZADEH, membre

Abdolmajid MOHAMMADIAN, membre externe

RÉSUMÉ

De nombreux procédés hydro-environnementaux, géotechniques et d'ingénierie impliquent des écoulements multiphasiques de matériaux granulaires immergés dans des fluides. Dans de tels problèmes, la phase fluide (par exemple, l'eau) et les grains solides (par exemple, les sédiments) interagissent et subissent différents régimes d'écoulement concernant l'écoulement du fluide ambiant et les forces corporelles (comme la gravité). Le transport de sédiments dans les environnements côtiers et fluviaux, la rupture de barrages hydrauliques, les coulées de débris et les glissements de terrain sont des exemples de ces écoulements granulaires immergés. Comprendre et prévoir le comportement mécanique de ces systèmes complexes est crucial pour optimiser les conceptions techniques et atténuer les risques environnementaux associés. De tels phénomènes sont caractérisés par des déformations de surface libre hautement dynamiques et des écoulements non linéaires de la phase granulaire. Les modèles numériques bien développés, avec moins de coûts et plus de flexibilité et de précision par rapport aux études théoriques et expérimentales, ont été introduits comme des outils puissants et fiables pour étudier la physique sous-jacente des écoulements à surface libre et granulaire. Néanmoins, les propriétés mécaniques complexes et les évolutions violentes de la surface libre de ces problèmes multiphysiques imposent des défis importants à la précision et à la stabilité des calculs pour leurs prédictions précises .

Les méthodes traditionnelles basées sur le maillage ont des difficultés à gérer les écoulements à surface libre avec de grandes déformations interfaciales. Les méthodes de particules sans maillage, telles que les particules mobiles semi-implicites (MPS) et l'hydrodynamique des particules lissées (SPH), grâce à leur nature lagrangienne, ont prouvé leurs avantages pour faire face à la complexité de tels écoulements de fluides. Pourtant, leur stabilité numérique, leur précision et leur efficacité sont des problèmes ouverts, en particulier pour des simulations précises d'écoulements granulaires violents à surface libre et immergés . De plus, les lois de comportement manquent d'une formulation unifiée et cohérente pour capturer différents régimes d'écoulements granulaires dynamiques. Pour combler ces lacunes dans les connaissances, nous devons améliorer la précision et la stabilité des méthodes numériques et des modèles rhéologiques granulaires.

L'objectif global de ce projet de recherche est de développer des méthodes de particules continues sans maillage robustes et cohérentes pour simuler des écoulements à surface libre et granulaire hautement dynamiques. Pour cela, nous proposons une méthode particulière conservatrice originale (basée sur la méthode MPS faiblement compressible) enrichie par

des algorithmes robustes de stabilisation des particules. Les développements incluent de nouveaux termes diffusifs artificiels et plusieurs techniques de régularisation des particules. Nous étudions le rôle des techniques de régularisation des particules proposées dans le contexte des méthodes MPS et SPH faiblement compressibles pour simuler des écoulements à surface libre hautement dynamiques. En outre, nous présentons un nouveau modèle de rhéologie avancé avec une formulation nouvelle et cohérente pour estimer la pression effective. Pour étudier la dynamique granulaire rapide, nous introduisons une nouvelle formulation MPS multi-résolution avec les nouvelles techniques de stabilisation et le modèle de rhéologie généralisée.

Nous validons les méthodes de particules améliorées pour des écoulements à surface libre hautement dynamiques caractérisés par des vagues déferlantes, des événements d'impact fluide-fluide et fluide-solide et une évolution d'écoulement non linéaire. De plus, nous étudions le comportement mécanique des écoulements granulaires immergés (entraînés par la gravité et les écoulements rapides de fluides), en simulant des cas de référence difficiles. Nous analysons les simulations numériques à travers des comparaisons qualitatives et quantitatives avec les données théoriques, analytiques et expérimentales disponibles. Les techniques de stabilisation des particules garantissent la précision numérique et la stabilité des grandes déformations de surface libre et des événements d'impact. Le modèle de rhéologie généralisée capture le comportement mécanique complexe et les régimes d'écoulement dynamiques des écoulements granulaires rapides entraînés par la gravité et les fluides. Les résultats numériques et les validations confirment l'efficacité et la nécessité des développements originaux présentés dans cette étude. Globalement, ce projet de recherche doctorale contribue à l'avancement des connaissances pour simuler des écoulements à surface libre et granulaire hautement dynamiques. Une telle compréhension des problèmes multiphysiques peut améliorer les processus décisionnels impliqués dans les activités de gestion des risques de divers problèmes hydro-environnementaux et géotechniques.

ABSTRACT

Many hydro-environmental, geotechnical, and engineering processes involve multiphase flows of granular materials immersed in fluids. In such problems, the fluid phase (e.g., water) and the solid grains (e.g., sediment) interact and experience different flow regimes concerning the ambient fluid flow and body forces (like gravity). Sediment transport in coastal and fluvial environments, water dam failure, debris flows, and landslides are examples of these immersed granular flows. Understanding and predicting the mechanical behavior of these complex systems are crucial for optimizing the engineering designs and mitigating the related environmental hazards. Such phenomena are characterized by highly dynamic free-surface deformations and non-linear flows of the granular phase. The well-developed numerical models, with fewer costs and more flexibility and accuracy over theoretical and experimental studies, have been introduced as powerful and reliable tools for studying the underlying physics of free-surface and granular flows. Nevertheless, the complex mechanical properties and violent free-surface evolutions of such multiphysics problems impose significant challenges to computational accuracy and stability for their accurate predictions.

The traditional mesh-based methods have difficulties in handling free-surface flows with large interfacial deformations. Mesh-free particle methods, such as Moving Particle Semi-implicit (MPS) and Smoothed Particle Hydrodynamics (SPH), thanks to their Lagrangian nature have proved their advantages for dealing with the complexities of such fluid flows. Yet, their numerical stability, accuracy, and efficiency are open problems, particularly, for accurate simulations of violent free-surface and immersed granular flows. In addition, the constitutive laws lack a unified and consistent formulation for capturing different regimes of dynamic granular flows. To address these knowledge gaps, we require to enhance the accuracy and stability of numerical methods and the granular rheological models.

The global objective of this research project is to develop robust and consistent mesh-free continuum particle methods for simulating highly dynamic free-surface and granular flows. To that end, we propose an original conservative particle method (based on the weakly-compressible MPS method) enhanced by robust particle stabilization algorithms. The developments include new artificial diffusive terms and several particle regularization techniques. We study the role of proposed particle regularization techniques within the context of the weakly-compressible MPS and SPH methods for simulating highly dynamic free-surface flows. Also, we present a new rheology model advanced with a novel and consistent formulation for estimating the effective pressure. To investigate rapid granular dynamics, we introduce

a novel multi-resolution MPS formulation with the new stabilization techniques and the generalized rheology model.

We validate the enhanced particle methods to highly dynamic free-surface flows characterized by breaking waves, fluid-fluid and fluid-solid impact events, and non-linear flow evolution. Furthermore, we investigate the mechanical behavior of immersed granular flows (driven by gravity and rapid fluid flows), simulating challenging benchmark cases. We analyze the numerical simulations through qualitative and quantitative comparisons with the available theoretical, analytical, and experimental data. The particle stabilization techniques ensure numerical accuracy and stability of large free-surface deformations and impact events. The generalized rheology model captures the complex mechanical behavior and dynamic flow regimes of rapid gravity- and fluid-driven granular flows. The numerical results and validations confirm the effectiveness and necessity of the original developments presented in this study. Overall, this doctoral research project contributes to the advancement of knowledge for simulating highly dynamic free-surface and granular flows. Such an understanding of the multiphysics problems can enhance the decision-making processes involved in hazard management activities of various hydro-environmental and geotechnical problems.

TABLE OF CONTENTS

RÉSUMÉ	iii
ABSTRACT	v
TABLE OF CONTENTS	vii
LIST OF TABLES	xi
LIST OF FIGURES	xiii
LIST OF SYMBOLS AND ABBREVIATIONS	xxix
CHAPTER 1 INTRODUCTION	1
1.1 Background and motivation	1
1.2 Dissertation outline	4
CHAPTER 2 LITERATURE REVIEW	5
2.1 Mesh-free particle methods	5
2.2 Immersed granular flows	11
CHAPTER 3 RESEARCH PROJECT	14
3.1 Research problems	14
3.1.1 Stability and accuracy of particle methods	14
3.1.2 Granular flow modeling	15
3.1.3 Research questions	16
3.2 Research objectives	16
3.3 Research originality and contributions	17
3.3.1 A conservative form of WC-MPS	17
3.3.2 Particle stabilization techniques	17
3.3.3 A generalized rheology model	18
3.3.4 A multi-resolution particle method for granular dynamics	19
3.4 Publications	19
3.5 Structure of thesis	22
CHAPTER 4 ARTICLE 1: AN ENHANCED WEAKLY-COMPRESSIBLE MPS METHOD FOR FREE-SURFACE FLOWS	24

4.1	Abstract	24
4.2	Introduction	24
4.3	MPS Methodology	28
4.3.1	Governing equations	28
4.3.2	Standard MPS discretization	29
4.3.3	Boundary treatments	31
4.4	Enhanced Weakly-Compressible MPS	32
4.4.1	Conservative pressure force	32
4.4.2	The continuity equation for the particle number density calculation	35
4.4.3	WC-MPS with Diffusion; WC-DMPS	36
4.4.4	A Corrected Particle Shifting technique; CPS + PC	38
4.5	Numerical Results and Discussions	44
4.5.1	Hydrostatic pressure	48
4.5.2	Elliptical water drops	52
4.5.3	Rotating square patch of fluid	56
4.5.4	Dam break	61
4.6	Conclusions	64

CHAPTER 5 ARTICLE 2: ENHANCED WEAKLY-COMPRESSIBLE

	MPS METHOD FOR VIOLENT FREE-SURFACE FLOWS: ROLE OF PARTICLE REGULARIZATION TECHNIQUES	66
5.1	Abstract	66
5.2	Introduction	67
5.3	Governing equations	71
5.4	The EWC-MPS model	71
5.4.1	The discrete system with the conservation properties	71
5.4.2	Particle regularization techniques for violent free-surface flows	75
5.4.3	Initial and solid boundary conditions	87
5.4.4	Time integration scheme	88
5.5	Numerical results and discussions	89
5.5.1	2D water dam-break	89
5.5.2	3D water sloshing in a rectangular reservoir	98
5.5.3	3D water dam-break against a rigid obstacle	104
5.6	Conclusion	111

CHAPTER 6 ARTICLE 3: STABILITY AND ACCURACY OF THE WEAKLY COM-

	PRESSIBLE SPH WITH PARTICLE REGULARIZATION TECHNIQUES	116
--	---	-----

6.1	Abstract	116
6.2	Introduction	117
6.3	SPH methodology	119
	6.3.1 Dynamic Particle Collision (DPC) technique for SPH	122
	6.3.2 Particle shifting algorithm coupled with DPC: <i>cPS</i>	124
6.4	Numerical simulations	127
	6.4.1 Oscillating droplet under a conservative force field	130
	6.4.2 2D water dam break	136
	6.4.3 2D water sloshing in a tank	138
	6.4.4 3D water dam-break against a rigid obstacle	140
6.5	Concluding remarks	143
CHAPTER 7 ARTICLE 4: ENHANCED WEAKLY-COMPRESSIBLE MPS METHOD FOR IMMERSSED GRANULAR FLOWS		155
7.1	Abstract	155
7.2	Introduction	155
7.3	Governing Equations and Constitutive laws	161
	7.3.1 Basic assumptions	161
	7.3.2 Flow equations	162
	7.3.3 A regularized visco-inertial model	163
	7.3.4 Consistent effective pressure	165
7.4	Numerical Model	166
	7.4.1 The discrete system	166
	7.4.2 Modified diffusive term	169
	7.4.3 A generalized rheology model for immersed granular flows	171
	7.4.4 Virtual moving gates	173
	7.4.5 Initial and boundary conditions	175
	7.4.6 Solution algorithm	176
7.5	Results and discussions	176
	7.5.1 Hydrostatic pressure for two fluid phases	177
	7.5.2 Immersed granular collapse	179
	7.5.3 Immersed granular landslide	192
7.6	Conclusion	199
CHAPTER 8 ARTICLE 5: FLUID-DRIVEN GRANULAR DYNAMICS THROUGH A CONSISTENT MULTI-RESOLUTION PARTICLE METHOD		213
8.1	Abstract	213

8.2	Introduction	213
8.3	Equations of motion	217
8.4	A consistent multi-resolution multiphase MPS method	218
8.4.1	Integral and summation interpolants	218
8.4.2	The discrete system of flow equations	219
8.4.3	Dynamic particle collision for multi-scale multiphase interactions . . .	221
8.4.4	Generalized rheology model	222
8.4.5	Boundary conditions and solution algorithm	224
8.5	Results and discussions	225
8.5.1	Numerical accuracy and convergence of the multi-resolution MPS model	225
8.5.2	Dam break waves on erodible granular beds	231
8.6	Conclusion	250
CHAPTER 9 GENERAL DISCUSSION		256
CHAPTER 10 CONCLUSION AND RECOMMENDATIONS		258
10.1	Future research	258
REFERENCES		260

LIST OF TABLES

Table 2.1	The kernel summation (for the density, ρ , and the particle number density, n , calculations), the particle approximation and gradient operators of an arbitrary function, f , with the standard SPH and MPS formulations.	7
Table 4.1	The elliptical water drop; The Root-Mean-Squared Error of the semi-minor and semi-major axes and ab variables	56
Table 5.1	Calculation time per iteration (i.e., $t^{iter.} = \text{Total calculation time}/\text{Total number of time steps}$) of the 2D water dam-break problem with different spatial resolutions, R . The last row of the table represents the rate of increase in the calculation time obtained by the CPS*+DPC versus the DPC technique. The GPU accelerated code is run on an NVIDIA V100 Volta GPU device.	98
Table 5.2	Calculation time per iteration (i.e., $t^{iter.} = \text{Total calculation time}/\text{Total number of time steps}$) of the 3D water sloshing problem with different spatial resolutions, R . The last row of the table represents the rate of increase of the calculation time with the CPS*+DPC versus the DPC technique. The GPU accelerated code is run on an NVIDIA V100 Volta GPU device.	101
Table 6.1	GPU specifications	144
Table 6.2	3D dam break: the simulation runtime per iteration denoted as $t_{iter.}$. In this 3D problem, the number of fluid particles would be (79, 380), (652, 212), and (5, 314, 295) where $R = 27.5, 55,$ and $110,$ respectively.	145
Table 6.3	3D dam break: the simulation runtime per physical second denoted as t_s . In this 3D problem, the number of fluid particles would be (79, 380), (652, 212), and (5, 314, 295) where $R = 27.5, 55,$ and $110,$ respectively. cPS and DPC reduce the runtime by 2.5-4.5 and 6-8.5 %, respectively.	145
Table 7.1	The strategies for the diffusive term to simulate the steady reservoir filled with the two fluid phases as $\rho_L/\rho_H = 0.5$	176
Table 7.2	The strategies for the diffusive term to simulate the steady reservoir filled with the two fluid phases as $\rho_L/\rho_H = 0.5$	179
Table 7.3	The material properties of the glass beads as the saturated granular phase	186

Table 7.4	Calculation and boundary conditions of the immersed granular collapse with different particle sizes, l_0	187
Table 7.5	The numerical test cases of the immersed granular collapse concerning the rheology model, the diffusive term, and the effective pressure equation.	187
Table 7.6	Time steps of the extracted data from the experimental and numerical simulations, $T = t\sqrt{g_y/H_0}$	187
Table 7.7	Calculation time per iteration for simulating Case 2A with different resolutions using NVIDIA V100 Volta GPU device	196
Table 7.8	The numerical test cases of the immersed granular landslide	198
Table 7.9	Time steps of the extracted data from the numerical simulations, $T = t\sqrt{g_y/H_0}$	199
Table 8.1	Material properties of coarse sand grains and PVC pellets.	234
Table 8.2	The normalized root-mean-square error (L_2) of A_e , $x_c A_e$, and x_f of case A-Sand with values for material properties in the rheology model (a , b , and μ_2) and where $q = 1$	236
Table 8.3	The normalized root-mean-square error (L_2) of A_e , $x_c A_e$, and x_f of case A-PVC with different material properties in the rheology model (a , b , and μ_2) and where $q = 1$	237
Table 8.4	The normalized root-mean-square-error (L_2) of A_e , $x_c A_e$, and x_f with $q = 1, 2$, and 4 for case A-PVC with and without the suspension equation (8.23).	238
Table 8.5	The normalized root-mean-square error (L_2) of A_e , $x_c A_e$, and x_f of cases A-Sand, A-PVC, B-Sand, and C-Sand simulated by the multi-resolution MPS model ($q = 4$).	247
Table 8.6	The normalized root-mean-square-error (L_2) of A_e , $x_c A_e$, and x_f with $q = 1, 2$, and 4 for case A with sand and PVC.	250

LIST OF FIGURES

Figure 1.1	Examples of granular dynamics in hydro-environmental problems: (a) Cecil Lake road landslide in Alberta 2016 (the inset photo is taken from the Geological Survey of Canada) and (b) dam failure in Quebec, 1999 (the inset photo is taken from Brooks & Lawrence [1]). (c): The co-presence of water and sediment in such phenomena.	2
Figure 1.2	Different flow regimes of the immersed granular collapse	3
Figure 1.3	(a) Representative volume of the fluid and submerged solid grains, (b) Homogenization of phase, and (c) the discretization of the computational domain into moving particles.	3
Figure 2.1	(a) The kernel approximation over the computational fluid domain, and (b) the particle interaction force, \mathbf{F}	6
Figure 3.1	The five interconnected research articles addressing the four research objectives (O1-O4). Articles 1-5 are represented as chapters 4, 5, 6, 7, and 8, respectively.	23
Figure 4.1	The fluid and solid boundary particles configuration	32
Figure 4.2	(a) Initial pressure field ($t = 0$) of a randomized particle distribution placed on a hexagonal lattice (maximum randomness level of $0.1l_0$ in the x and y directions) with the periodic boundary conditions, (b) the pressure field obtained with the new conservative form of the pressure gradient, $\frac{d}{n_0} \sum_{i \neq j}^N (n_i \frac{p_j}{n_j} + n_j \frac{p_i}{n_i}) \frac{\mathbf{e}_{ij}}{r_{ij}} W_{ij}$, and (c) the non-conservative form of the higher-order pressure gradient (including \mathbf{C}_i), $\frac{d}{n_0} \sum_{i \neq j}^N \frac{p_j - p_i}{r_{ij}} (\mathbf{C}_i \mathbf{e}_{ij}) W_{ij}$, at $t = 1.0$ second of simulation	35
Figure 4.3	A particle classification scheme in the context of the MPS method	41
Figure 4.4	Sketch of the Corrected Particle Shifting algorithm	44
Figure 4.5	The initial setups of the hydrostatic pressure (a), the elliptical water drop (b), the rotating square patch of fluid (c) and the water dam break test-cases (d). The colour contours represent the initial pressure fields.	47

Figure 4.6	The hydrostatic pressure contour; (a) The WC-MPS model with the conservative ∇p (Eq. 23) and the kernel summation equation (4.5) for calculating the particle number density, (b) with the Conservative WC-MPS model. The graph (c) represents the pressure parameter at the center of the reservoir (Mid-point, M) over the simulation time ($t = 2$ Seconds). In the original WC-MPS model (the gray dash line), Eq.(4.5) updates the particle number density and the gradient of pressure is approximated by Eq. (4.16) with added particle stabilizing term $\Delta p = p_i - \hat{p}_i$	49
Figure 4.7	The hydrostatic pressure contour; (a) the original WC-MPS, (b) the original WC-MPS + the pair-wise particle collision approach and (c) the Conservative WC-DMPS (using the conservative pressure gradient Eq. (4.23) and the added diffusive term to the continuity equation (4.39) with $\delta_{MPS} = 0.1$). The time history of the pressure at the mid-point for each case is plotted in the graph (d)	50
Figure 4.8	The role of the initial hexagonal particle distribution in the Conservative WC-MPS model; (a) Conservative WC-MPS model with the initial hexagonal particle distribution (b) Conservative WC-MPS model with the Cartesian particle distribution (same as the case (b) in Figure 6). The evolution of the pressure at the mid-point of the steady tank is represented in the graph (c) for the hexagonal particle distribution (the blue continues line) and the Cartesian particle distribution (the red dashed line).	51
Figure 4.9	The pressure field and the evolution of the water drop at $tw_0 = 0.1, 0.5$ and 0.8 ; (a) the Conservative WC-MPS model vs (b) the Conservative WC-DMPS with $\delta_{MPS} = 0.2$ + CPS algorithm. The black dash-dot line represents the analytical deformation of the elliptical bubble.	52
Figure 4.10	The particles distribution and pressure field of the water drop test case at $tw_0 = 0.8$ for the four different strategies (case a-d).	53
Figure 4.11	The effectiveness of the CPS algorithm for the long-term stability of the model and the tensile instability elimination: The water drop evolution and pressure contour at $tw_0 = 1.7$ without and with the CPS algorithm (Case (a) & (b)). The time history of the local numerical pressure at point A without any frequency filtering is represented in the graph (c) ($c_0 = 15Rw_0$).	54

Figure 4.12	The time history of local $(p_m - p_{anal.})/\rho\omega_0^2 R^2$ at the domain center without any frequency filtering; (a) Conservative WC-MPS ($\delta_{MPS} = 0$) vs (b) Conservative WC-DMPS with $\delta_{MPS} = 0.2$ ($c_0 = 15R\omega_0$).	55
Figure 4.13	The time evolution of the semi-minor, a , and semi-major, b , axes of the elliptical water drop.	55
Figure 4.14	Evolution of the square patch of fluid at $t\omega_0 = 1.08$. The white squares represent the LFDM-BEM results extracted from [2].	57
Figure 4.15	The square patch of fluid without the diffusive term at $t\omega_0 = 2.04$. . .	57
Figure 4.18	The robustness of the proposed enhancement techniques in capturing large deformations (The long-term simulations of the case (a) in Figure 4.16).	58
Figure 4.16	The square patch of fluid with different pressure gradient formulations at $t\omega_0 = 2.04$. The white squares represent the LFDM-BEM model results extracted from [2].	59
Figure 4.17	The local pressure at the domain center for the three strategies in Figure 4.16, without any frequency filtering and with $c_0 = 5L\omega_0$; (a) Conservative WC-DMPS, (b) Non-Conservative WC-DMPS and (c) Non-Conservative WC-DMPS with the higher-order $\langle \nabla p \rangle_i$ vs the δ^+ -SPH model [3] (In all three cases a-c the CPS+PC algorithm is activated.)	60
Figure 4.19	The square patch of fluid with (a) and without (b) the proposed corrections in the PS algorithm (i.e. the corrections II to IV), $re = 3.1l_0$. However, the other calculation conditions are the same as the case (c) in Figure 4.14.	61
Figure 4.20	Water dam break at $T = t\sqrt{g/H} = 1.62$ and 2.96 , The Conservative WC-MPS model with and without the diffusive term (case (b) vs (a) , respectively) where the CPS+PC algorithm is activated. ($H/l_0 = 100$)	63
Figure 4.21	Water dam break evolution with the Conservative WC-DMPS model and the CPS+PC algorithm at $T = t\sqrt{g/H} = 5.9, 6.5$ and 7.8 ($H/l_0 = 100$).	63
Figure 4.22	The effectiveness of the proposed corrections in the CPS technique (i.e. corrections II-IV in section 4.4.4) for determining the normal vectors to modify the particle shifting vector ($H/l_0 = 60, re = 3.1l_0$). Other calculation conditions are the same as the case (b) in Figure 4.20. . .	64
Figure 4.23	The numerical versus experimental [4] water pressure at $S1$ (Left) and the wave front propagation (Right) for the dam break test case. . . .	64
Figure 5.1	The graphical abstract	67

Figure 5.2	The Dynamic Particle Collision (DPC) algorithm consists of the proposed collision and repulsive terms and the dynamic coefficients defined by the Wendland kernel	76
Figure 5.3	The new particle classification algorithm and special treatments of the boundary particles for the corrected particle-shifting vector. The umbrella-shaped region used for identifying the free-surface particle is illustrated (i.e., R1 and R2 given by Eq. (5.19)). The results of the two-dimensional (2D) dam-break test case (with $H/l_0 = 100$) show the estimated normal vectors and the different categories of the fluid particles at $T = 2.18$ and $T = 6.43$, where $T = t\sqrt{g/H}$ is the non-dimensional time.	80
Figure 5.4	The sequential steps of the CPS*+DPC algorithm as a hybrid particle regularization approach. The new particle classification algorithm is represented in Figure 5.3, and the corrected particle-shifting vector is given by Eqs. (5.18) & (5.28).	87
Figure 5.5	Initial configuration and pressure contour of the 2D water dam-break based on the experimental setup by Lobovský et al. [4]. The dash-dot line is the expected free surface of the fluid flow filling the width of the tank at the final equilibrium state.	89
Figure 5.6	Numerical results of the models ($R = H/l_0 = 100$) with the CPS*+DPC, DPC, and without regularization techniques versus the experimental results of Lobovský et al. [4]: the time history of averaged local water pressure, p , at $S1$ (left) and the wave propagation (right).	91
Figure 5.7	The dam break problem without the particle regularization techniques ($R = 200$). The dash-dot line is the expected free surface of the fluid flow filling the width of the tank at the final equilibrium state.	91
Figure 5.9	Time history of the kinetic, ΔE_k , potential, ΔE_p , and mechanical, ΔE_m , energies of the dam break test case with the DPC vs PC methods (left graph). The total kinetic energy dissipation by the PC techniques (accumulated over time) is denoted as Q_{PC} . The right graph represents the particle convergence of the 2D dam-break simulation as the total energy dissipation reduces with increasing the spatial resolution, $R = H/l_0$	92

Figure 5.8	Time evolution of the dam break problem with the standard PC (left column) and the DPC (right column) techniques ($R = 200$). The color contour represents the non-dimensional pressure field at $T = t\sqrt{g/H} = 3.28, 5.70, 6.91, 9.83,$ and 17.47 (from the top row to the bottom row, respectively). The dash-dot line is the expected free surface of the fluid flow filling the width of the tank at the final equilibrium state.	93
Figure 5.10	Time evolution of the dam break problem simulated by the CPS*+DPC technique with and without the $\delta\hat{\mathbf{v}}$ -terms (represented in the right and left columns, respectively). The resolution is set to $R = 200$ and the expanded regions, i.e., $i \in \mathbb{X}$, are identified with the yellow particles. The dash-dot line is the expected free surface of the fluid flow filling the width of the tank at the final equilibrium state.	95
Figure 5.11	The evolution of energy components (E_p : the potential energy (top left), E_k : the kinetic energy (top right), and E_m : the mechanical energy (bottom left) (defined by Eq. (5.37)) of the 2D dam-break problem with different CPS techniques and resolutions. The bottom right graph shows the convergence of the potential energy to the expected final state (i.e., $\Delta E_p/\Delta E_m^{Fin} = -1$) by increasing the spatial resolution, $R = H/l_0$	96
Figure 5.12	Time evolution of the dam break problem with the CPS*+DPC (left column) and the DPC (right column) techniques ($R = 200$). The color contour represents the non-dimensional pressure field. The dash-dot line is the expected free surface of the fluid flow filling the width of the tank at the final equilibrium state.	97
Figure 5.13	Initial configuration and pressure field of the 3D water sloshing problem. The locations of the three pressure sensors ($P1, P2,$ and $P3$, which in the physical model by Rafiee et al. [5] correspond to sensors $P180, P078,$ and $P136$, respectively) are specified on the side view of the reservoir. Section A-A and Section B-B, identified on the top view of the reservoir, are used to represent the numerical results.	99
Figure 5.14	Local numerical pressure (with $R = L/l_0 = 200$) versus the experimental measurements of Rafiee et al. [5] at the $P1$ (top), $P2$ (middle), and $P3$ (bottom) points.	100
Figure 5.15	Flow evolutions and the pressure field of the water sloshing problem (at Section A-A) simulated by the model with the CPS*+DPC (left column) and the DPC (right column) techniques, where $R = 260$. . .	102

Figure 5.16	Time evolution of the 3D water sloshing problem (at Section A-A) using the CPS*+DPC techniques with and without the additional $\delta\hat{\mathbf{v}}$ -terms (represented in the right and the left columns, respectively). The resolution is set to $R = 200$, and the expanded regions, i.e., $i \in \mathbb{X}$, are identified with the yellow particles.	103
Figure 5.17	Particle classification and normal vectors of the 3D sloshing problem at Section A-A and Section B-B with the CPS*+DPC technique and $R = 200$	104
Figure 5.18	Evolution of energy components (E_m : the mechanical energy (top left), E_k : the kinetic energy (top right), E_p : the potential energy (bottom left), and Q_{PC} : the total kinetic energy dissipated by the DPC technique (bottom right) (defined by Eqs. (5.37) & (5.38)) of the 3D water sloshing test case with the DPC and CPS*+DPC (with and without the $\delta\hat{\mathbf{v}}$ -terms) techniques, where $R = 200$. The non-dimensional time, T , is given as $t\sqrt{g/L}$, and the energy variations, $\Delta E = E^t - E^0$, are normalized by the initial mechanical energy of the system, $E_m^0 = E_p^0 + E_k^0$	105
Figure 5.19	Initial configuration of the 3D water dam-break against the rigid obstacle, based on the physical model by Kleefsman et al. [6]. The pressure sensors, $P1$ and $P2$, are located on the side wall of the obstacle, and the vertical water heights in the y-direction at $H1$ and $H2$ are probed. Section A-A, shown on the top view of the channel, is used to represent the numerical results.	106
Figure 5.20	Numerical results (with the DPC and CPS*+DPC techniques and the different spatial resolutions, R) versus the experimental measurements from Kleefsman et al. [6]: Shown are the local pressure at points $P1$ and $P2$ (top row) and the depth of water in the y-direction at $H1$ and $H2$ lines, y_{max} (bottom row). The non-dimensional time and the spatial resolutions are given as $T = t\sqrt{g/H}$ and $R = H/l_0$, respectively.	107
Figure 5.21	Flow evolution and particles' velocity magnitude for the 3D water dam-break with the rigid obstacle simulated by the model with the CPS*+DPC (left column) and DPC (right column) techniques, where $T = t\sqrt{g/H}$ and $R = 55$	108
Figure 5.22	Non-dimensional pressure field of the 3D water dam-break with the rigid obstacle (at Section A-A) during the main impact events simulated by the model with the CPS*+DPC (left column) and DPC (right column) techniques, where $T = t\sqrt{g/H}$ and $R = 55$	109

Figure 5.23	Temporal changes of the energy components of the 3D water dam-break with the obstacle: The top left and right graphs represent the numerical convergence of the 3D model with the DPC and CPS*+DPC techniques (with various spatial resolutions), respectively. The bottom graph compares the energy evolutions with DPC versus CPS*+DPC.	110
Figure 5.24	Flowchart of the solution algorithm based on the symplectic time integration scheme. The main temporal loop of the calculation is implemented on a GPU device with CUDA C++ parallel programming. . .	114
Figure 6.1	The graphical abstract	117
Figure 6.2	The general form of the DPC transport-velocity formulation, $\delta\mathbf{v}_i^{DPC}$, (6.12) consists of the dynamic collision and repulsive terms for dealing with different states of inter-particle penetration where $r_{ij} < dp$. . .	124
Figure 6.3	The coupled Particle Shifting formulation (6.22). b_i , $\delta\mathbf{r}_i^{PS}$, and $\delta\mathbf{v}_i^{DPC}$ are given through equations (6.21), (6.18), and (6.12), respectively. .	127
Figure 6.4	Initial state and pressure field of the numerical test cases: (a) the oscillating droplet, (b) 2D water dam break, (c) 2D water sloshing, and (d) 3D dam break against an obstacle	130
Figure 6.6	Oscillating droplet: the time evolutions of a and b by the SPH + PS, cPS or DPC techniques compared with the theoretical solution in (a). Graph (b) illustrates the divergence of model with the PS method due to the unphysical volume expansion	132
Figure 6.5	Oscillating droplet: non-dimensional pressure fields by the SPH with either PS, cPS, or DPC techniques from top to bottom rows, respectively ($R = d_0/dp = 200$). The free-surface of the droplet is compared with the theoretical solution (the black dashed lines) at $t/T = 4.25, 6.50$, and 8.75	133
Figure 6.7	Oscillating droplet: graphs (a-d) represent the time evolution of the total potential (E_p), kinetic (E_k), and, mechanical (E_m) energies comparing the numerical results with the theoretical solution (the black dotted lines). Graphs (e-g) give L_2 errors and the convergence order of the numerical results.	134
Figure 6.8	Oscillating droplet: the spatial particle disorder, λ_i for the models with no particle regularization, PS, cPS, and DPC. The time evolution of the global particle disorder, Λ , is plotted in the graph for the different test cases. The spatial particle disorder formulation is implemented based on the work of Antuono et al. [7].	135

Figure 6.9	Dam break: the local averaged pressure on the front wall, at S , (left) and the wave propagation on the horizontal bed, x_f , (right) with $R = H/dp = 200$. Numerical results are extracted every 0.02 seconds. . . .	139
Figure 6.10	Dam break: flow evolutions and non-dimensional pressure fields with cPS and DPC (the left and right columns, respectively) with $R = 200$	139
Figure 6.11	Dam break: the particle distribution and the non-dimensional pressure field as the wave impacts the free-surface at $T = 6.31$ (simulated by PS, cPS and DPC techniques where $R = 200$)	140
Figure 6.12	Dam break: (a) the local spatial particle disorder, λ_i , at $T = 6.31$ and (b) the evolution of its global value, Λ , with PS, cPS, and DPC techniques where $R = 200$	141
Figure 6.13	Dam break: $\langle \nabla \cdot \mathbf{r} \rangle_i$ and the non-dimensional pressure field at $T = 8.90$ and the final stage, $T = 40.44$, with cPS and DPC where $R = 200$. The dash-dot line is the expected fluid height at the final equilibrium state.	142
Figure 6.14	Dam break: evolution of the global energies by cPS and DPC with different spatial resolutions, R , plotted in graphs (a) and (b), respectively. Graph (c) compares the energy evolution of the model with no particle regularization with the profiles of PS, cPS, and DPC where $R = 200$	143
Figure 6.15	Dam break: flow evolution and the non-dimensional pressure fields (a, b), the impact load, p , at S (c, d), and the energy evolution, ΔE , (e, f) with different viscosity models, i.e., the laminar+SPS model, the artificial viscosity term ($\alpha = 0.01$), and the inviscid fluid ($\alpha = 0$), simulated by cPS and DPC where $R = 200$. The dashed red line in (a) and (b) is the free surface at $T = 5.95$ predicted by the BEM solver from [8]. The dashed black line in (c) and (d) is the experimental measurement of the impact load from [4].	144
Figure 6.16	Water sloshing: the local averaged pressure obtained by PS, cPS, and DPC ($dp = 0.002$ (m)) compared with the experimental measurements at the probe location, S , reported by Souto-Iglesias et al. [9]. Numerical results are extracted every 0.01 seconds.	145
Figure 6.17	Water sloshing: the flow evolutions and the non-dimensional pressure fields with PS, cPS, and DPC ($dp = 0.002$ (m)) compared with snapshots of the experiment on the top-row (taken from [9])	146

Figure 6.18	Water sloshing: $\langle \nabla \cdot \mathbf{r} \rangle_i$ and the local spatial particle disorder, λ_i at $t = 7.50$ seconds where $dp = 0.002$ (m)	147
Figure 6.19	Water sloshing: the time evolution of the global spatial particle disorder, Λ , and the global potential energy, E_p , where $dp = 0.002$ (m) (represented in graphs (a) and (b), respectively)	148
Figure 6.20	3D dam break: the fluid height at $H1$ and $H2$, and the local pressure at $P1$ and $P2$ by PS, cPS, and DPC (where $R = H/dp = 55$) validated with the experimental measurements by Kleefsman et al. [6]. Numerical results are extracted every 0.1 seconds.	148
Figure 6.21	3D dam break: the flow evolution and the magnitude of velocity by PS, cPS, and DPC (the top, middle and bottom rows, respectively) at $T = 2.53$ and 5.06 , with $R = 110$	149
Figure 6.22	3D dam break: non-dimensional pressure field at the middle-section of the reservoir, $y = 0.5$ (m), by cPS and DPC (the left and right columns, respectively) at $T = 2.53$, 5.06 , and 8.45 , with $R = 110$	150
Figure 6.23	3D dam break: $\langle \nabla \cdot \mathbf{r} \rangle_i$ at the middle-section of the reservoir, $y = 0.5$ (m), by PS, cPS, and DPC (the top, middle, and bottom rows, respectively) at $T = 8.45$ and 33.79 , with $R = 110$	151
Figure 6.24	3D dam break: evolution of the energy components by cPS and DPC with different spatial resolutions ((a) and (b) graphs, respectively). Graph (c) compares the energy evolution by PS, cPS, and DPC where $R = 110$	152
Figure 6.25	Implementation of the DPC formulation within the GPU-accelerated framework of DualSPHysics. The DPC transport-velocity equation, $\delta \mathbf{v}_i^{DPC}$, is given by (6.12).	154
Figure 7.1	The graphical abstract	156
Figure 7.2	The homogenized water and mixture phases are treated as Newtonian and non-Newtonian fluids, respectively. The computational domain is discretized with moving particles representing the water (Ω_w), mixture (Ω_m), and solid boundary (Ω_s) particles.	168
Figure 7.3	The virtual moving gates implemented for modeling the effects of the physical gate in the numerical simulations.	174

Figure 7.4	The initial configuration of the steady reservoir ($g_y = 9.81 \text{ m/s}^2$) filled with the two fluid phases ($R = H/l_0 = 100$). The lighter phase with ρ_L is considered as the reference phase for calculating the bulk modulus, B_0 . The hexagonal lattice is used for the initial uniform distribution of the particles.	180
Figure 7.5	The position of the fluid particles (y_i) vs their numerical pressure (p_i , without any data averaging or filtering) at $t = 10.0 \text{ s}$ (All the fluid particles are plotted in the graph for cases 1A, 1B, and 1C defined in Table 7.2 with $R = 100$). The zoom-in plots show fluid particles at the free-surface, the interface, and the vicinity of the bottom wall.	180
Figure 7.6	Pressure field of the cases 1A, 1B, and 1C at $t = 10.0 \text{ s}$. The particles are initially located on the hexagonal configuration and $R = 100$	181
Figure 7.7	The theoretical versus the extracted numerical pressure (averaged at $x = 0.1 \text{ m}$ and $t = 10 \text{ s}$). The NRMSE of the pressure profiles for the cases 1A and 1C with the different spatial resolutions, $R = H/l_0 = 50, 100, \text{ and } 200$, are represented.	181
Figure 7.8	The velocity profiles (averaged at $x = 0.1 \text{ m}$ and $t = 10 \text{ s}$) and the evolution of the total kinetic energy of the system with $R = 50$. The NRMSE for the cases 1A and 1C are represented.	182
Figure 7.9	The NRMSE of the pressure profiles and the total kinetic energy (in the log-log plot) for the cases 1A and 1C representing the order of convergence of the numerical results.	182
Figure 7.10	The three-dimensional configuration and the initial setup of the physical (a) and numerical (b) models	188
Figure 7.11	The immersed granular collapse via the three-dimensional numerical model based on the enhanced weakly-compressible MPS method (Case 2A- $l_0 = 0.003 \text{ m}$). See the supplementary results as the movies of the experiment and the numerical simulations.	189
Figure 7.12	The temporal evolution of the immersed granular collapse; the experimental vs numerical results (Case 2A- $l_0 = 0.003 \text{ m}$) at the sidewall section.	190
Figure 7.13	Time evolutions of the non-dimensional interface profiles of the immersed granular collapse; the experimental results vs the numerical simulations (Case 2A with $l_0 = 0.004, 0.0035, 0.003, 0.002, 0.0015 \text{ m}$ at the sidewall section and T2, T6, and the final stage).	193

Figure 7.14	Normalized run-out distances (L/L_0-1) (left-graph) and the RMS Errors of (L/L_0-1) (right-graph and the inset table) of the immersed granular collapse (Case 2A with $l_0= 0.004, 0.0035, 0.003, 0.002, 0.0015 m$). The mean diameter of the solid grains is $d_g = 0.0008 m$ and N_g is the number of solid grains that the macroscopic scale of the particle method (i.e., a mixture particle) represents in the 3D problem (with $\phi = 0.64$).	194
Figure 7.15	The pressure field of the fluid particles at the sidewall section; Case 2A vs Case 2B ($l_0 = 0.003 m$). The black squares correspond to the interface profiles of the experimental results. The long-dashed lines represent the interface of the water and the mixture particles in the numerical model.	194
Figure 7.16	The viscosity field of the mixture particles at the middle section; Case 2A vs Case 2B ($l_0 = 0.003 m$). The water particles detected as the free-surface particles are identified.	195
Figure 7.17	The total pressure of the mixture particles concerning their vertical position ($p_i - y_i$) at the final stage of the simulation, $t = 1.60$ second; Case 2A vs Case 2C ($l_0 = 0.003 m$)	195
Figure 7.18	The non-dimensional numbers of the visco-inertial rheology model (I_v , I and I_m defined in Eq. (7.5) and St) at the middle section of the channel (Case 2A- $l_0 = 0.003 m$)	203
Figure 7.19	The approximated volume fraction of the mixture particles, $\langle\phi\rangle_i$, and the nondimensional scale of the water particles' effective viscosity, η_i/μ_w , at the middle section (Case 2A- $l_0 = 0.003 m$)	204
Figure 7.20	The dynamic viscosity field of the mixture particles at the sidewall section; Case 2A vs Case 2D ($l_0 = 0.003 m$). The black squares represent the interface profiles of the experimental results.	204
Figure 7.21	The effective pressure within the mixture particles at the sidewall section; Case 2A vs Case 2E ($l_0 = 0.003 m$). The black squares represent the interface profiles of the experimental results.	205
Figure 7.22	The normalized runout distance at the sidewall section; Case 2A vs Case 2D and Case 2E ($l_0 = 0.003 m$)	205
Figure 7.23	The immersed granular landslide; the initial setup of the numerical model and the virtual gates.	206
Figure 7.24	The three-dimensional numerical results of the immersed granular landslide at the middle section of the channel with a 45-degree slope (Case 3A)	207

Figure 7.25	The immersed granular landslide; The 3D numerical results of case 3A (from the sidewall view) versus the experimental results of test case S7 extracted from [10] (The orange dash line represents the initial stage of the granular phase (at T0) and the green lines plotted on the scaled snapshots correspond to the outline of the mixture phase in the numerical simulation at each time step. The dark blue particles are the free-surface particles detected by the CPS algorithm).	208
Figure 7.26	The velocity contour and vectors of the submerged landslide at the middle section of the channel at T4 showing the circulation formed by the drag force in the fluid flow (Case 3A)	209
Figure 7.27	The normalized runout distance of the immersed granular landslide; the numerical versus the experimental results (Test case S7 in [10] with a 45-degree slope, smooth surfaces, and glass beads)	209
Figure 7.28	The non-dimensional numbers of the visco-inertial rheology model (I_v , I_m and St defined by Eq. (7.5)) at the middle section of the channel (Case 3A)	210
Figure 7.29	The approximated volume fraction of the mixture particles, $\langle\phi\rangle_i$, and the nondimensional scale of the water particles' effective viscosity, η_i/μ_w , at the middle section (Case 3A)	211
Figure 7.30	The role of the effective pressure in the evolution of the immersed granular landslide; Case 3A vs 3C at the middle section of the channel at T3.	211
Figure 7.31	Solution algorithm based on the explicit second-order symplectic time integrator by Monaghan and Rafiee [11]. The host part of the code, run on the CPU, initializes the model, and prints the results, while the main temporal loop and the neighbor search algorithm (within the gray box) are run on the GPU.	212
Figure 8.1	(a): The multiphysics system containing water and submerged solid grains. (b): The representative volumes of water and mixture phases homogenized into the representative elementary volume, V , in the single-continuum model. (c): The particle discretization in the single- or multi-resolution particle method. (d): The discretized computational domain with different spatial resolutions for the water and mixture particles.	216

Figure 8.2	Kernel function of the MPS method for the multi-resolution particle interactions. d is the space dimension equal to 2 and 3 for the two- and three-dimensional simulations, respectively. k determines the smoothing length of the kernel, r_{ei} , and is set to 3.1 regardless of the particle size, l_{0i}	221
Figure 8.3	Initial configuration of the numerical simulations: (a) the multi-viscosity Poiseuille flow, and (b) the hydrostatic pressure for two fluid phases.	226
Figure 8.4	Poiseuille flow: velocity of fluid particles ($\forall i \in \Omega_f$) at $T = tU_0/L = 100$ with $M = 25, 50,$ and 100 , simulated by the single-resolution ($q = l_{02}/l_{01} = 1$) and multi-resolution ($q = 2, 4$) MPS models. The spatial resolution of the second fluid phase (Ω_2) is $R = L/l_{02} = 40$. The solid black lines represent the analytical velocity profiles. The magnitude of velocity is normalized by U_0	228
Figure 8.5	Poiseuille flow: (a) $L_2(\ \mathbf{v}\)$ over the simulation time for $M = 50$ with different spatial resolutions (R), and (b) the numerical errors and order of convergence ($O(\cdot)$) for $M = 25, 50,$ and 100 , simulated by the single- and multi-resolution MPS models. In (b), $L_2(\ \mathbf{v}\)$ is averaged over $T = 90 - 100$ identified as the gray regions in (a).	229
Figure 8.6	Hydrostatic pressure: particle distributions and pressure fields (with $R = H/l_{02} = 100$) at $t = 10$ s (represented in the top and the middle rows, respectively). The local pressures extracted at $x = 0.1$ m are plotted against the theoretical hydrostatic pressure (in the bottom row).	232
Figure 8.7	Hydrostatic pressure: (a) $L_2(p)$ over the simulation time with different spatial resolutions (R), and (b) the numerical errors and order of convergence, simulated by the single- and multi-resolution MPS models. In (b), $L_2(p)$ is averaged over $T = 60 - 70$ identified as the gray regions in (a). The local numerical pressures are averaged on the extraction points (i.e., at $x = 0.05, 0.10,$ and 0.15 m, shown in Figure 8.3-b).	233
Figure 8.8	Water dam break, under the gravitational force, $\mathbf{g} = (0, -9.81\text{m/s}^2)^t$, on movable beds. (a) The initial configuration of the two-dimensional numerical simulations, and (b) the experimental data by Spinewine and Zech [12]. Considering different levels of sediment on the left side of the gate, ΔH_b , we simulate cases A, B, and C (denoted as (a), (b), and (d) in the experiments, respectively). The fluid particles ($i \in \Omega_f = \Omega_w \cup \Omega_m$) are packed before the initialization of the main simulations.	235

- Figure 8.9 Sensitivity analysis of the fluid-driven granular flow (case A-Sand) to the rheology parameters (a , b , and μ_2) through the single-resolution MPS model ($q = 1$). The experimental profiles of the eroded area, A_e , the first moment of the eroded area, $x_c A_e$, and the wavefront position, x_f , are extracted from the interface data by Spinewine and Zech [12]. 237
- Figure 8.10 Sensitivity analysis of the fluid-driven granular flow (case A-PVC) to the rheology parameters (a , b , and μ_2) through the single-resolution MPS model ($q = 1$). The experimental profiles are extracted from the interface data by Spinewine and Zech [12]. 238
- Figure 8.11 Dam break waves over the flat erodible bed (case A-Sand). The first row shows the snapshots and the interface data from the experiments by Spinewine and Zech [12]. The results of the multi-resolution MPS model (with $q = 4$) (i.e., the velocity magnitude, $\|\mathbf{v}\|$, the log of the effective viscosity, $\log_{10}(\eta)$, the approximated volume fraction, $\langle\phi\rangle/\phi_0$, and the mixed number of the rheology model, I_m) are represented at $t = 0.5$ and 1.0 seconds. The experimental interface data (the black squares) are plotted on the numerical results. Except for the close-up plots/snapshots, the vertical scale is stretched by a factor of 1.5. . . . 241
- Figure 8.12 Dam break waves over the flat erodible bed (case A-PVC). The first row shows the snapshots and the interface data from the experiments by Spinewine and Zech [12]. The experimental interface data (the black squares) are plotted on the numerical results (where $q = 4$). Except for the close-up plots/snapshots, the vertical scale is stretched by a factor of 1.5. 242
- Figure 8.13 Dam break waves over the erodible bed (case B-Sand). The first row shows the snapshots and the interface data from the experiments by Spinewine and Zech [12]. The experimental interface data (the black squares) are plotted on the numerical results (where $q = 4$). Except for the close-up plots/snapshots, the vertical scale is stretched by a factor of 1.5. 243
- Figure 8.14 Dam break waves over the erodible bed (case C-Sand). The first row shows the snapshots and the interface data from the experiments by Spinewine and Zech [12]. The experimental interface data (the black squares) are plotted on the numerical results. Except for the close-up plots/snapshots, the vertical scale is stretched by a factor of 1.5. . . . 244

- Figure 8.15 Vertical velocity profiles of dam break waves over the flat erodible bed (case A-PVC) in comparison with the experimental data at $t = 0.6$, 1.0, and 1.4 seconds. The local numerical velocity, $x + 0.05u_{num.}$, is identified by the delta markers and the color map. The experimental data, $x + 0.05u_{exp.}$ (shown as the black x markers) are extracted from the work of Spinewine and Capart [13]. Except for the close-up plots, the vertical scale is stretched by a factor of 4. 246
- Figure 8.16 Vertical profiles of the granular concentration, c , and sediment transport intensity, cu , of case A-PVC at $t = 0.6$ seconds (on the left and right graphs, respectively). The numerical results of the multi-resolution model ($q = 4$) are compared with the experimental measurements by Spinewine and Capart [13] (plotted as the delta and the black x markers, respectively). The vertical scale is stretched by a factor of 1.5. 247
- Figure 8.17 Flow evolution and the eroded region, $i \in \Omega_{ed}$, of case A, B, and C, at $t = 1.25$ s, simulated by the multi-resolution MPS model ($q = 4$) compared with the experimental snapshots and interface data (the black squares) from the work of Spinewine and Zech [12]. The vertical scale is stretched by a factor of 5.0. 248
- Figure 8.18 Temporal evolution of A_e , $x_c A_e$, and x_f of cases A-Sand, A-PVC, B-Sand, and D-Sand with the multi-resolution MPS model ($q = 4$) compared with the experimental profiles (extracted from the interface data reported by Spinewine and Zech [12]). A_e and $x_c A_e$ are normalized by the corresponding reference values of case A-Sand (denoted as $(A_e)_{exp.:A-Sand}^f$ and $(x_c A_e)_{exp.:A-Sand}^f$, respectively). 249
- Figure 8.19 Flow evolution and the detected eroded region, $i \in \Omega_{ed}$, for case A-sand with the single-resolution ($q = 1$) and multi-resolution ($q = 2, 4$) MPS models compared with the experimental interface data (the black squares) from [12]. Except for the close-up plots, the vertical scale is stretched by a factor of 5.0. 251
- Figure 8.20 Flow evolution and the detected eroded region, $i \in \Omega_{ed}$, for case A-PVC with the single-resolution ($q = 1$) and multi-resolution ($q = 2, 4$) MPS models compared with the experimental interface data (the black squares) from [12]. Except for the close-up plots, the vertical scale is stretched by a factor of 5.0. 252

Figure 8.21	Temporal evolution of the eroded area, A_e , the first moment of the eroded area, $x_c A_e$, and the wavefront position, x_f , with the single-resolution ($q = 1$) and multi-resolution ($q = 2, 4$) MPS models for case A with sand and PVC compared with the experimental measurements by Spinewine and Zech [12].	253
Figure 8.22	The global kinetic energy of the mixture particles ($E_k = 0.5 \sum \rho_{0i} l_{0i}^2 \ \mathbf{v}\ _i^2$ for $\forall i \in \Omega_m$) with the single-resolution ($q = 1$) and multi-resolution ($q = 2, 4$) MPS models for case A with sand and PVC.	253

LIST OF SYMBOLS AND ABBREVIATIONS

α	A constant coefficient for the particle collision technique
β	A constant coefficient for free-surface detection
δ	The non-dimensional coefficient of the diffusive term
η	The dynamic viscosity
γ	The shear rate
μ	The friction coefficient
ν	The kinetic viscosity
ν_t	The eddy viscosity
Ω	Computational domains
ϕ	The volume fraction of the solid phase
ρ	Fluid density
ρ_g	The true density of the solid grains
$\boldsymbol{\tau}$	The shear force tensor
θ	The internal friction angle
a	A constant material parameter in the visco-inertial rheology model
A	A dimensionless constant in the particle shifting equation
A_e	The eroded area
b	A constant material parameter in the visco-inertial rheology model
\mathbb{B}	Boundary particles
B_0	The bulk modulus of the equation of state
\mathbf{C}	Particle concentration in the particle shifting equation
\mathbf{C}	The correction matrix
C_{CFL}	The Courant–Friedrichs–Lewy stability condition coefficient
c_0	Speed of sound
C_v	The viscosity condition coefficient
d	The number of space dimensions
D	The diffusive term in the continuity equation

D^m	The modified diffusive term in the continuity equation
d_g	The mean diameter of the solid grains
\mathbf{e}	The unit vector of the inter-particle distance
\mathbf{E}	The strain rate tensor
\mathbb{E}	External particles
E_k	The kinetic energy
E_m	The mechanical energy
E_p	The potential energy
f	An arbitrary scalar or vector function
\mathbf{F}	Body forces
\mathbb{F}	Free-surface particles
\mathbf{g}	The gravitational force
h	The smoothing length in Smoothed Particle Hydrodynamics
i	A target particle in the approximation operators
I	The inertial number of the rheology model
\mathbb{I}	Internal particles
I_m	The mixed number of the rheology model
I_v	The viscous number of the rheology model
II_E	The magnitude of the strain rate tensor
j	neighbor particle
k	The coefficient of the kernel function
l_0, dp	The initial particle distance
L_2	The normalized root-mean-square error
m	The particle mass
Ma	Mach number
n	Particle number density
\mathbf{n}	The normal vector to the free surface
N	Number of neighbor particles
\mathbf{N}	The unit normal vector to the free surface
n_0	The normalization factor

p	Pressure
$p_{eff.}$	The effective pressure
p_{max}	The maximum pressure in the particle collision technique
p_{min}	The minimum pressure in the particle collision technique
q	The particle size ratio in the multi-resolution method
R	Spatial resolution
\mathbf{r}	The position vector
R_1	The search region 1 in the particle shifting technique
R_2	The search region 2 in the particle shifting technique
r_e	The smoothing length in MPS
r_{ij}	The inter-particle distance
St	The Stokes number
t	Time
T	Non-dimensional time
\mathbf{T}	The total stress tensor
u	The thermal energy
\mathbf{v}	Velocity vector
V	Volume
W	Kernel function
\mathbb{X}	Expanded particles
x_c	The geometric center of the eroded area
x_f	The wavefront position
BEM	Boundary Element Method
CFL	Courant Friedrichs Lewy
CPS	Corrected Particle Shifting
CPU	Central Processing Unit
DEM	Discrete Element Method
DPC	Dynamic Particle Collision
EOS	Equation Of State
EWCMPS	Enhanced Weakly Compressible Moving Particle Semi-implicit

FDM	Finite Difference Method
FVM	Finite Volume Method
GPU	Graphics Processing Unit
GVF	Generalized Visco-plastic Fluid
ISPH	Incompressible Smoothed Particle Hydrodynamics
LES	Large Eddy Simulation
MPM	Material Point Method
MPS	Moving Particle Semi-implicit
OPS	Optimized Particle Shifting
PC	Particle Collision
PPE	Pressure Poisson Equation
PS	Particle Shifting
PVC	Polyvinyl Chloride
SPH	Smoothed Particle Hydrodynamics
SPS	Sub-Particle Scale
VOF	Volume Of Fraction
WCMPs	Weakly Compressible Moving Particle Semi-implicit
WCSPH	Weakly Compressible Smoothed Particle Hydrodynamics

CHAPTER 1 INTRODUCTION

1.1 Background and motivation

Highly dynamic free-surface flows, granular (sediment) flows, and their interactions are ubiquitous in various hydro-environmental, geotechnical, and engineering processes. Examples include fluvial and coastal flows, sediment dynamics, flash floods, debris flows, sub-aerial and submerged landslides, and water and tailings dam failure. The socio-economic impact of such phenomena can be devastating as they can threaten human life, the environment, and infrastructures. For example, the 2016 landslide in Alberta destroyed Cecil Lake road (Figure 1.1-(a)), and the 1996 dam-failure of Lake Ha!Ha! in Quebec due to a severe rain-storm caused significant sediment erosion upstream and downstream of the failed earthfill dyke (Figure 1.1-(b)) [1]. The 2014 tailings dam breach at the Mount Polley Mine in British Columbia released eight million cubic meters of pollution into Polley Lake, Hazeltine Creek, and Quesnel Lake [14]. The 2017 flooding events in Quebec inundated more than 5,000 homes with \$223 million property damages [15]. Climate changes and immoderate human activities have further intensified their environmental impacts. Understanding the processes and mechanisms associated with these highly dynamic systems is crucial for many engineering designs and the prevention and mitigation of related risks. Granular materials (macroscopic small particles, e.g., gravel and sand) and the ambient fluids (water) (Figure 1.2-c) are the two main components whose interactions create a complex and hard-to-predict system.

Such multiphysics problems, including rapid flows of fluid and granular materials, demonstrate complex nonlinear mechanical behaviors challenging their predictions. Highly-dynamic fluid problems consist of breaking waves, fluid sloshing, and impact events characterized by high velocity, high-pressure gradients, and large interfacial deformations. The granular phase manifests dynamic fluid- and solid-like behaviors driven by fluid flows and body forces (like gravity). The main characteristic of granular flows is the simultaneous presence of quasi-static (solid), dense-flow (liquid), and kinetic (suspended) regimes [16] (Figure 1.2). The granular phase transitions between these flow states concerning the flow and material properties. The inertia, viscosity, and pore pressure of the fluid phase play role in the mechanical behavior of the granular phase [17]. Particularly, in rapid flows, the mixture of solid grains and pore water (or simply the mixture phase) experiences dilatation and compaction that change flow evolution.

Understanding the underlying physics of highly dynamic fluid and granular flows is essential for predicting and mitigating the related environmental hazards [1]. Engineers employ

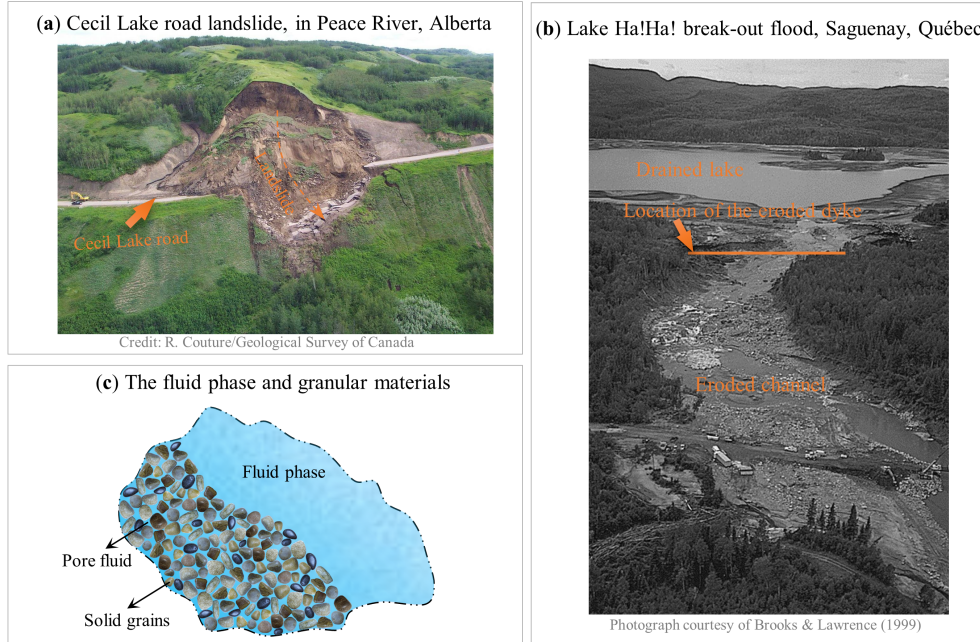


Figure 1.1 Examples of granular dynamics in hydro-environmental problems: (a) Cecil Lake road landslide in Alberta 2016 (the inset photo is taken from the Geological Survey of Canada) and (b) dam failure in Quebec, 1999 (the inset photo is taken from Brooks & Lawrence [1]). (c): The co-presence of water and sediment in such phenomena.

experimental, theoretical, and numerical approaches to provide insights into the mechanical and flow evolution of such problems. Experiments require highly sensitive measurement instruments and are limited to laboratory size test cases [18,19]. Theoretical studies use simplifying assumptions based on empirical shear stress functions, and thus, can only provide rough estimation of flow evolution [13,18]. On the other hand, with the current advancement of computing resources and algorithms, computational methods have proven to be practical alternatives for studying free-surface and immersed granular flows in various hydrodynamic conditions [20].

Numerical methods have been widely developed for simulating rapid free-surface and immersed granular flows. While discrete-based methods (e.g., the Discrete Element Method [21]) provide in-depth analysis of solid grains' microscopic behavior, they are computationally expensive for dealing with engineering problems that involve a large volume of materials. On the other hand, continuum-based numerical methods homogenize the solid grains or the mixture of solid and fluid into bulk properties at the macroscopic level (Figure 1.3-(a) & (b)). Thus, they are introduced as scalable models and computationally affordable for large-scale modeling. Mesh-based continuum methods, despite their remarkable advancements in simulating interfacial flows, due to their mesh dependency require particular treatments to

deal with highly dynamic flows (e.g., see [22, 23]). In contrast, mesh-free continuum-based methods, or simply particle methods (such as the Material Point Method (MPM) [24], the Moving Particle Semi-implicit (MPS) method [25], and the Smoothed Particles Hydrodynamics (SPH) method [26]), discretize the fluid domain into moving particles carrying flow and material properties (Figure 1.3-(c)). Such particle methods, owing to their Lagrangian nature, have become powerful computational tools for studying free-surface flows and granular dynamics in hydro-environmental and geotechnical studies [27–29].

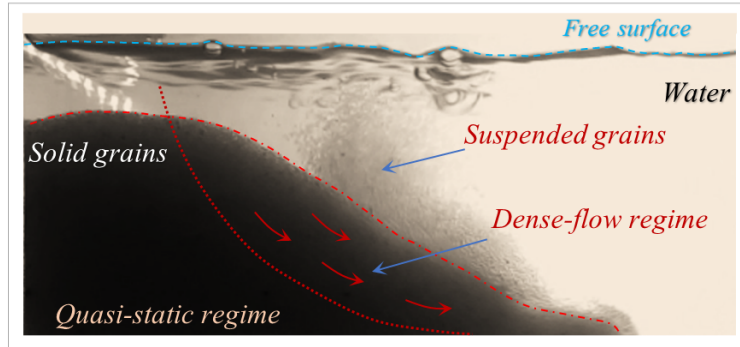


Figure 1.2 Different flow regimes of the immersed granular collapse

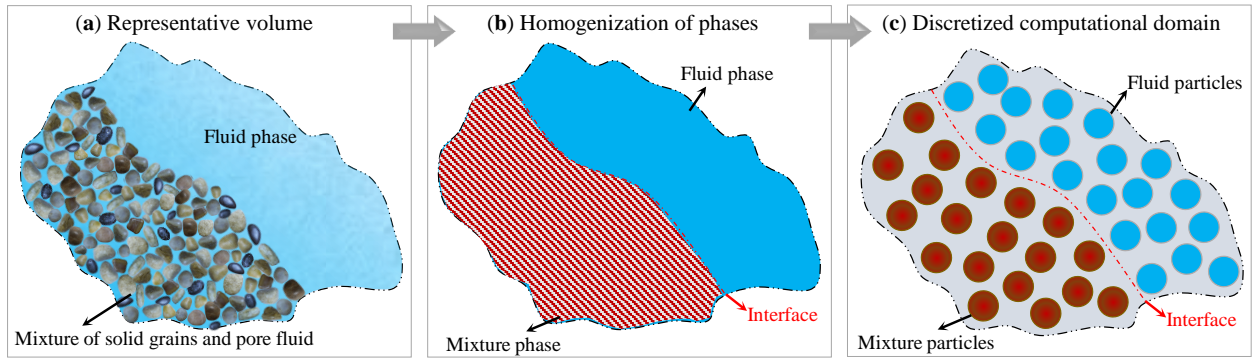


Figure 1.3 (a) Representative volume of the fluid and submerged solid grains, (b) Homogenization of phase, and (c) the discretization of the computational domain into moving particles.

Nevertheless, accurate simulation of the multiphase flows with large free-surface deformations is still challenging for numerical methods. Inconsistent governing equations and discretization errors affect the reliability of the computational tools and thus, surmounting them remain subjects of ongoing investigations. The numerical stability and accuracy of the models require further improvements for predicting the violent interfacial and dense granular flows.

Moreover, the constitutive laws (i.e., the rheology models) predicting the mechanical behavior of the mixture of solid grains and fluid (at the macroscopic level) lack a unified formulation capable of considering the dynamic flow regimes with variable material and flow properties. This doctoral research project aims at developing consistent mesh-free particle methods for accurate simulation of highly dynamic free-surface and immersed granular flows. The numerical model solves Lagrangian governing equations based on the SPH and MPS formulations. We introduce several enhancement techniques concerning the stability and accuracy of the particle methods for dealing with large interfacial flow deformations. Moreover, we propose a generalized rheology model and a multi-resolution particle method to investigate the mechanical behavior of sediment dynamics driven by gravity and rapid fluid flows. Overall, this doctoral research project contributes to the advancement of knowledge for the in-depth analysis of complex and highly dynamic fluid and dense granular flows over a broad range of conditions.

1.2 Dissertation outline

We have organized this dissertation in nine chapters including the introduction. In Chapter 2, we present a critical literature review on particle methods and immersed granular flow modeling. In Chapter 3, we discuss the research questions, identify the main research objectives, and summarize the research contributions. We have addressed the main objectives in five research articles that constitute Chapters 4, 5, 6, 7, and 8. At the end, we discuss the general achievements and present the concluding remarks of this research project in Chapters 9 and 10.

CHAPTER 2 LITERATURE REVIEW

2.1 Mesh-free particle methods

Eulerian mesh-based and Lagrangian mesh-free methods are two conceptually distinct approaches adopted for the continuum-based modeling of fluid dynamics. Mesh-based methods (e.g., the Finite Volume Method (FVM) [30], the Finite Difference Method (FDM) [31], and the Volume of Fraction (VOF) method [32]) construct a computational grid system for discretizing the fluid domain. In such numerical methods, the governing equations solve the convection of flow and material properties passing through the mesh faces while the spatial position of the calculation nodes remains semi or fully fixed. The conventional mesh-based methods struggle to simulate the complex fragmentation of interfacial flows. Thus, for handling extreme flow deformations, mesh-based methods should be further developed with special implementations regarding their grid system, e.g., the moving-mesh method [33], and the reference map technique [22]. On the other hand, mesh-free methods (e.g., the Material Point Method (MPM) [24], the Moving Particle Semi-implicit (MPS) method [25], and the Smoothed Particles Hydrodynamics (SPH) method [26]) discretize the fluid domain into moving nodes (i.e., particles) that carry the flow and material properties. The movements of particles, based on the Lagrangian-form governing equations, introduces such methods as powerful computational tools for capturing highly dynamic free-surface flows involved in complex hydro-environmental system [34, 35]. Due to their Lagrangian characteristic, SPH and MPS have attracted a great deal of attention for numerical modeling of free-surface and multiphase flows [11, 36, 37].

SPH and MPS are the two most popular and well-developed particle methods for various scientific and engineering studies (e.g., in coastal and ocean engineering [27, 38], nuclear engineering [39], and industrial applications [40]). Gingold and Monaghan [26] and Koshizuka and Oak [25] proposed the original SPH and MPS formulations, respectively. Both particle methods discretize the Lagrangian form of the Navier-Stokes equations into moving particles without any connectivity [34, 35]. The particle approximation operators, $\langle \cdot \rangle_i$, employ a compact weighting function (W , so-called the kernel) to smooth the flow and material properties, e.g., f , over a target particle, i , interacting with its neighboring particles, j , inside the finite smoothing radius, r_e (where the inter-particle distance, $r_{ij} = \|\mathbf{r}_{ij} = (\mathbf{r}_j - \mathbf{r}_i)\| \leq r_e$, N is the number of neighbor particles, and \mathbf{r}_i is the position of particle i) (Figure 2.1-a). The kernel is a positive function of the smoothing length and the inter-particle distance, i.e., $W_{ij} = W(r_{ij}, r_e)$ and $W_{ij} \geq 0$. The particles interact with each other through the discretized

form of the governing equations (including the pressure and shear forces). The particle interaction is conservative if the force, \mathbf{F} , is anti-symmetric with respect to i and j indexes, i.e., if $\mathbf{F}_{ij} = -\mathbf{F}_{ji}$; otherwise, the particle interaction is non-conservative based on Newton's third law (excluding body and dissipative forces of the system) (Figure 2.1-b).

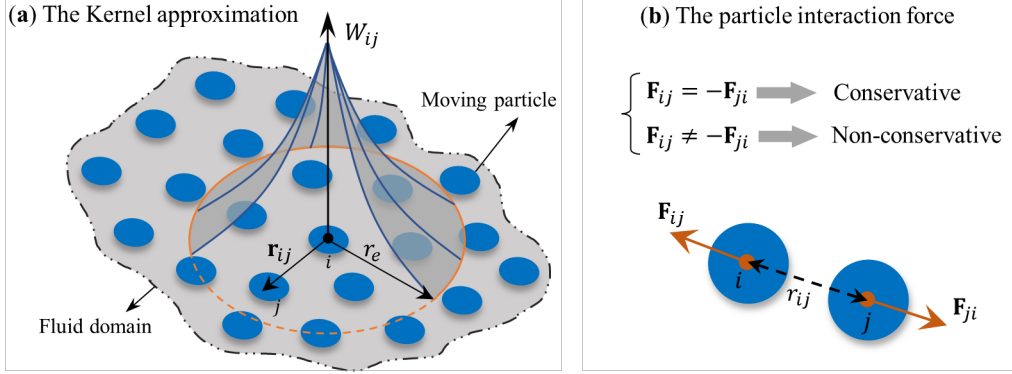


Figure 2.1 (a) The kernel approximation over the computational fluid domain, and (b) the particle interaction force, \mathbf{F} .

SPH and MPS, as two sister methods, while differ in their basic approximation techniques yet share similar solution algorithms and numerical issues. Table 2.1 compares the kernel summation, the particle approximation and gradient operators of an arbitrary function, f , with the standard SPH and MPS formulations. SPH retains the fluid density, ρ , in its approximation operators; the MPS formulations are independent of the density substituted by the non-dimensional particle number density, n . For multiphase flows, the standard SPH formulations require special treatments at the interface for treating the density-discontinuity [36]. MPS by using the non-dimensional particle number density can be a natural choice for resolving the density-discontinuity issues of the interfacial flows [41]. The kernel of SPH (W^{SPH}) is a dimensional term $((\rho/m)^{-1}$ where m is the particle mass) which should respect the unity condition [35, 42]; nevertheless, the kernel of MPS (W^{MPS}) is a non-dimensional smoothing function without the need for respecting the unity condition as a constant normalization factor (n_0) appears in its operators [34, 43] (Table 2.1). Moreover, SPH derivatives include the gradients of kernel, i.e., $\nabla_i W_{ij}^{SPH} = (\mathbf{r}_{ji}/r_{ij})(\partial W_{ij}^{SPH}/\partial r_{ij})$ where $\partial W_{ij}^{SPH}/\partial r_{ij} \leq 0$ [35, 42]; MPS directly uses the non-dimensional kernel within its approximation terms. Accordingly, MPS (as a kernel-derivative-free approach) does not suffer from the numerical instability associated with the kernel derivative that exists in the force terms of the standard SPH formulations [44, 45]. d is the space dimension equal to 1, 2, and 3 for the one-, two-, and three-dimensional problems (i.e., for 1D, 2D, and 3D, respectively).

Table 2.1 The kernel summation (for the density, ρ , and the particle number density, n , calculations), the particle approximation and gradient operators of an arbitrary function, f , with the standard SPH and MPS formulations.

Operator	SPH	MPS
The kernel summation:	$\rho_i = \sum_j^N m_j W_{ij}^{SPH}$	$n_i = \sum_{i \neq j}^N W_{ij}^{MPS}$
The particle approximation, $\langle f \rangle_i =$	$\sum_j^N \frac{m_j}{\rho_j} f_j W_{ij}^{SPH}$	$\frac{1}{n_0} \sum_{i \neq j}^N f_j W_{ij}^{MPS}$
The gradient operator, $\langle \nabla f \rangle_i =$	$\sum_j^N \frac{m_j}{\rho_j} f_j \nabla_i W_{ij}^{SPH}$	$\frac{d}{n_0} \sum_{i \neq j}^N \frac{f_j - f_i}{r_{ij}^2} \mathbf{r}_{ij} W_{ij}^{MPS}$

The original SPH method [26] considers the fluid flow as a weakly-compressible and barotropic phase, and therefore, solves the equation of state (EOS) to update the thermodynamic pressure. The original MPS method [25, 46] treats the fluid flow as a fully incompressible phase, keeping the density of particles constant by solving the Pressure Poisson Equation Equation (PPE). While the weakly-compressible SPH (WC-SPH) methods solve the time integration algorithm explicitly, the fully-incompressible particle methods, including SPH and MPS, have to solve PPE implicitly. Numerically solving the PPE matrix is one of the most time-consuming parts of the incompressible models. On the other hand, solving the equation of state is straight forward and significantly reduces the computational costs. Shakibaeinia and Jin [47] introduced the weakly-compressible version of the MPS method (WC-MPS) for free-surface flows by proposing the equation of state as a function of the particle number density and the normalization factor. The main focus of the current research project is to develop and validate enhancement techniques, compatible with both the WC-MPS and WC-SPH methods, for highly dynamic free-surface and immersed granular flows.

In the standard weakly-compressible SPH and MPS methods, the kernel summation operator estimates the local fluid density and the particle number density, respectively (Table 2.1). The accuracy of this equation greatly depends on the type of the kernel function, the kernel truncation issues at the boundaries, and the particle distribution. Particularly, the kernel summation operator act poorly at the vicinity of the free surface where the kernel support is incomplete causing numerical instability and non-uniform particle distributions [48]. Furthermore, such models neglect the velocity divergence (i.e., they consider $\nabla \cdot \mathbf{v} = 0$), and thus, the conservation properties of the discrete system (considering the energy equation [49]). To surmount this inaccuracy in the standard SPH formulation, Bonet and Lok [48] employed the continuity equation as an alternative model for the density calculation. Including the

continuity equation into the governing equations provides the model the opportunity to be variationally consistent, assign initial density and pressure fields, and improve the pressure estimations close to the boundaries [42, 48, 49].

SPH and MPS suffer from several numerical issues associated with the Lagrangian movement of the particles and the discretization errors (i.e., the particle approximation errors). Particularly, in the WC-SPH methods, the discretization errors and numerical (false) diffusion affect the density estimation manifested as high-frequency pressure fluctuations (i.e., pressure noises). Moreover, the long-term stability and accuracy of such methods depend on the conservation properties of the discrete system and uniformity of particle distribution [49, 50]. Over the past years, SPH and MPS have gone through significant enhancements concerning their numerical accuracy, stability, and efficiency. The developments include adopting high-order derivatives [51, 52], implementing artificial repulsive force and diffusive terms into the governing equations [53, 54], and imposing uniform particle distribution [55, 56]. We review the numerical solutions and their limitations as follows:

- *High-order approximation operators*

In SPH and MPS, the numerical accuracy of the approximation operators (i.e., the gradient, divergence, and Laplacian operators) depends on the uniformity of the particle distributions, as well as, the order of accuracy of the derivatives. High-order approximation operators are introduced in the discrete system of particles to increase the convergence order and numerical accuracy of the derivatives. Such high-order formulations can also improve the numerical stability and smoothness of the pressure field [51]. Considering the Taylor expansion series, different corrective matrices (also called the renormalization tensors) for the first- and second-order numerical accuracy are derived [52, 57, 58]. Oger et al. [52] proposed a high-order convergence SPH by introducing the correction matrix for the continuity and momentum equations. Khayyer and Gotoh [57] proposed a modified multi-term source with the higher-order operator for the Poisson’s pressure equation. Khayyer and Gotoh [57] implemented a corrective matrix into the standard pressure gradient operator similar to the renormalization matrix Oger et al. [52] employed to apply higher-order calculations. One should note that inconsistent implementation of the high-order gradient and divergence operators ignores the conservative properties of the particle interactions (as they are not anti-symmetric with respect to the particle indexes, see Figure 2.1 and Table 2.1). This feature of high-order terms is not in favor of the stability of weakly-compressible SPH and MPS methods [49]. Gotoh and Khayyer [59] pointed out that the implementation of particle stabilization techniques is essential for the models with the corrective matrix. Duan et al. [60] also confirmed that

even with implementing high-order derivatives, stabilizing techniques are still required for ensuring numerical stability of the simulations.

- *Artificial diffusive terms*

High-frequency and unphysical pressure fluctuations affect the numerical stability and accuracy of the WC-SPH methods [54]. To eliminate pressure noises, artificial viscosity and density diffusion terms are proposed. Gingold and Monaghan [61] introduced the artificial viscosity term into the pressure gradient term of the momentum equation. This numerical correction has shown to be an effective technique for improving the pressure oscillations (e.g., see [3, 62–64]). Using the same concept, Molteni and Colagrossi [54] proposed the standard density diffusion term as the Laplacian of the density added to the right-hand side of the continuity equation. This approach (so-called δ -SPH) leads to robust numerical results for simulation of the free-surface flows [65]. However, the standard form of the density diffusive term diverges the density field (from the hydrostatic solution) near the boundaries with the kernel truncation [66, 67]. Antuono et al. [66] proposed a convergent form of this term by the Taylor expansion series and a corrective interpolator for the kernel gradient. Antuono et al. [65] compared different numerical diffusive terms in the WC-SPH method. Meringolo et al. [68] employed the sub-particle scale turbulence closure to determine the coefficients of viscosity and density diffusive terms dynamically according to the local and instantaneous flow conditions. Fourtakas et al. [69] introduced a new form of the density diffusive term by substituting the dynamic density with the total density; however, their formulation violates the conservation of mass considering that it is not an anti-symmetric term [65].

For multiphase flow problems, the divergence issue of the density diffusion terms requires adopting special boundary treatments at the interface. Sun et al. [70] and Hammani et al. [71] employed the convergent diffusive term for the multiphase flows restricting its application to the fluid particles of the same phase. Zheng and Chen [72] substituted the oscillation of density increment for the density variable in the multiphase SPH model. In such developed formulations of WC-SPH methods, the corrective matrix and the first-order density gradient operators are also limited to the same phase particles. In this case, although the higher-order gradient formulation reduces the associated errors at the interface, this solution remains incompetent for highly dynamic interfacial flows.

- *Particle regularization techniques*

Another common numerical issue of the standard SPH and MPS methods is the unphysical inter-particle penetrations (so-called particle clustering and tensile instability) [44]. Such

numerical instabilities originate from the Lagrangian equation, which moves the particles along the streamlines [50, 52]. Irregular positions of particles (i.e., non-isotropic particle distribution) increase the approximation errors leading to numerical instabilities and inaccurate estimations of flows. Also, in the standard SPH formulation, the kernel gradient reduces to zero at its center, and thus underestimates the magnitude of the inter-particle repulsive force [44, 45]. To improve the uniformity of the particles, different particle regularization techniques are developed in SPH and MPS. In the context of the SPH method, Xu et al. [55] proposed the Particle Shifting (PS) method, which shifts particles to the area with less particle concentration. Lind et al. [50] and Skillen et al. [73] adapted PS to free-surface flows involving body-water impacts. Khayyer et al. [74] optimized the PS formulation by canceling its normal component at the free surface. On another approach, the pair-wise Particle Collision (PC) techniques, based on the momentum transfer between a pair of colliding physical solid or gas particles, are developed. Lee et al. [56] formulated the PC within the context of the fully-incompressible MPS method for free-surface flows. Shakibaeinia and Jin [75] extended the PC formulation for multiphase flows within the context of the weakly-compressible MPS method.

- *Multi-resolution particle methods*

To further improve efficiency and accuracy, multi-resolution particle methods are introduced as desirable approaches for capturing more flow/solid deformations over a refined computational domain/element. In general, they aim at eliminating the computational costs of a fully refined single-resolution simulation. Several SPH and MPS methods pair their multi-resolution formulations with dynamic particle splitting and merging algorithms [76–78], adaptive particle refinement techniques [79–81], and overlapping methods [82, 83], to simulate complex flow problems. In a different approach, Sun et al. [84] have proposed a volume adaptive scheme to limit particle volume variations of compressible multiphase flows. Applications of these multi-resolution particle methods include wave body interactions, high Reynolds number flows past a bluff body, and rapid multiphase flows (e.g., see [76], [85], and [86]). Moreover, multi-resolution SPH and MPS approaches are extended for modeling of fluid-structure interactions where the higher spatial resolution of the structure elements allows more accurate deformations [70, 87–89]. In such developed models, it is imperative to implement conservative approximation operators in a consistent manner concerning particle interactions with different sizes and mechanical properties. In the standard MPS formulation, the approximation terms consider an identical spatial resolution for the entire domain. In other words, the discrete equations ignore the particle size and the smoothing length [43].

This feature of the MPS operators should be noted for deriving consistent and conservative multi-resolution models.

2.2 Immersed granular flows

Over the past decades, many experimental and theoretical studies have focused on presenting physical and mathematical explanations for granular flows' mechanical behavior (e.g., [18, 19, 90–93]). Both approaches have been employed for analyzing the mechanism of granular avalanches and slides, e.g., [10, 19, 94, 95], and intense bed-load transports [12, 13, 18]. The granular phase, under gravity and fluid flows, undergoes different flow states identified as quasi-static (solid or viscous), dense-flow (liquid), and free-fall (suspended) regimes [16, 17]. With the presence of ambient fluid (like water), the situation becomes more complex as the mechanical and flow properties of the interstitial fluid influence on the granular flow behavior [17]. The empirical models (obtained from the experimental and theoretical investigations) aim at capturing such complex granular dynamics. However, the experiments rely on the accuracy of the measurement instruments and are limited to laboratory-scale cases. Also, the theoretical solutions adopt simplifying assumptions (like the steady flow conditions and the shallow-water equations) and can only provide an overall estimation of the granular flow [18]. As another alternative, numerical methods, in the discrete and continuum-based formats, have been widely developed for investigating the underlying physics of granular flows. Discrete-based methods (e.g., the Discrete Element Method [21]) deal with the individual grains subjected to macroscopic and microscopic forces (e.g., [96, 97]). Although they are effective methods for in-depth analysis of granular mechanical behavior, computational costs associated with microscopic simulations of solid particles limit their application to small-scale problems [20]. On the other hand, the continuum-based methods homogenize the granular phase into macroscopic properties. The scalability of the continuum-based methods makes them computationally less expensive and appropriate for large-scale simulations involved in engineering studies (e.g., [20, 33]).

In the continuum-based models of immersed granular flows, the rheology model estimates the mechanical properties of fluid and solid grains. The numerical method implements the rheology formulation within the governing equations as the single- or two-phase continuum models [16, 17]. The single-phase model treats the solid grains and ambient fluid as a single mixture phase; the mixture interacts with the fluid phase directly through one set of governing equations. The two-phase model simulates the relative motion of the fluid and the homogenized solid phase (as two separate and continuous fluid phases), solving two sets of governing equations coupled by the inter-phase forces (i.e., the buoyant, drag, and non-drag

forces) [17, 95]. Therefore, unlike the single-phase model, the two-phase model includes the effects of volume fraction variations in the constitutive formulations [20, 95, 98]. Nevertheless, in the two-phase model, solving the computational domain over two sets of calculation points is computationally expensive (particularly for three-dimensional simulations); also, the phases' mechanical properties depend on empirical equations used for estimating the inter-phase forces.

Many empirical and numerical studies have been devoted to introducing general and reliable constitutive laws for different regimes of the granular flows [17, 99]. For the immersed condition, different non-Newtonian models are developed (e.g., see [92, 93, 100, 101]). Guazzelli and Pouliquen [17] presented a comprehensive review of the rheology of concentrated granular suspensions. Among them, the local $\mu(I)$ rheology (proposed by Jop et al. [99] and Forterre and Pouliquen [102]) has drawn attention for the dry and submerged cases (e.g., [96, 103, 104]). Considering low Stokes immersed granular flows, Boyer et al. [101] conducted a series of experiments to derive a unified rheology equation. Amarsid et al. [100] with some dimensional analysis and simulating the inertial and viscous regimes of the mixture introduced a unified rheology model for the dry and immersed granular flows. Baumgarten and Kamrin [20] combined the former models (i.e., the models by [101] and [100]) in a single formulation to capture different states of the dense granular flows using a two-continuum mixture model. It should be highlighted that in the adopted rheology models, the inertial number, I , is a pre-defined function according to the expected flow regime. Therefore, the standard $\mu(I)$ models are not unified for simulating viscous, inertial, and free-fall regimes of the granular flows. Particularly, for the immersed and dense granular flows, both inertial and viscous regimes may control the mechanical behavior of the flow; thus, predicting the underlying physics of the mixture would be more challenging [100].

In the context of SPH and MPS methods, the adopted constitutive laws include the Bingham plastic formulation [105–107], the Herschel-Bulkley model [107, 108], the Herschel-Bulkley-Papanastasiou model [109], the regularized $\mu(I)$ [110–113], and the elastic-viscoplastic model [114]. Moreover, to improve the prediction of the flow threshold of the mixture, some methods have employed an additional yielding threshold based on Shields' erosion criterion [106, 115, 116]. Particularly, in the standard WC-MPS framework, Shakibaeinia and Jin [108] simulated the mobile-bed dam-break including the non-linear behavior of the granular material by the Generalized Visco-plastic Fluid (GVF) model (proposed by Chen et al. [117]). Nodoushan and Shakibaeinia [118] employed the regularized form of the local $\mu(I)$ rheology to model the submerged and dry granular collapses. Further, Tajnesaie and Shakibaeinia [112] developed the same model to simulate the granular landslide in a two-dimensional configuration and compared the results with the Heschel-Bulkley model. Recently, Ke et al. [119] investigated

the role of the $\mu(I)$ rheology for the dry granular slide and dam-break via the standard WC-MPS method.

An accurate and dynamic estimation of effective pressure is essential for detecting the yielded and non-yielded flow regions. SPH and MPS methods (e.g., [105, 113, 116, 120]) assume the lithostatic condition for predicting the pore-water pressure within the mixture phase. Ghaïtanellis et al. [114] appended an additional term into the constitutive model to calculate the effective pressure independently (via solving the Laplacian of the field accompanied by the boundary conditions of the model). In general, these approaches involve the free-surface and interface detection which limits the capability of the particle methods for dealing with highly dynamic granular flows. In another approach, Fourtakas and Rogers [109] and Zubeldia et al. [115] employed a modified equation of state (EOS) for their WC-SPH model by using the density of the saturated sediment to estimate the pore-water pressure. However, their models consider different reference pressures within the EOS (for the total pressure and the pore-water pressure); thus, the pressure oscillations due to the slight compressibility of the fluid model affect the estimation of the viscosity of the submerged granular flows [114]. Moreover, in standard particle methods, the unphysical pressure noises and the particle clustering can significantly affect the accuracy of the granular modeling. Resolving these numerical issues put great emphasis on adopting the particle regularization techniques and the artificial diffusive terms for ensuring the stability and accuracy of the numerical simulations.

CHAPTER 3 RESEARCH PROJECT

3.1 Research problems

The previous chapter reviewed the past research works and highlighted the gaps in knowledge and the needs for the research, which define our research questions here. These knowledge gaps are related to numerical aspects of the particle methods and their application for free-surface and granular flows.

3.1.1 Stability and accuracy of particle methods

To study the multiphysics of complex flows, the discrete system of governing equations should respect the mechanical properties of the problem (i.e., the mass and momentum conservation laws). Also, the numerical model should implement high-order approximation operators to improve the accuracy and convergence order of the results. SPH and MPS can not achieve both noting that the high-order derivatives of the Lagrangian equations violate the momentum conservation law. Particularly, the WC-MPS method does not benefit from a conservative system of equations (even without the high-order terms). In this method, the kernel summation operator estimates the particle number density, and the pressure gradient terms ignore the linear momentum conservation in the particle interactions. In addition, the approximated shear force violates the conservation of the angular momentum of the discrete system. The kernel truncation (at the free surface) and the non-conservative pressure and shear forces increase the numerical errors and pressure noises leading to particle clustering and instability affecting the flow accuracy.

Particle stabilization techniques have shown promising outcomes for eliminating unphysical pressure oscillations and improving particle clustering issues. Such numerical developments include artificial diffusion terms (like the density diffusion term) and particle regularization techniques (like the PC and PS methods). Yet, the efficiency and convergence behavior of their implementations are limited to low Reynolds numbers. To simulate highly dynamic free-surface deformations (with fluid-fluid and fluid-solid impacts) and deal with negative pressure fields, the particle stabilization techniques still lack conservative and convergent formulations. The standard form of the density diffusion term causes the divergence of the pressure field close to the boundaries and interfaces. This divergence of density parameter affects the long-term stability of multiphase and violent free-surface flows. Moreover, the effectiveness of PS techniques greatly depends on the accuracy of the free-surface detection algorithm. Without

special boundary treatments, the developed PS techniques struggle to present uniform particle distribution in large flow deformations and where impact events occur. In cases with several impact events and where the potential energy is dominant, the standard form of PS methods alters the system’s potential energy (manifested as unphysical volume expansions in the fluid domain). This numerical anomaly is due to the non-Lagrangian displacement of the particles without respecting the conservative properties of the system. To accurately model rapid free-surface and multiphase flows (particularly with high viscosity and extreme deformations), resolving such numerical inconsistencies is essential.

3.1.2 Granular flow modeling

In the constitutive laws, the rheology model predicts the mechanical behavior of the mixture phase as a function of the material and flow properties. Submerged granular material undergoes dynamic fluid- and solid-like behaviors driven by gravity and ambient fluid flows. The implemented rheology models in particle methods lack a unified formulation for simulating different states (i.e., the viscous, inertial, and suspension regimes) of the immersed granular flows. Also, the yield stress and post-failure terms of the rheology models, as functions of the mixture effective pressure (i.e., the normal stress in the solid phase), are sensitive to the accuracy and smoothness of the estimated pressure field. Thus, unphysical pressure noises can directly affect the shear force estimation. This inaccuracy in particle methods not only threatens the stability of the simulation but also leads to unrealistic granular evolution. In addition, the lithostatic stress (commonly adopted for the effective pressure of the mixture) neglects the dynamics of the interstitial fluid flow in the rheological model. To deal with the large deformation of the sediment continuum, we require a consistent formulation to estimate the effective pressure without the hydrostatic assumption and the interface tracking for the pore-water pressure.

In the continuum-based methods, the macroscopic scale representing the continuum (i.e., the representative elementary volume) must be large enough to contain a sufficient number of solid grains [17, 121]. Otherwise, the numerical element would reach the size of the discrete elements (i.e., the solid grains), and therefore, the continuum assumption of the constitutive law would become invalid. On the other hand, the spatial resolution of the discretized computational domain should be small enough (concerning the characteristic length-scale of the case study) to mathematically represent its vicinity and minimize the numerical approximation errors [114, 122]. Furthermore, to capture highly dynamic and high Reynolds number fluid flows (e.g., the fluid-driven sediment erosion), the numerical solution requires a higher spatial resolution for the fluid phase than that of the mixture. The current contin-

uum particle methods, developed for immersed granular flows, adopt a single particle size for discretizing the entire fluid domain. Considering an identical spatial resolution for both water and mixture particles restricts the capability of the particle methods in simulating large interfacial deformations and minimizing the numerical discretization errors.

3.1.3 Research questions

Accordingly, we summarize the key questions of this research project as follows:

- Q1: How to develop a conservative form of the governing equations for the WC-MPS method?
- Q2: How to enhance stability and accuracy of particle methods for violent free-surface flows?
- Q3: How to model multiphysics of immersed granular flows through a unified rheology model?
- Q4: How to develop a consistent particle method for highly-dynamic sediment transport?

Overall, the identified questions target filling the research gaps in particle methods for simulating accurate flow evolution of highly dynamic free-surface and granular flows. To reduce numerical errors and instability (associated with the non-conservative discrete system, high-frequency pressure noises, and unphysical inter-particle penetrations), particle methods should be enhanced by addressing Q1 and Q2. As for understanding the underlying physics of immersed granular flows, the rheology equation should be generalized to model different flow regimes (Q3). Moreover, to simulate multi-scale fluid-sediment interactions (while respecting the continuum assumption of the constitutive law), developing a multi-resolution approach becomes essential (Q4).

3.2 Research objectives

This research project aims at developing and validating a consistent mesh-free particle method capable of accurate simulation of violent free-surface flows and dynamics of immersed granular flows. It contributes to a longer-term objective of providing the scientific community and engineers with the predictive tools that can help in engineering designs, protecting the environment, and managing the risk associated with the hydro-environmental systems. Based on the four research questions, Q1-Q4, respectively, we identify the specific research objectives as follows:

- O1: Proposing and evaluating conservative forms of the WC-MPS method,
- O2: Developing effective particle stabilization techniques for free-surface flows,

- O3: Elaborating the theoretical foundation and developing a generalized rheology model for immersed granular flows,
- O4: Developing a consistent multi-resolution particle method for immersed granular flows.

3.3 Research originality and contributions

This research project contributes to the advancement of knowledge in different aspects. We propose and validate several new developments to mesh-free particle methods to provide a reliable numerical model for simulating highly dynamic free-surface and immersed granular flows

We represent the original contributions of this research project, corresponding to the four research objectives, in the following sections:

3.3.1 A conservative form of WC-MPS

We develop a novel version of the WC-MPS method considering the conservative properties of the governing equations. We derive new conservative operators for the pressure gradient and the shear stress calculations. The new model employs the continuity equation for updating the particle number density to reduce the kernel truncation errors at the boundaries. The new conservative pressure force implements anti-symmetric particle interactions and acts as an artificial repulsive force between the fluid particles. To conserve the system's global energy, we present the conjugate form of the approximation operator for the velocity divergence term in the new continuity equation. This original conservative WC-MPS method provides a unique and novel platform for studying the numerical accuracy of the simulations and convergence properties of the approximation operators.

3.3.2 Particle stabilization techniques

We propose several enhancement techniques to ensure numerical stability and accuracy of the particle methods. They include developing new artificial density diffusive terms and effective particle regularization algorithms. We develop the particle stabilization techniques by considering the conservative feature of the discrete system. Hereinafter, we denote the conservative WC-MPS method coupled with the particle stabilization techniques as the Enhanced WC-MPS (EWC-MPS) method. A summary of the new developments are listed as follows:

- *WC-MPS with diffusion*

In the context of the conservative WC-MPS method, we propose a novel diffusive term as the Laplacian of the particle number density. We further improve the accuracy of this diffusive term by implementing the convergent form of the Laplacian operator and high-order gradient derivatives (presented as the modified diffusive term). We consider the mass conservation of the system in the derivation of these new diffusive terms and keep their formulations independent of the density variable.

- *Particle regularization techniques*

To improve stability of particle methods, we propose and develop several particle regularization techniques, within the framework of WC-MPS and WC-SPH formulations:

- A corrected particle shifting technique: CPS + PC

We propose a new conservative equation for the PS technique (within the MPS framework) advanced with effective free-surface detection algorithms. We couple the proposed PS method with the standard form of the PC techniques, given rise to a novel hybrid approach (CPS + PC), to improve particle distribution at the free-surface boundary layer.

- Dynamic pair-wise Particle Collision technique: DPC

We propose a new formulation of the PC technique presenting dynamic coefficients for the collision term and adding a dynamic background pressure. We introduce and validate DPC, in SPH and MPS, as a powerful particle regularization technique for dealing with different states of inter-particle penetrations in violent free-surface flows.

- The consistent form of CPS: CPS* + DPC

We advance our CPS by deriving the additional diffusive terms (due to the PS transport-velocity term) to resolve the non-conservative-volume issue of its formulation. Including the diffusive terms into the CPS technique and proposing further developments for the boundary treatment algorithm results in the consistent form of CPS (denoted as CPS*). By coupling CPS* with our novel DPC, CPS* + DPC, we present a robust hybrid particle regularization technique.

3.3.3 A generalized rheology model

We propose a new generalized rheology model for estimating the mechanical properties of the immersed granular flows. The generalized rheology formulation treats the fluid (here, water)

and mixture (i.e., the mixture of water and solid granules) phases as Newtonian and non-Newtonian flows, respectively. For the fluid phase, the model includes a turbulence model (based on the Sub-Particle Scale (SPS) formulation in particle methods) and the effects of the solid phase volume fraction. For the mixture phase, we adopt the visco-inertial rheology model by Baumgarten and Kamrin [20] that can capture the dominant regimes of dense granular flows through its post-failure terms. To resolve the singularity issue of this friction equation (when the strain rate magnitude is strictly zero), we derive a new regularized form of the dynamic viscosity equation (denoted as the regularized visco-inertial rheology model). Furthermore, we develop a novel and consistent equation to calculate the effective pressure dynamically based on the mass conservation law of the pore-water phase (within the mixture phase). The consistent effective pressure incorporates the flow dynamics of the mixture within the rheology model by estimating the true density of the pore-water phase without any interface detection.

3.3.4 A multi-resolution particle method for granular dynamics

As a part of this research project, we propose a novel multi-resolution particle method for fluid-driven granular dynamics. The main idea behind the multi-resolution model for granular flows is to respect the continuum assumption of the rheology model while reducing the size of the fluid/water particles. To that end, we derive new approximation operators respecting the conservative properties of the discrete system based on the conservative WC-MPS formulation (according to the objective O1). To ensure numerical stability and avoid unphysical oscillations, we adapt the modified diffusive term and the DPC technique to the newly developed multi-resolution framework (i.e., following the objective O2). Further, we couple the developed method with the generalized rheology model supplied with a suspension equation for rapid and immersed granular flows (i.e., following the objective O3). We employ the validated numerical method to investigate the importance of multi-scale multiphase water-sediment interactions in rapid fluid-driven problems.

3.4 Publications

This research project has directly contributed to five journal articles included as chapters of the thesis. In addition, it has led to the publication of two conference papers and one journal article. These articles are listed below:

- **Article 1:** "An enhanced weakly-compressible MPS method for free-surface flows" [123]
Authors: Mojtaba Jandaghian and Ahmad Shakibaenia

Journal: Computer Methods in Applied Mechanics and Engineering

Publication date: March 2020

Authorship statement: The first author proposed and developed the conservative formulations and the stabilization techniques. He implemented the new methods within the 2D serial code and simulated the benchmark cases. He validated and analyzed the numerical results, prepared the figures, wrote and revised the original draft, responded to the comments, and revised the manuscript in the review process of the article.

- **Article 2:** "Enhanced weakly-compressible MPS method for violent free-surface flows: Role of particle regularization techniques" [124]

Authors: Mojtaba Jandaghian, Abdelkader Krimi, Amir Reza Zarrati, and Ahmad Shakibaeinia

Journal: Journal of Computational Physics

Publication date: June 2021

Authorship statement: The first author proposed the new methodology including the new particle regularization techniques. He developed a GPU-accelerated code (for the 3D modeling) and implemented the new techniques. He conducted the simulations, validated and analyzed the numerical results, prepared the graphs and figures, wrote and revised the original draft. In the review process of the article, he responded to the comments and revised the manuscript. The second co-author provided general comments on the quality of the figures and participated in the related discussions. The third co-author provided detailed comments and revised the original draft of the article.

- **Article 3:** "Stability and accuracy of the weakly-compressible SPH with particle regularization techniques" [125]

Authors: Mojtaba Jandaghian, Herman Musumari Siaben, and Ahmad Shakibaeinia

Journal: European Journal of Mechanics - B/Fluids

Submitted in October 2021 and accepted on March 17, 2022

Authorship statement: The first author derived the new particle regularization techniques in the SPH method. He implemented the new formulations inside the open-source code DualSPHysics software. He conducted the simulations, validated and analyzed the numerical results, prepared the graphs and figures, wrote the original draft, and responded to the comments and revisions received from the reviewers. The second co-author numerically solved the analytical solution of the first test case and wrote the code for calculating the spatial particle disorder. Also, he revised the original draft and provided general comments on the quality of the visualizations.

- **Article 4:** "Enhanced weakly-compressible MPS method for immersed granular flows"

[126]

Authors: Mojtaba Jandaghian, Abdelkader Krimi, and Ahmad Shakibaeinia

Journal: Advances in Water Resources

Publication date: June 2021

Authorship statement: The first author proposed the new methodology including the generalized rheology model and the modified diffusive term. He developed the GPU-accelerated code and implemented the new techniques in the software. He validated and analyzed the numerical simulations, extracted the experimental data, prepared the graphs and figures, wrote and revised the original draft. In the review process of the article, he responded to the comments and revised the manuscript. The second co-author reviewed the article and provided general comments.

- **Article 5:** "Fluid-driven granular dynamics through a consistent multi-resolution particle method" [127]

Authors: Mojtaba Jandaghian and Ahmad Shakibaeinia

Journal: Journal of Fluid Mechanics

Submission date: February 2022

Authorship statement: The first author proposed the new multi-resolution method and the adapted stabilization techniques. He developed the GPU-accelerated code and implemented the new model. He validated and analyzed the numerical simulations versus the theoretical solutions and the post-processed experimental data, visualized the results, and wrote and revised the original draft.

- **Conference paper 1:** "A Moving Particle Semi-implicit numerical method for modeling sediment dynamic" [111]

Authors: Mojtaba Jandaghian and Ahmad Shakibaeinia

Conference: E-proceedings of the 38th IAHR World Congress

Publication date: September 2019

Authorship statement: The first author developed the 2D serial code with the new methodology for the particle stabilization. He simulated the test cases, analyzed the results, prepared the figures, and wrote the original draft. He presented this paper at the conference in Panama City.

- **Conference paper 2:** "Dynamic particle collision technique for free-surface flows in SPH" [128]

Authors: Mojtaba Jandaghian, Herman Musumari Siaben, Abdelkader Krimi, and Ahmad Shakibaeinia

Conference proceeding: 2021 International SPHERIC Workshop

Publication date: June 2021

Authorship statement: The first author derived the new DPC technique for SPH. He implemented the formulation inside the open-source code DualSPHysics and simulated the test cases. He validated and analyzed the numerical results, prepared the graphs and figures, and wrote and revised the original draft. He presented the paper at the online conference. The second co-author provided the analytical solution of the first test case and revised the manuscript. The third co-author also provided the analytical solution and participated in the related discussions.

- **Article 6:** "A WC-SPH particle shifting strategy for simulating violent free surface flows" [64]

Authors: Abdelkader Krimi, Mojtaba Jandaghian, and Ahmad Shakibaeinia

Journal: Water

Publication date: November 2020

Authorship statement: The second co-author revised the original draft, provided comments on the quality of the results, and participated in the related discussions.

3.5 Structure of thesis

This thesis is presented in an article-based format. Following the Introduction and Literature Review chapters (i.e., chapters 1 and 2, respectively), five interconnected journal articles are presented in chapters 4-8 (see Figure 3.1). While chapters 4-6 concentrate on enhancing the stability and accuracy of particle methods for general free-surface flows, chapters 7 and 6, employ and further develop the new enhanced techniques for the particular cases of immersed gravity-driven and fluid-driven granular flows, respectively. These chapters are organized as follows:

- Chapter 4 (Article 1) addresses the research objectives O1 and O2 proposing the conservative form of the WC-MPS method. It also introduces the artificial density diffusive term and the CPS + PC particle regularization technique.
- Chapter 5 (Article 2) also contribute to the research objectives O1 and O2. It investigates the role of particle regularization techniques in simulating violent free-surface flows by the EWC-MPS method. It also proposes the modified density diffusive term and the DPC and CPS*+DPC particle regularization techniques.

- Chapter 6 (Article 3) addresses the research objectives O2 in the context of the WC-SPH method. It validates the effectiveness of the developed DPC formulation and a new hybrid PS technique (PS + DPC, denoted as cPS) for highly dynamic free-surface flows.
- Chapter 7 (Article 4) primarily addresses the research objective O3 by proposing the generalized rheology model for the immersed granular flows in the EWC-MPS method. It also contribute to objectives O1 and O2 by presenting and evaluating a modified diffusive term for multiphase flows.
- Chapter 8 (Article 5) focuses on developing a consistent multi-resolution particle method for fluid-driven granular flows. Furthermore, it contributes to adapting the rheology model and stabilization techniques to the multi-resolution formulations, which are aligned with the objectives O1-O3.

Finally, chapters 9 and 10 summarize and conclude the outcomes and the key findings of this research project.

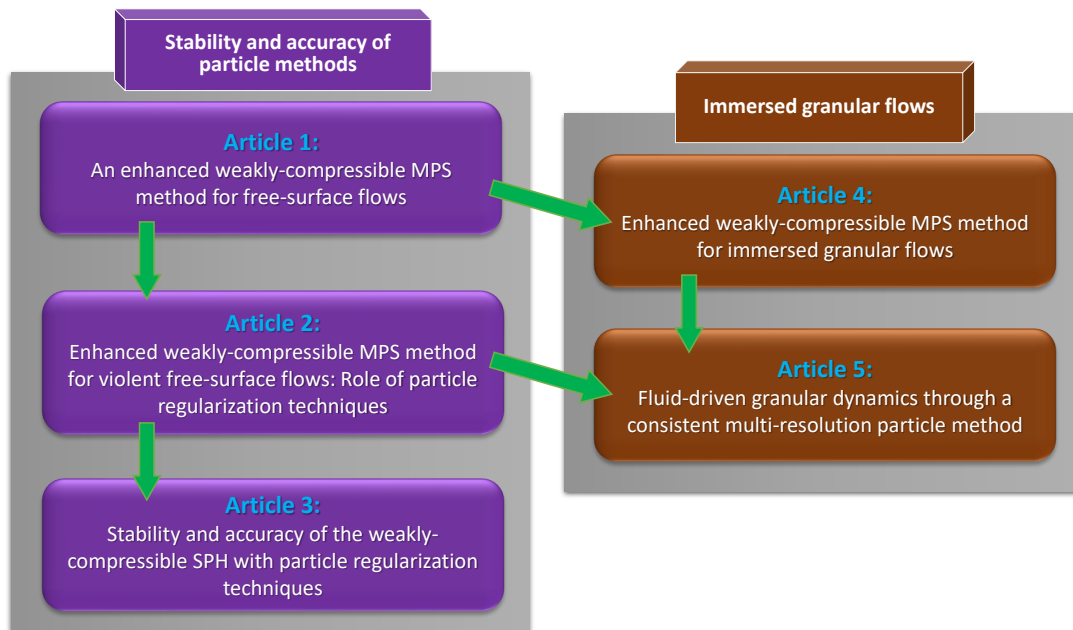


Figure 3.1 The five interconnected research articles addressing the four research objectives (O1-O4). Articles 1-5 are represented as chapters 4, 5, 6, 7, and 8, respectively.

CHAPTER 4 ARTICLE 1: AN ENHANCED WEAKLY-COMPRESSIBLE MPS METHOD FOR FREE-SURFACE FLOWS

Authors: Mojtaba Jandaghian¹ and Ahmad Shakibaeinia¹

¹Department of Civil, Geological and Mining Engineering, Polytechnique Montréal, Canada
Computer Methods in Applied Mechanics and Engineering

4.1 Abstract

Similar to other particle methods, the Weakly-Compressible MPS (WC-MPS) is known to suffer from numerical instabilities and unphysical pressure fluctuations. Here we develop, adapt and evaluate a series of enhancement techniques to improve the stability and accuracy of this numerical approach. This includes a new conservative pressure gradient formulation and its conjugate form of the continuity equation supplied with a new diffusive term to reduce the numerical error related to the false diffusion. As a regularization technique, we have also adapted and modified the particle shifting algorithm (with near-surface special treatment) in combination with the pair-wise particle collision method to avoid particle clustering and associated noises. The impact of each of these enhancement techniques is evaluated and quantified using popular benchmark cases, i.e. hydrostatic pressure tank, elliptical water drops, rotating square patch of fluid, and dam-break problems. While the results confirm the effectiveness of all the enhancement techniques, the additional diffusive term is found to play a key role in increasing stability and eliminating the high-frequency pressure noises. Furthermore, results show that for the cases with large interfacial deformations, the developed particle shifting algorithm is essential for maintaining the smoothness of the free-surface region and avoiding unwanted fragmentation.

4.2 Introduction

Mesh-free particle methods (or simply particle methods) are a group of numerical techniques, which are recognized for their abilities in the simulation of challenging problems, especially those with large interfacial deformation and fragmentations. Despite the capabilities of these methods, they are known to be associated with instabilities and accuracy problems, particularly in prediction of the pressure field. Over past years, much effort has focused on dealing with such issues (e.g., in [3, 34, 129–131]), yet they have remained to be open problems. The issues such as high-frequency unphysical pressure fluctuations, particle clustering and the so-

called tensile instability, affect the stability of the particle method and requires implementing enhancement algorithms such as the higher-order approximations (e.g., [51, 132]), the artificial diffusive terms (e.g., [53, 54]) and the particle stabilizing and regularization techniques (e.g., [50, 132]).

The widely-used particle models are the Smoothed Particle Hydrodynamics (SPH) and the Moving Particle Semi-implicit (MPS) approaches, which have become powerful tools for simulating complex hydro-environmental problems (e.g., [59, 114, 115, 133–135]). These two sister methods differ in their basic approximation techniques yet share a lot in terms of solution algorithms. The MPS method proposed by Koshizuka and Oak [25] is widely used and validated for various hydrodynamic problems (e.g., in [105, 113, 136]). Shakibaeinia and Jin [47] introduced the weakly compressible version of the MPS method (WC-MPS) by employing an equation of state as the substitute for the Poisson’s Pressure Equation (PPE) to solve the governing equations explicitly and reduce the calculation costs. This method is the focus of the present study.

We can evaluate the accuracy and stability of the numerical models from the mathematical (exact derivatives) and mechanical (exact momentum conservation) point of view. A numerical model that conserves the momentum of the system (in the absence of external forces) and estimates the derivatives with a high-order of accuracy is an ideal model for the fluid flow simulations. Nevertheless, SPH and MPS are incapable to accomplish both, since the exact derivatives of acceleration terms ignore the conservation of momentum [49]. Considering the Taylor expansion series for the higher-order calculations and antisymmetric pressure gradient formulations to conserve the momentum of a system, various approximation formulas for the governing equations are proposed (refer to [51, 60, 133, 137, 138]). Particularly for MPS, Koshizuka and Oka [25] added a particle stabilizing term ($\Delta p = p_i - \hat{p}_i$, $\hat{p}_i = \min(p_i, p_j)$, $j \in$ neighbor of i) to the standard form of the pressure gradient to keep the interparticle forces positive and exterminate particle clumping, however, it violates the momentum conservation and reduces the order of accuracy. Khayyer and Gotoh [139] presented another equation for the gradient of pressure in the MPS framework conserving the momentum, while estimating inaccurate gradient values with incorrect gradient vector directions [140]. Suzuki et al. [141] derived the Hamiltonian MPS formulations (similar to the SPH approximation equations using the gradient of kernel function) conserving the mechanical energy of the system for the fully incompressible fluid flows. Lee et al. [56] evaluated the role of a conservative pressure gradient with $\Delta p = 2p_i$ in an improved incompressible MPS model. Khayyer and Gotoh [57] implemented a corrective matrix into the standard pressure gradient operator similar to the renormalization matrix Oger et al. [52] employed to apply higher order calculations. Gotoh and Khayyer [59] pointed out that the stability of the model with the corrective matrix is

uncertain without implementing a particle regularization technique for simulating real test cases. Duan et. al [60] showed that by including this corrective matrix in the gradient and divergence formulations, the order of convergence mathematically increases from zero-order to exactly first order, nevertheless the particle stabilizing techniques for the free-surface and interior regions are required.

Furthermore, the particle methods suffer from particle clustering so-called tensile instability as a result of the insufficient repulsive force between particles [44]. From a microscopic point of view, an internal repellent force avoids molecules from clustering even when they attract each other under external stretching forces. If a mathematical model underestimates the repulsive force as the particles approach, the tensile instability occurs due to a negative pressure field or an extreme compressive external force. This pairing instability originates from the approximation errors and the sudden decrease of the repulsive force as the particles cluster in particle methods with the kernel derivative (in SPH). Different solutions have been suggested to eliminate the particles clumping and represent a smooth pressure field based on the source of instability and disturbance. This includes implementing an artificial repulsive force and diffusive terms into the governing equations, imposing uniform particle distribution to avoid the collision of the particles, and smoothing the density and pressure field approximation.

Molteni and Colagrossi [54] added a diffusion term as Laplacian of density into the continuity equation to compensate for the numerical (false) diffusion associated with the numerical technique in the weakly compressible SPH model. The concept behind this diffusion term comes from the artificial viscosity term that Monaghan and Gingold [61] implemented into the momentum equation to eliminate the shock discontinuities [54]. This approach (so-called δ -SPH) leads to robust results in SPH for simulation of the free-surface flows [65]. However, near the fluid free-surface due to the kernel truncation, the standard diffusion term diverges [66,67]. Antuono et al. [66] proposed a diffusion term by the Taylor expansion series and a corrective interpolator for the kernel gradient to present a conservative form of the Laplacian of density over the fluid domain. Antuono et al [65] compared different numerical diffusive terms in the WC-SPH framework. Sun et al. [85,130] presented a modified δ -SPH algorithm, denoted as δ plus-SPH, improved by the optimized particle shifting approach. Recently, Meringolo et al. [142] employed the sub-particle scale turbulence closure to determine the diffusive parameters dynamically according to the local and instantaneous flow conditions.

The focus of some of the past studies has been on applying particle rearrangement/regularization to achieve a uniform density field and overcome the problem with tensile instability and particle clustering. Monaghan [44] implemented a positive force term denoted as the repulsive

force (i.e. an artificial pressure term) into the momentum equation in a weakly compressible SPH model. Also, he proposed the XSPH method [143] that avoids particle interpenetration by repositioning the particles based on the average velocity of the neighbouring particles. Adami et al. [144] regularized the particle motions by introducing a stress term into the momentum equation that stands for the effect of a background pressure applied to modify the particle's transport velocity. They implemented the approach only for internal flows working with the density summation formula in the weakly compressible SPH model. To enhance the stability and accuracy of the MPS method and suppress the tensile instability, Khayyer and Gotoh [57] proposed a modified multi-term source with the higher-order derivation of Poisson's pressure equation. Lind et al. [50] presented the generalized particle shifting (PS) algorithm for an ISPH model that repositions particles to the area with less particle concentration. In the PS approach, the gradient of particle concentration and the Fickian diffusion coefficient determine the magnitude and direction of the particle shifting. Skillen et al. [73] further generalized the PS method and applied it to test cases with the body-water slam and wave-body interaction. Khayyer et al. [74] Optimized the PS method (OPS) for the ISPH model by removing the false particles shifting in the normal direction to the free-surface. The OPS indirectly simulates the physical role of free-surface tension in a numerical model [50]. Sun et al. [130] developed the PS approach for multi-resolution problems in the context of the weakly compressible SPH method. Xu and Yu [145] employed the PS method to suppress the tensile instability in viscoelastic free-surface flows using a weakly compressible SPH model. Recently, Duan et al. [60,136] developed PS approach with a new shifting vector as a function of direction vector and employing the conservative form of pressure gradient for the stability of free-surface particles in the context of multiphase incompressible MPS scheme.

The pair-wise Particle Collision (PC) method applied in the MPS [75, 146] also aims to eliminate particle clustering and tensile instability. The main concept of this approach comes from the collision of granular particles considering their elasticity and mechanical energy dissipation [147]. Shakibaeinia and Jin [75] implemented the PC method to remove the particle clumping from the proposed weakly compressible MPS for multiphase flows. Xu and Jin [146] and Lee et al. [56] evaluated the effects of the collision distance and coefficient on MPS stability and the distribution of the particles.

Nonetheless, the WC-MPS model still suffers from instabilities (esp., in its pressure field) and requires improvements to become robust for dealing with complex fluid flows. Therefore, this research aims to address the well-known instabilities recognized in the particle methods (including WC-MPS) by proposing and evaluating a series of enhancement techniques for the WC-MPS formulations, some which of are new while the others are adapted from other particle methods. To remove the weaknesses of the kernel summation equation in the par-

particle number density calculation and reduce the kernel truncations errors, we will derive the continuity-based method for calculation of the particle number density. Moreover, we propose a new diffusive term in the context of the WC-MPS method, by adding an artificial density diffusion term into the continuity equation to compensate for the false diffusion and obtain a noise-free pressure field. To represent a conservative model, we will propose a new formulation for the pressure gradient reproducing particle self-rearranging via a repulsive force in positive pressure fields. With developing a dynamic free-surface detection algorithm for our WC-MPS model and enhancing the particle shifting algorithm, we will provide an effective tool for eliminating the tensile instability through small continuous particle displacements. The effectiveness and stability of the proposed algorithms are discussed and validated via simulating the challenging and popular free-surface flow benchmark cases.

4.3 MPS Methodology

4.3.1 Governing equations

The governing equations consist of mass and momentum conservation laws. In a particle method, we can interpret the right-hand sides of the momentum and continuity equations as the interaction forces and the particle's expansion rate, respectively [34]. A general form of the equations is given by:

$$\frac{1}{\rho} \frac{D\rho}{Dt} = -\nabla \cdot \mathbf{v} \quad (4.1)$$

$$\frac{D\mathbf{v}}{Dt} = -\frac{1}{\rho} \nabla p + \mathbf{F} + \frac{1}{\rho} \nabla \cdot \boldsymbol{\tau} \quad (4.2)$$

$$\frac{D\mathbf{r}}{Dt} = \mathbf{v} \quad (4.3)$$

where \mathbf{v} is the velocity vector, p is the scalar value of the pressure, \mathbf{F} is the acceleration vector due to body forces, $\boldsymbol{\tau}$ is the viscous stresses tensor and ρ is the fluid density. The viscous stresses tensor ($\boldsymbol{\tau}$) contains the laminar viscous stresses and the turbulence effects. With a stiff Equation of State (EOS), $p = f(\rho)$, the behavior of an incompressible fluid is predicted as a weakly compressible fluid. Neglecting the divergence of velocity for a weakly-compressible model, the Laplacian of velocity field times the viscosity of the fluid ($\mu \nabla^2 \mathbf{v}$) represents the viscous shear stresses [148].

4.3.2 Standard MPS discretization

The mesh-free particle methods discretize the continuous medium into free-moving particles and update their position (\mathbf{r}_i) in each time step (Δt) using the equation of motion (4.3). The fluid particles carry the flow properties. In a Lagrangian frame, the temporal derivative of the velocity field (Left-hand side of Eq. (4.2)) already contains the convection terms. The MPS method uses a weight averaging (kernel smoothing) function, $W(r_{ij}, r_e)$, to approximate quantities and derivatives over a target particle i , from its neighboring particles. When the distance between particle i and j , $r_{ij} = |\mathbf{r}_j - \mathbf{r}_i|$, is less than the smoothing length of the kernel function, r_e , they are considered as neighbors. The smoothing length is usually selected to be 2-4 times of the initial average particle distance l_0 . The most popular kernel function in MPS is the rational kernel function with the compact support [25]. Shakibaeinia and Jin [47] investigated the effects of different types of kernel functions and introduced a third-order polynomial spiky function for MPS. In this study, we utilize the rational kernel function.

Using kernel smoothing process, the MPS approximation, $\langle \rangle$, of an arbitrary function, f , for particle i is given by:

$$\langle f \rangle_i = \frac{\sum_{i \neq j}^N f_j W_{ij}}{\sum_{i \neq j}^N W_{ij}} \quad (4.4)$$

in which $W_{ij} = W(r_{ij}, r_e)$ and N = the total number of neighbour particles of particle i . The summation of kernel function for particles at the vicinity of particle i ($r_{ij} \leq r_e$) defines a dimensionless parameter called particle number density, n , as:

$$n_i = \sum_{i \neq j}^N W_{ij}(r_{ij}, r_e) \quad (4.5)$$

The particle number density for an incompressible fluid should remain invariant to satisfy the continuity equation [46]. Modifying Eq. (4.4), a reference particle number density value, n_0 , can be used as a normalization factor:

$$\langle f \rangle_i = \frac{1}{n_0} \sum_{i \neq j}^N f_j W_{ij} \quad (4.6)$$

The relation between ρ_i and n_i is given by [46]:

$$\langle \rho \rangle_i = \frac{m n_i}{\int W dV} \quad (4.7)$$

Therefore, we can substitute ρ_i/ρ_0 with n_i/n_0 in every derived equation. In this equation, m is the mass of particle and $\int W dV$ is a constant value (by neglecting the kernel truncation

near the boundaries and V : the volume of particles).

In MPS, the gradient of an arbitrary scalar on a target particle is approximated using the weight averaging of gradient vector between that particle and each of its neighbors:

$$\begin{cases} \langle \nabla f \rangle_i = \frac{d}{n_0} \sum_{i \neq j}^N \frac{f_{ij}}{r_{ij}} \mathbf{e}_{ij} W_{ij} \\ \nabla f_i = \frac{f_j - f_i}{\|\mathbf{r}_j - \mathbf{r}_i\|} \mathbf{e}_{ij} = \frac{f_{ij}}{\|\mathbf{r}_{ij}\|} \mathbf{e}_{ij}, \quad \mathbf{e}_{ij} = \frac{\mathbf{r}_{ij}}{r_{ij} = \|\mathbf{r}_{ij}\|} \end{cases} \quad (4.8)$$

in which \mathbf{e}_{ij} is the unit direction vector between particle i and j , and d ($=1, 2, 3$) is the number of space dimensions. Similarly, one can approximate the divergence of an arbitrary vector, \mathbf{F} , as:

$$\langle \nabla \cdot \mathbf{F} \rangle_i = \frac{d}{n_0} \sum_{i \neq j}^N \frac{\mathbf{F}_{ij}}{r_{ij}} \cdot \mathbf{e}_{ij} W_{ij}. \quad (4.9)$$

By implementing the Taylor series, the approximation formula for the Laplacian of a vector \mathbf{F} (Divergence of a vector gradient) is:

$$\langle \nabla^2 \mathbf{F} \rangle_i = \frac{2d}{n_0} \sum_{i \neq j}^N \frac{\mathbf{F}_{ij}}{r_{ij}^2} W_{ij}. \quad (4.10)$$

If we neglect the kernel truncations in a continuum field, r_{ij}^2 has a constant value over the fluid flow domain as:

$$\lambda = \frac{\sum_{i \neq j}^N r_{ij}^2 W_{ij}}{\sum_{i \neq j}^N W_{ij}}. \quad (4.11)$$

Hence, the final form of the Laplacian of a vector \mathbf{F} in the MPS framework will be as:

$$\langle \nabla^2 \mathbf{F} \rangle_i = \frac{2d}{\lambda n_0} \sum_{i \neq j}^N \mathbf{F}_{ij} W_{ij}. \quad (4.12)$$

The MPS operators (Eqs. (4.8)-(4.12)) can be used to approximate the spatial derivative in the flow governing equations. To solve the governing equation, the model requires an additional equation to calculate the pressure field. The original MPS considers the flow as fully incompressible and solves the Poisson's pressure equation. The WC-MPS, however, allows slight compressibility, making it possible to employ an equation of state (EOS) to explicitly calculate the pressure field [34]. The equation of state in WC-MPS gives the pressure as a function of n_i by [47]:

$$p_i = \frac{c_0^2 \rho_0}{\gamma} \left(\left(\frac{n_i}{n_0} \right)^\gamma - 1 \right), \quad \gamma = 7 \quad (4.13)$$

where ρ_0 and c_0 are reference density and numerical sound speed, respectively. To limit the density variation to less than 1% (i.e., $Ma < 0.10$) numerical speed of sound is selected to 10 times the maximum possible flow velocity ($\|\mathbf{v}_{max}\|$) [53].

We can solve the governing equations by employing the first-order prediction-correction scheme (See [47]) or the second-order Symplectic time integrator (See [11]). As the time integration schemes solve the weakly compressible fluid flows with an explicit approach, the time steps of the time integration scheme (Δt) should satisfy the Courant-Friedrichs-Lewy stability condition (i.e., the CFL condition) [67]. We implement the CFL condition to determine Δt as:

$$\Delta t \leq CFL \frac{l_0}{c_0} \quad (4.14)$$

where CFL is the Courant number ($0 < CFL \leq 1$) [47]. In this study, the CFL condition controls the time step of calculations for the benchmark cases, since the shear forces are negligible (i.e. the fluid is inviscid or $\mu \ll 1$).

4.3.3 Boundary treatments

To assign the boundary values to the free-surface, the free-surface particles must be identified. Standard MPS uses the decrease of particle number density near the free-surface as a condition for detecting the free-surface particles. Particle i is a free-surface particle if:

$$n_i \leq \beta_n n_0 \quad (4.15)$$

in which β_n is a threshold parameter between 0.8 and 0.99 and should be tuned based on the test cases [46, 47]. This condition is simple to implement and computationally affordable. However, to deal with complex flows with extreme surface deformations and patterns, more accurate free-surface detection is necessary for enforcing suitable boundary conditions [149].

We employ fixed wall and ghost particles to simulate the solid boundaries (Figure 4.1). The wall particles contribute in the momentum and particle number density calculations to apply appropriate repulsive force to the approaching fluid particles, however, they remain fixed similar to the model employed by [67]. The ghost particles prevent incomplete kernel support near walls. The pressure parameter of the ghost particles is extrapolated from the nearest wall particle. We assign the velocity of the nearest fluid particle (or zero velocity) to the fixed wall and ghost particles to simulate the slip (or non-slip) boundary conditions. One should note that for dealing with complex boundary geometries (e.g. curved solid boundaries) special treatments become necessary [114, 150].

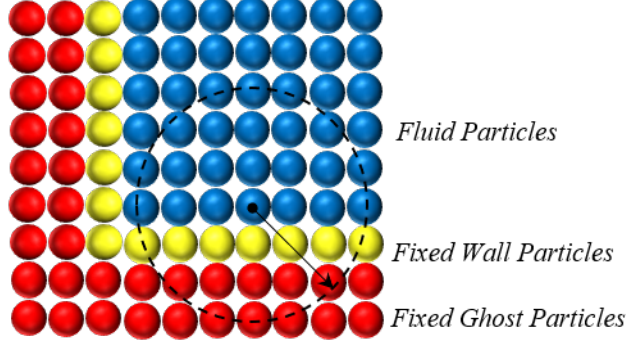


Figure 4.1 The fluid and solid boundary particles configuration

4.4 Enhanced Weakly-Compressible MPS

4.4.1 Conservative pressure force

For incompressible MPS, different formulations are proposed to estimate the force terms by considering the higher-order calculations and particle stabilizing terms (refer to [51, 57, 60, 133, 137, 138, 151]). The standard MPS formulation (Eq. (4.8)) approximates the pressure gradient as [25]:

$$\langle \nabla p \rangle_i = \frac{d}{n_0} \sum_{i \neq j}^N \frac{p_j - p_i}{r_{ij}} \mathbf{e}_{ij} W_{ij}. \quad (4.16)$$

To increase the accuracy of approximation to exact linear order, with the Taylor series expansion a non-dimensional corrective matrix (\mathbf{C}_i) is implemented into the gradient of pressure as [57, 60, 133]:

$$\langle \nabla p \rangle_i = \frac{d}{n_0} \sum_{i \neq j}^N \frac{p_j - p_i}{r_{ij}} (\mathbf{C}_i \mathbf{e}_{ij}) W_{ij} \quad (4.17)$$

where

$$\mathbf{C}_i = \left(\frac{d}{n_0} \sum_{i \neq j}^N \frac{\mathbf{r}_{ij}}{r_{ij}} \otimes \mathbf{e}_{ij} W_{ij} \right)^{-1} \quad (4.18)$$

and will be an identity matrix for a uniform particle distribution (away from free-surfaces). Given that $\mathbf{e}_{ij} = -\mathbf{e}_{ji}$, $\mathbf{C}_i \neq \mathbf{C}_j$ and $W_{ij} = W_{ji}$, equations (4.16) and (4.17) violate the momentum preservation of the system as they are not anti-symmetric ($\nabla p_{ij} \neq -\nabla p_{ji}$) [75, 139]. Although the approximation errors of derivatives on the randomly distributed (but fixed) particles can be reduced using the higher-order derivatives, the role of symmetry and conservation properties of the numerical method is missing in such accuracy and convergence evaluations. Therefore, implementing stabilizing techniques for rearranging particles toward

a uniform distribution (e.g., using particle shifting or pair-wise particle collision method) are necessary [60]. Price [49] and Lind et al. [50] discussed this issue in more detail by presenting numerical examples showing the importance of respecting momentum conservation for the long term stability and accuracy of a weakly compressible SPH method.

In order to improve the conservation features (considering the non-linear properties of the system) of the weakly-compressible MPS method, here we propose a new formulation for the pressure gradient to produce an anti-symmetric momentum equation (with respect to the particle index). If particle i is at the center of its neighbouring particles and far from boundaries (i.e. no kernel truncation occurs), the kernel summation of vector \mathbf{r}_{ij}/r_{ij}^2 is zero [25]:

$$\sum_{i \neq j}^N \frac{\mathbf{r}_{ij}}{r_{ij}^2} W_{ij} = 0 \quad (4.19)$$

therefore, the approximation of the gradient of pressure (Eq. (4.16)) can be reduced to:

$$\langle \nabla p \rangle_i = \frac{d}{n_0} \sum_{i \neq j}^N \frac{p_j}{r_{ij}^2} \mathbf{r}_{ij} W_{ij}. \quad (4.20)$$

To obtain an anti-symmetric formulation for the pressure gradient in the SPH method, the density is placed into the gradient operator as [42, 49, 152, 153]:

$$\frac{\nabla f_i}{\phi_i} = \nabla \left(\frac{f_i}{\phi_i} \right) + \frac{f_i}{\phi_i^2} \nabla \phi_i. \quad (4.21)$$

We consider $\phi_i = \rho_i$ and substitute ρ_i with $\rho_0 n_i / n_0$ to have the MPS form of Eq. (4.21) for the pressure gradient:

$$\frac{\nabla p_i}{n_i} = \nabla \left(\frac{p_i}{n_i} \right) + \frac{p_i}{n_i^2} \nabla n_i \quad (4.22)$$

If we employ Eq. (4.20) to estimate the RHS of Eq. (4.22), we gain the final shape of the new pressure gradient in the MPS framework as:

$$\langle \nabla p \rangle_i = \frac{d}{n_0} \sum_{i \neq j}^N \left(n_i \frac{p_j}{n_j} + n_j \frac{p_i}{n_i} \right) \frac{\mathbf{e}_{ij}}{r_{ij}} W_{ij}. \quad (4.23)$$

Consequently, the new gradient of pressure equation determines the inter-particle forces as

follow ($\rho_i = \rho_j = \rho_0$):

$$\begin{cases} \mathbf{T}_{ij}^p = \frac{m\langle\nabla p\rangle_i}{\rho_0} = \frac{md}{n_0\rho_0} \left[\left(n_i \frac{p_j}{n_j} + n_j \frac{p_i}{n_i} \right) \frac{\mathbf{r}_{ij}}{r_{ij}^2} W_{ij} \right] \\ \mathbf{T}_{ji}^p = \frac{m\langle\nabla p\rangle_j}{\rho_0} = \frac{md}{n_0\rho_0} \left[\left(n_j \frac{p_i}{n_i} + n_i \frac{p_j}{n_j} \right) \frac{\mathbf{r}_{ji}}{r_{ji}^2} W_{ji} \right] \end{cases}. \quad (4.24)$$

Given that $\mathbf{r}_{ij} = -\mathbf{r}_{ji}$ and $W_{ij} = W_{ji}$, the interparticle forces are equal in magnitude and opposite in direction ($\mathbf{T}_{ij}^p = -\mathbf{T}_{ji}^p$) and as a result, the linear and angular momentum conservation exists by implementing the new gradient pressure formula in MPS (in the absence of external and shear forces).

We can interpret the conservative pressure gradient model as a particle stabilizing technique, in which the dynamic particle stabilizing term (Δp) includes $n_{i,j}$ and $p_{i,j}$ as:

$$\Delta p = \left(\frac{n_j}{n_i} + 1 \right) p_i + \left(\frac{n_i}{n_j} - 1 \right) p_j. \quad (4.25)$$

If we assume a constant particle number density field surrounding particle i ($n_i = n_j$), the pressure gradient model is similar to the gradient model evaluated by Lee et al. [56] in which $\Delta p = 2p_i$ is added to the standard pressure gradient. It should be highlighted that these models are more sensitive to the tensile instability in negative pressure fields (i.e. $p_i < 0$), since particles purely attract each other in the absence of any repulsive force [85].

To illustrate the importance of the momentum conservation and the role of the particle stabilizing term in our model, we present a simple numerical test case called “*Settling a random particle distribution*” suggested by Price [49]. In a 2-D square domain of $x, y \in [-0.5, 0.5]$ with the periodic boundary conditions, we initially place particles on a hexagonal lattice ($l_0 = 0.02$). To achieve a non-uniform particle distribution, we randomly displace particles as:

$$\mathbf{r}'_i = \mathbf{r}_i + \delta\mathbf{r}_i = \mathbf{r}_i + [kl_0(R_{nx} - 0.5), kl_0(R_{ny} - 0.5)], \quad (4.26)$$

where $0 \leq R_{nx, y} \leq 1$ is a random number, and the dimensionless coefficient, k , determines the level of randomness. Here we use $k = 0.2$ to limit $|\delta\mathbf{r}_i|$ to $0.1l_0$ in x and y directions. The kernel summation equation (4.5) and the equation of state (4.13) calculate n_i and p_i for the randomized particle distribution (Figure 4.2-a). The smoothing length for the kernel approximation is $3l_0$ and $\rho_0 = 1000 \text{ kg/m}^3$. The sound speed and calculation time steps are set to 1 m/s and 0.002 s , respectively. Since no external and viscous shear forces exist, a uniform pressure field is expected ($\nabla p = 0$). As Price [49] suggests, a gradient of pressure with local momentum conservation should be able to rearrange the non-uniformly distributed

particles toward a uniform one. The result (Figure 4.2) shows that our new MPS pressure gradient contains this self re-arrangement (i.e. keeping particles uniformly distributed) which gives an accurate estimation of the derivatives without including the higher-order calculations (i.e. the corrective matrix, Eq. (4.18)) or any particles stabilizing technique. Employing the new conservative form of the pressure gradient (Eq. (4.23)) leads to a stable condition with uniform particle distribution and pressure equilibrium after 1 second of simulation (Figure 4.2-b), while the model with the non-conservative form of the higher-order pressure gradient (Eq. (4.17)) reaches an unstable condition due to particle clustering (Figure 4.2-c).

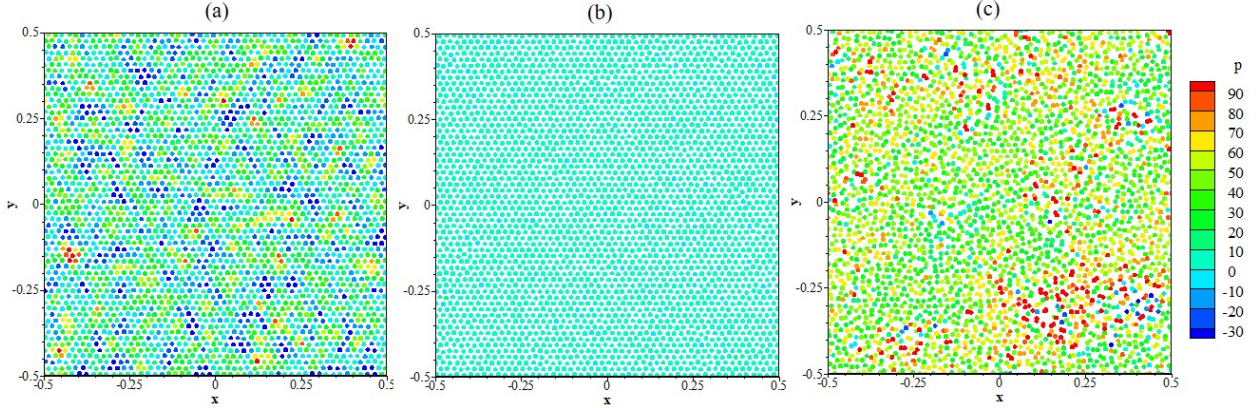


Figure 4.2 (a) Initial pressure field ($t = 0$) of a randomized particle distribution placed on a hexagonal lattice (maximum randomness level of $0.1l_0$ in the x and y directions) with the periodic boundary conditions, (b) the pressure field obtained with the new conservative form of the pressure gradient, $\frac{d}{n_0} \sum_{i \neq j}^N (n_i \frac{p_j}{n_j} + n_j \frac{p_i}{n_i}) \frac{\mathbf{e}_{ij}}{r_{ij}} W_{ij}$, and (c) the non-conservative form of the higher-order pressure gradient (including \mathbf{C}_i), $\frac{d}{n_0} \sum_{i \neq j}^N \frac{p_j - p_i}{r_{ij}} (\mathbf{C}_i \mathbf{e}_{ij}) W_{ij}$, at $t = 1.0$ second of simulation

4.4.2 The continuity equation for the particle number density calculation

In MPS, a stable and accurate pressure field highly depends on a non-oscillatory particle number density field. The standard MPS and WC-MPS directly calculate n_i using particles' position by summing the kernel function values over the neighbour particles (Eq. (4.5)). The accuracy of this zeroth-order approximation is highly sensitive to the type of kernel function and the small changes in the distribution of the particles [49]. There will be also a sudden drop of pressure near free-surfaces due to low density. In addition, in this method, the initial pressure field will have no impact on the simulation. Therefore, here to calculate n_i we solve the continuity equation to limit the errors near boundaries [48] and include the expansion

rate of particles (i.e. the velocity divergence) in calculating the pressure field. This will also allow us to apply initial pressure to smoothen the initial rearrangement of particles.

To discretize the continuity equation one should note that a model will conserve the total energy of the particles, E , only if the conjugate operators estimate the pressure gradient and the velocity divergence in the governing equations [49]. The conjugate divergence operator to the gradient Eq. (4.22) employed to derive the new pressure gradient (Eq. (4.23)) is:

$$\nabla \cdot \mathbf{F}_i = \frac{1}{n_i} [\nabla \cdot (\mathbf{F}_i n_i) - \mathbf{F}_i \cdot \nabla n_i] \quad (4.27)$$

by having $\phi_i = \rho_i$ and Eq. (4.7). Considering equations (4.9) and (4.27) for the divergence of the velocity vector and condition (4.19), the MPS approximation of the continuity equation (4.1) is given by:

$$\frac{1}{n_i} \frac{Dn_i}{Dt} = -\frac{d}{n_0} \sum_{i \neq j}^N \left(\frac{n_j}{n_i} \right) \frac{\mathbf{v}_{ij}}{r_{ij}} \cdot \mathbf{e}_{ij} W_{ij}, \quad (4.28)$$

where $\mathbf{v}_{ij} = \mathbf{v}_j - \mathbf{v}_i$. Hence, with the conjugate operators the discretized form of the momentum and thermal (internal) energy equations will satisfy the condition below for the total energy conservation (in the absence of external forces and dissipation):

$$\frac{dE}{dt} = \sum_i m (\mathbf{v}_i \cdot \frac{d\mathbf{v}_i}{dt} + \frac{du_i}{dt}) = 0, \quad (4.29)$$

in which u_i is the thermal energy of particle i . By substituting equations (4.23) and (4.28) into Eq. (4.29) and considering $\rho_i = \rho_0$ and $du_i/dt = -p_i/\rho_i \nabla \cdot \mathbf{v}_i$ at a constant entropy, we have

$$\frac{dE}{dt} = -\sum_i m \frac{d}{\rho_0 n_0} \sum_{i \neq j}^N \left(n_i \frac{\mathbf{v}_i p_j}{n_j} + n_j \frac{\mathbf{v}_j p_i}{n_i} \right) \cdot \frac{\mathbf{e}_{ij}}{r_{ij}} W_{ij} = 0 \quad (4.30)$$

which due to its antisymmetric feature (with respect to the particle index) confirms the total energy preservation of the system provided with the discretized form of the governing equations.

4.4.3 WC-MPS with Diffusion; WC-DMPS

In order to eliminate the particle number density fluctuations arising from the numerical (or false) diffusion and discretization errors, we here introduce a new diffusive term in the equations. Using the Laplacian of particle number density and the equation of state (Eq. (4.13)), we add this diffusive term to the continuity equation (Eq. (4.28)). The basic idea of this such diffusive term originates from the work of Molteni and Colagrossi [54] on the δ -SPH

method.

Ideally, the particle number density is supposed to remain constant for an incompressible fluid. However due to the physical (allowed by weak compressibility) as well as unphysical density fluctuations, one can be having variation in the particle number density denoted as n'_i . This variation is the correction that must be made to keep the particle number density constant. Using the continuity equation one can calculate the velocity variation (\mathbf{v}') corresponding to the variation of particle number density as:

$$\frac{1}{n_i} \frac{n'_i}{\Delta t} = -\nabla \cdot \mathbf{v}'_i. \quad (4.31)$$

The projection methods calculate the velocity variation (correction) from the momentum equation, excluding the shear stress terms, as:

$$\mathbf{v}'_i = -\frac{\Delta t}{\rho_0} \nabla p_i. \quad (4.32)$$

Taking divergence of the left and right-hand sides of Eq. (4.32) results in the Laplacian of the pressure field:

$$\frac{1}{n_i} \frac{n'_i}{\Delta t} = \frac{\Delta t}{\rho_0} \nabla^2 p_i; \quad (4.33)$$

with Eq. (4.12) the approximation form of Laplacian of pressure is given by:

$$\langle \nabla^2 p \rangle_i = \frac{2d}{\lambda n_i} \sum_{i \neq j}^N (p_j - p_i) W_{ij}. \quad (4.34)$$

From the equation of state (Eq. (4.13)) where $\gamma = 1$, we have p_{ij} as:

$$p_{ij} = p_j - p_i = \rho_0 c_0^2 \left(\frac{n_j - n_i}{n_0} \right). \quad (4.35)$$

Substituting Eq. (4.35) into Eq. (4.34) determines the relation between the Laplacian of p and n as:

$$\langle \nabla^2 p \rangle_i = \rho_0 c_0^2 \frac{2d}{\lambda n_i} \sum_{i \neq j}^N \left(\frac{n_j - n_i}{n_0} \right) W_{ij} = \frac{\rho_0 c_0^2}{n_0} \langle \nabla^2 n_i \rangle. \quad (4.36)$$

Finally, we derive the new diffusion term, D_i , by substituting the Laplacian of pressure with the Laplacian of the particle number density (Eq. (4.36)) in Eq. (4.33):

$$D_i = \delta_{MPS} \frac{\Delta t c_0^2}{n_0} \nabla^2 n_i. \quad (4.37)$$

We introduce a non-dimensional coefficient, $0 < \delta_{MPS} \leq 1$, into the diffusion term (in analogy with δ -SPH models [65]) to adjust the intensity of the term according to test cases. The modified continuity equation then is given by:

$$\frac{1}{n_i} \frac{Dn_i}{Dt} = -\nabla \cdot \mathbf{v}_i + \delta_{MPS} \frac{\Delta t c_0^2}{n_0} \nabla^2 n_i. \quad (4.38)$$

Consequently, we update the particle number density of particle i through

$$\frac{1}{n_i} \frac{Dn_i}{Dt} = -\frac{d}{n_0} \sum_{i \neq j}^N \left(\frac{n_j}{n_i} \right) \frac{\mathbf{v}_{ij}}{r_{ij}} \cdot \mathbf{e}_{ij} W_{ij} + \left(\delta_{MPS} \frac{\Delta t c_0^2}{n_0} \right) \frac{2d}{\lambda n_0} \sum_{i \neq j}^N n_{ij} W_{ij}. \quad (4.39)$$

It should be highlighted that the new diffusive term is consistent with the global mass conservation law by satisfying $\sum_i n_i D_i V_i = 0$ condition (where $V_i = \int W dV / n_i$ from Eq. (4.7)). Besides we apply the diffusive term only between the fluid particles to exclude the effects of the solid boundary particles on the conservation features of the system (i.e. if i or $j \in$ the solid boundary particles, then $D_i = 0$). Overall, the effect of this pure numerical correction shall reduce by increasing the spatial resolution [65, 142]. Further, for tuning the non-dimensional coefficient one should note that the diffusive term should not introduce large energy dissipation into the system affecting the time steps and the mechanical behaviour of the fluid flow [53]. The proposed diffusive term reduces by decreasing the time steps of calculations as the function of the CFL coefficient and the initial distance between particles (l_0). Considering some dimensional analysis and the CFL condition (4.14) determines the relationship between the magnitude of δ_{MPS} and the delta parameter employed in the δ -SPH method by $\delta_{SPH} = \delta_{MPS} (l_0 CFL / h)$ (in which h represents the smoothing length of the kernel approximation, $r_e = 2h$ and $h = 1.55l_0$). In this study, we justify the intensity of the proposed diffusive term in the simulations by confirming the compatibility between the numerical and the reference results and ensuring that it has the same order of magnitude as the diffusive term in the δ -SPH method. (e.g. for the dam break test case with $CFL = 0.5$ and $h/l_0 = 1.55$, the equivalent of the selected $\delta_{MPS} = 0.35$ in SPH is 0.11, which is compatible with the common constant $\delta_{SPH} = 0.1$ used in the δ -SPH methods [65, 68].)

4.4.4 A Corrected Particle Shifting technique; CPS + PC

Particle regularization/rearrangement techniques are common methods for improving particle distribution uniformity to avoid problems like density fluctuations and particle clustering. The original WC-MPS uses a pair-wise Particle Collision (PC) approach [75]. Here, however, we have adapted and developed a particle shifting (PS) algorithm, whose idea originates from

“Fick’s law of diffusion” implemented by Lind et al. [50] in SPH to shift fluid particles to the area with less particle concentration. Fick’s law determines the magnitude and direction of the particle shifting vector as:

$$\delta \mathbf{r}_i = -F_i \nabla C_i \quad (4.40)$$

in which C_i and F_i are the particle concentration and Fickian diffusion coefficient, respectively. Lind et al. [50] considered the Von Neumann stability analysis of the advection-diffusion equation and the CFL condition to estimate F_i as:

$$F_i = Al_0 \|\mathbf{v}\|_{max} dt \quad (4.41)$$

where A is a dimensionless constant between 1-6 and $\|\mathbf{v}\|_{max}$ is the magnitude of maximum expected velocity. Considering Eq. (4.19) (the CFL condition for stability of an explicit model) and the Mach number (Ma) we can rewrite F_i as [130]:

$$F_i = Al_0^2 \cdot CFL \cdot Ma \quad (4.42)$$

(in this study, $A = 2$). In MPS, one can determine the particle concentration (volume fraction) of i using Eq. (4.5) as:

$$C_i = \frac{\sum_{i \neq j}^N W_{ij}}{n_0} . \quad (4.43)$$

Using Eq. (4.8) to approximate the gradient of C_i , the particle shifting equation (Eq. (4.40)) would become non-conservative (i.e. $\delta \mathbf{r}_{i \rightarrow j} \neq -\delta \mathbf{r}_{j \rightarrow i}$ where $\delta \mathbf{r}_{j \rightarrow i} = -F_i \frac{d}{dt} \frac{C_j - C_i}{r_{ij}} \mathbf{e}_{ij} W_{ij}$) leading to unstable conditions in a non-uniform particles distribution. To derive an anti-symmetric form of this equation we employ Eq. (4.21) with $\phi_i = \rho_i$ to approximate ∇C_i as:

$$\langle \nabla C \rangle_i = \frac{d}{n_0} \sum_{i \neq j}^N \frac{C_i + C_j}{r_{ij}} \mathbf{e}_{ij} W_{ij} \quad (4.44)$$

by which the particle shifting vector lies on \mathbf{r}_{ij} and has the conservation feature of the shifting procedure. Unlike in SPH [50, 130], in our proposed concentration gradient equation (Eq. (4.44)), no additional artificial pressure-like function (f_{ij}) is necessary, because the presence of the kernel function (as $W_{ij} \neq 0$ at its origin) overcomes the pairing instability problem (arises from the SPH kernel derivative).

The pure PS technique requires special treatment near free-surface because of the incomplete kernel support, where Eq. (4.44) predicts a false particle shifting toward the free-surface [50]. To overcome this issue, the scheme should correct the displacement vector by restricting the particle diffusion in the normal direction to the free-surface [74]. Skillen et al. [73] proposed

the following formulation to implement the modified particle shifting approach with \mathbf{t}_i and \mathbf{n}_i (the unit tangential and normal vectors to the free-surface of fluid flow, respectively):

$$\delta \mathbf{r}_i = -F_i \left[\frac{\partial C_i}{\partial s} \mathbf{t}_i + \alpha \left(\frac{\partial C_i}{\partial n} - \beta \right) \mathbf{n}_i \right] \quad (4.45)$$

where α and β are the dimensionless parameters that can be set to zero to remove the particle shifting normal to the free-surface. To implement the PS algorithm with Eq. (4.45), particles belonging to the free-surface region and the unit normal vector to the free-surface should be determined.

Here, a dynamic algorithm in the context of MPS is developed to classify the fluid particles into four groups of, (4.1) free-surface ($i \in \text{Type-}\mathbb{F}$), (4.2) free-surface vicinity ($i \in \text{Type-}\mathbb{B}$), (4.3) inner ($i \in \text{Type-}\mathbb{I}$) and (4.4) external or splashed ($i \in \text{Type-}\mathbb{E}$) particles (The types \mathbb{E} , \mathbb{F} , \mathbb{B} and \mathbb{I} refer to external/splashed (detached from the free surface), free surface, free surface vicinity, and internal particles, respectively.) (Figure 4.3).

In this scheme, we employ the local particle number density ($\sum_{i \neq j}^N W_{ij}$) without additional calculation costs instead of the eigenvalue of the renormalization tensor used by [149, 151]. First, the detection algorithm evaluates the particle concentration parameter ($C_i = \sum_{i \neq j}^N W_{ij} / n_0$) with

$$\left\{ \begin{array}{l} 1) C_i < \beta_E \\ 2) \beta_E \leq C_i \leq \beta_F \\ 3) \beta_F < C_i \end{array} \right. \quad (4.46)$$

conditions, where β_F and β_E are the tunable threshold of C_i based on the type of kernel function and the smoothing length ($0 < \beta_E < \beta_F < 1$). For the rational and spiky kernel functions with $re = 3.1l_0$, we set β_E and β_F to 0.4 and 0.9, respectively. If $C_i < \beta_E$, the fluid particle i is an external or splashed particle ($i \in \mathbb{E}$). With the conditions two or three being true, the scheme moves to the next step to detect the free-surface particles. For a particle satisfying the second condition, we define an umbrella-shaped region proposed by Marrone et al. [149] with the local normal vector to the free-surface (\mathbf{n}_i in Eq. (4.49)) and scan the region for the neighbor particles. With the point S at the distance l_0 from particle i in the normal direction to the free-surface, we search R1 and R2 regions for the neighboring particle j (Figure 4.3-b). The criteria to check for the candidate particle to eventually distinguish the free-surface particles are as follow:

$$\left\{ \begin{array}{ll} |\mathbf{r}_{ij}| \geq \sqrt{2}l_0 \text{ and } |\mathbf{r}_{jS}| < l_0, & \text{R1} \rightarrow i \notin \mathbb{F} \\ |\mathbf{r}_{ij}| < \sqrt{2}l_0 \text{ and } |\mathbf{n}_i \cdot \mathbf{r}_{jS}| + |\mathbf{t}_i \cdot \mathbf{r}_{jS}| < l_0, & \text{R2} \rightarrow i \notin \mathbb{F} \\ j \notin \text{R1} \cup \text{R2} \text{ or } N_i < \beta_N N_0 & \rightarrow i \in \mathbb{F} \end{array} \right. \quad (4.47)$$

If no particle is detected inside R1 and R2 regions or the number of neighbour particles surrounding the particle i , N_i , is less than the maximum initial number of neighbors, N_0 , multiplied by β_N (i.e. $N_i < \beta_N N_0$, β_N is set to 0.75), the algorithm labels particle i as a free-surface particle ($i \in \mathbb{F}$). Otherwise, with satisfying the third condition of (4.46) or if particle i is a neighbor of a free-surface particle ($j \in \mathbb{F}$) while $\mathbf{r}_{ij} \leq \alpha l_0$, the scheme considers i as a particle in the vicinity of the free-surface, $i \in \mathbb{B}$. The rest are classified as inner fluid particles, $i \in \mathbb{I}$. We determine α based on the smoothing length to eliminate the kernel truncation of inner particles (with $re = 3.1l_0$, α is set to 2.01).

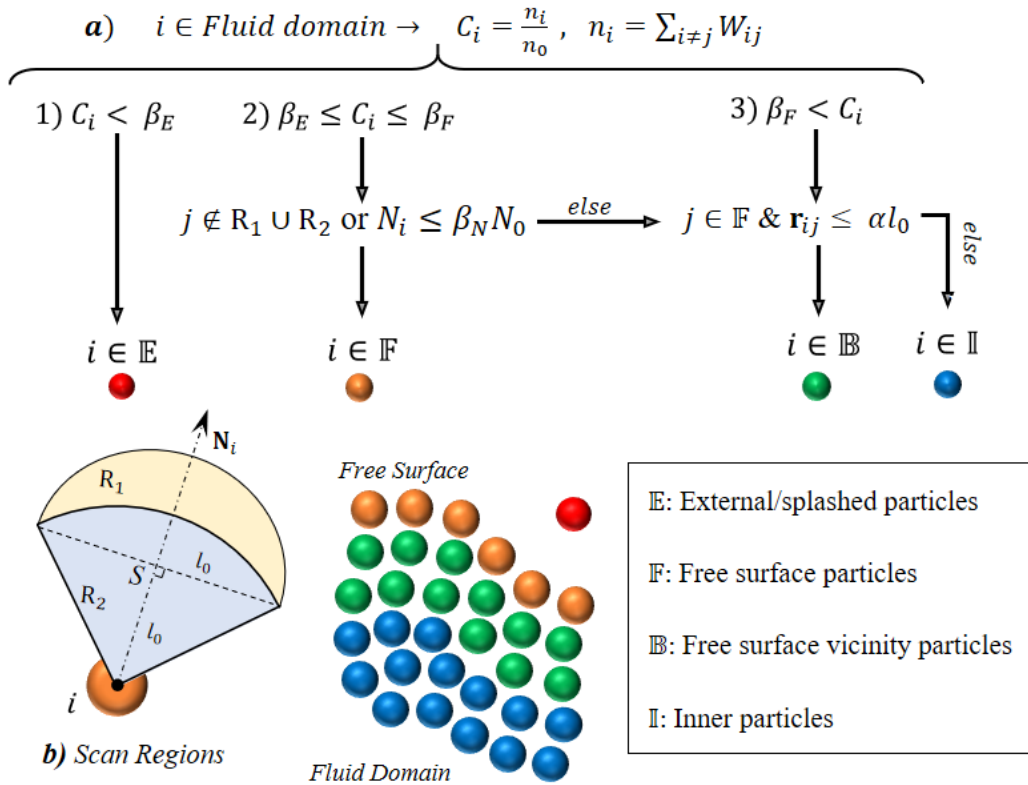


Figure 4.3 A particle classification scheme in the context of the MPS method

Based on the particle classification scheme, our proposed PS approach determines the shifting vector of the fluid particle i as [74]:

$$\delta \mathbf{r}_i = \begin{cases} -F_i \nabla C_i, & \text{if } i \in \mathbb{I} \\ -F_i (\mathbf{I} - \hat{\mathbf{n}}_i \otimes \hat{\mathbf{n}}_i) \cdot \nabla C_i, & \text{if } i \in \mathbb{B} \\ -F_i (\mathbf{I} - \mathbf{n}_i \otimes \mathbf{n}_i) \cdot \nabla C_i, & \text{if } i \in \mathbb{F} \\ 0 & \text{if } i \in \mathbb{E} \end{cases} \quad (4.48)$$

in which \mathbf{I} is the identity matrix. We can calculate the normal vector to the free-surface by the kernel estimation of any arbitrary parameter representing the type of particles [154]. Similar to the work of Duan et al. [60], we employ the unit direction vector, \mathbf{e}_{ij} , for the free-surface particles ($i \in \mathbb{F}$) where the kernel truncation is intense ($C_i \leq 0.9$) to define the local normal vector, \mathbf{n}_i . However, for the free-surface vicinity particles ($i \in \mathbb{B}$), we introduce the non-local normal vector, $\hat{\mathbf{n}}_i$, with respect to the neighbour free-surface particles ($j \in \mathbb{F}$ & $r_{ij} \leq 2.10l_0$) making the normal vector of particles in this category independent of their local kernel truncations and neighbour particles distribution (Eq.(4.49)).

$$\left\{ \begin{array}{l} \text{If } i \in \mathbb{F} \rightarrow \text{Local normal vector :} \\ \text{If } i \in \mathbb{B} \rightarrow \text{Non - local normal vector :} \end{array} \right. \quad \begin{array}{l} \mathbf{N}_i = \sum_{i \neq j}^N \mathbf{e}_{ji} W_{ij}, \quad \mathbf{n}_i = \frac{\mathbf{N}_i}{\|\mathbf{N}_i\|} \\ \hat{\mathbf{N}}_i = \sum_{j \in \mathbb{F}}^N \mathbf{n}_j W_{ij}, \quad \hat{\mathbf{n}}_i = \frac{\hat{\mathbf{N}}_i}{\|\hat{\mathbf{N}}_i\|} \end{array} \quad (4.49)$$

The ultimate purpose of such a Corrected PS method is to modify the particles shifting vector in the free-surface region to cancel the particle's diffusion in the normal direction to the free-surface. The gradient of particle concentration (Eq. (4.44)) may shift a particle in the vicinity of the free-surface in the opposite direction to the free-surface regardless of its incomplete kernel support. Therefore, here, based on the non-local normal vector for the free-surface vicinity particles, we neglect modifying the shifting vector, if particle $i \in \mathbb{B}$ is not shifted toward the free-surface by Eq. (4.40) (i.e. If $\hat{\mathbf{n}}_i \cdot \delta \mathbf{r}_i < 0$, then $\delta \mathbf{r}_{i \in \mathbb{B}} = -F_i \nabla C_i$ and particle i is classified as inner particles in the shifting procedure). However, for the rest of the free-surface particles ($i \in \mathbb{F}$), we always implement the free-surface correction as $\mathbf{n}_i \cdot \delta \mathbf{r}_i > 0$ due to the intense incomplete kernel support ($C_i \leq 0.9$).

In addition, as the Corrected PS scheme deactivates the imaginary repulsive force between the fluid particles in the normal direction to the free-surface ($\delta \mathbf{r}_{i \in \mathbb{F} \cup \mathbb{B}} \perp \mathbf{n}_i, \hat{\mathbf{n}}_i$), the stability of particles in the free-surface region is still vulnerable to negative pressure fields and highly dynamic deformations. To overcome the tensile instability in the free-surface region, we add the pair-wise PC method to our proposed PS algorithm. Here, the PC method modifies the velocity vector by transferring linear momentum between colliding particles as:

$$\begin{cases} \dot{\mathbf{v}}_i = \mathbf{v}_i - \frac{1+\varepsilon}{2}\mathbf{v}_{ij}^{coll} \\ \dot{\mathbf{v}}_j = \mathbf{v}_j + \frac{1+\varepsilon}{2}\mathbf{v}_{ij}^{coll} \end{cases} \quad (4.50)$$

where ε is the collision ratio ($0 \leq \varepsilon \leq 1$) and $\dot{\mathbf{v}}_i$ is the velocity of particle i after the collision with particle j . To do so, for the fluid particles in the free-surface region ($j, i \in \mathbb{F} \cup \mathbb{B}$) if the collision conditions are satisfied ($r_{ij} \leq 0.90l_0$ & $\mathbf{v}_{ij} \cdot \mathbf{r}_{ij} < 0$), we calculate the collision velocity ($\mathbf{v}_{ij}^{coll} = (\mathbf{v}_{ij} \cdot \mathbf{e}_{ij})\mathbf{e}_{ij}$) and summate the velocity variations of each colliding particle i and j ($\delta\mathbf{v}_i = -\frac{1+\varepsilon}{2}\mathbf{v}_{ij}^{coll}$ and $\delta\mathbf{v}_j = +\frac{1+\varepsilon}{2}\mathbf{v}_{ij}^{coll}$ where in this study, $\varepsilon = 0.5$). Hence, in the free-surface region ($i \in \mathbb{F} \cup \mathbb{B}$), the PC method updates the velocity of the particles colliding with each other, while the Corrected PS algorithm regulates particles in the tangential direction to prevent the tensile instability.

It should be highlighted that the PC method conserves the total linear momentum of the system while indirectly repositions particles on the basis of the collision velocity (i.e. Since the mass of particles remains constant, only the momentum moves from particle i to particle j) [75]. However, the PS approach violates the momentum conservation of the system [50]. Since $\delta\mathbf{r}_i < 0.05l_0$ in each time step of the numerical test cases, we ignore the velocity and density changes due to the particle shifting to keep the particle number density invariant as we reposition particles according to Eq. (4.48) [130, 155].

Eventually, the proposed particle regularization technique modifies the position and velocity vectors of the fluid particles by $\dot{\mathbf{r}}_i = \mathbf{r}_i + \delta\mathbf{r}_i$ (for $i \in \mathbb{F} \cup \mathbb{B} \cup \mathbb{I}$) and $\dot{\mathbf{v}}_i = \mathbf{v}_i + \delta\mathbf{v}_i$ (for $i \in \mathbb{F} \cup \mathbb{B}$), respectively. Further, the CPS technique includes the solid boundary particles in detecting the free-surface region and calculating the shifting vector of the fluid particles. In summary, we represent the Corrected PS approach in the context of MPS, hereafter denoted as (CPS), by implementing the following items:

- (I) A new conservative equation for the particle shifting vector (Eq. (4.29)) with the kernel function surmounting the tensile instability issue derived from the kernel derivative function.
- (II) A non-local normal vector for the free-surface layer particles (Eq. (4.49) for $i \in \mathbb{B}$) determined by the free-surface neighbor particles ($j \in \mathbb{F}$) to improve the accuracy of PS in cancelling the particles' diffusion in the normal direction to the free-surface.
- (III) Applying the particle shifting without any modification by the free-surface normal vector in the free-surface vicinity layer ($i \in \mathbb{B}$), if the particle shifting vector (Eq. (4.40)) is in the opposite direction to the free-surface, i.e.:

If $i \in \mathbb{B}$ & $\hat{\mathbf{n}}_i \cdot \delta \mathbf{r}_i < 0$, then $\delta \mathbf{r}_i = -F_i \nabla C_i$ as if $i \in \mathbb{I}$

- (IV) Appending the pair-wise Particle Collision (PC) method to the Corrected PS (denoted as CPS + PC) to eliminate the possible tensile instability in the free-surface region ($i \in \mathbb{F} \cup \mathbb{B}$) with the highly dynamic deformations and negative pressure fields.

Figure 4.4 summarizes the equations and correction techniques in the CPS+PC method. We discuss the effectiveness of this particle regularization technique in the stability of the free-surface region and the interior part of the fluid domain in the following section 4.5.

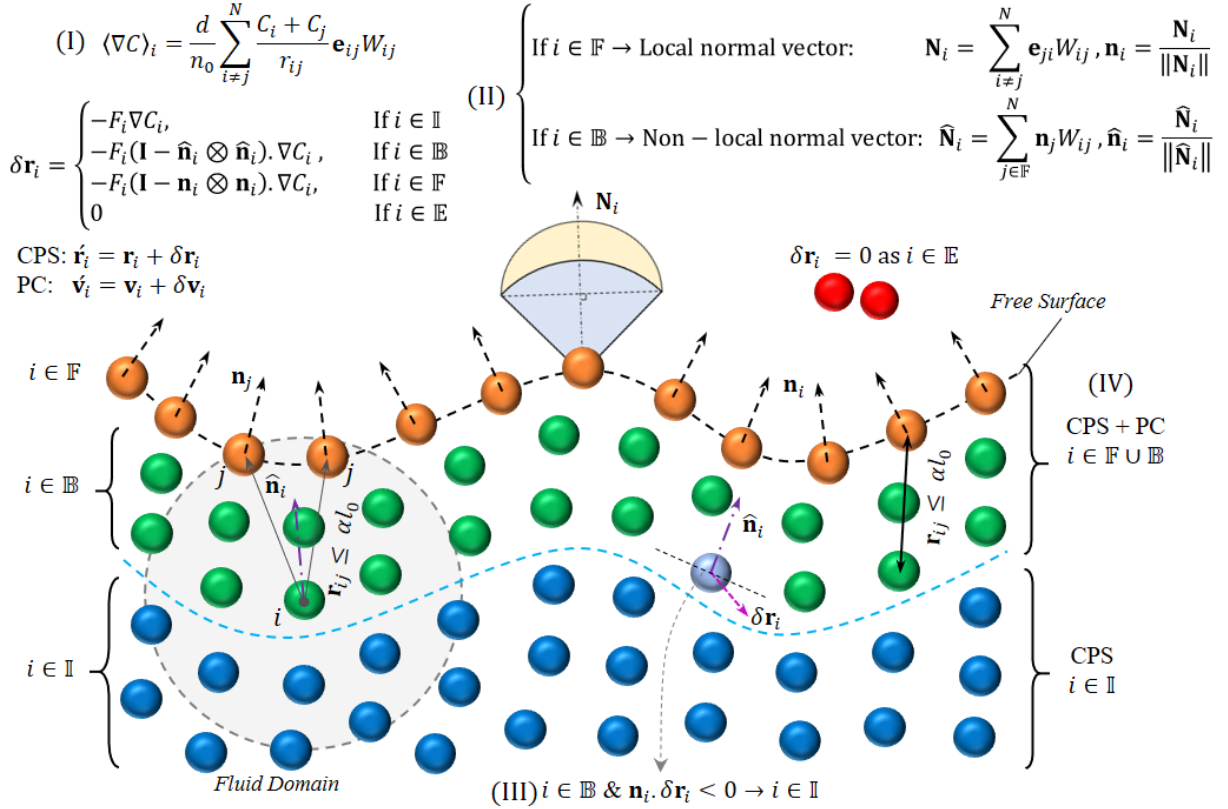


Figure 4.4 Sketch of the Corrected Particle Shifting algorithm

4.5 Numerical Results and Discussions

Here, we denote the enhanced WC-MPS model which employs the conservative pressure gradient (Eq.(4.23)) and its conjugate form of the continuity equation (Eq. (4.39)), as the

Conservative WC-MPS model. By activating the diffusive term inside the continuity equation, the model is denoted as the Conservative WC-DMPS model.

To validate and evaluate the enhanced WC-MPS model, we simulate four classical free-surface flow benchmarks including (4.1) hydrostatic pressure tank, (4.2) elliptic water drop, (4.3) rotating square patch, and (4.4) water dam break. The first two cases deal with the positive pressure fields without and with deformations, respectively. The third test case is highly deformative and requires overcoming the tensile instability due to the dominant negative pressure field. Considering all the improvement techniques, we simulate and validate the two-dimensional water dam break (the fourth test case) to illustrate the robustness of the proposed schemes in handling such a complex free-surface flow. The characteristics of the benchmark cases are presented as follow:

1. *Hydrostatic pressure tank*

With the particle arrangement 100×100 ($l_0 = 0.002$ m), we simulate a steady tank filled with water ($\rho = 1000$ kg/m³) as a two-dimensional problem to validate the stability of the numerical model in predicting the linear pressure field. A hydrostatic initial pressure field is assigned (Figure 4.5-a). The simulation is done for two seconds. The prediction-correction time integration scheme is employed and the CFL coefficient and the reference speed of sound are set to 0.5 and $10\sqrt{2gH} \cong 20$ m/s, respectively. We plot the pressure contours and the time evolution of local pressure at the midpoint of the steady reservoir (M) to validate and compare with the theoretical hydrostatic pressure (i.e. $p_{theo.} = \rho gh_M$). In this test case, we adopt the initial Cartesian (cubic) and the hexagonal particle distributions to evaluate their effects on the stability and convergence of the results.

2. *Elliptic water drops*

A circular water drops under the initial velocity field, $\mathbf{v}_0 = (-w_0x, w_0y)$, stretches in the y -direction preserving the elliptical shape (i.e. ab remains equal to 1) in absence of external forces and energy dissipation (i.e. $\mu = 0$) [47]. Because of its simplicity and the availability of the analytical solution [156], this case has been popular for the validation of particle methods (e.g., [48, 60, 157]). The irrotational initial velocity forms a positive pressure field within the bubble (Figure 4.5-b). We simulate the time evolution of the water bubble with radius 1.0 m and the initial particle distance 0.01 and 0.02 m (i.e. $R/l_0 = 100$ and 50). In this test case, the second-order Symplectic time integration scheme solves the system of equations and the CFL coefficient and the reference speed of sound are set to 0.6 and $15Rw_0$, respectively.

We evaluate the impact of the proposed enhancements achieved by employing the diffusive term in the continuity equation (the Conservative WC-DMPS model) and the Corrected PS approach on the time evolution and the pressure field. We initially allocate the fluid particles on the hexagonal lattice (instead of adopting the packing algorithms used in [3, 7] or the damping technique implemented in [158]) to eliminate the noise that the initial fluid particle rearrangement produces in the Cartesian configuration. Accordingly, we will be able to solely study the effectiveness of the proposed enhancement techniques.

3. *Rotating square patch of fluid*

The square patch of an inviscid fluid ($L = 1.0$ m) rotates by the initial angular velocity ($\omega_0 = 1.0 \text{ s}^{-1}$). Similar to the water drops test case, the fluid particles are initially located on a hexagonal lattice to avoid the initial particle rearrangement ($l_0 = 0.005$ m where $L/l_0 = 200$) and their initial pressure is assigned by solving Poisson's Pressure Equation ([2]) (Figure 4.5-c). We set the reference sound speed and the CFL coefficient to $5L\omega_0$ and 0.2, respectively. The second-order Symplectic time integration scheme is employed. The main characteristics of this test-case are the negative pressure field (due to the centrifugal force) and the extreme fluid domain distortion. At the four corners of the square, in the absence of any external force, the gradient of pressure should remain zero and accordingly the four vertices preserve their initial velocity [2]. This is a popular and challenging benchmark case for particle methods (due to extreme deformations) (e.g., [3, 74, 129, 130]). We simulate this case to evaluate the effects of the newly proposed CPS + PC, pressure gradients, and diffusive term on tensile instability and the pressure field. Since no analytical solution for this benchmark is available, we compare the time evolution of the free-surface and the pressure at the center of the rotating fluid (point A) with the numerical results of the Lagrangian Finite Difference Method (LFDM) supplied with the Boundary Element Method (BEM) [2, 156] and the δ^+ -SPH models [3, 130].

4. *Water dam break*

Dam break is a widely used test case for particle methods (e.g., in [131, 142, 155, 159]). In this test case, the dam gate is suddenly removed, the water column collapses and flows on the horizontal bed then impacts the right wall and forms a returning wave. The large free-surface deformations and the high flow velocity are the main characteristics of the dam break problem making its simulation challenging. We set the dam break setup with $H = 0.5B$ and $L = 5.366H$ (Figure 4.5-d) to simulate the water collapse evolution and determine the effectiveness of the enhancement techniques in removing the pressure noise. The initial Cartesian

(square) particle distribution with $H/l_0 = 60$ and 100 resolutions is implemented. With the Symplectic time integration scheme, the reference sound speed and the CFL coefficient are set to $10\sqrt{gH} = 25 \text{ m/s}$ and 0.5, respectively. The wave front propagation and the pressure parameter probed on the right wall (at $S1$ in Figure 4.5-d) are validated with the experimental results of Lobovský et al. [4].

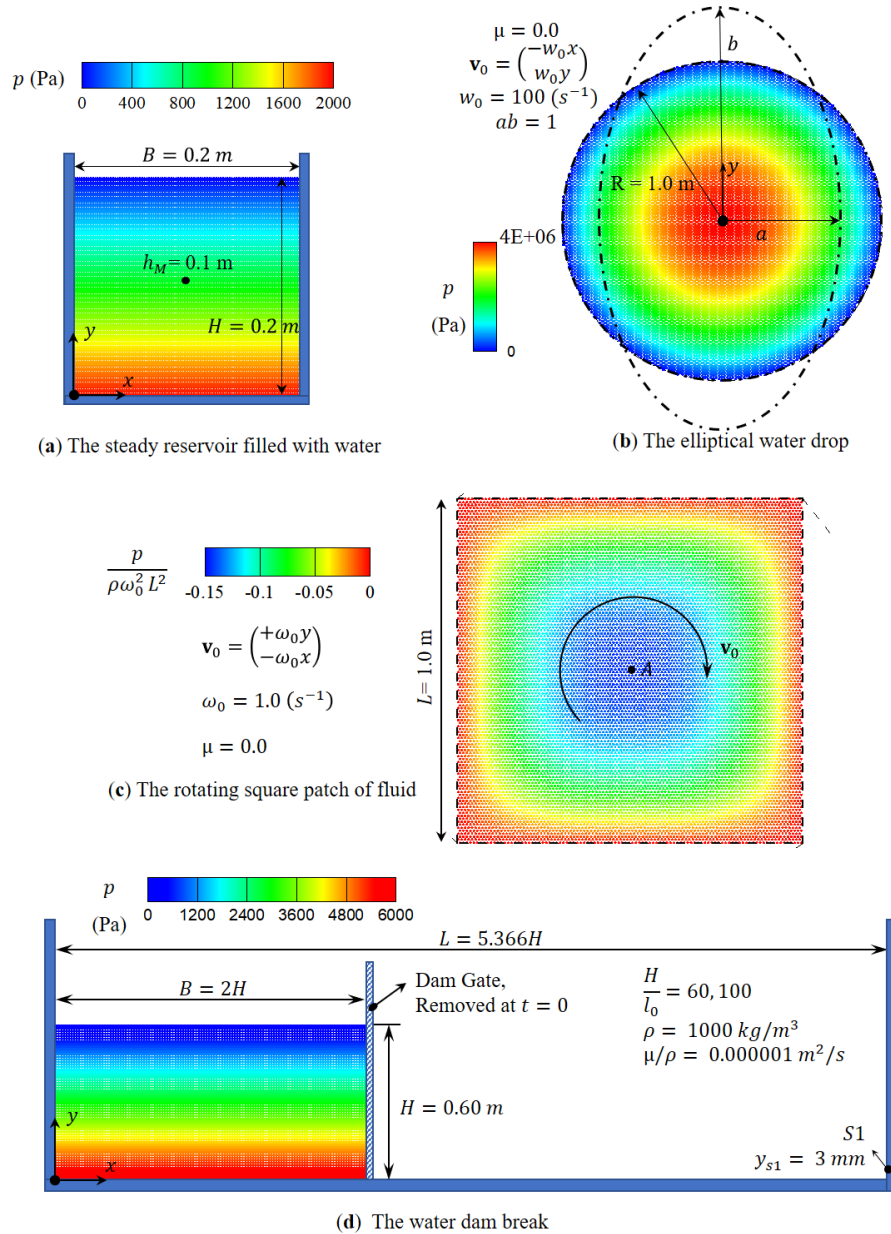


Figure 4.5 The initial setups of the hydrostatic pressure (a), the elliptical water drop (b), the rotating square patch of fluid (c) and the water dam break test-cases (d). The colour contours represent the initial pressure fields.

4.5.1 Hydrostatic pressure

We simulate the hydrostatic pressure in a steady reservoir filled with water to evaluate the stability of the Conservative WC-MPS model by implementing the new pressure gradient equation (Eq. (4.23)) and the continuity equation for the particle number density calculation (Eq. (4.39)).

Using the proposed antisymmetric pressure gradient formulation activates a repulsive force between the fluid particles leading to an accurate pressure field and a speedup in the convergence stability (Figure 4.6). In Figure 4.6, comparing case (a) vs (b) shows that the continuity equation (as the substitute for Eq. (4.5)) and the assigned initial pressure field reduce the errors of the kernel truncation at the fluid free-surface resulting in a uniform particle distribution and acceleration of the pressure convergence at the midpoint (graph (c)). In the original WC-MPS model the kernel summation equation (4.5) and the pressure gradient (4.16) with added $\Delta p = p_i - \hat{p}_i$ term (where $\hat{p}_i = \min(p_i, p_j)$ and $j \in \text{neighbor of } i$) approximate n_i and ∇p_i , respectively. This model shows instabilities (before $t = 1.0$ second) at the free-surface and the pressure field as it violates the conservation feature (Figure 4.7-a & graph (d)). By applying the pair-wise particle collision technique to the original WC-MPS model, the model becomes numerically stable (Figure 4.7-b), however, the pressure oscillates at the mid-point and does not converge to the theoretical result before $t = 2.0$ s (Figure 4.7-graph (d)). The Conservative WC-MPS model reaches the stable pressure field in less than 1.0 s and the proposed diffusion term (the Conservative WC-DMPS model with $\delta_{MPS} = 0.1$ which is equivalent to $\delta_{SPH} = 0.03$) eliminates the noise in the pressure field originated from the fixed Cartesian boundary particles arrangement (Figure 4.7-c).

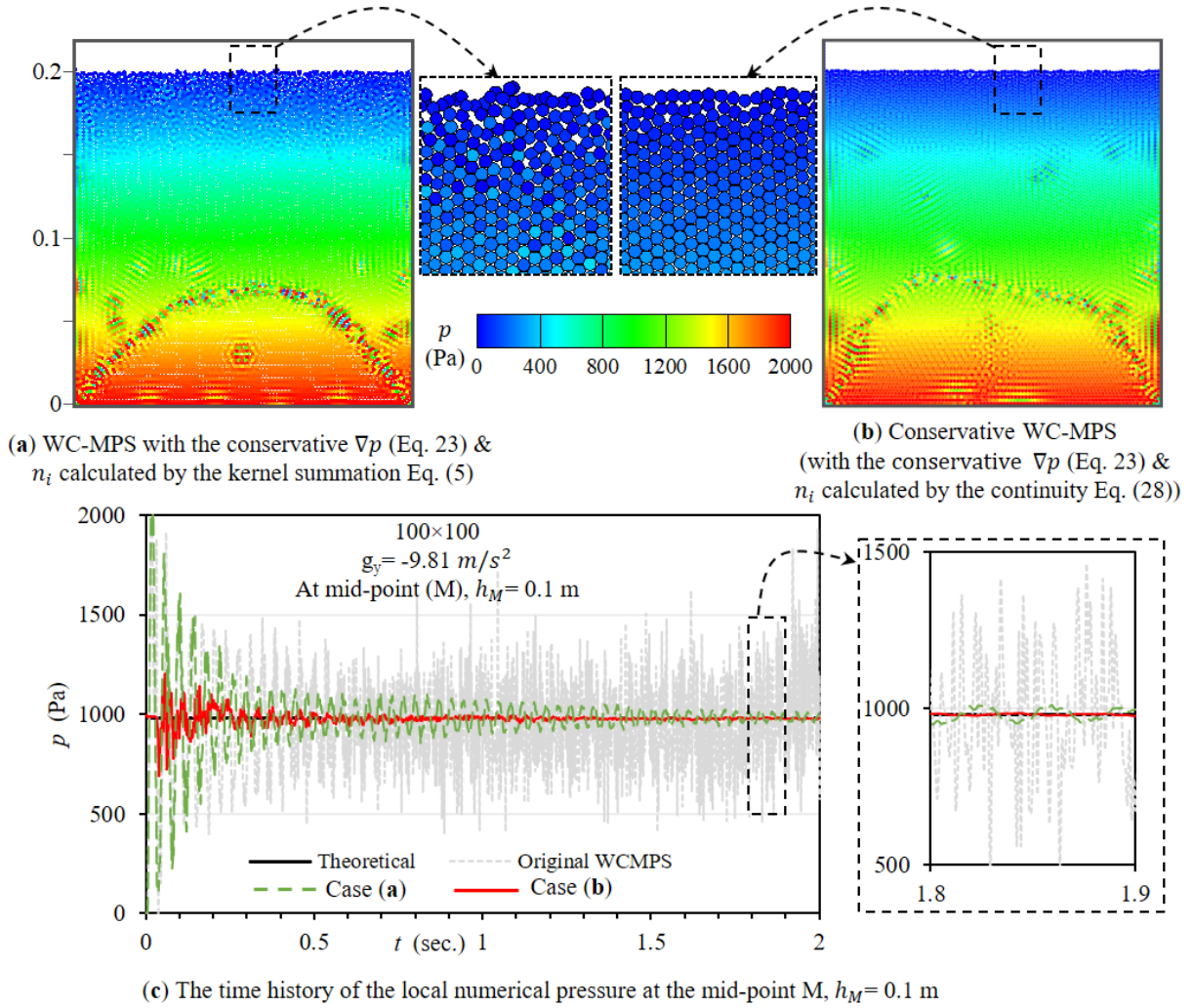


Figure 4.6 The hydrostatic pressure contour; (a) The WC-MPS model with the conservative ∇p (Eq. 23) and the kernel summation equation (4.5) for calculating the particle number density, (b) with the Conservative WC-MPS model. The graph (c) represents the pressure parameter at the center of the reservoir (Mid-point, M) over the simulation time ($t = 2$ Seconds). In the original WC-MPS model (the gray dash line), Eq.(4.5) updates the particle number density and the gradient of pressure is approximated by Eq. (4.16) with added particle stabilizing term $\Delta p = p_i - \hat{p}_i$.

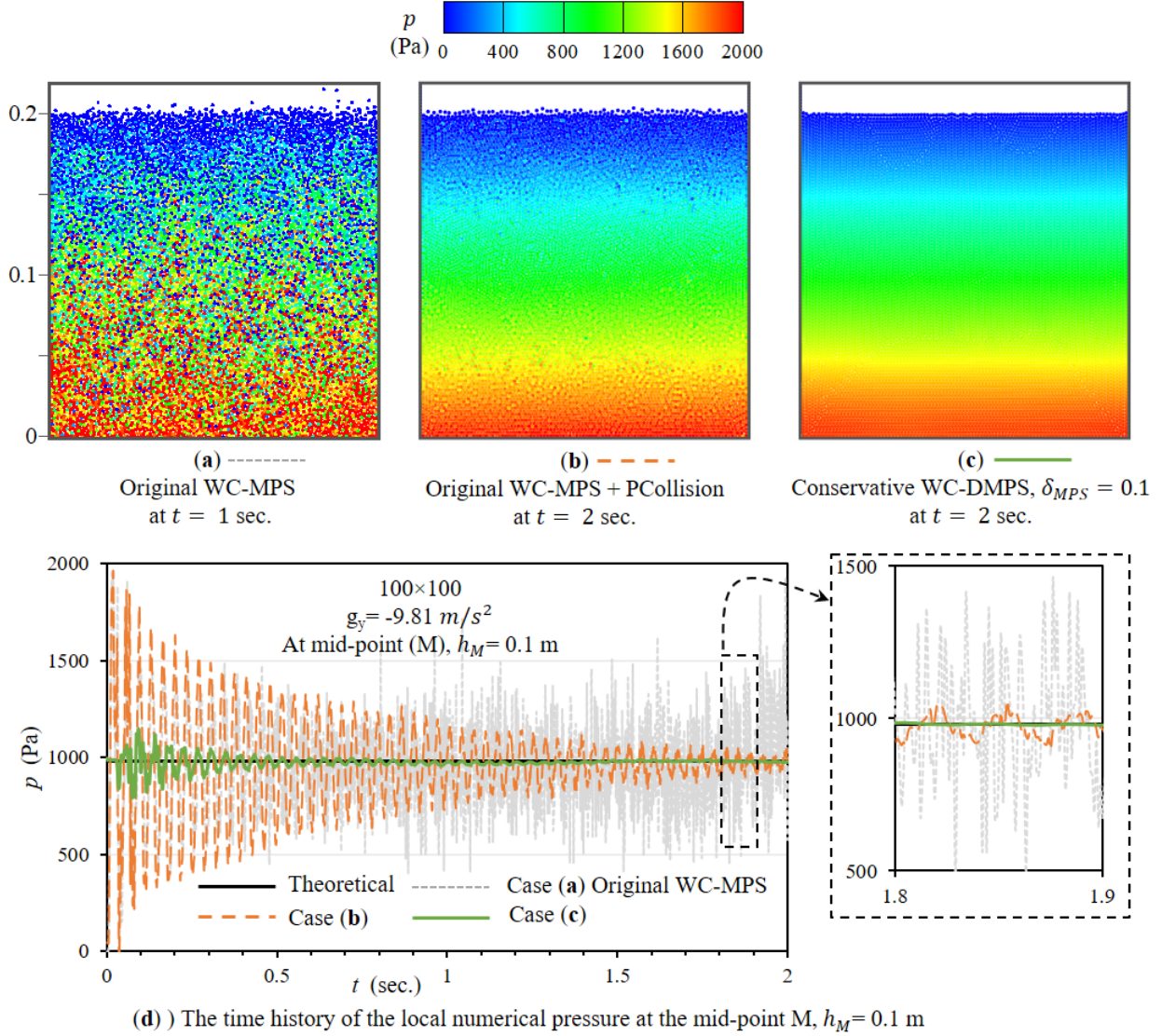


Figure 4.7 The hydrostatic pressure contour; (a) the original WC-MPS, (b) the original WC-MPS + the pair-wise particle collision approach and (c) the Conservative WC-DMPS (using the conservative pressure gradient Eq. (4.23) and the added diffusive term to the continuity equation (4.39) with $\delta_{MPS} = 0.1$). The time history of the pressure at the mid-point for each case is plotted in the graph (d).

In a similar setup, we initially allocate the particles on a hexagonal lattice where the energy of the system would be at the minimum state and no transition from the cubic lattice to the hexagonal-close-packed occurs [49]. In this test case, without the diffusion term ($\delta_{MPS} = 0.0$) or the particle regularization techniques, the Conservative WC-MPS model gives a noise-free

and stable hydrostatic pressure field (Figure 4.8-a). Since the fluid particles are in the stable isotropic particle arrangement, the initial hydrostatic pressure assigned remains constant with no oscillation at the mid-point of the tank in the absence of any external disturbance (Figure 4.8- graph (c)).

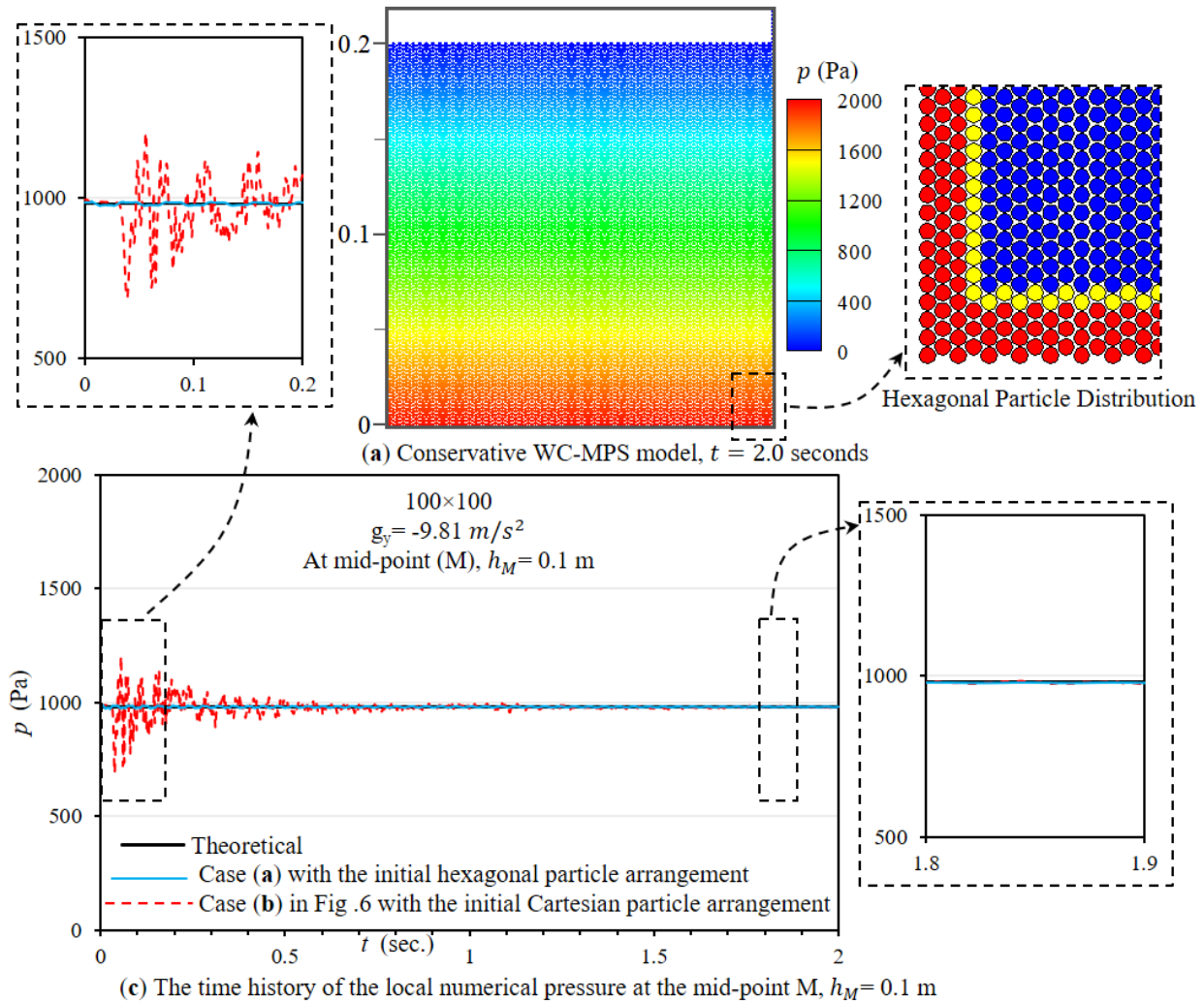


Figure 4.8 The role of the initial hexagonal particle distribution in the Conservative WC-MPS model; (a) Conservative WC-MPS model with the initial hexagonal particle distribution (b) Conservative WC-MPS model with the Cartesian particle distribution (same as the case (b) in Figure 6). The evolution of the pressure at the mid-point of the steady tank is represented in the graph (c) for the hexagonal particle distribution (the blue continues line) and the Cartesian particle distribution (the red dashed line).

4.5.2 Elliptical water drops

In the second test case, we model the time evolution of the water drops deformed by an irrotational initial velocity field. Figure 4.9 compares the results of the Conservative WC-MPS models with and without the diffusive term and the CPS technique (b & a). Even without the improvement techniques, the proposed Conservative WC-MPS model provides stable and uniform particle arrangement obeying the analytical deformation of the elliptical bubble (for $tw_0 \leq 1.2$). Nevertheless, undesirable pressure fluctuations are observed (Figure 4.9-a). Activating the diffusion term in the particle number density calculation ($\delta_{MPS} = 0.2$ equivalent to $\delta_{SPH} = 0.08$) and the CPS regularization technique eliminates these high-frequency fluctuations (Figure 4.9-b).

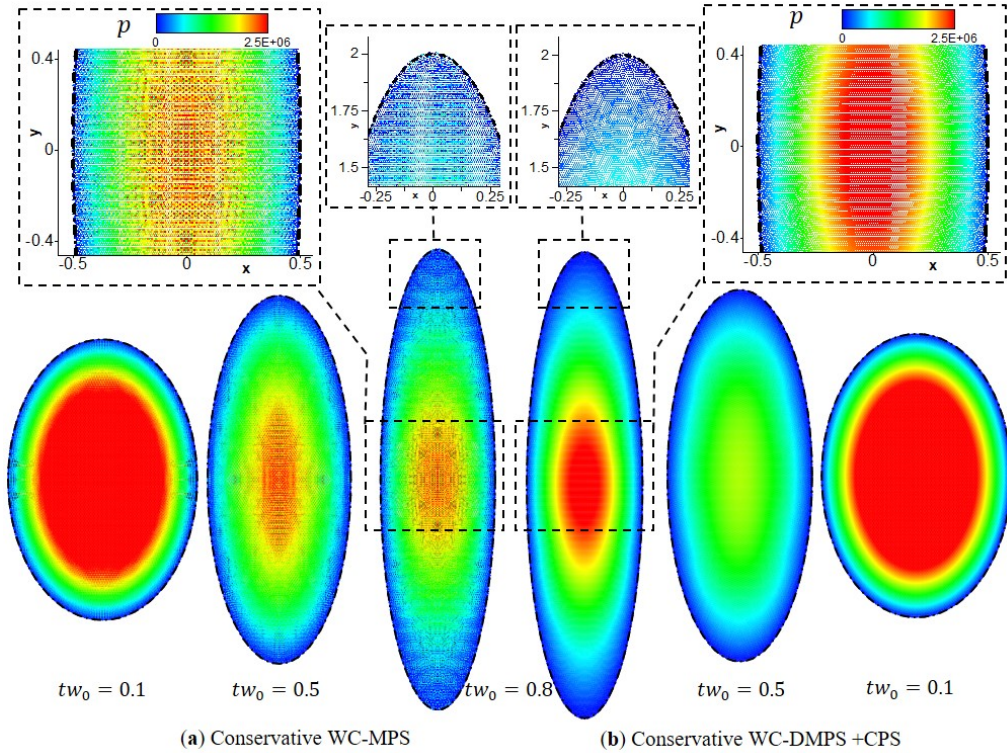


Figure 4.9 The pressure field and the evolution of the water drop at $tw_0 = 0.1, 0.5$ and 0.8 ; (a) the Conservative WC-MPS model vs (b) the Conservative WC-DMPS with $\delta_{MPS} = 0.2$ + CPS algorithm. The black dash-dot line represents the analytical deformation of the elliptical bubble.

The pressure fields shown in Figure 4.10 illustrate that the particle shifting approach alone is incapable of reducing the approximation errors (a vs b), while the diffusive term (with $\delta_{MPS} = 0.2$) effectively removes the pressure noise (c). However, the CPS technique accompanied by

the diffusive term represents a more uniform particle arrangement, especially in the area close to the free-surface, where the kernel support truncates (Figure 4.10-c vs d). Moreover, applying the particle shifting algorithm is required to surmount the particle clustering for the long-term stability of the simulation (Figure 4.11-a vs b, at $tw_0 = 1.7$). Without the CPS, the tensile instability becomes dominant affecting the pressure field smoothness and the water drops stability (Figure 4.11-graph (c) in which p_m is the local numerical pressure at the center of the water drops).

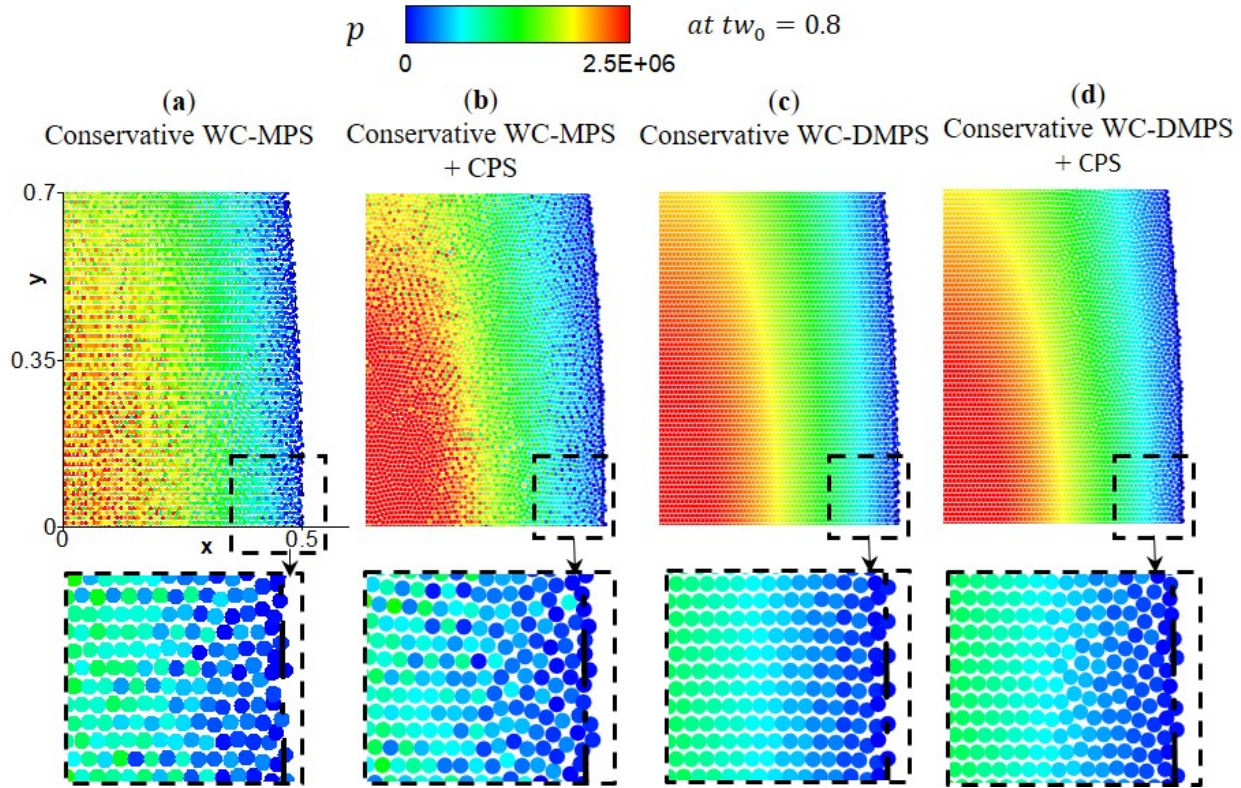


Figure 4.10 The particles distribution and pressure field of the water drop test case at $tw_0 = 0.8$ for the four different strategies (case **a-d**).

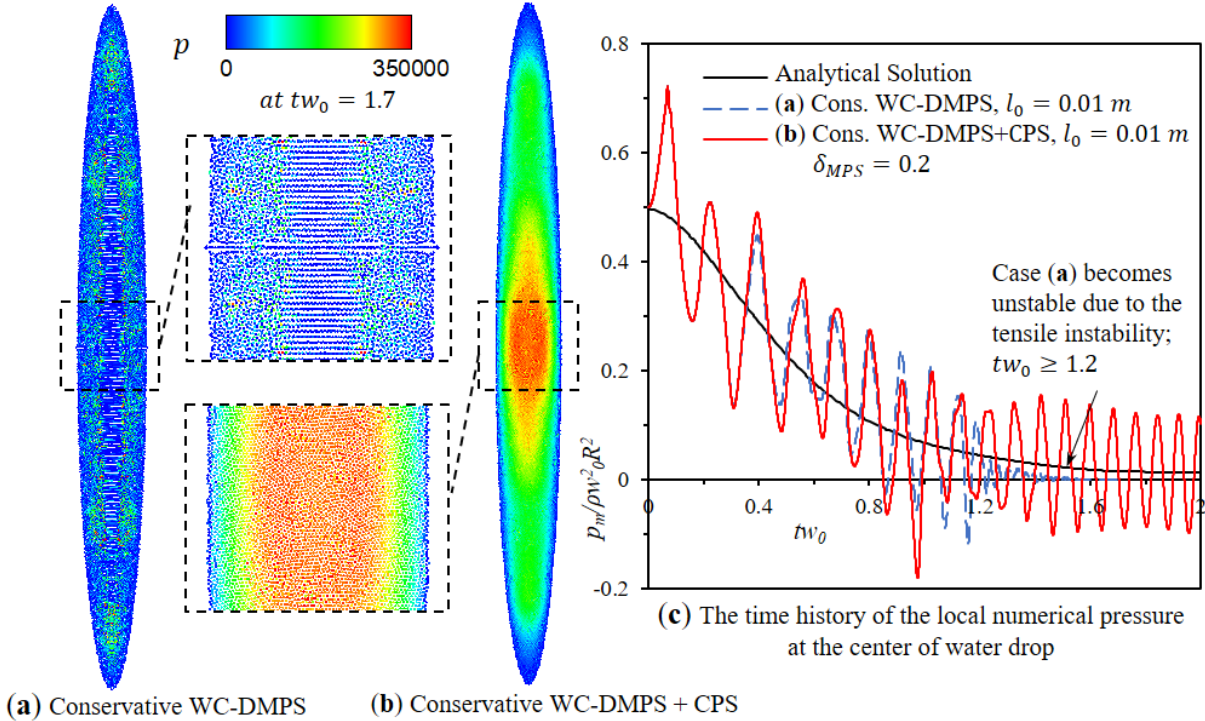


Figure 4.11 The effectiveness of the CPS algorithm for the long-term stability of the model and the tensile instability elimination: The water drop evolution and pressure contour at $tw_0 = 1.7$ without and with the CPS algorithm (Case (a) & (b)). The time history of the local numerical pressure at point A without any frequency filtering is represented in the graph (c) ($c_0 = 15Rw_0$).

For the quantitative comparison, we have plotted $(p_m - p_{Anal.}) / \rho w_0^2 R^2$ with respect to tw_0 in Figure 4.12, where $p_{Anal.}$ is the analytical pressure at the domain center. The figure shows the effectiveness of the diffusive term in eliminating the high-frequency pressure noise. One should note that the low-frequency pressure oscillations around the analytical solution (Figure 4.11-graph (c) and Figure 4.12) originates from the compressibility allowed by the numerical model since the exchange between the mechanical energy and the internal energy exists throughout the simulation [160]. The reference sound speed controls the frequency of this pressure oscillation. By selecting $c_0 = 15Rw_0$ (where Mach number < 0.1) the pressure signal propagates faster than $\|\mathbf{v}_{max}\|$ not affecting the fluid flow [2]. To show the role of the proposed diffusive term in removing the high-frequency pressure fluctuations we presented the results without any frequency filtering and data averaging.

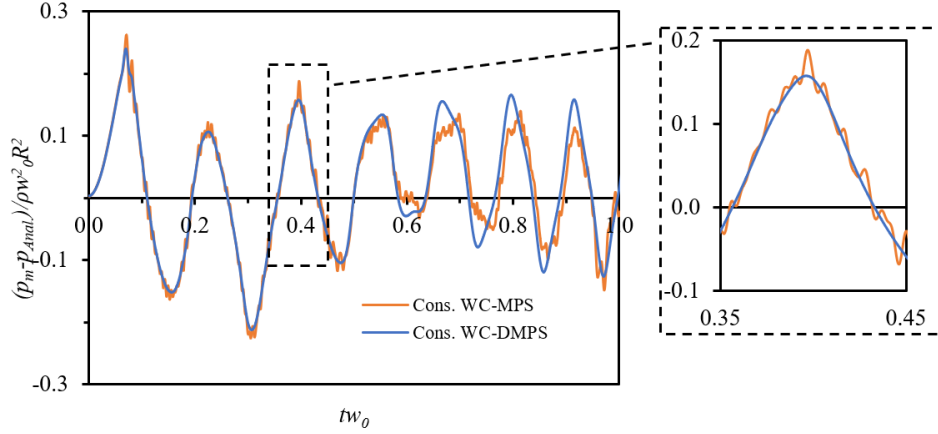


Figure 4.12 The time history of local $(p_m - p_{anal.})/\rho w_0^2 R^2$ at the domain center without any frequency filtering; (a) Conservative WC-MPS ($\delta_{MPS} = 0$) vs (b) Conservative WC-DMPS with $\delta_{MPS} = 0.2$ ($c_0 = 15Rw_0$).

Moreover, the time evolution of the semi-minor, a , and semi-major, b , axes of the drop (Figure 4.13), confirms the compatibility of the numerical and analytical results. Table 4.5.2 summarizes the Root-Mean-Squared Error (RMSE) of a , b and ab variables for the Conservative WC-MPS with $l_0 = 0.01$ m, and the Conservative WC-DMPS+CPS with $l_0 = 0.01$ m and $l_0 = 0.02$ m. Hence, adopting the improvement techniques as well as using a finer resolution, reduces the RMSE, showing a convergence.

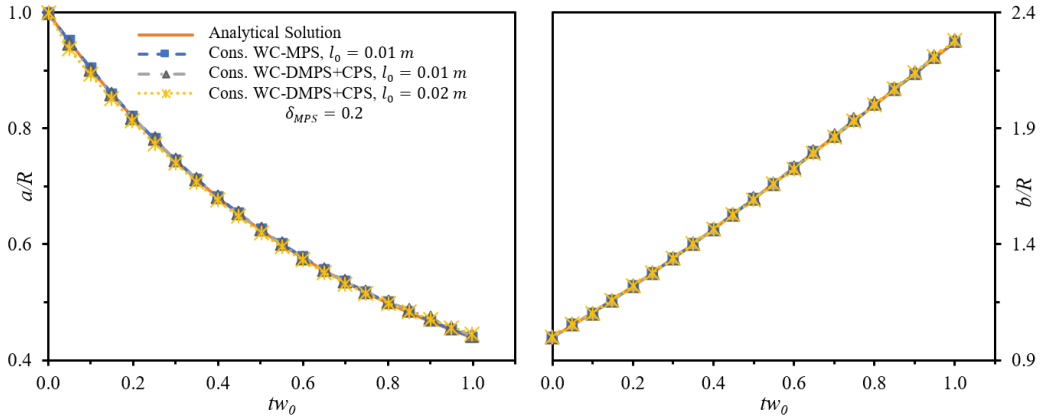


Figure 4.13 The time evolution of the semi-minor, a , and semi-major, b , axes of the elliptical water drop.

Table 4.1 The elliptical water drop; The Root-Mean-Squared Error of the semi-minor and semi-major axes and ab variables

Strategy	l_0 (m)	Root-Mean-Squared Error (RMSE) of		
		Semi-minor, a , axis	Semi-major, b , axis	ab
Conservative WC-MPS	0.01	1.349E-02	1.349E-02	3.166E-02
Conservative WC-DMPS+CPS, $\delta_{MPS} = 0.2$	0.01	9.382E-03	1.239E-02	1.979E-02
Conservative WC-DMPS+CPS, $\delta_{MPS} = 0.2$	0.02	3.018E-02	1.181E-02	4.557E-02

4.5.3 Rotating square patch of fluid

Dealing with the dominant negative pressure field for simulating the rotation of the initially square fluid patch, requires the particle stabilizing techniques to eliminate the fluid particle clustering. To do so, we implement the CPS algorithm for the whole fluid domain and the pair-wise PC method only for the free-surface layer of particles (the model is denoted as the CPS + PC algorithm). In this test case, we investigate the role of the different pressure gradient formulations. This includes the conservative pressure gradient (Eq. (4.23)), the non-conservative pressure gradient (Eq. (4.16)) and the non-conservative higher-order pressure gradient (Eq. (4.17)). For stability purposes, we use the conservative pressure gradient equation for the fluid particles detected as the free-surface particles ($i \in \mathbb{F} \cup \mathbb{B}$) in the models with the non-conservative formulations (similar to the work of Duan et al. [60]). In all these cases, the continuity equation (4.39) approximates the particle number density for updating the pressure field.

Figure 4.14 compares the evolved fluid patch at $t\omega_0 = 1.08$ using the Conservative WC-MPS with and without implementing the diffusion term and the CPS+PC algorithm. The Conservative WC-DMPS ($\delta_{MPS} = 0.5$ equivalent to $\delta_{SPH} = 0.065$) shows tensile instability even with activating the pair-wise PC method for the whole fluid particles (Figure 4.14-a). Nonetheless, by implementing the CPS+PC algorithm without the diffusive term the simulation overcomes the tensile instability, although the pressure field still suffers from the approximation errors (i.e. the noisy pressure field exists) (Figure 4.14-b and Figure 4.15). Including the diffusive term results in a smooth pressure field (Figure 4.14-c). Moreover, the overall deformations of the fluid patch obtained via the enhanced WC-MPS models are in good agreement with the numerical simulation of [2] using the LFDM-BEM model (Figure 4.14-b & c and Figure 4.15).

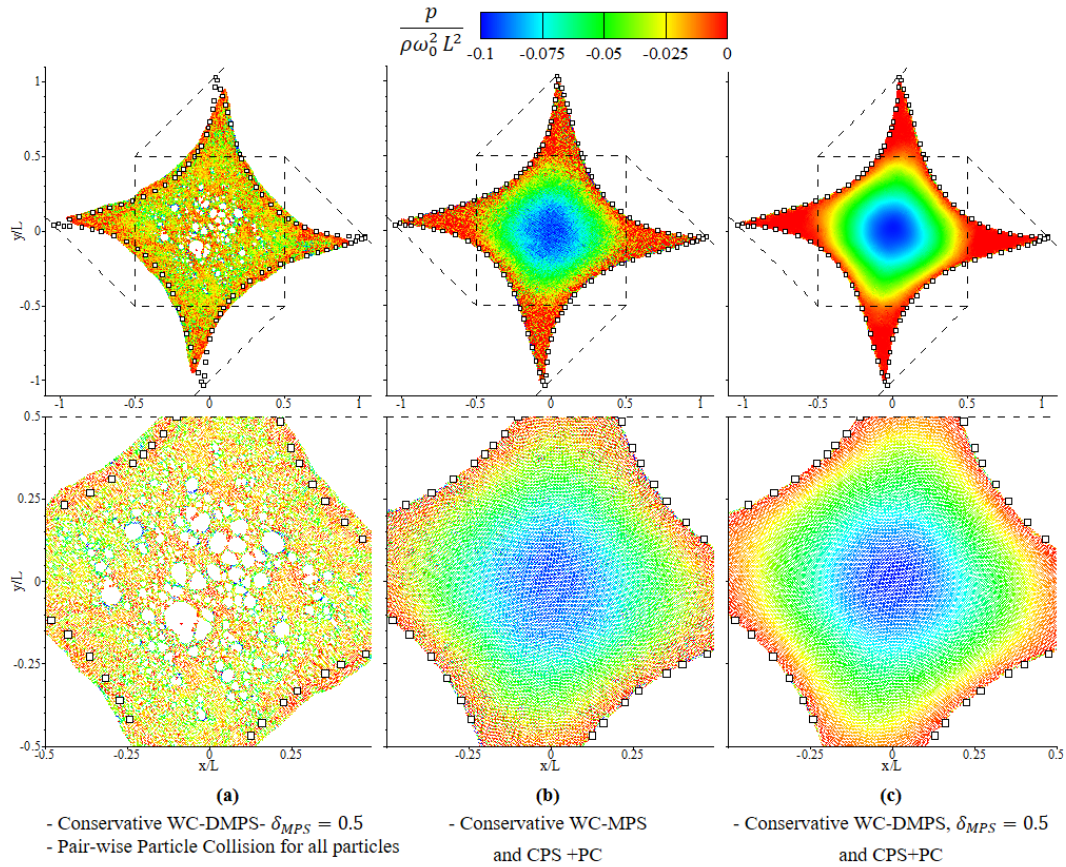


Figure 4.14 Evolution of the square patch of fluid at $t\omega_0 = 1.08$. The white squares represent the LFDM-BEM results extracted from [2].

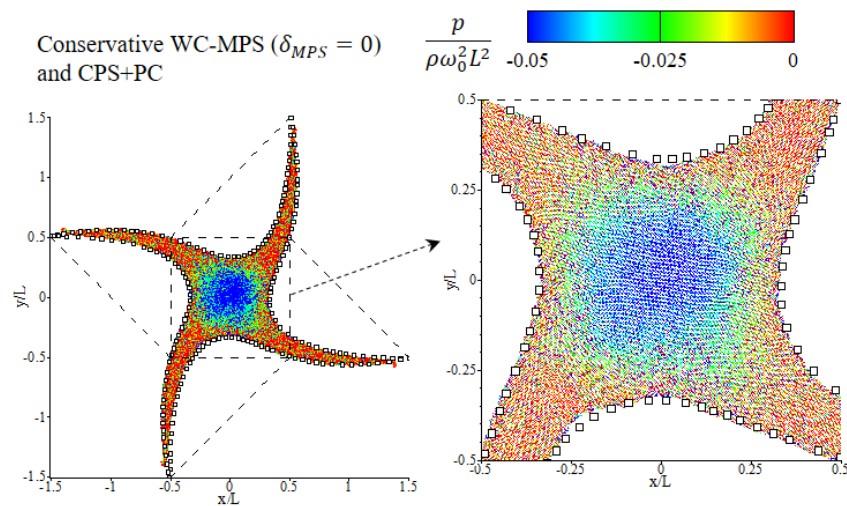


Figure 4.15 The square patch of fluid without the diffusive term at $t\omega_0 = 2.04$.

Since the initial centrifugal force causes a negative pressure field, the conservative pressure gradient equation simulates attractive forces instead of the desirable repulsive force between two fluid particles. Nevertheless, the CPS+PC algorithm as an effective regularization technique controls this issue and forms a uniform arrangement of the fluid particles eliminating the tensile instability (Figure 4.16-a). The WC-DMPS models using the standard pressure gradient formulations (with and without the corrective matrix) as well as the proposed conservative pressure gradient equation all result in the smooth pressure fields. This is since the CPS+PC algorithm is activated in all three cases (case (a-c) in Figure 4.16). Figure 4.17 compares the time history of the local pressure at the domain center (without any frequency filtering or data averaging) using the different pressure gradient formulations versus the numerical results of the δ^+ -SPH [130], showing a good compatibility. Figure 4.18 shows the robustness of the proposed WC-DMPS+CPS+PC model for simulation of the extremely deformed fluid patch at the late stages (at $t\omega_0 = 4.0$, 6.0 and 8.0).

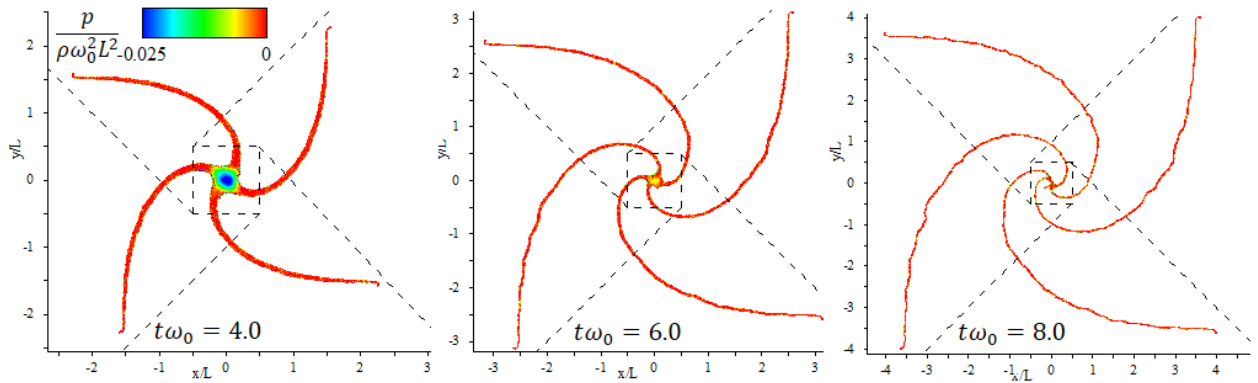


Figure 4.18 The robustness of the proposed enhancement techniques in capturing large deformations (The long-term simulations of the case (a) in Figure 4.16).

The improvements achieved by the CPS algorithm in determining the normal vectors to update the particle shifting vector and eliminating the tensile instability among the free-surface particles are apparent in Figure 4.19. Both (a) and (b) test cases use Eq. (4.44) for calculating the shifting vector and the classification algorithm represented in Figure 4.3. In case (a) the CPS+PC method with all the proposed corrections is implemented. However, in case (b) the PC method is not applied and the local normal vector in the free-surface vicinity layer modifies the shifting vector (i.e. without corrections II and IV in section 4.4.4). Also, the fluid particles in the free-surface layer with the shifting vector toward the interior domain are not detected to be considered as the inner particles (i.e. without correction III). As shown

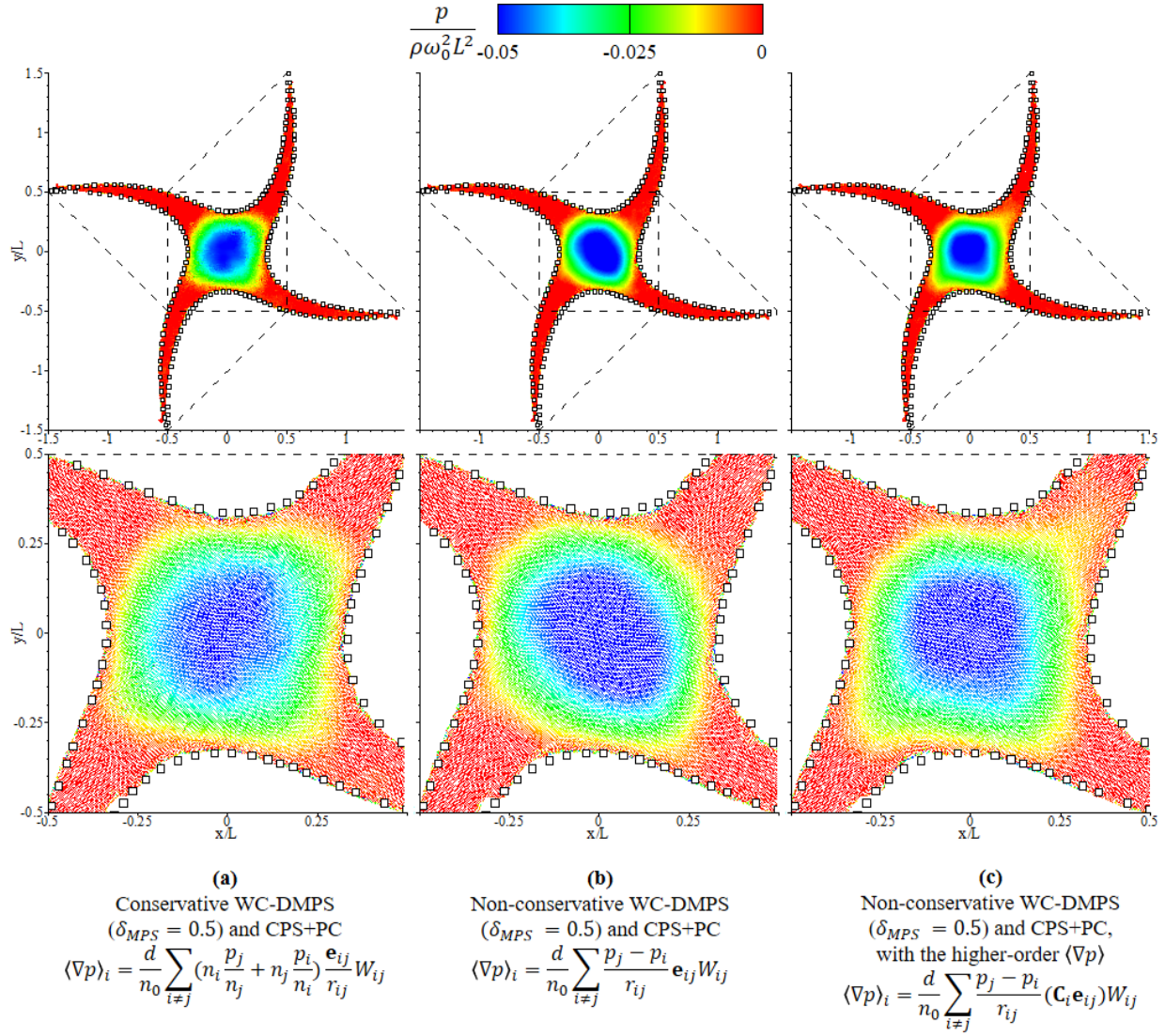


Figure 4.16 The square patch of fluid with different pressure gradient formulations at $t\omega_0 = 2.04$. The white squares represent the LFD-M-BEM model results extracted from [2].

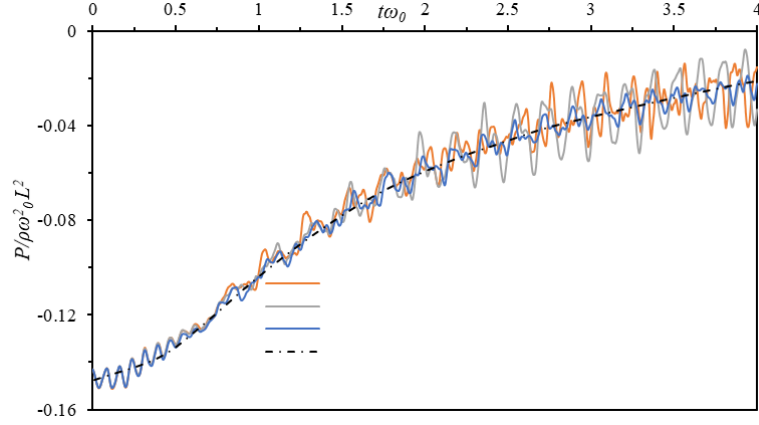


Figure 4.17 The local pressure at the domain center for the three strategies in Figure 4.16, without any frequency filtering and with $c_0 = 5L\omega_0$; **(a)** Conservative WC-DMPS, **(b)** Non-Conservative WC-DMPS and **(c)** Non-Conservative WC-DMPS with the higher-order $\langle \nabla p \rangle_i$ vs the δ^+ -SPH model [3] (In all three cases a-c the CPS+PC algorithm is activated.)

in Figure 4.19-b, without the modifications appended to the PS method the instability in the free-surface region leads to unphysical fluid fragmentations and the non-uniform normal vectors. However, the CPS+PC method surmounts these issues by representing uniform normal vectors and particle distributions in the free-surface region (Figure 4.19-a).

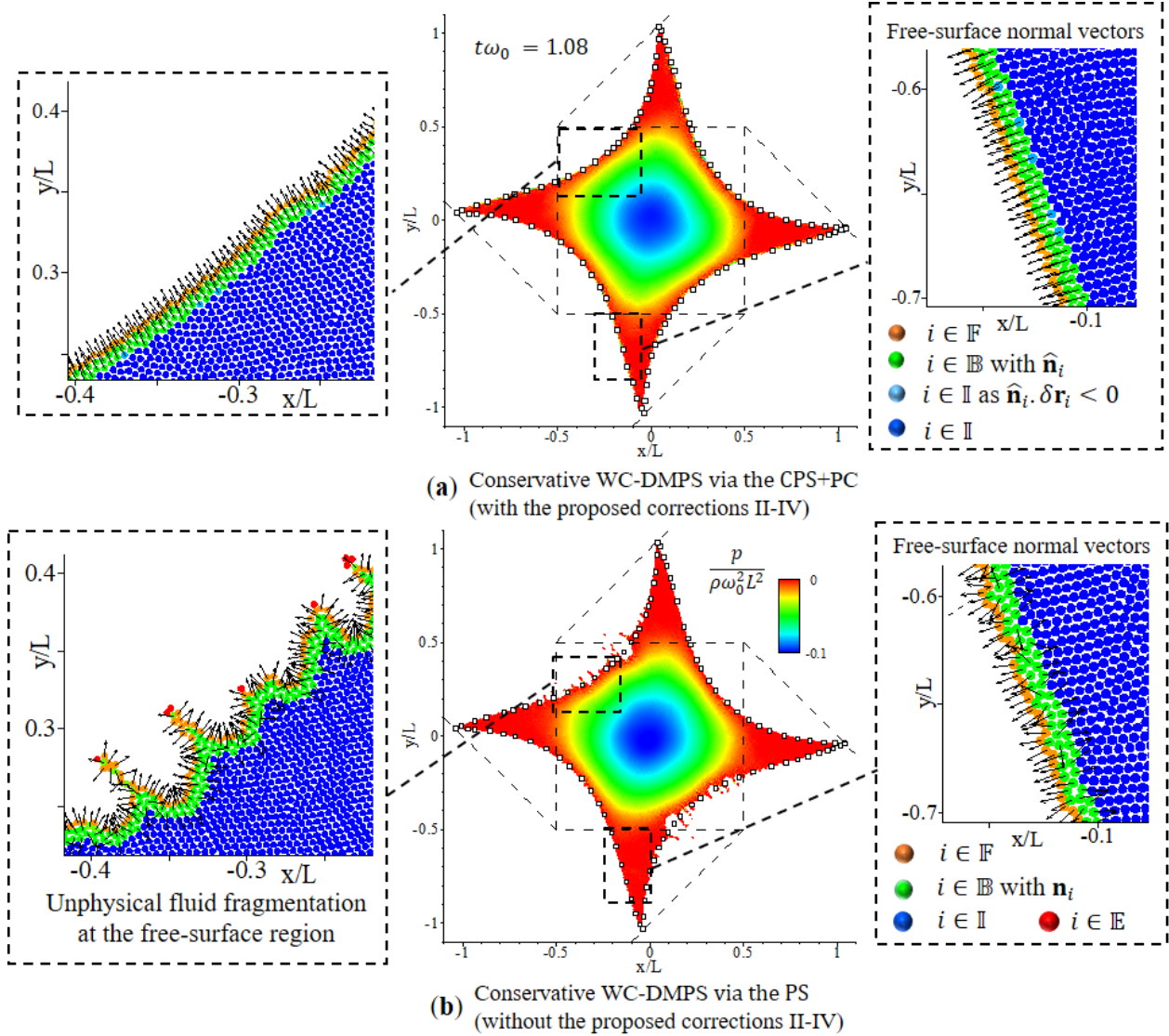


Figure 4.19 The square patch of fluid with (a) and without (b) the proposed corrections in the PS algorithm (i.e. the corrections II to IV), $re = 3.1l_0$. However, the other calculation conditions are the same as the case (c) in Figure 4.14.

4.5.4 Dam break

In the dam break test case, as the water flow impacts the right wall at $T = t\sqrt{g/H} \approx 2.5$, a plunging wave forms followed by a collapse at about $T \approx 6.5$. Figure 4.20 shows the snapshots of the evolution before and after the impact ($T = 1.62$ and 2.96), where the effectiveness of the proposed diffusive term in reducing the high-frequency pressure noise is well illustrated.

The model with the conservative pressure gradient, the continuity equation and the diffusive term ($\delta_{MPS} = 0.35$ which is equivalent to $\delta_{SPH} = 0.11$) represents a smooth pressure field, while the same model without the diffusive term suffers from the noisy pressure field (Figure 4.20-b vs a). To ensure the stability of the simulation in both test cases the CPS+PC algorithm is implemented.

Furthermore, to show the robustness of the particle stabilizing techniques we plot the evolution of the dam break forming the plunging wave at $T = 5.9, 6.5$ and 7.8 in Figure 4.21. Thanks to the stability achieved by the CPS+PC algorithm and the proposed diffusive term, the Conservative WC-DMPS model represents accurate flow evolutions and a smooth pressure field during the wave formations. A close snapshot of the wave at $T = 5.9$ confirms the tensile instability elimination and the uniform particle arrangement achieved by the developed WC-DMPS model (Figure 4.21).

Figure 4.22 shows the effectiveness of the CPS method for determining the free-surface normal vectors. Both (a) & (b) test cases have similar calculation conditions (Conservative WC-DMPS, $\delta_{MPS} = 0.35$) and $H/l_0 = 60$ and modify the shifting vectors calculated by Eq. (4.44) at the free-surface region. Nevertheless, unlike case (a) in which the local normal vector is used, case (b) employs the non-local normal vector. Also, in case (a) corrections III and IV are deactivated. As shown in Figure 4.22, the CPS+PC method represents accurate and uniform normal vectors required for modifying the shifting vector at the free-surface region.

Figure 4.23 provides a quantitative comparison between the numerical and experimental (from [4]) wave front propagation (with $H/l_0 = 60$ and 100) and the local pressure (for point $S1$). The results show good compatibility, specially for the wave propagation. One should note that the initial underestimation of the wave propagation can be related to the effects of the gate removal mechanism, which has been neglected in the numerical simulations. The local numerical pressure at point $S1$ is more oscillatory (comparing to those digitized from experiments) and the second pressure increase (related to back wave) has a slight delay (occurs at $T \approx 6.5$ instead of $T \approx 6.0$). Such discrepancy that can also be observed in the results of other single-phase particle models (e.g., SPH [65,142]), can be related to the slightly allowed compressibility, boundary effect, and absence of air-phase.

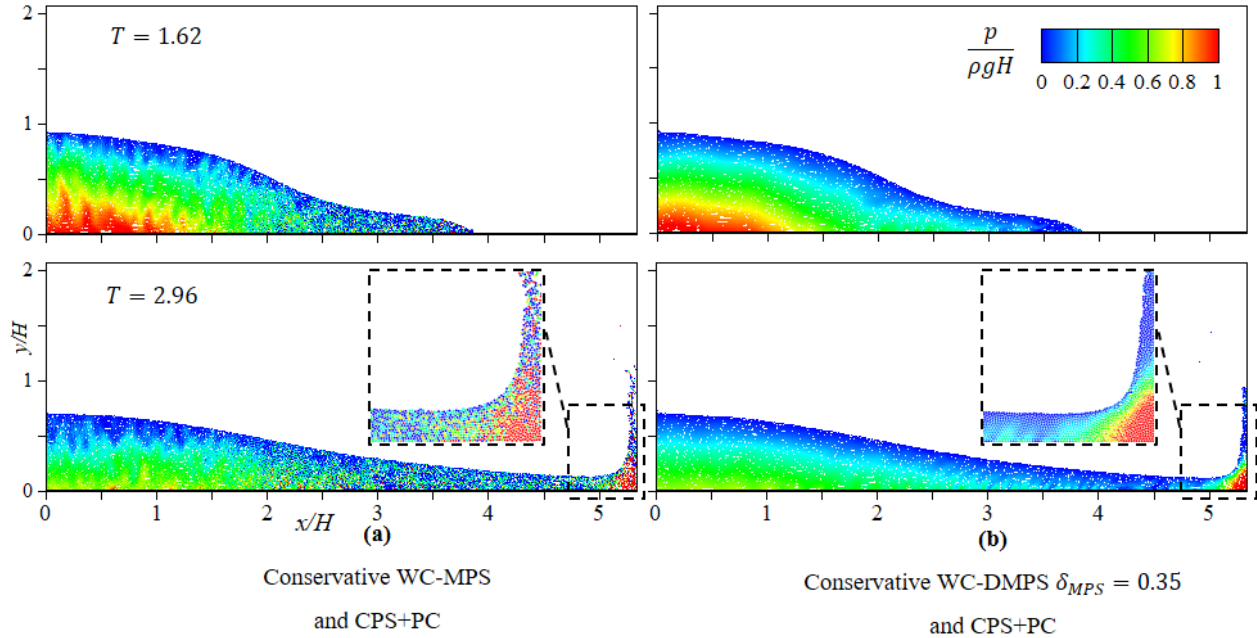


Figure 4.20 Water dam break at $T = t\sqrt{g/H} = 1.62$ and 2.96 , The Conservative WC-MPS model with and without the diffusive term (case (b) vs (a), respectively) where the CPS+PC algorithm is activated. ($H/l_0 = 100$)

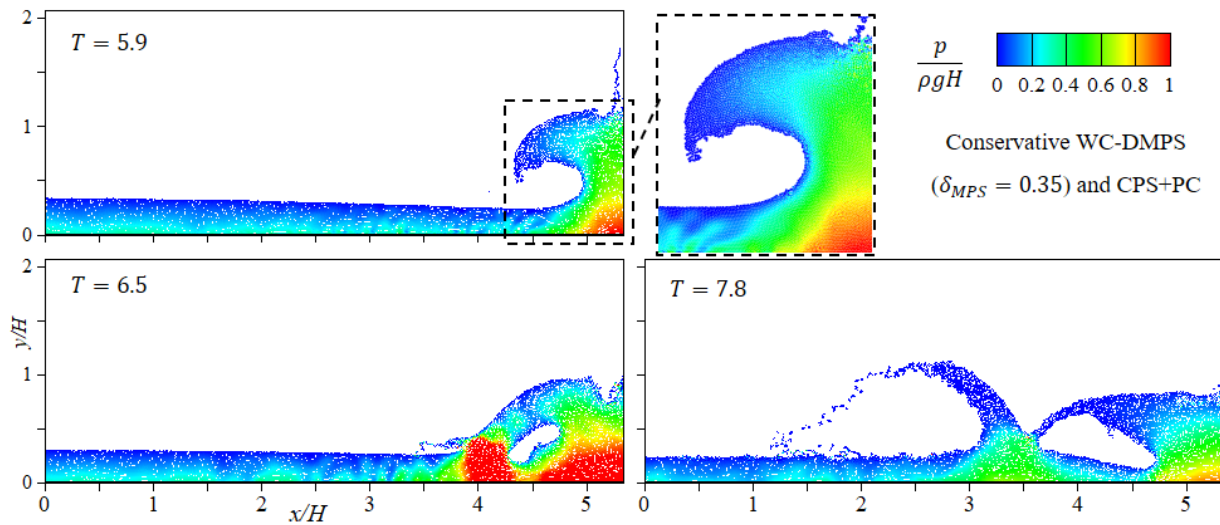


Figure 4.21 Water dam break evolution with the Conservative WC-DMPS model and the CPS+PC algorithm at $T = t\sqrt{g/H} = 5.9, 6.5$ and 7.8 ($H/l_0 = 100$).

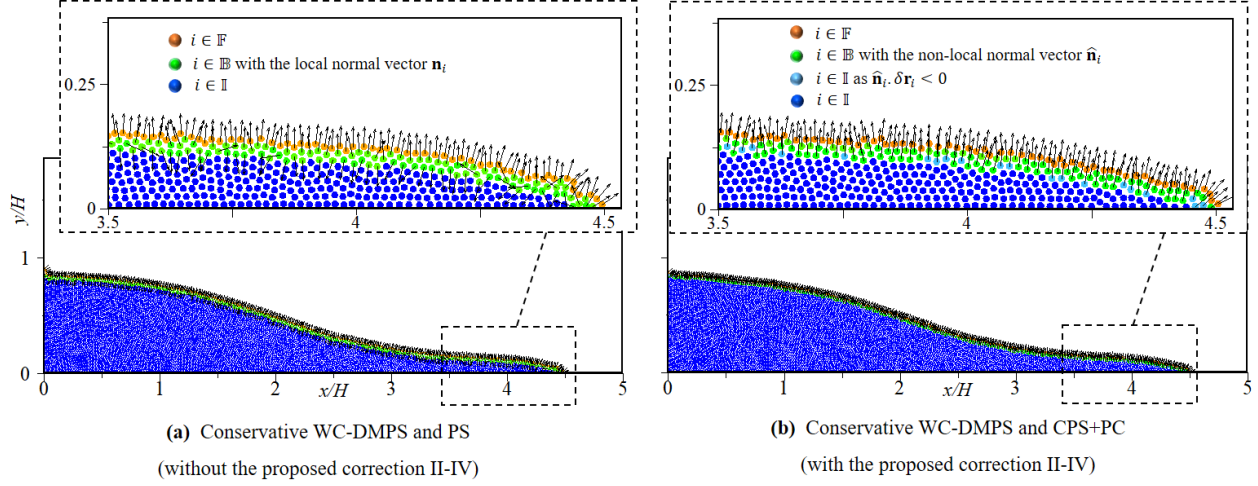


Figure 4.22 The effectiveness of the proposed corrections in the CPS technique (i.e. corrections II-IV in section 4.4.4) for determining the normal vectors to modify the particle shifting vector ($H/l_0 = 60$, $re = 3.1l_0$). Other calculation conditions are the same as the case (b) in Figure 4.20.

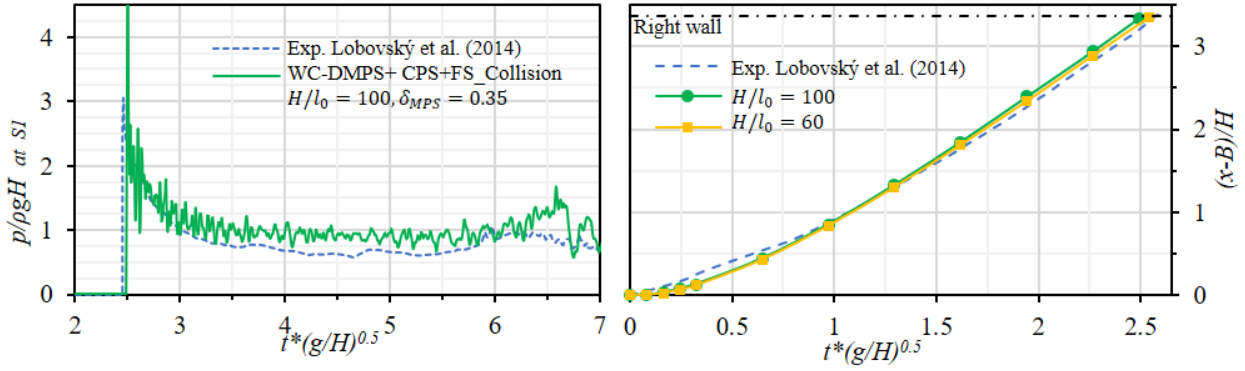


Figure 4.23 The numerical versus experimental [4] water pressure at $S1$ (Left) and the wave front propagation (Right) for the dam break test case.

4.6 Conclusions

A series of enhancement techniques were developed, adapted and evaluated for the WC-MPS particle method, to improve the stability and accuracy of this numerical approach. We introduced a *Conservative WC-MPS* model by employing an antisymmetric pressure gradient

formulation and its conjugate form of the continuity equation. A new diffusive term was proposed (*WC-DMPS technique*) to reduce the numerical errors (false diffusion). We adapted and corrected the particle shifting (*CPS*) algorithm to modify the normal vector and hence the particle shifting vector of particles detected as the free-surface particles. Moreover, the pairwise Particle Collision approach was combined with the CPS method (*CPS+PC*) as a particle stabilizing technique for the free-surface particles. The proposed enhancement techniques were evaluated using four benchmark cases (each with its special flow characteristics).

In general, the proposed techniques proved to be effective in increasing the stability and accuracy and overcoming issues associated with the tensile instability and unphysical pressure fluctuations. The results showed that the conservative pressure gradient regulates particles via the repulsive force activated in the positive pressure fields. While the developed particle shifting algorithm is still required to guarantee long-term stability and eliminate particle clustering especially in the negative pressure fields. Moreover, the CPS+PC technique successfully removed the fluid fragmentation problem in highly dynamic cases at the free-surface regions.

We observed that without the diffusive term the other enhancement techniques are incapable of removing the unphysical pressure noise. By assigning the initial pressure and activating the diffusive term via the proposed continuity equation, the smooth pressure fields are achieved in all four benchmark cases.

For future work, we suggest studying the role of the proposed conservative model in the energy conservation of the system and extending the developments to the multiphase and three-dimensional WC-MPS method. This requires the sensitivity analysis of the diffusive term in the energy dissipation and its treatment at the free-surface and solid boundaries for further improvements. Moreover, it is worthwhile to investigate the proposed particle shifting method for the long-term simulations of violent free-surface flows where the potential energy is dominant, and several breaking events occur.

CHAPTER 5 ARTICLE 2: ENHANCED WEAKLY-COMPRESSIBLE MPS METHOD FOR VIOLENT FREE-SURFACE FLOWS: ROLE OF PARTICLE REGULARIZATION TECHNIQUES

Mojtaba Jandaghian¹, Abdelkader Krimi¹, Amir Reza Zarrati²,
and Ahmad Shakibaeinia¹

¹Department of Civil, Geological and Mining Engineering, Polytechnique Montréal, Canada

²Department of Civil and Environmental Engineering, Amirkabir University of Technology, Iran

Journal of Computational Physics

5.1 Abstract

This paper develops a consistent particle method for capturing the highly non-linear behavior of violent free-surface flows, based on an Enhanced Weakly Compressible Moving Particle Semi-implicit (EWC-MPS) method. It pays special attention to the evaluation and improvement of two particle regularization techniques, namely, pairwise particle collision (PC) and particle shifting (PS). To improve the effectiveness of PC in removing noisy pressure field, and volume conservation issue of PS, we propose and evaluate several enhancements to these techniques, including a novel dynamic PC technique, and a consistent PS algorithm with new boundary treatments and additional terms (in the continuity and momentum equations). Besides, we introduce modified higher-order and anti-symmetric operators for the diffusive and shear force terms. Evaluation of the proposed developments for violent free-surface flow benchmark cases (2D dam-break, 3D water sloshing, and 3D dam-break with an obstacle) confirms an accurate prediction of the flow evolution and rigid body impact, as well as long-term stability of the simulations. The dynamic PC reduces pressure noises with low energy dissipation, and the consistent PS conserves the volume even for extreme deformations. Comparing the role of these new particle regularization techniques demonstrates the effectiveness of both in assuring the uniformity of the particle distribution and pressure fields; nevertheless, the implementation of PS is found to be more complex and time-consuming, mainly due to its need for free surface detection and boundary treatment with many tuning parameters. (Figure 5.1)

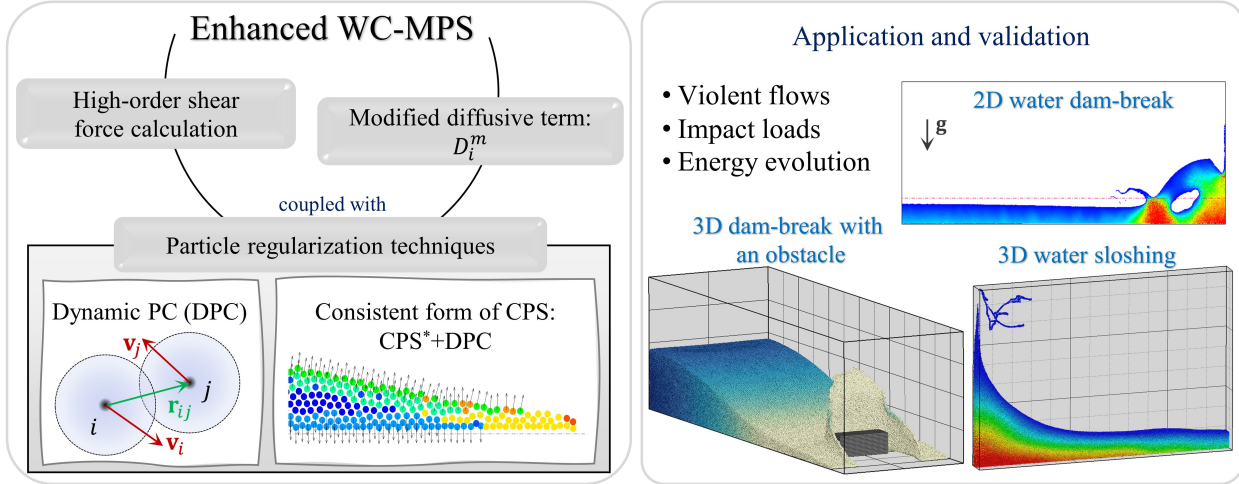


Figure 5.1 The graphical abstract

5.2 Introduction

Continuum-based particle methods have been developed and applied for solving many scientific and engineering problems (see e.g., [38–40, 42]). The Lagrangian nature of these approaches has attracted many research projects involving complex fluid flow physics. In contrast to the traditional Eulerian methods identified with semi- or fixed grids, the moving particles carrying the flow and material properties provide an effective computational tool for capturing extreme flows and interface deformations. Nevertheless, the numerical stability and convergence of these particle methods are still open problems that require robust stabilization techniques (e.g., [3, 161]).

Smoothed Particle Hydrodynamics (SPH) and Moving Particle Semi-implicit (MPS) (initially developed by Gingold and Monaghan [26] and Koshizuka and Oka [25], respectively) are two popular particle methods for fluid flow problems. Shakibaeinia and Jin [47] introduced the Weakly Compressible MPS (WC-MPS) method, with the equation of state being the function of the particle number density. This method has been the focus of many studies, particularly for simulating hydro-environmental problems (e.g., see [75, 162] for free-surface and multiphase fluid flows, and [29, 108] for sediment dynamic modeling). Jandaghian and Shakibaeinia [123] recently proposed a new version of the WC-MPS approach, denoted as the Enhanced WC-MPS (EWC-MPS). The EWC-MPS method, as a continuity-based model, employs a diffusive term and particle regularization techniques to reduce/eliminate numerical instability. In the present study, we further improve this method and investigate its stability and convergence for the long-term modeling of violent free-surface flows by introducing several

new enhancements.

Numerical instabilities in particle methods mainly arise from errors due to the discretization methods and the Lagrangian motion, which lead to non-uniform particle distributions recognized as noisy pressure fields, particle clustering, and tensile instability. These drawbacks of the particle methods not only cause numerical instabilities but also affect the modeling accuracy, particularly in regions with high-pressure and/or tension forces and extreme flow deformations [59]. To decrease the high-frequency unphysical pressure fluctuations, particle methods implement higher-order operators (e.g., [52, 58, 157]) and artificial viscosity/diffusion terms (e.g., [54, 61]). Moreover, particle regularization techniques have been developed to assure uniform particle distributions and overcome the common pairing instabilities. Among these regularization techniques, the pair-wise Particle Collision (PC) (e.g., [56, 75, 146]), the Particle Shifting (PS) (e.g., [3, 50, 55, 60, 74]), and the transport-velocity formulations (e.g., [144, 163, 164]) approaches have shown to be promising in surmounting these instabilities by regulating the particles.

Unphysical high-frequency pressure noises, as the common numerical issue of the weakly compressible SPH and MPS methods, originate from the particle approximation and the kernel truncation errors [54, 123]. To reduce these pressure fluctuations, Monaghan and Gingold [61] inserted an artificial viscosity term into the momentum equation of the weakly compressible SPH method for shock simulations. The artificial viscosity term has shown to be an effective numerical technique for eliminating the pressure fluctuations and ensuring numerical stability, and is being implemented in well-developed SPH models (e.g., see [3, 62–64]). Molteni and Colagrossi [54] introduced a novel diffusive term defined as the Laplacian of the density field in the continuity equation to surmount the pressure oscillations in the weakly compressible SPH method. Antuono et al. [66] proposed the convergent form of this diffusive term using high-order Laplacian and gradient operators. In the context of the weakly compressible MPS, Jandaghian and Shakibaeinia [123] derived a new version of this diffusive term as a function of the particle number density for free-surface flows. Furthermore, high-order approximation operators have been employed to increase the accuracy of the numerical calculations and remove the pressure noises [57]. Oger et al. [52] improved the SPH method through a renormalization-based formulation for increasing the accuracy of the gradient approximations. Similarly, Khayyer and Gotoh [57] represented a first-order accuracy pressure gradient equation in the incompressible MPS framework. Duan et al. [58] implemented a second-order corrective matrix and showed that in their incompressible MPS model the stabilization errors are more dominant compared to the truncation errors. Jandaghian and Shakibaeinia [123] by comparing a conservative pressure gradient operator versus the non-conservative high-order pressure force illustrated that respecting the conservation properties of the system plays an

important role in the numerical stability of the weakly compressible MPS method.

To increase the numerical stability, the particle methods adopt the PC technique developed based on the concept of the momentum transfer in the collision of physical solid or gas particles. This approach utilizes empirical coefficients to indirectly apply a repulsive force between a pair of colliding particles. Lee et al. [56] represented the PC technique as a particle regularization technique in the MPS formulations for simulating violent free-surface flows and impact loads. Shakibaeinia and Jin [108] developed the PC formulation for simulating sediment dynamic problems in the context of the multiphase weakly compressible MPS method. Further, Shakibaeinia and Jin [75] extended the application of the PC method to high-density ratio multiphase flows, and Xu and Jin [146] validated this technique as the particle stabilization approach of the weakly compressible MPS method for free-surface flows involving impact events.

Moreover, PS techniques aim at eliminating particle-clustering and tensile instability by moving particles to the area with less particle concentration. In the context of the incompressible SPH method, Xu et al. [55] originally implemented the PS method for solving internal flows. Lind et al. [50] represented the PS approach based on Fick's law of diffusion and corrected the PS vector for free-surface flows. Shadloo et al. [165] adopted the Lennard-Jones repulsive force to derive the PS vector and validated the improved SPH method for simulating rapid fluid flows over solid bodies. Zainali et al. [166] employed this PS formulation for multiphase incompressible SPH simulations. Khayyer et al. [74] proposed an optimized version of the PS scheme to enhance the performance of the incompressible SPH method for interfacial flows. Mokos et al. [167] developed the PS technique for multiphase violent fluid flows in the weakly compressible SPH framework. Duan et al. [60] implemented the PS technique within an incompressible multiphase MPS model considering the free-surface corrections of the PS vector. Sun et al. [130] appended the PS technique to the weakly compressible SPH method with special treatments of particles in the free-surface region. Further, Sun et al. [3] developed the consistent form of this PS method by including additional diffusive terms of the PS transport velocity within the governing equations. Jandaghian and Shakibaeinia [123] proposed the corrected-PS algorithm coupled with the PC technique (i.e., the hybrid method denoted as CPS+PC) for their enhanced weakly compressible MPS method, and the developed model was shown to be effective and essential for avoiding unphysical fluid fragmentations.

Violent free-surface flows are particularly challenging for the well-developed particle methods for capturing long-term mechanical behaviors (see e.g., [85, 164]). These complex flows are usually associated with breaking waves, impact events, and water sloshing, and are characterized by high Reynolds numbers, highly non-linear deformations, and fluid-fluid and

fluid-solid impacts [62]. Hence, increasing stability and reducing the approximation errors of the particle methods while conserving the global momentum/energy of the system become critical issues for simulating these problems. For this purpose, in addition to employing higher-order formulations and diffusive terms, eliminating the particle-pairing instabilities requires rigorous particle regularization techniques [3]. The PS techniques (e.g., [62, 167]), transport-velocity algorithms (e.g., [164, 168]), and the PC method (e.g., [56, 146]) have been specifically developed and utilized to surmount the numerical instability of violent free-surface flows. Nevertheless, despite their success in improving the particle distributions, many existing particle-shifting methods and the associated free-surface detection algorithms introduce some new challenges in simulating such complex flows (e.g., [123, 161]). Particularly in weakly compressible particle methods, where the potential energy is dominant and several breaking events occur (e.g., water dam break and sloshing problems), the continuous shifting of the particles leads to an unphysical expansion of the fluid field [3, 64]. Further developments to overcome these numerical issues involve implementing more accurate particle classification algorithms and treatment of the free-surface particles (e.g., [64, 74, 161]). Moreover, including some additional advection terms in the governing equations may dissipate the excessive potential energy inserted via the particle-shifting technique [3]. On the other hand, the conservative PC technique has advantages over PS because of its simplicity and being free from many exceptions and boundary treatments; however, by using empirical coefficients, this technique has been shown to be less effective for highly violent flows (see e.g., [56, 146]).

The main objective of this paper is to propose a robust numerical tool based on the EWC-MPS method for simulating the long-term stability of violent free-surface flows while predicting the system's global energy. To accomplish that, we propose a conservative form of the three-dimensional EWC-MPS method by employing a higher-order gradient and Laplacian operators (Section). Moreover, we implement a modified diffusive term in the MPS framework (based on the formulation of [66]) to reduce the high-frequency pressure fluctuations and kernel truncation errors. Regarding the particle regularization techniques, we investigate the role and impact of PC and PS techniques on stability, accuracy, and conservation properties, then to address the issues with these techniques we propose and evaluate a new dynamic PC approach (Section) and a consistent form of the CPS technique (Section). By simulating and validating two-dimensional dam-breaks and three-dimensional water sloshing and obstacle impacts, we investigate and compare the performance of the proposed developments for the long-term stability of relevant problems (Section).

5.3 Governing equations

The mathematical model governs the fluid flows through the momentum and mass conservation laws. The Lagrangian form of the governing equations in the continuum mechanics is as follows [169]:

$$\left\{ \begin{array}{l} \frac{D\rho}{Dt} = -\rho\nabla\cdot\mathbf{v} \\ \rho\frac{D\mathbf{v}}{Dt} = -\nabla p + \rho\mathbf{F} + \nabla\cdot\boldsymbol{\tau} \\ \frac{D\mathbf{r}}{Dt} = \mathbf{v} \end{array} \right. \quad (5.1)$$

In this system, the continuity equation updates the fluid density, ρ , by the divergence of the velocity, $\nabla\cdot\mathbf{v}$, stated as the mass volume expansion rate. The momentum equation updates the velocity vector, \mathbf{v} , used to move the position of the material points, \mathbf{r} . The gradient of pressure, ∇p , the divergence of the shear stress tensor, $\nabla\cdot\boldsymbol{\tau}$, and the body force, $\rho\mathbf{F}$, represent the interaction forces per unit volume. With the weak compressibility assumption, the pressure, p , is a function of the density as a barotropic fluid given by the Equation of State (EOS) (i.e., $p = f(\rho)$). The shear force, $\nabla\cdot\boldsymbol{\tau}$, introduces the laminar and turbulence properties of the viscous fluid within the numerical model. For a Newtonian incompressible fluid (with $\nabla\cdot\mathbf{v} \simeq 0$), the shear stress tensor is given as a function of the dynamic viscosity, μ , and the strain rate tensor of the fluid phase (i.e., $\boldsymbol{\tau} = 2\mu\mathbf{E}$ where $\mathbf{E} = 0.5 [(\nabla\mathbf{v}) + (\nabla\mathbf{v})^T]$).

5.4 The EWC-MPS model

5.4.1 The discrete system with the conservation properties

The particle methods discretize the computational domain, Ω , into particles that represent the fluid phase, Ω_f , and the solid walls, Ω_s (i.e. $\Omega = \Omega_f \cup \Omega_s$). In the EWC-MPS method using the symbolic notation, the approximation operator, $\langle \cdot \rangle$, forms the differential equations (5.1) for a target particle i into:

$$\left\{ \begin{array}{l} \frac{1}{n_i} \frac{Dn_i}{Dt} = -\langle \nabla\cdot\mathbf{v} \rangle_i + D_i^m \\ \frac{D\mathbf{v}_i}{Dt} = -\frac{1}{\rho_i} \langle \nabla p \rangle_i + \mathbf{F}_i + \frac{1}{\rho_i} \langle \nabla\cdot\boldsymbol{\tau} \rangle_i \\ \frac{D\mathbf{r}_i}{Dt} = \mathbf{v}_i \end{array} \right. \quad (5.2)$$

in which the model calculates the particle number density, n_i , (as the substitute for the density, ρ_i) via the continuity equation supplied with the modified diffusive term, D_i^m [123]. The momentum equation estimates the interparticle forces (i.e., the pressure force, $\langle \nabla p \rangle_i$, the shear force, $\langle \nabla \cdot \boldsymbol{\tau} \rangle_i$, and the body force, $\rho_i \mathbf{F}_i$ per unit volume) for updating the velocity, \mathbf{v}_i , and eventually the position of the particle, \mathbf{r}_i , while the model keeps the fluid density constant in the momentum equation (i.e., $\rho_i = \rho_0$: the reference density of the fluid phase; for water, $\rho_0 = 1000 \text{ kg/m}^3$), the equation of state updates the pressure field as a function of n_i with:

$$p_i = \frac{c_0^2 \rho_0}{\gamma} \left(\left(\frac{n_i}{n_0} \right)^\gamma - 1 \right) \quad (5.3)$$

where n_0 is the normalization factor and $\gamma = 7$ [47]. With the artificial speed of sound, c_0 , being considerably larger than the maximum velocity corresponding to the problem, $\|\mathbf{v}\|_{max}$, (e.g., $c_0 \geq 10 \|\mathbf{v}\|_{max}$), the equation of state limits the compressibility of the fluid phase to 1%, as the Mach number (Ma) remains less than 0.1. The kernel function, $W(r_{ij}, r_e)$, defines the interaction of particle i with its neighboring particles ($j \in N$) through the approximation procedure. The neighbor search algorithm updates the neighbor lists in each time step with the kernel influence radius, $r_e = 3.1l_0$, where $r_{ij} = \|\mathbf{r}_j - \mathbf{r}_i\| \leq r_e$ and l_0 is the initial particle distance. The conjugate form of the gradient and divergence operators for the pressure force and the velocity field, respectively, gives:

$$\left\{ \begin{array}{l} \langle \nabla p \rangle_i = \frac{d}{n_0} \sum_{i \neq j}^N \left(n_i \frac{p_j}{n_j} + n_j \frac{p_i}{n_i} \right) \frac{\mathbf{e}_{ij}}{r_{ij}} W_{ij} \\ \langle \nabla \cdot \mathbf{v} \rangle_i = \frac{d}{n_0} \sum_{i \neq j}^N \left(\frac{n_j}{n_i} \right) \frac{\mathbf{v}_{ij}}{r_{ij}} \cdot \mathbf{e}_{ij} W_{ij} \end{array} \right. \quad (5.4)$$

in which \mathbf{e}_{ij} is the unit direction vector between particle i and j (i.e. $\mathbf{e}_{ij} = (\mathbf{r}_{ij} = \mathbf{r}_j - \mathbf{r}_i)/r_{ij}$), $W_{ij} = W(r_{ij}, r_e)$, and $d (= 1, 2, 3)$ is the number of space dimensions [123]. The normalization factor, n_0 , is calculated at the initial stage ($t = 0$) by the kernel summation over the fluid particles with the complete kernel support (i.e., $n_0 = \max(\sum_{i \neq j}^N W_{ij})$ at $t = 0$). We employ the rational kernel function [75] for all the approximated terms of the governing equation (5.2).

Employing the conjugate form of the approximation operators in (5.4) ensures that the particle system preserves the total energy of the numerical model (in the absence of the shear and body forces and the diffusion terms) [49, 123]. Further, this model conserves the linear and angular momentums, since the pressure force is antisymmetric (with respect to the particle indexes) and with the same direction as the \mathbf{r}_{ij} vector. In the presence of viscous

stresses, we should approximate the shear force, $\langle \nabla \cdot \boldsymbol{\tau} \rangle_i$, with an antisymmetric formulation in order to still conserve the linear momentum of the system. To do so, in this study we implement the following divergence operator:

$$\langle \nabla \cdot \boldsymbol{\tau} \rangle_i = \frac{d}{n_0} \sum_{i \neq j}^N \left(\frac{n_i}{n_j} \boldsymbol{\tau}_j + \frac{n_j}{n_i} \boldsymbol{\tau}_i \right) \cdot \frac{\mathbf{e}_{ij}}{r_{ij}} W_{ij} \quad (5.5)$$

derived based on the formulation by Jandaghian and Shakibaeinia [123] proposed for the conservative pressure force in Eq. (5.4). In this equation, the shear stress tensor of particle i is given by $\boldsymbol{\tau}_i = 2\mu_i \mathbf{E}_i$, where \mathbf{E}_i is the deviatoric part of the strain rate tensor estimated by $0.5(\langle \nabla \mathbf{v} \rangle_i + \langle \nabla \mathbf{v} \rangle_i^T)$ for incompressible flows. Furthermore, we implement a turbulence model to simulate unresolved fluid motions smaller than the filter size [170]. Based on the Sub Particle Scale (SPS) turbulence model, we add the turbulent viscosity, μ_{ti} , to the dynamic viscosity of the fluid phase (i.e., $\mu_i = \mu + \mu_{ti}$ and for water $\mu = 10^{-3}$ Pa.s), where $\mu_{ti} = \rho_0 (C_s r_e)^2 \sqrt{4II_{E_i}}$ and $II_{E_i} = 0.5 \mathbf{E}_i : \mathbf{E}_i$ is denoted as the second main invariant of the strain rate tensor and C_s is the Smagorinsky coefficient set to 0.12 in this study [29, 37].

Even with Eq. (5.5) being an antisymmetric equation with respect to the particle indexes, the direct methods are incapable of confirming the conservation of the angular momentum within the discrete system [48]. Considering the variational procedure, Bonet and Lok [48] showed that the numerical model preserves the angular momentum if the potential energy remains invariant as the rigid body rotates. This is achieved by implementing a gradient operator that correctly estimates the true velocity gradient, \mathbf{W} , of an angular velocity vector, $\boldsymbol{\omega}$, where $\mathbf{v}_i = \boldsymbol{\omega} \times \mathbf{r}_i$ (i.e., ideally $\langle \nabla \mathbf{v} \rangle_i = \mathbf{W}$) [48]. In the MPS framework, the gradient of this velocity field is approximated via:

$$\langle \nabla \mathbf{v} \rangle_i = \frac{d}{n_0} \sum_{i \neq j}^N \frac{\mathbf{W} \mathbf{r}_{ij}}{r_{ij}} \otimes \mathbf{e}_{ij} W_{ij} \quad (5.6)$$

in which \otimes is the outer product of two vectors. Therefore, the condition that assures the preservation of the related potential energy will be:

$$\frac{d}{n_0} \sum_{i \neq j}^N \frac{\mathbf{r}_{ij}}{r_{ij}} \otimes \mathbf{e}_{ij} W_{ij} = \mathbf{I} \quad (5.7)$$

which is required for estimating the true velocity gradient (\mathbf{I} being the identity matrix).

Satisfying this condition leads to a corrective matrix identical to \mathbf{C}_i , given as:

$$\mathbf{C}_i = \left(\frac{d}{n_0} \sum_{i \neq j}^N \frac{\mathbf{r}_{ij}}{r_{ij}} \otimes \mathbf{e}_{ij} W_{ij} \right)^{-1} \quad (5.8)$$

which ensures the exact calculation of the gradient of any linear velocity field [48, 52, 57]. Accordingly, we include the corrective matrix into the gradient operator of the velocity vector as follows:

$$\langle \nabla \mathbf{v} \rangle_i^C = \frac{d}{n_0} \sum_{i \neq j}^N \frac{\mathbf{v}_{ij}}{r_{ij}} \otimes (\mathbf{C}_i \mathbf{e}_{ij}) W_{ij} \quad (5.9)$$

which is used in the shear force calculations (i.e., in the $\boldsymbol{\tau}_i$ and μ_{ti} terms) and $\mathbf{v}_{ij} = \mathbf{v}_j - \mathbf{v}_i$. By implementing this first-order accuracy operator, we aim to conserve the angular momentum of the system (similar to the incompressible SPH method proposed by Khayyer et al. [170]).

Based on the flow equations in the MPS framework, Jandaghian and Shakibaeinia [123] introduced the diffusive term into the continuity-based WC-MPS model to eliminate high-frequency pressure fluctuations. We modify the standard diffusive term by employing a higher-order Laplacian operator to implement its convergent form (like the formulation proposed by Antuono et al. [66] for the δ -SPH models). This eliminates kernel truncation errors at the free surface and in the vicinity of the solid boundary, converging the diffusive term over the fluid domain, which is required to obtain a stable pressure field for long-term simulations [66]. In the context of the WC-MPS method, the modified the diffusive term forms to:

$$D_i^m = \left(\delta_{MPS} \frac{\Delta t c_0^2}{n_0} \right) \frac{2d}{n_0} \sum_{i \neq j}^N \left[(n_j - n_i) - \frac{1}{2} \left[\langle \nabla n \rangle_i^C + \langle \nabla n \rangle_j^C \right] \cdot \mathbf{r}_{ij} \right] \frac{W_{ij}}{r_{ij}^2} \quad (5.10)$$

in which the time step of the calculation, Δt , the reference sound speed, c_0 , the normalization factor, n_0 , and the adjusting coefficient, $0 < \delta_{MPS} \leq 1$ determine the strength of the numerical diffusion (in this study, $\delta_{MPS} = 0.7$ for all test cases). Using the higher-order gradient equation produces the gradient of the particle number density, as follows:

$$\langle \nabla n \rangle_i^C = \frac{d}{n_0} \sum_{i \neq j}^N \frac{n_j - n_i}{r_{ij}} (\mathbf{C}_i \mathbf{e}_{ij}) W_{ij} \quad (5.11)$$

where the corrective matrix, \mathbf{C}_i , imposes the first-order accuracy on the gradient operator. It should be noted that the modified diffusive terms conserve the total mass of the system, as equations (5.8), (5.10), and (5.11) are limited to the fluid particles (i.e. $i, j \in \Omega_f$) and $\sum_i n_i D_i^m V_i = 0$, V_i is the volume of the particle.

5.4.2 Particle regularization techniques for violent free-surface flows

Dynamic pair-wise Particle Collision technique: DPC

The idea behind the pair-wise Particle Collision (PC) approach originates from the momentum transfer between colliding physical solid or gas particles in the normal direction [75,147]. In the particle methods (e.g., [56,75,146]), the standard PC technique modifies the velocity of fluid particles penetrating each other considering the collision velocity, a constant coefficient of restitution, and a threshold as the collision distance (\mathbf{v}_{ij}^{Coll} , ε and θl_0 , respectively) through $\mathbf{v}'_i = \mathbf{v}_i + \delta\mathbf{v}_i$ as:

$$\delta\mathbf{v}_i = \sum_{i \neq j}^N \left(\frac{1 + \varepsilon}{2} \right) \mathbf{v}_{ij}^{Coll}$$

in which:

$$\mathbf{v}_{ij}^{Coll} = \begin{cases} (\mathbf{v}_{ij} \cdot \mathbf{e}_{ij}) \mathbf{e}_{ij} & \text{for } r_{ij} \leq \theta l_0 \text{ and } \mathbf{v}_{ij} \cdot \mathbf{r}_{ij} < 0 \\ 0 & \text{otherwise} \end{cases} \quad (5.12)$$

and ε specifies the kinetic energy variation of the particles after the collision and θ is a non-dimensional threshold coefficient usually set to 0.8 – 0.9 [75,147]. The time integration algorithm dispositions the particle with the post-collision velocity \mathbf{v}'_i [75]. This velocity modification ignores the inter-particle penetration of other neighboring particles, j , that are not approaching particle i (i.e., for $\mathbf{v}_{ij} \cdot \mathbf{r}_{ij} \geq 0 \rightarrow \mathbf{v}_{ij}^{Coll} = 0$ even if $r_{ij} < l_0$). Moreover, the constant coefficient and the predefined threshold of collision distance restrict the effectiveness of the PC method for dealing with extreme flow deformations.

Here, we propose a new formulation of the PC technique to resolve the numerical instabilities associated with particle-clustering in violent free-surface flows. The developed algorithm employs variable coefficients and the local gradient of a dynamic background pressure to update the transport velocity. This particle regularization technique, hereinafter denoted as the Dynamic pair-wise Particle Collision (DPC) technique, modifies the velocity by:

$$\delta\mathbf{v}_i = \left(\sum_{i \neq j}^N \kappa_{ij} \mathbf{v}_{ij}^{Coll} - \frac{\Delta t}{\rho_0} \sum_{i \neq j}^N \phi_{ij} \frac{p_{ij}^b}{r_{ij}} \mathbf{e}_{ij} \right)$$

where

$$(\mathbf{v}_{ij}^{Coll}, \phi_{ij}) = \begin{cases} ((\mathbf{v}_{ij} \cdot \mathbf{e}_{ij}) \mathbf{e}_{ij}, 0) & \text{if } \mathbf{v}_{ij} \cdot \mathbf{r}_{ij} < 0, \\ (0, 1) & \text{otherwise} \end{cases} \quad (5.13)$$

acting between the fluid particles (i.e., $i, j \in \Omega_f$). For pairs of interpenetrated particles still approaching each other, i.e., $\mathbf{v}_{ij} \cdot \mathbf{r}_{ij} < 0$, only the collision term (i.e., the first term

on the right-hand side) modifies their velocity vectors with a variable coefficient, given as $0 \leq \kappa_{ij} \leq 1$, and a binary multiplier set to $\phi_{ij} = 0$. Otherwise, when they are receding from each other, the second term, as the local gradient of dynamic background pressure, p_{ij}^b , activates an artificial repulsive force between the two target particles by setting $\phi_{ij} = 1$.

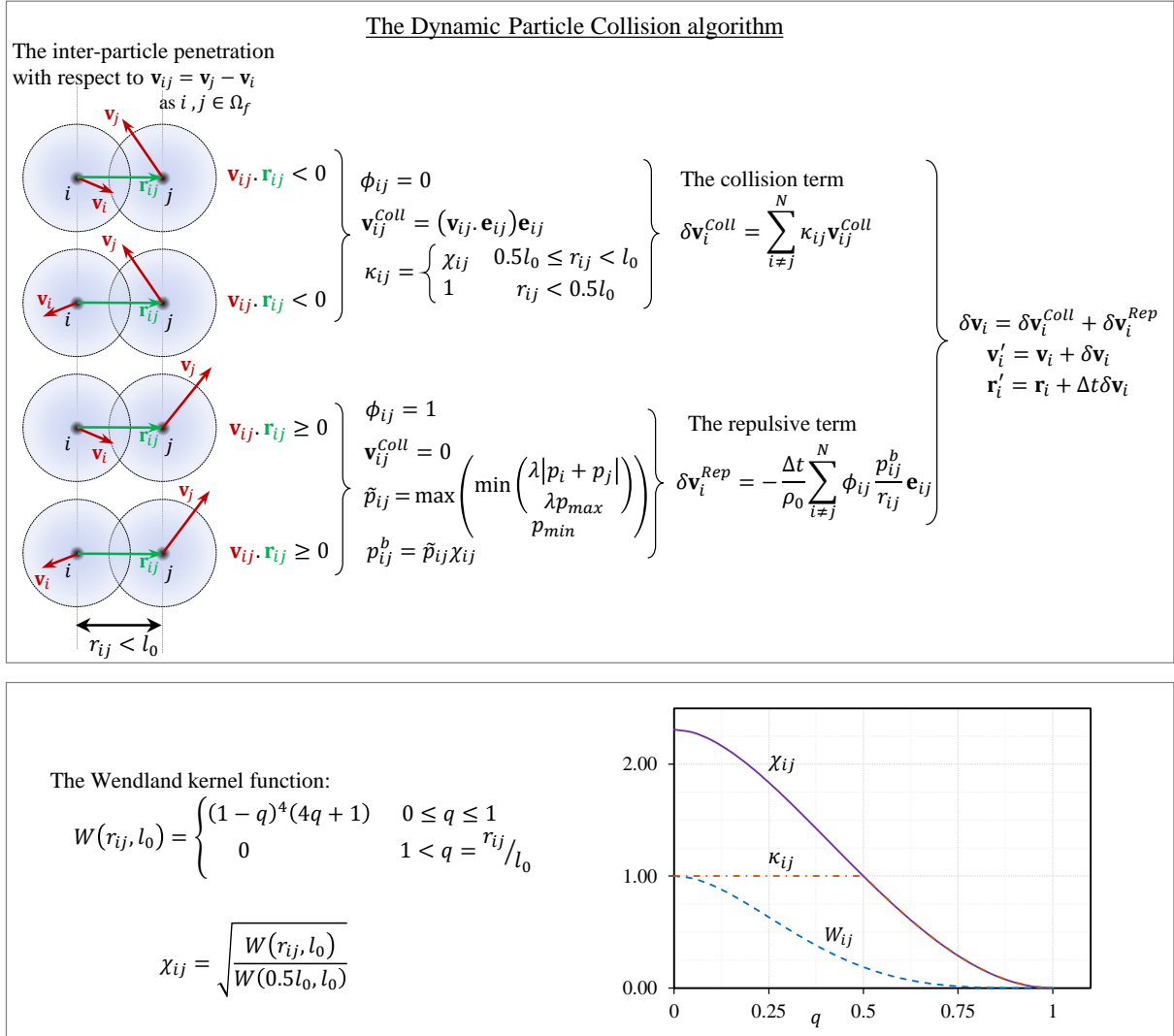


Figure 5.2 The Dynamic Particle Collision (DPC) algorithm consists of the proposed collision and repulsive terms and the dynamic coefficients defined by the Wendland kernel

This new formulation (i.e., Eq. (5.13)) covers the different conditions that demonstrate inter-particle penetration, i.e., particle-clustering (shown in Figure 5.2). By calculating the velocity variation of all the fluid particles, the proposed DPC technique updates the velocities

and positions of the fluid particles as follows:

$$\begin{cases} \mathbf{v}'_i = \mathbf{v}_i + \delta\mathbf{v}_i \\ \mathbf{r}'_i = \mathbf{r}_i + \Delta t\delta\mathbf{v}_i \end{cases} \quad (5.14)$$

We define the dynamic background pressure by the local pressure of the particles and the inter-particle distance as follows:

$$\begin{cases} p_{ij}^b = \tilde{p}_{ij}\chi_{ij} \\ \tilde{p}_{ij} = \max(\min(\lambda|p_i + p_j|, \lambda p_{max}), p_{min}) \\ \chi_{ij} = \sqrt{\frac{W(r_{ij}, l_0)}{W(0.5l_0, l_0)}} \end{cases} \quad (5.15)$$

where λ is a non-dimensional coefficient (typically with a constant value of 0.1~0.2). This formulation limits the background pressure by the expected minimum and maximum values of the pressures (i.e., p_{min} and λp_{max} , respectively, considered as positive constants in the problem). The minimum pressure keeps the repulsive force non-zero, while the maximum pressure eliminates large velocity variations (particularly in regions where flow impacts solid walls or forms a plunging wave). The proposed dynamic background pressure (within the repulsive term) increases the stability particularly close to the free-surface where attractive forces may become dominant through the conservative pressure force. In this study, we set $\lambda = 0.2$ for all benchmark cases and assign p_{min} and p_{max} considering the minimum hydrostatic pressure on the free-surface and the maximum impact load on the walls, respectively. In test cases where the gravitational force is not dominant, these parameters can be determined according to the analytical solution and/or the local particle pressure. The kernel function, with a smoothing length equal to the initial particle distance, adjusts the strength of the repulsive force through χ_{ij} , defined as a non-dimensional variable. This function increases as the particle distance decreases and becomes greater than the unit where $r_{ij} < 0.5l_0$. Similarly, we utilize χ_{ij} as the variable coefficient of the collision term considering the following conditions:

$$\kappa_{ij} = \begin{cases} \chi_{ij} & 0.5l_0 \leq r_{ij} < l_0 \\ 1 & r_{ij} < 0.5l_0 \end{cases} \quad (5.16)$$

by which the magnitude of the velocity variation decreases smoothly with the particle separation. Further, the latter condition avoids excessive transfer of linear momentum between

the colliding particles (i.e., with $\kappa_{ij} = 1.0$, the coefficient of restitution, ε , reaches its maximum value which is unit). Through the dynamic coefficients, both the collision and repulsive terms only modify the velocities and positions considering the nearest-neighbor particles that penetrate the target particle (i.e., if $r_{ij} \geq l_0$, $W(r_{ij}, l_0) = 0 \rightarrow \chi_{ij} = 0$). Note that since Eq. (5.13) is an antisymmetric term, the proposed DPC still conserves the total linear momentum of the system (i.e., $\sum_i m \delta \mathbf{v}_i = 0$ with the constant mass of particles m).

The repulsive term in Eq. (5.13) regulates particles based on the pressure gradient term of the momentum equation (i.e., $d\mathbf{v}/dt = -\nabla p/\rho_0$, similar to the generalized transport-velocity approach of Zhang et al. [163] and the artificial repulsive forces of Monaghan et al. [44] and Tsuruta et al. [132]). However, the proposed repulsive force coupled with the new collision term still acts as a pair-wise technique without the smoothing procedure over all the neighbor particles. Further, this term is antisymmetric, and the velocity is directly updated by Eq. (5.14) without implementing any additional term in the momentum equation (i.e., without $(\nabla \cdot (\mathbf{v} \otimes \delta \mathbf{v}) - \mathbf{v} \nabla \cdot (\delta \mathbf{v}))$ terms). It should be noted that the effectiveness of the DPC technique depends on the type of kernel function used for the χ_{ij} variable (e.g., the kernel functions with the singularity issues (like the rational kernel function [47]) may lead to large values of the repulsive force when $r_{ij} \rightarrow 0$). In this study, we use the Wendland kernel function [67], where $0 \leq \chi_{ij} \leq 2.31$. Figure 5.2 illustrates the numerical implementation of the DPC algorithm and plots the Wendland kernel and χ_{ij} functions.

A consistent form of the corrected particle shifting technique: CPS*+DPC

The particle shifting (PS) algorithm regulates the distribution of fluid particles, thus eliminating the tensile instability and increasing the numerical accuracy and stability. Here, we propose and develop a consistent form of the corrected-PS algorithm (i.e., the hybrid approach originally proposed in [123] denoted as CPS+PC) for the EWC-MPS method. To that end, we implement a more restricted criterion for boundary treatments of the particle-shifting vector. We also re-derive the MPS formulation of the additional diffusive terms included in the continuity and momentum equations resulting from the particle-shifting velocity (based on the work of Sun et al. [3]). The former introduces new criteria to classify the fluid particles required for dealing with corners and extreme curvatures of the interfaces. The latter aims to include the effects of the gradients' advection due to the particle shifting transport-velocity within the governing equations. Eventually, coupling the new CPS algorithm with the DPC technique, we propose a consistent form of the corrected particle-shifting technique, denoted as CPS*+DPC, for the free-surface flows.

- *Numerical treatment of the particle-shifting vector*

Here, the conservative particle shifting vector of the fluid particles, $i \in \Omega_f$, is given by:

$$\delta \mathbf{r}_i = -F \nabla C_i = -F \frac{d}{n_0} \sum_{i \neq j | i, j \in \Omega_f}^N \frac{C_i + C_j}{r_{ij}} \mathbf{e}_{ij} W_{ij} \quad (5.17)$$

where j only belongs to the fluid particles, Ω_f , and $F = Al_0^2 C_{CFL} Ma$ is the Fickian diffusion coefficient with A and C_{CFL} being a dimensionless number ($A = 2$ in this study) and the Courant condition coefficient of the explicit model, respectively. Unlike in [123], Eq. (5.17) excludes the contribution of the solid boundary particles to the particle-shifting of the fluid particles. This vector dispositions the fluid particles to the area with less particle concentration, quantified by $C_i = \sum_{i \neq j}^N W_{ij} / n_0$ as $j \in \Omega$. Thus, the CPS algorithm should modify/cancel the particle-shifting vector with the incomplete kernel support (i.e., the particles in the vicinity of the free-surface and solid boundaries) to eliminate false particle-shifting.

For this purpose, the new dynamic particle classification algorithm, in addition to the internal particles ($i \in \mathbb{I}$), the free-surface vicinity particles ($i \in \mathbb{B}_F$), the free-surface particles ($i \in \mathbb{F}$), and the external/splashed particles ($i \in \mathbb{E}$), identifies the wall vicinity particles ($i \in \mathbb{B}_w$) and the fluid particles that signify the local volume expansion ($i \in \mathbb{X}$). Note that these classes represent the entire fluid domain (i.e., $\Omega_f = \mathbb{I} \cup \mathbb{F} \cup \mathbb{B}_F \cup \mathbb{B}_w \cup \mathbb{X} \cup \mathbb{E}$), whereas the wall and ghost solid boundary particles are denoted as \mathbb{W} and \mathbb{G} , respectively (i.e., $\Omega_s = \mathbb{W} \cup \mathbb{G}$). Based on the particle shifting correction proposed by Lind et al. [50] and Khayyer et al. [74], the false diffusion of the fluid particles toward the free surface should be avoided. In this study, with the fluid particles being categorized, the new CPS formulation modifies the particle-shifting vector through:

$$\delta \mathbf{r}_i = \begin{cases} -F \nabla C_i, & i \in \mathbb{I} \\ -F [\alpha_i \mathbf{I} - \beta_i (\hat{\mathbf{n}}_i \otimes \hat{\mathbf{n}}_i)] \cdot \nabla C_i, & i \in \mathbb{B}_F \cup \mathbb{B}_w \\ -F [\alpha_i \mathbf{I} - \beta_i (\mathbf{n}_i \otimes \mathbf{n}_i)] \cdot \nabla C_i, & i \in \mathbb{F} \\ 0 & i \in \mathbb{E} \cup \mathbb{X} \end{cases} \quad (5.18)$$

in which \mathbf{I} is the identity matrix. This formulation removes the normal component of the particle-shifting vector of the free-surface particles ($i \in \mathbb{F}$) and the particles identified in the vicinity of the free-surface and the solid boundary particles ($i \in \mathbb{B}_F \cup \mathbb{B}_w$) via their unit local normal vector, \mathbf{n}_i , and the non-local normal vectors $\hat{\mathbf{n}}_i$, respectively [123]. The binary coefficients α_i and β_i (which are either equal to 1 or 0) in the new equation impose some restricting conditions on the particle-shifting vector of the free-surface and boundary particles

(through Eqs. (5.24)-(5.27)).

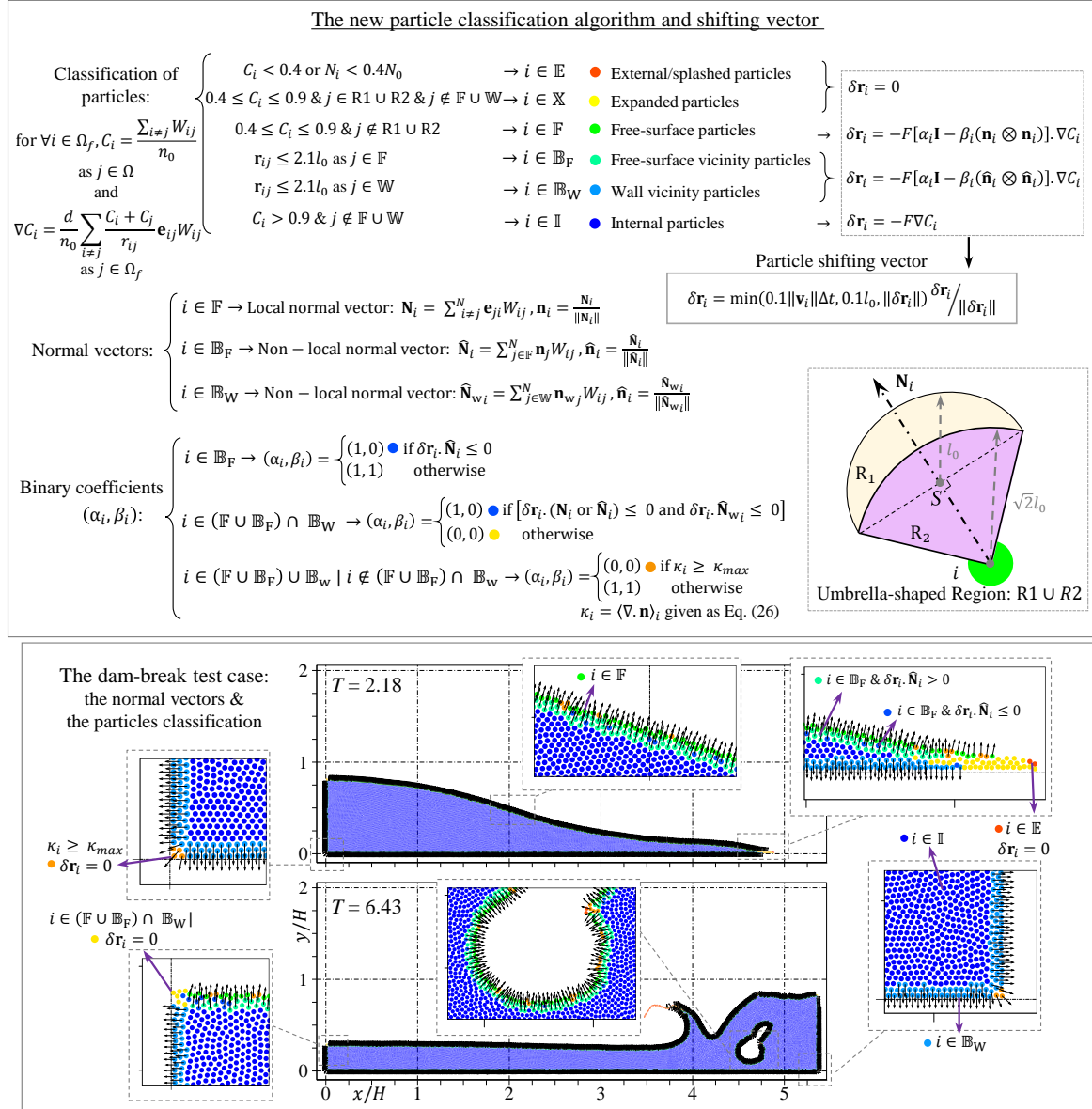


Figure 5.3 The new particle classification algorithm and special treatments of the boundary particles for the corrected particle-shifting vector. The umbrella-shaped region used for identifying the free-surface particle is illustrated (i.e., $R1$ and $R2$ given by Eq. (5.19)). The results of the two-dimensional (2D) dam-break test case (with $H/l_0 = 100$) show the estimated normal vectors and the different categories of the fluid particles at $T = 2.18$ and $T = 6.43$, where $T = t\sqrt{g/H}$ is the non-dimensional time.

Firstly, the algorithm distinguishes the free-surface particles and the regions with unphysi-

cal volume expansion (due to manipulation of the potential energy by the particle-shifting procedure). To do so, the model evaluates C_i with the predefined limits and then searches for the neighboring particles, $j \in \Omega$, within the umbrella-shaped region: R1 and R2, defined in [123] as:

$$\begin{cases} \text{R1 : } |\mathbf{r}_{ij}| \geq \sqrt{2}l_0 \text{ and } |\mathbf{r}_{jS}| < l_0 \\ \text{R2 : } |\mathbf{r}_{ij}| < \sqrt{2}l_0 \text{ and } |\mathbf{n}_i \cdot \mathbf{r}_{jS}| + |\mathbf{t}_i \cdot \mathbf{r}_{jS}| < l_0 \end{cases} \quad (5.19)$$

where S is at the distance l_0 from particle $i \in \Omega_f$ in the normal direction and the unit local normal vector of the fluid particles, \mathbf{n}_i , is given as:

$$\mathbf{n}_i = \frac{\mathbf{N}_i}{\|\mathbf{N}_i\|} \quad \text{as } \mathbf{N}_i = \sum_{i \neq j \in \Omega}^N \mathbf{e}_{ji} W_{ij}, \quad (5.20)$$

noting that the unit tangential vector, \mathbf{t}_i , satisfies $\mathbf{t}_i \cdot \mathbf{n}_i = 0$ condition (see R1 and R2 illustrated in Figure 5.3). Fluid particles with incomplete kernel support and without a neighboring particle inside their search regions are identified as free-surface particles (i.e., if $0.4 \leq C_i \leq 0.9$ and $j \notin \text{R1} \cup \text{R2} \rightarrow i \in \mathbb{F}$). A particle that still satisfies the $0.4 \leq C_i \leq 0.9$ condition while finding a neighboring particle within the $\text{R1} \cup \text{R2}$ region not detected as a free-surface or a wall particle, indicates an unphysical local expansion of volume in the internal region. To reduce the accumulation of errors in the potential energy of the system, we cancel the shifting of these particles (i.e., if $0.4 \leq C_i \leq 0.9$ and $j \in \text{R1} \cup \text{R2} \ \& \ j \notin \mathbb{F} \cup \mathbb{W} \rightarrow i \in \mathbb{X} \ \& \ \delta \mathbf{r}_i = 0$). Further, for detecting particles that are detached from the main body of the fluid domain, i.e., $i \in \mathbb{E}$, we consider the number of surrounding neighbors, N_i , (as $r_{ij} \leq r_e$ with $j \in \Omega$) and C_i satisfying the $C_i < 0.4$ or $N_i < 0.4N_0$ condition (where N_0 is the maximum number of neighbors as the isotropic particle distribution forms (e.g., with $r_e = 3.1l_0$ in the two- and three-dimensional problems, N_0 is set to 34 and 140, respectively). In this case, its particle-shifting vector is neglected due to the extreme kernel truncations and the insufficient number of neighboring particles.

In the next step, the fluid particles that contain free-surface particles within their neighbor list (i.e., $r_{ij} \leq (r_e - l_0)$ as $j \in \mathbb{F}$) are identified as free-surface-vicinity particles ($i \in \mathbb{B}_F$) [123]. For these particles, the non-local normal vector, $\hat{\mathbf{n}}_i$, defined by [123] as:

$$\hat{\mathbf{n}}_i = \frac{\hat{\mathbf{N}}_i}{\|\hat{\mathbf{N}}_i\|} \quad \text{as } \hat{\mathbf{N}}_i = \sum_{j \in \mathbb{F}}^N \mathbf{n}_j W_{ij} \text{ for } i \in \mathbb{B}_F \quad (5.21)$$

cancels the shifting vector in the direction normal to the free surface. Furthermore, the new algorithm considers fluid particles that interact with the wall particles (i.e., $r_{ij} \leq (r_e - l_0)$ as

$j \in \mathbb{W}$) in the vicinity of the wall ($i \in \mathbb{B}_w$). The non-local normal vectors of the wall-vicinity particles are specified by:

$$\hat{\mathbf{n}}_i = \frac{\hat{\mathbf{N}}_{w_i}}{\|\hat{\mathbf{N}}_{w_i}\|} \quad \text{as } \hat{\mathbf{N}}_{w_i} = \sum_{j \in \mathbb{W}} \mathbf{n}_{w_j} W_{ij} \quad \text{for } i \in \mathbb{B}_w, \quad (5.22)$$

where the unit normal and normal vectors of the wall particles (i.e., \mathbf{n}_{w_i} and \mathbf{N}_{w_i} , respectively) are given as follows:

$$\mathbf{n}_{w_i} = \frac{\mathbf{N}_{w_i}}{\|\mathbf{N}_{w_i}\|} \quad \text{as } \mathbf{N}_{w_i} = \sum_{i \neq j \in \mathbb{W} \cup \mathbb{G}} \mathbf{e}_{ij} W_{ij} \quad \text{for } i \in \mathbb{W}. \quad (5.23)$$

With the unit normal vector given by (5.22), particle-shifting toward the solid boundary is ignored through Eq. (5.18). Finally, the fluid particles that are not in the vicinity of the free-surface and solid boundaries (i.e., $i \notin \mathbb{F} \cup \mathbb{B}_F \cup \mathbb{B}_w$) and the kernel support is almost complete (i.e., $C_i > 0.9$) are labeled as internal particles.

Considering the local curvature of the surfaces and the direction of the shifting vector against the normal vectors, the algorithm determines the binary coefficients α_i and β_i . In case the shifting vector of a fluid particle located in the vicinity of the free surface is toward the interior domain, the algorithm treats the particle as an internal one, i.e.:

$$\text{for } i \in \mathbb{B}_F \rightarrow (\alpha_i, \beta_i) = \begin{cases} (1, 0) & \text{if } \delta \mathbf{r}_i \cdot \hat{\mathbf{N}}_i \leq 0 \\ (1, 1) & \text{otherwise} \end{cases} \quad (5.24)$$

where $\delta \mathbf{r}_i$ is given by Eq. (5.17). To deal with fluid particles that are detected inside both the $\mathbb{F} \cup \mathbb{B}_F$ and \mathbb{B}_w regions, special treatment of the shifting vector becomes necessary. This occurs at the intersection of the free surface region and the solid boundary. If this fluid particle's shifting vector (given by Eq. (5.17)) is toward either its free-surface or wall-normal vectors, the algorithm ignores its shifting, i.e.:

$$\text{for } i \in (\mathbb{F} \cup \mathbb{B}_F) \cap \mathbb{B}_w \rightarrow (\alpha_i, \beta_i) = \begin{cases} (1, 0) & \text{if } [\delta \mathbf{r}_i \cdot (\mathbf{N}_i \text{ or } \hat{\mathbf{N}}_i) \leq 0 \text{ and } \delta \mathbf{r}_i \cdot \hat{\mathbf{N}}_{w_i} \leq 0] \\ (0, 0) & \text{otherwise} \end{cases} . \quad (5.25)$$

Moreover, for large surface curvatures (such as the corners of the fluid domain), correction of the shifting vector with the normal vector in a direction tangential to the surface still leads to inaccurate particle-shifting. Therefore, we introduce a criterion for distinguishing regions with large curvatures in order to ignore their particle-shifting. To calculate the scalar value

of curvature, we estimate the divergence of the unit normal vectors by:

$$[ll]\kappa_i = \langle \nabla \cdot \mathbf{n} \rangle_i = \frac{d}{n_0} \sum_{i \neq j}^N \frac{\mathbf{n}'_j - \mathbf{n}'_i}{r_{ij}} \cdot \mathbf{e}_{ij} W_{ij}$$

for $i \in (\mathbb{F} \cup \mathbb{B}_F) \cup \mathbb{B}_w$ while $i \notin (\mathbb{F} \cup \mathbb{B}_F) \cap \mathbb{B}_w$ (5.26)

in which, if $i \in \mathbb{F} \rightarrow \mathbf{n}'_i = \mathbf{n}_i$ and if $i \in (\mathbb{B}_w \text{ or } \mathbb{B}_F) \rightarrow \mathbf{n}'_i = \hat{\mathbf{n}}_i$. Further, $\mathbf{n}'_j = \mathbf{n}_{j \in \mathbb{F}}$ and $\mathbf{n}'_j = \mathbf{n}_{w_j \in \mathbb{W}}$ for $i \in (\mathbb{F} \cup \mathbb{B}_F)$ and $i \in \mathbb{B}_w$, respectively, while the neighbor particles that belong to intersecting free-surface and wall boundary particles are ignored (i.e., $j \in (\mathbb{W} \cup \mathbb{F}) \mid j \notin (\mathbb{F} \cap \mathbb{B}_w)$). With the scalar value of the curvature, κ_i , exceeding the predefined limit, κ_{max} , the binary coefficients set the shifting vector to null, i.e.:

$$i \in \mathbb{F} \cup (\mathbb{B}_F \text{ or } \mathbb{B}_w) \rightarrow (\alpha_i, \beta_i) = \begin{cases} (0, 0) & \text{if } \kappa_i \geq \kappa_{max} \\ (1, 1) & \text{otherwise} \end{cases} \quad (5.27)$$

wherein both two- and three-dimensional problems κ_{max} is adjusted to 5.0, validated for the rational kernel function with $r_e = 3.1l_0$. This condition entirely cancels the shifting of free-surface and boundary particles in regions where the normal vectors are non-uniform. It should be highlighted that the only intersection between the particle categories occurs with fluid particles belonging to both the $\mathbb{F} \cup \mathbb{B}_F$ and \mathbb{B}_w regions, specifically treated by Eq. (5.25); whereas no other identified regions overlap.

Altogether, the new particle-shifting vector, i.e., Eq. (5.18), modifies the positions of the fluid particles as $\mathbf{r}'_i = \mathbf{r}_i + \delta \mathbf{r}_i$. To avoid extreme deviation of the flow variables, we limit the magnitude of the particle-shifting vector by [50]:

$$\delta \mathbf{r}_i = \min(0.1 \|\mathbf{v}_i\| \Delta t, 0.1l_0, \|\delta \mathbf{r}_i\|) \delta \mathbf{r}_i / \|\delta \mathbf{r}_i\|. \quad (5.28)$$

Figure 5.3 summarizes the dynamic particle classification algorithm with the special treatment of the free-surface and boundary particles by the new particle-shifting formulation. Also, this figure shows the particles' categories and the unit-normal vectors on the dam-break test case as an example (with $H/l_0 = 100$, H being the initial height of the water column).

- *Additional diffusive terms due to the particle-shifting transport velocity*

The role of transport velocity of the particle-shifting in the governing equations (5.2) and the total energy of the system is negligible with invariant (or zero) potential energy (e.g.,

[74, 85, 171]). However, for long-term simulations and to capture the correct dynamics of violent free-surface flows (esp. with body forces), consideration of the deviation of velocity in the continuity and momentum equations becomes essential [123]. Here, in the context of the MPS method, we re-derive the additional terms (implemented by Sun et al. [3] in the SPH framework) to include the effects of the particle-shifting velocity in the governing equations. The particle shifting velocity, $\delta\hat{\mathbf{v}}_i$, is defined as the corrected particle shifting vector (Eq. (5.18)) divided by the time step, i.e.:

$$\delta\hat{\mathbf{v}}_i = \delta\mathbf{r}_i/\Delta t. \quad (5.29)$$

In Lagrangian derivatives of any arbitrary value (or vector), f , this velocity deviation modifying the transport velocity, $\mathbf{v} + \delta\hat{\mathbf{v}}$, appears as an extra term, $\nabla f \cdot \delta\hat{\mathbf{v}}$ [3, 144]. Considering the particle number density and the momentum velocity, this term reads:

$$\begin{cases} \nabla n \cdot \delta\hat{\mathbf{v}} = \nabla \cdot (n\delta\hat{\mathbf{v}}) - n\nabla \cdot (\delta\hat{\mathbf{v}}) \\ \nabla \mathbf{v} \cdot \delta\hat{\mathbf{v}} = \nabla \cdot (\mathbf{v} \otimes \delta\hat{\mathbf{v}}) - \mathbf{v} \nabla \cdot (\delta\hat{\mathbf{v}}) \end{cases} \quad (5.30)$$

rewriting the governing equations of the EWC-MPS method (including the modified diffusive terms and the shear force) to:

$$\begin{cases} \frac{1}{n_i} \frac{Dn_i}{Dt} = -\langle \nabla \cdot (\mathbf{v} + \delta\hat{\mathbf{v}}) \rangle_i + \frac{1}{n_i} \langle \nabla \cdot (n\delta\hat{\mathbf{v}}) \rangle_i + D_i^m \\ \frac{D\mathbf{v}_i}{Dt} = -\frac{1}{\rho_i} \langle \nabla p \rangle_i + \mathbf{F}_i + \frac{1}{\rho_i} \langle \nabla \cdot \boldsymbol{\tau} \rangle_i + \langle \nabla \cdot (\mathbf{v} \otimes \delta\hat{\mathbf{v}}) \rangle_i - \mathbf{v}_i \langle \nabla \cdot (\delta\hat{\mathbf{v}}) \rangle_i \\ \frac{D\mathbf{r}_i}{Dt} = \mathbf{v}_i + \delta\hat{\mathbf{v}}. \end{cases} \quad (5.31)$$

To estimate the additional terms, we should consider the mass and momentum conservation properties of the system [3]. The terms containing the velocity deviation are estimated by the following operators in the new system of equations:

$$\begin{cases} \frac{1}{n_i} \langle \nabla \cdot (n\delta\hat{\mathbf{v}}) \rangle_i = \frac{d}{n_0^2} \sum_{i \neq j}^N (n_j \delta\hat{\mathbf{v}}_j + n_i \delta\hat{\mathbf{v}}_i) \cdot \frac{\mathbf{e}_{ij}}{r_{ij}} W_{ij} \\ \langle \nabla \cdot (\mathbf{v} \otimes \delta\hat{\mathbf{v}}) \rangle_i = \frac{d}{n_0} \sum_{i \neq j}^N (\mathbf{v}_j \otimes \delta\hat{\mathbf{v}}_j + \mathbf{v}_i \otimes \delta\hat{\mathbf{v}}_i) \cdot \frac{\mathbf{e}_{ij}}{r_{ij}} W_{ij} \\ \mathbf{v}_i \langle \nabla \cdot (\delta\hat{\mathbf{v}}) \rangle_i = \mathbf{v}_i \frac{d}{n_0} \sum_{i \neq j}^N \frac{\delta\hat{\mathbf{v}}_j - \delta\hat{\mathbf{v}}_i}{r_{ij}} \cdot \mathbf{e}_{ij} W_{ij}. \end{cases} \quad (5.32)$$

We approximate the first additional term inserted in the continuity equation, i.e., $\nabla \cdot (n\delta\hat{\mathbf{v}})$, by the antisymmetric divergence operator and setting $1/n_i = 1/n_0$ to preserve the total mass as $\sum_i \frac{n_i}{n_0} \langle \nabla \cdot (n\delta\hat{\mathbf{v}}) \rangle_i V_i = 0$ [3]. Note that the transport velocity inside the divergence equation of the continuity equation contains the second additional term, $-n\nabla \cdot (\delta\hat{\mathbf{v}})$. Similarly, for the momentum equation, we approximate the first additional term, $\nabla \cdot (\mathbf{v} \otimes \delta\hat{\mathbf{v}})$, with the antisymmetric divergence in order to conserve the linear momentum of the system. Unlike the SPH model by Adami et al. [144] (further generalized by Zhang et al. [163]), we include the divergence of the velocity deviation (i.e., the second additional term, $-\mathbf{v}\nabla \cdot (\delta\hat{\mathbf{v}})$) within the momentum equation. Although the approximated form of this additional term violates the momentum conservation law, it should be noted that the energy conservation of the system is not satisfied by the PS techniques [74, 130]. With the additional terms, the new formulation (5.31) aims to dissipate/eliminate the excessive energy inserted into the system by shifting the fluid particles.

Coupling the additional $\delta\hat{\mathbf{v}}$ -terms in the governing equations with the new particle classification algorithm and the shifting vector (summarized in Figure 5.3), we introduce a new form of the CPS approach identified as CPS*. This algorithm updates the velocity and particle number density fields by the discretized form of Eq. (5.31) after dispositioning the particles with $\delta\mathbf{r}_i$, given by Eq. (5.18) and (5.28). As originally pointed out by Jandaghian and Shakibaeinia [123], in problems with highly dynamic flow deformations, the fluid particles at the free-surface region are still vulnerable to particle-clustering, leading to unphysical fluid fragmentations (as their particle-shifting vector is canceled in the normal direction to the free surface). Similar to Jandaghian and Shakibaeinia [123], to improve the numerical stability of the free surface and the external particles, we append the DPC approach to the CPS* method. This hybrid technique, denoted as CPS*+DPC, applies a corrected particle-shifting vector with the additional $\delta\hat{\mathbf{v}}$ -terms over the fluid domain, while implementing the DPC method only among the free-surface, free-surface boundary, and splashed particles (i.e., $i, j \in \mathbb{F} \cup \mathbb{B}_F \cup \mathbb{E}$ in Eqs. (5.13) & (5.14)). It should be noted that the DPC would act as the only particle regularization technique of the particles with null particle-shifting in these regions (where $i \in \mathbb{E}$ or $(\alpha_i, \beta_i) = (0, 0)$ by Eqs. (5.25) & (5.27)).

Figure 5.4 represents the numerical implementation of the new CPS*+DPC technique. We summarize the proposed enhancements of the CPS*+DPC scheme as follows:

- The new particle classification scheme:
 - recognizes the internal regions where unphysical volume expansion occurs ($i \in \mathbb{X}$),
 - identifies the fluid particles at the vicinity of the wall with the proposed non-local

- normal vectors ($i \in \mathbb{B}_w$),
- detects the fluid particles at the intersections of the free-surface region and the vicinity of the wall ($i \in (\mathbb{F} \cup \mathbb{B}_F) \cap \mathbb{B}_w$), and
 - calculates the curvature of the interfaces by Eq. (5.26).
 - The new particle-shifting formulation (Eq. (5.18)):
 - ignores the solid boundary particles in the shifting process of the fluid particles (Eq.(5.17)),
 - cancels the shifting vectors of the particles with the unphysical volume expansion ($i \in \mathbb{X} \rightarrow \delta \mathbf{r}_i = 0$),
 - through the binary multipliers, α_i and β_i , imposes some restricting conditions to the magnitude and/or direction of the particle shifting vector in the free-surface boundary and the vicinity of the wall, and the regions with extreme flow curvatures (Eqs.(5.24)-(5.27)), and
 - limits the magnitude of the shifting vector according to the particle's velocity and the spatial resolution (Eq. (5.28)).
 - The additional diffusive terms due to the particle-shifting transport velocity (i.e., the $\delta \hat{\mathbf{v}}$ -terms), which are re-derived in the context of the MPS method (Eq.(5.32)), update the velocity, position, and density of the particles based on the governing equations (5.31).
 - The new DPC formulation, coupled with the CPS* algorithm, acts as the particle regularization technique of the particles within the free-surface regions and splashed particles (i.e., $i, j \in \mathbb{F} \cup \mathbb{B}_F \cup \mathbb{E}$) through equations (5.13) & (5.14).

```

CPS*+DPC {
  For  $\forall i \in \Omega_f$ :
    • Define the category of the particle (based on the new particle classification algorithm, Figure 2)
    • Calculate the corrected particle shifting vector:  $\delta \mathbf{r}_i$  (Eqs. (18) & (28))
    • Update the position:  $\mathbf{r}'_i = \mathbf{r}_i + \delta \mathbf{r}_i$ 
    • Estimate and include the additional  $\delta \hat{\mathbf{v}}_i$ -terms in the governing equations (Eqs. (31) & (32):
      • Determine the particle shifting velocity:  $\delta \hat{\mathbf{v}}_i = \delta \mathbf{r}_i / \Delta t$ 
      • Calculate the transport-velocity:  $\delta \mathbf{v}_i = (\langle \nabla \cdot (\mathbf{v} \otimes \delta \hat{\mathbf{v}}) \rangle_i - \mathbf{v}_i \langle \nabla \cdot (\delta \hat{\mathbf{v}}) \rangle_i) \Delta t$ 
      • Update the velocity and position:  $\begin{cases} \mathbf{v}'_i = \mathbf{v}_i + \delta \mathbf{v}_i \\ \mathbf{r}'_i = \mathbf{r}'_i + \delta \mathbf{v}_i \Delta t \end{cases}$ 
      • Calculate the density variation:  $\delta n_i = n_i (1/n_0 \langle \nabla \cdot (n \delta \hat{\mathbf{v}}) \rangle_i - \langle \nabla \cdot (\delta \hat{\mathbf{v}}) \rangle_i) \Delta t$ 
      • Update the particle number density:  $n_i = n_i + \delta n_i$ 
    • Apply the DPC technique among the free-surface, the free-surface boundary, and the
      external particles ( $i, j \in \mathbb{F} \cup \mathbb{B}_F \cup \mathbb{E}$  in Eqs. (13) & (14))
}

```

Figure 5.4 The sequential steps of the CPS*+DPC algorithm as a hybrid particle regularization approach. The new particle classification algorithm is represented in Figure 5.3, and the corrected particle-shifting vector is given by Eqs. (5.18) & (5.28).

5.4.3 Initial and solid boundary conditions

Here, we apply the initial hydrostatic pressure to all the particles at $t = 0$ based on their initial position with respect to the free surface and considering the gravitational force as $g = 9.81 \text{ m/s}^2$ in the negative y-direction. The inverse form of the EOS (i.e., $n_i^0 = n_0 (p_i^0/B_0 + 1)^{1/\gamma}$, in which $B_0 = c_0^2 \rho_0 / \gamma$), calculates the initial particle number density, n_i^0 , which will be updated by the continuity equation.

The solid boundary particles consist of the wall and ghost particles (see [123]). The position of these particles remains fixed with respect to each other constructing the rigid walls. In this study, to simulate fluid-wall interactions, we adopt either the dynamic boundary condition [67] or the generalized wall boundary condition [172]. In these models, the pressure of the fluid particles approaching the wall increases through the continuity equation (i.e., in Eq. (5.4) considering the true velocity of the reservoir, \mathbf{v}_w , for the neighbor boundary particles). To implement the free-slip boundary condition for violent flow simulations, both models ignore

the solid boundary particles in the fluid particle shear force calculations [62, 158].

Regarding the pressure of the wall particles, these boundary models implement different formulations. In the dynamic boundary condition, the continuity equation updates the density of the wall particles (with an adjusted wall velocity), and the equation of state calculates their pressure. Furthermore, the divergence of the velocity ignores the presence of ghost particles in the fluid and wall particle continuity equations. In the generalized wall boundary condition, the fluid particles' pressure at the vicinity of the wall is smoothed on the wall particles by including the gravity force and the wall's accelerations [172]. Then, the inverse form of the equation of state determines the wall's particle number density. However, in both methods, we directly assign the pressure of the nearest wall particle to the ghost particles.

5.4.4 Time integration scheme

We employ the second-order symplectic algorithm [11] for the temporal integration of the equations. This algorithm updates the interaction forces, the pressure field, and the particles' positions by dividing each time step, Δt , into two calculation stages with $\Delta t/2$ (see Appendix 5.6). The viscosity of particles is recalculated at the beginning of each stage by estimating the gradient of velocity and the magnitude of the strain rate tensor. The adopted particle regularization techniques are implemented only in the second stage of the scheme before calculating the new particle number density and pressure fields (Figure 5.24). Thus, to determine the transport velocity and regulate the particles' positions, Δt is substituted by $\Delta t/2$ in Figure 5.4 and Eq. (5.14) for the CPS* and DPC techniques, respectively.

To determine the invariant time step of the integration scheme, Δt , we employ the Courant–Friedrichs–Lewy (CFL) stability condition as:

$$\Delta t = C_{CFL} \frac{l_0}{c_0} \quad (5.33)$$

in which C_{CFL} is the CFL coefficient and the artificial sound speed, c_0 , is a problem-dependent parameter determined based on the expected Mach number [47, 173]. One should note that in the problems studied as the violent and impact flows, even with the turbulence viscosity included in the shear stress calculations, the acoustic and the kinetic constraints remain dominant for determining the time step of the explicit model [173]. The solution algorithm is implemented on a parallel accelerated code run on the Graphical Processing Unit (GPU) using Compute Unified Device Architecture (CUDA) parallel programming language based on C++ (see Appendix 5.6 for more details).

5.5 Numerical results and discussions

In this study, we simulate challenging violent free-surface flow benchmark cases to evaluate the role of the proposed enhancements. The cases include the two-dimensional (2D) water dam-break and three-dimensional (3D) sloshing and obstacle impact problems.

5.5.1 2D water dam-break

This benchmark case has been the focus of numerous particle methods (e.g., [25,75,164,174]). Capturing these complex flows, dominated by water-water and water-solid impacts, requires robust particle regularization techniques to eliminate possible numerical instabilities while conserving the total momentum and energy of the system [3].

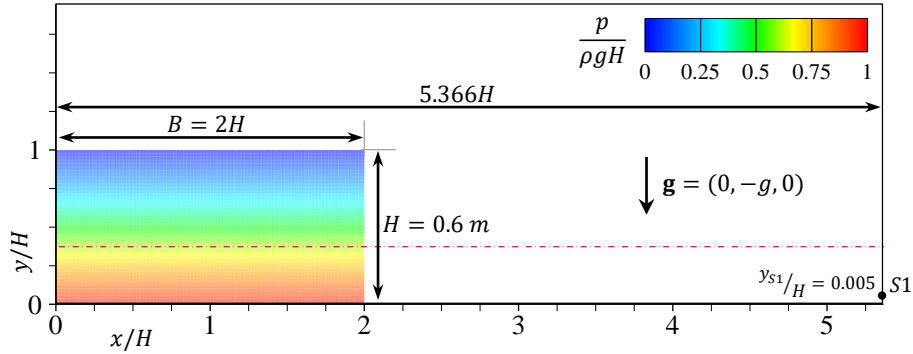


Figure 5.5 Initial configuration and pressure contour of the 2D water dam-break based on the experimental setup by Lobovský et al. [4]. The dash-dot line is the expected free surface of the fluid flow filling the width of the tank at the final equilibrium state.

We set up the initial configuration of the dam break based on the physical model by Lobovský et al. [4] (shown in Figure 5.5). With the initial height of the water column, H , and the initial particle distance, l_0 , located on the Cartesian lattice, the spatial resolution is identified as $R = H/l_0$ (where in this study $R = 60, 100$, and 200 , which correspond to 11,840, 27,696, and 95,312 total numbers of particles, respectively). We simulate the time evolution of the dam break for 10 seconds and define the non-dimensional time as $T = t\sqrt{g/H}$. Based on the kinetic energy pressure constraint (for specifying the artificial sound speed of the weakly compressible model) and the maximum expected velocity, which is given as $\|\mathbf{v}\|_{max} = 2.0\sqrt{gH}$, we set the sound speed to 100 m/s, limiting the Mach number to 0.049 (see [175]). In all the cases, the C_{CFL} coefficient is equal to 0.5, except in the model without the regularization technique, in which $C_{CFL} = 0.25$. We employ the dynamic boundary condition to simulate the interaction

forces between the fluid and the rigid walls. In the DPC scheme, the maximum and minimum pressures of Eq. (5.15) are given as $2.3\rho gH$ (based on the analytical solution discussed in [175]) and ρgl_0 , respectively. In the case of the standard PC method being implemented, we set the constants of Eq. (5.12), $\varepsilon = 0.5$ and $\theta = 0.9$. In this problem, we normalize the global energies (E_p : the potential energy, E_k : the kinetic energy, E_m : the mechanical energy, and Q_{PC} : the total kinetic energy dissipated by the DPC technique, for which the formulations are given in Appendix 5.6) by $\Delta E_m^{Fin} = E_m^\infty - E_m^0$, in which E_m^0 is the initial mechanical energy (equal to E_p^0) and E_m^∞ is the final mechanical energy of the system (equal to the final expected potential energy with the water phase filling the width of the tank and reaching the equilibrium state).

Concerning the short-term evolution of the flow ($T < 8$), we first validate the numerical (i.e., from the models with either the DPC or the CPS*+DPC techniques or with no regularization technique) versus the experimental results of [4]. Figure 5.6 compares the time history of the local pressure signal at point $S1$ and the propagation of the wave on the horizontal bed. To measure the local pressure, the pressure of the fluid particles inside the support radius, set to $1.6l_0$ from the sensor, are linearly averaged every 0.004 s without kernel-smoothing or any data-filtering (i.e., $p_{S1} = \sum_1^{N_s} p_j / N_s$, as N_s is the number of fluid particles, j , where $\|\mathbf{r}_j - \mathbf{r}_{S1}\| \leq 1.6l_0$). For both parameters, the results of the simulations followed the same trends as the experimental measurements. Incompatibilities between the experimental and numerical results originate from the weak compressibility of the flow, ignoring the air phase, and the implemented solid boundary model. The numerical stability of the test case without the regularization technique can be evaluated from Figure 5.7. In this model, the particle-clustering becomes dominant with the progress of the impact events (i.e., as the wave impacts the front wall at $T \simeq 2.5$, a plunging jet forms and impinges the free surface at $T \simeq 6.06$). Numerical instability due to extreme inter-particle penetration terminated the simulation at $T \simeq 9.0$ (as the unphysical inter-particle forces ejected the clustered particles outside the predefined computational domain). Furthermore, as shown in the zoomed-in sections of Figure 5.7, unphysical fluid fragmentations exist, especially in the flow regions with highly dynamic deformations. Eliminating these numerical issues, which hinder long-term simulations of violent flows and affect flow evolutions, requires a great emphasis on the adoption of rigorous particle regularization techniques.

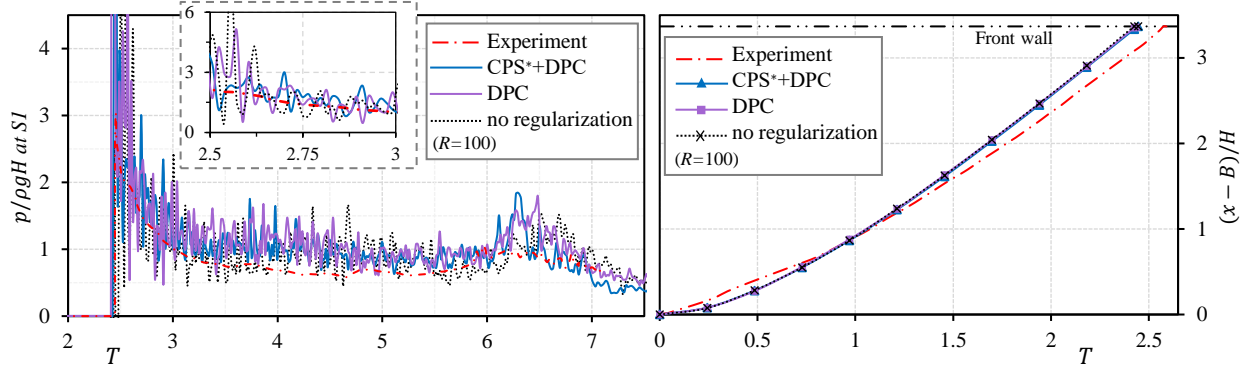


Figure 5.6 Numerical results of the models ($R = H/l_0 = 100$) with the CPS*+DPC, DPC, and without regularization techniques versus the experimental results of Lobovský et al. [4]: the time history of averaged local water pressure, p , at $S1$ (left) and the wave propagation (right).

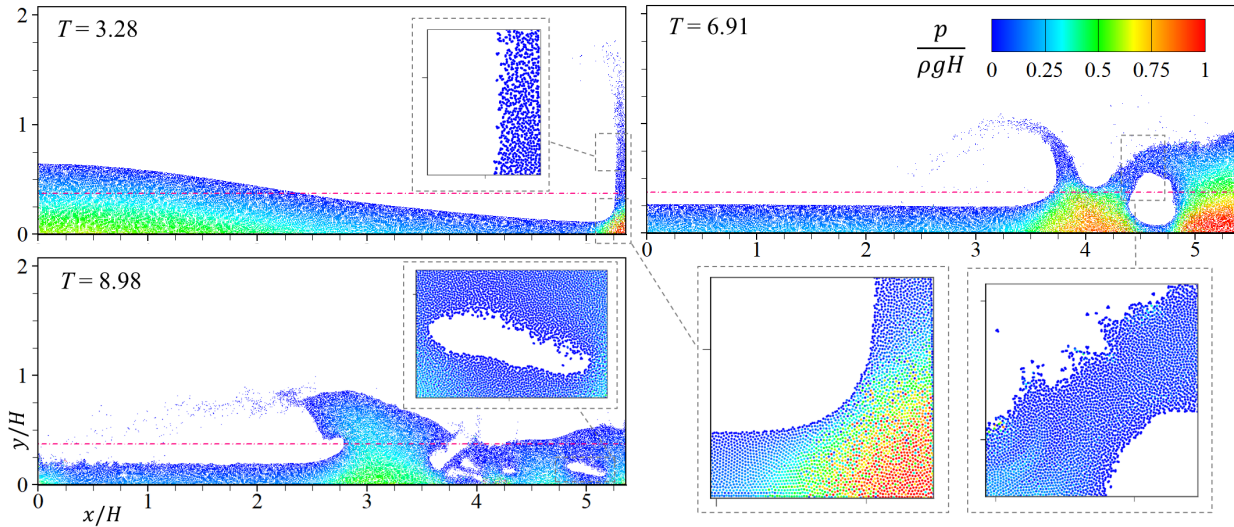


Figure 5.7 The dam break problem without the particle regularization techniques ($R = 200$). The dash-dot line is the expected free surface of the fluid flow filling the width of the tank at the final equilibrium state.

In this part, we investigate the role of the proposed DPC regarding the stability and energy evolution of the system. Figure 5.8 depicts that both the DPC and PC techniques

guarantee the long-term simulation of the dam break by resolving the numerical stabilities. However, the model with the PC method still suffers from noisy pressure fields, which may lead to inaccurate flow predictions. In contrast, the DPC technique effectively reduces the high-frequency pressure fluctuations (specifically illustrated in the zoomed-in sections of Figure 5.8). Regarding the energy variations of the fluid phase, Figure 5.9 shows that both the PC and DPC methods reached the final expected equilibrium state (i.e., $\Delta E_p/\Delta E_m^{Fin} = -1$) without any manipulation of the potential energy. The kinetic, potential, and mechanical energies of these models followed almost identical patterns during the impact events (between $T = 2.5$ and 17.5), since their formulations did not affect the total linear momentum of the system. Moreover, in comparison to the model without regularization (which is stable till $T \simeq 9.0$), both the PC and DPC techniques represent similar energy profile evolutions. However, the DPC dissipates the kinetic energy almost two times as much as the standard PC technique. This confirms that the DPC ensures numerical stability without changing the overall energy of the system, while acts as an efficient artificial viscosity formulated by the pairwise and dynamic repulsive and collision terms. Furthermore, Figure 5.9 depicts that with the higher spatial resolutions ($R = 60, 100, \text{ and } 200$), the heat produced by the DPC, i.e., Q_{PC} , reduces which confirms the numerical convergence of the model (especially during the violent dam break flow).

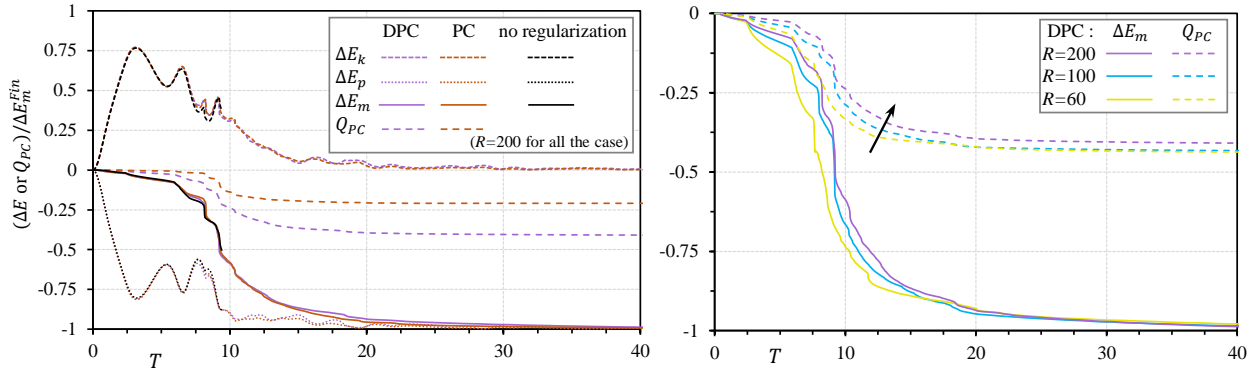


Figure 5.9 Time history of the kinetic, ΔE_k , potential, ΔE_p , and mechanical, ΔE_m , energies of the dam break test case with the DPC vs PC methods (left graph). The total kinetic energy dissipation by the PC techniques (accumulated over time) is denoted as Q_{PC} . The right graph represents the particle convergence of the 2D dam-break simulation as the total energy dissipation reduces with increasing the spatial resolution, $R = H/l_0$.

In the next step, we study the effectiveness of the corrected particle-shifting algorithms in

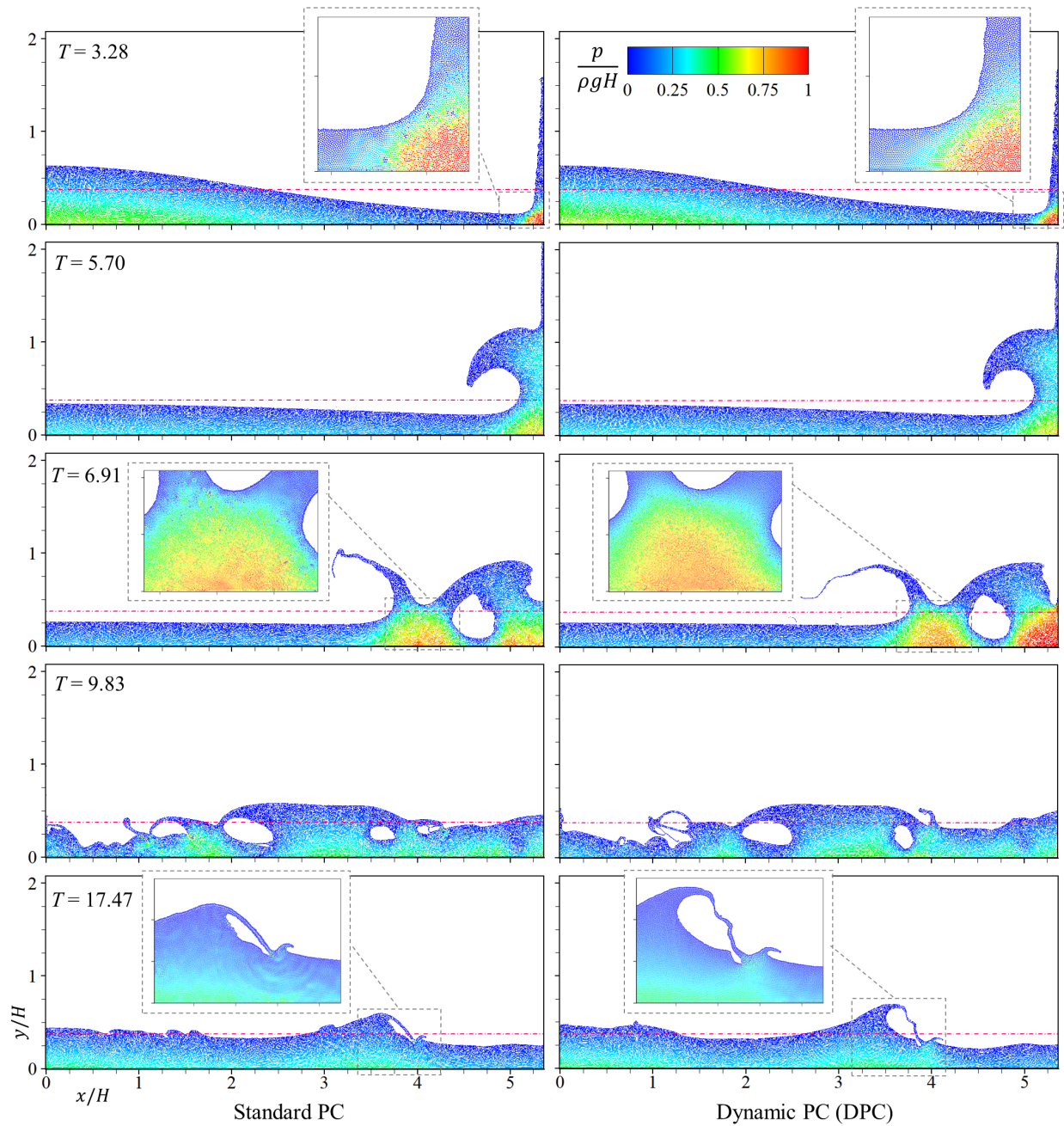


Figure 5.8 Time evolution of the dam break problem with the standard PC (left column) and the DPC (right column) techniques ($R = 200$). The color contour represents the non-dimensional pressure field at $T = t\sqrt{g/H} = 3.28, 5.70, 6.91, 9.83,$ and 17.47 (from the top row to the bottom row, respectively). The dash-dot line is the expected free surface of the fluid flow filling the width of the tank at the final equilibrium state.

capturing the flow and energy evolutions. As shown in the right column of Figure 5.10, the CPS*+DPC algorithm simulates the evolution of the dam break without unphysical volume expansion; however, the same model without the additional $\delta\mathbf{v}$ -terms expands the volume of the fluid phase, particularly when $T \gtrsim 8.0$ (Figure 5.10, left column). To further clarify the role of the $\delta\hat{\mathbf{v}}$ -terms, Figure 5.11 compares the energy profiles of the CPS*+DPC method (with and without the $\delta\hat{\mathbf{v}}$ -terms) versus the original CPS+PC [123]. It shows that the continuous application of particle-shifting with the original CPS+PC increases the potential energy of the system considerably after $T \gtrsim 8.0$. Even limiting the magnitude of the shifting vector (by Eq. (5.28)) in the original CPS+PC does not reduce the accumulation of errors, which leads to inaccurate estimation of the mechanical energy in a long-term simulation. The new CPS scheme without the $\delta\hat{\mathbf{v}}$ -terms decreases these errors by canceling the shifting vectors of the expanded particles (i.e., $i \in \mathbb{X} \rightarrow \delta\mathbf{r}_i = 0$). The consistent CPS*+DPC method completely dissipates the excess energy inserted into the system noting that the potential energy converges to the final expected value (i.e., no volume expansion occurs). Moreover, by increasing the spatial resolution, the CPS*+DPC formulations represent slightly fewer errors in predicting the final potential energy. Nevertheless, as shown in Figure 5.11, the kinetic energy is noticeably dissipated with the CPS*+DPC technique (between $T = 6.0$ and 17.5). This shows that although implementation of the $\delta\hat{\mathbf{v}}$ -terms is required for long-term simulations (to avoid unphysical volume expansion), these terms can affect the kinetic energy and therefore the mechanical behavior of the 2D dam-break flow during impact events. We should also note that the additional terms might only be essential for the weakly compressible models and can be neglected for a fully incompressible model (subjected to further investigations).

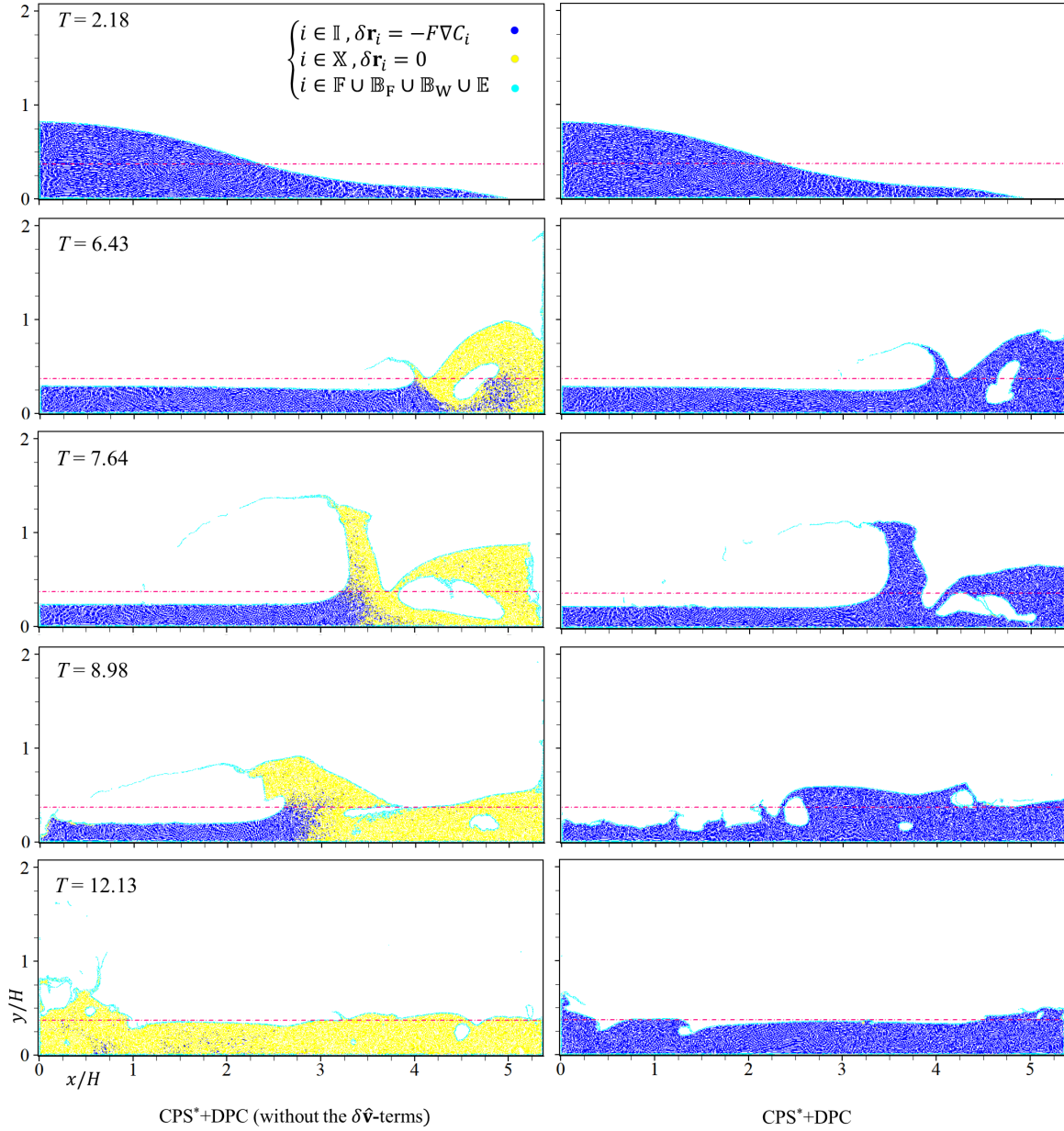


Figure 5.10 Time evolution of the dam break problem simulated by the CPS*+DPC technique with and without the $\delta \hat{\mathbf{v}}$ -terms (represented in the right and left columns, respectively). The resolution is set to $R = 200$ and the expanded regions, i.e., $i \in \mathbb{X}$, are identified with the yellow particles. The dash-dot line is the expected free surface of the fluid flow filling the width of the tank at the final equilibrium state.

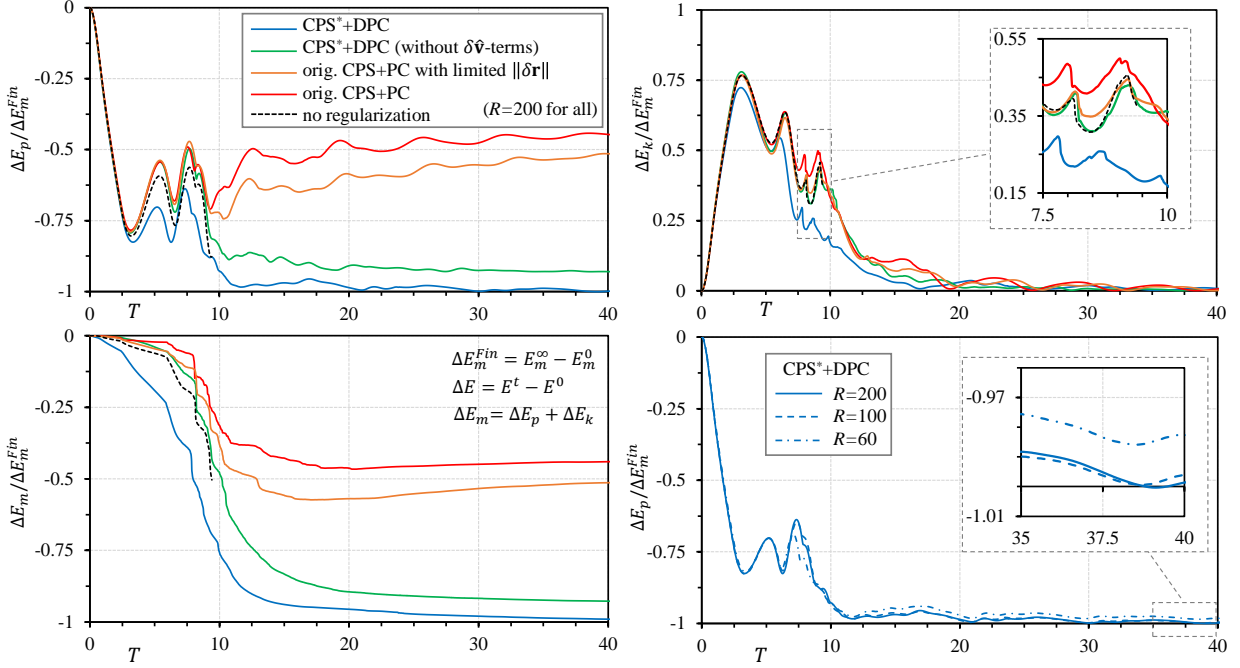


Figure 5.11 The evolution of energy components (E_p : the potential energy (top left), E_k : the kinetic energy (top right), and E_m : the mechanical energy (bottom left) (defined by Eq. (5.37)) of the 2D dam-break problem with different CPS techniques and resolutions. The bottom right graph shows the convergence of the potential energy to the expected final state (i.e., $\Delta E_p/\Delta E_m^{Fin} = -1$) by increasing the spatial resolution, $R = H/l_0$.

Figure 5.12 demonstrates that the EWC-MPS with the proposed stabilization techniques ensures the long-term-simulations of these complex flows and represents noise-free pressure fields. However, we observe that the CPS*+DPC method slightly alters the flow evolution (particularly at $T = 8.98$) by excessive dissipation of the kinetic and potential energies (also shown in Figure 5.11). Meanwhile, the model with the DPC technique predicts the flow and pressure evolutions without the numerical instabilities or affecting the evolutions of the global energies. One should also note that in the CPS*+DPC technique although the PS vector is neglected for the splashed particles and where $(\alpha_i, \beta_i) = (0, 0)$ (through Eqs. (5.25) & (5.27)), the DPC technique is effectively ensuring the numerical stability in these regions (e.g., see the corners of the fluid domain of the dam-break problem in Figure 5.3).

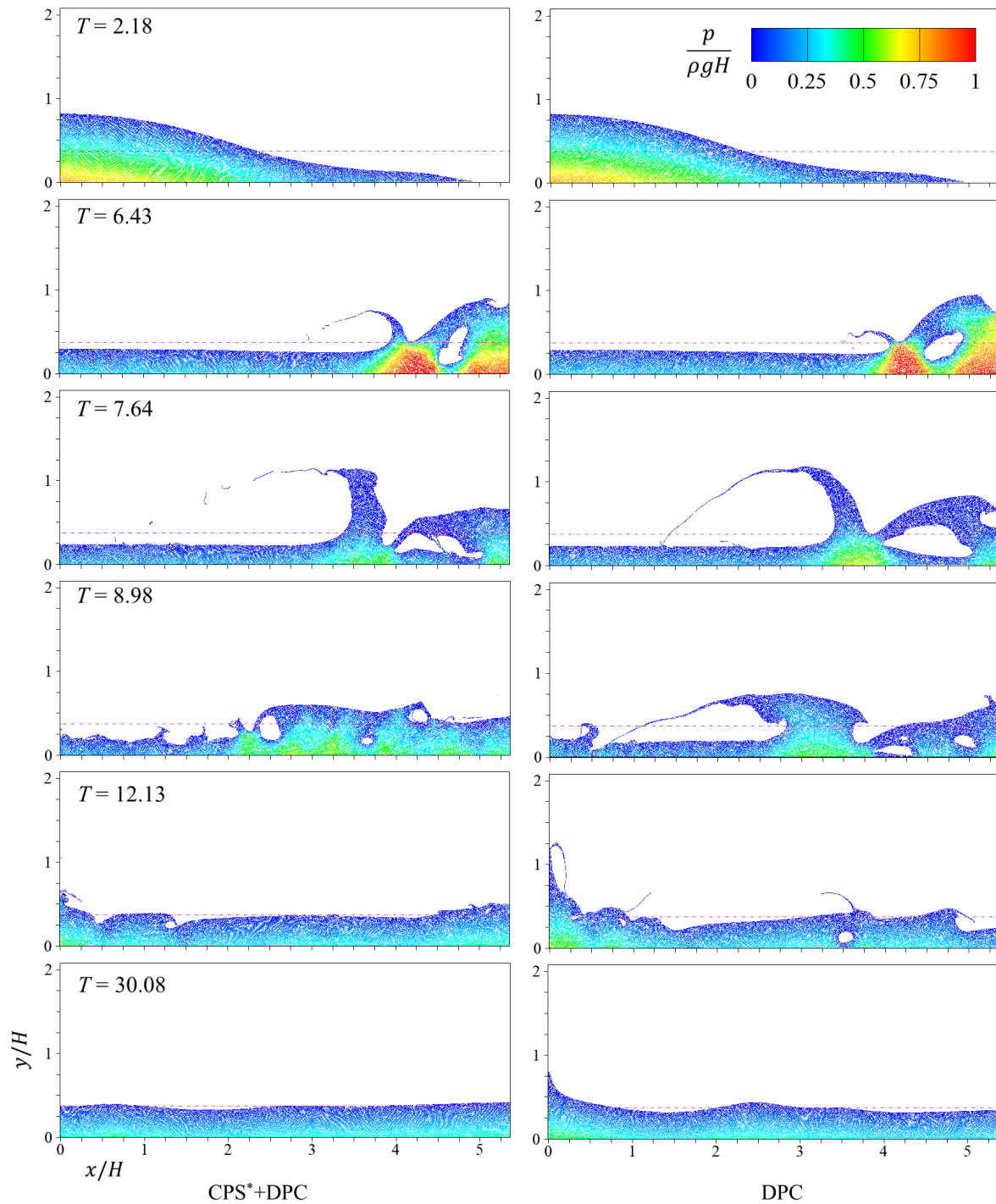


Figure 5.12 Time evolution of the dam break problem with the CPS*+DPC (left column) and the DPC (right column) techniques ($R = 200$). The color contour represents the non-dimensional pressure field. The dash-dot line is the expected free surface of the fluid flow filling the width of the tank at the final equilibrium state.

5.5.2 3D water sloshing in a rectangular reservoir

Here we simulate 3D water sloshing in a rectangular reservoir that moves with a harmonic motion in the longitudinal direction. Under the gravitational force and with this motion's frequency being close to the natural frequency of water, a violent flow consisting of bore breaks and impact events forms within the tank [168]. This highly non-linear free-surface flow has been modeled by particle methods to show their effectiveness in dealing with such complex features (e.g., [5, 55, 164, 168]).

We set up the numerical model based on the physical model by Rafiee et al. [5]. A horizontal channel with dimensions $L \times D \times W$ (in the x-, y-, and z-directions, where $L = 1.3$, $D = 0.9$, and $W = 0.1$ m) is partially filled with water with an initial height of $H = 0.2D$ (Figure 5.13). To validate the results with the experimental measurements, we extract the local pressure (every 0.004 seconds) on the side-wall of the channel at points $P1$, $P2$, and $P3$ as identified in Figure 5.13 (with the same formulation used in the 2D dam-break test case). The numerical results are represented for 8 seconds of the simulations. The frequency, f , and amplitude, A_0 , of the harmonic motion are set to 0.496 s^{-1} and 0.1 m , respectively. Sinusoidal excitation updates the positions and velocities of the solid boundary particles ($i \in \Omega_s$) in the x-direction as $\mathbf{r}_i = \mathbf{r}_i^0 + \{A_0 \sin(2\pi f_0 t), 0, 0\}$ and $\mathbf{v}_i = \{2\pi A_0 f_0 \cos(2\pi f_0 t), 0, 0\}$ at the midpoint and the end of each time step. Furthermore, we assign the initial hydrostatic pressure and the velocity as equal to $\mathbf{v}_i^0 = \{2\pi A_0 f_0, 0, 0\}$ for all the particles at $t = 0$. In this problem, we implement the generalized wall boundary condition from Adami et al. [172], which includes the gravity force, \mathbf{g} , and the acceleration of the rigid walls, $\mathbf{a}_{w_i} = \{-4A_0 (\pi f_0)^2 \sin(2\pi f_0 t), 0, 0\}$, in the pressure calculation for the wall particles. We define the spatial resolution of the simulations as $R = L/l_0$ set to 100, 200 and 260, which corresponds to the total numbers of 90,972, 365,464 and 661,952 particles located on the cubic lattice. For all the test cases $C_{CFL} = 0.25$

Table 5.1 Calculation time per iteration (i.e., $t^{iter.} = \text{Total calculation time}/\text{Total number of time steps}$) of the 2D water dam-break problem with different spatial resolutions, R . The last row of the table represents the rate of increase in the calculation time obtained by the CPS*+DPC versus the DPC technique. The GPU accelerated code is run on an NVIDIA V100 Volta GPU device.

$R = H/l_0$		60	100	200
Number of fluid particles, Ω_f		7,200	20,000	80,000
Calculation time per iteration, $t^{iter.}$ (sec.)	DPC	7.42E-03	8.49E-03	2.04E-02
	CPS*+DPC	8.69E-03	1.01E-02	2.41E-02
$[t^{iter.}(\text{CPS}^* + \text{DPC})/t^{iter.}(\text{DPC}) - 1] \times 100$		17.11	18.96	18.13

and $c_0 = 50$ m/s, the maximum expected velocity, given as $\|\mathbf{v}\|_{max} = 2.0\sqrt{gH}$, limits the Mach number to 0.053 [175]. The maximum and minimum pressures of the DPC technique (in Eq. (5.15)) are determined as 15 kPa (according to the experimental measurements in [5]) and ρgl_0 , respectively.

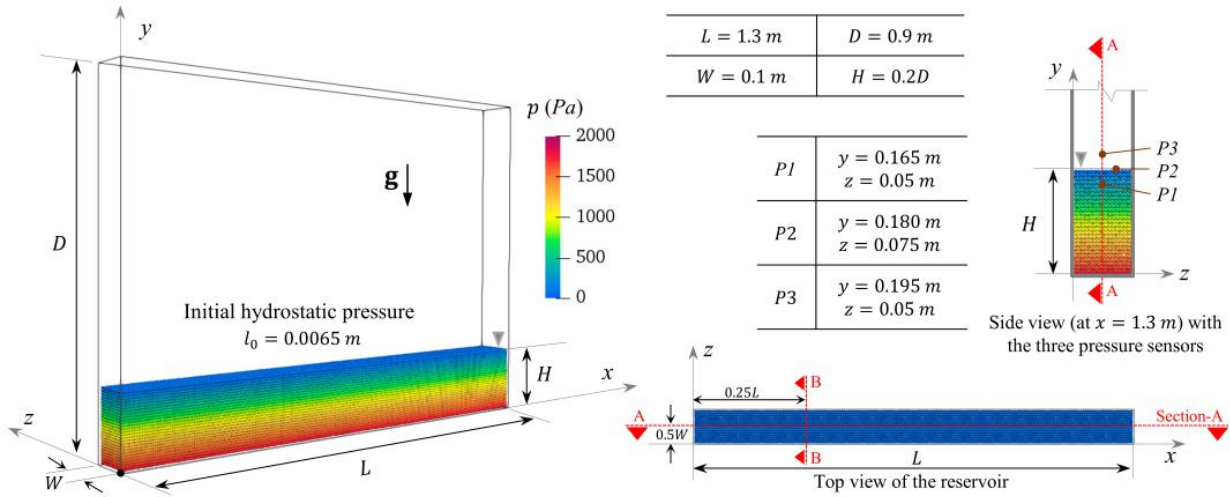


Figure 5.13 Initial configuration and pressure field of the 3D water sloshing problem. The locations of the three pressure sensors ($P1$, $P2$, and $P3$, which in the physical model by Rafiee et al. [5] correspond to sensors $P180$, $P078$, and $P136$, respectively) are specified on the side view of the reservoir. Section A-A and Section B-B, identified on the top view of the reservoir, are used to represent the numerical results.

Figure 5.14 plots the numerical local pressure at points $P1$, $P2$, and $P3$ versus the experimental results of [5]. The time evolutions of the pressure profiles with either the DPC or the CPS*+DPC techniques are in good agreement with those from the experimental measurements. In the physical model, the air pockets entrapped as the flow impacts the wall avoid a sudden increase in local pressure; however, the single-phase numerical models, by ignoring the air phase, neglect the cushioning effects [5, 164, 168]. This issue results in a discrepancy between the numerical and experimental measurements, manifested as overestimations of the numerical pressure when the wave reaches the sidewall at $t = 2.5$, 4.5, and 6.5 seconds (Figure 5.14).

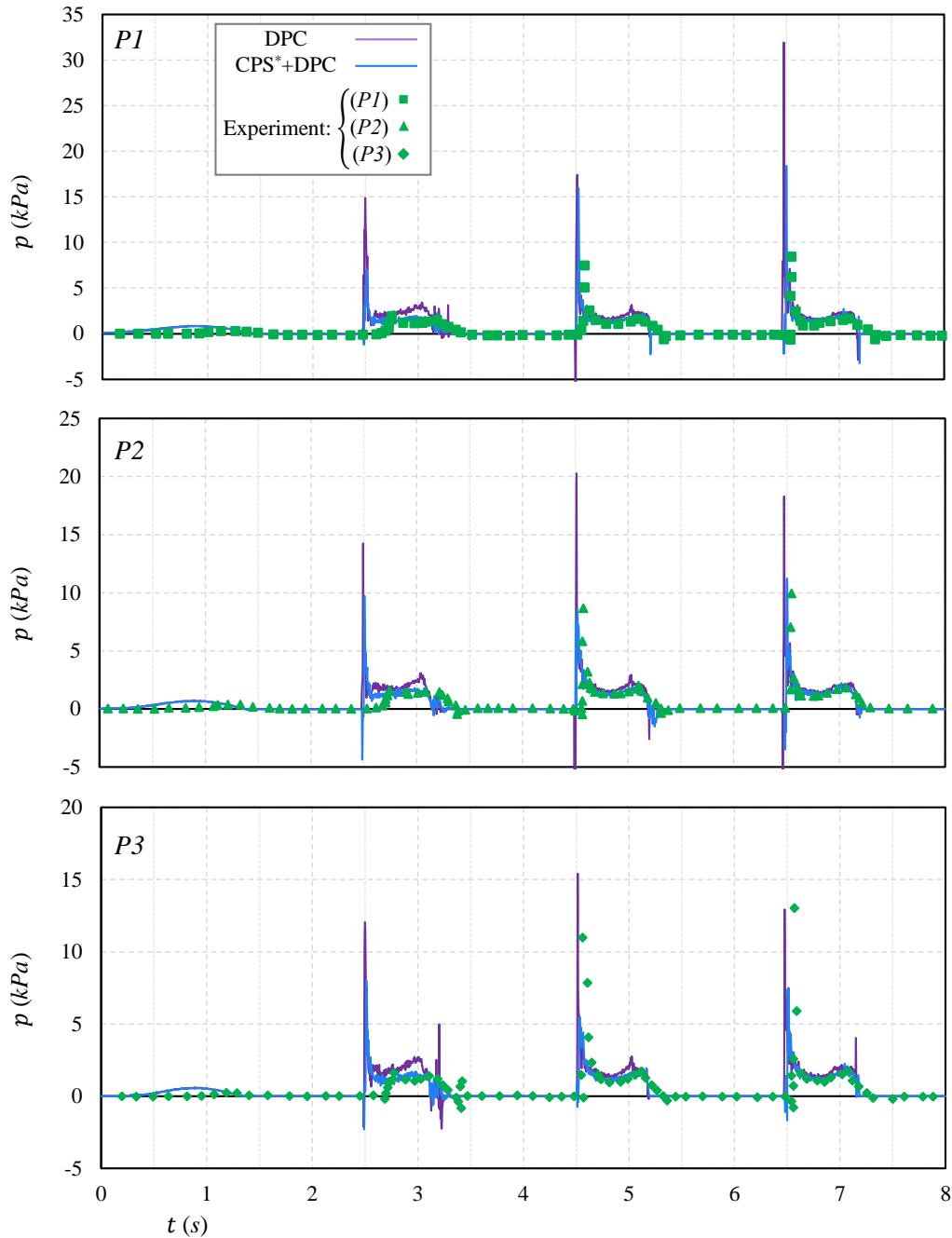


Figure 5.14 Local numerical pressure (with $R = L/l_0 = 200$) versus the experimental measurements of Rafiee et al. [5] at the $P1$ (top), $P2$ (middle), and $P3$ (bottom) points.

Figure 5.15 illustrates the flow evolution and pressure fields, comparing the simulations with the CPS*+DPC and DPC where $R = 260$. Both models show identical flow evolutions while ensuring long-term numerical stability by resolving the particle-clustering problem.

Moreover, with the modified diffusive term, the simulations represent smooth pressure fields. In Figure 5.16, the new CPS*+DPC technique with the implemented $\delta\hat{\mathbf{v}}$ -terms preserves the overall volume of the fluid phase (shown in the right column); nevertheless, the same model without the additional $\delta\hat{\mathbf{v}}$ -terms leads to unphysical volume expansion after a few cycles (see left column). Figure 5.17 represents the new dynamic particle classification in the 3D configuration of the fluid flow. With this algorithm, the CPS*+DPC technique deals dynamically with the extreme flow curvatures (including the corners) and the intersection of the particles detected as the free-surface boundary and the wall boundary particles.

The temporal evolutions of the global energies of the system are illustrated in Figure 5.18, where the non-dimensional time is given as $T = t\sqrt{g/L}$. Here, the components of energy, i.e., ΔE and Q_{PC} (see Appendix 5.6), are normalized by the initial mechanical energy, $E_m^0 = E_p^0 + E_k^0$. We observe that CPS*+DPC without the $\delta\hat{\mathbf{v}}$ -terms increases the potential energy over time (also shown in the left column of Figure 5.16). On the other hand, implementing the $\delta\hat{\mathbf{v}}$ -terms dissipates the excessive potential energy and predicts less kinetic energy versus the DPC technique. Furthermore, the results show that with a higher spatial resolution ($R = 200$ and 260), the heat produced by the DPC technique, i.e., Q_{PC} , decreases.

Moreover, Table 5.2 represents the calculation time per iteration ($t^{iter.}$) of the 3D simulations with the three spatial resolutions using an NVIDIA V100 Volta GPU device for solving the main temporal loop of the algorithm. Comparing the calculation time per iteration demonstrates that the CPS*+DPC algorithm increases the calculation cost by $\sim 20\%$. This result highlights that the DPC technique while being as effective as the CPS*+DPC technique with less energy dissipation is simple to numerically implement since does not involve the time-consuming conditional operations of the CPS*+DPC algorithm (required for the particle classifications and approximating the additional terms).

Table 5.2 Calculation time per iteration (i.e., $t^{iter.} = \text{Total calculation time}/\text{Total number of time steps}$) of the 3D water sloshing problem with different spatial resolutions, R . The last row of the table represents the rate of increase of the calculation time with the CPS*+DPC versus the DPC technique. The GPU accelerated code is run on an NVIDIA V100 Volta GPU device.

$R = L/l_0$		100	200	260
Number of fluid particles, Ω_f		11,700	81,000	187,200
Calculation time per iteration, $t^{iter.}$ (sec.)	DPC	5.83E-02	1.33E-01	3.67E-01
	CPS*+DPC	6.68E-02	1.66E-01	4.47E-01
$[t^{iter.}(\text{CPS}^* + \text{DPC})/t^{iter.}(\text{DPC}) - 1] \times 100$		14.58	24.81	21.79

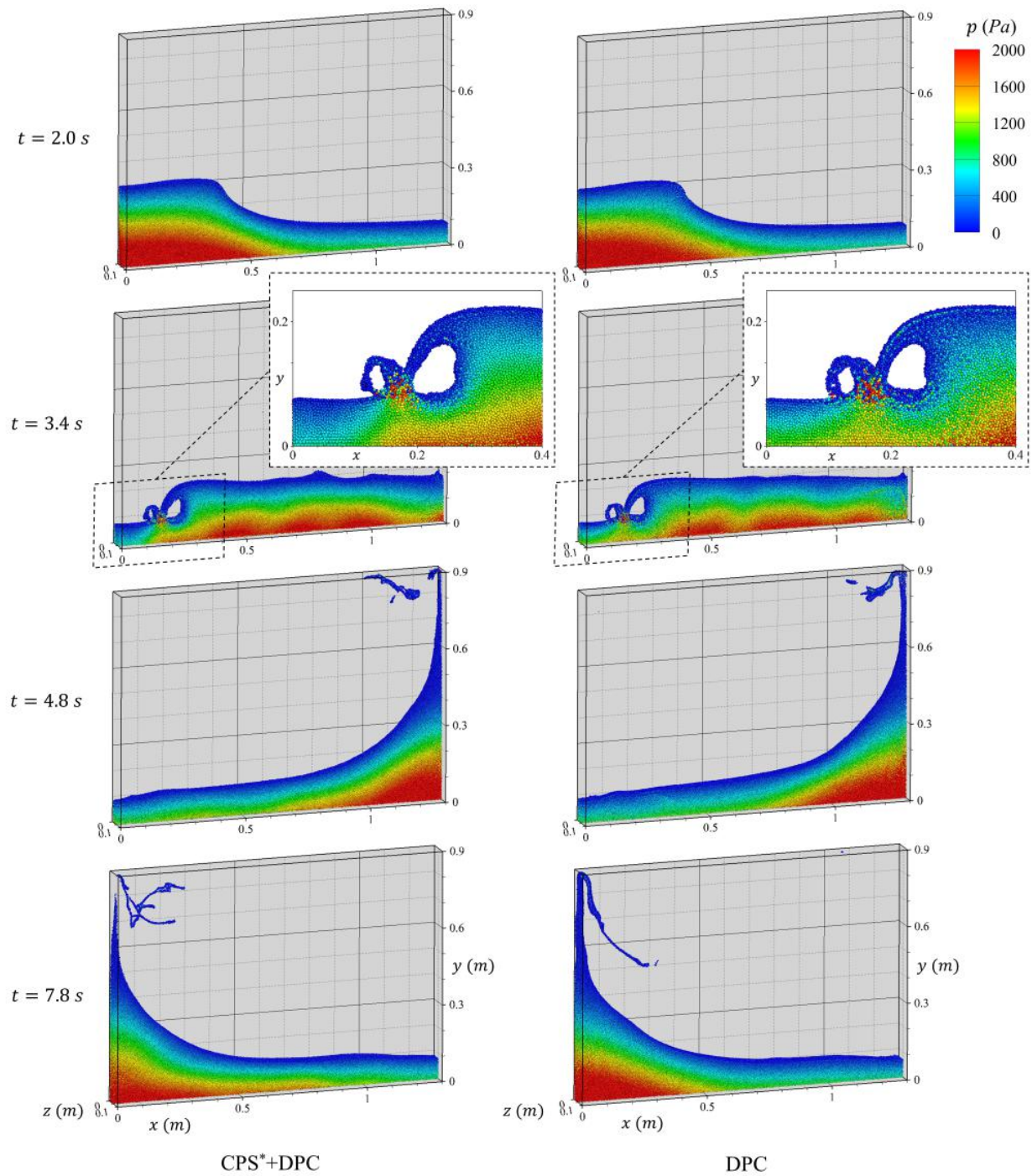


Figure 5.15 Flow evolutions and the pressure field of the water sloshing problem (at Section A-A) simulated by the model with the CPS*+DPC (left column) and the DPC (right column) techniques, where $R = 260$.

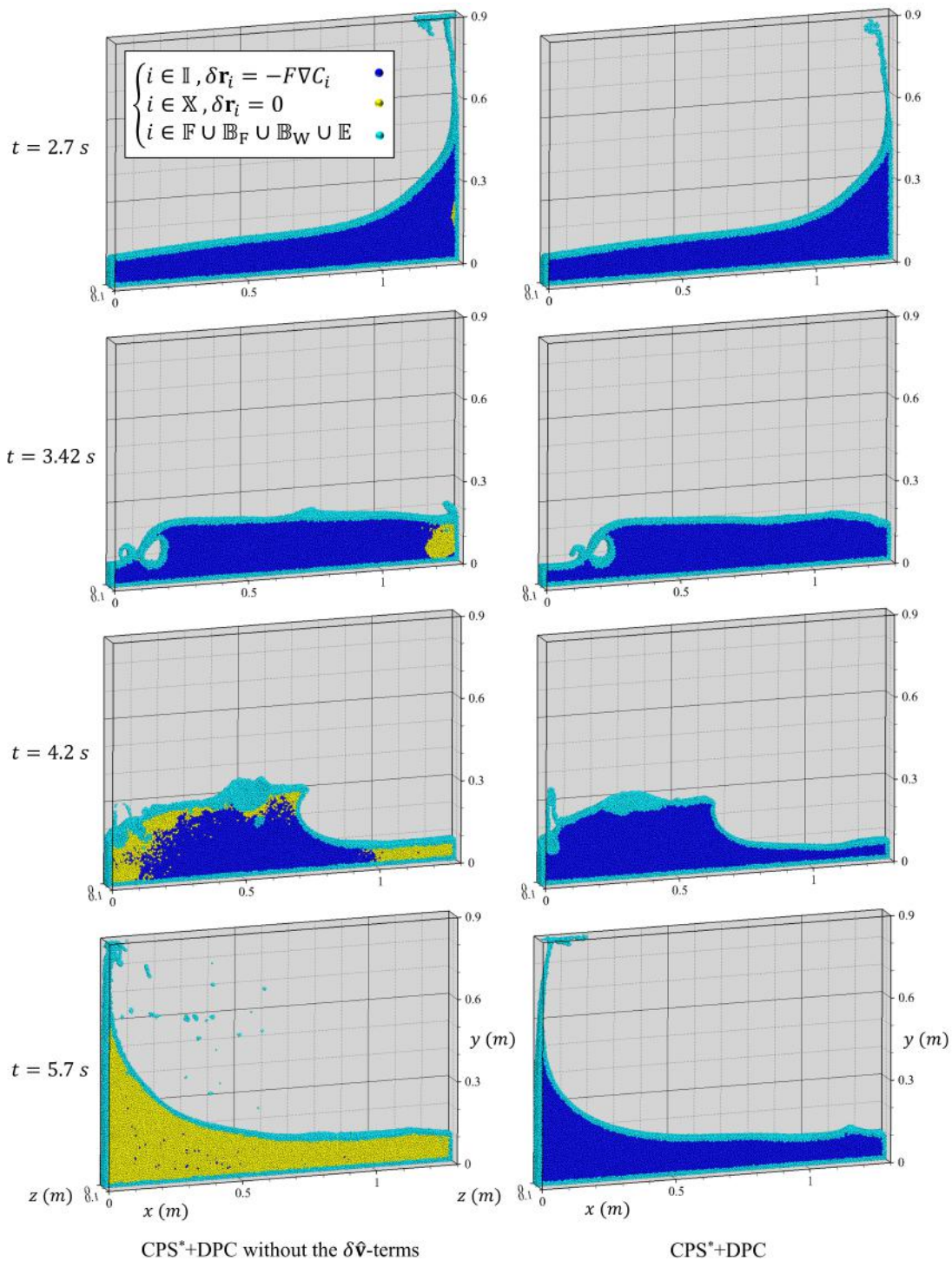


Figure 5.16 Time evolution of the 3D water sloshing problem (at Section A-A) using the CPS*+DPC techniques with and without the additional $\delta \hat{\mathbf{v}}$ -terms (represented in the right and the left columns, respectively). The resolution is set to $R = 200$, and the expanded regions, i.e., $i \in \mathbb{X}$, are identified with the yellow particles.

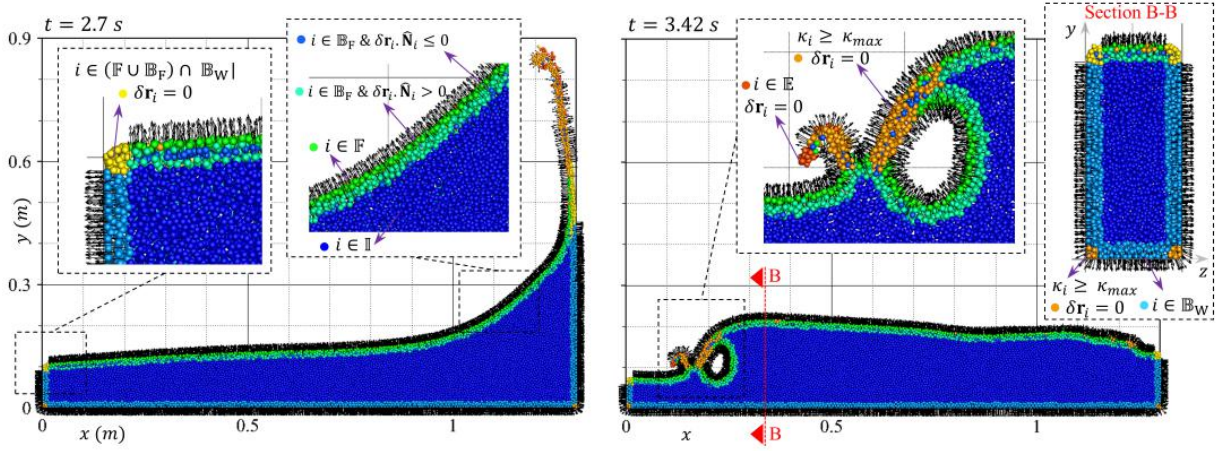


Figure 5.17 Particle classification and normal vectors of the 3D sloshing problem at Section A-A and Section B-B with the CPS*+DPC technique and $R = 200$.

5.5.3 3D water dam-break against a rigid obstacle

In this test case, under the gravitational force, a column of water collapses and impacts a rigid cuboid obstacle. Particle methods have widely simulated this problem as a benchmark case for studying violent flows and fluid-structure interactions (e.g., [62, 167, 168, 176–178]).

We employ the experimental model from Kleefsman et al. [6] to set up and validate the numerical simulations. Figure 5.19 illustrates the initial configuration of the problem, the location of points $P1$ and $P2$, and the vertical lines $H1$ and $H2$ used for probing the local pressure and the depth of the water, respectively. With the spatial resolution given as $R = H/l_0 = 55$, the simulation contains 1,044,444 particles, including the fluid and solid boundary particles located on the cubical lattice. In this benchmark case, the generalized wall boundary model from Adami et al. [172] simulates the interaction forces between the fluid and the rigid bodies. The CFL coefficient and the Mach number are equal to 0.5 and 0.046, respectively, with the sound speed set to 100 m/s and $\|\mathbf{v}\|_{max} = 2.0\sqrt{gH}$. Like the dam-break test case, the maximum and minimum background pressures of the DPC formulation are determined as $2.3\rho gH$ and $\rho g l_0$, respectively.

The numerical results of the proposed model with either the DPC or CPS*+DPC represent trends almost similar to the experimental measurements (Figure 5.20). The depth of water at the $H1$ and $H2$ lines (extracted every 0.05 seconds for three spatial resolutions, $R = 13.75, 27.5,$ and 55) shows that the flow evolutions are comparable with the experimental profiles. However, the absence of the air phase and its cushioning effects in the numerical

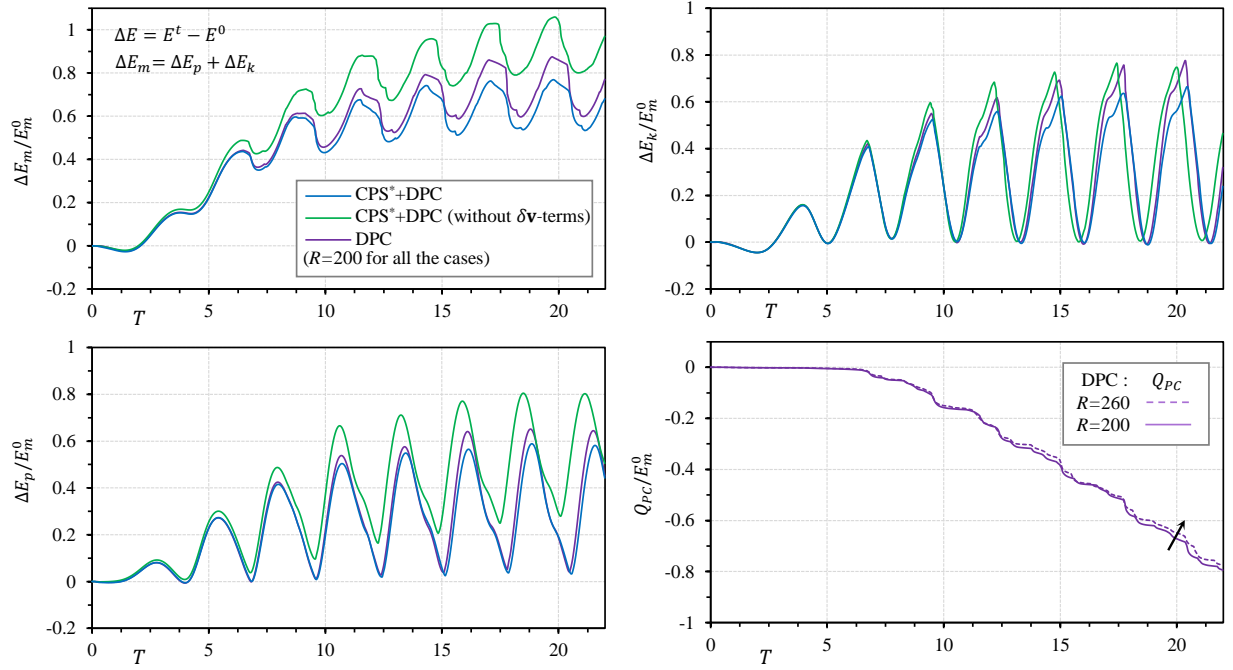


Figure 5.18 Evolution of energy components (E_m : the mechanical energy (top left), E_k : the kinetic energy (top right), E_p : the potential energy (bottom left), and Q_{PC} : the total kinetic energy dissipated by the DPC technique (bottom right) (defined by Eqs. (5.37) & (5.38)) of the 3D water sloshing test case with the DPC and CPS*+DPC (with and without the $\delta\hat{\mathbf{v}}$ -terms) techniques, where $R = 200$. The non-dimensional time, T , is given as $t\sqrt{g/L}$, and the energy variations, $\Delta E = E^t - E^0$, are normalized by the initial mechanical energy of the system, $E_m^0 = E_p^0 + E_k^0$.

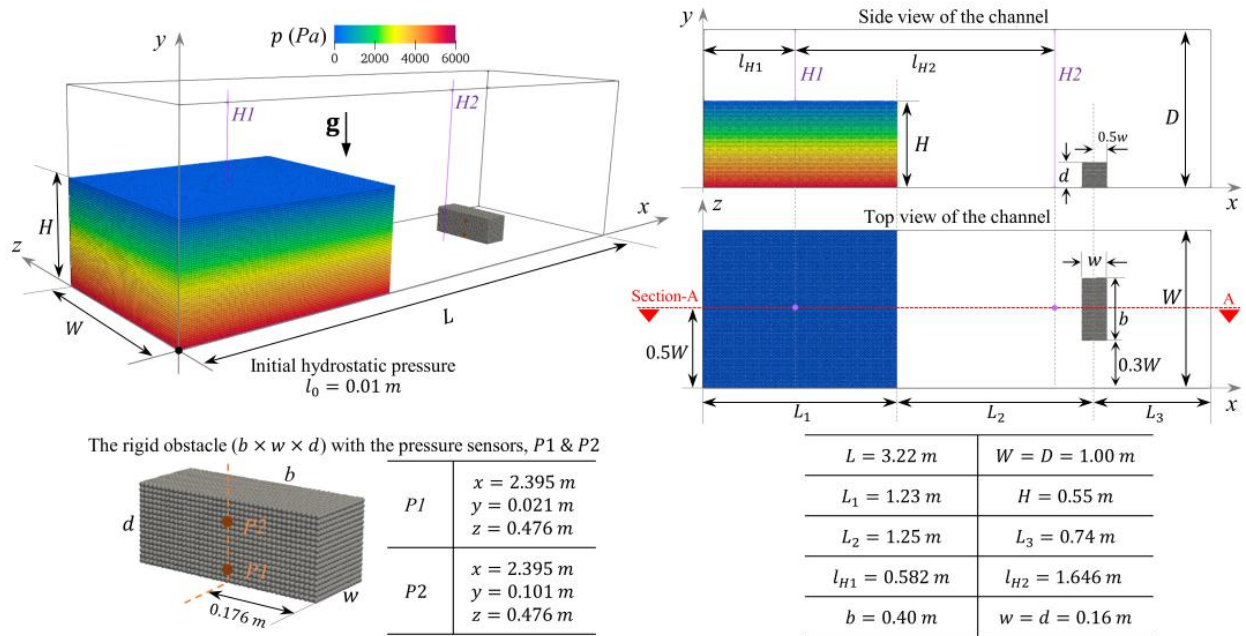


Figure 5.19 Initial configuration of the 3D water dam-break against the rigid obstacle, based on the physical model by Kleefsman et al. [6]. The pressure sensors, $P1$ and $P2$, are located on the side wall of the obstacle, and the vertical water heights in the y -direction at $H1$ and $H2$ are probed. Section A-A, shown on the top view of the channel, is used to represent the numerical results.

simulation introduces some discrepancies between the measurements, particularly during the main impact events (i.e., $1.75 \lesssim T = t\sqrt{g/H} \lesssim 8.5$). This issue results in oscillatory impact pressures at points $P1$ and $P2$ (extracted every 0.004 seconds) and leads to a delay in the second wave that impacts the obstacle at $T \approx 20.0$. These incompatibilities between the numerical and experimental results are also noticeable in the measurements of other single-phase particle methods, e.g., [176, 177]. However, the results confirm that with increasing the spatial resolution the pressure fluctuations considerably decrease showing the numerical convergence of the 3D model (Figure 5.20).

Figure 5.21 compares the flow evolution with the DPC versus the CPS*+PC techniques. We observe that the proposed EWC-MPS method, by resolving the numerical instabilities, can capture the complex flow deformations of this benchmark case. As the wave impacts at the rigid step, the flow splashes up and two jets form on the horizontal bed and impact the vertical wall of the reservoir; the flow, while overtopping the obstacle, collides with the returning jets and forms plunging waves [167, 168]. Furthermore, Figure 5.22 shows that the diffusive model represents regular pressure fields at Section A-A during the impact events. The evolution

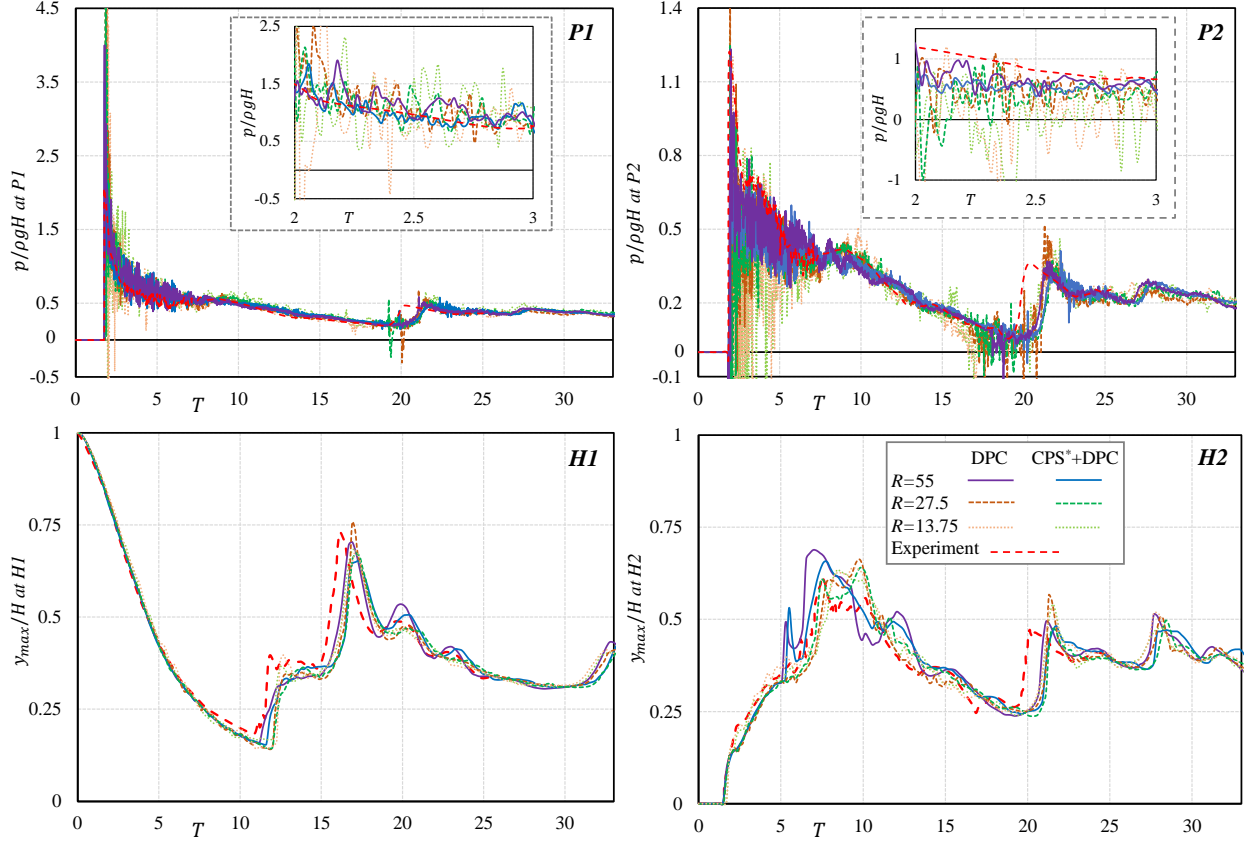


Figure 5.20 Numerical results (with the DPC and CPS*+DPC techniques and the different spatial resolutions, R) versus the experimental measurements from Kleefsman et al. [6]: Shown are the local pressure at points $P1$ and $P2$ (top row) and the depth of water in the y -direction at $H1$ and $H2$ lines, y_{max} (bottom row). The non-dimensional time and the spatial resolutions are given as $T = t\sqrt{g/H}$ and $R = H/l_0$, respectively.

of the energy components of the system, normalized by $\Delta E_m^{Fin} = E_m^\infty - E_m^0$, is plotted in Figure 5.23. Both particle regularization techniques introduce less energy dissipation by increasing the spatial resolution, confirming the numerical convergence of the 3D simulations. Also, similar to the previous test case, the DPC technique is slightly less dissipative than the CPS*+DPC formulations. Overall, the evolution of the global energies obtained by both techniques is almost identical (with $R = 55$), and they eventually reach the expected potential energy at $T \approx 25$ (i.e., $\Delta E_p/\Delta E_m^{Fin} = -1$).

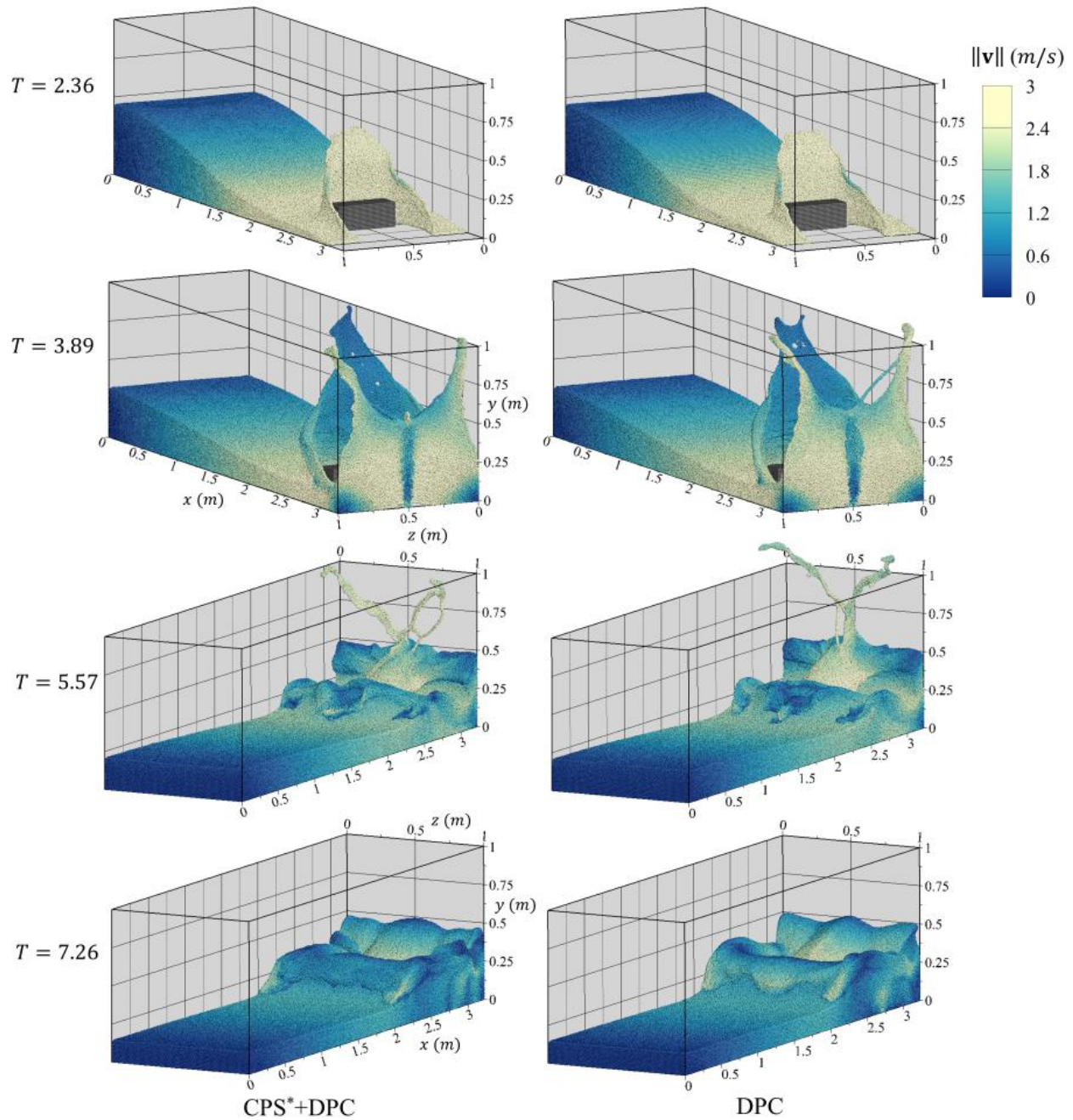


Figure 5.21 Flow evolution and particles' velocity magnitude for the 3D water dam-break with the rigid obstacle simulated by the model with the CPS*+DPC (left column) and DPC (right column) techniques, where $T = t\sqrt{g/H}$ and $R = 55$.

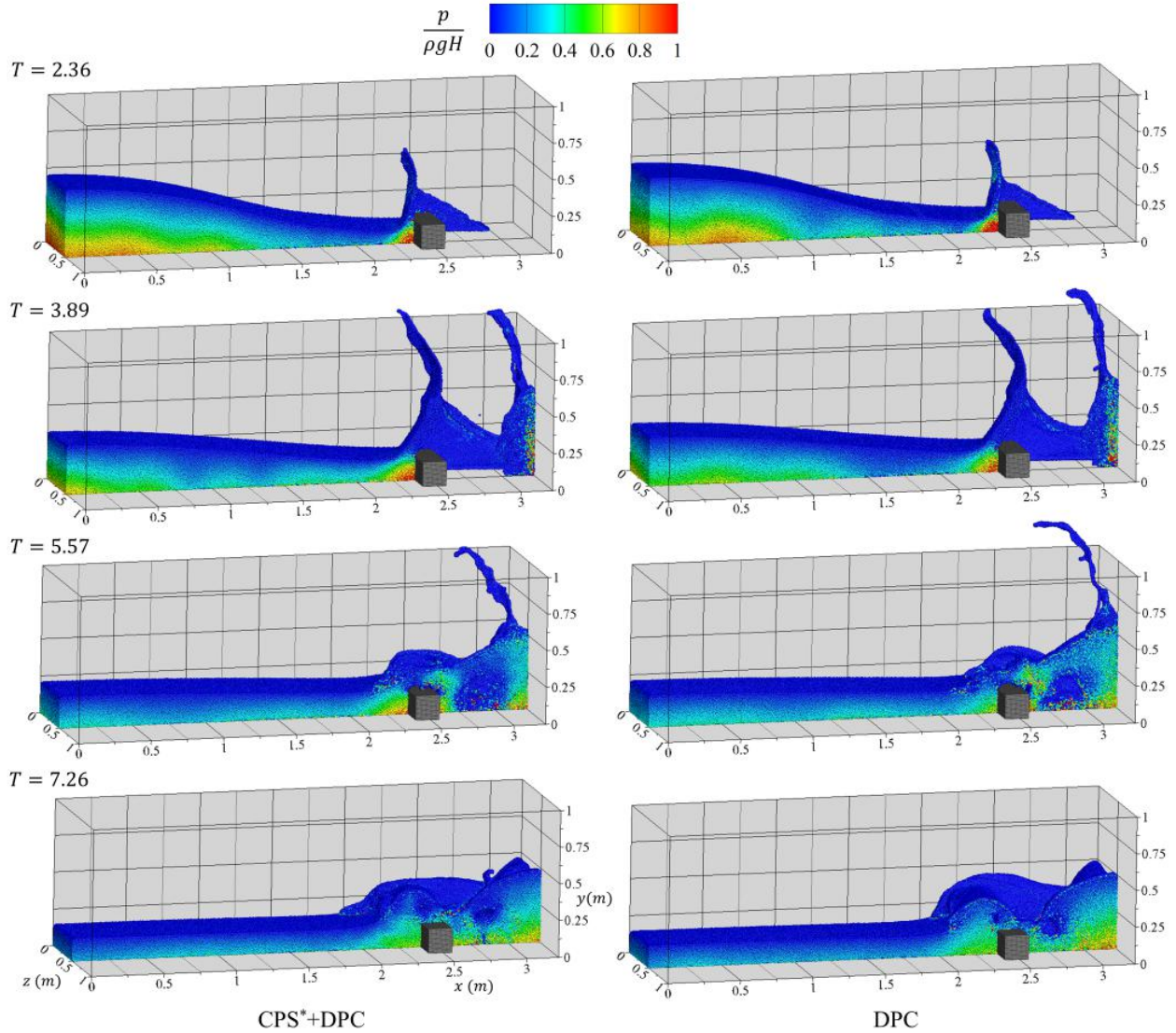


Figure 5.22 Non-dimensional pressure field of the 3D water dam-break with the rigid obstacle (at Section A-A) during the main impact events simulated by the model with the CPS*+DPC (left column) and DPC (right column) techniques, where $T = t\sqrt{g/H}$ and $R = 55$.

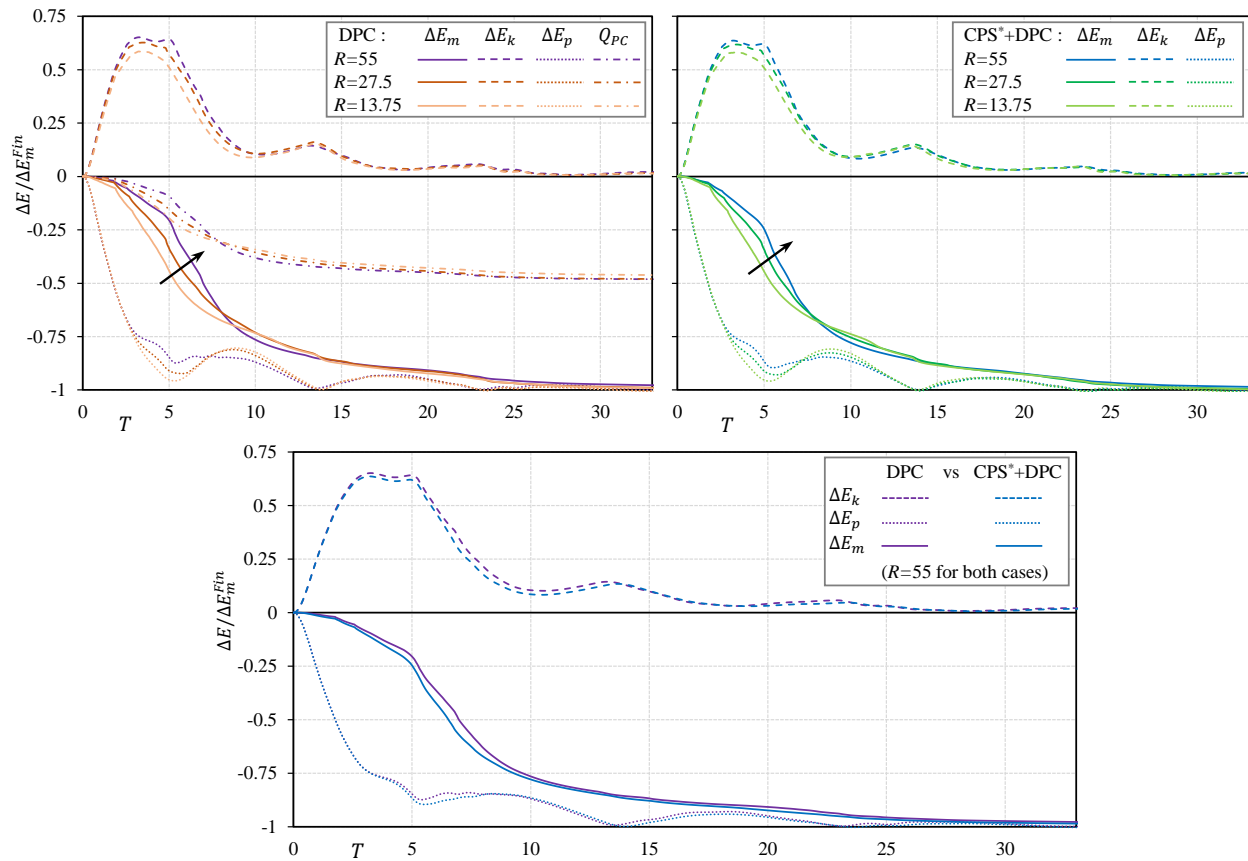


Figure 5.23 Temporal changes of the energy components of the 3D water dam-break with the obstacle: The top left and right graphs represent the numerical convergence of the 3D model with the DPC and CPS*+DPC techniques (with various spatial resolutions), respectively. The bottom graph compares the energy evolutions with DPC versus CPS*+DPC.

5.6 Conclusion

We developed and validated the three-dimensional EWC-MPS method for simulating violent free-surface flows. In a conservative framework of governing equations, we introduced several enhancement techniques that are shown to be essential for dealing with fluid-fluid and fluid-solid impact events. To include the turbulence shear force, we adopted the SPS scheme with a higher-order gradient operator to estimate the magnitude of the strain rate tensor. Furthermore, we employed a convergent form of the diffusive term in the context of the MPS formulations to reduce high-frequency pressure noises and kernel truncation errors at the boundaries.

We evaluated and compared the impact of the two particle regularization techniques, particle shifting (PS) and pairwise particle collisions (PC), on the accuracy, stability, and convergence of the model. We found that the corrected-PS (in its original form proposed in [123] as CPS+PC) is more effective in reducing the unphysical pressure noises but has a problem with volume conservation in simulating violent free-surface flows (i.e., it expands the volume and deviates the system's potential energy). To resolve the issues with these two regularization techniques, we proposed a dynamic pairwise particle collision and a consistent form of the corrected particle-shifting techniques, denoted as DPC and CPS*+DPC, respectively. The new DPC technique benefits from a dynamic formulation that deals with different states of inter-particle penetration. Unlike the particle-shifting approaches, the DPC is simple to numerically implement, as it does not require any particle classification or free-surface detection. The CPS*+DPC technique consists of a new particle classification algorithm and a modified shifting vector coupled with additional $\delta\hat{v}$ -terms. Moreover, this hybrid approach implements the DPC technique among free-surface and splashed particles in order to avoid unphysical fluid fragmentations.

The overall results confirm the effectiveness and necessity of adopting the proposed regularization techniques for dealing with extreme flow deformations of free-surface violent flows where the potential energy is dominant, and several impact events occur. Both regularization techniques represent accurate flow evolutions of the benchmark cases and eliminate particle-clustering over the fluid domain. Although these techniques require some parameter adjustments, the robustness of both implementations is well demonstrated. The DPC technique, while ensuring numerical stability, results in a smoother pressure field in comparison to the standard PC method. We have shown that the new particle classification algorithm can dynamically detect large domain curvatures and expanded regions required for adjusting the direction and/or magnitude of the particle-shifting vector. The proposed CPS*+DPC technique predicts the final expected potential energy; however, the same model without the

$\delta\hat{\mathbf{v}}$ -terms still leads to a volume expansion manifested as an increase in the global potential energy of the violent free-surface flow. In all three benchmark cases, the evolution of the energy components showed that the DPC technique is a low-dissipative approach and reduces the calculation costs of the 2D and 3D simulations compared to the CPS*+DPC algorithm that requires the particle classifications and approximating the $\delta\hat{\mathbf{v}}$ -terms.

The EWC-MPS method developed and validated in this study can be extended to multiphase flow problems with high-density ratios and complex mechanical behaviors. The robust regularization techniques, along with the modified diffusive term which act independently from the density discontinuity and empirical coefficients, make the method a powerful computational tool for large-scale hydro-environmental and industrial applications. It is also worthwhile to investigate the role of the current developments within the framework of fully incompressible MPS and SPH methods. To do so, further enhancements may include implementing strategies for optimizing the parallel programming (e.g., [177,179]), acquiring advanced turbulence formulations (e.g., [180]), and consistent solid boundary models (e.g., [174,181]).

Appendix A. The symplectic scheme with the diffusive terms

The second-order symplectic time integration scheme divides the time step into two stages of calculation [11]. In the first stage, the position, velocity, and particle number density of the particles are updated at the midpoint, $t + \Delta t/2$, as follows:

$$\begin{cases} \mathbf{r}_i^{t+\Delta t/2} = \mathbf{r}_i^t + \frac{\Delta t}{2} \mathbf{v}_i^t \\ \mathbf{v}_i^{t+\Delta t/2} = \mathbf{v}_i^t + \frac{\Delta t}{2} \left[-\frac{1}{\rho_i} \langle \nabla p \rangle_i + \mathbf{F}_i + \frac{1}{\rho_i} \langle \nabla \cdot \boldsymbol{\tau} \rangle_i \right]^t \\ n_i^{t+\Delta t/2} = n_i^t + n_i^t \frac{\Delta t}{2} [-\langle \nabla \cdot \mathbf{v} \rangle_i + D_i^m]^t \end{cases} \quad (5.34)$$

with the midpoint density, the equation of state (5.3) gives the midpoint pressure, $p_i^{t+\Delta t/2}$. In the second stage, with the midpoint values, the right-hand side of the momentum equation estimates the new velocity, and then the new position of the particles is updated at $t + \Delta t$, according to:

$$\begin{cases} \mathbf{v}_i^{t+\Delta t} = \mathbf{v}_i^t + \Delta t \left[-\frac{1}{\rho_i} \langle \nabla p \rangle_i + \mathbf{F}_i + \frac{1}{\rho_i} \langle \nabla \cdot \boldsymbol{\tau} \rangle_i \right]^{t+\Delta t/2} \\ \mathbf{r}_i^{t+\Delta t} = \mathbf{r}_i^{t+\Delta t/2} + \frac{\Delta t}{2} \mathbf{v}_i^{t+\Delta t}. \end{cases} \quad (5.35)$$

Thus, the scheme updates the particle number density (and consequently the pressure, $p_i^{t+\Delta t}$) as follows:

$$n_i^{t+\Delta t} = n_i^{t+\Delta t/2} + n_i^{t+\Delta t/2} \frac{\Delta t}{2} \left[-\langle \nabla \cdot \mathbf{v} \rangle_i^{t+\Delta t} + D_i^{mt+\Delta t/2} \right] \quad (5.36)$$

in which the particle number density at the mid-point is used in the $\langle \nabla \cdot \mathbf{v} \rangle_i^{t+\Delta t}$ term.

The solution algorithm is implemented on a GPU accelerated code (Figure 5.24). The initialization of the simulation and saving data for the post-processing jobs run on the Computer Processing Unit (CPU) as the host part of the code. Nevertheless, the main temporal loop, including the neighbor search algorithm and the particle regularization techniques, run on the Graphical Processing Unit (GPU) as the device section. The subroutines of this loop are written with the Compute Unified Device Architecture (CUDA) parallel programming language based on C++. This allows the numerical model to use the massive parallelization on the GPU to process a large number of particles simultaneously [177]. Figure 5.24 summarizes the numerical implementation of the solution algorithm.

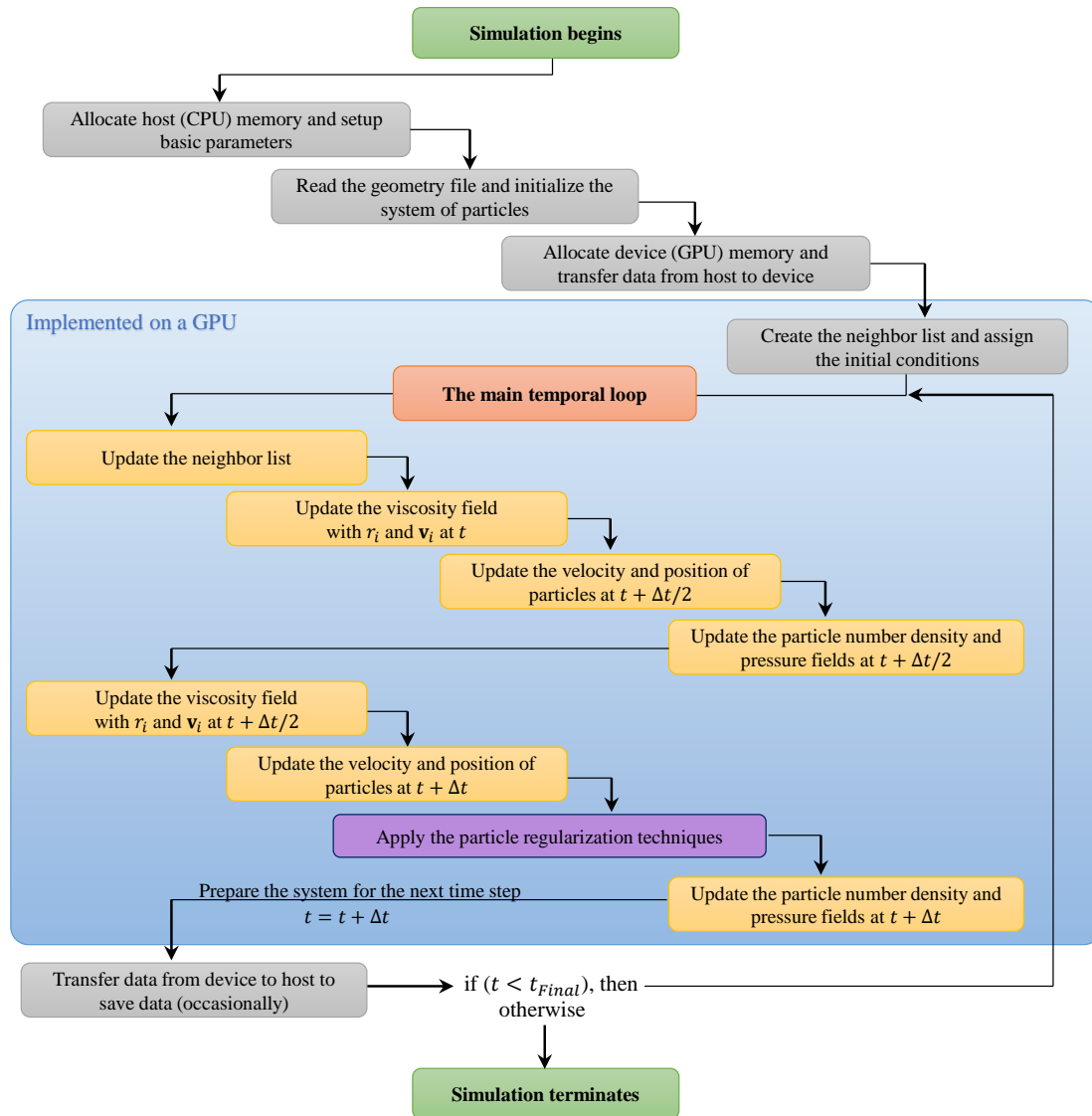


Figure 5.24 Flowchart of the solution algorithm based on the symplectic time integration scheme. The main temporal loop of the calculation is implemented on a GPU device with CUDA C++ parallel programming.

Appendix B. The energy components of the system

By plotting the time evolution of the global energies of the system, we investigate the effect of the particle regularization techniques on the overall mechanical behavior of the system. For this purpose, we calculate the global kinetic energy, E_k , the global potential energy, E_p ,

and the global mechanical energy, E_m , at each time step, t , as follows:

$$E_k^t = \frac{\rho l_0^d}{2} \sum_{i \in \Omega_f} \|\mathbf{v}\|_i^2, \quad E_p^t = -\rho l_0^d \sum_{i \in \Omega_f} \mathbf{g} \cdot \mathbf{r}_i, \quad E_m^t = E_k^t + E_p^t, \quad (5.37)$$

where ρl_0^d is the constant mass of the fluid particles. The variation of the energies with respect to their initial values, E^0 , is given as $\Delta E = E^t - E^0$. Furthermore, the total kinetic energy dissipated by the particle collision technique during the simulation time is calculated by:

$$Q_{PC}^t = \sum_{t=0}^t (E'_k - E_k)^t \quad (5.38)$$

in which E_k and E'_k are the global kinetic energies before and after updating the velocity of the particles at each time step, respectively.

CHAPTER 6 ARTICLE 3: STABILITY AND ACCURACY OF THE WEAKLY COMPRESSIBLE SPH WITH PARTICLE REGULARIZATION TECHNIQUES

Authors: Mojtaba Jandaghian¹, Herman Musumari Siaben¹, and Ahmad Shakibaeinia¹

¹Department of Civil, Geological and Mining Engineering, Polytechnique Montréal, Canada
European Journal of Mechanics - B/Fluids

6.1 Abstract

This paper proposes and validates two new particle regularization techniques for the Smoothed Particle Hydrodynamics (SPH) numerical method to improve its stability and accuracy for free surface flow simulations. We introduce a general form of the Dynamic pair-wise Particle Collision (DPC) regularization technique that we recently proposed in the context of the Moving Particle Semi-implicit (MPS) method in [124]. The DPC coupled with the standard Particle Shifting (PS) technique has given rise to a hybrid approach that we propose to alleviate particle clustering issues in the free-surface and splashed regions. We validate the proposed techniques to four benchmark cases: (i) the oscillating droplet, (ii) the two-dimensional water dam-break, (iii) the two-dimensional water sloshing, and (iv) the three-dimensional water dam break against a rigid obstacle. We evaluate their impacts on the stability, accuracy and the conservation properties of the test cases. The qualitative and quantitative analysis of the results shows that despite its simplicity, the DPC technique is more effective in reducing the spatial disorder and capturing the impact events compared with the standard and the newly improved hybrid PS methods. Although the hybrid PS technique improves particle distribution at the free surface, it still suffers from the inconsistent implementation of the PS equation which unphysically increases the fluid volume and violates the conservation of potential energy in the long-term simulations. Overall, the conservative DPC algorithm proves to be a simple and efficient alternative regularization technique for simulating such highly dynamic free-surface flows. (Figure 6.1)

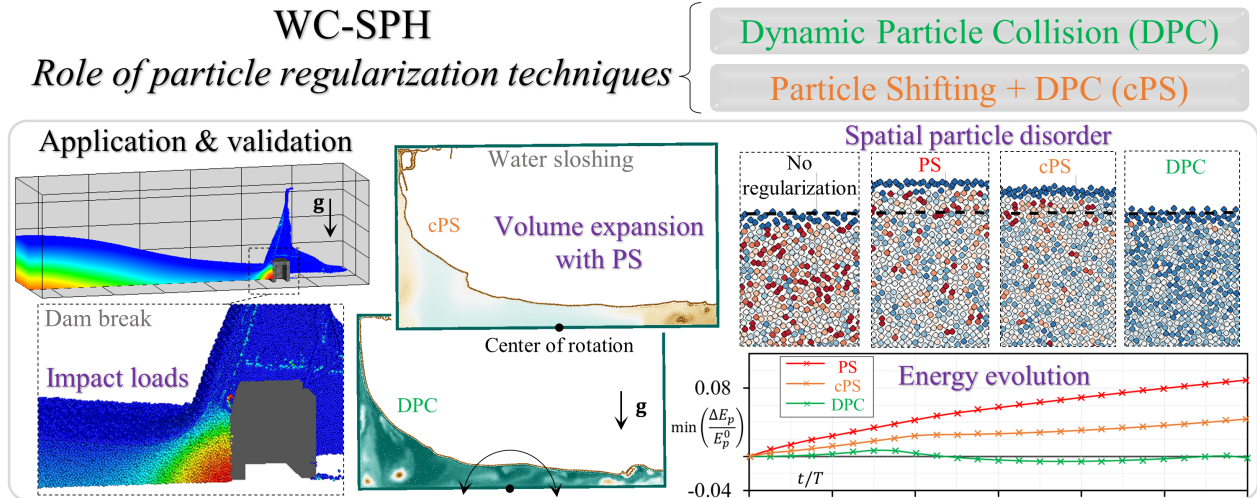


Figure 6.1 The graphical abstract

6.2 Introduction

Continuum-based mesh-free particle methods, such as the Smoothed Particle Hydrodynamics (SPH) [26] and Moving Particle Semi-implicit (MPS) [25] methods, have remarkable capabilities for simulating highly dynamic free-surface and interfacial flows (e.g., for solving multiphysics problems in industry [39, 40] and in hydro-environmental fields [27, 126]). Nevertheless, due to their Lagrangian nature, they are prone to non-uniform particle distribution and unphysical spurious pressure noises that compromise their accuracy and stability. To deal with these issues some of the past studies have proposed higher-order approximation operators (e.g., [126, 137]) or added the numerical diffusion terms to the continuity [54, 123] and momentum [61] equations. But even with these improvements, the particle methods can still suffer from particle distribution anomalies. Therefore, another group of enhancement techniques works on the regularization of the particle distribution, among which, the particle shifting (PS) technique [50, 55], the pair-wise particle collision (PC) method [56, 75], and the transport-velocity formulation [144, 163] are common approaches developed for SPH and MPS methods.

In the SPH framework, Xu et al. [55] proposed the PS method, which moves particles to the area less populated, avoiding therefore inter-particle penetrations. Lind et al. [50] and Skillen et al. [73] adapted PS to free-surface flows involving body-water impacts. Further, Khayyer et al. [74] proposed the optimized PS method which cancels the normal component of PS at the free-surface and its neighborhood. The pair-wise particle collision technique,

which is based on the collision of physical solid or gas particles, was first time formulated within the context of the incompressible MPS by Lee et al. [56] (for free-surface flows) and for the weakly compressible MPS by Shakibaeinia and Jin [75] (for multiphase flows).

Without special treatments of free-surface particles and considering the effects of the shifting transport-velocity, the PS algorithms (particularly implemented in the weakly compressible models) have shown to affect the mechanical behavior of the complex flows where the potential energy is dominant and several breaking events occur [3, 64]. By applying PS, the potential energy of the system increases as observed by unphysical volume expansions discussed in [124] and [64]. In SPH, Sun et al. [3] derived additional diffusive terms (added to the continuity and momentum equations) and implemented restricted boundary conditions to resolve the excessive potential energy due to continuous activation of PS. In MPS, Jandaghian et al. [124] proposed a consistent form of a corrected PS method by including the additional transport-velocity terms and implementing special boundary treatments (for large flow curvatures and by excluding the solid boundary particles). Sun et al. [3] and Jandaghian et al. [124] showed that their developed PS algorithms, applied to weakly compressible particles methods, renders the latter free from unphysical volume expansions and numerical results divergence.

More recently, Lyu and Sun [182] enhanced the SPH method by introducing a corrective cohesive force to tackle the volume-non-conservative issue of the original shifting equation. Antuono et al. [183] considered the consistent form of PS within an arbitrary Lagrangian-Eulerian SPH framework (presented by Oger et al. [155]) improving the stability of the developed model by adopting artificial diffusion terms. Antuono et al. [184] coupled a Large-Eddy Simulation SPH (LES-SPH) method with the consistent PS and the Tensile Instability Control (TIC) scheme (proposed by Sun et al. [85]) for simulating high Reynolds number problems. Also, Lyu et al. [185] appended the PS formulation to the TIC method to surmount the tensile instability issue due to strong negative pressures in fluid-structure interactions with SPH. Marrone et al. [186] evaluated the dissipation mechanism in sloshing problems through the developed LES-SPH model with the enhanced particle stabilization techniques. Other research works, e.g., [187–189], have successfully validated SPH models supplied with PS and artificial diffusion terms to study violent sloshing problems and dam-breaking flows with complex breaking waves. Further, Wen et al. [190] adopted the multiphase particle collision model to ensure numerical stability of their developed incompressible MPS method for simulating violent multiphase flows.

Jandaghian et al. [124] developed a new version of the particle collision technique within their enhanced weakly compressible MPS method for simulating violent free-surface flows.

They validated that the proposed algorithm, denoted as the Dynamic pair-wise Particle Collision (DPC) technique, captures the impact events of such complex flows and eliminates particle pairing instability over the fluid domain. Moreover, they confirmed that DPC is a simple technique characterized by low-dissipation with cheap computation costs and is more effective and efficient than the consistent form of PS. This technique employs a dynamic pair-wise repulsive force and a variable coefficient of restitution for the collision term for dealing with different conditions of inter-particle penetrations. They showed that for the case of MPS, unlike the widely used Particle Shifting (PS) method, the DPC transport-velocity equation conserves the linear momentum of the system. Moreover, the DPC technique is more straightforward as it is free from the complexities of interface treatments.

This paper aims at developing the DPS technique for the weakly compressible SPH method to demonstrate its role in the accuracy and stability of the highly dynamic free-surface flow modeling. It also represents and evaluates a hybrid PS-DPC technique. We re-derive the general form of the DPC algorithm in the SPH framework for multiphysics problems (Section 8.4.3). We append DPC to the standard form of the PS equation (as a hybrid technique) to resolve the particle clustering issue present on the free-surface and external particles while exempting the model from complex free-surface treatments (Section 6.3.2). We implement these techniques in the GPU-accelerated subroutines of the open-source code DualSPHysics (see [67] and [179]). We simulate four benchmark cases: (i) the oscillating droplet under a conservative force field, (ii) the two-dimensional (2D) water dam-break, (iii) the 2D water sloshing in a tank, and (iv) the three-dimensional (3D) water dam break against a rigid obstacle (Section 6.4). By qualitative and quantitative validations, we evaluate the convergence and consistency of SPH with the DPC technique compared to the existing and newly developed PS algorithms.

6.3 SPH methodology

In SPH, the Lagrangian form of the Navier-Stokes equations represent the physical laws of the fluid flows [35]. The numerical method discretizes the governing equations over the entire computational domain, Ω , into moving particles (or simply particles) categorized as the fluid particles, Ω_f , and the solid boundary particles, Ω_b (i.e., $\Omega = \Omega_f \cup \Omega_b$). The approximation operator, $\langle \bullet \rangle$, forms the continuity and momentum equations, respectively, to:

$$\frac{D\rho_i}{Dt} = -\rho_i \langle \nabla \cdot \mathbf{v} \rangle_i \quad (6.1)$$

and

$$\rho_i \frac{D\mathbf{v}_i}{Dt} = -\langle \nabla p \rangle_i + \langle \nabla \cdot \boldsymbol{\tau} \rangle_i + \rho_i \mathbf{F}_i, \quad (6.2)$$

in which the material time derivative, $D(\cdot)/Dt$, updates the density, ρ_i , and velocity, \mathbf{v}_i , of the generic particle, $i \in \Omega_f$. In the momentum equation (6.2), the pressure, the total shear stress tensor, and the body force per unit volume, are denoted as p_i , $\boldsymbol{\tau}_i$, and $\rho_i \mathbf{F}_i$ respectively. The fluid particle carries the material and flow properties as its local position, \mathbf{r}_i , moves by

$$\frac{D\mathbf{r}_i}{Dt} = \mathbf{v}_i. \quad (6.3)$$

Considering the fluid phase as a weakly compressible and barotropic fluid, the equation of state,

$$p_i = B_0 \left(\left(\frac{\rho_i}{\rho_0} \right)^\gamma - 1 \right), \quad (6.4)$$

explicitly updates p_i where the fluid bulk modulus is $B_0 = c_s^2 \rho_0 / \gamma$. The reference density of the fluid and the polytropic index are denoted as ρ_0 and $\gamma = 7$, respectively. With the numerical speed of sound, c_s , being much greater than the maximum expected velocity, $\|\mathbf{v}\|_{max}$, this model restricts the density variations, e.g., with $c_s \geq 10 \|\mathbf{v}\|_{max}$, the Mach number, $Ma \leq 0.1$, and the density variation would be limited to less than %1.

In the variationally consistent framework, the SPH formulation estimates the divergence of velocity, $\langle \nabla \cdot \mathbf{v} \rangle_i$, and the gradient of pressure, $\langle \nabla p \rangle_i$, terms as follows [179]:

$$\begin{cases} \langle \nabla \cdot \mathbf{v} \rangle_i = \sum_j \frac{m_j}{\rho_j} \mathbf{v}_{ji} \cdot \nabla_i W_{ij} \\ \langle \nabla p \rangle_i = \sum_j \frac{m_j}{\rho_j} (p_i + p_j) \nabla_i W_{ij} \end{cases} \quad (6.5)$$

in which $W_{ij} = W(r_{ij}, kh)$ is the smoothing kernel function, m_i denotes the constant mass of the particle, and $(\cdot)_{ij} = (\cdot)_i - (\cdot)_j$. The neighbor particle, $j \in \Omega$, is within the support domain of W with the influence radius of kh , i.e., the inter-particle distance, $r_{ij} = \|\mathbf{r}_i - \mathbf{r}_j\| \leq kh$ (where k is a positive real number and the smoothing length, $h = 2dp$, dp being the initial particle distance). The gradient of kernel, $\nabla_i W_{ij} = (\mathbf{r}_{ij}/r_{ij})(\partial W_{ij}/\partial r_{ij})$ noting that $\partial W_{ij}/\partial r_{ij} \leq 0$ [35, 42]. The shear force in (6.2), i.e., $\langle \nabla \cdot \boldsymbol{\tau} \rangle_i$, includes the momentum dissipation due to the laminar flow regime and the turbulence effects. Adopting the Laplacian and the variationally consistent approximation operators, respectively, for the laminar viscosity

and the turbulence dissipation terms, gives [67, 179]:

$$\langle \nabla \cdot \boldsymbol{\tau} \rangle_i = \sum_j m_j \frac{4\rho_i \nu_0 \mathbf{r}_{ij} \cdot \nabla_i W_{ij}}{(\rho_i + \rho_j)(r_{ij}^2 + \eta^2)} \mathbf{v}_{ij} + \sum_j \frac{m_j}{\rho_j} (\boldsymbol{\tau}_i^* + \boldsymbol{\tau}_j^*) \cdot \nabla_i W_{ij}. \quad (6.6)$$

in which ν_0 is the reference kinematic viscosity of the fluid and $\eta = 0.01h$ is a small value added to avoid the singularity issue. The large eddy simulation sub-particle scale model (SPS), using the Favre averaging for the weakly compressible model, determines the turbulence stress tensor, $\boldsymbol{\tau}_i^*$, as follows [37, 191]:

$$\boldsymbol{\tau}_i^* = 2\nu_{ti}\rho_i \left(\mathbf{S}_i - \frac{1}{3} \text{tr}(\mathbf{S}_i) \mathbf{I} \right) - \frac{2}{3} \rho_i C_I \Delta^2 |\mathbf{S}_i|^2 \mathbf{I} \quad (6.7)$$

in which \mathbf{S}_i is the strain rate tensor, \mathbf{I} is the identity matrix, $\nu_{ti} = (C_s \Delta)^2 |\mathbf{S}_i|$ is the eddy viscosity, and $C_I = 0.00066$. The Smagorinsky coefficient, $C_s = 0.12$, and the filter width, Δ (which is as a constant proportional to dp) determine the mixing length-scale of the SPS turbulence model. The magnitude of the strain rate tensor, denoted as $|\mathbf{S}_i|$, reads $\sqrt{2S_i^{\alpha\beta} S_i^{\alpha\beta}}$ (in Einstein notation where $S_i^{\alpha\beta}$ is an element of \mathbf{S}_i considering α and β as the coordinate directions).

Appending an artificial density diffusion term to the right-hand side of the continuity equation (6.1) has been an effective and essential solution (see the δ -SPH method of Molteni and Colagrossi [54] and the enhanced MPS method of Jandaghian and Shakibaenia [123]) to eliminate high-frequency pressure noises of the weakly compressible models. In the weakly compressible SPH formulation, the general form of the density diffusion term, D_i , is written as follows:

$$D_i = \delta h c_s \sum_{j \in \Omega_f} \frac{m_j}{\rho_j} \boldsymbol{\psi}_{ij} \cdot \nabla_i W_{ij} \quad (6.8)$$

where the preset non-dimensional coefficient, δ , adjusts the magnitude of this numerical correction. The standard form of the density diffusion term is given by [54]:

$$\boldsymbol{\psi}_{ij} = 2(\rho_j - \rho_i) \frac{\mathbf{r}_{ji}}{(r_{ij}^2 + \eta^2)}. \quad (6.9)$$

This term causes the density field close to the boundaries to diverge from the hydrostatic solution [66, 126]. To improve the pressure estimation at the vicinity of the solid boundary, Fourtakas et al. [69], proposed a new form of (6.9) by replacing the total density with the dynamic density as:

$$\boldsymbol{\psi}_{ij} = 2(\rho_{ji} - \rho_{ij}^H) \frac{\mathbf{r}_{ji}}{(r_{ij}^2 + \eta^2)}. \quad (6.10)$$

The hydrostatic pressure difference, $p_{ij}^H = \rho_0 \mathbf{g} \cdot \mathbf{r}_{ji}$, gives the hydrostatic density difference, ρ_{ij}^H , through the inverse form of the equation of state as [69]:

$$\rho_{ij}^H = \rho_0 \left(\sqrt[\gamma]{1 + \frac{p_{ij}^H}{B_0}} - 1 \right), \quad (6.11)$$

with \mathbf{g} being the gravitational acceleration set to $\{0, 0, -g = -9.81 m.s^{-2}\}^T$.

To solve the governing equations (6.1-6.4), we adopt in this study the second-order symplectic scheme in which the explicit model dynamically updates the time steps of calculation, Δt , based on the Courant–Friedrichs–Lewy (CFL) stability conditions (see [179]). We employ the modified Dynamic Boundary Condition (mDBC) method implemented by English et al. [192] for solid boundaries.

6.3.1 Dynamic Particle Collision (DPC) technique for SPH

The pair-wise particle collision method (originally implemented in MPS by Lee et al. [56] and Shakibaeinia and Jin [75]) regularizes the particle distribution based on the momentum transfer between a pair of colliding particles. Jandaghian et al. [124] proposed a new version of this technique, denoted as the Dynamic pair-wise Particle Collision (DPC) technique, by adopting dynamic form of the collision and repulsive terms to improve the pressure field. Here, we represent the DPC formulation in the framework of the weakly compressible SPH method. Considering mass, m_i , and volume, $V_i = m_i/\rho_i$, of particles, the general form of the DPC transport-velocity equation, \mathbf{v}_i^{DPC} , reads:

$$\delta \mathbf{v}_i^{DPC} = \sum_{j \in \Omega_f} \kappa_{ij} \frac{2m_j}{m_i + m_j} \mathbf{v}_{ij}^{coll} + \frac{\Delta t}{\rho_i} \sum_{j \in \Omega_f} \phi_{ij} \frac{2V_j}{V_i + V_j} \frac{p_{ij}^b}{r_{ij}^2 + \eta^2} \mathbf{r}_{ij}, \quad (6.12)$$

in which

$$(\mathbf{v}_{ij}^{coll}, \phi_{ij}) = \begin{cases} \left(\frac{\mathbf{v}_{ij} \cdot \mathbf{r}_{ij}}{r_{ij}^2 + \eta^2} \mathbf{r}_{ji}, 0 \right), & \text{for } \mathbf{v}_{ij} \cdot \mathbf{r}_{ij} < 0 \\ (0, 1) & \text{Otherwise} \end{cases}, \quad (6.13)$$

and in single fluid phase simulations $m_i = m_j$. The DPC transport-velocity equation consists of the collision and repulsive terms (i.e., the first and second terms at its right-hand side, respectively). It deals with different states of inter-particle penetration and uses a variable coefficient of restitution, κ_{ij} , and the dynamic background pressure, p_{ij}^b [124] (see Figure 6.2). When a pair of particles overlap and approach each other (i.e., when $r_{ij} < dp$ and

$\mathbf{v}_{ij} \cdot \mathbf{r}_{ij} < 0$) the collision term reduces their normal collision velocity, \mathbf{v}_{ij}^{coll} , and the binary multiplier $\phi_{ij} = 0$. Otherwise, when $\mathbf{v}_{ij} \cdot \mathbf{r}_{ij} \geq 0$ and still the inter-particle penetration occurs, by setting $\phi_{ij} = 1$ and $\mathbf{v}_{ij}^{coll} = 0$, the model activates the repulsive force (derived from the pressure gradient term without any smoothing procedure). The dynamic background pressure of the repulsive term is limited to the expected maximum and minimum pressures of the test case (denoted as p_{max} and p_{min} , respectively) and is written as [124]:

$$\begin{cases} p_{ij}^b = \tilde{p}_{ij} \chi_{ij} \\ \tilde{p}_{ij} = \max(\min(\lambda |p_i + p_j|, \lambda p_{max}), p_{min}) \end{cases} \quad (6.14)$$

where λ is a non-dimensional adjusting parameter (set to 0.1). DPC dynamically determines the variable coefficients, χ_{ij} and κ_{ij} , through:

$$\chi_{ij} = \sqrt{\frac{w(r_{ij}, dp)}{w(0.5dp, dp)}} \text{ and } \kappa_{ij} = \begin{cases} \chi_{ij} & 0.5 \leq r_{ij}/dp < 1 \\ 1 & r_{ij}/dp < 0.5 \end{cases}, \quad (6.15)$$

respectively. These coefficients control the strength of the repulsive and collision terms as functions of the inter-particle distance via the non-dimensional part of the Wendland kernel given as:

$$w(r_{ij}, dp) = \left(1 - \frac{r_{ij}}{dp}\right)^4 \left(4 \frac{r_{ij}}{dp} + 1\right), 0 \leq r_{ij} < dp \quad (6.16)$$

(where for $r_{ij} \geq dp$, $w(r_{ij}, dp) = 0$). Eventually, DPC updates the velocity and position of the fluid particles by

$$\begin{cases} \mathbf{v}'_i = \mathbf{v}_i + \delta \mathbf{v}_i^{DPC} \\ \mathbf{r}'_i = \mathbf{r}_i + \Delta t \delta \mathbf{v}_i^{DPC} \end{cases}. \quad (6.17)$$

We should highlight that the DPC formulations (6.12-6.15) keep the velocity corrections small by implementing pair-wise particle interactions and the dynamic coefficients. Therefore, DPC avoids excessive manipulation of the mechanical properties of the flow (including the mass and volume of particles) without the need for the additional diffusion terms due to the non-Lagrangian velocity changes (derived based on the Leibniz–Reynolds transport theorem in the consistent PS formulations (e.g., [3, 124]) and the Arbitrary Lagrangian Eulerian (ALE) schemes coupled with the PS equation (e.g., [155, 183])). Unlike standard PS methods that shift fluid particles to the area with less concentration (e.g., [50, 130]), DPC conserves the linear momentum of the two colliding particles by being an anti-symmetric

formulation and considering a constant mass for the particles [124]. Furthermore, DPC implements the regularization process of the fluid particles without any boundary treatments eliminating the complexities of the free surface and normal vectors detection. In section 6.4, simulating benchmark cases, we evaluate the evolution of system's global energy to confirm the negligible effects of the DPC transport-velocity equation on the overall flow properties. The implementation of DPC in DualSPHysics is represented in 6.5.

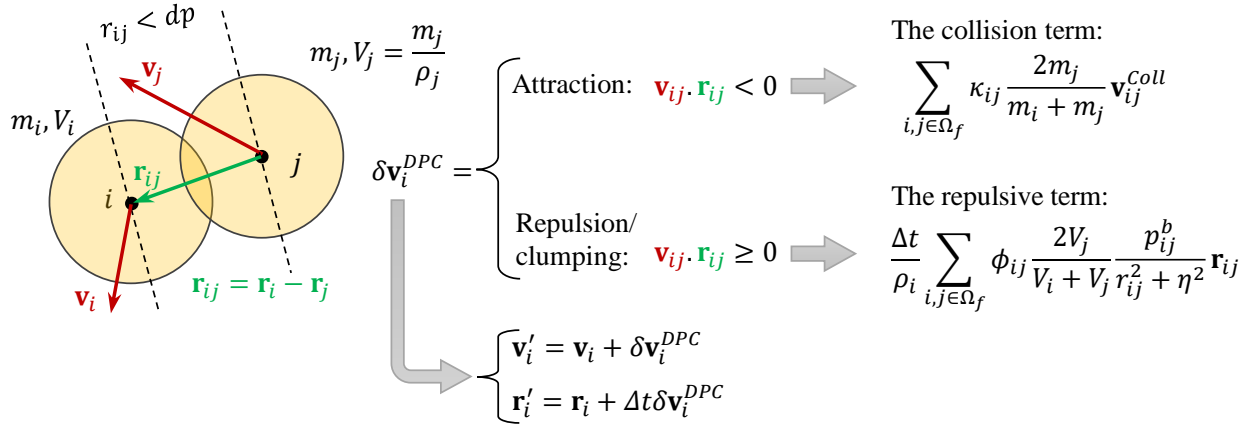


Figure 6.2 The general form of the DPC transport-velocity formulation, $\delta \mathbf{v}_i^{DPC}$, (6.12) consists of the dynamic collision and repulsive terms for dealing with different states of inter-particle penetration where $r_{ij} < dp$

6.3.2 Particle shifting algorithm coupled with DPC: *cPS*

The standard Particle Shifting (PS) technique, implemented in DualSPHysics, regularizes the distribution of fluid particles ($i \in \Omega_f$) using the Fickian-based formulation (proposed by Lind et al. [50] and Skillen et al. [73]):

$$\delta \mathbf{r}_i^{PS} = -D_i^F \langle \nabla C \rangle_i \quad (6.18)$$

where the particle shifting vector, $\delta \mathbf{r}_i^{PS}$, has the same direction as the gradient of the local particle concentration, $\langle \nabla C \rangle_i$, estimated as:

$$\langle \nabla C \rangle_i = \sum_{j \in \Omega} \frac{m_j}{\rho_j} \nabla_i W_{ij}. \quad (6.19)$$

A variable Fickian diffusion coefficient, $D_i^F = Ah\Delta t \|\mathbf{v}_i\|$, controls the intensity of shifting based on the Von Neumann stability analysis and the CFL condition [73]. The non-

dimensional constant, A , is suggested to be set between 1-6 [73]. One should note that D_i^F is a function of the variable time step and the local velocity magnitude (unlike the other PS formulations that employ constant D^F using the maximum expected velocity of the test case, e.g., in [123, 130]). Also, the model limits the magnitude of $\delta\mathbf{r}_i^{PS}$ in each coordinate directions to $0.1dp$. Accordingly, this PS algorithm, through the variable Fickian diffusion coefficient and limiting the magnitude of shifting, aims at avoiding excessive movement of particles [179].

Inside the free-surface region, the kernel truncation causes (6.18) to introduce false diffusion of particles toward and beyond the interface [50, 130]. Thus, special treatments of (6.18) become necessary to control particle shifting at the free-surface and its vicinity. This includes detecting the free-surface particles and modifying/canceling the shifting normal to the interface. Accuracy of the particle shifting corrections greatly depends on the efficiency of the particle detection algorithm and the estimated normal vectors (especially in violent free-surface flows) [130]. With inaccurate estimation of normal vectors and canceling the component of PS normal to the interface, the highly dynamic flows would be susceptible to particle clustering at the interface [123].

The standard PS method, for single-phase flow simulations, simply adjusts the magnitude of shifting by multiplying $\delta\mathbf{r}_i^{PS}$ by a correction coefficient, A_{Ci} . It also neglects the shifting of the particles with extreme kernel truncation (i.e., $\delta\mathbf{r}_i^{PS} = 0$ for $A_{Ci} < 0$). The correction coefficient is defined as $A_{Ci} = (\langle\nabla\cdot\mathbf{r}\rangle_i - A_{FST})/(dim. - A_{FST})$ in which

$$\langle\nabla\cdot\mathbf{r}\rangle_i = \sum_{j\in\Omega} \frac{m_j}{\rho_j} \mathbf{r}_{ji}\cdot\nabla_i W_{ij}, \quad (6.20)$$

and the free-surface threshold coefficient, A_{FST} , is a preset value less than the domain dimension, $dim. = 2$ or 3 for the two- and three-dimensional simulations, respectively [167, 193]. We refer to the equations (6.18-6.20) as the standard PS formulation (which exists in Dual-SPHysics).

To improve particle distribution in the free-surface region and ensure numerical stability, Jandaghian et al. [123, 124] coupled the PS formulation with the particle collision technique within the context of MPS method. Here, similar to the work of Jandaghian et al. [123], we couple the standard PS equation with the DPC technique, represented in section (8.4.3). In this hybrid method, hereinafter denoted as cPS, the PS equation (6.18) is directly applied to the internal particles, while the DPC transport-velocity term (6.12) regularizes the distribution of particles detected inside the free-surface region or as splashed particles. We first

classify the fluid particles into two categories identified by a binary multiplier, b_i , given as:

$$b_i = \begin{cases} 1 & \text{If } A_{C_i} < 0 \text{ or } N_i < 0.75N_0 \\ 0 & \text{Otherwise} \end{cases}. \quad (6.21)$$

in which N_i , and N_0 are the number of neighbor particles and the expected number of neighbor particles in an isotropic particle distribution, respectively. If $b_i = 0$ the model considers the fluid particle as an internal particle; if $b_i = 1$ the particle belongs to the free-surface region or the splashed (i.e., external) particles' category due to the extreme kernel truncation and insufficient number of neighbor particles (see Figure 6.3). Considering $k = 2$ in the smoothing functions, we estimate $N_0 = 52$ and 260 for the 2D and 3D simulations, respectively. Employing the binary multiplier (6.21) and the DPC term (6.12), we implement the cPS equation as:

$$\delta \mathbf{r}_{i \in \Omega_f}^{cPS} = (1 - b_i) A_{C_i} \delta \mathbf{r}_i^{PS} + b_i \Delta t \delta \mathbf{v}_i^{DPC} \quad (6.22)$$

which finally updates the position and velocity of the fluid particles through

$$\begin{cases} \mathbf{r}'_i = \mathbf{r}_i + \delta \mathbf{r}_i^{cPS} \\ \mathbf{v}'_i = \mathbf{v}_i + b_i \delta \mathbf{v}_i^{DPC} \end{cases}. \quad (6.23)$$

We implement cPS only in the correction stage of the time integration scheme (compatible with the DPC implementation shown in Figure 6.2). This coupling of PS with DPC exempts the model from complex free-surface treatments which would involve time-consuming operations (required for estimating the normal vectors and the renormalization tensor), noting that DPC improves the particle clustering issue in the free-surface and splashed regions (i.e., where $b_i = 1$). Figure 6.3 summarizes the cPS algorithm. It should be highlighted that the proposed cPS method still lacks the consistent particle shifting algorithms developed by implementing additional diffusion/cohesion terms to encounter the volume-non-conservation issue of the standard PS models (e.g., see [3, 124, 182]).

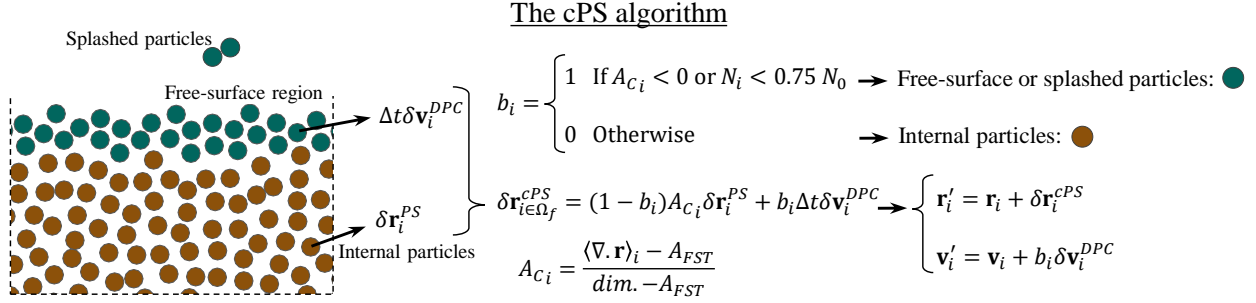


Figure 6.3 The coupled Particle Shifting formulation (6.22). b_i , $\delta \mathbf{r}_i^{PS}$, and $\delta \mathbf{v}_i^{DPC}$ are given through equations (6.21), (6.18), and (6.12), respectively.

6.4 Numerical simulations

We simulate challenging benchmark cases to investigate the stability and accuracy of the weakly compressible SPH method supplied with the proposed particle regularization techniques. We choose numerical cases in which violent free-surface flows and the potential forces are dominant. Through a comprehensive evaluations of the numerical results, we discuss the effectiveness and efficiency of the proposed models for capturing the impact events and long-term modeling of highly dynamic flows. For all the simulations, we adopt the fifth-order Wendland kernel and set $k = 2$. In the symplectic time integration scheme the CFL coefficient is set to 0.2. In the PS formulation, we use the recommended values of the shifting coefficients, i.e., $A = 2$ and $A_{FST} = 1.5$ and 2.75 for the 2D and 3D problems, respectively [179]. To quantitatively study the effectiveness of the particle regularization techniques, we calculate and plot the spatial particle disorder, denoted as λ_i (which its formulations are proposed by Antuono et al. [7]). By averaging λ_i over the internal fluid particle (i.e., for $b_i = 0$ given by (6.21)) the global value of the spatial particle disorder, Λ , is estimated [7]. Moreover, the evolution of global energy is identified as $\Delta E = E^t - E^0$ (where E^t and E^0 refer to the global energy at t and the initial condition); the global potential, kinetic, and mechanical energies, are denoted as E_p , E_k , and E_m , respectively (see [124] for their general formulation). Videos of the simulations are provided in the supplementary material of the online version of this article.

Herein, we denote the weakly compressible SPH model (Section (6.3)) coupled either with the proposed DPC formulation (Section (8.4.3)), the cPS algorithm (Section (6.3.2)), or the standard PS method as DPC , cPS , or PS , respectively.

We represent flow characteristics and numerical properties of the test cases as follows:

1. *Oscillating droplet under a conservative force field:* This numerical test case is a periodic free-surface flow. By long-term simulations of this benchmark case, we can directly investigate the conservative properties of the particle method considering that no solid boundary exists and the fluid is inviscid [130, 160]. A conservative central body force, $\mathbf{F}_i = -A_0^2 \mathbf{r}_i$, periodically stretches an initially circular droplet, with the radius of d_0 , along the x and z -directions (Figure 6.4-a). The flow frequency, $1/T \simeq A_0/4.827$, and the constant parameter $A_0 = 1.5$ (1/s) control the time evolution of this free-surface flow. We distribute the particles on the Cartesian lattice where $d_0 = 0.5$ (m) and assign the initial condition based on the theoretical solution by Monaghan and Rafiee [11] (i.e., $p_i = \rho_0 A_0^2 (d_0^2 - \|\mathbf{r}_i\|^2)$ and $\mathbf{v}_i = \{A_0, 0, -A_0\} \mathbf{r}_i$ at $t = 0$). Moreover, we set $c_s = 15A_0 d_0$ and $\rho_0 = 1000$ (kg/m³) and identify the spatial resolution of the test case by $R = d_0/dp$. To avoid high-frequency pressure noises, we only activate the density diffusion term of Molteni and Colagrossi [54] (6.9) with $\delta = 0.1$ (without the artificial viscosity term as $\nu_0 = 0$). We assign the initial maximum and minimum pressures at the center and the free-surface of the droplet to $p_{max} = 2\rho_0 A_0^2 d_0^2$ and $p_{min} = (\rho_0 A_0^2 (d_0^2 - (d_0 - 0.5dp)^2))$ in the DPC repulsive term (6.14), respectively.
2. *2D dam break:* This problem has become a popular benchmark case for showing the robustness of the enhanced particle methods capable of simulating highly dynamic free-surface flows (e.g., [50, 54, 124, 182, 194]). It involves complex fluid-fluid and fluid-solid impacts that challenge the standard SPH methods for dealing with their associated numerical issues. Here, we simulate the experimental case by Lobovský et al. [4] in which the height and width of the water column are $H = 0.6$ (m) and $B = 2H$, respectively, and the length of channel is $5.366H$ (in the x -direction) (Figure 6.4-b). The initial hydrostatic pressure is assigned to the particles and the sound speed is set to $c_0 = 10\sqrt{gH}$ where the gravitational acceleration is $g = 9.81$ (m/s²) in the negative z -direction. Unless specified, the model implements the laminar viscosity and the SPS equations (6.6) where $\nu_0 = 10^{-6}$ (m²/s) and $\rho_0 = 1000$ (kg/m³) for water. We activate the density diffusion model of Fourtakas et al. [69] (6.10) and set $\delta = 0.1$. The non-dimensional time and the spatial resolution of the model are identified by, $T = t\sqrt{g/H}$ and $R = H/dp$, respectively. For simulating the solid walls, we adopt the modified Dynamic Boundary Condition (mDBC) introduced by [192]. Similar to [124], we assign $p_{max} = 2.3\rho gH$ and $p_{min} = \rho gdp$ in the DPC formulation (6.14). The impact load on the front wall, the probe location S , is locally averaged to be compared with the experimental measurements.

3. *Water sloshing:* Accurate estimation of the sloshing loads are essential for optimum design of fluid storage tanks and vessels [195]. The movement of the solid boundary with the presence of the gravitational acceleration, \mathbf{g} , forms plunging waves and lateral water impacts. Here, we simulate the water sloshing in a rectangular reservoir identical to the experimental case of Souto-Iglesias [195]. In this test case, the tank rotates periodically under a sinusoidal excitation with the rotation center at the middle point of the bottom side and the frequency of $1/T$ (Figure 6.4-c). We simulate this test case as a 2D and single phase problem. The tank length and height, L_b and H_b , are 0.90 and 0.508 (m), respectively. Water fills the width of the reservoir with the initial height, $H = 0.093$ (m). The model assigns the initial hydrostatic pressure to the particles and sets $c_0 = 30\sqrt{gH}$. The density and kinematic viscosity of the water are set to $\rho = 1000$ (kg/m^3) and $\nu_0 = 10^{-6}$ (m^2/s), respectively. The SPS model calculates the shear forces in the numerical model. The density diffusion term of Fourtakas et al. [69] (6.10) is implemented with $\delta = 0.1$. We adopt a single spatial resolution for all the simulations where $dp = 0.002$ (m). The mDBC model updates the pressure of the solid boundary particles. In (6.14), we set $p_{max} = 15$ (kPa) and $p_{min} = \rho g dp$ based on the expected maximum pressure from the experimental data and the minimum hydrostatic pressure on the free-surface. We extract the local averaged pressure at the location of the pressure sensor, S , (identified on Figure 6.4-c) to validate the lateral impact with those from the experiment.

4. *3D dam break against a rigid obstacle:* In this test case, the water column collapses under the gravitational force, \mathbf{g} , on the horizontal bed and impacts a rigid cuboid obstacle. Plunging jets form and fluid-solid interactions occur as water flows over the obstacle and impacts the front-wall of the reservoir. The 3D configuration of this free-surface violent flow challenges the developed particle method in capturing its highly dynamic deformations and impact events (e.g., [124,164,167,192]). Figure 6.4-d shows the initial hydrostatic pressure and the geometrical properties of the problem. The reservoir, water column and obstacle dimensions are chosen according to the experimental setup of Kleefsman et al. [6] employed for validating the flow evolution and impact loads. The vertical lines probed for the fluid heights are at $H1:(x = 0.992, y = 0.5)$ and $H2:(x = 2.638, y = 0.5)$ and the local pressure is extracted on the front-vertical face of the obstacle at $P1:(x = 0.8245, y = 0.471, z = 0.021)$ and $P2:(x = 0.8245, y = 0.471, z = 0.101)$ points (units in meter). The initial height of the water column is $H = 0.55$ (m) in the z-direction. The non-dimensional time is denoted as, $T = t\sqrt{g/H}$ and the sound speed is set to $c_0 = 20\sqrt{gH}$. Similar to the previous test cases, we implement the Laminar+SPS model (6.6) (with $\rho = 1000$

(kg/m^3) and $\nu_0 = 10^{-6}$ (m^2/s)), the diffusion term of Fourtakas et al. [69] (6.10) (with $\delta = 0.1$), and the mDBC solid boundary model. In the dynamic background pressure (6.14), we adopt $p_{max} = 2.3\rho gH$ and $p_{min} = \rho gdp$. Simulating this 3D problem with various spatial resolutions ($R = H/dp = 27.5, 55, \text{ and } 110$), we specifically investigate the efficiency and computational performance of the new numerical implementations in DualSPHysics.

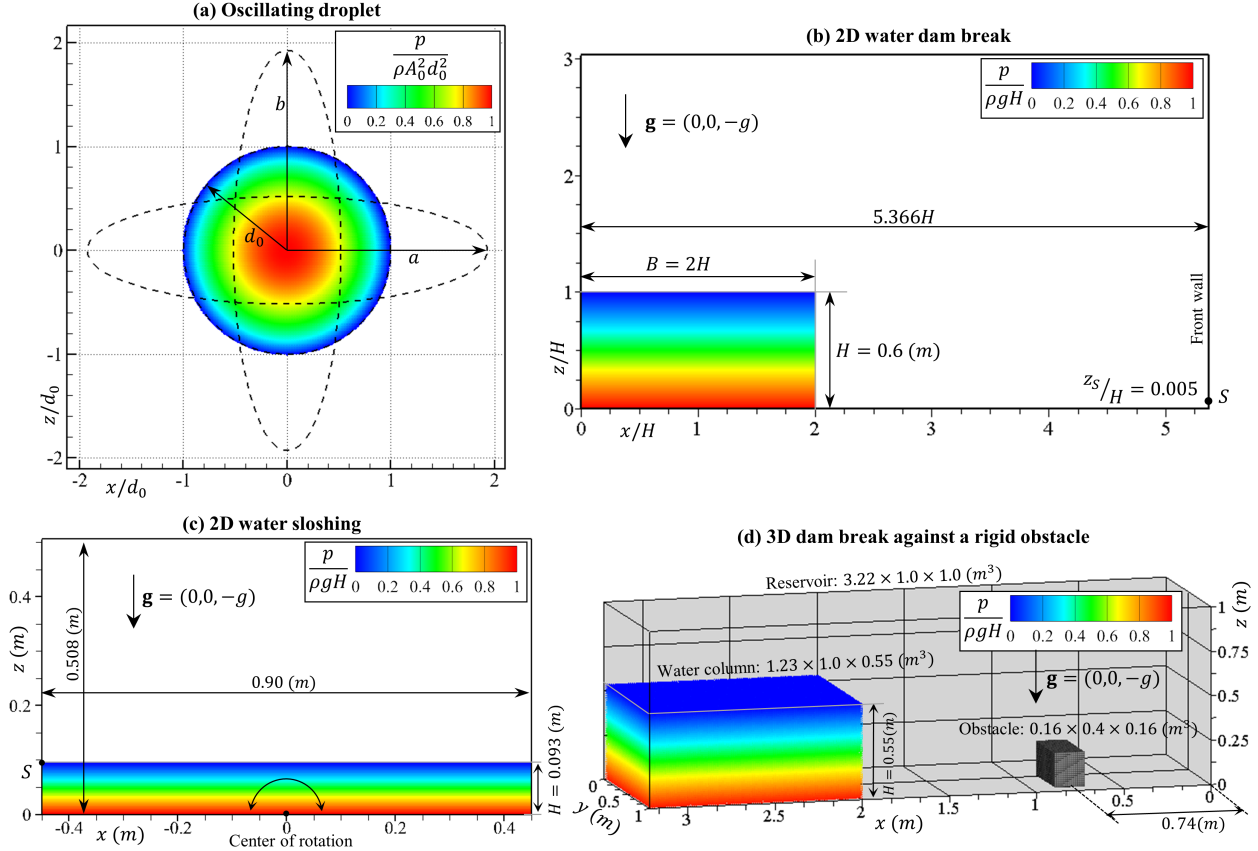


Figure 6.4 Initial state and pressure field of the numerical test cases: (a) the oscillating droplet, (b) 2D water dam break, (c) 2D water sloshing, and (d) 3D dam break against an obstacle

6.4.1 Oscillating droplet under a conservative force field

We validate the numerical simulations of this periodic free-surface flow versus its theoretical solution (represented in [11]). Figure 6.5 illustrates the pressure fields and flow evolutions simulated with the PS, cPS, and DPC techniques, where the spatial resolution, $R = d_0/dp = 200$.

Thanks to the density diffusion term, the pressure field is smooth over the fluid domain. However, the particle clustering issue at the free-surface region is notable with PS (as PS ignores the fluid particles with $A_{C_i} < 0$). On the other hand, cPS improves particle distribution at the free-surface and its vicinity by applying DPC between the detected free-surface particles. Comparing the flow evolution with the analytical free-surface (indicated with the black dashed lines) manifests the unphysical volume expansion due to the inconsistent implementation of the particle shifting (particularly at $t/T = 6.50$ and 8.75); however, with cPS the volume expansion slightly reduces. The DPC method not only represents uniform particle distribution at the free-surface region ensuring the numerical stability, but also predicts accurate evolution of the oscillating droplet.

We plot the time evolution of semi-axes, a and b , and their theoretical profiles to quantify the accuracy of the simulated flow. Figure 6.6-a shows that the shifting formulation leads to overestimation of a/d_0 and b/d_0 , while the model with DPC gives more accurate evolution of the semi-axes. Theoretically, we expect the numerical model to conserve the total volume satisfying $ab/d_0^2 = 1$ condition. Figure 6.6-b shows that DPC successfully conserves the total volume with less than ~ 1 % error. The naive implementation of PS diverges this value (i.e., the volume expands by ~ 8 % after 12 cycles); nevertheless, the free-surface stability achieved by cPS reduces this error to less than 3 %.

In Figure 6.7, we evaluate the time evolution of the global energies, ΔE . Figure 6.7-a shows that DPC predicts more accurate evolution of the potential energy in comparison to PS that increases fluid volume over the simulation time. We observe that the minimum of potential energy evolution in each cycle, $\min(\Delta E_p/E_p^0)$, (which should ideally be zero) diverges with PS by more than 8 % error after 12 cycles, but cPS reduces the error to only ~ 4 % (Figure 6.7-b). On the other hand, DPC shows convergence behaviors as it keeps $\min(\Delta E_p/E_p^0)$ to less than 1 %. The global mechanical energy theoretically should remain identical to its initial value (i.e., ideally $\Delta E_m = 0$). However, the numerical dissipation of the weakly compressible SPH algorithm (especially with implementing the density diffusion term) reduces the mechanical energy over the simulation (i.e., numerically $\Delta E_m < 0$). Figure 6.7-c & d plot the mechanical energy evolution of the models with different spatial resolutions ($R = 50, 100, 200, \text{ and } 400$). Figure 6.7-d confirms that with DPC and cPS the mechanical energy converges toward its theoretical value as the spatial resolution increases. In contrast, PS results in positive values of mechanical energy evolution, i.e., $\Delta E_m > 0$ (by inserting unphysical potential energy into the system). Also, PS does not establish a clear convergence behavior by increasing R (Figure 6.7-c). The normalized root mean square error (i.e., L_2) of the kinetic, potential, and mechanical energies are plotted in Figure 6.7, graphs (e), (f), and (g), respectively. In comparison to PS and cPS, the numerical error of the potential and

kinetic energies significantly reduces by DPC. Yet, DPC and cPS result in almost identical order of convergence (1.0-1.2). Moreover, the PS affecting the global energies of the flow affects the convergence order reducing by one order of magnitude to 0.1-0.5.

Here, we evaluate the local spatial particle disorder, λ_i , and its global value Λ (represented by Antuono et al. [7]) comparing the effectiveness of the particle regularization techniques. The results show that the shifting formulation implemented in PS and cPS reduces Λ (averaged over $t/T = 10-12$) from 0.115, obtained by the case with no particle regularization technique, to 0.084 and 0.079, respectively (Figure 6.8). The improvement of particle distribution at the free-surface region with cPS is well illustrated in the zoom-in snapshots. It should be highlighted that DPC successfully represents more regular particle distribution ($\Lambda = 0.054$) compared to the shifting technique.

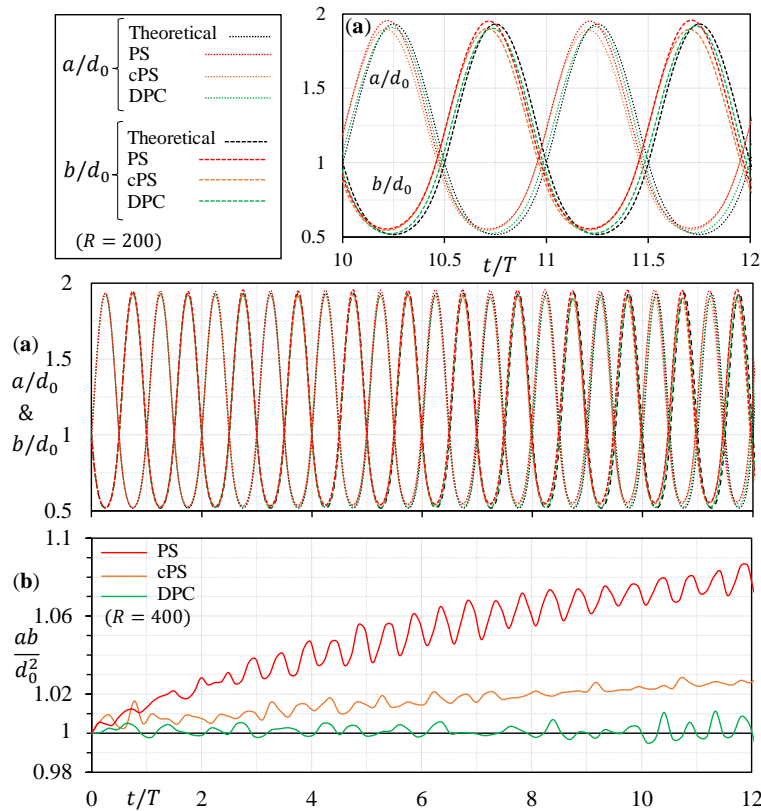


Figure 6.6 Oscillating droplet: the time evolutions of a and b by the SPH + PS, cPS or DPC techniques compared with the theoretical solution in (a). Graph (b) illustrates the divergence of model with the PS method due to the unphysical volume expansion

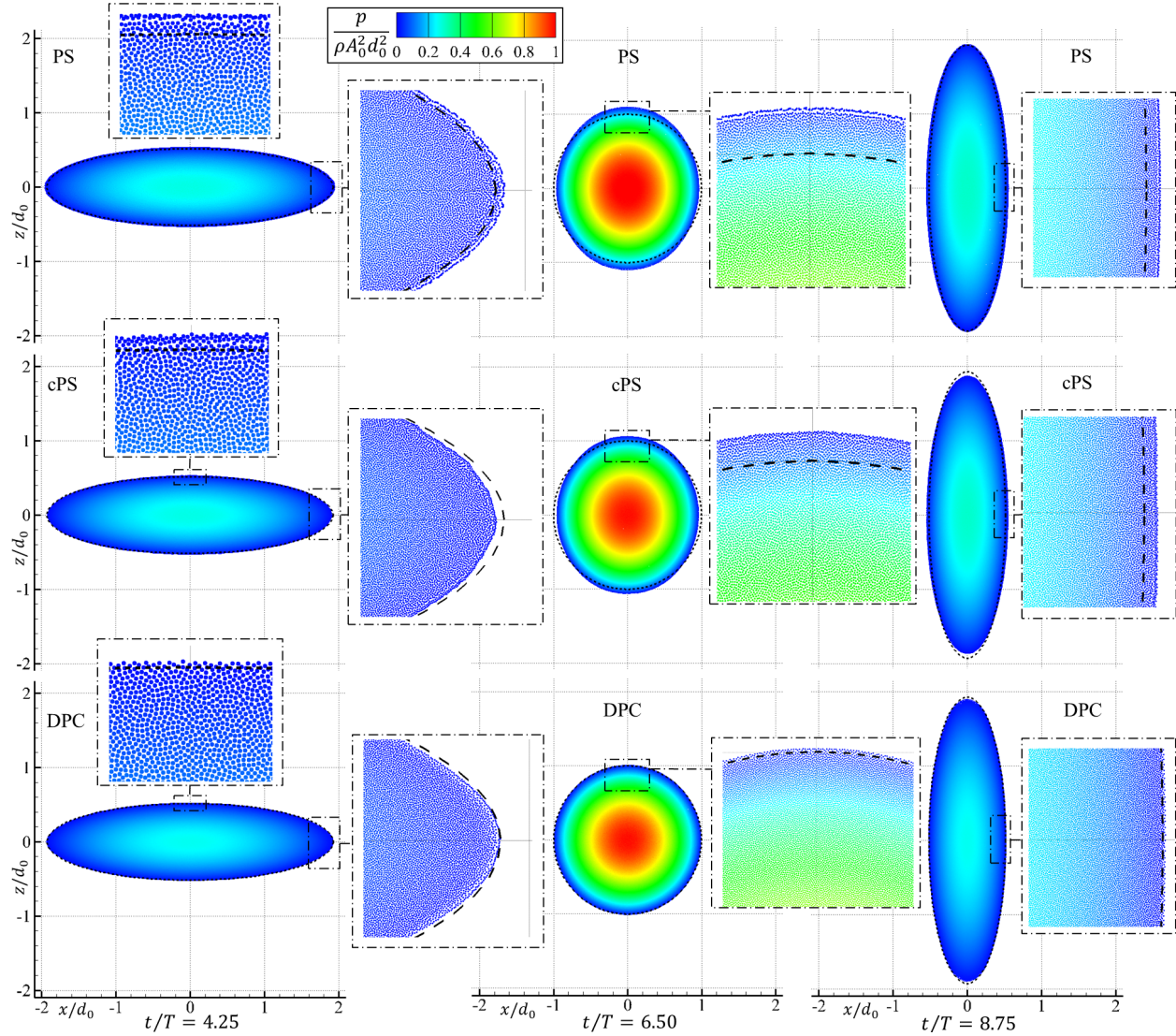


Figure 6.5 Oscillating droplet: non-dimensional pressure fields by the SPH with either PS, cPS, or DPC techniques from top to bottom rows, respectively ($R = d_0/dp = 200$). The free-surface of the droplet is compared with the theoretical solution (the black dashed lines) at $t/T = 4.25, 6.50$, and 8.75 .

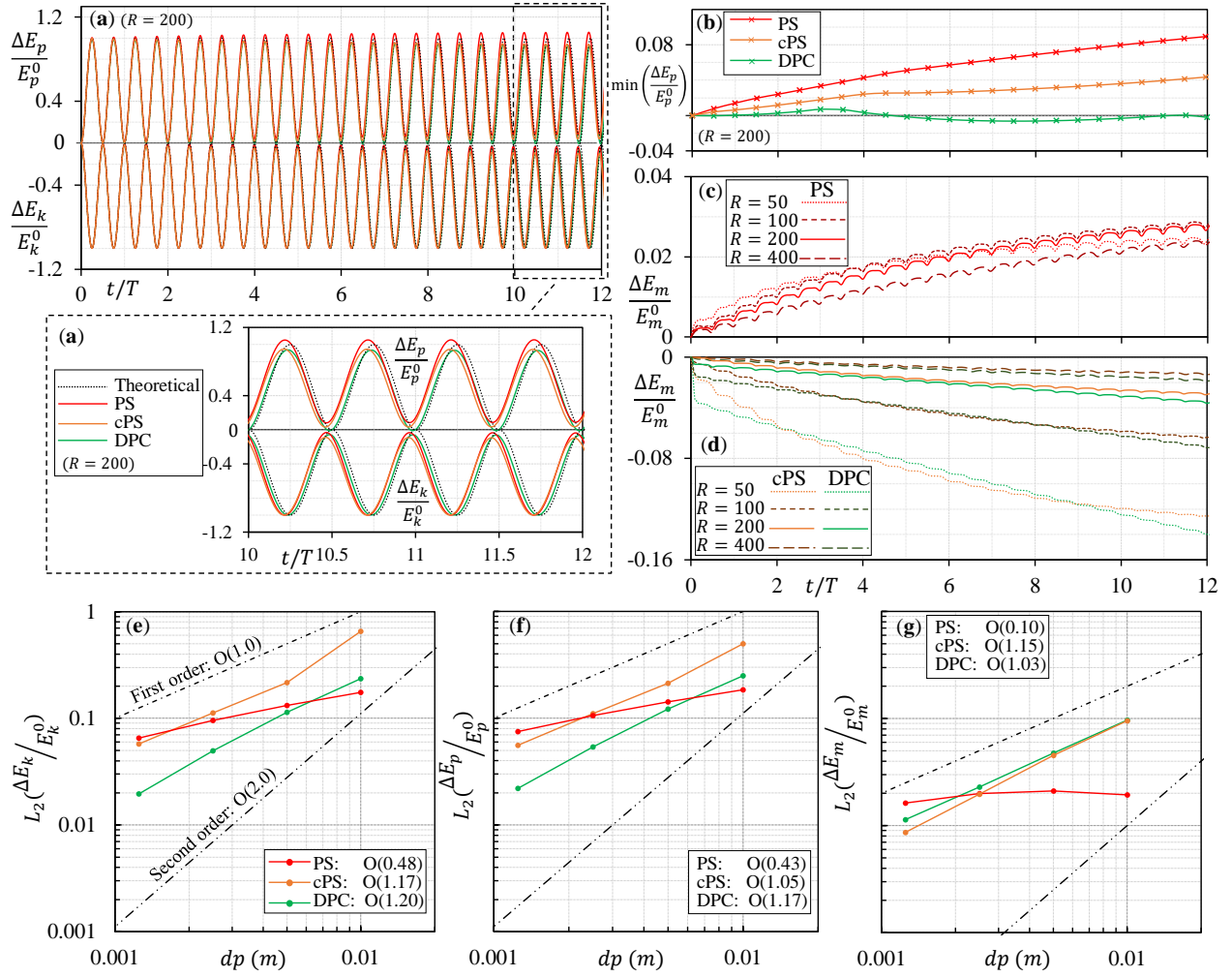


Figure 6.7 Oscillating droplet: graphs (a-d) represent the time evolution of the total potential (E_p), kinetic (E_k), and, mechanical (E_m) energies comparing the numerical results with the theoretical solution (the black dotted lines). Graphs (e-g) give L_2 errors and the convergence order of the numerical results.

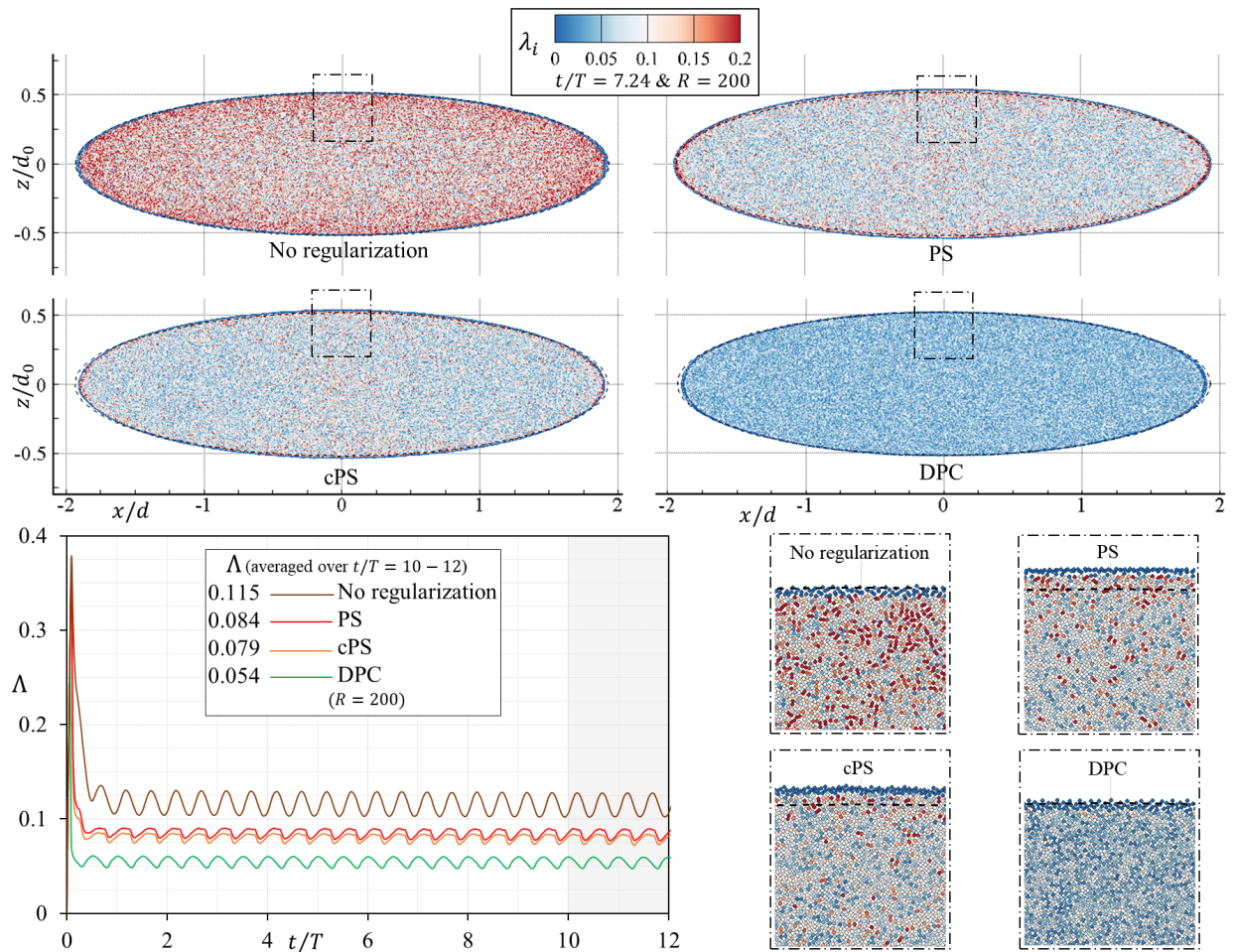


Figure 6.8 Oscillating droplet: the spatial particle disorder, λ_i for the models with no particle regularization, PS, cPS, and DPC. The time evolution of the global particle disorder, Λ , is plotted in the graph for the different test cases. The spatial particle disorder formulation is implemented based on the work of Antuono et al. [7].

6.4.2 2D water dam break

We validate the numerical simulation of the 2D dam break versus the experimental results of Lobovský [4] and evaluate the role of the particle regularization techniques. Figure 6.9 shows that DPC and cPS (with the spatial resolution, $R = H/dp = 200$) accurately estimate the impact load at the pressure measurement point, S , and the wave propagation on the horizontal bed, x_f , compared with the experimental results. The discrepancies between the numerical and experimental measurements are related to the air-cushioning effects neglected in the single fluid phase simulations and the solid boundary conditions [167]. We should highlight that the local pressure extracted every 0.02 seconds may not reflect the high-frequency pressure fluctuations due to the weak compressibility of the fluid phase.

Figure 6.10 represents the flow evolution and the non-dimensional pressure field simulated by cPS and DPC. The overall flow evolution with both approaches are almost identical, however, we observe that DPC reduces pressure fluctuations during highly dynamic flows and impact events at $T = 7.60$ and 8.90 . To illustrate the efficiency of the regularization techniques, we display snapshots of the plunging wave at $T = 6.31$ (Figure 6.11). The results shown confirm the effectiveness of DPC embedded into the PS method through equations (6.22) and (6.23) (i.e., the cPS method) for improving the particle distribution at the impact and free-surface regions compared with PS. Moreover, DPC (i.e., equation (6.12)) applied among all the fluid particles results in more uniform particle distribution without involving any boundary treatments (Figure 6.11).

To quantify the improvements, we compare the local spatial particle disorder and the time evolution of its global value, i.e., λ_i and Λ , respectively, simulated by PS, cPS, and DPC (Figure 6.12). cPS reduces spatial particle disorder at the vicinity of the free-surface compared to PS; yet, both PS and cPS manifest irregular particle distribution at the impact location as $\lambda > 0.2$. DPC proves to be capable of reducing the spatial particle disorder where the wave impacts the free-surface and pressure suddenly increases (Figure 6.12-a). Also, the global particle disorder with DPC is considerably less than the models with PS and cPS, especially during the violent flow of the dam beak (Figure 6.12-b); with DPC, Λ remains less than 0.06, while with cPS and PS, Λ exceeds 0.11 at $T = 8$.

Next, we study the conservation of the fluid volume and the global energy evolution of the simulations. In a volume conservative model, the local value of $\langle \nabla \cdot \mathbf{r} \rangle_i$ is expected to remain equal to the space dimension of the test case (i.e., for this 2D case, we expect $\langle \nabla \cdot \mathbf{r} \rangle_i \cong 2$). Figure 6.13 manifests the unrealistic volume expansion of the fluid phase due to the shifting of the internal particles (as $\langle \nabla \cdot \mathbf{r} \rangle_i < 1.75$ in some regions at $T = 8.90$ and over the entire fluid domain, at $T = 40.44$); DPC does not suffer from this numerical issue

(noting that $\langle \nabla \cdot \mathbf{r} \rangle_i > 1.8$ over the main fluid domain). We also observe that the unphysical volume expansion diverges the hydrostatic pressure expected in the late stages of the flow (at $T = 40.44$ shown in Figure 6.13). Furthermore, we plot the energy evolution of the system normalized by $\Delta E_m^{fin} = E_p^0 - E_p^\infty$ in Figure 6.14 (where E_p^0 is the initial potential energy and E_p^∞ is the final expected potential energy with the fluid flow reaching the equilibrium state in the rectangular tank). For both cPS and DPC, increasing R reduces the dissipation of the mechanical energy during the main impact events showing the numerical convergence of the results (Figure 6.14-a & b). DPC estimates accurate evolution of the global energy (i.e., $\Delta E_p / \Delta E_m^{fin} \cong -0.975$ as ideally should reach -1.0). The energy evolution with DPC is almost identical to the results of the model with no particle regularization (Figure 6.14-c); thus, DPC effectively improves the particle distribution without manipulating the global flow properties. In contrast, the unphysical volume expansion with the particle shifting (in either PS or cPS forms) increases the potential energy of the system not reaching the expected value (i.e., $\Delta E_p / \Delta E_m^{fin} \cong -0.875$ and -0.85 with cPS and PS, respectively). Particularly during the violent flow deformations (i.e., $T \cong 8 - 10$), the standard PS excessively increases the global mechanical energy of the system (shown in the zoomed view of graph (c) in Figure 6.14).

To investigate the role of the shear force term in the pressure and flow evolution, we compare the results of the dam-break case simulated by cPS and DPC (with $R = 200$) considering different viscosity models, i.e., the Laminar+SPS model (equation (6.6)), the artificial viscosity term (see [179]), and with no viscosity (as if water is an inviscid fluid). A non-dimensional coefficient, α , adjusts the intensity of the artificial viscosity [61, 179]. We implement the artificial viscosity term by setting α to 0.01 and considering the slip boundary condition at the solid walls. To simulate water as an inviscid fluid, α is set to 0.0. As illustrated in Figure 6.15- (a) and (b), in all the cases, the pressure field is smooth, and the free surface match quite well with the reference solution (the dashed red line reported by Greco et al. [8] using a Boundary Element Method (BEM)) at $T = 5.95$. Figure 6.15- (c) and (d) show that the averaged local pressure of all the viscosity models evolves similarly during the impact events and is compatible with the experimental measurement (the dashed black line from [4]). These results confirm that the smoothness of the pressure field and the evolution of the estimated impact load (with the adopted density diffusion term (6.8) and the cPS or DPC technique) are almost independent of the viscosity formulation. Moreover, Figure 6.15- (e) and (f) indicate that the Laminar+SPS formulation (in the form implemented in DualSPHysics) dissipates slightly less mechanical energy in comparison with the artificial viscosity term. Accordingly, we choose the Laminar+SPS model for the shear force calculation to evaluate the effect of particle regularization techniques on the system's conservation

properties without incorporating energy dissipation of the artificial term.

6.4.3 2D water sloshing in a tank

Here, we present and discuss the numerical simulations of the 2D water sloshing and its lateral water impacts. The time history of the impact loads at the location of the pressure sensor, S , is compared with the experimental measurements by [9]. Figure 6.16 shows that while PS and cPS slightly overestimate the local averaged pressure (at $t/T \cong 2.6, 3.7, 4.75$), DPC predicts more accurate impact loads with less pressure noises. The remaining incompatibility between the numerical and experimental results is due to the fact that the single phase simulation ignores the air-cushioning effects. Also, the periodic rotation of the solid walls may affect the accuracy of the estimated impact load increasing local pressure fluctuations observed in Figure 6.16 [192]. Figure 6.17 illustrates snapshots of the flow evolution (taken from the experiment represented by [9]) and the non-dimensional pressure fields with PS, cPS, and DPC. Although all the models capture the overall flow evolution, yet, DPC results in isotropic and more compact particle distributions during the lateral impacts (see the zoom-in sections of Figure 6.17). With the extreme kernel truncation at the free surface, the standard approximation operators diverge the pressure and velocity fields affecting the dynamic free-surface boundary condition [196]. The numerical errors due to the incomplete kernel support with no special treatment of PS near the free surface lead to dominant particle clustering. DPC and cPS improve the particle distribution in this region; nevertheless, to further resolve the accumulation of particles at the free-surface vicinity, one can implement high-order discretization operators (e.g., the high-order density diffusion terms [66, 126]) and virtual background nodes (e.g., the virtual particle technique by Duan et al. [197] and the Background Mesh scheme by You et al. [196]).

To quantify the effectiveness of the models, we represent the estimated value of $\langle \nabla \cdot \mathbf{r} \rangle_i$ and the local spatial disorder of particles, λ_i (in Figure 6.18). DPC retains $\langle \nabla \cdot \mathbf{r} \rangle_i > 1.8$ (which is expected to be $\cong 2$); due to the unphysical volume expansion by PS and cPS, $\langle \nabla \cdot \mathbf{r} \rangle_i < 1.75$ becomes dominant over the entire fluid domain. Moreover, DPC improves uniform particle distribution in comparison to PS and cPS by which λ_i increases to more than 0.2 where the lateral impact occurs at $t = 7.50$ seconds. We also observe that, with PS and cPS, the volume expansion and the extreme particle clustering issue within the interior domain of the flow make conditions (6.21) incapable of accurately detecting the boundary and splashed particles (noting that in some internal regions λ_i is incorrectly set to zero).

Next, we plot the time evolution of the global particle disorder, Λ , and the global potential energy, E_p , in Fig 6.19-a and b, respectively. The potential energy is normalized by its initial

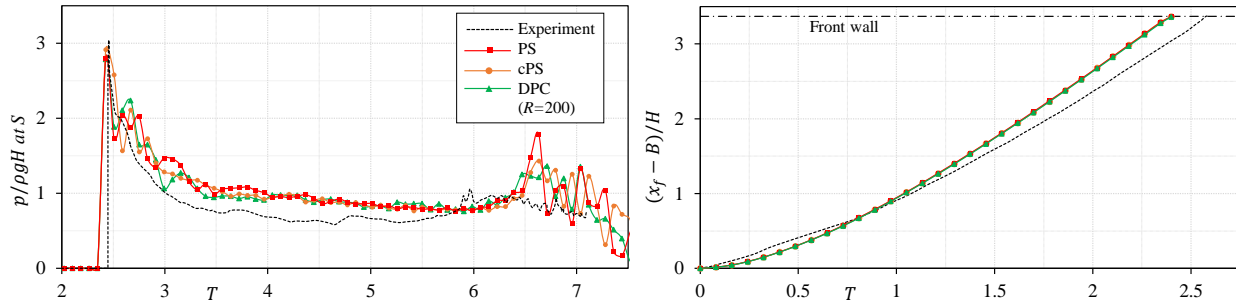


Figure 6.9 Dam break: the local averaged pressure on the front wall, at S , (left) and the wave propagation on the horizontal bed, x_f , (right) with $R = H/dp = 200$. Numerical results are extracted every 0.02 seconds.

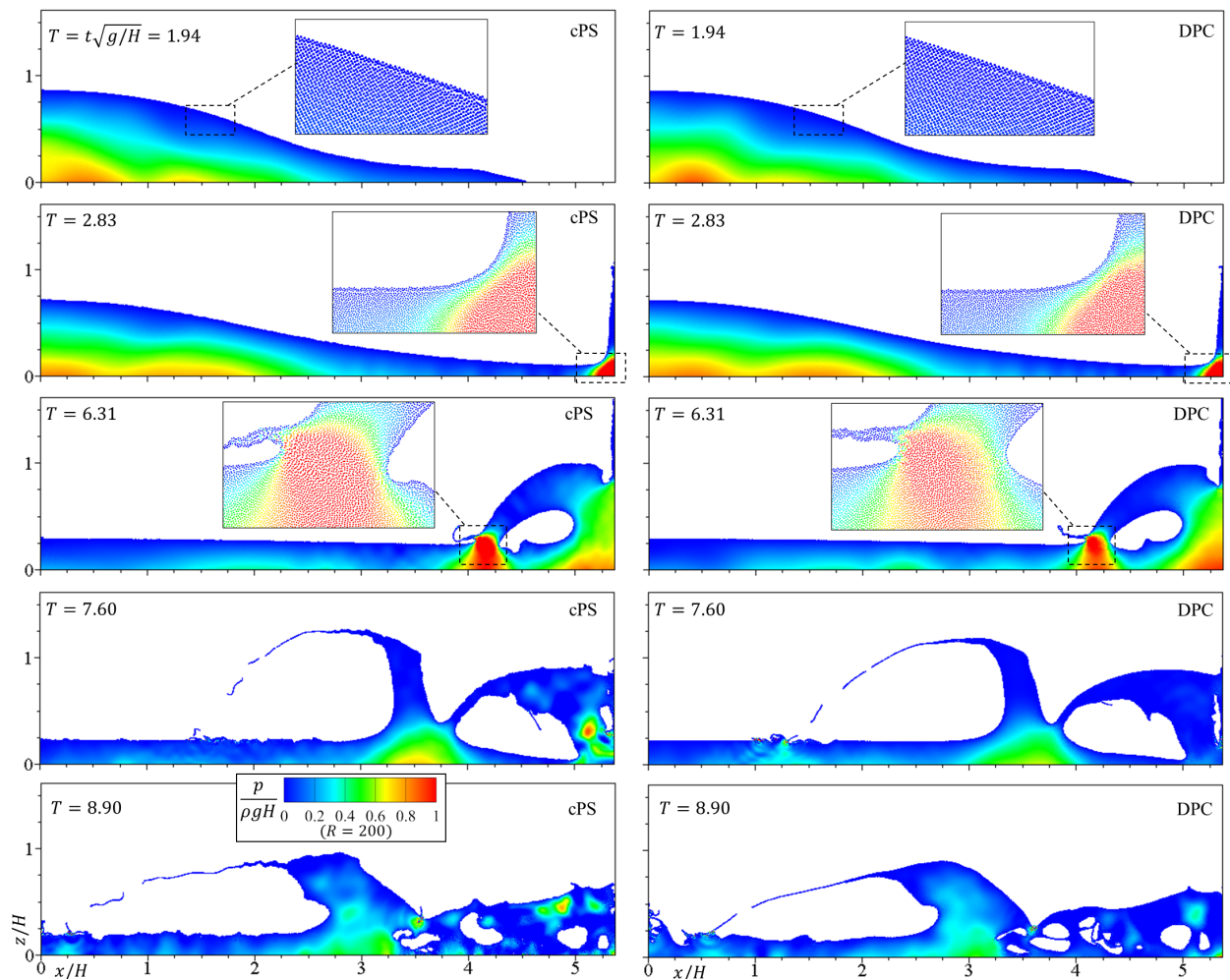


Figure 6.10 Dam break: flow evolutions and non-dimensional pressure fields with cPS and DPC (the left and right columns, respectively) with $R = 200$

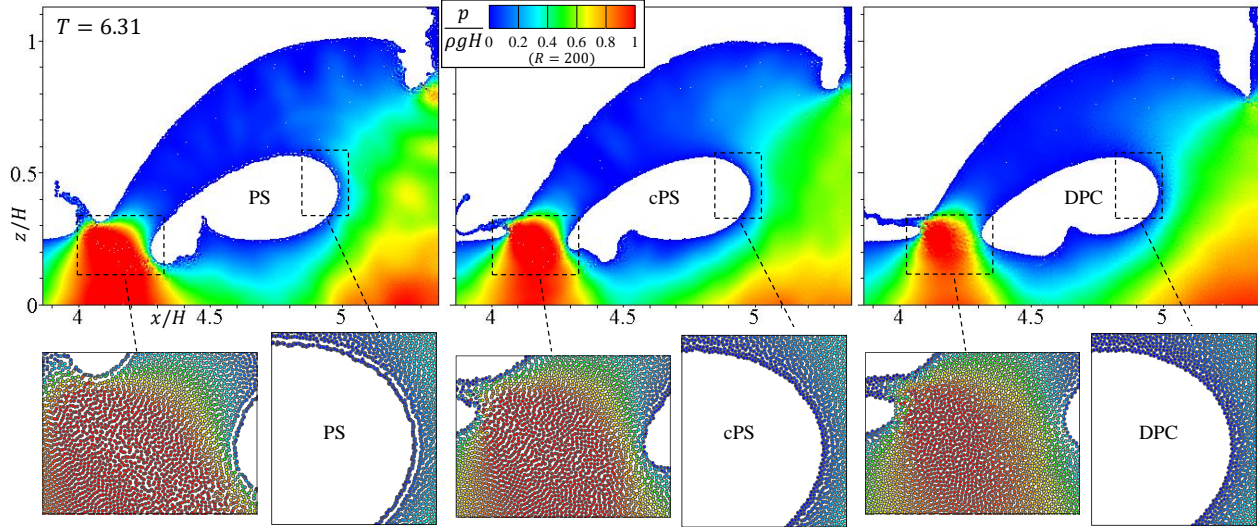


Figure 6.11 Dam break: the particle distribution and the non-dimensional pressure field as the wave impacts the free-surface at $T = 6.31$ (simulated by PS, cPS and DPC techniques where $R = 200$)

global value, E_p^0 . After 5 cycles of rotation, Λ increase to more that 0.11 by PS and cPS, while DPC keeps Λ less than 0.07 showing more regular particle distribution over the entire domain. We again observe that, unlike DPC, PS and cPS diverge the minimum potential energy of the system in the long-term simulation of this violent free-surface flow. This divergence of potential energy, manifested as the unphysical volume expansion, originates from the inconsistent implementation of the shifting equation (i.e., without considering the additional diffusion/cohesion terms of the particle shifting transport-velocity [3, 124, 182]).

6.4.4 3D water dam-break against a rigid obstacle

In Figure 6.20, by plotting the extracted numerical results against the experimental measurements (by [6]), we show that the implemented models predict the fluid flow evolutions and the impact loads on the rigid obstacle. The temporal evolution of the fluid heights over $H1$ and $H2$ lines and the local pressures on $P1$ and $P2$ points (with PS, cPS, and DPC, where the spatial resolution, $R = H/dp = 55$) are compatible with the experimental results. Similar to the other single fluid phase simulations (e.g., [124, 189, 192]), a delay occurs in the impact load of the returning wave (at $T \cong 20$).

Figure 6.21 illustrates the violent free-surface deformations and the magnitude of the velocity field as the water flow impacts the obstacle (at $T \cong 2.5$), and further, climbs up the front wall

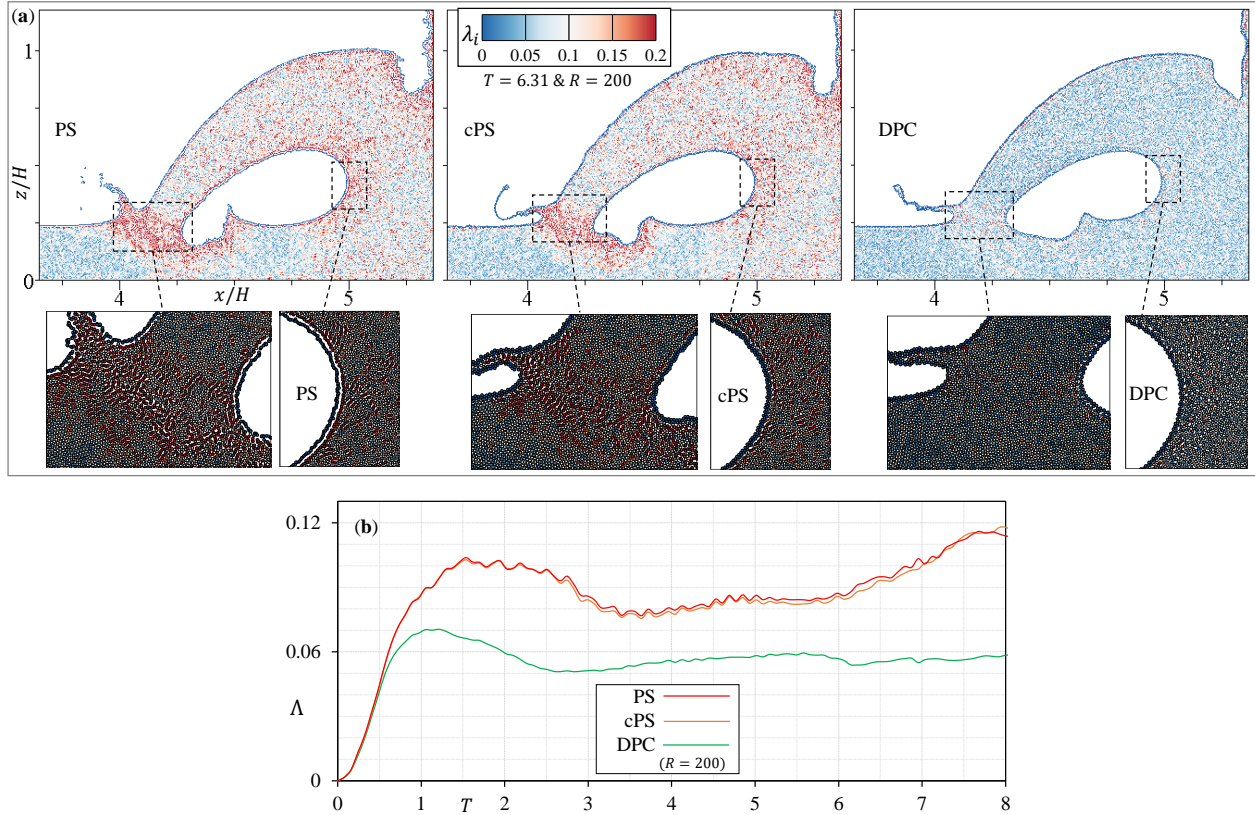


Figure 6.12 Dam break: (a) the local spatial particle disorder, λ_i , at $T = 6.31$ and (b) the evolution of its global value, Λ , with PS, cPS, and DPC techniques where $R = 200$

of the reservoir (at $T = 5.06$). The standard PS cannot eliminate fluid fragmentation due to highly dynamic flow deformations (shown in the zoomed view of the splashed flow); however, cPS and DPC simulate more uniform flow evolution. Figure 6.22 displays the pressure field at the middle-section of the tank (where $y = 0.5$ (m)) simulated by cPS and DPC. During the formation of the submerged waves, DPC shows slightly less pressure noises (e.g., at $T = 5.06$ and 8.45). Moreover, the inconsistent PS models (in the PS and cPS forms) clearly result in the volume-non-conservation issue as $\langle \nabla \cdot \mathbf{r} \rangle_i < 2.87$ in the internal regions of the fluid flow (shown in Figure 6.23, at $T = 7.45$ and $T = 33.79$). The divergence of $\langle \nabla \cdot \mathbf{r} \rangle_i$ highlights that employing a variable shifting coefficient (D_i^F) and limiting the magnitude of the shifting vector are numerically insufficient for avoiding the unphysical volume expansion by the PS equation. This places emphasis on the implementation of the consistent PS algorithm (i.e., adopting the additional diffusive terms due to the shifting transport-velocity and the special free-surface treatments, e.g. in [124, 130]) being essential for the long-term simulation of such complex free-surface flow. On the other hand, the results confirm that DPC, with being

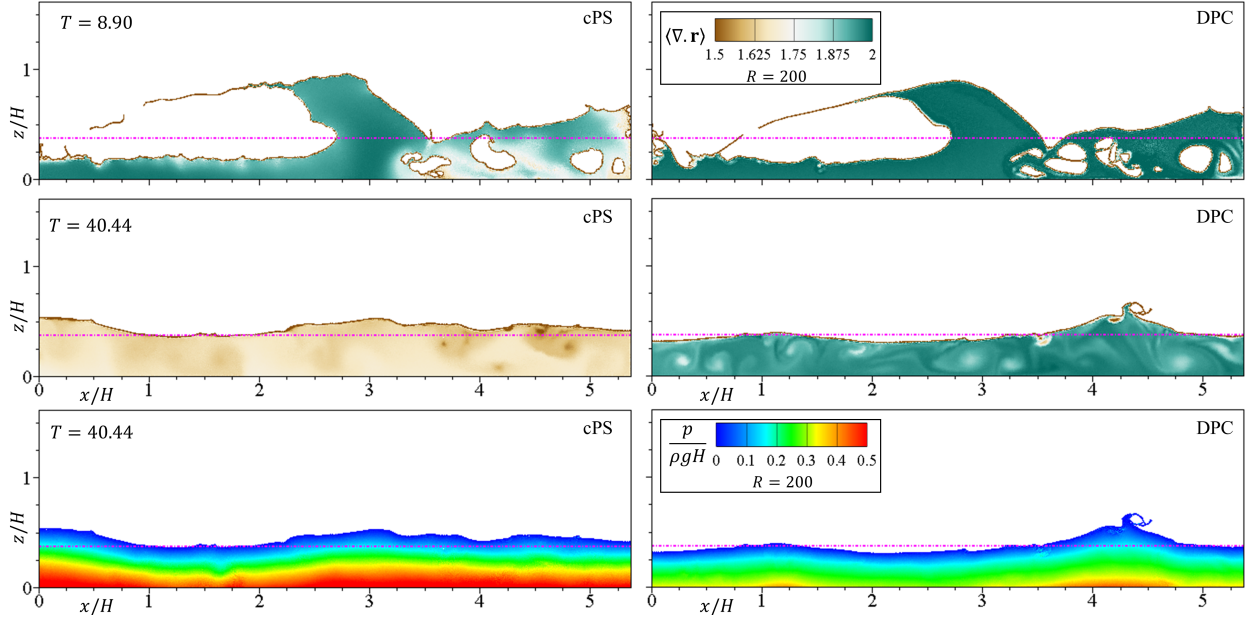


Figure 6.13 Dam break: $\langle \nabla \cdot \mathbf{r} \rangle_i$ and the non-dimensional pressure field at $T = 8.90$ and the final stage, $T = 40.44$, with cPS and DPC where $R = 200$. The dash-dot line is the expected fluid height at the final equilibrium state.

exempted from the complex boundary treatments and a conservative formulation, avoids numerical instabilities eliminating the particle clustering issue and representing smoother pressure fields.

Figure 6.24 compares the time evolution of system's global energies. Increasing the spatial resolution reduces the energy dissipation during the impact events showing the numerical convergence of the simulations with either cPS or DPC (Figure 6.24-a & b). Figure 6.24-c compares the energy evolutions where $R = 110$. While DPC predicts the expected final potential energy (i.e., $\Delta E_p / \Delta E_m^{fin} \cong -0.975$ as ideally should reach -1.0) the increase in the potential energy by PS (which starts from $T \cong 7.5$ and remains over the simulation) evidences its inability for dealing with complex flow deformations.

Finally, we evaluate the efficiency of the new implementations in DualSPHysics by comparing the simulation runtime with different regularization techniques (Tables 6.2 and 6.3). The runtime per physical second and per iteration are denoted as t_s and $t_{iter.}$, respectively. We simulate all the test cases using an NVIDIA Tesla V100 PCIe device (see the GPU specifications in Table 6.1). In this 3D problem, the number of fluid particles would be (79, 380), (652, 212), and (5, 314, 295) where $R = 27.5$, 55, and 110, respectively. In Tables 6.2 and 6.3, $(t_{(.)} / t_{(.)}^{PS} - 1) \times 100$ gives the speed-up of runtime (in percent) with respect to the original

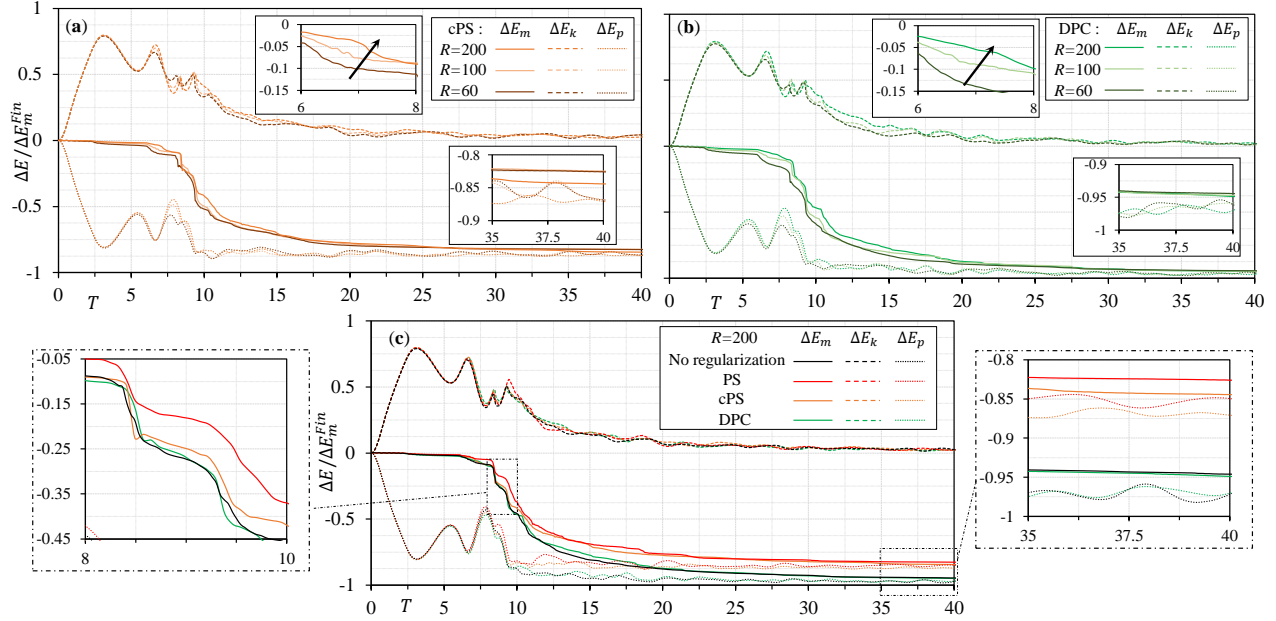


Figure 6.14 Dam break: evolution of the global energies by cPS and DPC with different spatial resolutions, R , plotted in graphs (a) and (b), respectively. Graph (c) compares the energy evolution of the model with no particle regularization with the profiles of PS, cPS, and DPC where $R = 200$.

model that implements the standard PS technique. Table 6.2 shows that the implemented modifications (associated with the DPC and cPS formulations) increase the simulation runtime per iteration, $t_{iter.}$, by 2-6.5 %. Nevertheless, the numerical stability achieved by the proposed regularization techniques allows the model to adopt larger time steps as the total runtime, t_s , reduces by 2.5-4.5 % and 6-8.5 % by cPS and DPC, respectively. The time step of calculation is updated after every time step according to the CFL condition as a function of the maximum viscous diffusion and acceleration of particles [179]. DPC eliminates unphysical high values of particle acceleration (at the impact events where pressure increases suddenly and inter-particle penetration occurs), and therefore, reduces the number of iterations over the simulation. Overall, this reduction of simulation runtime (especially with DPC) justifies the implementation of effective particle regularization techniques not only for improving the numerical stability and accuracy, but also for increasing the efficiency of the computations.

6.5 Concluding remarks

In this study, we introduced effective particle regularization techniques within the framework of the weakly compressible SPH method for the long-term simulation of violent free-surface

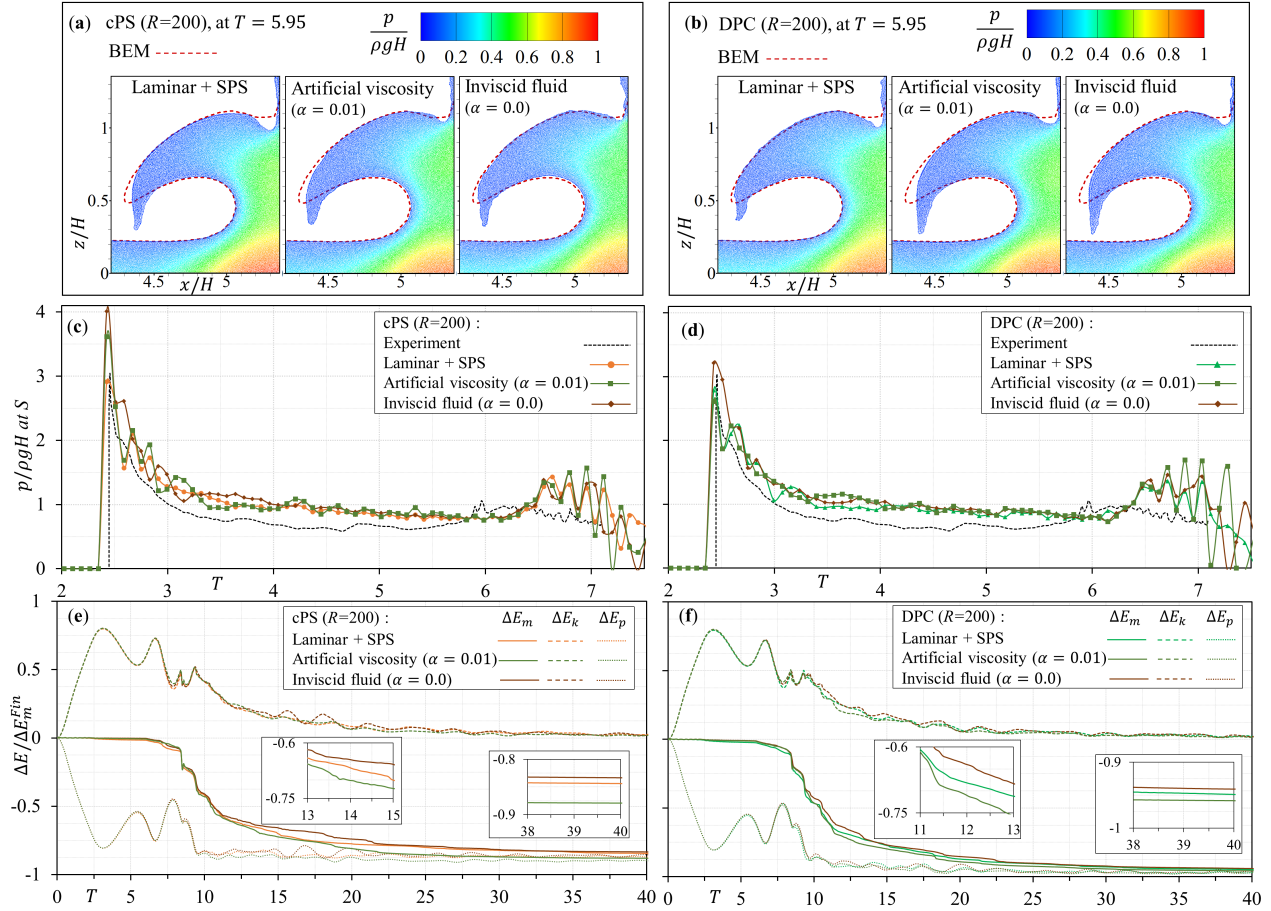


Figure 6.15 Dam break: flow evolution and the non-dimensional pressure fields (a, b), the impact load, p , at S (c, d), and the energy evolution, ΔE , (e, f) with different viscosity models, i.e., the laminar+SPS model, the artificial viscosity term ($\alpha = 0.01$), and the inviscid fluid ($\alpha = 0$), simulated by cPS and DPC where $R = 200$. The dashed red line in (a) and (b) is the free surface at $T = 5.95$ predicted by the BEM solver from [8]. The dashed black line in (c) and (d) is the experimental measurement of the impact load from [4].

Table 6.1 GPU specifications

NVIDIA Tesla V100 PCIe	
CUDA compatibility	7.0
CUDA cores	5120
Multiprocessors	80
Global memory (MB)	16160
GPU Maximum clock rate (MHz)	1380
Memory clock rate (MHz)	877
Memory bus width (bits)	4096

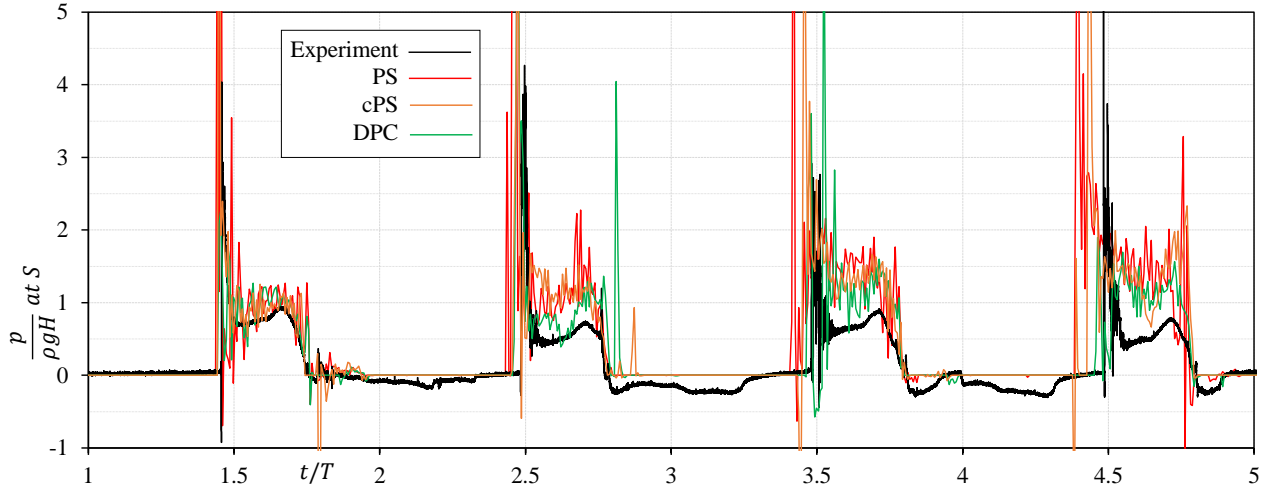


Figure 6.16 Water sloshing: the local averaged pressure obtained by PS, cPS, and DPC ($dp = 0.002$ (m)) compared with the experimental measurements at the probe location, S , reported by Souto-Iglesias et al. [9]. Numerical results are extracted every 0.01 seconds.

Table 6.2 3D dam break: the simulation runtime per iteration denoted as $t_{iter.}$. In this 3D problem, the number of fluid particles would be (79, 380), (652, 212), and (5, 314, 295) where $R = 27.5$, 55, and 110, respectively.

Model	$t_{iter.}/10^{-3}$ (seconds)			$(t_{iter.}/t_{iter.}^{PS} - 1) \times 100$		
	$R = 27.5$	$R = 55$	$R = 110$	$R = 27.5$	$R = 55$	$R = 110$
Standard PS	7.79	31.94	213.35	0	0	0
cPS	8.20	32.52	224.52	+5.16	+1.83	+5.24
DPC	7.98	32.59	227.13	+2.40	+2.06	+6.46

Table 6.3 3D dam break: the simulation runtime per physical second denoted as t_s . In this 3D problem, the number of fluid particles would be (79, 380), (652, 212), and (5, 314, 295) where $R = 27.5$, 55, and 110, respectively. cPS and DPC reduce the runtime by 2.5-4.5 and 6-8.5 %, respectively.

Model	t_s (seconds)			$(t_s/t_s^{PS} - 1) \times 100$		
	$R = 27.5$	$R = 55$	$R = 110$	$R = 27.5$	$R = 55$	$R = 110$
Standard PS	53.76	471.84	7326.52	0	0	0
cPS	52.38	442.88	7008.10	-2.58	-6.14	-4.35
DPC	50.57	431.54	6859.17	-5.93	-8.54	-6.38

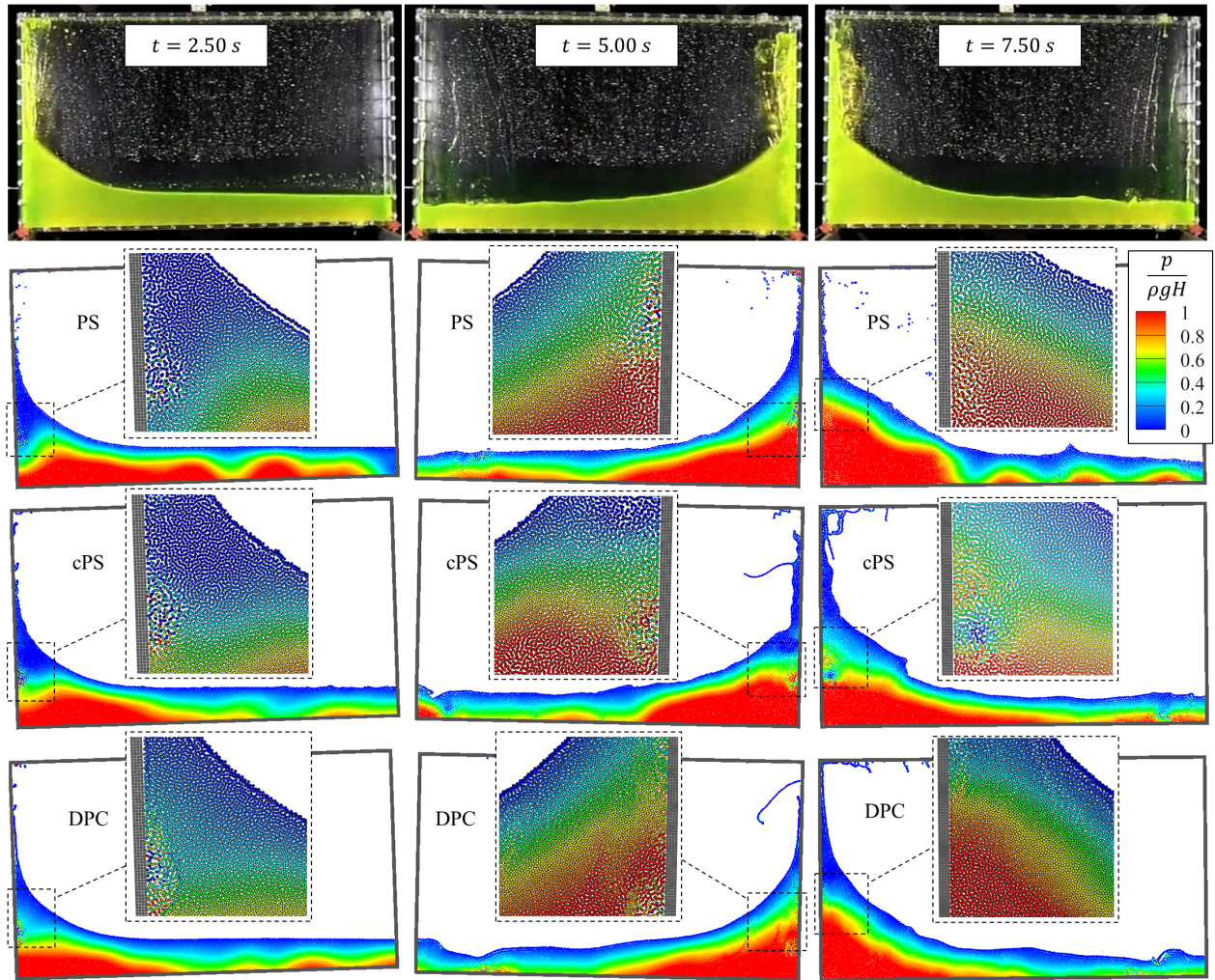


Figure 6.17 Water sloshing: the flow evolutions and the non-dimensional pressure fields with PS, cPS, and DPC ($d_p = 0.002\text{ (m)}$) compared with snapshots of the experiment on the top-row (taken from [9])

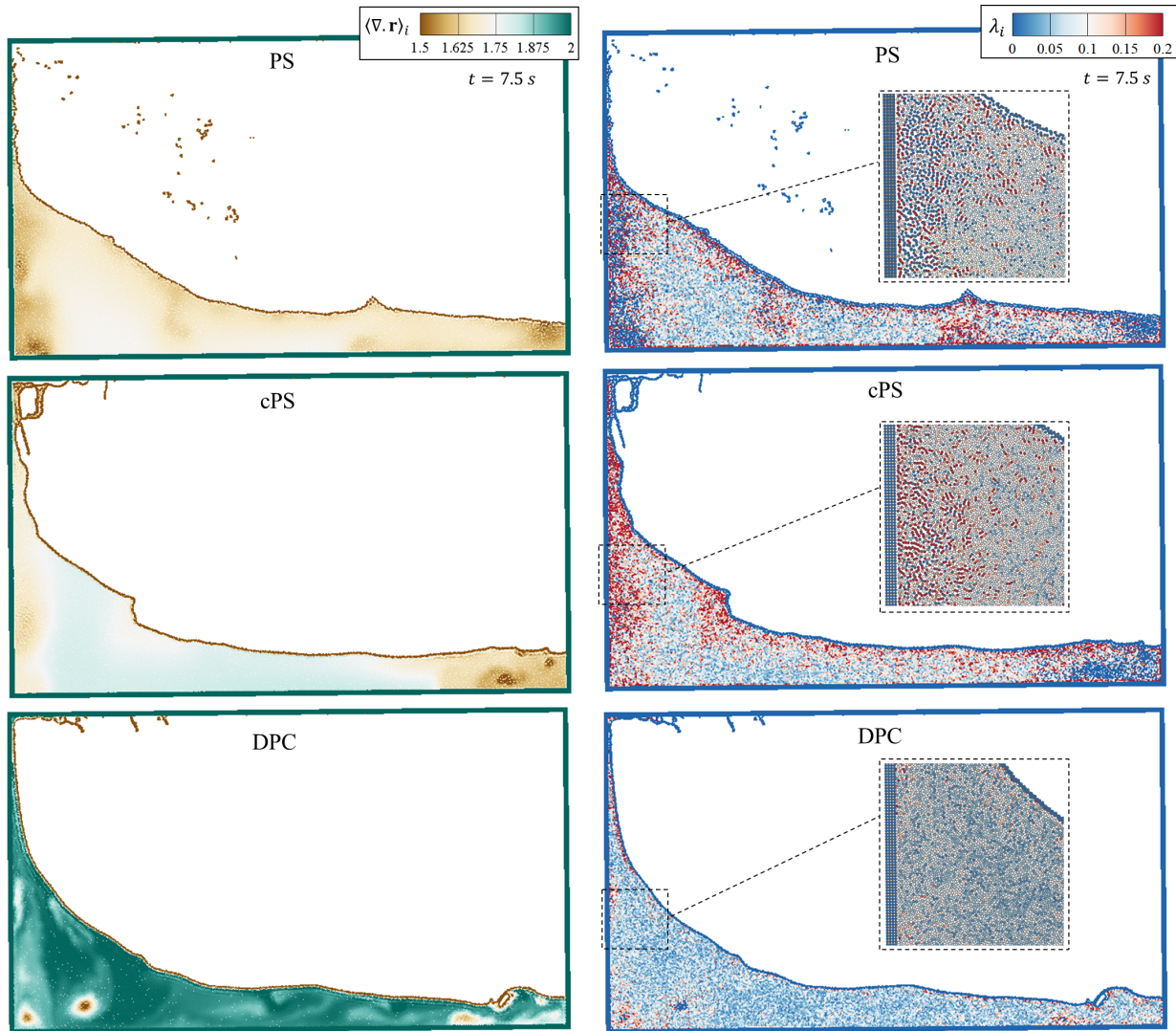


Figure 6.18 Water sloshing: $\langle \nabla \cdot \mathbf{r} \rangle_i$ and the local spatial particle disorder, λ_i at $t = 7.50$ seconds where $dp = 0.002$ (m)

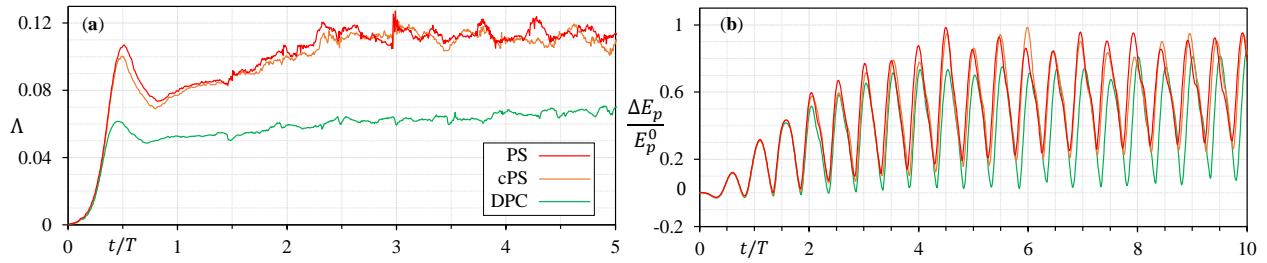


Figure 6.19 Water sloshing: the time evolution of the global spatial particle disorder, Λ , and the global potential energy, E_p , where $dp = 0.002$ (m) (represented in graphs (a) and (b), respectively)

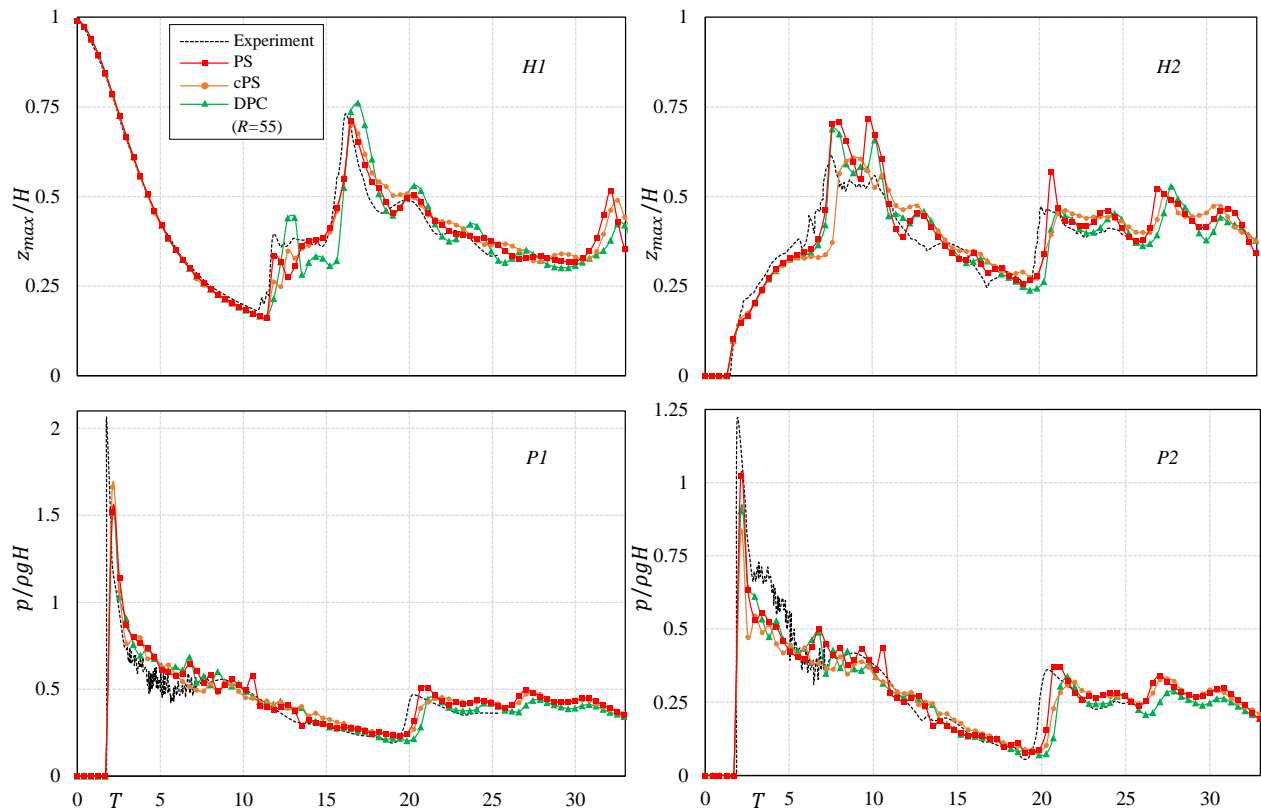


Figure 6.20 3D dam break: the fluid height at $H1$ and $H2$, and the local pressure at $P1$ and $P2$ by PS, cPS, and DPC (where $R = H/dp = 55$) validated with the experimental measurements by Kleefsman et al. [6]. Numerical results are extracted every 0.1 seconds.

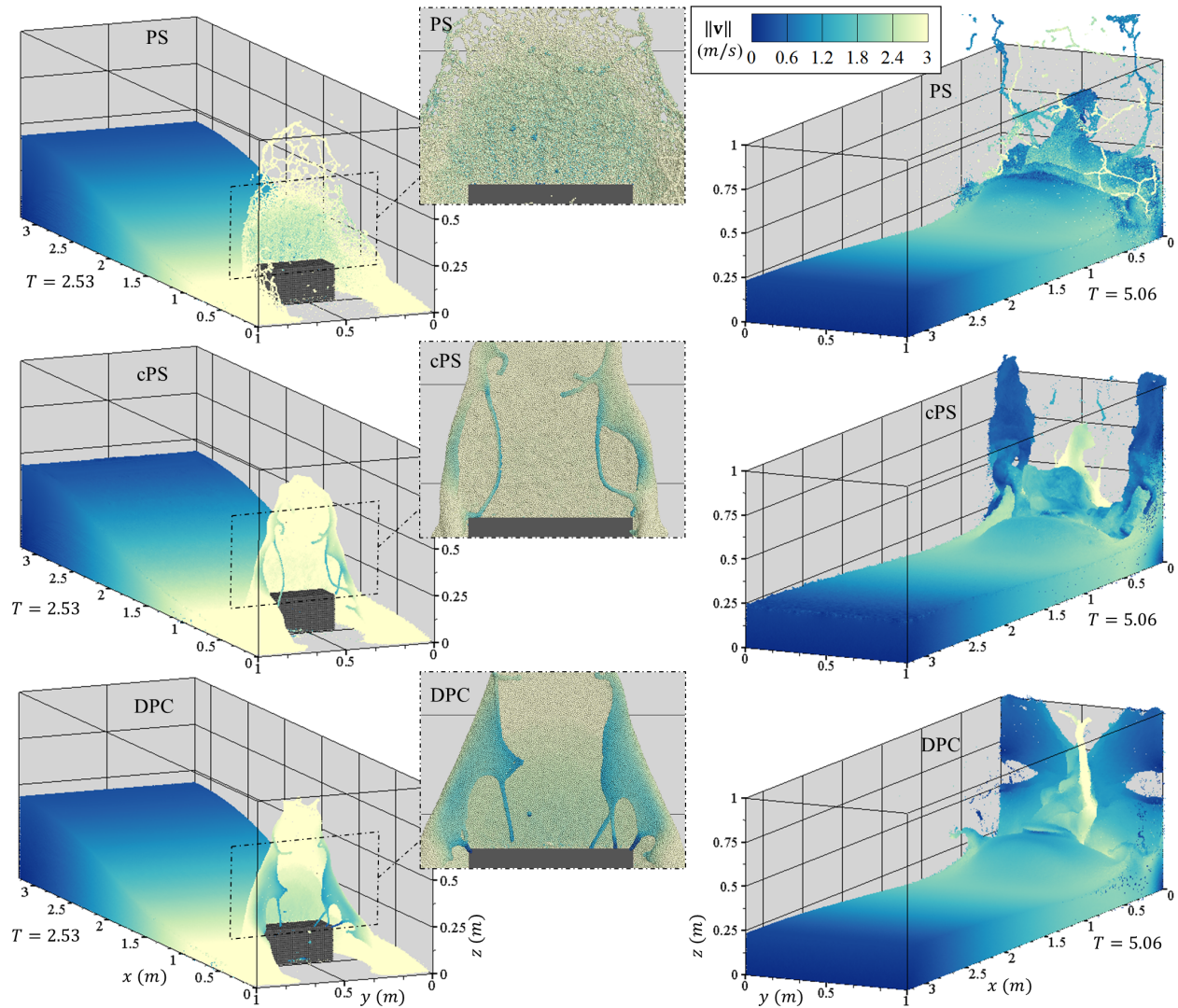


Figure 6.21 3D dam break: the flow evolution and the magnitude of velocity by PS, cPS, and DPC (the top, middle and bottom rows, respectively) at $T = 2.53$ and 5.06 , with $R = 110$.

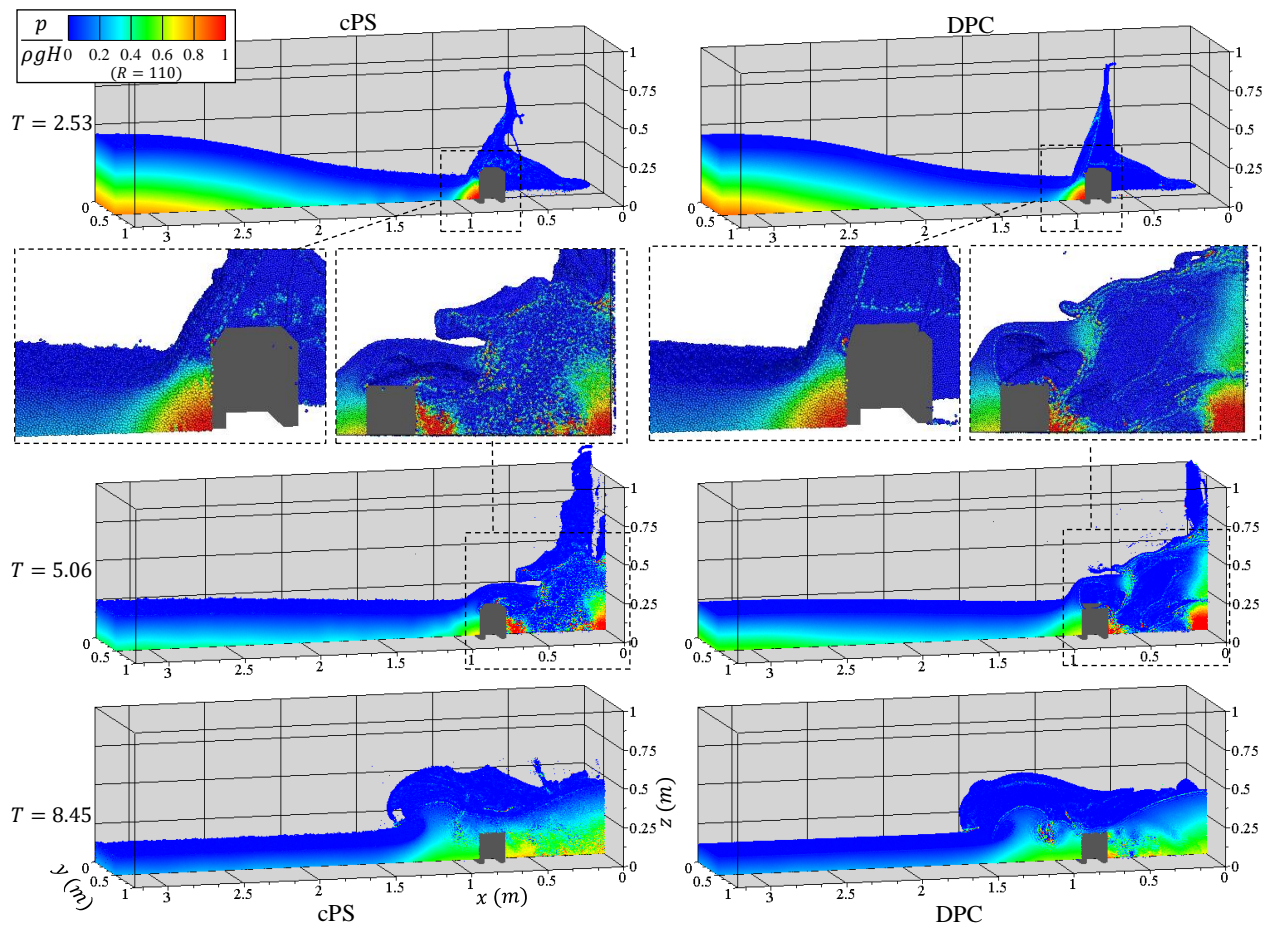


Figure 6.22 3D dam break: non-dimensional pressure field at the middle-section of the reservoir, $y = 0.5$ (m), by cPS and DPC (the left and right columns, respectively) at $T = 2.53$, 5.06, and 8.45, with $R = 110$.

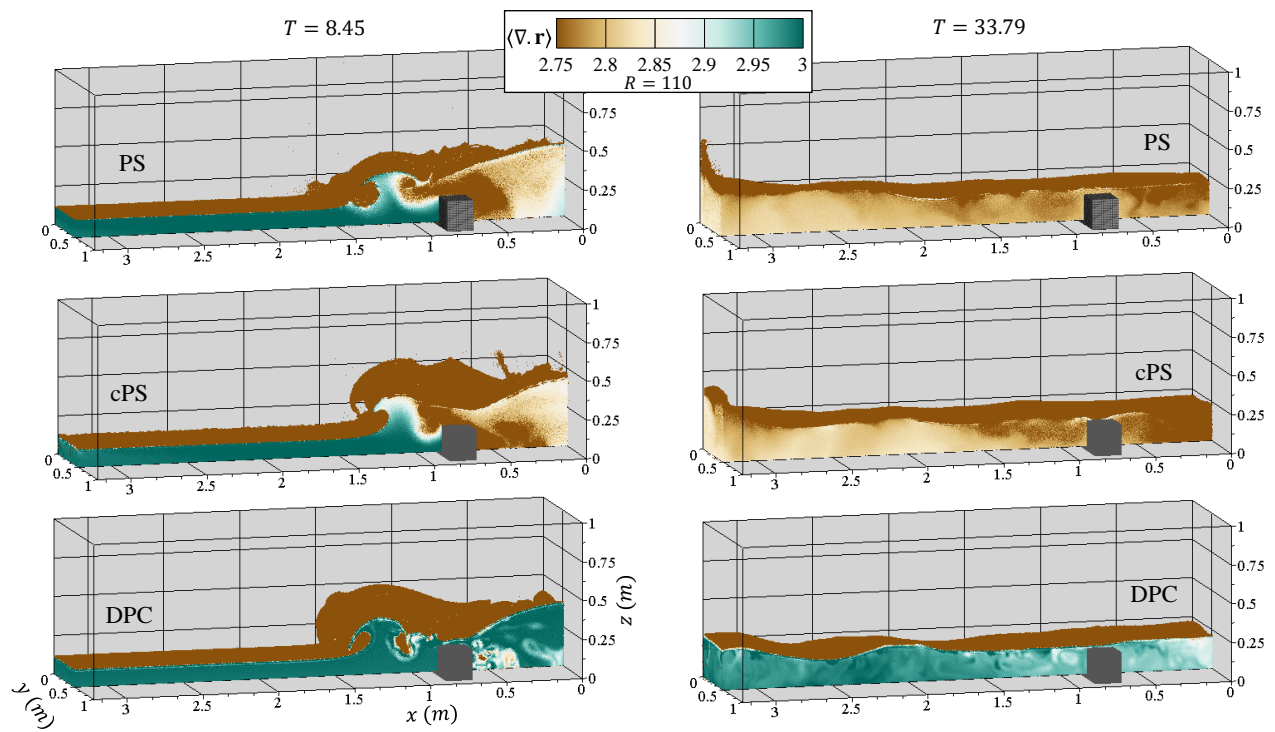


Figure 6.23 3D dam break: $\langle \nabla \cdot \mathbf{r} \rangle_i$ at the middle-section of the reservoir, $y = 0.5$ (m), by PS, cPS, and DPC (the top, middle, and bottom rows, respectively) at $T = 8.45$ and 33.79 , with $R = 110$.

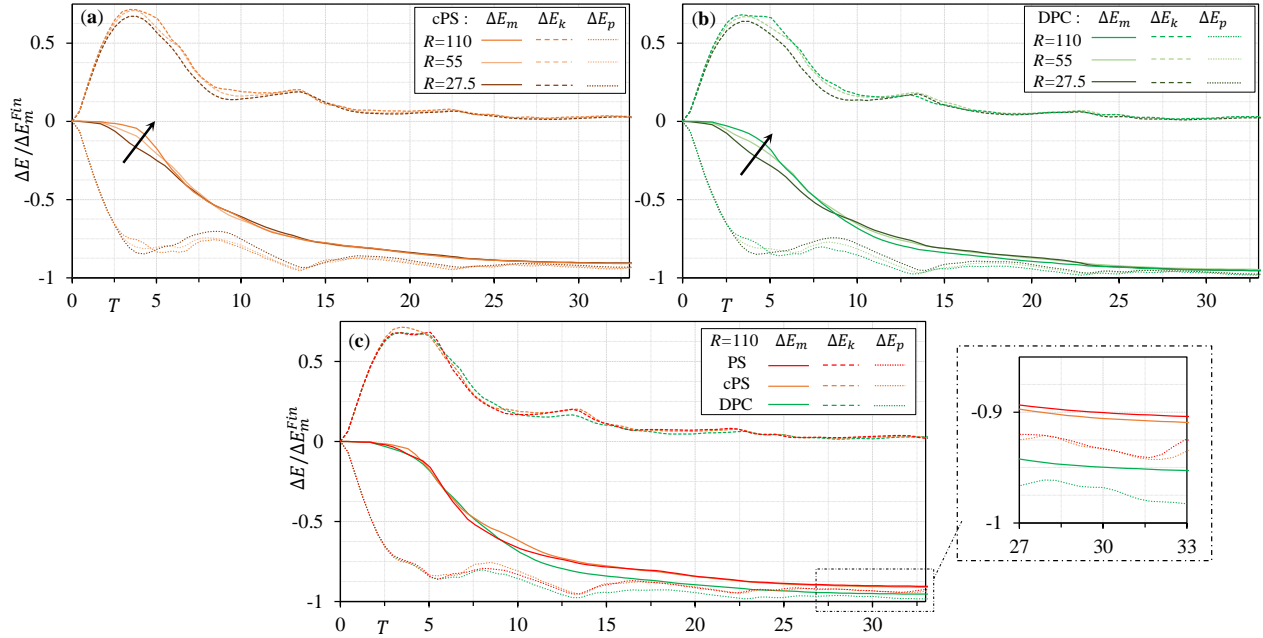


Figure 6.24 3D dam break: evolution of the energy components by cPS and DPC with different spatial resolutions ((a) and (b) graphs, respectively). Graph (c) compares the energy evolution by PS, cPS, and DPC where $R = 110$.

flows. We represented the dynamic pair-wise particle collision technique (DPC) (originally proposed by [124] for the MPS method) and a particle shifting equation coupled with the DPC method (cPS). We implemented these regularization techniques in the DualSPHysics software and simulated four benchmark cases. We validated the numerical simulations with the theoretical solution and the available experimental measurements analyzing the accuracy and convergence of the numerical model. Overall, the qualitative and quantitative results confirmed that the shifting equation (in both the PS and cPS forms) affects the conservation of volume in the long-term simulation of the violent free-surface flows. On the other hand, DPC not only represents more regular particle distribution ensuring numerical stability, but also accurately predicts global evolutions of the system conserving the linear momentum.

We summarize the key remarks of this study as follows:

- SPH with DPC predicts stable and accurate flow evolution for long-term simulations of free-surface flows.
- DPC improves the particle clustering at the free-surface regions and where impact events occur.

- DPC respects the linear momentum conservation of the system, while PS affects the global potential energy and unphysically expands the fluid volume.
- Numerical results of SPH with DPC converge to the theoretical and expected solutions, however, with PS the convergence behavior of the model would be affected.
- The numerical stability achieved by DPC allows the SPH model to adopt larger time steps compared to the PS formulation implemented in DualSPHysics (reducing the simulation runtime by 6-8.5 %).

We should highlight that the more recent improvements to PS formulation (e.g., the works of Jandaghian et al. [124] in MPS and Sun et al. [3] and Hong-Guan and Sun [182] in SPH) resolve its numerical issues manifested as the unphysical volume expansion and the particle clustering at the free surface regions. However, the proposed DPC (as a more effective and efficient alternative technique to the standard PS and the cPS method studied in the present work) is exempted from complex boundary treatments, additional diffusive terms, and their associated computational costs.

Future research works may include validating and improving the DPC technique for dealing with the tensile instability issues (i.e., strong negative pressures) in viscous flows with high Reynolds number (like viscous flow past a bluff body). Moreover, it is worthwhile to extend the DPC formulation for simulating high-density ratio multiphase flows.

Appendix A. Implementation of DPC in DualSPHysics

We implement the DPC formulations within the GPU-accelerated subroutines of the DualSPHysics software (v5.0.4). In the initialization stage of the model, the preset parameters of DPC are loaded into the program. In the main temporal loop of calculation, we define a device function, denoted as `DynamicParticleCollision()`, that implements the DPC term (6.12) using the Compute Unified Device Architecture (CUDA) C++ parallel programming language (Figure 6.25). This function is nested inside the existing device function that contains the *for loop* responsible for calculating the interaction forces by calling the neighboring particles and loading their variables. The output of the DPC function is $\Delta t \delta \mathbf{v}_i^{DPC}$ which updates the velocity and position vectors of the fluid particles in the second stage (i.e., the correction step) of the symplectic algorithm. We changed the present global and device subroutines considering that the developed model can still execute the existing PS method; the user can choose to substitute the PS execution with the DPC technique. One should note that since DPC does not require free-surface detection and is implemented in the current

framework of the GPU-accelerated code (without additional *for loop* for the calculations), we expect the efficiency of the application to remain intact.

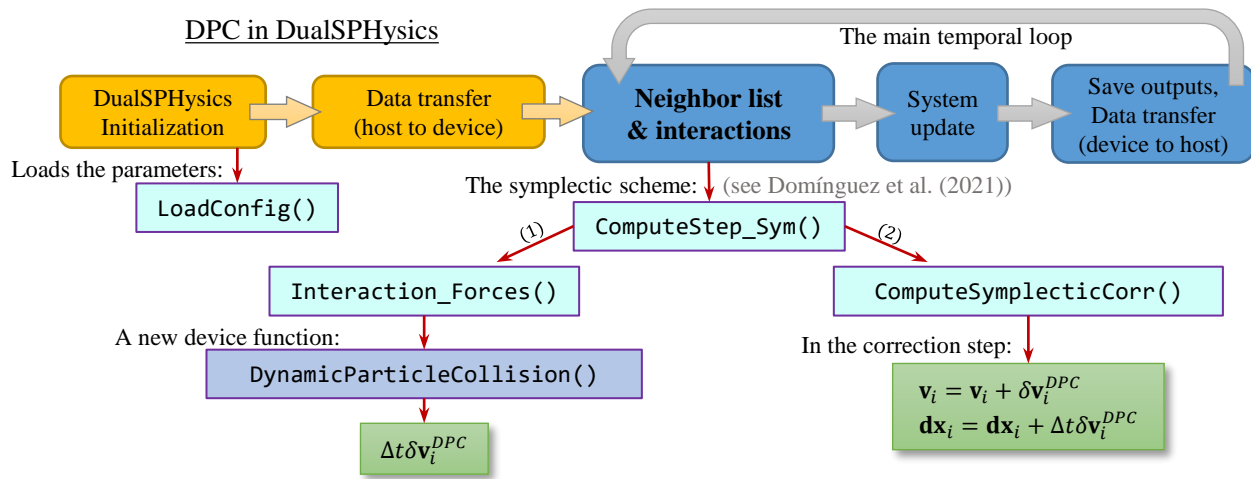


Figure 6.25 Implementation of the DPC formulation within the GPU-accelerated framework of DualSPHysics. The DPC transport-velocity equation, $\delta\mathbf{v}_i^{DPC}$, is given by (6.12).

CHAPTER 7 ARTICLE 4: ENHANCED WEAKLY-COMPRESSIBLE MPS METHOD FOR IMMERSED GRANULAR FLOWS

Mojtaba Jandaghian¹, Abdelkader Krimi¹, and Ahmad Shakibaeinia¹

¹Department of Civil, Geological and Mining Engineering, Polytechnique Montréal, Canada

Advances in Water Resources

7.1 Abstract

We develop and validate a three-dimensional particle method based on an Enhanced Weakly-Compressible MPS approach for modeling immersed dense granular flows. For this purpose, we adopt a unified and generalized rheological model, using a regularized visco-inertial rheology, for all regimes of multiphase granular flow. Moreover, we propose a new consistent formulation to estimate the effective pressure of the solid skeleton based on the continuity equation of the pore-water. To improve the accuracy of the multiphase particle methods, especially near boundaries and interfaces, we introduce a modified high-order diffusive term by employing the convergent form of the Laplacian operator. The effectiveness of the new diffusive term is particularly demonstrated by modeling the hydrostatic pressure of two fluid phases. Further, coupling the generalized rheology model with the flow equations, we investigate the gravity-driven granular flows in the immersed granular collapse and slide in three dimensions. As a part of this study, we represent the experiment on the immersed granular collapse to validate the model. The evolution and runout length of the granular bulk are compared with those from experiments confirming good compatibility. Overall, the qualitative and quantitative results justify the proposed developments shown to be essential for predicting different states of the immersed granular flows. (Figure 7.1)

7.2 Introduction

Multiphase flow of solid grains interacting with fluid exists in many hydro-environmental systems such as sediment erosions, debris flows, and submarine avalanches [17, 198]. These so-called multiphase granular flows can have devastating socio-economic impacts [199, 200]. The experimental measurements and numerical models are the engineers' tools to understand the complex physics of these problems to optimize the engineering designs and mitigate related hazards. The numerical models have advantages in eliminating the expenses and surmounting the limits of the experimental researches. However, dealing with the highly

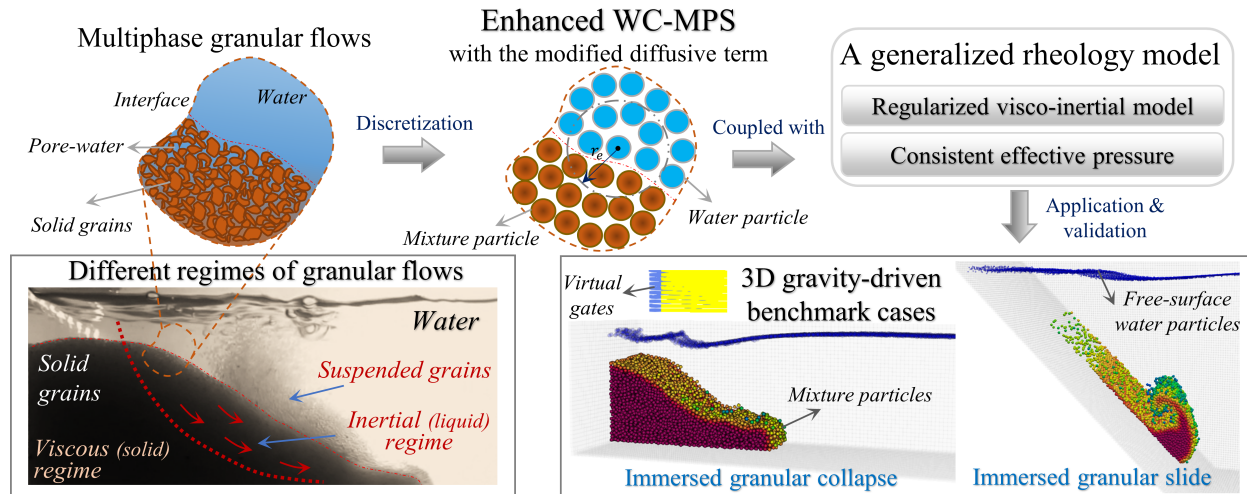


Figure 7.1 The graphical abstract

dynamic interfacial flows including mixing processes of the solid grains and fluid phase requires advanced rheology models and numerical developments [17,20]. The conventional mesh-based Eulerian approaches struggle to simulate the complicated deformations and fragmentations of interfacial flows [22,33]. Meanwhile, mesh-free Lagrangian methods have been shown to be effective for simulating such problems including complex interactions of fluids and sediments (e.g., [201–205]). Discrete-based mesh-free models (e.g., the Discrete Element Method) are known to be accurate models for in-depth analysis while are computationally expensive [20]. In contrast, the continuum-based mesh-free particle methods at the macroscopic level (or simply particle methods, such as Moving Particle Semi-implicit (MPS) and Smoothed Particle Hydrodynamic (SPH) methods) homogenize the bulk volume of the mixture into moving particles being scalable and hence more computationally affordable. In these models, the Lagrangian form of governing equations coupled with the constitutive laws calculates the interaction forces as the moving particles are the material points simulating the advection process.

Particle methods, due to their Lagrangian nature, have demonstrated promising capabilities in solving scientific and engineering problems [59]. SPH and MPS, as the two most popular particle methods (initially proposed by Gingold and Monaghan [26] and Koshizuka et al. [25,46], respectively) have been widely applied and developed for simulating complex fluid flow targeting hydro-environmental problems (e.g., [88, 178, 202, 204, 206, 207]). These methods share many algorithms and techniques and produce similar results in many cases [43,178]. However, MPS as a kernel-derivative-free method has more flexibility in the choice of the ker-

nel function and resolves the instability issues that arise from the derivative of the kernel function in the inter-particle force terms of the original SPH formulations [44, 45]. Furthermore, MPS uses the non-dimensional particle number density (as a substitute for the real density), which naturally addresses the density discontinuities at the phase interfaces of multiphase simulations [41].

Shakibaeinia and Jin [47] proposed the Weakly Compressible version of the MPS method (denoted as WC-MPS) by solving the equation of state instead of the Poisson equation for updating the pressure field. Shakibaeinia and Jin [29, 75, 108] have extended and validated the WC-MPS method for incompressible and multiphase problems in various hydrodynamic conditions. Furthermore, this method has been the focus of many research studies for simulating complex flows (e.g., [146, 208–210]) and specifically developed for the dry and saturated granular flows (e.g., [112, 118, 119, 211, 212]). Jandaghian and Shakibaeinia [123] enhanced the WC-MPS method by introducing a conservative system of equations supplied with the diffusive term and the corrected particle shifting technique. Recently, Jandaghian et al. [124] developed the particle regularization techniques of this so-called Enhanced WC-MPS (EWC-MPS) model for capturing the non-linear behavior of violent free-surface problems. In this study, the EWC-MPS method is coupled with the rheological models and further improved and validated for simulating the multiphase granular flows.

Many empirical and numerical studies have been devoted to introducing general and reliable constitutive equations for capturing the different regimes of the granular flows (i.e., the free-fall, inertial, and viscous regimes) [17, 99] (e.g., [20, 100, 213]). Particularly, for the immersed and dense granular flows, representing a versatile model for understanding the underlying physics of the mixture is more challenging since both inertial and viscous regimes may control the mechanical behavior of the flow [100]. Furthermore, in these rheology models, an accurate estimation of the normal-stress (i.e., the effective pressure) within the solid-skeleton is essential for detecting the yielded and non-yielded flow regions. With this regard, the commonly used hydrostatic assumption (for calculating the pore-water pressure) includes the complexity and limitations of detecting interfaces and ignores the hydrodynamic aspects of the granular flows in the rheology equation. Moreover, the unphysical pressure noises (as the common problem of particle methods [66]) arising from the numerical and approximation errors can significantly affect the accuracy of the results. Resolving these modeling issues requires developing a unified framework for the immersed granular flow rheology model (e.g., [20, 100, 101]) and implementing higher-order operators (e.g., [66, 146]), the particle regularization techniques (e.g., [64, 130]), and the artificial diffusive terms (e.g., [66, 153]) for ensuring the stability and accuracy of the numerical simulations.

The rheology models in the continuum-based methods consider non-Newtonian behaviors for the dense granular flows [17]. Bingham types viscoplastic models (the Bingham-plastic and the Herschel-Bulkley models) have been frequently utilized and validated in particle methods (e.g., [29,109,115,116,134]). More recently, the local $\mu(I)$ rheology (proposed by Job et al. [99] and Forterre and Pouliquen [102]) as a function of the flow and material properties has drawn attention for the dry and submerged problems (e.g., [104,112,119]). For immersed conditions of the dense granular flows, different non-Newtonian models are developed according to the experimental and numerical results (e.g., see [17,92,93,100,101]). Guazzelli and Pouliquen [17] presented a comprehensive review of the rheology of concentrated granular suspensions. Regarding the immersed granular flow in the low Stokes limit, Boyer et al. [101] conducted a series of (pressure-imposed shearing) experiments to represent unified rheology. Amarsid et al. [100] with some dimensional analysis and simulating the inertial and viscous regimes of the mixture (by a coupled molecular dynamics-lattice Boltzmann method) introduced a unified rheology model for capturing the dry and immersed granular flows. Baumgarten and Kamrin [20] combined the former models in a single formulation to simulate the granular flows using a two-phase model. In the context of particle methods, Rodriguez-Paz and Bonet [107] employed the Generalized Visco-plastic Fluid (GVF) model proposed by Chen et al. [117] as a semiempirical model to calculate the total shear stress of the debris flow with a corrected SPH method. Hosseini et al. [214] modeled single-phase non-Newtonian fluid flows using the power-law, Bingham-Plastic, and Herschel-Bulkley constitutive models with an explicit SPH approach. Nabian and Farhadi [105] utilized the Bingham and the GVF rheological models to simulate the granular multiphase flows in an incompressible MPS scheme. To eliminate the numerical problem of pressure-dependent erosion at the interface, Khanpour et al. [106] and Zubeldia et al. [115] employed the Shields criterion in the weakly compressible SPH framework to determine the sediment erosion threshold, while the constitutive model determines the effective viscosity of the sublayer sediment phase based on Bingham viscoplastic models. In the WC-MPS framework, Shakibaeinia and Jin [108] simulated the two-phase mobile-bed dam break including the non-linear behavior of the granular material by the GVF model. Nodoushan and Shakibaeinia [118] employed the regularized form of the local $\mu(I)$ rheology to model the submerged and dry granular collapses. Further, Tajnesaie and Shakibaeinia [112] developed the same model to simulate the granular landslide in a two-dimensional configuration and compared the results with the Heschel-Bulkley model. Recently, Ke et al. [119] investigated the role of the $\mu(I)$ rheology for the dry granular slide and dam-break via the standard WC-MPS method.

The sediment rheology model is pressure-dependent and requires determining the granular effective pressure within the mixture phase for calculating the effective viscosity. The two-phase

mixture models (which solve separate sets of equations for each granular and fluid phase) calculate the effective pressure within the solid phase directly (e.g., [20, 215, 216]). However, the single-phase multi-density/multi-viscosity models require a supplementary approach to estimate the pore-water pressure of the mixture phase. In particle methods, different approaches are proposed for determining the effective pressure within the granular material. The majority of the SPH and MPS models (e.g., [105, 113, 116, 120]) assume the lithostatic condition for the fluid and/or sediment phases to predict the pore-water pressure neglecting the hydrodynamics of the mixture flow. Ghaitanellis et al. [114] appended an additional equation to the sediment model to calculate the soil-skeleton stress independently via solving the Laplacian of the effective pressure accompanied by the boundary conditions of the model. In general, these approaches involve the free-surface and interface detections limiting the capability of the particle method for dealing with highly deformed multiphase flows. To avoid this issue, Fourtakas and Rogers [109] and Zubeldia et al. [115] employed a modified equation of state (EOS) of the WC-SPH model by using the density of the saturated sediment to estimate the pore-water pressure. However, since their model considers different reference pressure within the EOS (for the total and pore-water pressure), the pressure oscillations due to the slight compressibility affect the sediment model overestimating the viscosity for the submerged conditions [114].

Since in the MPS/SPH methods, the kernel truncates at the free surface of the fluid and in the vicinity of the solid boundary, the standard diffusive term added to the continuity equation diverges the density field. This leads to unphysical pressure prediction affecting the overall mechanical behavior of the fluid flow (particularly in the long-term simulations). In the case of granular flows, where the constitutive equation and yield/flow behavior are highly sensitive to the pressure field and its vibrations, such unphysical divergence can largely affect the results. In general, by adding a numerical diffusion term to the continuity equation (e.g., in the δ -SPH [54, 66] and the EWC-MPS methods [123]) the high-frequency pressure fluctuations have been eliminated; however, dealing with the density discontinuity at the interfaces of multiphase problems still requires special treatments. To overcome these numerical issues, Sun et al. [70] applied the diffusive term by the convergent form of the Laplacian operator (originally proposed by Antuono et al. [66] for the single fluid phase problems), for the multiphase problems restricting the diffusive term between the fluid particles within the same phase. In this case, the renormalization matrix and the first-order density gradient operators are also limited to the same phase particles. Similarly, Zheng and Chen [72] proposed the convergent formulation for the diffusive term in the multiphase SPH model employing the oscillation of density increment instead of the density variable. Krimi et al. [158] proposed another form of the diffusive term for the multiphase WC-SPH method for

dealing with the density discontinuity at the interface. However, the proposed term violates the mass conservation and ignores the higher-order spatial terms required for reducing the kernel truncation errors at the free-surface and in the vicinity of the solid boundary. Fourtakas et al. [69] introduced a new form of the diffusive term (for the single fluid phase problems) by substituting the dynamic density with the total density in the original formulation of Molteni and Colagrossi [54]. They showed that the new diffusive term by removing the hydrostatic density from the total density improves the pressure estimation close to the boundaries (only for problems where the gravitational force is dominant [69]). Nevertheless, it should be noted that the proposed diffusive term (unlike the diffusive term proposed by Antuono et al. [66] with the higher-order gradient) violates the conservation of mass considering that it is not an antisymmetric equation (see [65]).

In this paper, we aim to develop a robust and accurate EWC-MPS method for predicting the evolution of the immersed granular flows concerning its different regimes. This model benefits from the enhancement techniques required for the stability and accuracy of such fluid flow. Besides, the particle number density updated via the continuity and diffusive equations deals with the density discontinuity issues which affect the pressure field. Here, we extend the developments to three-dimensional and multiphase problems. Developing a generalized rheology model, we adopt and regularize the visco-inertial rheology model to capture the inertial and viscous regimes through a single formulation. Moreover, based on the continuity equation of the pore-water phase as a barotropic fluid, we propose a consistent formulation to eliminate the complexity for detecting the interface, meanwhile, include the dynamics of the fluid flow within the effective pressure estimation. In the proposed model, we implement the Sub-Particle Scale (SPS) turbulent model for the fluid phase and the higher-order velocity gradient operator. To improve the accuracy of the numerical model, we modify the diffusive term in the context of MPS for dealing with multiphase problems including the pressure-dependent shear models. The new diffusive term aims to alleviate the kernel truncation and density discontinuity issues of the multiphase problems and remove the unphysical pressure noises. To include the physical effects of the removable gate in the initial stage of the fluid flow, we implement virtual gates imposing the shear and pressure interactions. First, a simple hydrostatic pressure is modeled to show the effectiveness of the modified diffusive term. Further, we simulate and validate challenging benchmark cases of the granular flows: the immersed granular collapse and landslide. The mixture behavior in the former is identified by the viscous and inertial regimes whilst in the latter, the inertial regime is dominant due to the extreme flow deformation. To validate the immersed granular collapse, we conduct a complementary experiment representing the evolution and runout length of the deposit. The submerged and deformable landslide is validated by the available experimental results.

We investigate and fully characterize the flow regimes of these problems and evaluate the effectiveness of the proposed developments for capturing the complex mechanical behavior of such multiphase flows.

7.3 Governing Equations and Constitutive laws

7.3.1 Basic assumptions

The immersed granular flows consist of a mixture of solid grains and viscous fluid (i.e., water). In this study, the mixture of solid grains and interstitial/pore-water is considered as a single continuum. Further, the constitutive laws represent the ambient water (Ω_w) as a Newtonian and the mixture (Ω_m) as non-Newtonian fluid phases (see Figure 7.2). The mathematical models correspond to the mechanical behavior of the fluid phases and their interactions. Based on the following assumptions we derive the generic mathematical and numerical frameworks of the fluid domain:

1. The mixture of solid grains and water is a non-colloidal and non-Brownian suspension,
2. The water and mixture phases are barotropic fluids,
3. No mass exchange and heat transfer occur between the fluid phases,
4. Terzaghi's stress principle specifies the effective pressure of the sediment skeleton

With the first assumption, we employ the local rheology model that characterizes the granular flow with the volume fraction of the solid grains and the bulk friction coefficient considering the gravitational and shear forces [20, 100]. The second assumption allows the mathematical model to update the pressure of the fluid phases as a function of the density variations [100]. Considering the third assumption and neglecting the compressibility of the pore-water and the solid skeleton of the grains signify that the volume fraction of the granular phase remains invariant. Further, the single-phase and continuum-based models ignore the relative velocity between the interstitial fluid and solid grain. The fourth assumption is used to estimate the normal stress between the solid grains required for the rheological properties of the mixture.

In this paper, the subscripts, w , g , m , f , and pw denote the flow and material properties of water, the solid grains, the mixture of solid grains and water, the overall fluid domain (as the union of the water and mixture phases, i.e., $\Omega_f = \Omega_w \cup \Omega_m$), and the pore-water, respectively (see Figure 7.2). Also, 0 as a superscript (or subscript) of the flow properties stands for the initial condition (or the reference) values.

7.3.2 Flow equations

The Navier-Stokes governing equations in the Lagrangian framework describe the continuum flows as [169]:

$$\begin{cases} \frac{D\rho}{Dt} = -\rho\nabla\cdot\mathbf{v} \\ \rho\frac{D\mathbf{v}}{Dt} = -\nabla p + \nabla\cdot\boldsymbol{\tau} + \rho\mathbf{F} \\ \frac{D\mathbf{r}}{Dt} = \mathbf{v} \end{cases} \quad (7.1)$$

in which the pressure, the shear, and the body forces per unit volume (∇p , $\nabla\cdot\boldsymbol{\tau}$, and $\rho\mathbf{F}$, respectively) determine the acceleration ($D\mathbf{v}/Dt$) of a fluid with a density of ρ . The velocity vector and its divergence (i.e., \mathbf{v} and $-\nabla\cdot\mathbf{v}$: the mass volume expansion rate) updates the position (\mathbf{r}) and the rate of change of the density ($D\rho/Dt$), respectively. In the weakly compressible fluid models, the equation of state as a function of the material density calculates the mechanical pressure (i.e., $p = f(\rho)$).

The rheology models account for the viscous forces within the multiphase fluid flows. The general form of the rheology models considers the shear stress as a linear or non-linear function of the strain rate tensor, \mathbf{E} , and its principal invariants (the first, second, and third principal invariants; $I_E = \nabla\cdot\mathbf{v} = 0$, $II_E = 1/2\mathbf{E} : \mathbf{E}$ and III_E , respectively) based on the Reiner-Rivlin equation for an incompressible mixture flow [117]. Assuming the shear stress independent of III_E and \mathbf{E}^2 terms, represents the shear stress tensor as follows [117]:

$$\boldsymbol{\tau}(\mathbf{E}) = 2\eta\mathbf{E} \quad (7.2)$$

where η is the *effective (or apparent) dynamic viscosity* of the fluid phase. This effective viscosity includes the shear behaviors of the fluid flow considering the rate of deformation and the material and hydrodynamic properties. For both Newtonian and non-Newtonian fluids, the incompressibility assumption (i.e., $\nabla\cdot\mathbf{v} = 0$) sets \mathbf{E} equal to the deviatoric part of the rate of deformation, \mathbf{E}' (where $\mathbf{E} = 0.5 [(\nabla\mathbf{v}) + (\nabla\mathbf{v})^T]$ and the superscript T stands for the transpose of the matrix).

In the momentum equation, the divergence of the shear stress includes the viscous forces through the system of equations (7.1). Considering the incompressibility condition and neglecting the gradient of dynamic viscosity over the domain (i.e., $\nabla\eta = 0$, even at the interfaces) simplifies the viscous force to [108, 112]:

$$\nabla \cdot \boldsymbol{\tau} = \eta \nabla^2 \mathbf{v}. \quad (7.3)$$

This force stands for the shear behaviors of both Newtonian and non-Newtonian fluids. For Newtonian and incompressible fluids, a linear relationship exists between its true viscosity and the strain rate tensor. In the case of the granular flows, the solid grains immersed in Newtonian fluids (like water with the true viscosity of μ_w) increases the viscosity of the fluid as $\mu_w(1 + 5/2\phi)$ by the volume fraction, ϕ [17, 20]. Moreover, the turbulence eddy viscosity, ν_t , (based on the Large Eddy Simulation model [148]) can be added to include the turbulence effects within the effective dynamic viscosity of the water as follows:

$$\eta_w = \mu_w \left(1 + \frac{5}{2}\phi\right) + \rho_w \nu_t. \quad (7.4)$$

We calculate the turbulence eddy viscosity with $\nu_t = (C_s \Delta l)^2 \sqrt{4II_E}$ in which Δl is the mixing length and the Smagorinsky coefficient, C_s , is set to 0.12. For non-Newtonian fluids, ideally, the rheology model should be capable of capturing the mechanical behaviors such as the shear-thinning, the shear-thickening, and the flow threshold. The experimental studies show that granular flows contain these non-linear behaviors [92]. Accordingly, the continuum-based models consider the granular flows as non-Newtonian and incompressible fluids where the rheology model includes their shear behaviors through the effective viscosity.

7.3.3 A regularized visco-inertial model

Here, we employ the rheology model proposed by Baumgarten and Kamrin [20] combining Boyer et al. [101] and Amarsid et al. [100] models to simulate the viscous and inertial regimes of the granular flows within a single formulation. As analyzed by Amarsid et al. [100], in this model the non-dimensional numbers controlling the flow behaviors are the inertial number, I , the viscous number, I_v , and the mixed number, I_m , defined as follows:

$$I_m = \sqrt{I^2 + 2I_v}, \quad I = |\dot{\gamma}| d_g \sqrt{\frac{\rho_g}{p_g}}, \quad I_v = \frac{\mu_w |\dot{\gamma}|}{p_g} \quad (7.5)$$

where d_g and ρ_g are the mean diameter and the true density of the solid grains, respectively. The normal stress between the solid grains, p_g , is the effective pressure of the solid skeleton, p_{eff} , in the immersed condition. The magnitude of the shear rate, $|\dot{\gamma}|$, is equal to $\sqrt{4II_E}$ for an incompressible fluid. The general form of the viscosity model, hereinafter denoted as the visco-inertial model, is given by [20]:

$$\mu(I_v, I_m, \phi) = \mu_1 + \frac{\Delta\mu}{(b/I_m) + 1} + \frac{5}{2} \left(\frac{\phi I_v}{a I_m} \right) \quad (7.6)$$

in which $\Delta\mu = \mu_2 - \mu_1$ and ϕ is the volume fraction of the solid grains. The material parameters (a and b) including the upper and lower limits of the friction coefficient (μ_2 and μ_1 , respectively) can be specified by fitting the numerical and experimental results in the steady-state shearing flows [20]. In the context of this model, the Stokes number defined as $St = I^2/I_v$ determines the regimes of the granular flows. If $St \rightarrow \infty$, the inertial number is dominant, i.e., $I_m \approx I$, and by setting $b = I_0$ and $\mu_f = 0$ Eq. (7.6) reproduces the $\mu(I)$ rheology implemented for the dry granular flows (I_0 being an empirical coefficient of the rheology). Baumgarten and Kamrin [20] showed that for $St \rightarrow 0$ (where $I_m \approx \sqrt{2I_v}$) Eq. (7.6) fits with the data collected from the viscosity models and experimental measurements represented by Chang and Powell [217], Stickel and Powell [92], and Boyer et al. [101] for the inertial and viscous regimes. These empirical models govern the dense granular flows suggesting $I \lesssim 0.2$, $I_v \lesssim 0.1$, $I_m \lesssim 0.6$ and $0 \leq St < \infty$ conditions [20].

Considering the visco-inertial model the effective viscosity for the incompressible mixture, η_m , forms to:

$$\eta_m = \frac{\mu(I_v, I_m, \phi) p_g}{|\dot{\gamma}|}. \quad (7.7)$$

To use Eq. (7.7) within the viscous force equation (7.3), the singularity issue (as $|\dot{\gamma}| \rightarrow 0$) should be resolved by employing the regularization techniques [104]. Here, we utilize a combination of the Bercovier and Engelman [218] regularization formulation and the simple regularization model represented by Frigaard and Nouar [219] within the term containing the yield stress, $|\tau_y| = \mu_1 p_g$, and the post-failure terms (i.e., the second and third terms on the right-hand side of Eq. (7.6)). Therefore, by substituting the dimensionless numbers (7.5) into $\mu(I_v, I_m, \phi)$, we obtain the effective viscosity formulation as follows:

$$\eta_m = \frac{|\tau_y|}{\sqrt{|\dot{\gamma}|^2 + \lambda_r^2}} + \frac{\Delta\mu p_g}{\left(b\sqrt{p_g}/\sqrt{d_g^2 \rho_g + 2\mu_w/(|\dot{\gamma}| + \lambda_r)} \right) + |\dot{\gamma}|} + \frac{5\phi}{2a} \left(\frac{\mu_w \sqrt{p_g}}{\sqrt{|\dot{\gamma}|^2 d_g^2 \rho_g + 2\mu_w |\dot{\gamma}| + \lambda_r^2}} \right) \quad (7.8)$$

in which the regularization parameter, λ_r , is a small value to avoid the singularity and the normal stress is assumed to remain positive over the mixture phase (i.e., $\lambda_r \ll 1$ and $p_g > 0$) (see Appendix A.). To specify the yield stress for the non-cohesive granular material

with the internal friction angle, θ , we employ the Drucker-Prager yield criteria as $|\tau_y| = \mu_1 p_g = 2\sqrt{3}\sin\theta p_g/(3 - \sin\theta)$. In Eq. (7.8) (unlike the Bingham types and the generalized viscoplastic models) the post-failure terms contain the material and flow properties within a single formulation for the dry and immersed conditions. Moreover, when $|\dot{\gamma}|$ is strictly zero the regularized effective viscosity is definite (unlike the Papanastasiou regularization technique [104]), and no further consideration is required.

7.3.4 Consistent effective pressure

For the immersed granular flows, the effective pressure of the sediment skeleton plays a key role in the constitutive model (Eq. (7.8)). To capture the mechanical behavior of the highly dynamic multiphase granular flows, the rheology model should predict a dynamic pore-water pressure. Applying the lithostatic condition not only requires detecting the interfaces beforehand but also ignores the dynamics of the mixture's motion for estimating the effective pressure. This has limited the capability of the well-developed particle methods (e.g., [111, 112, 114, 220]) for dealing with highly deformed interfaces in the immersed granular flows.

Here, we propose a consistent approach based on the mass conservation law of the pore-water (within the mixture phase) to calculate the effective pressure dynamically. For this purpose, we employ the main assumptions already considered in the single-phase continuum-based models for the fully submerged granular flows (the assumptions I-IV in Section 7.3.1).

The continuity equation governing the partial density of the pore-water, $\bar{\rho}_{pw} = (1 - \phi)\rho_w$, is given as:

$$\frac{1}{\bar{\rho}_{pw}} \frac{D^w \bar{\rho}_{pw}}{Dt} + \frac{1}{V_M} \frac{D^w V_M}{Dt} = 0 \quad (7.9)$$

where $D^w(./)Dt$ is the material time derivative on the water phase [221]. The second term of this equation stands for the rate of volume expansion and can be substituted by the divergence of the velocity field, $\nabla \cdot \mathbf{v}_{pw}$ (as V_M being the volume of the material particle). Eq. (7.9) specifies the evolution of the true water density of the mixture phase, ρ_w , (as a barotropic fluid) for calculating the pore-water pressure [20]. Since the single-phase models treat the mixture of grains and pore-water as a single continuum, the fluid flow within the solid skeleton is neglected. Accordingly, we can assume that the volume fraction remains invariant (i.e., $\phi = \text{constant}$) and the pore-water phase follows the same velocity and position as the mixture phase (i.e., $\mathbf{v}_{pw} = \mathbf{v}$ and $D^w(./)Dt = D(./)Dt$). Therefore, we summarize the general form of the constitutive relation for the pore-water pressure within the immersed granular phase as follows:

$$\begin{cases} \frac{1}{\rho_w} \frac{D\rho_w}{Dt} + \frac{1}{V_M} \frac{DV_M}{Dt} = 0 \\ p_{pw} = f(\rho_w). \end{cases} \quad (7.10)$$

By solving equation (7.10), we supply the continuum-based model with a direct method to update the pore-water pressure field within the mixture phase (without the need for detecting interfaces). With the initial hydrostatic condition for the density and pressure fields, the spatial divergence of the velocity field ($\nabla \cdot \mathbf{v}$) determines the evolution of ρ_w . Eventually, Terzaghi's effective stress and the equation of state for the mixture and pore-water phases determine the effective pressure, $p_{\text{eff}} = p - p_{pw}$. It should be highlighted that the rheology model only utilizes the effective pressure to calculate the effective viscosity and the mixture inertial numbers through Eq. (7.8). Meanwhile, the velocity field of the mixture phase (\mathbf{v}) along with the bulk properties of the fluid flow (p and ρ) are calculated via the system of equations represented as the multiphase model in Eq. (7.1).

7.4 Numerical Model

7.4.1 The discrete system

The continuum-based models homogenize the representative volume of the water and solid grains into continuous fluid phases. The approximation procedure of the particle methods discretizes the fluid domain into moving calculation points carrying the material and flow properties (Figure 7.2). The approximation operator, $\langle \rangle$, (for the quantities and derivatives of the flow variables) represents the discretize particle system [34, 35]. In the conservative WC-MPS method [123] the right-hand sides of the differential equations (7.1) are approximated for a generic particle i as follows:

$$\begin{cases} \frac{Dn_i}{Dt} = -n_i \langle \nabla \cdot \mathbf{v} \rangle_i \\ \rho_i \frac{D\mathbf{v}_i}{Dt} = -\langle \nabla p \rangle_i + \langle \eta \nabla^2 \mathbf{v} \rangle_i + \rho_i \mathbf{F}_i \\ \frac{D\mathbf{r}_i}{Dt} = \mathbf{v}_i \end{cases} \quad (7.11)$$

where the particle number density, n_i , is updated via the continuity equation, and η is the dynamic viscosity. The density of particles is constant in the momentum equation ($\rho_i = \rho_{0_i}$: the true density of fluid particles) while the pressure is updated by the equation of state given as:

$$p_i = B_0 \left(\left(\frac{n_i}{n_0} \right)^\gamma - 1 \right) \quad (7.12)$$

where $\gamma = 7$ [47]. For the multiphase fluid flows the fluid bulk modulus, B_0 , is set to be identical over the domain as $B_0 = c_0^2 \rho_0 / \gamma$ where c_0 and ρ_0 are the artificial sound speed and the true density of the reference fluid phase, respectively [36]. With $c_0 \geq 10 \|\mathbf{v}\|_{max}$ (where $\|\mathbf{v}\|_{max}$ is the maximum expected velocity of the problem), the Mach number remains less than 0.1 limiting the compressibility of the fluid to 1 %. It is worthy to mention that this MPS method for multiphase fluid flows resolves the discontinuity issue occurring at the interfaces via using the particle number density (as the substitute for the density variable like [41]) and the identical bulk modulus for all the fluid phases.

In the approximation procedure, the kernel function (W) smooths the differential operators of equations (7.11) over the particles (Figure 7.2). The normalization factor, n_0 , (as a constant value over the computational domain) is the kernel summation of the fluid particles over their neighbor particles (N) at the initial state of particles (l_0) and away from boundaries (i.e., $n_0 = \sum_{i \neq j}^N W(r_{ij}, r_e)$ at $t = 0$, as $r_{ij} = |\mathbf{r}_j - \mathbf{r}_i| \leq r_e$, and r_e being the influence radius of the kernel function set to $3.1l_0$). With considering the conjugate form of the gradient and divergence operators in the context of MPS formulations, we derive the approximation operators of the fluid flow variables as follows:

$$\begin{cases} \langle \nabla \cdot \mathbf{v} \rangle_i = \frac{d}{n_0} \sum_{i \neq j}^N \left(\frac{n_j}{n_i} \right) \frac{\mathbf{v}_{ij}}{r_{ij}} \cdot \mathbf{e}_{ij} W_{ij} \\ \langle \nabla p \rangle_i = \frac{d}{n_0} \sum_{i \neq j}^N \left(n_i \frac{p_j}{n_j} + n_j \frac{p_i}{n_i} \right) \frac{\mathbf{e}_{ij}}{r_{ij}} W_{ij} \\ \langle \eta \nabla^2 \mathbf{v} \rangle_i = \frac{2d}{n_0} \sum_{i \neq j}^N \eta_{ij} \frac{\mathbf{v}_{ij}}{r_{ij}^2} W_{ij} \end{cases} \quad (7.13)$$

in which $W_{ij} = W(r_{ij}, r_e)$ and d ($= 1, 2, 3$) is the number of space dimensions. The rational kernel function [46] is used in all the simulations. The pressure force vectors lie on the unit direction vectors between particle i and j ($\mathbf{e}_{ij} = \mathbf{r}_{ij}/r_{ij}$) conserving the linear and angular momentum of the system. While Laplacian of the velocity vector with the direction of $\mathbf{v}_{ij} = \mathbf{v}_j - \mathbf{v}_i$ only conserves the linear momentum. One should note that in the absence of shear stresses and external forces, the approximated form of the governing equations conserves the total energy of the system, E (i.e., $dE/dt = 0.0$). In our model, the harmonic mean determines the effective dynamic viscosity acting between particles i and j as $\eta_{ij} = 2\eta_i\eta_j/(\eta_i + \eta_j)$ [75].

To ensure the numerical stability and eliminate the particle clustering (i.e., the tensile instability), we implement the Corrected Particle Shifting algorithm (the CPS technique proposed in the EWC-MPS method [123]) regularizing their position vector by the corrected particle shifting vector, $\delta \mathbf{r}_i$, as $\mathbf{r}'_i = \mathbf{r}_i + \delta \mathbf{r}_i$. The proposed CPS is applicable to the three-dimensional problems without any adjustment regarding the implemented free-surface detection algorithm and the interface treatments. This approach utilizes the summation of the kernel function (i.e., the particle concentration defined as $\sum_{i \neq j}^N W_{ij}/n_0$) and hence, acts independently from the material properties of the fluid phases in the multiphase problems. In this study, the particle shifting coefficient is set to $0.04l_0^2$. Further, we limit the magnitude of the shifting vector as $\delta \mathbf{r}_i = \min \{0.25 \|\mathbf{v}_i\| \Delta t, 0.2l_0, \|\delta \mathbf{r}_i\|\} \delta \mathbf{r}_i / \|\delta \mathbf{r}_i\|$, to reduce the energy manipulation that may occur by the convection of material and flow properties of the fluid particles where the potential energy is dominant.

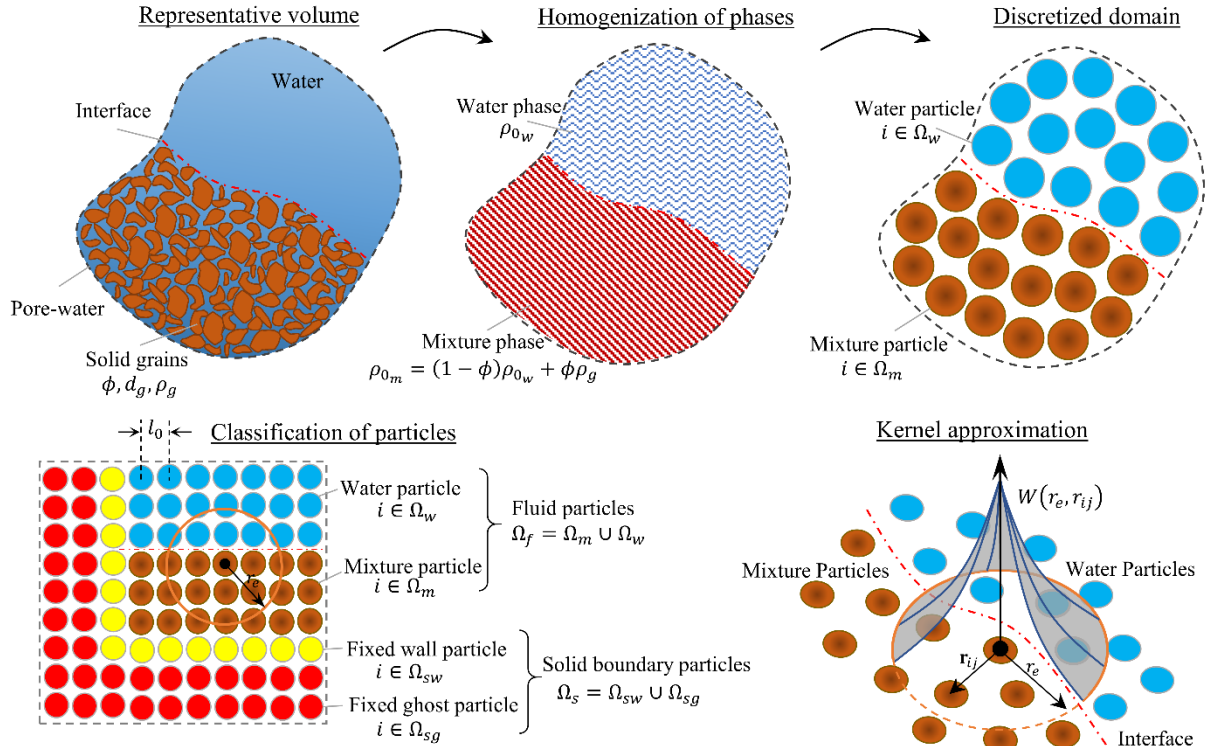


Figure 7.2 The homogenized water and mixture phases are treated as Newtonian and non-Newtonian fluids, respectively. The computational domain is discretized with moving particles representing the water (Ω_w), mixture (Ω_m), and solid boundary (Ω_s) particles.

7.4.2 Modified diffusive term

Jandaghian and Shakibaeinia [123] introduced the diffusive term in the WC-MPS method to eliminate high-frequency pressure fluctuations. By adding the diffusive term, D_i , to the right-hand side of the continuity equation, this numerical correction has proved to be effective and essential for obtaining a smooth pressure field in particle methods (e.g., [54, 123]).

Nevertheless, the standard form of the diffusive terms (proposed by Molteni and Colagrossi [54] for WC-SPH, and Jandaghian and Shakibaeinia [123] for WC-MPS) unphysically diverges the pressure field at the free-surface as the kernel function truncates [66]. The same issue exists in the vicinity of the solid boundary particles where the inner product of the normal vector to the solid wall and the gravitational force is non-zero (i.e., $\mathbf{n}_s \cdot \mathbf{g} \neq 0$). In this case, the density of the fluid particles close to the solid boundary particles decreases affecting the overall pressure field in the long-term simulations. This divergence occurs as the solid boundary particles are excluded from the diffusive term of the fluid particles required for conserving the total mass of the fluid phase. Particularly, for problems where the mechanical behavior of the fluid flow depends on the pressure parameter implementing a convergent diffusive term over the fluid domain becomes essential (e.g., for calculating the effective viscosity of the sediment phase in this study). Moreover, in the multiphase problems, the diffusive term (as a function of the density in the standard delta-SPH) requires special treatment at the interface of the fluid phases due to the discontinuity of the density field. By only applying the diffusive term among the same phase particles (e.g., in [70, 109]) the kernel function truncates at the interface diverging the density field. Although the higher-order gradient formulation reduces the associated errors, for highly deformable interfacial flows this is still incompetent.

Here, we represent a modified diffusive term in the context of the WC-MPS method to surmount the numerical issues arising from the kernel truncations at the boundaries. To do so, we employ the convergent form of Laplacian and Taylor's expansion series based on the work of Antuono et al. [66]. Further, utilizing the particle number density, n_i , gives an independent diffusive term with respect to the density discontinuities at the interfaces of multiphase problems. The general form of the modified diffusive term denoted by D_i^m , is given as:

$$D_i^m = \delta_{MPS} \frac{\Delta t c_0^2}{n_0} \langle \nabla^2 n \rangle_i \quad (7.14)$$

where the time step of calculation (Δt), the reference sound speed, and the normalization factor (c_0 and n_0 , respectively) and the non-dimensional coefficient ($0 < \delta_{MPS} \leq 1$) deter-

mine the intensity of the numerical correction [123]. To supply the model with the global-convergent equation for Laplacian of the particle number density, we consider:

$$\langle \nabla^2 n \rangle_i = \frac{2d}{n_0} \sum_{i \neq j}^N \psi_{ij} \frac{W_{ij}}{r_{ij}^2} \quad (7.15)$$

where based on Taylor's series, ψ_{ij} is given by:

$$\psi_{ij} = (n_j - n_i) - \frac{1}{2} [\langle \nabla n \rangle_i^C + \langle \nabla n \rangle_j^C \cdot \mathbf{r}_{ij}] \quad (7.16)$$

recovering the convergence all over the fluid domain [66]. The gradient of n_i in the MPS formulations is approximated via:

$$\langle \nabla n \rangle_i^C = \frac{d}{n_0} \sum_{i \neq j}^N \frac{n_j - n_i}{r_{ij}} (\mathbf{C}_i \mathbf{e}_{ij}) W_{ij} \quad (7.17)$$

in which the corrective matrix, \mathbf{C}_i , increases the operator's order of accuracy and is as follows [123]:

$$\mathbf{C}_i = \left(\frac{d}{n_0} \sum_{i \neq j}^n \frac{\mathbf{r}_{ij}}{r_{ij}} \otimes \mathbf{e}_{ij} W_{ij} \right)^{-1} \quad (7.18)$$

while i and $j \in \Omega_f$ and \otimes is the outer product of two vectors. Eventually, the modified diffusive term denoted as D_i^m , forms to:

$$D_i^m = \left(\delta_{MPS} \frac{\Delta t c_0^2}{n_0} \right) \frac{2d}{n_0} \sum_{i \neq j}^N \left[(n_j - n_i) - \frac{1}{2} [\langle \nabla n \rangle_i^C + \langle \nabla n \rangle_j^C \cdot \mathbf{r}_{ij}] \right] \frac{W_{ij}}{r_{ij}^2} \quad (7.19)$$

limited among the fluid particles (i.e., i and $j \in \Omega_f$). Therefore, by adding this term to the continuity equation proposed in the enhanced WC-MPS model, we obtain:

$$\frac{1}{n_i} \frac{Dn_i}{Dt} = - \langle \nabla \cdot \mathbf{v} \rangle_i + D_i^m \quad (7.20)$$

for updating the particle number density field in the multiphase problems. The modified diffusive term acts independently from the density discontinuity at the fluid interfaces and benefits from the continuous particle number density field. This is possible as the identical bulk modulus ($B_0 = \rho_0 c_0^2 / \gamma$) and the normalization factor are used to define the particle number density and calculate the pressure fields in all the fluid phases. Further, this diffusive

model conserves the total mass of the system (i.e., $\sum_i n_i D_i^m V_i = 0$ as V_i is the volume of the particle) in multiphase test cases. The implementation and effectiveness of the modified diffusive term are specifically discussed in section 7.5.1. Recently, Jandaghian et al. [124] adapted this diffusive term (Eq. (7.19)) for simulating and validating violent free-surface flows.

7.4.3 A generalized rheology model for immersed granular flows

The numerical model calculates the effective viscosity of each fluid particle concerning its material properties and flow variables. Here, we propose a generalized rheology model to couple with the EWC-MPS method by implementing the regularized visco-inertial rheology model along with the consistent effective pressure. The regularized visco-inertial model (Eq. (7.8)) determines the effective viscosity of the fluid particles containing the granular material, $i \in \Omega_m$, through:

$$\eta_i = \frac{|\tau_y|_i}{\sqrt{|\dot{\gamma}|_i^2 + \lambda_r^2}} + \frac{\Delta\mu p_{g_i}}{\left(b\sqrt{p_{g_i}}/\sqrt{d_g^2\rho_g + 2\mu_w/(|\dot{\gamma}|_i + \lambda_r)}\right) + |\dot{\gamma}|_i} + \frac{5\langle\phi\rangle_i}{2a} \left(\frac{\mu_w\sqrt{p_{g_i}}}{\sqrt{|\dot{\gamma}|_i^2 d_g^2\rho_g + 2\mu_w|\dot{\gamma}|_i + \lambda_r^2}} \right) \quad (7.21)$$

in which the normal stress between the solid grains, p_{g_i} , (wherein the immersed condition $p_{g_i} = p_{\text{eff}_i}$) gives the yield stress as $|\tau_y|_i = \mu_1 p_{g_i}$ and $|\dot{\gamma}|_i = \sqrt{4II_{Ei}}$. In this study we choose $\lambda_r = 0.001$ to avoid the singularity issue. The constitutive model for Newtonian fluid (Eq. (7.4)) updates the effective viscosity of the water particles, $i \in \Omega_w$, (as a function of the shear rate magnitude, $|\dot{\gamma}|_i$, and the smoothed volume fraction, $\langle\phi\rangle_i$) by:

$$\eta_i = \mu_w \left(1 + \frac{5}{2} \langle\phi\rangle_i\right) + \rho_{0_w} (C_s r_e)^2 |\dot{\gamma}|_i \quad (7.22)$$

where $\mu_w = 0.001 \text{ Pa}\cdot\text{s}$, $\rho_{0_w} = 1000 \text{ kg}/\text{m}^3$ for water and the smoothing length, r_e , is considered as the mixing length for the turbulence Sub-Particle Scale model with $C_s = 0.12$ (See [148, 180]). Here, we have ignored the implementation of Favre-averaging for the turbulence viscosity calculations (see [191]) by neglecting the weak compressibility of the fluid model. The numerical model estimates the volume fraction over the fluid particles as follows:

$$\langle\phi\rangle_i = \frac{\sum_{i \neq j}^N \phi_j W_{ij}}{\sum_{i \neq j}^N W_{ij}} \quad (7.23)$$

considering that for $\forall i \in \Omega_w$, $\phi_i = 0$ and for $\forall i \in \Omega_m$, $\phi_i = \phi$, ϕ being the volume fraction of the solid grains. It should be noted that the local volume fraction of the fluid particles, ϕ_i , remains invariant during the simulation, although its approximated value varies in the immersed problems as the interface deforms. Overall, the terms containing $\langle \phi \rangle_i$ in the rheology model aim to include the effects of the suspended granular materials through the effective viscosities at the interface (where $\langle \phi \rangle_i$ for $i \in \Omega_m$ decreases, while for $i \in \Omega_w$ increases) [20]. Moreover, we set $|\tau_y|_{i \in \Omega_m} = 0$ if $\langle \phi \rangle_i$ becomes less than 0.25ϕ .

We employ the corrective matrix, \mathbf{C}_i , (Eq. (7.18)) to increase the order of accuracy for estimating the velocity gradient, through:

$$\langle \nabla \mathbf{v} \rangle_i^C = \frac{d}{n_0} \sum_{i \neq j}^N \frac{\mathbf{v}_{ij}}{r_{ij}} (\mathbf{C}_i \mathbf{e}_{ij}) W_{ij} \quad (7.24)$$

used to calculate the second invariant of the strain rate tensor, $II_{E_i} = 0.5 \mathbf{E}_i : \mathbf{E}_i$, (where $\mathbf{E}_i = 0.5(\langle \nabla \mathbf{v} \rangle_i^C + \langle \nabla \mathbf{v} \rangle_i^{CT})$).

To implement the consistent effective pressure (proposed in section 7.3.4), we consider the rate of volume expansion of the particles (i.e., $V^{-1}_i DV_i/Dt$) by the velocity divergence and the diffusive term as $\langle \nabla \cdot \mathbf{v} \rangle_i - D^m_i$ to update the true density of the pore-water. Hence, we discretize the system of equations (7.10) in the Lagrangian framework for the mixture particles as follows:

$$\begin{cases} \frac{1}{\rho_{wi}} \frac{D\rho_{wi}}{Dt} = -\langle \nabla \cdot \mathbf{v} \rangle_i + D^m_i, & i \in \Omega_m \\ p_{pw_i} = B_0 \left(\left(\frac{\rho_{wi}}{\rho_{0w}} \right)^\gamma - 1 \right) \end{cases} \quad (7.25)$$

assuming invariant pore-water porosity for the particles. Note that the right-hand-side of the continuity equation of (7.25) is already estimated for updating the particle number density field through Eq. (7.20). With Terzaghi's effective stress, $p_{\text{eff}_i} = p_i - p_{pw_i}$, and the equation of state (7.12) (for p_i and p_{pw_i} as the functions of $n_i = n_0 \rho_i / \rho_{0m}$ and the identical B_0 where the true density of the mixture phase, $\rho_{0m} = (1 - \phi) \rho_{0w} + \phi \rho_g$), the general form of the effective pressure reduces to:

$$p_{\text{eff}_i} = B_0 \left[\left(\frac{n_i}{n_0} \right)^\gamma - \left(\frac{\rho_{wi}}{\rho_{0w}} \right)^\gamma \right], \quad i \in \Omega_m. \quad (7.26)$$

The proposed model not only calculates the effective pressure dynamically but also removes the need for tracking the interfaces without additional calculation costs. It is worthy to

note that since the presented model updates p_i and p_{pwi} with an identical bulk modulus, the pressure oscillations due to the slight compressibility of the numerical model are filtered out from the effective pressure calculation. Otherwise, using different reference pressures in the equation of state (or the hydrostatic assumption for the pore-water pressure) affects the stable viscosity field required for capturing the mechanical behavior of the submerged granular flows (since this introduces the low-frequency oscillations into the effective pressure field).

7.4.4 Virtual moving gates

In experimental setups of the immersed granular flows (including the gravity/flow driven problems), a physical gate contains the fluid phases at the initial stage. Different mechanisms have been implemented for removing the gate to release the mixture (or fluid) phase and form the granular flow (e.g., a sluice gate is lifted or withdrawn into a bottom cavity of the channel (see [91] and [222])). The gate as a moving object interacts with the fluid and granular phases through the pressure and friction forces. These interactions may have impacts on the initial stage of the flow as the gate is being removed (depending on the thickness and the roughness of the gate and the material properties of the fluid phases). Including the physical effects of the gate (associated with its high true velocity) within the numerical simulations has been a challenge in terms of stability and accuracy of the model. Therefore, the numerical models mostly ignore the presence of the gate and its influence on the initial condition of the fluid flows (e.g., [98, 114, 134]).

Here, we employ virtual moving gates to include the effects of the removable gate in the governing equations of the fluid particles while ignoring its physical thickness. Representing the thickness of the physical gate requires the use of extremely small particles affecting the computational efficiency. We explain the implementation of the virtual gate method through a simple example in which a gate separates the fluid phases as being lifted in the y -direction (Figure 7.3). We model the virtual gates by two sets of virtual particles with the particle distance of l_0 arranged in three layers (parallel to the centerline of the gate). The virtual particles at the left side interact with the fluid at the right side of the gate and vice versa. Each set of virtual particles (which are fixed with respect to each other) represents a virtual gate denoted as VG1 and VG2 delimiting the two regions of the channel (i.e., the left and right sides of the gate's centerline). These virtual gates are faced on the interface of the two regions identified as R1 and R2 (see Figure 7.3). The true velocity of the gate, v_g , updates the vertical position (y_g) of the virtual gates and R1 and R2 regions. It should be noted that the fluid particles within R1 (or R2) only interact with the virtual particles of VG1 (or VG2)

at the other side of the centerline while ignoring the fluid particles within R2 (or R1) and the virtual particles of VG2 (or VG1). Further, VG1 and VG2 neglect the presence of each other and the solid boundary particles.

Regarding the flow properties of the virtual particles, we update their pressure via the generalized wall boundary condition by Adami et al. [172] smoothing the fluid particles' pressure on the virtual particle as $p_i = \sum_{i \neq j}^N p_j W_{ij} / \sum_{i \neq j}^N W_{ij}$ where $i \in \text{VG1}$ (or VG2) and $j \in \text{R1}$ (or R2). The velocity and viscosity of the virtual particles included in the continuity and momentum equations of the fluid particles need to be adjusted based on the spatial resolution and the expected initial stage of the case study (e.g., see Table 7.4). However, they are moved with the true velocity of the gate, v_g . Hence, the pressure of the virtual particles repels the fluid particles from passing the centerline (to the other region) and their assigned velocity and viscosity simulate the friction between the gate and the fluid particles.

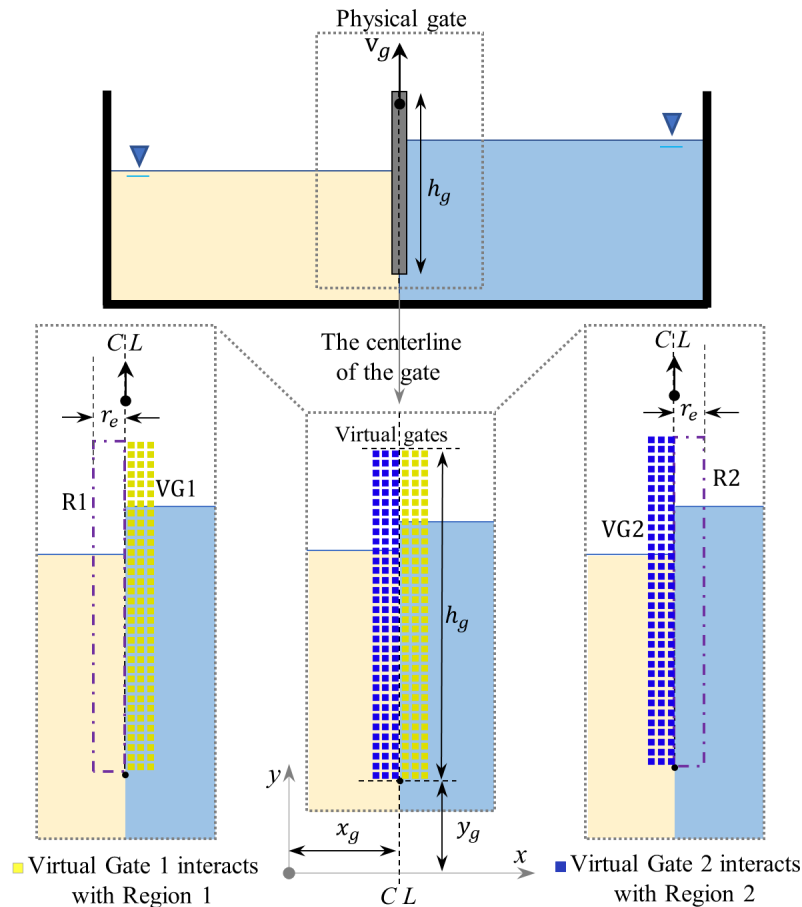


Figure 7.3 The virtual moving gates implemented for modeling the effects of the physical gate in the numerical simulations.

7.4.5 Initial and boundary conditions

The continuity equation in the EWC-MPS method enables assigning the initial pressure to the particles. Considering the theoretical solution of a problem (including the initial velocity, \mathbf{v}_i^0 , position, \mathbf{r}_i^0 , and the boundary conditions) the initial pressure of the fluid particles, p_i^0 , can be calculated. Then, the inverse form of the equation of state gives the initial particle number density of the particles through $n_i^0 = n_0 (p_i^0/B_0 + 1)^{1/\gamma}$. In this study, we assign the initial hydrostatic pressure to the fluid particles (without changing their positions). Subtracting the equivalent hydrostatic water pressure, $p_{pw_i}^0$, from the total initial pressure of the mixture particles, p_i^0 , determines the initial effective pressure of the mixture particles as $p_{\text{eff}i}^0 = p_i^0 - p_{pw_i}^0$. With the inverse form of the equation of state, we assign the initial true water density of the mixture particles, ρ_{wi}^0 , corresponding to the initial pore-water pressure.

We employ the fixed dynamic boundary condition for treating the wall and ghost particles denoted as the solid boundary particles, Ω_s (based on the work of Crespo et al. [67]). Figure 7.2 represents the classification of the particles including the fluid and solid boundary particles. In the dynamic boundary condition implemented in this study, the pressure of the closest wall particle is assigned to the ghost particles. Further, in the governing equations of the fluid particles, the velocity of the fluid particle interacting with the solid boundary is assigned to the ghost particles whereas the wall particles have zero velocity (Table 7.1). To update the particle number density of the wall particle via the continuity equation (without the diffusive term), the velocity of all the boundary particles remains zero. For approximating the gradient of the velocity of the fluid particles, $\langle \nabla \mathbf{v} \rangle_i$, we assign the fluid's velocity to the wall/ghost particles to avoid large amounts of II_{Ei} (i.e., $i \in \Omega_f, j \in \Omega_s$ and $r_{ij} \leq r_e \rightarrow \mathbf{v}_j = \mathbf{v}_i$ in Eq. (7.24)) (see Table 7.1).

At the vicinity of the solid boundary or the virtual gates, we assign the particle number density and a fraction of effective viscosity of the fluid particles, given by $\gamma_s \eta_i$, to the wall and ghost particles (i.e., $i \in \Omega_f, j \in (\Omega_s \text{ or } \text{VG1 (or VG2)})$ and $r_{ij} \leq r_e \rightarrow \eta_j = \gamma_s \eta_i$ and $n_j = n_i$ in Eq. (7.11)). The constant and dimensionless coefficient $0 \leq \gamma_s \leq 1$ adjusts the friction magnitude between the fluid and wall particles based on the problem specifics. Furthermore, the volume fraction of the fluid particles close to the solid boundaries is given to its neighbor boundary/virtual gate particles (i.e., $i \in \Omega_f, j \in (\Omega_s \text{ or } \text{VG1 (or VG2)})$ and $r_{ij} \leq r_e \rightarrow \phi_j = \phi_i$ in Eq. (7.23)). Regarding the particle stabilization technique, the CPS technique involves the solid boundary particles for determining the free surface regions and the shifting vector by assigning the particle concentration of the closest wall particle (calculated like the fluid particles) to the neighbor ghost particles.

Table 7.1 The strategies for the diffusive term to simulate the steady reservoir filled with the two fluid phases as $\rho_L/\rho_H = 0.5$.

$i \in \Omega_f, j \in \Omega_s = (\Omega_{sw} \cup \Omega_{sg})$ and $r_{ij} \leq r_e$		
$\langle \nabla \cdot \mathbf{v} \rangle_i, \langle \nabla^2 \mathbf{v} \rangle_i$	$\begin{cases} \mathbf{v}_j = 0 & j \in \Omega_{sw} \\ \mathbf{v}_j = \mathbf{v}_i & j \in \Omega_{sg} \end{cases}$	
$\langle \nabla \mathbf{v} \rangle_i$	$\mathbf{v}_j = \mathbf{v}_i$	$j \in \Omega_s$

7.4.6 Solution algorithm

The symplectic time integration algorithm by Monaghan and Rafiee [11] solves the discrete system of equations as a second-order and explicit scheme (see Appendix 7.6). In addition to the Courant-Friedrichs-Lewy stability condition, the shear force due to the maximum viscosity controls the time steps of the calculation (Δt) as follows [223]:

$$\Delta t = \min \left\{ C_{CFL} \frac{l_0}{c_0}, 0.125 \frac{\rho_m l_0^2}{\eta_{max}} \right\}. \quad (7.27)$$

In this study, we set the C_{CFL} coefficient to 0.5 for all the simulations; however, for simulating the granular flows, the diffusion stability condition is dominant and the maximum viscosity, η_{max} , enforces the shear force condition for the numerical stability of the time integration scheme. To accelerate the computations, we implement the numerical model in parallel frameworks with Compute Unified Device Architecture (CUDA) C++ programming language using the massive parallelism of the Graphical Processing Unit (GPU) devices (see Appendix 7.6 for more details). This speeds up simulating three-dimensional problems with high shear stresses studied in the present work. It should be highlighted that the developments proposed and validated in this paper are independent of the programming language and the parallel algorithms used and can be directly extended to other continuum-based particle methods.

7.5 Results and discussions

We implement the proposed developments in the three-dimensional model of the EWC-MPS method to capture the complex mechanical properties of the multiphase granular flows. First, we validate and discuss the role of the modified diffusive term by simulating the hydrostatic pressure in a simple multiphase problem. Further, we study the gravity-driven immersed granular flows through the granular collapse and landslide benchmark cases. We represent a set of experimental results for validating the granular collapse test case in the submerged

conditions. While for the immersed granular landslides, we validate the numerical simulations by the work of Pilvar et al. [10].

7.5.1 Hydrostatic pressure for two fluid phases

We simulate the hydrostatic pressure in a multiphase test case ([134, 164]), to show the effectiveness of the modified diffusive term. In this problem a steady reservoir is filled with two inviscid and immiscible fluids as the lighter phase (with the density $\rho_L = 1000 \text{ kg/m}^3$) is on the top of the heavier phase (with the density $\rho_H = 2000 \text{ kg/m}^3$), $\rho_L/\rho_H = 0.5$. Each fluid phase has 0.1 m height subjected to the constant gravitational force, $\mathbf{g} = \{0, -g_y, 0\}$, where $g_y = 9.81 \text{ m/s}^2$. The particles are initially located on a hexagonal lattice with the spatial resolution defined as $R = H/l_0$ (Figure 7.4). The Symplectic time integration scheme with $C_{CFL} = 0.5$ solves the governing equations for 10 seconds of simulation. Considering the lighter fluid as the reference phase, the reference sound speed and the bulk modulus are set to $c_0 = 10\sqrt{2g_y H}$ and $B_0 = \rho_L c_0^2/\gamma$, respectively. δ_{MPS} is set to 0.1 for all the test cases and the particle shifting technique is deactivated. The initial pressure, p_i^0 , of the fluid particles are calculated based on the initial hydrostatic condition. Then, the inverse form of the equation of state determines the initial particle number density field, n_i^0 (Figure 7.4).

Concerning the different formulations for ψ_{ij} in the diffusive term (Eq. (7.15)), we define three strategies to simulate this multiphase problem (the test cases 1A, 1B, and 1C in Table 7.2). The results show that the standard form of the diffusive term causes the pressure field to diverge at the free-surface and the vicinity of the bottom wall (Figure 7.5-1A). The kernel truncation at these regions locally manipulates the particle number density field leading to unstable pressure fields in the long-term simulation of the problem. Further, case 1A shows that this diffusive term overestimates pressure at the interface of the fluid phases. By employing the convergent form of Laplacian operator without the higher-order gradient formulation, i.e., with $\langle \nabla n \rangle_i$ (case 1B), the particle number density field still diverges close to the bottom wall. Nevertheless, the numerical pressure at the interface is compatible with the theoretical result and the overall pressure field becomes stable after $t = 3 \text{ s}$. In case 1C, the proposed diffusive term with the higher-order gradient (i.e., $\langle \nabla n \rangle_i^c$) is implemented in the convergent form of Laplacian operator acting between all the fluid particles (Eq. (7.19)). This diffusive term solves the kernel truncation issue at the free surface and the vicinity of the wall. Comparing case 1B vs 1C in Figure 7.5 exhibits the key role the first-order gradient plays in the accuracy of the pressure approximation as the kernel function truncates. Figure 7.6 illustrates the uniform particle distribution and the smooth pressure field obtained by the three cases at $t = 10 \text{ s}$. However, implementing the standard diffusive term underesti-

mates the pressure at the vicinity of the bottom wall in the long-term simulation (Figure 7.6-1A). Overall, the results confirm that the modified diffusive term as a function of the particle number density and without being limited to the same phase particles (unlike the multiphase SPH models e.g., [70]), estimates accurate pressure field over the fluid domain while is independent of the accuracy of the corrective matrix (Eq. (7.18)) at the interface of the fluid phases.

To quantify the improvement achieved by the modified diffusive term (similar to the work of Fourtakas et al. [69]), we conduct the particle convergence study considering different spatial resolutions set as $R = 50, 100, \text{ and } 200$. With the theoretical solution of this problem, we estimate the Normalized Root Mean Square Error (NRMSE) of the pressure, the magnitude of velocity, and the total kinetic energy of fluid particles (E_k). Figure 7.7 compares the theoretical hydrostatic pressure with the extracted numerical pressure at $x = 0.1 \text{ m}$ and $t = 10 \text{ s}$ of the cases 1A and 1C (where the errors are normalized by the maximum analytical pressure of the corresponding fluid phase). Although the NRMSE of the model with the standard diffusive term reduces by increasing the resolution, the pressure in the vicinity of the bottom wall still diverges considerably in the long-term simulation (as for Case 1A with $R = 200$, $\text{NRMSE} = 1.87\%$). However, the modified diffusive term decreases the NRMSE significantly by the order of one magnitude as the numerical pressure converges to the analytical pressure across the fluid phase (as for Case 1C with $R = 200$, $\text{NRMSE} = 0.154\%$). Figure 7.8 illustrates the velocity profile in the middle section (at $t = 10 \text{ s}$) and the temporal evolution of the total kinetic energy (where the errors of $\|\mathbf{v}\|$ and E_k are normalized by $\sqrt{g_y H}$ and the total potential energy (which in this problem is 45.05 (J)), respectively). The NRMSE of the velocity and the total kinetic energy are negligible for both 1A and 1C cases (i.e., $\text{NRMSE} < 0.01\%$); nevertheless, with the modified diffusive term, the velocity field convergence to the theoretical velocity of zero with fewer numerical errors. It should be noted that the initial hexagonal distribution of the particles has eliminated the initial particle rearrangement and its associated noises that occur with the cartesian particle distribution in the initial time steps of the simulation (see [123]). In Figure 7.9, we plot the NRMSE of the total kinetic energy and the pressure with the different resolutions using the logarithmic scale to identify the order of convergence. For the total kinetic energy, the order of convergence is estimated as 1.56 and 1.69, for 1A and 1C, respectively, showing satisfactory results as it slightly increases with implementing the modified diffusive term. The divergence of the pressure in the vicinity of the wall with the standard diffusive term affects the order of convergence of this variable as is approximately less than one (i.e., Case 1A: $O(0.74)$); whereas, with the modified diffusive term, i.e., Case 1C, the order of convergence increases considerably to $O(1.35)$, confirming the effectiveness of the model in predicting accurate

pressure field.

7.5.2 Immersed granular collapse

The immersed granular collapse has been widely modeled for understanding the mechanical properties of the granular flows in various hydrodynamic conditions (e.g., [19, 90, 91, 224]). Capturing the different states of the granular flow in this problem: the viscous and/or inertial regimes, has been a great challenge for numerical models (e.g., [20, 113, 225–227]). Here, by simulating this gravity-driven test case, we investigate the role of the modified diffusive term, the regularized visco-inertial model, and the consistent effective pressure. We validate the three-dimensional numerical model (developed in the context of the EWC-MPS method) by the experimental results conducted and presented as a part of the present work. Figure 7.10 illustrates the initial setup and geometrical properties of the physical and numerical models.

We conducted the experiment in a steady and horizontal channel of the rectangular cross-section ($W_b \times L_b$) with a sluice gate located at $x = L_0$. As the gate opens (with $v_g = 1 \text{ m/s}$ in the y -direction), the column of the mixture collapses under the gravitational force (with $\mathbf{g} = \{0, -g_y, 0\}$ and $g_y = 9.81 \text{ m/s}^2$) propagating on the smooth bottom wall of the channel. With the aspect ratio of the granular column equal to one (i.e., $H_0/L_0 = 1$), the final deposit is expected to form a triangular shape where the final height becomes less than the initial height [91]. Table 7.3 contains the material properties of the spherical glass beads with a mean diameter of 0.0008 m and $\rho_g = 2470 \text{ kg/m}^3$ fully submerged in ambient water with $\rho_{0w} = 1000 \text{ kg/m}^3$ and $\mu_w = 0.001 \text{ Pa}\cdot\text{s}$. We neglect Brownian effects as the grains are large enough (i.e., as $d_g > 100 \text{ }\mu\text{m}$). The physical properties used in the effective viscosity equation correspond to the rheology model Baumgarten and Kamrin [20] validated by the experimental data. We recorded the evolution of the collapse from the sidewall of the reservoir to extract the interface profiles and the spreading (runout) length of the granular deposit. Depending on the material properties of the fluid phase and the solid grains, the viscous and/or inertial regimes occur in the immersed granular collapse [90, 93]. Considering the

Table 7.2 The strategies for the diffusive term to simulate the steady reservoir filled with the two fluid phases as $\rho_L/\rho_H = 0.5$.

Strategy	ψ_{ij} in Laplacian operator of the diffusive term (Eq. (7.15))	
Case 1A	$\psi_{ij} = (n_j - n_i)$	$i, j \in \text{all the fluid particles}$
Case 1B	$\psi_{ij} = (n_j - n_i) - 0.5 \left[\langle \nabla n \rangle_i + \langle \nabla n \rangle_j \right] \cdot \mathbf{r}_{ij}$	$i, j \in \text{all the fluid particles}$
Case 1C	$\psi_{ij} = (n_j - n_i) - 0.5 \left[\langle \nabla n \rangle_i^C + \langle \nabla n \rangle_j^C \right] \cdot \mathbf{r}_{ij}$	$i, j \in \text{all the fluid particles}$

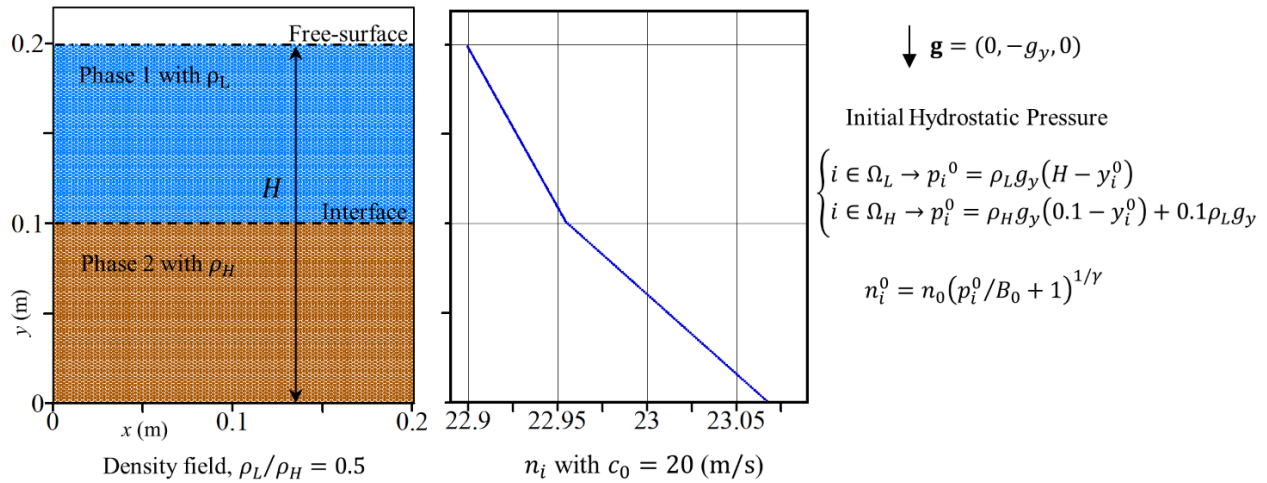


Figure 7.4 The initial configuration of the steady reservoir ($g_y = 9.81 \text{ m/s}^2$) filled with the two fluid phases ($R = H/l_0 = 100$). The lighter phase with ρ_L is considered as the reference phase for calculating the bulk modulus, B_0 . The hexagonal lattice is used for the initial uniform distribution of the particles.

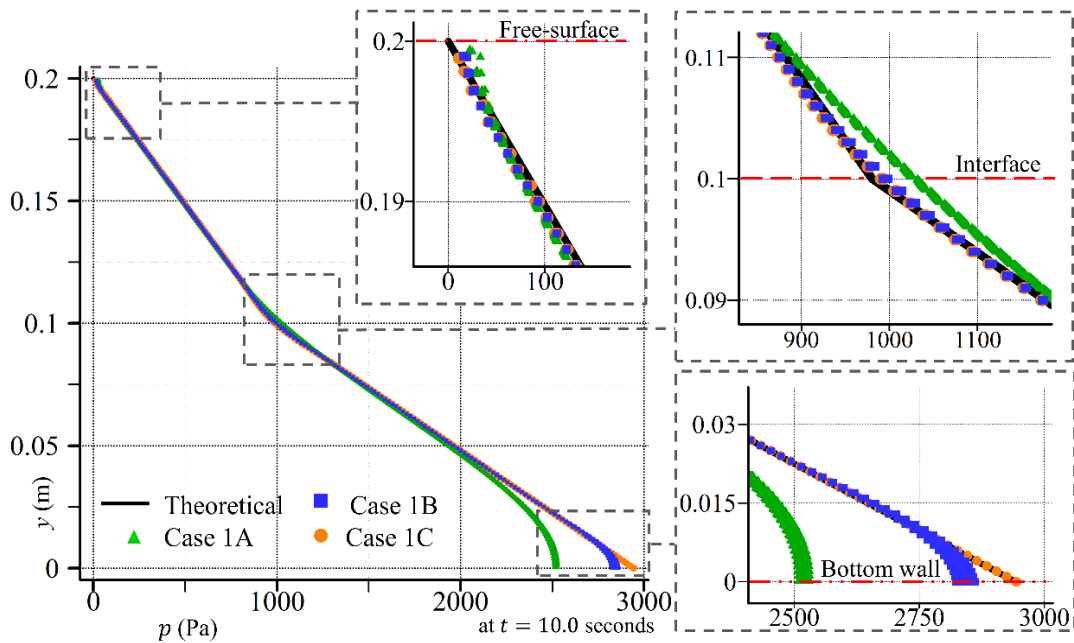


Figure 7.5 The position of the fluid particles (y_i) vs their numerical pressure (p_i , without any data averaging or filtering) at $t = 10.0 \text{ s}$ (All the fluid particles are plotted in the graph for cases 1A, 1B, and 1C defined in Table 7.2 with $R = 100$). The zoom-in plots show fluid particles at the free-surface, the interface, and the vicinity of the bottom wall.

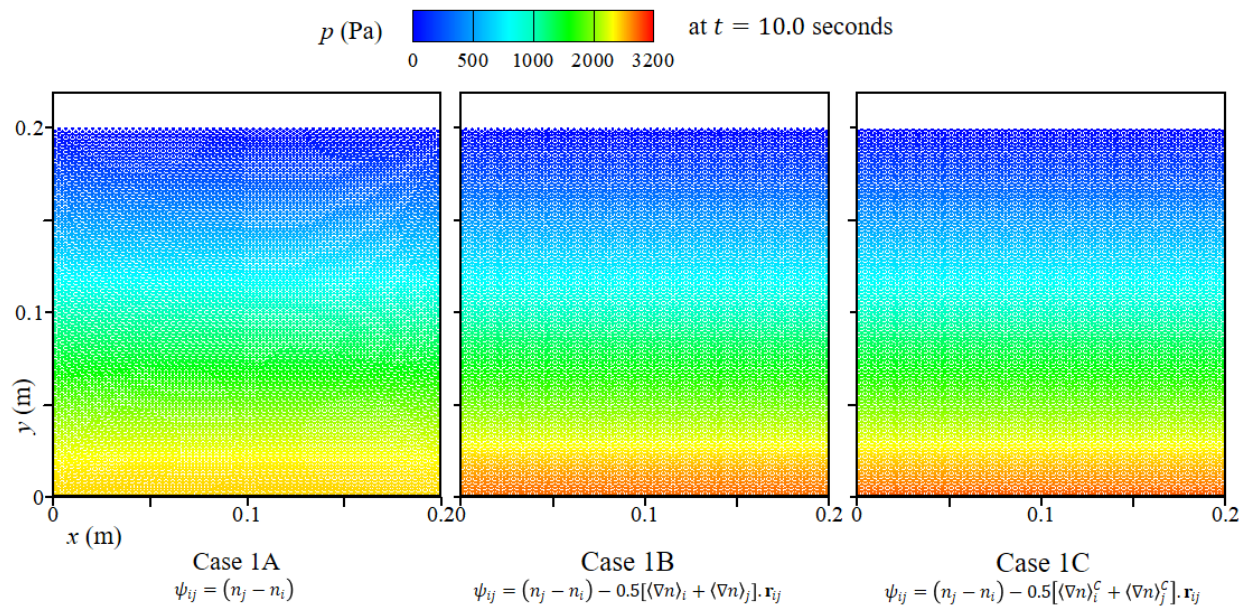


Figure 7.6 Pressure field of the cases 1A, 1B, and 1C at $t = 10.0$ s. The particles are initially located on the hexagonal configuration and $R = 100$.

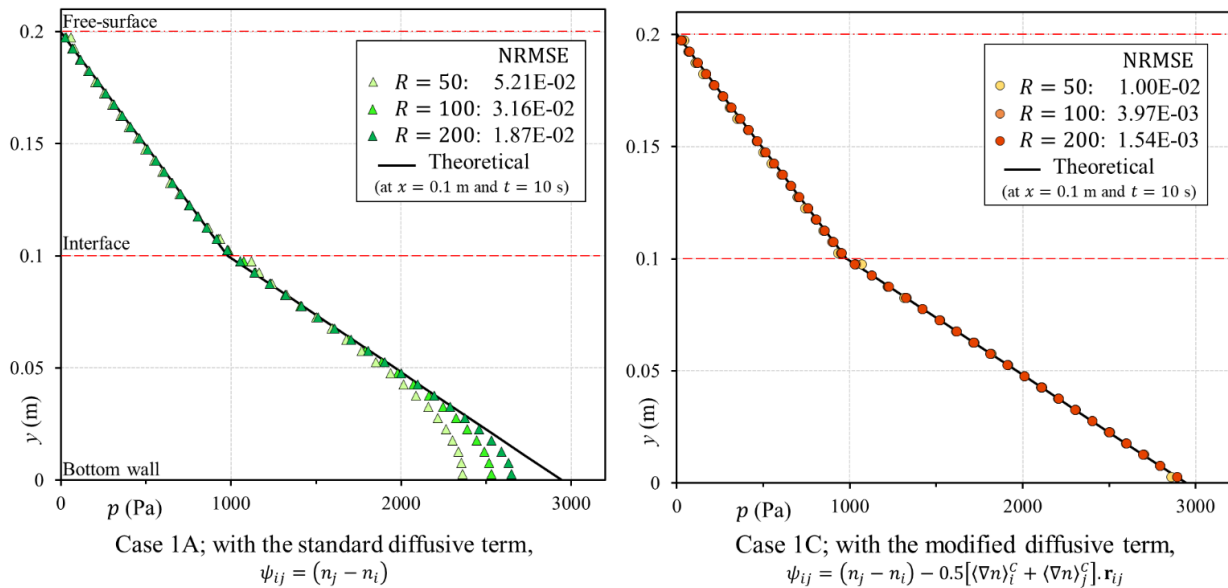


Figure 7.7 The theoretical versus the extracted numerical pressure (averaged at $x = 0.1$ m and $t = 10$ s). The NRMSE of the pressure profiles for the cases 1A and 1C with the different spatial resolutions, $R = H/l_0 = 50, 100$, and 200 , are represented.

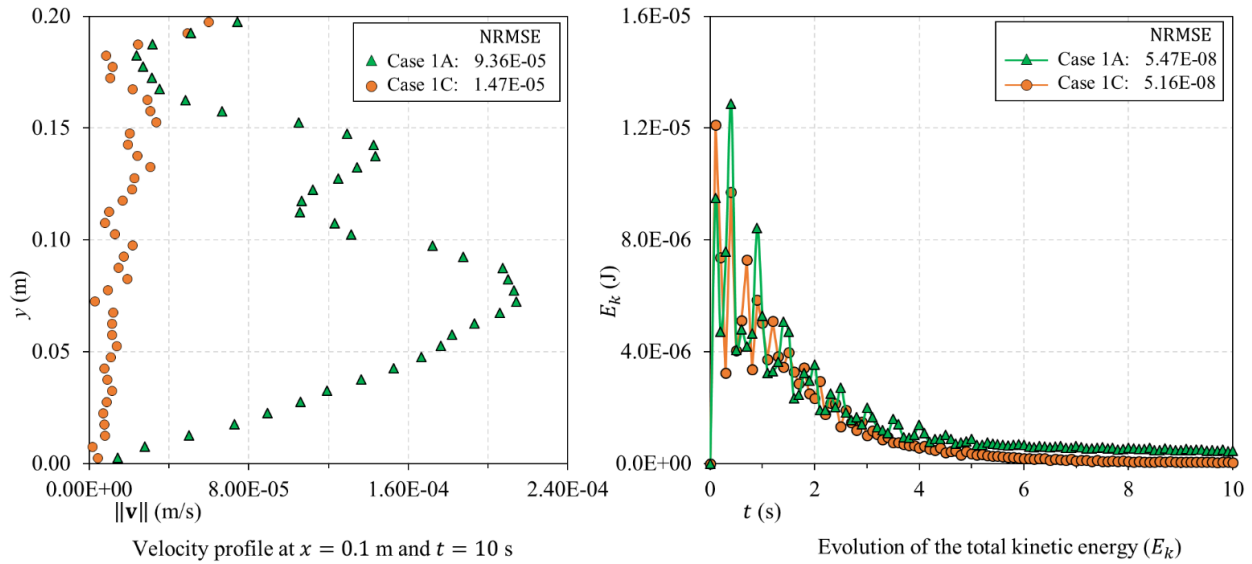


Figure 7.8 The velocity profiles (averaged at $x = 0.1$ m and $t = 10$ s) and the evolution of the total kinetic energy of the system with $R = 50$. The NRMSE for the cases 1A and 1C are represented.

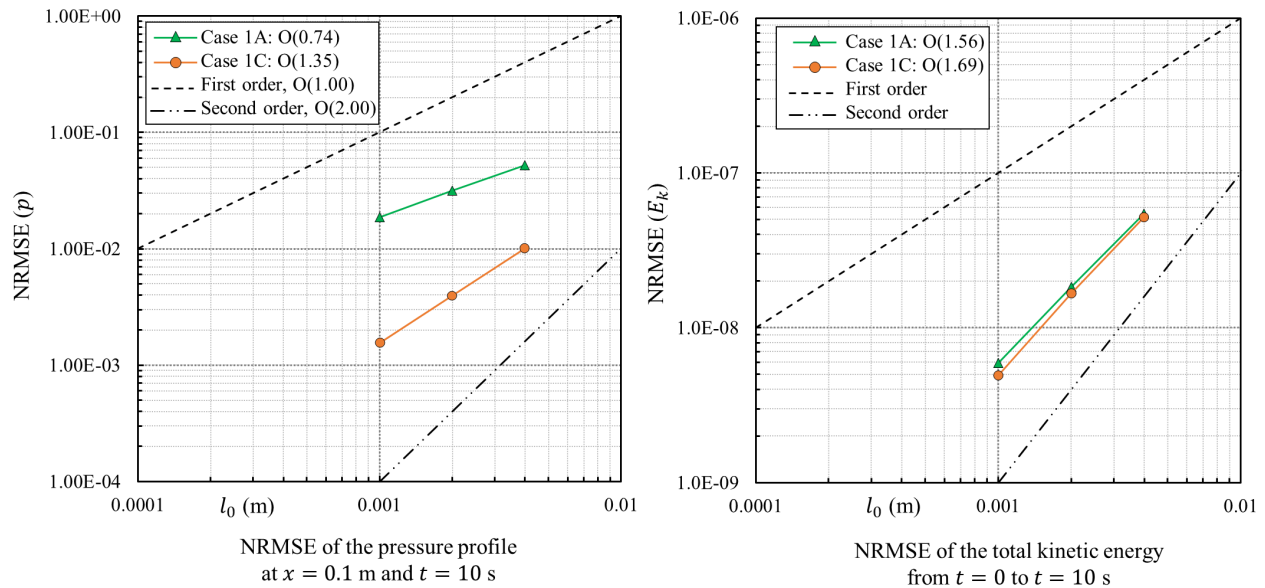


Figure 7.9 The NRMSE of the pressure profiles and the total kinetic energy (in the log-log plot) for the cases 1A and 1C representing the order of convergence of the numerical results.

dimensionless numbers: the Stokes number, St , (here is defined as the ratio of the viscous timescale to the free-fall timescale) and the grain-water density ratio, $r = (\rho_g/\rho_{0w})^{0.5}$, the immersed granular collapse in the present study falls within the viscous-inertial regime (as $St = 5.4$ and $r = 1.6$) [90].

In the numerical model, we discretize the computational domain with the initial particle distance, l_0 . The total particle count, presented in Table 7.4, consists of the water, mixture, solid boundary, and virtual gates particles. To ensure the incompressibility of the fluid model, we set the reference sound speed to 24 m/s . We should note that in this problem the viscous force limits the time steps of the calculation through Eq. (7.27) (as $\eta_{max} = 1000 \text{ Pa}\cdot\text{s}$). We implement the particle packing algorithm to eliminate the noise arising from the transition of the initial cubic particle distribution to the low-energy configuration (similar to [228]). The new position of the fluid particles are used to calculate n_0 (by averaging the kernel summation over the interior fluid particles) and initialize the main simulations (i.e., apply the initial hydrostatic condition) (Figure 7.10-b). The virtual particle, j , representing the moving gate interacts with the fluid particle, i , within R1 or R2 regions (in Figure 7.10-b) through the governing equations. Although the virtual particles are moved with the true velocity of the physical gate ($v_g = 1 \text{ m/s}$), their virtual velocity included in the momentum and continuity equations of the fluid particles is adjusted according to Table 7.4 for different spatial resolutions (e.g., with $l_0 = 0.003 \text{ m}$ for $\forall i \in \text{VG1 or VG2} \rightarrow \mathbf{v}_i = \{0.0, +0.2, 0.0\}$). Also, for the shear force between the fluid particles, i , and the virtual and wall particles, j , the dimensionless coefficient of the viscosity, γ_s , is given in Table 7.4 (e.g., with $l_0 = 0.003 \text{ m}$, $\eta_j = 0.2\eta_i$). We extract the numerical results from the middle and sidewall sections of the channel (specified in Figure 7.10) to represent them in two-dimensional (x - y) graphs. We define five different strategies for simulating the immersed granular collapse concerning the implementation of the diffusive term, the effective pressure, and the rheology model (Table 7.5). The test case 2A contains all the developments proposed in the present work and can be denoted as the reference numerical model. In the diffusive term, $\delta_{MPS} = 0.6$ for all the test cases except 2B. To detect the free-surface particles and for the stability of the model, the CPS technique is activated. Table 7.6 identifies the timesteps in which the comparison of the experimental and numerical results is carried out. The nondimensional time scale, T , is given by $t\sqrt{g_y/H_0}$ (H_0 being the initial height of the granular column). We consider the reference time, $T_0 = 0.0$, as the immersed granular column commences to collapse on the bottom wall of the channel (shown in Figure 7.12). While the gate is being opened and still $L = L_0$ (L is the length of granular deposit on the bottom wall in the x -direction), we re-initialize the true density of water within the mixture particles, ρ_{wi} , assuming the hydrostatic condition for the pore-water pressure.

We represent the three-dimensional configuration of the immersed granular collapse (Case 2A with $l_0 = 0.003 \text{ m}$) in Figure 7.11: the viscosity field (in the logarithmic scale) and the effective pressure within the mixture particles at T4 and T6, respectively, and the pressure field of the water particles at T8 (see the results in the supplementary materials for movies of the experiment and the numerical simulations). The physical effects of the virtual gate implemented at the initial stages of the granular flow are well illustrated in the movies. Also, the fixed solid boundary particles include the shear force between the walls of the channel and the fluid particles in the numerical simulations. This allows the 3D model to capture the effects of the reservoir's corners on the overall evolution of the granular deposit. Due to the confinement of the granular phase at the two corners, the maximum viscosity occurs forming the curve-shape surface of the mixture on the back wall, also observed in the experiments (Figure 7.11- a & d). It should be highlighted that the two-dimensional models are incapable of capturing this aspect of the granular collapse [111].

Plotting the interface profiles of the experimental results (the left column of Figure 7.12) on the sidewall sections of the numerical simulation of Case 2A with $l_0 = 0.003 \text{ m}$ (in the right column of Figure 7.21), we compare the time evolution of the granular collapse. The rapid opening of the vertical gate creates vortices suspending the solid grains in water at the initial stage (Figure 7.12-T0). This makes digitizing the interface profiles of the experiment difficult and slightly affects the deformation of the granular phase in the early stages (at T2). Furthermore, since the virtual gate neglects the physical thickness of the gate (which is 0.005 m in the experiment), the shear stress causing the suspension of the grains is partially simulated via the numerical model. However, comparing the interface profiles in the following steps of the granular collapse shows good compatibility between the numerical and experimental results.

Next, we investigate the effect of the initial particle distance (or size) on the time evolutions of the mixture phase. In the case of granular flows, the choice of the particle distance is not only controlled by the convergence of the numerical technique but also by the validity of the continuum assumption. Considering the continuum assumption in the governing equations, the smallest numerical elements (here the particles) must be much larger than the diameter of the physical elements (here the solid grains and pore water) [17, 122]. With the particle and grain sizes being close (i.e., $l_0 \approx d_g$), the mixture particles would contain a limited number of solid grains violating the continuum assumption of the numerical model [114]. On the other hand, the representative elementary volume should be much smaller than the characteristic length of the problem to mathematically represent its vicinity in the calculations [122]. Therefore, the initial particle spacing should satisfy both conditions simultaneously; otherwise, either the rheology model, defined for a continuous effective fluid, becomes invalid or

the approximation errors increase, affecting the mechanical behavior of the mixture phase. To determine the optimum particle size of the model, we simulate the immersed granular collapse with different spatial resolutions ($l_0 = 0.004, 0.0035, 0.003, 0.002, 0.0015$ m with the adjusted boundary conditions given by Table 7.4). Figure 7.13 compares the dimensionless interface profiles of the numerical simulations with those from the experiment at the sidewall of the reservoir (at T2, T6, and the final stage). The results of case 2A with $l_0 = 0.004$ and 0.0035 m show considerable incompatibilities between the numerical and experimental profiles. This apparent discrepancy can be explained by the large initial particle distance (with regards to the problem characteristic length) which increases the approximation errors and leads to inaccurate interaction forces between the solid boundaries and fluid particles. Nevertheless, the interface profiles with $l_0 \leq 0.003$ m are in good agreement with the experimental profiles; whereas, the case $l_0 = 0.0015$ m shows slightly more deformation of the granular collapse at T6. Furthermore, we plot the normalized runout distances (i.e., $L/L_0 - 1$) in the left graph of Figure 7.14. A clear discrepancy between the experimental and numerical runout distances of the immersed granular collapse with $l_0 = 0.004$ and 0.0035 m exists, while the runout lengths of cases with the smaller particle sizes, particularly with $l_0 = 0.003$ and 0.002 m, are consistent with the experimental measurement. Although the case with $l_0 = 0.0015$ m (considering the adjusted boundary conditions (Table 7.4)) predicts the final stage of the granular deposit, it overestimates the runout length during the collapse (i.e., $T_2 \leq T \leq T_7$).

To quantify the accuracy of the results, we compute the Root Mean Squared Error (RMSE) of the normalized runout distances and plot them against the non-dimensional ratio of l_0/d_g (in the right graph of Figure 7.14). The table presented in Figure 7.14 shows the number of solid grains that each mixture particle represents, N_g , (in 3D) and the corresponding errors of the normalized runout length. For coarse particle sizes (i.e., $l_0 = 0.004$ and 0.0035 m), the RMS Errors are considerable (equal to 0.4972 and 0.1597, respectively). By decreasing the particle size to 0.003 and 0.002 m the errors significantly reduce (RMSE = 0.0509 and 0.0499, respectively) confirming the good agreement between the numerical and experimental results and the convergence of the model; however, with the smallest particle size of $l_0 = 0.0015$ m, the RMSE increases to 0.0963. This illustrates that when the mixture particle contains a limited number of solid grains (for $l_0 = 1.875d_g$, $N_g = 8$ in the 3D problem) may violate the continuum assumption of the granular mass leading the rheology model to become incapable of capturing the accurate evolutions of the granular mass (in this case, overestimating the deformations). Through a similar study, Ghaïtanellis et al. [114] obtained equivalent outcomes showing the overestimation of sediment erosion with $l_0 < 2d_g$ and concluded that the minimum error is achieved by $l_0 \approx 3d_g$. That is due to the fact that with smaller particle sizes

the macroscopic scale would reach the size of the discrete elements of the system, and thus, it would no longer be the representative elementary volume of the continuum model [114]. Overall, the interface profiles and the spreading length of the case 2A (with $l_0 = 0.003$ and 0.002 m) are consistent with the experimental measurements as the model predicts the evolution of the immersed granular collapse with the RMSE of the normalized runout distance ≈ 0.05 . Accordingly, we choose $l_0 = 0.003$ m (where $l_0 = 3.75d_g$) for the following simulations of the immersed granular flows represented in this paper.

In Table 7.7 we can compare the calculation time per iteration (i.e., per time step) of the simulations concerning the number of fluid particles and the different particle sizes. An NVIDIA V100 Volta GPU device is used for running the parallel part of the code written by CUDA C++ parallel programming language (see Appendix 7.6). Since the results in Table 7.7 cannot be used for discussing the efficiency of the GPU implementation and also considering the scope of the current work, we postpone investigating the performance analysis and the scalability of the GPU-accelerated code to future works.

Role of diffusive term

Here, we study the role of the diffusive term in simulating the immersed granular collapse. The modified diffusive term included in the continuity equation presents a uniform pressure field (Figure 7.15-2A). Without the diffusive term, the high-frequency pressure noises affect the mechanical behavior of the granular collapse (Figure 7.15- case 2B). This leads to unphysical deformation of the granular flow by overestimating the effective viscosity as incompatibility exists between the experimental interface profiles and the numerical results of case 2B (Figure 7.15 and Figure 7.16- case 2B). However, the modified diffusive term shows a uniform viscosity field required for capturing the shear properties of the granular flow (Figure 7.16- case 2A). The results emphasize implementing the diffusive term as an effective numerical correction approach for eliminating the high-frequency pressure fluctuations that exist in the numerical model.

Moreover, we compare the modified diffusive term with the standard diffusive term where $\psi_{ij} = n_j - n_i$ (i.e., case 2A vs case 2C). We plot the mixture particles position against their total numerical pressure (i.e., $y_i - p_i$) (Figure 7.17). While the standard diffusive term

Table 7.3 The material properties of the glass beads as the saturated granular phase

Material Properties	$d_g(m)$	$\rho_g(kg/m^3)$	$\theta(\text{degree})$	$\Delta\mu$	a	b	ϕ
Glass beads	0.0008	2470	22	1.03	1.23	0.30	0.64

Table 7.4 Calculation and boundary conditions of the immersed granular collapse with different particle sizes, l_0

l_0 (m)	0.004	0.0035	0.003	0.002	0.0015
Total number of particles	62,808	91,812	171,582	418,008	919,176
True velocity of the virtual gates, v_g (m/s)	1.0	1.0	1.0	1.0	1.0
Velocity of the virtual gates in the governing equations of the fluid particles (m/s)	0.1	0.15	0.2	0.2	0.3
The non-dimensional coefficient, γ_s , for adjusting the viscosity of the boundary and virtual particles	0.1	0.15	0.2	0.3	0.6

Table 7.5 The numerical test cases of the immersed granular collapse concerning the rheology model, the diffusive term, and the effective pressure equation.

Case	Rheology model	ψ_{ij} in the diffusive term	Effective pressure, p_{eff} .
2A	Regularized $\mu(I_v, I_m, \phi)$	$\psi_{ij} = (n_j - n_i) - 0.5 \left[\langle \nabla n \rangle_i^C + \langle \nabla n \rangle_j^C \right] \cdot \mathbf{r}_{ij}$	Consistent p_{eff} .
2B	Regularized $\mu(I_v, I_m, \phi)$	Without diffusive term (as if $\delta_{MPS} = 0.0$)	Consistent p_{eff} .
2C	Regularized $\mu(I_v, I_m, \phi)$	$\psi_{ij} = (n_j - n_i)$	Consistent p_{eff} .
2D	Regularized $\mu(I)$	$\psi_{ij} = (n_j - n_i) - 0.5 \left[\langle \nabla n \rangle_i^C + \langle \nabla n \rangle_j^C \right] \cdot \mathbf{r}_{ij}$	Consistent p_{eff} .
2E	Regularized $\mu(I_v, I_m, \phi)$	$\psi_{ij} = (n_j - n_i) - 0.5 \left[\langle \nabla n \rangle_i^C + \langle \nabla n \rangle_j^C \right] \cdot \mathbf{r}_{ij}$	Hydrostatic assumption for p_{pw}

Table 7.6 Time steps of the extracted data from the experimental and numerical simulations, $T = t\sqrt{g_y/H_0}$

Labels	T0	T2	T4	T6	T8	T14 (Final)
Time (s)	0.00	0.17	0.33	0.49	0.65	1.16
T	0.00	1.98	3.96	5.89	7.81	13.93

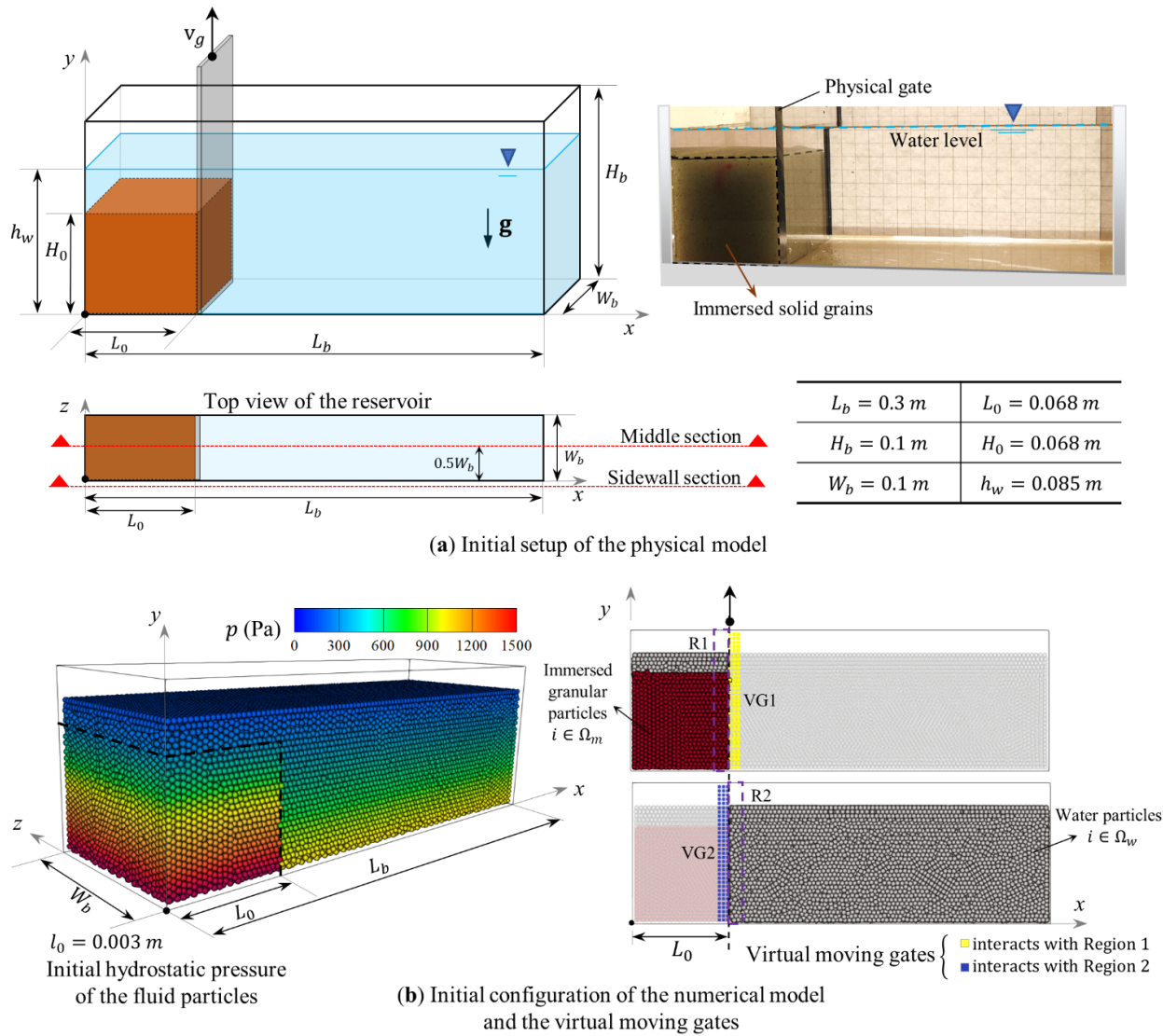


Figure 7.10 The three-dimensional configuration and the initial setup of the physical (a) and numerical (b) models

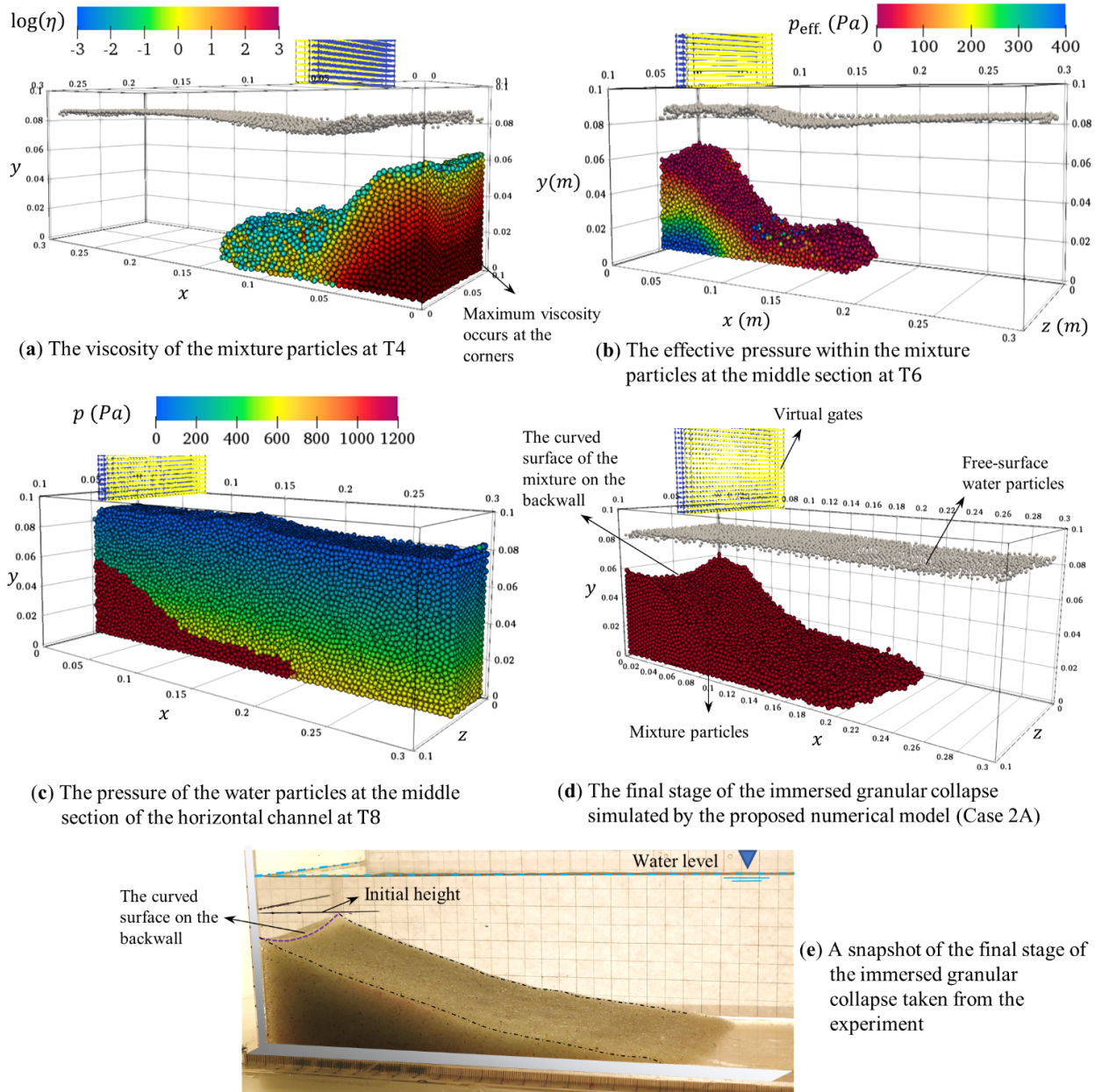


Figure 7.11 The immersed granular collapse via the three-dimensional numerical model based on the enhanced weakly-compressible MPS method (Case 2A- $l_0 = 0.003 \text{ m}$). See the supplementary results as the movies of the experiment and the numerical simulations.

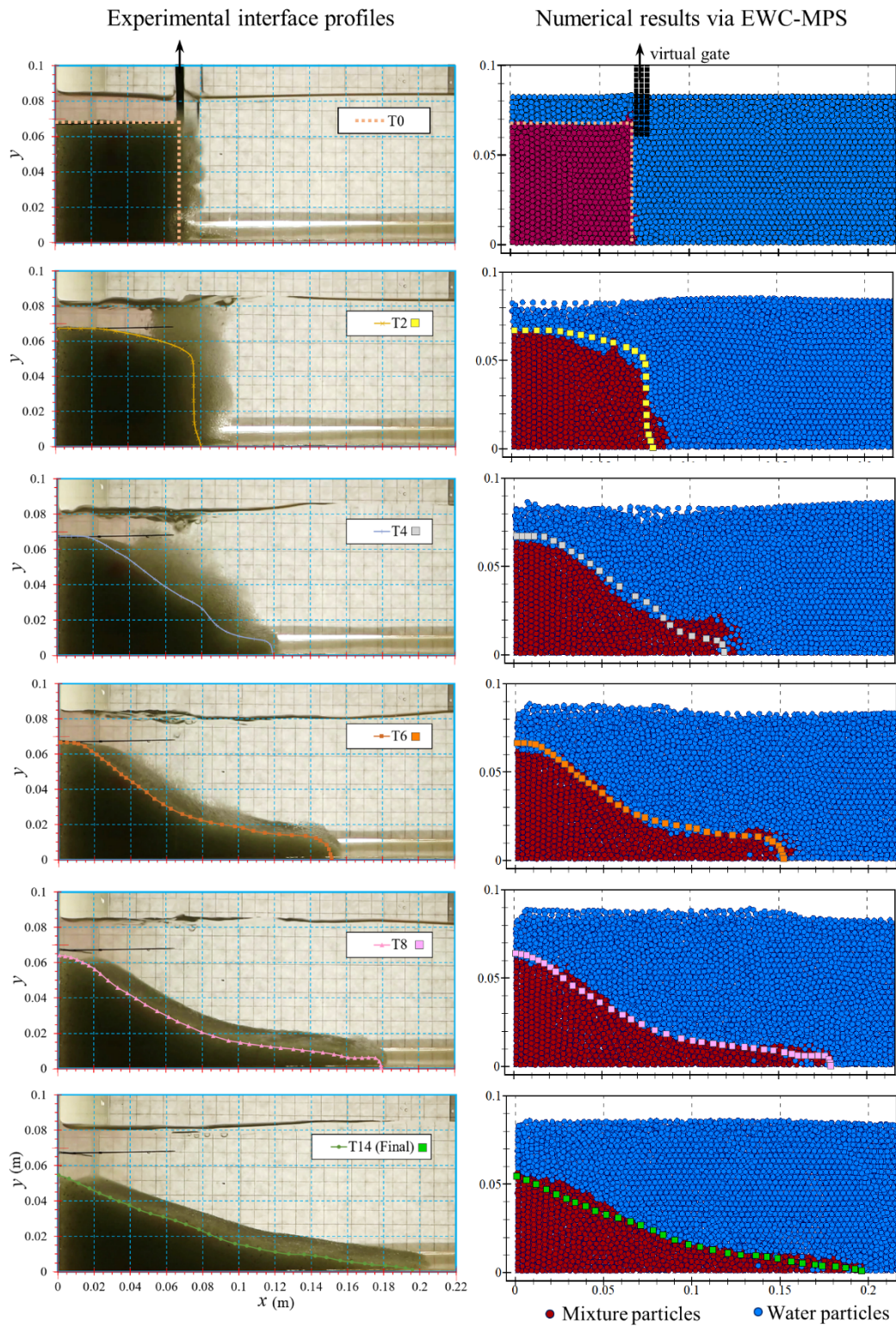


Figure 7.12 The temporal evolution of the immersed granular collapse; the experimental vs numerical results (Case 2A- $l_0 = 0.003 \text{ m}$) at the sidewall section.

reduces the total pressure in the vicinity of the bottom wall, the modified diffusive term eliminates the kernel truncation errors and represents a stable pressure field at the final stage of the collapse. It should be noted that the standard diffusive term manipulates the pressure (particularly in the vicinity of the wall) and hence, affects the mechanical properties of the immersed granular collapse where the effective pressure plays an essential role in the constitutive law.

Role of effective viscosity

We implemented the regularized visco-inertial rheology model to capture the viscous and inertial regimes of the immersed granular flows through a single formulation. Figure 7.18 indicates that the non-dimensional numbers (I_v , I and I_m defined in Eq. (7.5) and $St = I^2/I_v$) are within the limit defined for validating the visco-inertial model. The viscous number remains below 0.01 value, while the inertial number, I , is dominant in the yielded region controlling the post-failure terms of the effective viscosity (i.e., the second and third terms in the right-hand side of Eq. (7.6)). The range of the Stokes number (which varies from zero to ≈ 40 over the simulation) acknowledges the visco-inertial regime expected from this granular flow considering the material and flow characteristics. Furthermore, Figure 7.19 shows that the approximated volume fraction of the mixture particles, $\langle \phi \rangle_i$ from Eq. (7.23), reduces at the interface applying the effects of the suspension of the solid grains in their rheology model. The proposed model for the effective viscosity of the water particles (Eq. (7.22)) includes the turbulent properties of the fluid flow and the volume fraction of the solid grains at the interface. These effects are essential to be considered in the constitutive law as the dynamic viscosity of water particles increases considerably (≈ 30 times the reference viscosity of water, μ_w , in the highly deformed regions) impacting on the mechanical behavior of the granular flow (Figure 7.19).

Furthermore, we compare the $\mu(I_v, I_m, \phi)$ model with the $\mu(I)$ rheology (validated in [112, 135]) considering the same yield stress terms. The inertial number of the $\mu(I)$ rheology is a function of the drag coefficient, C_d , and water density ($I = |\dot{\gamma}| d_g \sqrt{\rho_{0w} C_d / p_{\text{eff}}}$) and is included in the post-failure term of case 2D as follows [104]:

$$\eta_i = \frac{|\tau_y|_i}{\sqrt{|\dot{\gamma}|_i^2 + \lambda_r^2}} + \frac{\Delta\mu p_{\text{eff}i}}{I_0 \sqrt{\frac{p_{\text{eff}i}}{d_g^2 \rho_{0w} C_d} + |\dot{\gamma}|_i + \lambda_r}} \quad (7.28)$$

where $I_0 = b$ and $C_d = 0.47$ for $i \in \Omega_m$ (the other calculation and boundary conditions of case 2D are identical to case 2A) (see Appendix 7.6 for more details regarding the regularized $\mu(I)$ rheology). The viscosity field of the mixture particles (in the logarithmic scale) obtained

via the rheology models is plotted in Figure 7.20. Thanks to the diffusive term implemented, cases 2A and 2D represent smooth viscosity fields. Comparing the interface profiles with the experimental results shows that the $\mu(I)$ rheology reproduces almost similar evolution of the granular collapse. This indicates that the yield stress term (as a function of the effective pressure and the strain rate magnitude) is dominant in the rheology of the granular collapse. However, the result shows that the $\mu(I)$ model underestimates the post-failure viscosity as the granular phase collapses, leading to incompatibility between the normalized runout distance of case 2D and the experimental result (Figure 7.22). While including the mixed number (I_m) and the term containing the volume fraction (ϕ) within the regularized visco-inertial model (Eq. (7.21) implemented in case 2A) simulates an accurate spreading length of the granular deposit.

Role of effective pressure

In the next step, we evaluate the role of the consistent effective pressure in the rheology of the immersed granular collapse. To do so, we employ the hydrostatic assumption for the pore-water pressure in test case 2E and compare the results with case 2A which contains the proposed equation (7.26). In case 2E with the same calculation and boundary conditions as case 2A, the hydrostatic assumption calculates the pore-water pressure according to the spatial position of the mixture particle and the free-surface of the water phase (i.e., $p_{\text{eff}_i} = p_i - \rho_{0w}g_y(h_{wi} - y_i)$ where h_{wi} is the height of water column in which the mixture particle is located and y_i is the position of the mixture particle from the bottom wall of the channel). Figure 7.21 compares the effective pressure fields of case 2A vs case 2E. The results show that the consistent effective pressure by including the hydrodynamics properties of the mixture particles within the rheology model predicts accurate evolutions of the mixture phase forming the granular deposit. However, in case 2E, the hydrostatic assumption overestimates the effective pressure at the yielded regions increasing the viscosity. This may result from the low-frequency oscillation of the pressure inserted in the effective pressure estimation. Hence, the evolution of the granular collapse simulated by case 2E becomes inconsistent with the experimental results (Figure 7.21). Particularly, the runout distance of case 2E versus the other test cases and the experimental results confirms the overestimation of effective pressure affecting the granular flow (Figure 7.22).

7.5.3 Immersed granular landslide

Simulating the immersed granular landslide deals with complex mechanical behaviors concerning the mixture of solid grains and water due to the highly dynamic granular flow. This

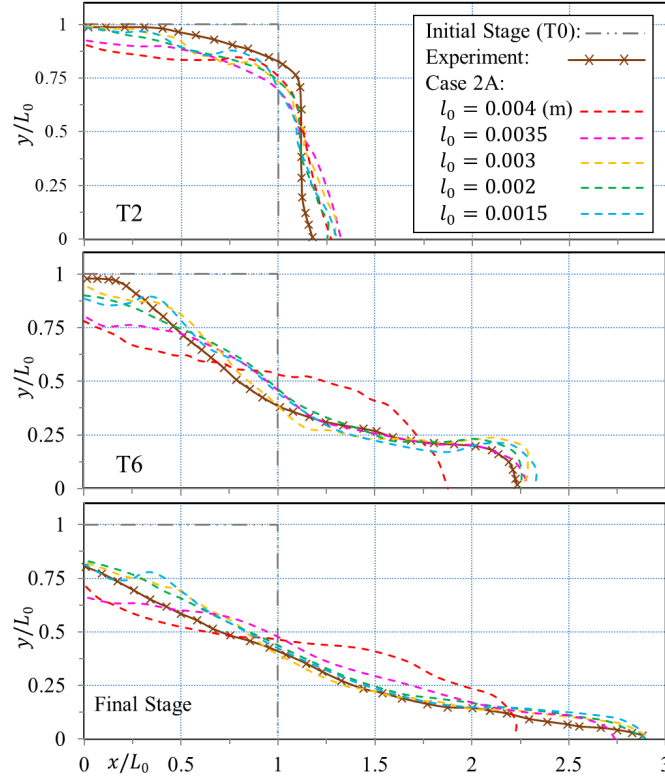


Figure 7.13 Time evolutions of the non-dimensional interface profiles of the immersed granular collapse; the experimental results vs the numerical simulations (Case 2A with $l_0 = 0.004, 0.0035, 0.003, 0.002, 0.0015$ m at the sidewall section and T2, T6, and the final stage).

characteristic of the granular landslide challenges the numerical models for capturing and predicting its evolution. Several experimental and numerical studies have focused on the landslides to represent a practical tool for predicting the mixture flow and generated waves (e.g., [10, 93, 222, 229–232]). Particle methods have been widely applied for dealing with such a problem (e.g., [112, 134, 200, 206, 212, 233, 234]). Here, to show the effectiveness of the proposed developments, we simulate the immersed granular landslide in the three-dimensional configuration via the EWC-MPS method. We set up the numerical model based on the physical model of test case S7 in [10] (Figure 7.23). In this multiphase problem, the triangle heap of the solid grains (with $l_g \times h_g$ dimensions and the same material properties presented in Table 7.3) is submerged within ambient water on an inclined plane with a slope angle of 45-degree. As the physical gate is lifted (with $v_g = 1$ m/s), the granular bulk (as the mixture phase) slides on the smooth wall under the gravitational forces (\mathbf{g}). Meanwhile, the drag force induced by water suspends the solid grains forming vortices rolling the mixture phase [10].

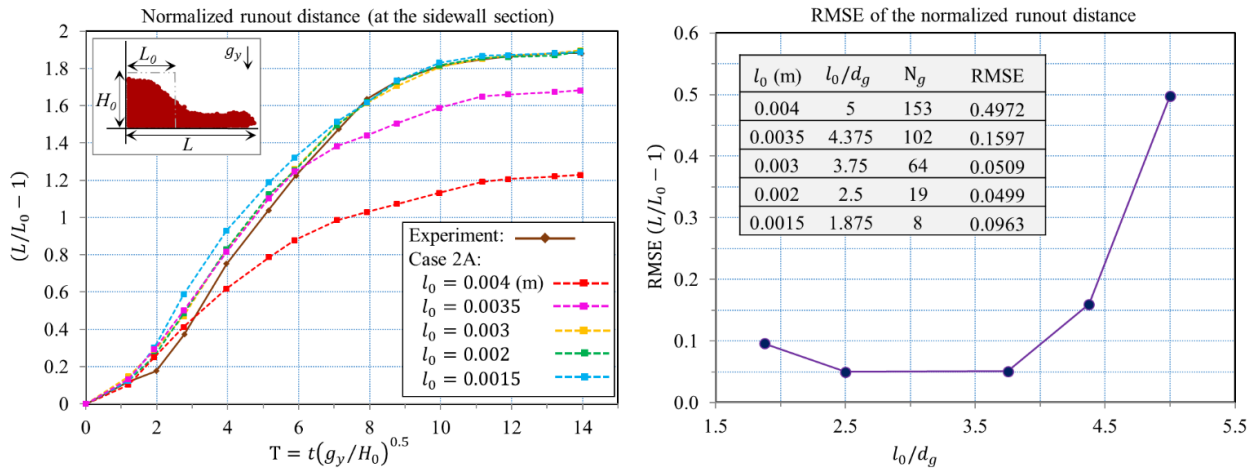


Figure 7.14 Normalized run-out distances (L/L_0-1) (left-graph) and the RMS Errors of (L/L_0-1) (right-graph and the inset table) of the immersed granular collapse (Case 2A with $l_0=0.004, 0.0035, 0.003, 0.002, 0.0015$ m). The mean diameter of the solid grains is $d_g = 0.0008$ m and N_g is the number of solid grains that the macroscopic scale of the particle method (i.e., a mixture particle) represents in the 3D problem (with $\phi = 0.64$).

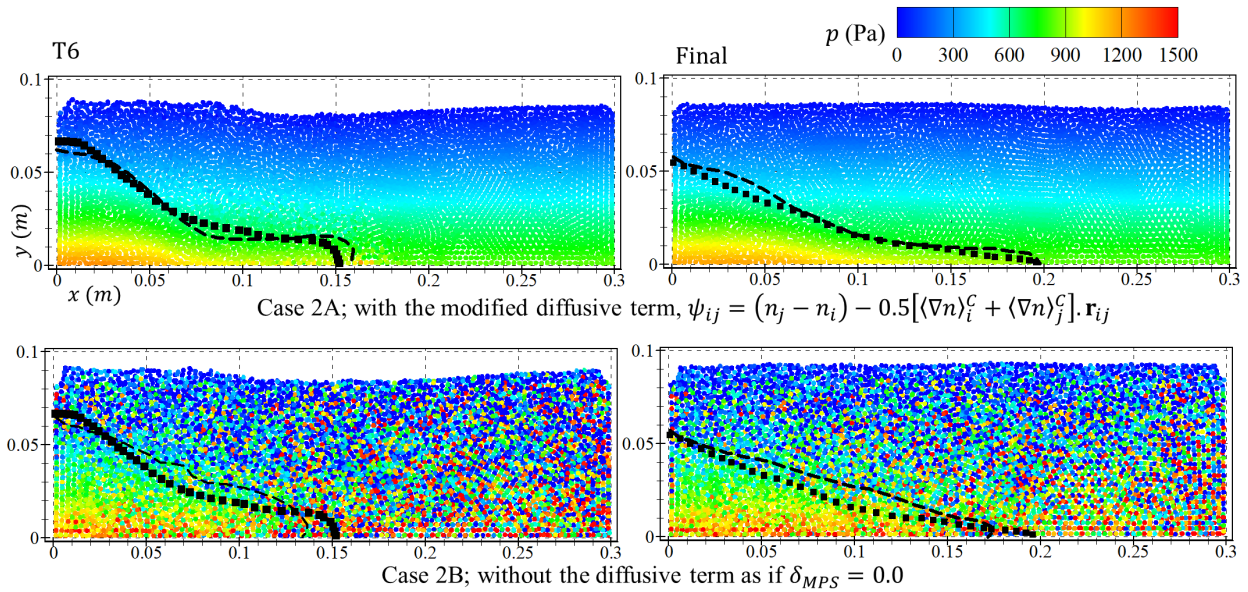


Figure 7.15 The pressure field of the fluid particles at the sidewall section; Case 2A vs Case 2B ($l_0 = 0.003$ m). The black squares correspond to the interface profiles of the experimental results. The long-dashed lines represent the interface of the water and the mixture particles in the numerical model.

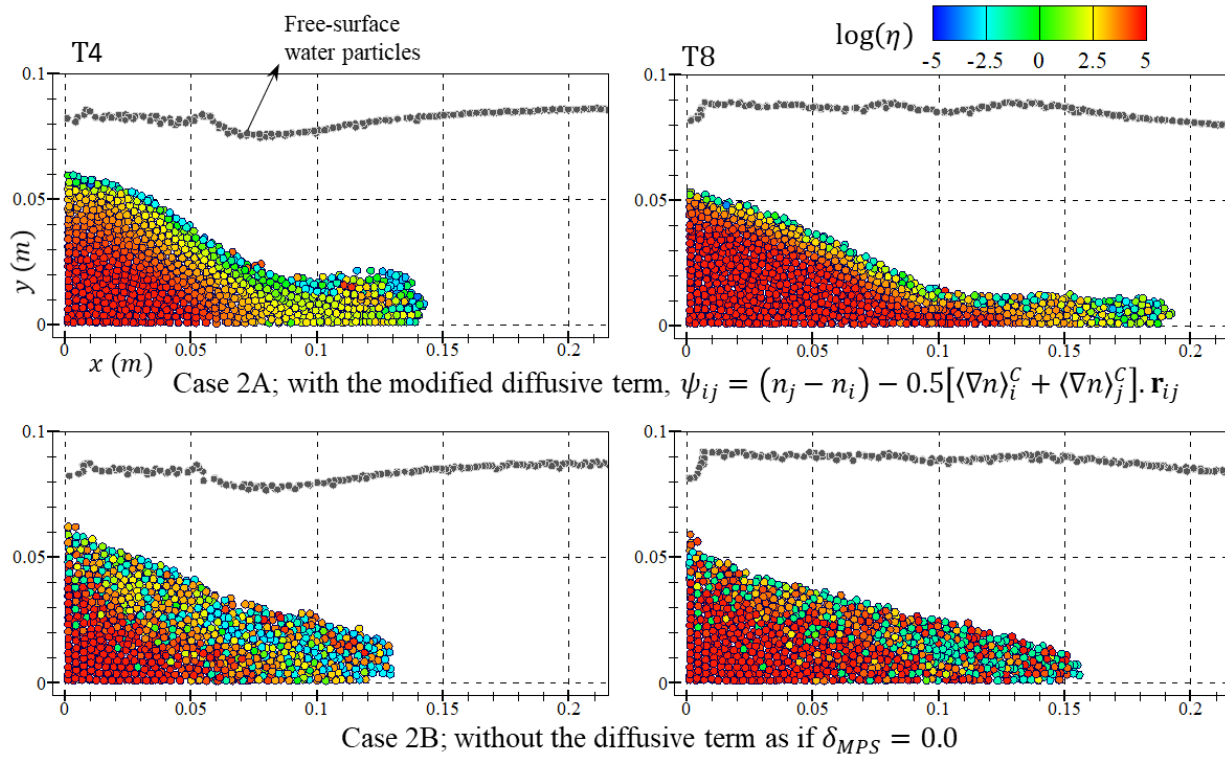


Figure 7.16 The viscosity field of the mixture particles at the middle section; Case 2A vs Case 2B ($l_0 = 0.003 \text{ m}$). The water particles detected as the free-surface particles are identified.

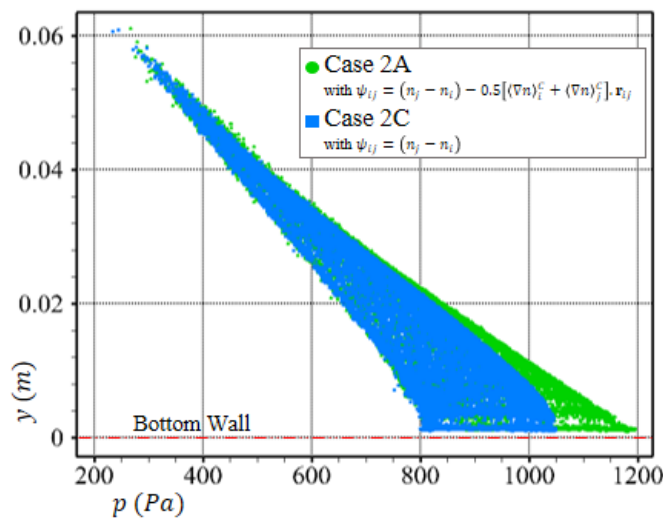


Figure 7.17 The total pressure of the mixture particles concerning their vertical position ($p_i - y_i$) at the final stage of the simulation, $t = 1.60 \text{ second}$; Case 2A vs Case 2C ($l_0 = 0.003 \text{ m}$)

Table 7.7 Calculation time per iteration for simulating Case 2A with different resolutions using NVIDIA V100 Volta GPU device

l_0 (m)	0.004	0.0035	0.003	0.002	0.0015
Number of fluid particles	39,375	47,012	92,400	315,000	739,200
Time per iteration (s)	0.051	0.098	0.143	0.349	0.851

With three different strategies defined in Table 7.8, we simulate the immersed granular landslide in which the particles with the initial spacing of 0.003 m discretize the computational domain. The corresponding particle count including the solid boundaries and virtual gates is 895,912. The output of the particle packing method is considered as the initial distribution of particles for calculating the averaged n_0 of the internal particles and applying the initial hydrostatic pressure (Figure 7.23). The nondimensional time scale is set to $T = t\sqrt{g_y/H_0}$, H_0 being the initial height of the granular phase from the bottom wall equal to 0.22 m . We extract the numerical results (from the middle and sidewall sections of the channel) to validate with the experimental measurements at the time steps given in Table 7.9. The sound speed within the bulk modulus is set to 24 m/s and $\eta_{max} = 400 Pa.s$. In all the test cases in this section, we implement the CPS method as the particle regularization technique and the modified diffusive term (Eq. (7.19)) with $\delta_{MPS} = 0.6$. In analogy to the previous test case, the virtual moving particles representing the physical gate are moved with the true velocity of 1.0 m/s in the y -direction, while their velocity parameter included in the governing equations of the fluid particles is set to $0.2v_g$. To simulate the semi-slip boundary condition, we reduce the viscosity of the wall (or the virtual) particle, j , interacting with the fluid particle, i , to 0.1 of the effective viscosity of the fluid particle (i.e., $\eta_j = 0.1\eta_i$ as if $\gamma_s = 0.1$). As the virtual gate is being opened and until the runout length, L , remains almost equal to l_g (i.e., until T0 shown in Figure 7.24-a) the model reinitializes the pore-water density imposing the hydrostatic condition.

We represent the three-dimensional results of the immersed granular landslide (case 3A) in Figure 7.24: the initial stage at T0, the approximated volume fraction and the velocity of the mixture particles at T3 and T4, respectively, and the final stage of the granular landslide (see the supplementary results for the movies of the simulated granular slide). With the free-surface detection algorithm (implemented as a part of the CPS technique) the generated wave formed by the submerged landslide is identified. Figure 7.24-b shows that the approximated volume fraction reduces at the interface due to the inter-phase shear forces suspending the mixture particles and forming circulations within the fluid flow. The bulk of the mixture with an average velocity of around 0.5 m/s approaches the slope toe at T4 and the mixture

particles come to rest on the bottom wall at $t = 1.49$ seconds (Figure 7.24-c & d). However, few mixture particles remain suspended within the water phase (as the viscous forces damp the kinetic energy and balance their weight).

To validate the developed three-dimensional model, we extract the numerical results from a viewpoint almost identical to the position of the camera used in the experiment (which is perpendicular to the sidewall and above the bottom wall of the channel). We represent the evolution of the submerged granular landslide simulated by case 3A and the scaled snapshots taken from the multimedia file of the experiment (provided in [10]) in the right and left columns of Figure 7.25, respectively. Plotting the outlines of the mixture particles (the continuous green lines) on the corresponding snapshots of the experiment, we compare the overall deformation of the landslide. In the experiment, as the gate opens the rapid fluid flow suspends the solid grains in the water expanding the volume of the mixture (i.e., reducing the local mass). The numerical model needs to simulate the water flow between the solid grains (as a deformable porous media) to capture this mixing process. Since the governing equations (Eq. (7.11)) do not simulate the mass exchange between the fluid particles, the current model overlooks the volume expansion observed at the initial stages of the landslide. Particularly at T2, the evolution of the mixture becomes incompatible with the experimental profile. This occurs as the numerical model initially overestimates the velocity of the mixture particles with the constant mass. However, we should note that the overall deformations of the landslide simulated by the proposed model are comparable to the experimental figures (Figure 7.25). Further, the results show that the constitutive laws implemented (through equations (7.21) and (7.22)) indirectly include the interphase drag force creating vortices and suspending the mixture particles from the interface (for $T > T2$). Figure 7.26 illustrates the velocity vectors representing the counterclockwise circulation of the fluid flow as the mixture particles approach the slope toe (at T4).

Moreover, we observe that the normalized runout distance of case 3A is in good agreement with the experimental measurement (almost identical to the experimental profile), particularly for $T \leq T6$, where the main evolution of the landslide occurs (Figure 7.27). Nevertheless, the particles separated from the granular bulk remain suspended for $T \geq T7$, while in the experiment the solid grains settle increasing the runout distance in the x -direction. Treating the mixture as an effective fluid in the single-phase formulations (represented by the mixture particles) might cause this discrepancy between the numerical and experimental runout distances at the late stages.

The non-dimensional numbers governing the visco-inertial model are represented in Figure 7.28. While the viscous number remains below 0.015, the inertial number surpasses the limit

suggested for the rheology model. However, the mixed number in the main body of the mixture phase is below its maximum limit (i.e., $I_m \lesssim 0.6$). The local Stokes number varies between 0 and 100 over the mixture phase indicating the different states of the immersed granular flow captured by the regularized visco-inertial model. We implement the local $\mu(I)$ rheology (based on the inertial number given by Eq. (7.28)) in case 3B and achieved almost identical results to case 3A. Comparing the runout distances of case 3A with 3B (in Figure 7.27) confirms that both rheology models predict the same evolution of the granular since the inertial regime is dominant in this landslide (unlike the immersed granular collapse test case). Figure 7.29 shows that in regions where the separation from the granular bulk occurs the approximated volume fraction of the mixture particles reduces to almost half of the reference volume fraction of the mixture phase (ϕ). Further, considering the turbulence model within the dynamic viscosity of the water particles, is shown to be effective and essential for simulating the interphase forces (as η_i/μ_w increases considerably in the region with the high strain rate magnitudes). It should be noted that the free-surface detection algorithm implemented within the CPS technique represents the generated wave by the landslide in Figure 7.29 at T2, T4, and T6.

In test case 3C, we implement the hydrostatic pore-water pressure to update the effective pressure within the mixture particles. The evolution of the landslide simulated by case 3A and 3C are compared in Figure 7.30 (at T3). Like the granular collapse test case (2E), the hydrostatic assumption in case 3C overestimates the viscosity field (by neglecting the hydrodynamic aspects of the fluid flow). In the case of 3A, with the consistent effective pressure included in the rheology model, the fluidity expected in the mixture is well captured. Particularly, the runout length of case 3C compared with the experimental and the other test cases (in Figure 7.27) indicates the overestimation of the effective pressure via the hydrostatic assumption for the pore-water pressure. Moreover, Figure 7.30 shows the effectiveness of the modified diffusive term for estimating a smooth pressure field (i.e., by eliminating the high-frequency pressure noises) over the fluid domain.

Table 7.8 The numerical test cases of the immersed granular landslide

Case	Rheology model	Effective pressure
3A	Regularized $\mu(I_v, I_m, \phi)$	Consistent effective pressure
3B	Regularized $\mu(I)$	Consistent effective pressure
3C	Regularized $\mu(I_v, I_m, \phi)$	With the hydrostatic assumption for p_{pw}

Table 7.9 Time steps of the extracted data from the numerical simulations, $T = t\sqrt{g_y/H_0}$

Labels	T0	T1	T2	T3	T4	T5	T6	T8
Time (s)	0.00	0.15	0.30	0.45	0.60	0.75	0.90	1.20
T	0	1	2	3	4	5	6	8

7.6 Conclusion

We represented a developed single-phase particle method based on the EWC-MPS method capable of simulating mechanical behaviors of the immersed granular flows. This multi-viscosity multi-density system proved to be effective and essential for simulating the interactions between water and mixture phases. We developed the rheology model via the regularized visco-inertial model, the consistent effective pressure, and higher-order operators for the velocity gradient and the diffusive term in the context of multiphase problems. Further, we included the turbulent viscosity and the linear effects of the suspension at the interface within the constitutive laws.

We showed the effectiveness of the modified diffusive term by predicting the hydrostatic pressure in a two-dimensional steady tank filled with two fluid phases. The convergence study that we conducted for this benchmark case confirmed that the modified diffusive term significantly reduces the numerical errors and increases the order of convergence of the results by eliminating the kernel truncation errors and thus, predicting accurate particle number density near the boundaries. We simulated the three-dimensional gravity-driven granular collapse and the deformable landslide to verify and validate the multiphase model. The results represented the capability of the proposed developments in capturing the complex flow deformation including the viscous and inertial regimes. Further, the modified diffusive term proved to be essential for removing the noisy pressure field and obtain an accurate viscosity prediction. The regularized visco-inertial rheology model consists of non-dimensional numbers and the approximated volume fraction of the mixture particles simulated the time evolution and the dominant flow regimes of the immersed granular problems. Furthermore, utilizing the proposed constitutive relation for calculating the pore-water pressure, not only exempts the model from the complexity of detecting the interface but also results in an accurate and stable viscosity field. Although the single-phase and continuum-based model is still incapable of modeling the fluid flow between the solid grains, the developed model represents promising outcomes in simulating the suspension process and forming the flow circulations within the mixture and water phases. Overall, the compatibility between the numerical results and the presented experimental measurements confirmed the robustness

of the proposed developments for studying the underlying physics of the immersed granular flows.

The model we have developed in this study can be employed for validating the generated waves by the transitional and submerged landslides in large-scale problems. This may require conducting three-dimensional experiments of the granular flows in various hydrodynamic conditions and with different granular materials (e.g., [230, 232]). It is also worthwhile to investigate the GPU implementation of this work for demonstrating the efficiency of the 3D code in simulating large-scale problems. Moreover, the non-local rheology models [235] can be coupled with the governing equations to study the nonlocal effects of the granular shear properties in the multiphase flows. Meanwhile, the EWC-MPS method of this work can be extensible to the two-phase mixture models [20, 98] capable of simulating the fluid flow through the solid grains to include the role of saturation degree in the rheology model.

Appendix A. Derivation of the regularized rheology equations

Here, we derive the regularized constitutive equations of the visco-inertial rheology, $\mu(I_v, I_m, \phi)$, and the $\mu(I)$ rheology used in the simulations (in the form of equations (7.21) and (7.28), respectively). Both rheology models diverge as the magnitude of the strain rate tensor vanishes (i.e., $|\dot{\gamma}| = 0$). The regularization techniques have been represented to resolve this singularity issue in the computational models (see [104]).

For the visco-inertial rheology equation (7.6), we employ Eq. (7.7) to write the effective viscosity of the mixture phase, η_m , as follows:

$$\eta_m = \frac{\mu_1 p_g}{|\dot{\gamma}|} + \frac{\Delta\mu p_g}{(b/I_m)|\dot{\gamma}| + |\dot{\gamma}|} + \frac{5\phi}{2a} \left(\frac{I_v p_g}{I_m |\dot{\gamma}|} \right) \quad (7.29)$$

which contains the yield stress (the first term on the right-hand side, denoted as Term – 1) and the post-failure (the second and third terms denoted as Term – 2 and 3) terms. In our proposed rheology model, the Bercovier and Engleman [218] formulation regularizes the yield stress term given as:

$$\text{Term – 1 : } \frac{|\tau_y|}{\sqrt{|\dot{\gamma}|^2 + \lambda_r^2}} \quad (7.30)$$

in which $|\tau_y| = \mu_1 p_g$ and λ_r being the regularization parameter set as $\lambda_r \ll 1$. With inserting the non-dimensional numbers (7.5) and some mathematical simplifications, we can rewrite the second term, as:

$$\text{Term} - 2 : \frac{\Delta\mu p_g}{\frac{b\sqrt{p_g}}{\sqrt{d_g^2\rho_g + \frac{2\mu_w}{|\dot{\gamma}|}}} + |\dot{\gamma}|}. \quad (7.31)$$

Using the simple model for the regularization (represented in Frigaard and Nouar [219]) of the $2\mu_w/|\dot{\gamma}|$ term, and by noting that $p_g > 0$, the second term reduces to:

$$\text{Term} - 2 : \frac{\Delta\mu p_g}{\frac{b\sqrt{p_g}}{\sqrt{d_g^2\rho_g + \frac{2\mu_w}{|\dot{\gamma}| + \lambda_r}}} + |\dot{\gamma}|}. \quad (7.32)$$

The third term by substituting the non-dimensional numbers (7.5) into the equation is given as follows:

$$\text{Term} - 3 : \frac{5\phi}{2a} \left(\frac{\mu_w \sqrt{p_g}}{\sqrt{|\dot{\gamma}|^2 d_g^2 \rho_g + 2\mu_w |\dot{\gamma}|}} \right) \quad (7.33)$$

and considering the Bercovier and Engleman [218] regularization equation, reads:

$$\text{Term} - 3 : \frac{5\phi}{2a} \left(\frac{\mu_w \sqrt{p_g}}{\sqrt{|\dot{\gamma}|^2 d_g^2 \rho_g + 2\mu_w |\dot{\gamma}| + \lambda_r^2}} \right). \quad (7.34)$$

Eventually, substituting the terms (7.30), (7.31), (7.32), and (7.34) into Eq. (7.29), the regularized visco-inertial model would be the following equation:

$$\eta_m = \frac{|\tau_y|}{\sqrt{|\dot{\gamma}|^2 + \lambda_r^2}} + \frac{\Delta\mu p_g}{\left(\frac{b\sqrt{p_g}}{\sqrt{d_g^2\rho_g + 2\mu_w/(|\dot{\gamma}| + \lambda_r)}} + |\dot{\gamma}| \right) + \frac{5\phi}{2a} \left(\frac{\mu_w \sqrt{p_g}}{\sqrt{|\dot{\gamma}|^2 d_g^2 \rho_g + 2\mu_w |\dot{\gamma}| + \lambda_r^2}} \right)} \quad (7.35)$$

used as Eq. (7.21) in the numerical model.

For the $\mu(I)$ rheology model, proposed by Jop et al. [99] as:

$$\mu(I) = \mu_1 + \frac{\Delta\mu}{(I_0/I) + 1} \quad (7.36)$$

the effective dynamic viscosity of the mixture phase given by Eq. (7.7) would be:

$$\eta_m = \frac{\mu(I) p_g}{|\dot{\gamma}|} = \frac{\mu_1 p_g}{|\dot{\gamma}|} + \frac{\Delta \mu p_g}{(I_0/I) |\dot{\gamma}| + |\dot{\gamma}|} \quad (7.37)$$

where the yield stress term can be regularized similar to Eq. (7.30). By substituting the inertial number of the immersed granular flows (i.e., $I = |\dot{\gamma}| d_g \sqrt{\rho_{0w} C_d / p_{\text{eff}}}$) [93, 112] and the simple model for regularizing the post-failure term, the regularized $\mu(I)$ rheology equation is represented as follows [104]:

$$\eta_m = \frac{|\tau_y|}{\sqrt{|\dot{\gamma}|^2 + \lambda_r^2}} + \frac{\Delta \mu p_g}{I_0 \sqrt{\frac{p_g}{d_g^2 \rho_{0w} C_d} + |\dot{\gamma}| + \lambda_r}} \quad (7.38)$$

which in the numerical model is implemented as Eq. (7.28).

Appendix B. The solution algorithm based on the symplectic scheme

In this paper, we employed the explicit second-order symplectic scheme represented by Monaghan and Rafiee [11] as the time integration algorithm. This time integrator solves the governing equations and applies the boundary conditions in two stages of calculations identified in Figure 7.31. The first stage calculates the flow properties at the mid-point, $t + \Delta t/2$. With the mid-point values, the second stage updates the velocity field, and therefore the position and the particle number density fields, at $t + \Delta t$. In this stage, the divergence of the velocity (Eq. (7.13)) and the modified diffusive term (Eq. (7.19)) are functions of the particle number density at the mid-point, i.e., $n^{t+\Delta t/2}$.

The numerical model consists of subroutines run on the Computer Processing Unit (CPU) or the Graphical Processing Unit (GPU) (as the host and device parts of the code, respectively). We adopted CUDA C++ as the parallel programming language to utilize the massive parallelism of the GPU's threads. The host section of the code initializes the model (i.e., allocates memories, reads the geometry file, and transfers data from the host to the GPU's memories) and saves the data for the post-processing tasks. The device section implements the neighbor search algorithm (see [47]) and the main temporal loop of solving the governing equations (i.e., Eq. (7.11), (7.12)) supplied with the modified diffusive term (Eq. (7.20)) and the corrected particle shifting technique (see [123]) (Figure 7.31). In the temporal loop of the calculation, the viscosity field, η_i , is calculated at the beginning of the first and second half of each time step. Moreover, the particle stabilization technique only regulates the fluid particles in the second stage of the scheme in advance of estimating the particle number density field. Also, the properties of the solid boundary and the virtual gates are updated at the end of each stage of the scheme.

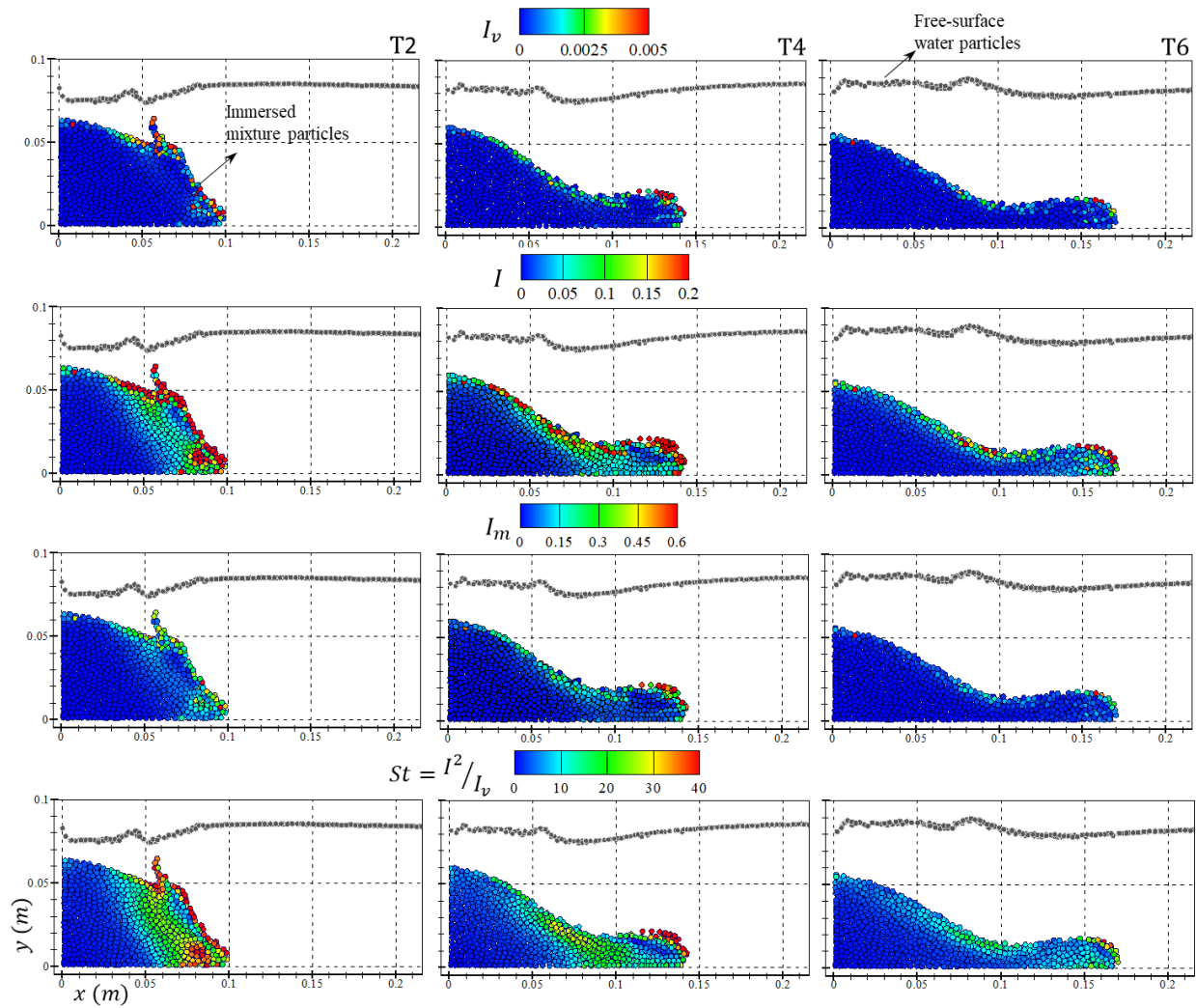


Figure 7.18 The non-dimensional numbers of the visco-inertial rheology model (I_v , I and I_m defined in Eq. (7.5) and St) at the middle section of the channel (Case 2A- $l_0 = 0.003$ m)

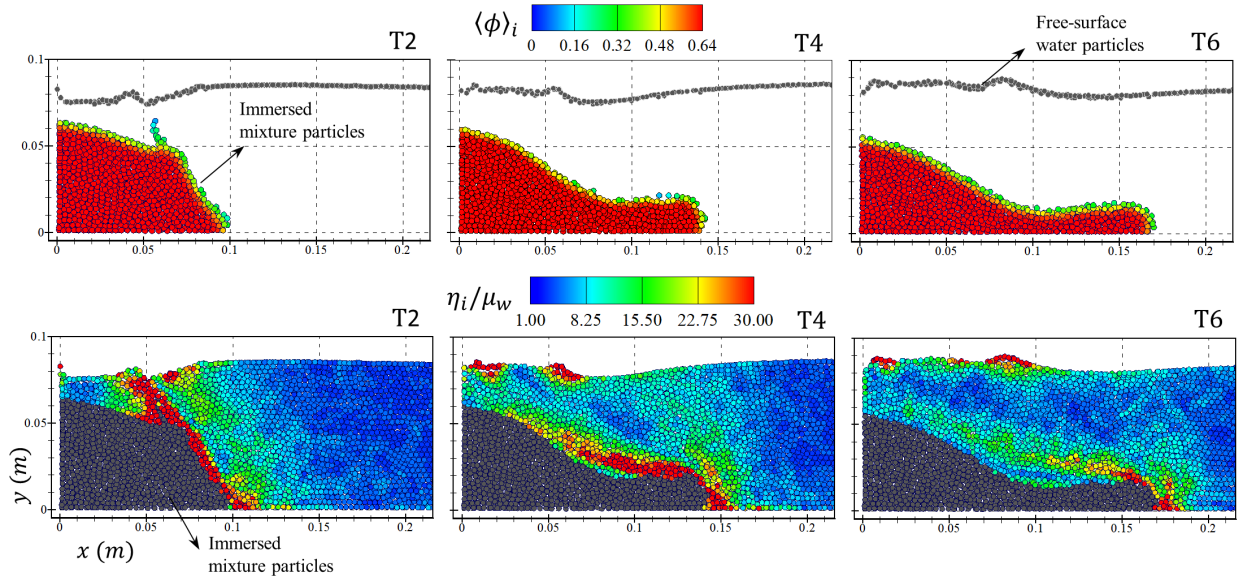


Figure 7.19 The approximated volume fraction of the mixture particles, $\langle \phi \rangle_i$, and the nondimensional scale of the water particles' effective viscosity, η_i/μ_w , at the middle section (Case 2A- $l_0 = 0.003$ m)

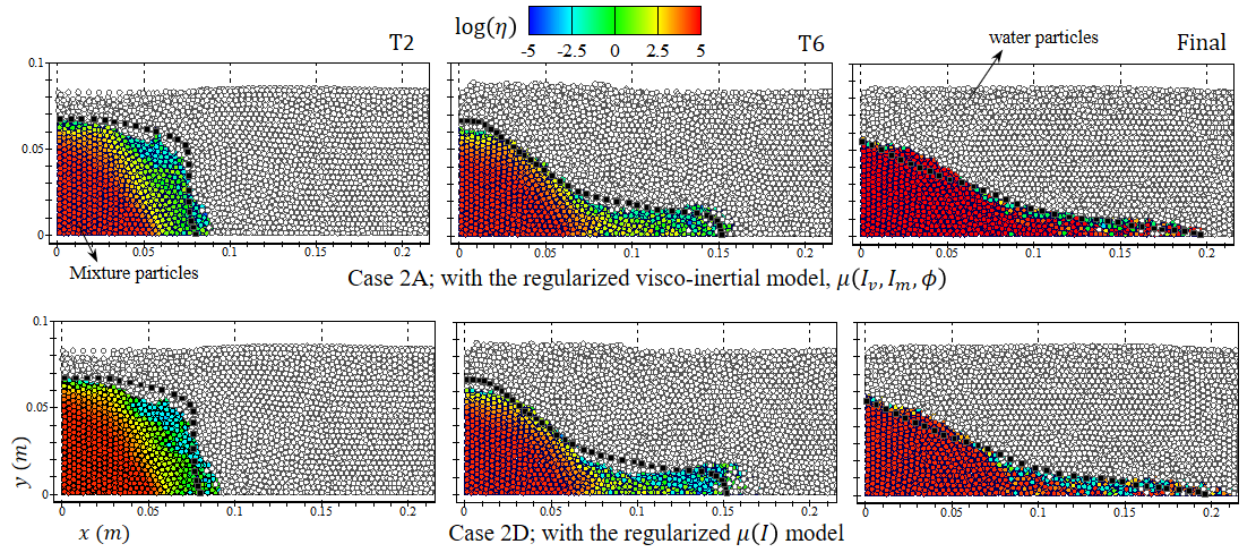


Figure 7.20 The dynamic viscosity field of the mixture particles at the sidewall section; Case 2A vs Case 2D ($l_0 = 0.003$ m). The black squares represent the interface profiles of the experimental results.

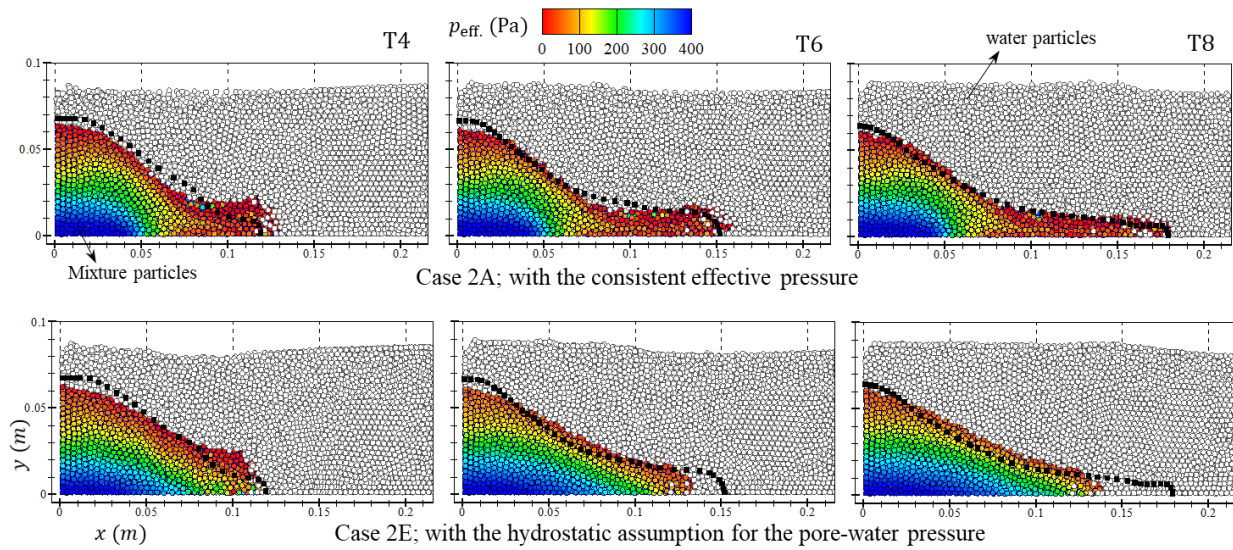


Figure 7.21 The effective pressure within the mixture particles at the sidewall section; Case 2A vs Case 2E ($l_0 = 0.003 \text{ m}$). The black squares represent the interface profiles of the experimental results.

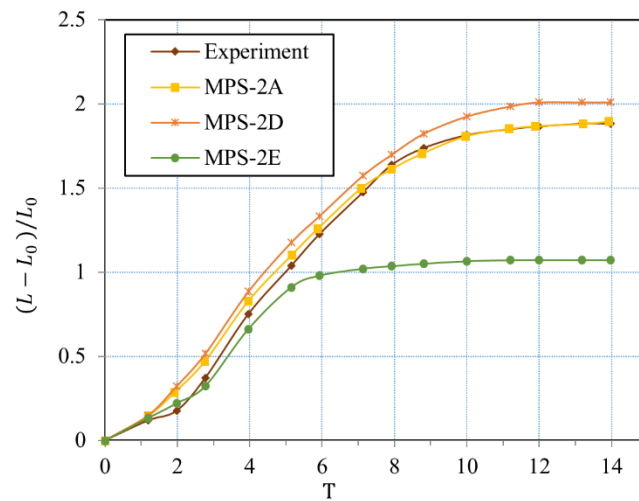


Figure 7.22 The normalized runout distance at the sidewall section; Case 2A vs Case 2D and Case 2E ($l_0 = 0.003 \text{ m}$)

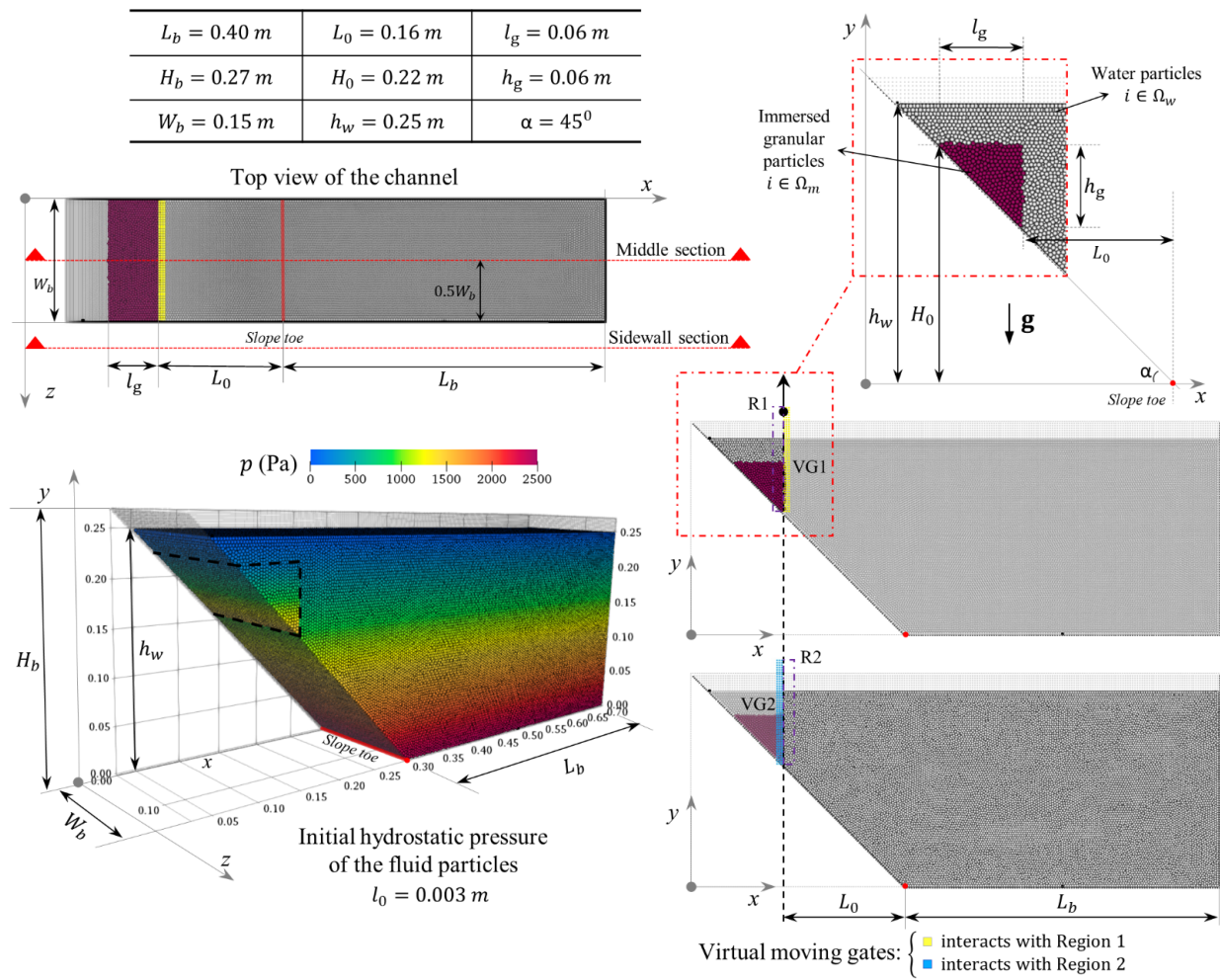


Figure 7.23 The immersed granular landslide; the initial setup of the numerical model and the virtual gates.

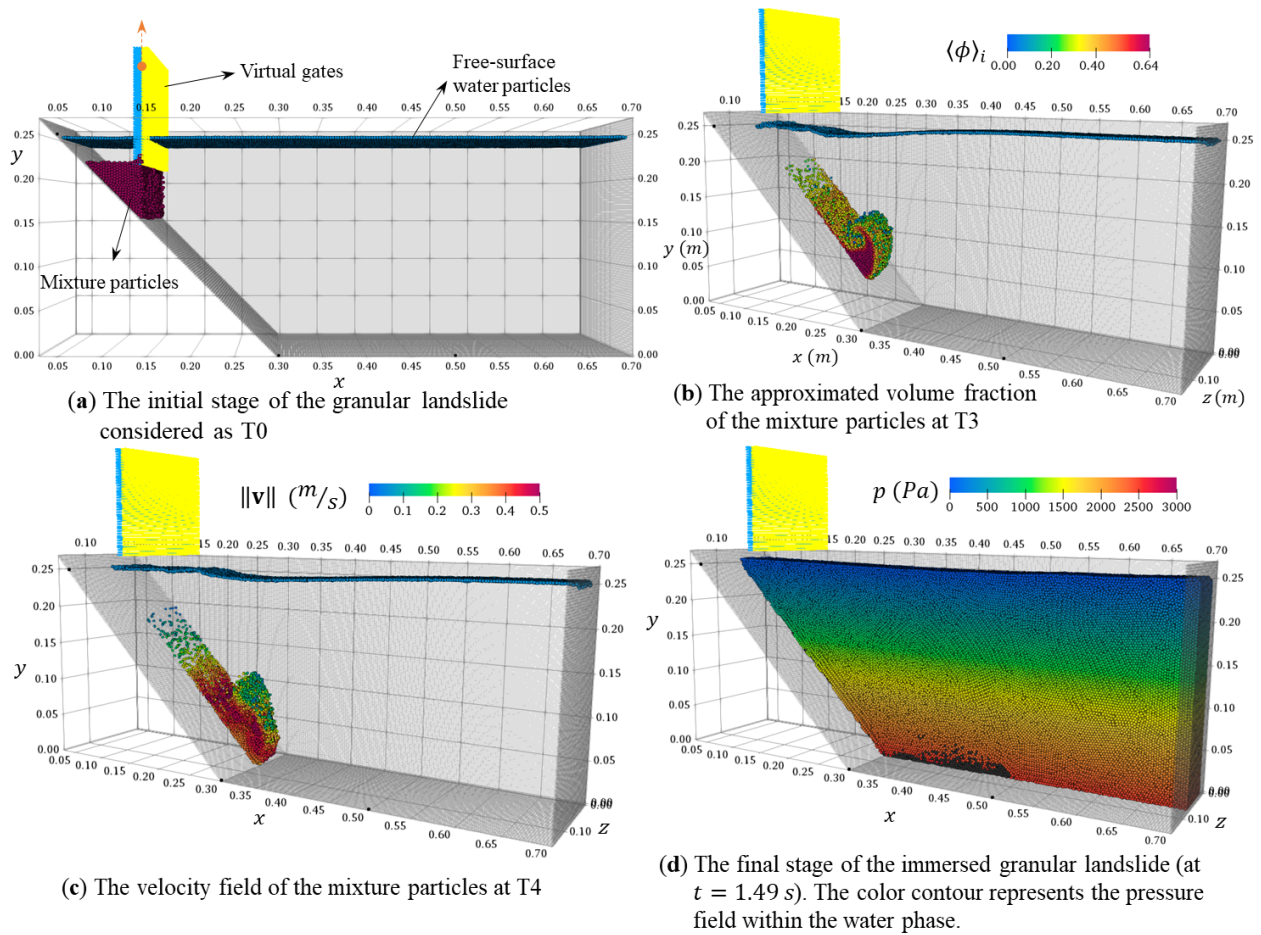


Figure 7.24 The three-dimensional numerical results of the immersed granular landslide at the middle section of the channel with a 45-degree slope (Case 3A)

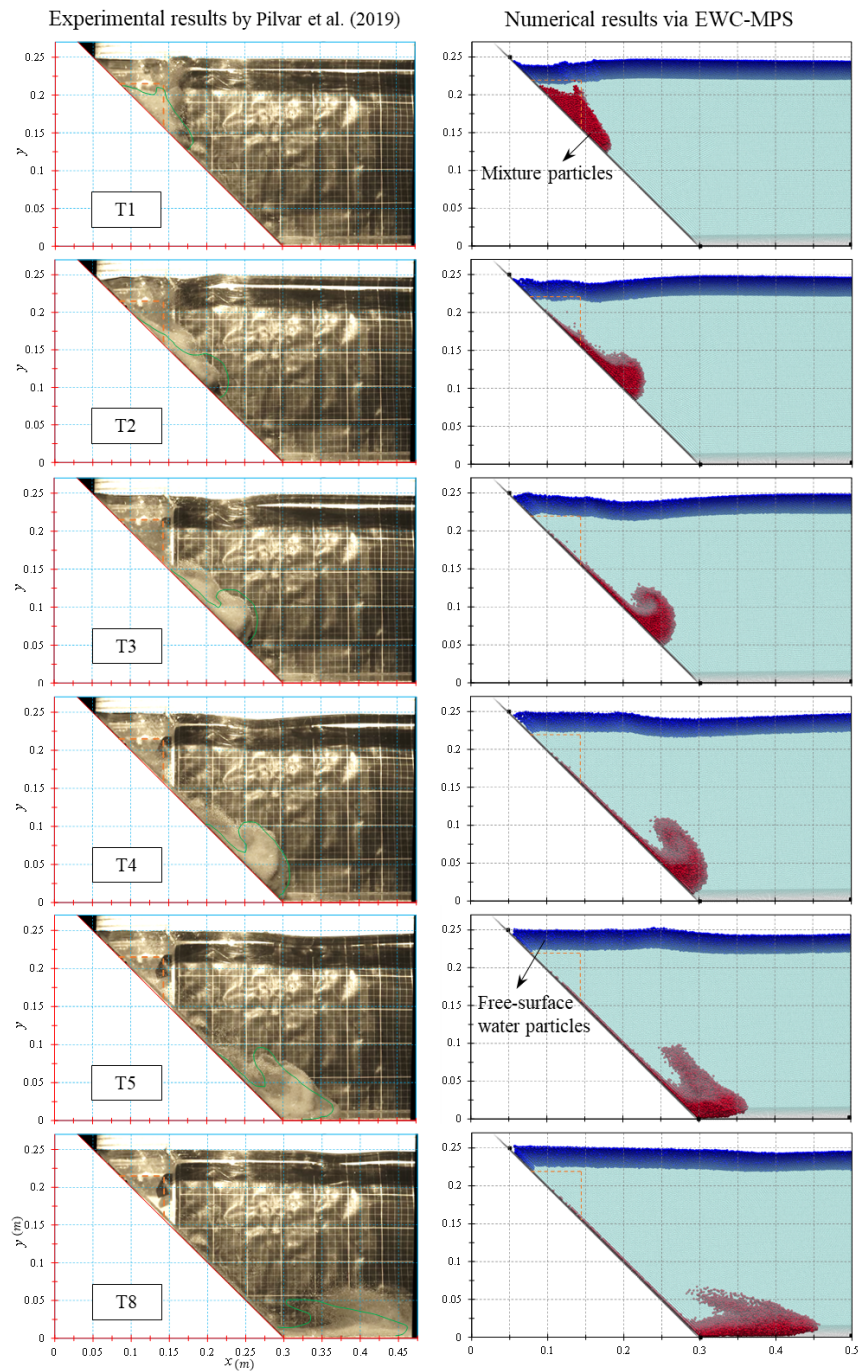


Figure 7.25 The immersed granular landslide; The 3D numerical results of case 3A (from the sidewall view) versus the experimental results of test case S7 extracted from [10] (The orange dash line represents the initial stage of the granular phase (at T0) and the green lines plotted on the scaled snapshots correspond to the outline of the mixture phase in the numerical simulation at each time step. The dark blue particles are the free-surface particles detected by the CPS algorithm).

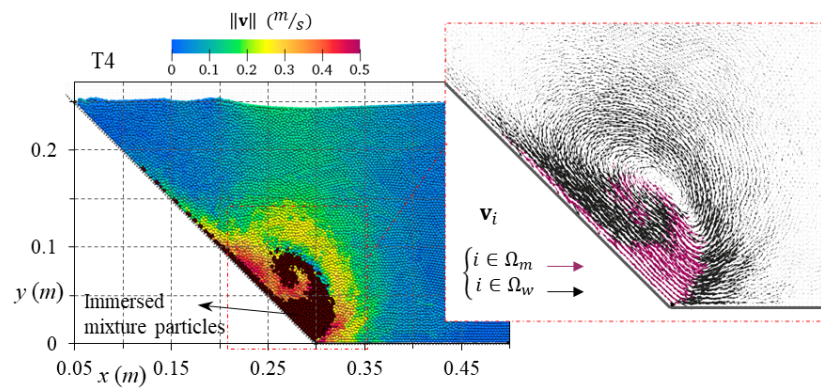


Figure 7.26 The velocity contour and vectors of the submerged landslide at the middle section of the channel at T4 showing the circulation formed by the drag force in the fluid flow (Case 3A)

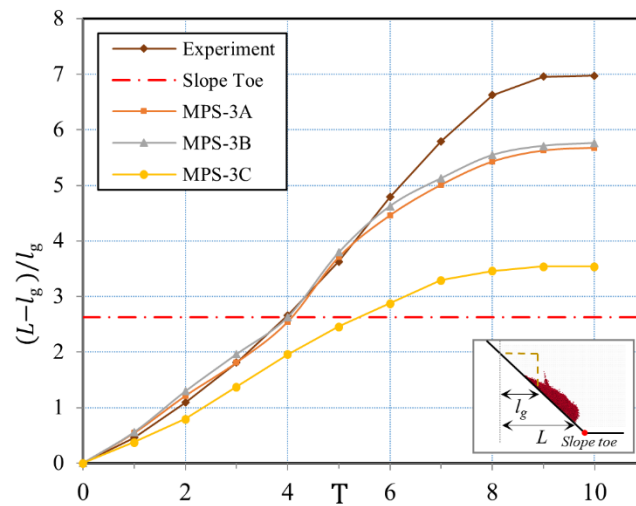


Figure 7.27 The normalized runout distance of the immersed granular landslide; the numerical versus the experimental results (Test case S7 in [10] with a 45-degree slope, smooth surfaces, and glass beads)

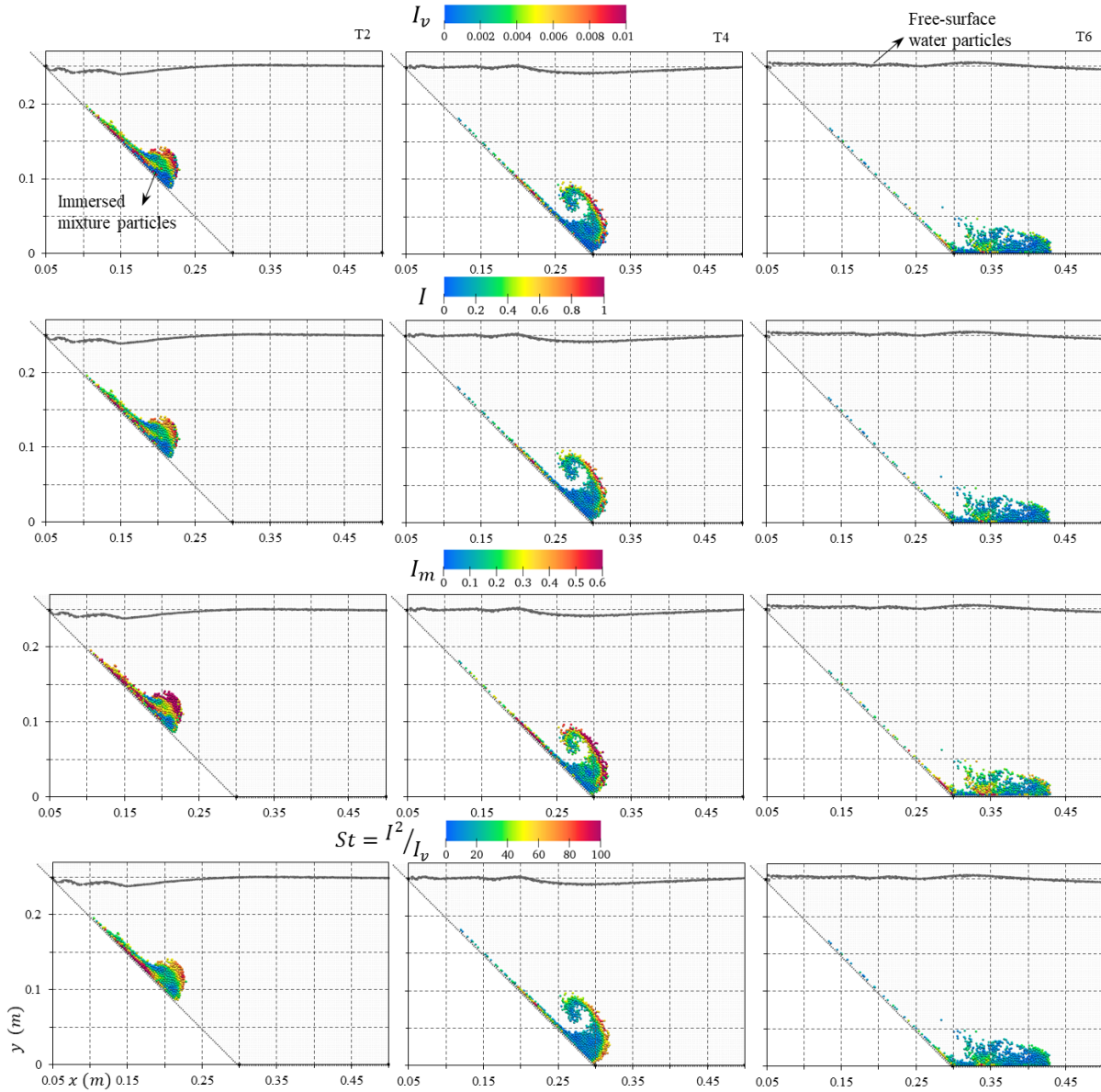


Figure 7.28 The non-dimensional numbers of the visco-inertial rheology model (I_v , I_m and St defined by Eq. (7.5)) at the middle section of the channel (Case 3A)

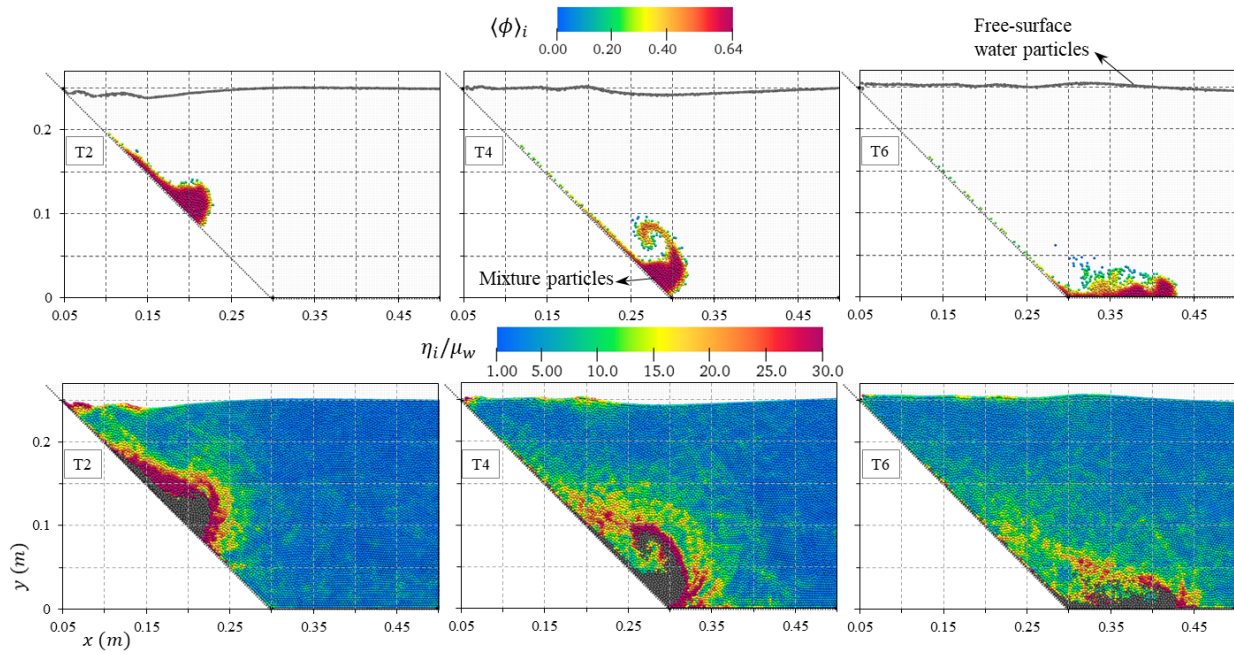


Figure 7.29 The approximated volume fraction of the mixture particles, $\langle \phi \rangle_i$, and the nondimensional scale of the water particles' effective viscosity, η_i/μ_w , at the middle section (Case 3A)

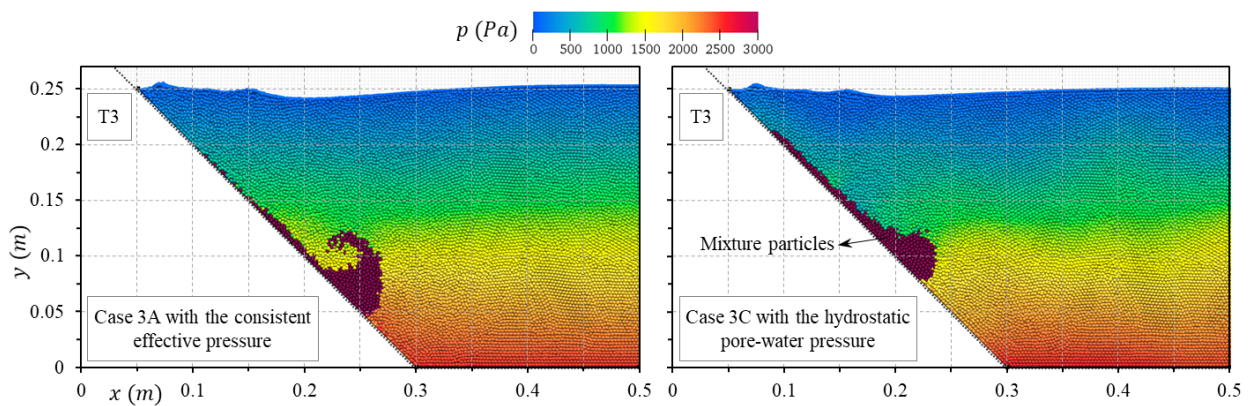


Figure 7.30 The role of the effective pressure in the evolution of the immersed granular landslide; Case 3A vs 3C at the middle section of the channel at T3.

```

Solution Algorithm{
  Initialization:
  • Allocate host memory and assign the basic parameters
  • Read the input file and initialize the system of particles
  • Allocate device memories and transfer data from host to device

  Implemented on a GPU
  • Assign the initial conditions and create the neighbor list

  Main temporal loop:
  While  $t \leq t_{final}$  do {
    • Update the neighbor list
    • Stage 1:
    for  $\forall i \in \Omega_f$  {
      - Update  $\eta_i$  (Eq. (21) for  $i \in \Omega_m$  & Eq. (22) for  $i \in \Omega_w$ )
      -  $\mathbf{r}_i^{t+\Delta t/2} = \mathbf{r}_i^t + 0.5\Delta t \mathbf{v}_i^t$ 
      -  $\mathbf{v}_i^{t+\Delta t/2} = \mathbf{v}_i^t + 0.5\Delta t [-1/\rho_i \langle \nabla p \rangle_i + \mathbf{g} + 1/\rho_i \langle \eta \nabla^2 \mathbf{v} \rangle_i]^t$ 
      -  $n_i^{t+\Delta t/2} = n_i^t + 0.5n_i^t \Delta t [-\langle \nabla \cdot \mathbf{v} \rangle_i + D_i^m]^t$ 
      -  $p_i^{t+\Delta t/2} = B_0 [(n_i^{t+\Delta t/2}/n_0)^Y - 1]$ 
    }
    - Update the solid boundary and the virtual gates

    • Stage 2:
    for  $\forall i \in \Omega_f$  {
      - Update  $\eta_i$  (Eq. (21) for  $i \in \Omega_m$  & Eq. (22) for  $i \in \Omega_w$ )
      -  $\mathbf{v}_i^{t+\Delta t} = \mathbf{v}_i^{t+\Delta t/2} + \Delta t [-1/\rho_i \langle \nabla p \rangle_i + \mathbf{g} + 1/\rho_i \langle \eta \nabla^2 \mathbf{v} \rangle_i]^{t+\Delta t/2}$ 
      -  $\mathbf{r}_i^{t+\Delta t} = \mathbf{r}_i^{t+\Delta t/2} + 0.5\Delta t \mathbf{v}_i^{t+\Delta t}$ 
      - Apply the corrected particle shifting;  $[\mathbf{r}_i' = \mathbf{r}_i + \delta \mathbf{r}_i]^{t+\Delta t}$ 
      -  $n_i^{t+\Delta t} = n_i^{t+\Delta t/2} + 0.5n_i^{t+\Delta t/2} \Delta t [-\langle \nabla \cdot \mathbf{v} \rangle_i^{t+\Delta t} + D_i^{m,t+\Delta t/2}]$ 
      -  $p_i^{t+\Delta t} = B_0 [(n_i^{t+\Delta t}/n_0)^Y - 1]$ 
    }
    - Update the solid boundary and the virtual gates

    • Prepare data for the next time step,  $t = t + \Delta t$ 

  }
  • Save the results occasionally (transfer data from device to host)
}

```

Figure 7.31 Solution algorithm based on the explicit second-order symplectic time integrator by Monaghan and Rafiee [11]. The host part of the code, run on the CPU, initializes the model, and prints the results, while the main temporal loop and the neighbor search algorithm (within the gray box) are run on the GPU.

CHAPTER 8 ARTICLE 5: FLUID-DRIVEN GRANULAR DYNAMICS THROUGH A CONSISTENT MULTI-RESOLUTION PARTICLE METHOD

Authors: Mojtaba Jandaghian¹ and Ahmad Shakibaeinia¹

¹Department of Civil, Geological and Mining Engineering, Polytechnique Montréal, Canada

Journal of Fluid Mechanics

8.1 Abstract

Granular dynamics driven by fluid flow is ubiquitous in many industrial and natural processes, such as fluvial and coastal sediment transport. Yet, their complex multiphysics nature challenges the accuracy and efficiency of numerical models. Here, we study the dynamics of rapid fluid-driven granular erosion through a mesh-free particle method based on the enhanced weakly-compressible Moving Particle Semi-implicit (MPS) method. To that end, we develop and validate a new multi-resolution multiphase MPS formulation for the consistent and conservative form of the governing equations, including particle stabilization techniques. First, we discuss the numerical accuracy and convergence of the proposed approximation operators through two numerical benchmark cases: the multi-viscosity Poiseuille flow and the multi-density hydrostatic pressure. Then, coupling the developed model with a generalized rheology equation, we investigate the water dam-break waves over movable beds. The particle convergence study confirms that the proposed multi-resolution formulation predicts the analytical solutions with acceptable accuracy and order of convergence. Validating the multiphase granular flow reveals that the mechanical behavior of this fluid-driven problem is highly sensitive to the water-sediment density ratio; the bed with lighter grains experiences extreme erosion and interface deformations. For the bed with a heavier material but different geometrical setups, the surge speed and the transport layer thickness remain almost identical (away from the gate). Furthermore, while the multi-resolution model accurately estimates the global sediment dynamics, the single-resolution model underestimates the flow evolution. Overall, the qualitative and quantitative analysis of results emphasizes the importance of multi-scale multi-density interactions in fluid-driven modeling.

8.2 Introduction

Many hydro-environmental and geotechnical problems involve the multiphase flow of granular material, like sediment, immersed in a fluid, like water (Figure 8.1-a). In such multiphysics

systems, the granular phase demonstrates dynamic solid- and fluid-like behaviors induced by gravity and the ambient fluid flow (e.g., in the cases of submarine landslides [10, 19, 90, 91, 94] and fluvial and coastal sediment transport [1, 18, 236]). Particularly, rapid shearing flows over granular beds cause large interfacial deformations leading to the erosion, suspension, and deposition of grains [17]. The complex and simultaneous presence of the quasi-static, dense-flow, and kinetic (suspended) regimes [16] makes the accurate prediction of such immersed granular flows challenging. This paper studies the fluid-driven granular dynamics through a consistent numerical method.

Discrete-based and continuum-based methods have been widely developed for simulating immersed granular flows. While discrete-based methods, such as the Discrete Element Method (DEM) [21], provide an in-depth grain-scale understanding of the granular behavior, they are computationally expensive for practical problems that involve a large volume of materials. On the other hand, the continuum-based numerical methods homogenize the assembly of solid grains (or the mixture of solid granules and interstitial fluid) into a body of continuum at the macroscopic level (Figure 8.1-b). Thus, they are scalable and computationally affordable for large-scale modeling. Such methods employ a rheology model to estimate the mechanical behavior of the granular continuum [17].

Mesh-based continuum methods have been developed for various granular simulations [96, 103]. However, due to their mesh dependency, they require particular treatments to deal with highly dynamic interfaces [22, 23]. In contrast, mesh-free Lagrangian continuum methods, or simply particle methods, discretize the continuum using moving particles without any connectivity (Figure 8.1-c). This feature of particle methods introduces them as reliable numerical approaches for handling interfacial deformations, and hence, suitable for highly dynamic granular flows [27–29]. The Material Point Method (MPM) [24], the Moving Particle Semi-implicit (MPS) method [25], and the Smoothed Particles Hydrodynamics (SPH) method [26] are some of the most widely adopted continuum particle methods. We establish the numerical method of this study based on the MPS formulation.

SPH and MPS have gone through significant developments to improve their accuracy and stability for highly dynamic and multiphase flows [74, 75, 124, 125, 164, 184, 197]. Shakibaeinia and Jin [47] introduced the weakly compressible MPS method (WC-MPS). Jandaghian and Shakibaeinia [123] and Jandaghian et al. [124] enhanced the accuracy and stability of the WC-MPS method by proposing artificial diffusive terms and particle regularization techniques. SPH and MPS, coupled with various rheological equations, have simulated immersed granular flows; the adopted constitutive laws include the Bingham plastic formulation [105–107], the Herschel-Bulkley model [107, 108], the Herschel-Bulkley-Papanastasiou

model [109], the regularized $\mu(I)$ equation by Jop et al. [99] [110–113], and the elastic-viscoplastic model [114]. Moreover, to improve the prediction of the incipient motion of the granular particles, some methods employed an additional yielding threshold based on Shields' erosion criterion [106, 115, 116]. Recently, Jandaghian et al. [126] proposed a generalized constitutive law to simulate three-dimensional immersed granular collapses and slides. They introduced the regularized form of the visco-inertial rheology model by Baumgarten and Kamrin [20] and the consistent effective pressure term for rapid granular deformation considering non-hydrostatic pore-water pressure and without shear stress threshold. While the previous advanced particle methods have mostly focused on the gravity-driven granular flows, a few have attempted to simulate the fluid-driven cases.

The continuum-based models treat the dense multiphase granular flow system using either single-continuum or two-continuum models [16, 17]. The single-continuum models consider the solid grains and interstitial (pore) fluid as a single uniform dense mixture. The mixture interacts with the ambient fluid phase directly through one set of governing equations. The two-continuum models simulate the relative motion of the interstitial fluid and the solid grains and solve separate sets of governing equations (including inter-phase forces) [17, 95]. In both approaches, the numerical element representing the continuum (i.e., the representative elementary volume, V , in Figure 8.1-b) must be large enough to contain a sufficient number of solid grains. Otherwise, the continuum assumption and the constitutive law would become invalid [17, 121, 126]. On the other hand, the numerical element should be small enough (with respect to the characteristic length-scale of the problem) to mathematically represent its vicinity and minimize the numerical approximation errors [114, 122, 126]. The computational model shall respect these two conflicting constraints in determining the spatial resolution of the discretized domain. Moreover, to capture highly dynamic and high Reynolds number fluid flows, the numerical solution requires a higher spatial resolution for the fluid phase (e.g., $V/4$) than that of the granular (or mixture). Accordingly, one can conceive a multi-resolution approach for simulating the fluid-driven granular flows (Figure 8.1-c & d).

Several multi-resolution SPH and MPS methods have been developed for improving numerical accuracy and capturing more accurate flow/solid deformations over a refined computational domain. They implement dynamic particle splitting and merging [76–78], adaptive particle refinement [79–81], overlapping methods [82, 83], and volume adaptive scheme [84]. Such multi-resolution methods are employed for various single-phase and multiphase flows (e.g., [76, 85, 86]) and fluid-structure interactions [70, 87–89]. Nevertheless, no multi-resolution particle method has been reported for multiphase granular flows.

In the present study, we propose a consistent multi-resolution particle method, based on

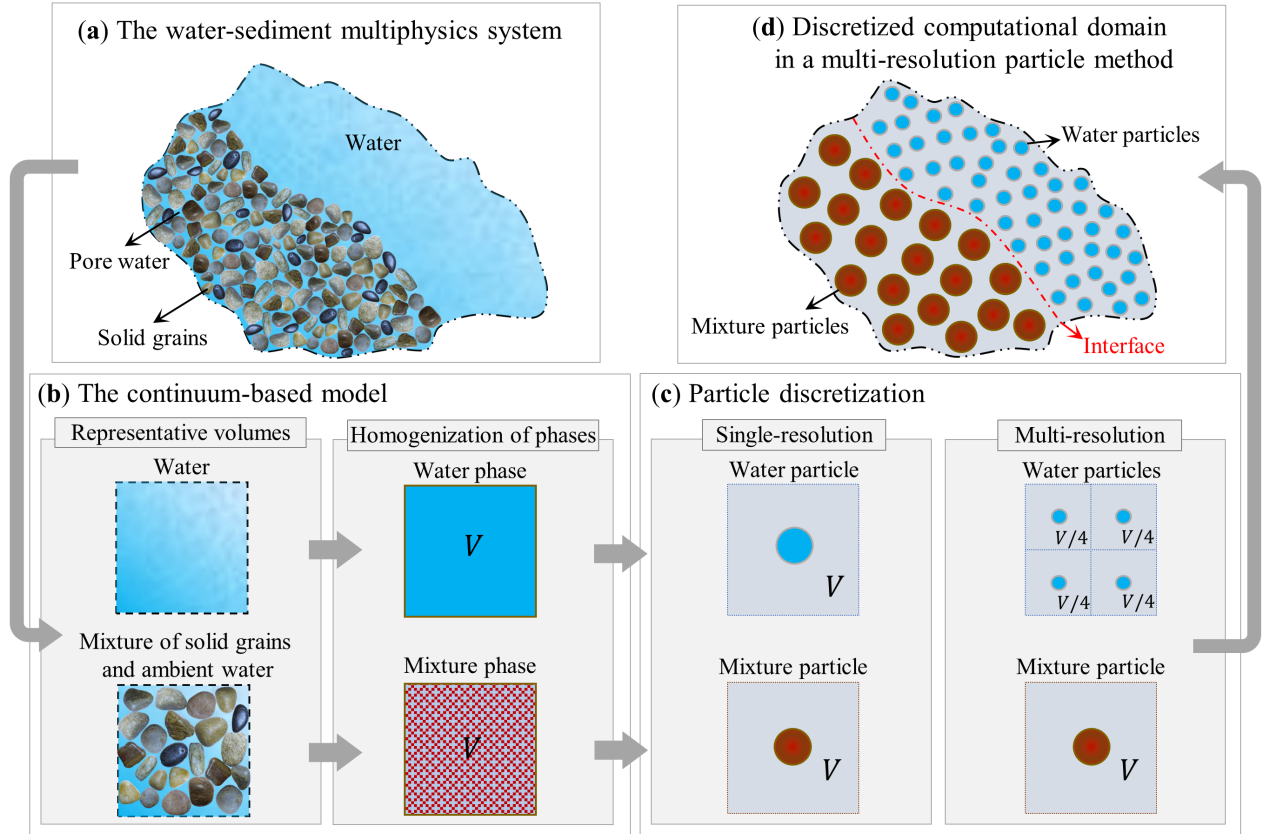


Figure 8.1 (a): The multiphysics system containing water and submerged solid grains. (b): The representative volumes of water and mixture phases homogenized into the representative elementary volume, V , in the single-continuum model. (c): The particle discretization in the single- or multi-resolution particle method. (d): The discretized computational domain with different spatial resolutions for the water and mixture particles.

the enhanced WC-MPS formulation (by Jandaghian and Shakibaeinia [123] and Jandaghian et al. [124, 126]), to investigate the mechanical behavior of immersed granular dynamics primarily driven by rapid fluid flow. We derive new approximation operators respecting the conservative properties of the multi-scale multiphase system. We present the novel multi-resolution MPS method in section 8.4. To ensure numerical stability and avoid unphysical oscillations (which can largely affect the granular yield behavior), we adapt the modified diffusive term [126] and the Dynamic Particle Collision (DPC) technique [124] to the newly developed multi-resolution framework. Further, we couple the developed MPS method with the generalized rheology model by Jandaghian et al. [126] supplied with a suspension equation for rapid and immersed granular flows (section 8.4.4). First, we validate the numerical model to two multiphase benchmark cases, i.e., the multi-viscosity Poiseuille flow and the multi-

density hydrostatic pressure, quantifying the numerical accuracy and convergence of the multi-resolution formulation (section 8.5.1). Next, by simulating water dam-break waves on erodible sediment beds, we provide a comprehensive study on the dynamics of rapid sediment erosion induced by a sudden collapse of a water column (section 8.5.2). Validating the numerical solutions with the available experimental data [12, 13], we present internal flow properties and the global mechanical behavior of this fluid-driven problem. We also parameterize the rheology and analyze the phenomenology of sediment dynamics concerning different bed materials and initial configurations of the test case. Comparing the results of the single- and multi-resolution MPS simulations, we evaluate the role of multi-scale interactions in capturing the flow evolution.

8.3 Equations of motion

Here, the system of granular material and the ambient fluid is considered as a multiphase continuum, which in a Lagrangian framework is described by the continuity equation:

$$\frac{D\rho}{Dt} = -\rho\nabla \cdot \mathbf{v}, \quad (8.1)$$

the momentum equation:

$$\frac{D\mathbf{v}}{Dt} = \frac{\nabla \cdot \mathbf{T}}{\rho} + \mathbf{F}, \quad (8.2)$$

and the advection equation:

$$\frac{D\mathbf{r}}{Dt} = \mathbf{v}, \quad (8.3)$$

calculating the time evolution ($D(\cdot)/Dt$) of the fluid density, ρ , velocity, \mathbf{v} , and position, \mathbf{r} , respectively [169]. The total stress tensor, \mathbf{T} , consists of the pressure scalar value, p , and the shear stress tensor, t , as $\mathbf{T} = -p\mathbf{I} + t$ (\mathbf{I} being the identity matrix) and $\rho\mathbf{F}$ is the body force per unit volume. Considering the barotropic fluids, the equation of state calculates the pressure, i.e., $p = f(\rho)$. For incompressible fluid flows and by neglecting the gradient of dynamic viscosity, η , over the fluid domain (i.e., considering $\nabla \cdot \mathbf{v} \approx 0$ and $\nabla\eta \approx 0$), the divergence of the stress tensor reduces to:

$$\nabla \cdot \mathbf{T} = -\nabla p + \eta\nabla^2\mathbf{v} \quad (8.4)$$

which is valid for Newtonian and non-Newtonian mechanical behaviors. Constitutive laws determine η as a function of hydrodynamic and material characteristics [17]. For water, we include a simple turbulence model (based on the Large Eddy Simulations) in the shear force calculations. We treat the mixture phase as a non-Newtonian fluid through the visco-inertial

rheology model (proposed by Baumgarten and Kamrin [20], and then represented in the regularized form by Jandaghian et al. [126]).

8.4 A consistent multi-resolution multiphase MPS method

8.4.1 Integral and summation interpolants

In continuum-based particle methods, the approximation operator transforms the integral representation of functions into the summation interpolant. By discretizing the computational domain, Ω , moving calculation points (or simply particles) carry flow and material properties [35]. Here, we adopt the general integral formulation of the MPS method to derive the summation operator of the multi-resolution model.

MPS integral representation of an arbitrary function, $f(\mathbf{r})$, reads [46]:

$$f(\mathbf{r}) = \frac{\int_{\Omega} f(\mathbf{r}') W(\|\mathbf{r}' - \mathbf{r}\|, r_e) d\mathbf{r}'}{\int_{\Omega} W(\|\mathbf{r}' - \mathbf{r}\|, r_e) d\mathbf{r}'} \quad (8.5)$$

where $d\mathbf{r}'$ is a differential volume element. The positive non-dimensional weighting function, W , (so-called the kernel) with a compact support smooths f over the influence radius, r_e . MPS introduces a normalization factor, denoted by n_0 , into the equations which corresponds to the reference physical fluid density, ρ_0 , and the mass of volume element, m , via:

$$n_0 = \frac{\rho_0}{m} \int_{\Omega} W(\|\mathbf{r}' - \mathbf{r}\|, r_e) d\mathbf{r}'. \quad (8.6)$$

Nevertheless, n_0 only depends on the type of kernel and the ratio of r_e to the size of spatial discretization, l_0 (i.e., $k = r_e/l_0$) [43]. With considering a constant k for the multi-resolution model, we employ (8.6) to rewrite (8.5) as:

$$f(\mathbf{r}) = \frac{1}{n_0} \int_{\Omega} f(\mathbf{r}') \frac{W(\|\mathbf{r}' - \mathbf{r}\|, r_e) k^d}{r_e^d} d\mathbf{r}' \quad (8.7)$$

in which d is the number of space dimensions and $m/\rho_0 = (r_e/k)^d$.

The original MPS formulation derives the summation operator of the integral representation (8.7) by considering identical smoothing length and spatial resolution for the entire fluid domain. Here, we propose a new formulation for the kernel, \widetilde{W} , to account for multi-resolution particle interactions through the general form of approximation operator:

$$\langle f \rangle_i = \frac{1}{n_0} \sum_{i \neq j}^N f_j \widetilde{W}(r_{ij}, \bar{r}_{eij}, V_{0j}) \quad (8.8)$$

for a target particle, $i \in \Omega$, surrounded by N number of neighbour particles, identified as $j \in \Omega$, where $r_{ij} = \|\mathbf{r}_j - \mathbf{r}_i\| \leq r_{ei}$. The modified kernel, which is non-dimensional, would be:

$$\widetilde{W}_{ij} = \widetilde{W}(r_{ij}, \bar{r}_{eij}, V_{0j}) = \frac{W(r_{ij}, \bar{r}_{eij})V_{0j}k^d}{\bar{r}_{eij}^d}, \quad (8.9)$$

in which V_{0i} , being the reference volume of particle, is equal to $(l_{0i})^d$ for incompressible fluid flows (as l_{0i} stands for the initial particle spacing of i). To respect the symmetric feature of the smoothing procedure in the governing equations (see section 9 and Figure 8.2), we have substituted r_e with $\bar{r}_{eij} = (r_{ei} + r_{ej})/2$ (similar to the formulations used by [130] and [77]). The new definition of kernel (8.9) includes the various sizes and smoothing lengths of particles within the approximation operator required for considering the multi-resolution interactions (where $V_{0i} \neq V_{0j}$); while in the same resolution interactions (where $V_{0i} = V_{0j}$), (8.9) automatically reduces to its original shape as $\widetilde{W}_{ij} = W(r_{ij}, r_{ei})$. By neglecting the kernel truncations at the interfaces and away from boundaries, n_0 keeps its standard definition as the summation of kernel at the initial uniform distribution of particles, i.e., $n_0 = \max \sum_{i \neq j}^N W(r_{ij}, r_{ei})$ at $t = 0$. Thus, it can be identified as a global constant for all the particle sizes and their interactions (as $k = r_{ei}/l_{0i}$ is invariable over Ω). In this study, we set $k = 3.1$ and use the third-order polynomial spiky kernel function [47] for all the approximation operators.

8.4.2 The discrete system of flow equations

In particle methods, the moving particles are the representative elementary volume of the ambient water phase, Ω_w , or the mixture of pore water and solid grains, Ω_m , or the solid walls, Ω_s , forming the computational domain, Ω (where $\Omega_w \cup \Omega_m$ would be the fluid phase, Ω_f , and $\Omega = \Omega_f \cup \Omega_s$). Using the summation operator for a target particle $i \in \Omega_f$, the flow equations read:

$$\begin{cases} \frac{1}{n_i} \frac{Dn_i}{Dt} = -\langle \nabla \cdot \mathbf{v} \rangle_i + D_i^m \\ \frac{D\mathbf{v}_i}{Dt} = -\frac{1}{\rho_i} \langle \nabla p \rangle_i + \frac{1}{\rho_i} \langle \eta \nabla^2 \mathbf{v} \rangle_i + \mathbf{F}_i \\ \frac{D\mathbf{r}_i}{Dt} = \mathbf{v}_i, \end{cases} \quad (8.10)$$

in which n_i is the non-dimensional particle number density (given as $n_0 \rho_i / \rho_{0i}$) and independent of the density discontinuity at the interfaces [126]. In this model, the momentum equation considers the density of particle, ρ_i , to be equal to the reference density of the fluid phase respecting the original form of the incompressible MPS method (i.e., in the momentum

equation: $\rho_i = \rho_{0i}$ where for $i \in \Omega_w \rightarrow \rho_{0i} = \rho_{0w}$ and $i \in \Omega_m \rightarrow \rho_{0i} = \rho_{0m} = \rho_{0w}(1-\phi_0) + \phi_0\rho_g$ as ϕ_0 and ρ_g are the reference volume fraction and the true density of the solid grains, respectively).

For the multi-resolution multi-phase MPS model, we use the kernel (8.9) to discretize the right-hand side terms of (8.10) based on the conservative WC-MPS formulation [123]:

$$\left\{ \begin{array}{l} \langle \nabla \cdot \mathbf{v} \rangle_i = \frac{d}{n_0} \sum_{i \neq j}^N \left(\frac{n_j}{n_i} \right) \frac{\mathbf{v}_j - \mathbf{v}_i}{r_{ij}} \cdot \mathbf{e}_{ij} \widetilde{W}_{ij} \\ \langle \nabla p \rangle_i = \frac{d}{n_0} \sum_{i \neq j}^N \left(n_i \frac{p_j}{n_j} + n_j \frac{p_i}{n_i} \right) \frac{\mathbf{e}_{ij} \widetilde{W}_{ij}}{r_{ij}} \\ \langle \eta \nabla^2 \mathbf{v} \rangle_i = \frac{2d}{n_0} \sum_{i \neq j}^N \eta_{ij} \frac{\mathbf{v}_j - \mathbf{v}_i}{r_{ij}^2} \widetilde{W}_{ij}. \end{array} \right. \quad (8.11)$$

$\mathbf{e}_{ij} = \mathbf{r}_{ij}/r_{ij}$ is the unit direction vector and the harmonic mean of the dynamic effective viscosity of i and j (i.e., η_i and η_j) gives $\eta_{ij} = 2\eta_i\eta_j/(\eta_i + \eta_j)$. With the new kernel function the interaction of particles with various size and density remains anti-symmetric within the governing equations; thus, the conjugate gradient and divergence operators ensure the conservation of the total energy (in the absence of shear and external forces) (see [49] and [123]) (Figure 8.2).

Considering the barotropic fluid as a weakly compressible phase, we employ the equation of state to calculate the pressure by Shakibaeinia and Jin [47]:

$$p_i = B_0 \left(\left(\frac{n_i}{n_0} \right)^\gamma - 1 \right) \quad (8.12)$$

where the bulk modulus, $B_0 = c_0^2\rho_0/\gamma$ and $\gamma = 7$ are constant for all the fluid phases as ρ_0 and c_0 are the true density and the artificial sound speed of the reference phase, respectively (here, we consider water as the reference phase, thus, $\rho_0 = \rho_{0w}$ and $c_0 = c_{0w}$). To limit the compressibility to less than 1%, the reference sound speed should satisfy $c_0 \geq 10\|\mathbf{v}\|_{max}$ condition by which the Mach number is kept less than 0.1 ($\|\mathbf{v}\|_{max}$ being the maximum expected velocity magnitude).

Next, we adapt the modified diffusive term by Jandaghian et al. [124] to the multi-resolution framework with the new kernel (8.9) as follows:

$$D_i^m = \left(\delta_{MPS} \frac{\Delta t c_0^2}{n_0} \right) \frac{2d}{n_0} \sum_{i \neq j}^N \left[(n_j - n_i) - \frac{1}{2} [\langle \nabla n \rangle_i^c + \langle \nabla n \rangle_j^c] \cdot \mathbf{r}_{ij} \right] \frac{\widetilde{W}_{ij}}{r_{ij}^2} \quad (8.13)$$

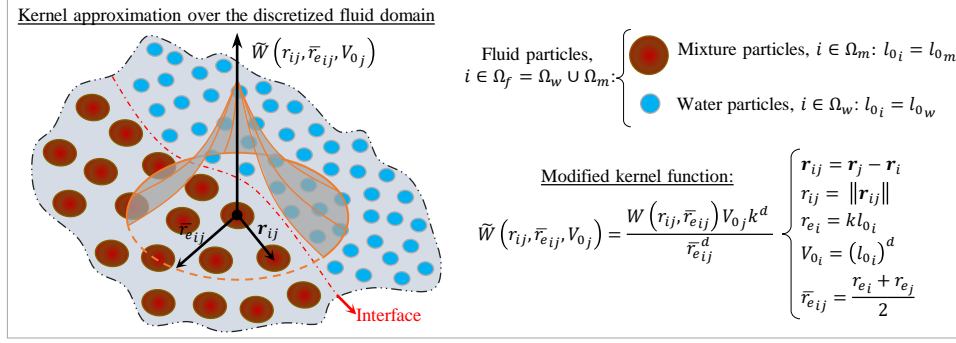


Figure 8.2 Kernel function of the MPS method for the multi-resolution particle interactions. d is the space dimension equal to 2 and 3 for the two- and three-dimensional simulations, respectively. k determines the smoothing length of the kernel, r_{ei} , and is set to 3.1 regardless of the particle size, l_{0i} .

in which $\langle \nabla n \rangle_i^c$ is the high-order gradient operator of n_i estimated by:

$$\langle \nabla n \rangle_i^c = \frac{d}{n_0} \sum_{i \neq j}^N \frac{n_j - n_i}{r_{ij}} (C_i \mathbf{e}_{ij}) \tilde{W}_{ij}, \quad (8.14)$$

and the correction matrix, C_i , is given as:

$$\mathbf{C}_i = \left(\frac{d}{n_0} \sum_{i \neq j}^N \frac{\mathbf{r}_j - \mathbf{r}_i}{r_{ij}} \otimes \mathbf{e}_{ij} \tilde{W}_{ij} \right)^{-1}. \quad (8.15)$$

where \otimes stands for the outer product of vectors. The non-dimensional coefficient, $0 < \delta_{MPS} \leq 1$, the calculation time step, Δt , and c_0 adjust the magnitude of this numerical correction. The diffusive term obeys the mass conservation law, if $\sum_i n_i V_i D_i^m = 0$ (as $V_i = n_0 V_{0i} / n_i$ from (8.6)); with $i, j \in \Omega_f$ in (8.13-8.15), the diffusive term would be an anti-symmetric formulation which conserves the total mass of the multi-resolution multiphase system.

8.4.3 Dynamic particle collision for multi-scale multiphase interactions

Here, we implement the Dynamic pair-wise Particle Collision (DPC) method (proposed by Jandaghian et al. [124]) as the particle regularization technique which ensures the numerical stability by eliminating particle clustering and high-frequency pressure noises. Considering the velocity variation of two particles colliding with different masses and volumes, we develop

the DPC formulation for the multi-resolution multi-phase interactions as:

$$\delta \mathbf{v}_i = \left(\sum_{i \neq j}^N \kappa_{ij} \frac{2m_{0j}}{m_{0i} + m_{0j}} \mathbf{v}_{ij}^{coll} - \frac{\Delta t}{\rho_{0i}} \sum_{i \neq j}^N \alpha_{ij} \frac{2V_{0j}}{V_{0i} + V_{0j}} \frac{p_{ij}^b}{r_{ij}} \mathbf{e}_{ij} \right) \quad (8.16)$$

where $i, j \in \Omega_f$ and $m_{0i} = \rho_{0i}V_{0i}$. The collision velocity, \mathbf{v}_{ij}^{coll} , and the binary multiplier, α_{ij} , are given by:

$$(\mathbf{v}_{ij}^{coll}, \alpha_{ij}) = \begin{cases} ((\mathbf{v}_{ij} \cdot \mathbf{e}_{ij})\mathbf{e}_{ij}, 0), & \text{for } \mathbf{v}_{ij} \cdot \mathbf{e}_{ij} < 0 \\ (0, 1) & \text{otherwise} \end{cases} \quad (8.17)$$

and the dynamic background pressure, p_{ij}^b , is defined as $p_{ij}^b = \tilde{p}_{ij}\chi_{ij}$ where $\tilde{p}_{ij} = \max(\min(\lambda|p_i + p_j|, \lambda p_{max}), p_{min})$, and, $\chi_{ij} = \left(W(r_{ij}, \bar{l}_{0ij}) / W(0.5\bar{l}_{0ij}, \bar{l}_{0ij}) \right)^{0.5}$. The non-dimensional variable, χ_{ij} , is a function of the kernel with the smoothing length set to $\bar{l}_{0ij} = (l_{0i} + l_{0j})/2$ (where for $r_{ij} \geq \bar{l}_{0ij} \rightarrow \chi_{ij} = 0$). The preset maximum and minimum pressure of the test case (p_{max} and p_{min} respectively) and the non-dimensional constant, λ , specify the strength of the repulsive term. For the collision term, the variable coefficient, κ_{ij} , dynamically sets the coefficient of restitution as a function of r_{ij} via:

$$\kappa_{ij} = \begin{cases} \chi_{ij} & 0.5\bar{l}_{0ij} \leq r_{ij} < \bar{l}_{0ij} \\ 1 & r_{ij} < 0.5\bar{l}_{0ij}. \end{cases} \quad (8.18)$$

Eventually, $\delta \mathbf{v}_i$ from (8.16) updates the velocity and position of particles within the solution algorithm (i.e., we have $\mathbf{v}'_i = \mathbf{v}_i + \delta \mathbf{v}_i$ and $\mathbf{r}'_i = \mathbf{r}_i + \delta \mathbf{v}_i \Delta t$). The proposed DPC through equations (8.16-8.18) conserves the linear momentum of the multi-resolution multi-phase particle interactions (i.e., with $i, j \in \Omega_f$ then $\sum_i m_{0i} \delta \mathbf{v}_i = 0$). In this study, we use the Wendland kernel for χ_{ij} and set $\lambda = 0.2$ [124].

8.4.4 Generalized rheology model

We employ the generalized rheology model of Jandaghian et al. [126] for calculating the effective viscosity of the water and mixture particles. For water as a Newtonian fluid with the true viscosity, μ_w , the effective viscosity increases by the presence of solid grains (i.e., with the approximated volume fraction, $\langle \phi \rangle_i$) and including the turbulence effect:

$$i \in \Omega_w \rightarrow \eta_i = \mu_w \left(1 + \frac{5}{2} \langle \phi \rangle_i \right) + \rho_{0w} \nu_{ti}. \quad (8.19)$$

as the eddy viscosity is given by $\nu_{ti} = (C_s r_{ei})^2 |\dot{\gamma}|_i$ and the Smagorinsky constant coefficient is set to $C_s = 0.12$. The pressure-imposed rheology treats the mixture of water and solid grains as a non-Newtonian fluid through the mixture effective viscosity formulated by $\eta_i = \mu_i p_{g_i} / |\dot{\gamma}|_i$ in which p_{g_i} is the solid grains' normal stress (i.e., the effective pressure), μ_i is the friction coefficient, and $|\dot{\gamma}|_i$ is the magnitude of strain rate tensor [17]. With the visco-inertial model of Baumgarten and Kamrin [20] (as the friction coefficient) and the regularized formulation (for avoiding the singularity issue when $|\dot{\gamma}|_i = 0$), [126] represented the effective viscosity of the mixture particles as:

$$i \in \Omega_m \rightarrow \eta_i = \frac{\tau_{y_i}}{\sqrt{|\dot{\gamma}|_i^2 + \lambda_r^2}} + \frac{(\mu_2 - \mu_1) p_{g_i}}{b \sqrt{p_{g_i}} / \sqrt{d_g^2 \rho_g + 2\mu_w / (|\dot{\gamma}|_i + \lambda_r)} + |\dot{\gamma}|_i} + \frac{5 \langle \phi \rangle_i}{2a} \left(\frac{\mu_w \sqrt{p_{g_i}}}{\sqrt{|\dot{\gamma}|_i^2 d_g^2 \rho_g + 2\mu_w |\dot{\gamma}|_i + \lambda_r^2}} \right) \quad (8.20)$$

where a and b are material constants. The upper and lower limits of the solid grains' friction are denoted as μ_2 and $\mu_1 = \tan(\theta)$, respectively. ρ_g , d_g , and θ stand for the true density, the mean diameter, and the internal friction angle of the solid grains, respectively. The yield stress, τ_y , is given by the Drucker-Prager yield criteria as $\tau_{y_i} = 2\sqrt{3} \sin(\theta) p_{g_i} / (3 - \sin(\theta))$ noting that $p_{g_i} > 0$. The regularization parameter, λ_r , is set to 0.001. For incompressible fluid flows, $|\dot{\gamma}|_i = \sqrt{4II_{E_i}}$, as the strain rate tensor, $E_i = 0.5[\langle \nabla \mathbf{v} \rangle_i^c + (\langle \nabla \mathbf{v} \rangle_i^c)^\dagger]$ and its second principal invariant, $II_{E_i} = 0.5 E_i : E_i$. For the derivation of (8.20) readers are referred to [126]. We estimate the gradient of velocity and the volume fraction of the water and mixture particles through:

$$\langle \nabla \mathbf{v} \rangle_i^c = \frac{d}{n_0} \sum_{i \neq j}^N \frac{\mathbf{v}_j - \mathbf{v}_i}{r_{ij}} (\mathbf{C}_i \mathbf{e}_{ij}) \widetilde{W}_{ij} \quad (8.21)$$

and

$$\langle \phi \rangle_i = \frac{\sum_j^N \phi_j \widetilde{W}_{ij}}{\sum_j^N \widetilde{W}_{ij}}, \quad (8.22)$$

respectively, noting that for $j \in \Omega_w \rightarrow \phi_j = 0$ and $j \in \Omega_m \rightarrow \phi_j = \phi_0$.

The non-dimensional parameters, i.e., the inertial number, $I_i = |\dot{\gamma}|_i d_g \sqrt{\rho_g / p_{g_i}}$, the viscous number, $I_{\nu i} = \mu_w |\dot{\gamma}|_i / p_{g_i}$, and the mixed number, $I_m = \sqrt{I^2 + 2I_\nu}$ govern the visco-inertial rheology model [100,101]. This model is validated against the experimental data of immersed granular flows where $I_m \leq 0.6$ [20]. In rapid fluid-driven granular erosion, mixture particles at the interface are subjected to high shear forces leading to their suspension with low volume concentration. In the dilute and semi-dilute conditions, the dynamic viscosity turns to be a

function of the volume fraction and independent of the shear rate magnitude [17]. Thus, to incorporate the role of suspension effects, we calculate the effective viscosity of the mixture particles where $\langle\phi\rangle_i/\phi_0 < 0.5$ or $I_{m_i} > 0.6$ through the suspension equation of [237]:

$$\eta_i = \mu_w \exp\left(\frac{2.5\langle\phi\rangle_i}{1 - \frac{39}{64}\langle\phi\rangle_i}\right). \quad (8.23)$$

Coupling the visco-inertial formulation with the Vand's equation aims at simulating the suspension process of mixture particles. Previously, Zubeldia et al. [115] and Fourtakas and Rogers [109] used this equation with the Herschel-Bulkley-Papanastasiou constitutive model for sediment dynamics modeling in SPH. One should not that our implemented constitutive model treats the different regimes of the immersed granular flow through the failure and post-failure terms and the suspension equation without any shear stress threshold (e.g., Shield's erosion criterion in [106,115]) to distinguish the yielded particles from the un-yielded ones.

Moreover, we implement the consistent effective pressure, $p_{\text{eff},i}$, proposed by Jandaghian et al. [126] to estimate p_{g_i} of the immersed granular flow where for $i \in \Omega_m$, $p_{g_i} = p_{\text{eff},i}$ and,

$$p_{\text{eff},i} = B_0 \left[\left(\frac{n_i}{n_0}\right)^\gamma - \left(\frac{\rho_{w_i}}{\rho_{0w}}\right)^\gamma \right] \quad (8.24)$$

in which the density of the pore-water, ρ_{w_i} , is updated by its continuity equation derived for the single-phase continuum model as follows:

$$\frac{1}{\rho_{w_i}} \frac{D\rho_{w_i}}{Dt} = -\langle\nabla \cdot \mathbf{v}\rangle_i + D_i^m. \quad (8.25)$$

The right-hand side of (8.25) is identical to the right-hand side of the continuity equation used for updating n_i (in (8.10)).

8.4.5 Boundary conditions and solution algorithm

In the numerical model, the fixed boundary particles ($i \in \Omega_s$) simulate the solid walls. The fluid particles interact with the solid boundary particles through the governing equations (8.11) [126]. To update the pressure of the wall boundary particles (p_i), we implement the dynamic solid boundary condition by Crespo et al. [67]. The pressure of the closest wall particle is assigned to the ghost particles. The velocity of the solid boundary particles, \mathbf{v}_i , is considered to be zero in the continuity equation of fluid particles. In the shear force calculations, the velocity assigned to the solid boundary particles applies slip or no-slip boundary conditions. For viscous flow simulations, we consider the viscosity of the fluid

particle for the boundary particle (i.e., $\eta_{j \in \Omega_s} = \eta_{i \in \Omega_f}$ in $\langle \eta \nabla^2 \mathbf{v} \rangle_i$).

For solving the governing equations, we implement the second-order and explicit symplectic time integration scheme (represented by Jandaghian et al. [126]). The time step of calculation, Δt , is given based on the the Courant–Friedrichs–Lewy (CFL) stability condition and the shear force corresponding to the density, the spatial resolution and the dynamic viscosity of each phase (i.e., Ω_w and Ω_m) as follows:

$$\Delta t = \min \left\{ C_{CFL} \frac{l_0}{c_0}, C_v \frac{\rho_0 l_0^2}{\eta_{max}} \right\}_{\Omega_w, m}, \quad (8.26)$$

in which C_{CFL} and C_v are non-dimensional coefficients of the time steps (identical for both phases) and η_{max} is the maximum expected dynamic viscosity. Considering Ω_w as the reference phase for the bulk module (in (8.12)), we set the sound speed of the second phase as $c_{0m} = c_{0w} \sqrt{\rho_{0w}/\rho_{0m}}$.

8.5 Results and discussions

The reliability of water-sediment dynamics modeling depends on the accuracy of the approximated governing equations and their capability in capturing the multiphysics flow properties. To investigate the consistency of the proposed multi-resolution MPS formulation, we begin with studying the numerical accuracy and convergence of two benchmark cases, i.e., the multi-viscosity Poiseuille flow and the hydrostatic pressure of two fluid phases (section 8.5.1). Then, we investigate and validate rapid fluid-driven granular erosion through simulating dam break waves over movable beds (section 8.5.2). A movie containing the numerical simulations and results is provided as the supplementary data of this paper.

8.5.1 Numerical accuracy and convergence of the multi-resolution MPS model

Here, we evaluate the numerical accuracy of the multi-resolution operator in estimating the shear force by modeling the multi-viscosity Poiseuille flow. Further, we simulate the hydrostatic pressure of two fluid phases to investigate the new conservative form of governing equations in the multi-resolution configuration. Figure 8.3 represents the initial setup of the test cases and their parameters.

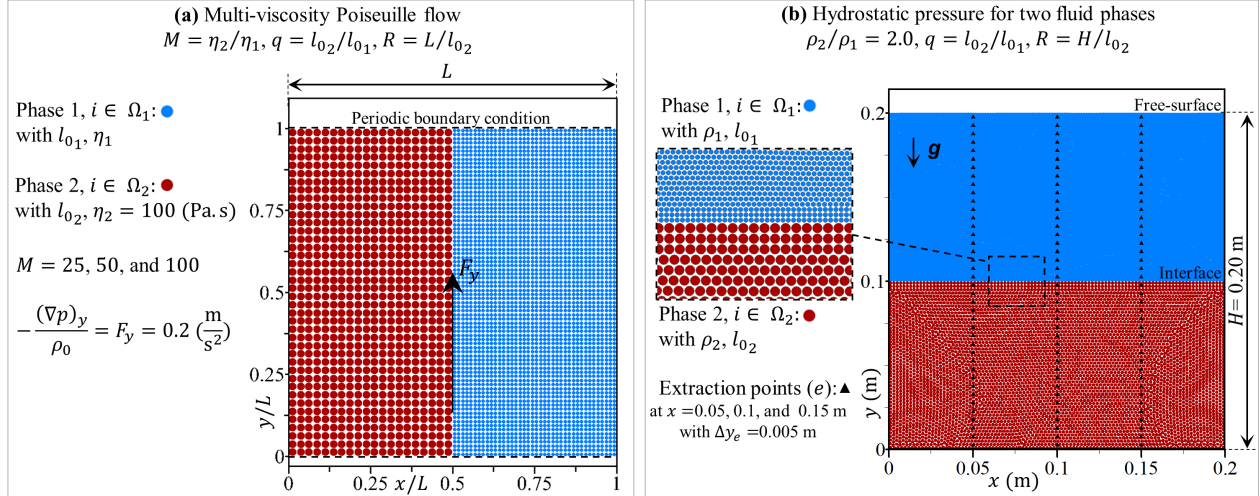


Figure 8.3 Initial configuration of the numerical simulations: (a) the multi-viscosity Poiseuille flow, and (b) the hydrostatic pressure for two fluid phases.

Multi-viscosity Poiseuille flow

This benchmark case has been widely simulated for studying the numerical accuracy and convergence characteristics of particle methods [75,114,238]. Two fluid phases, with different viscosity, flow between two stationary and parallel plates under a constant body force applied as a gradient of pressure, $\rho_0 F_y = -\nabla p_y$, in the positive y -direction (shown in Figure 8.3-a). The fluid phases, denoted as Ω_1 and Ω_2 , fill the channel with identical width (equal to $L/2$) and density, i.e., $\rho_1 = \rho_2 = \rho_0 = 1000 \text{ kg}\cdot\text{m}^{-3}$. We set the viscosity ratio, $M = \eta_2/\eta_1$, to 25, 50, and 100 with the dynamic viscosity of the second phase, η_2 , set to 100 Pa.s. No-slip boundary condition determines the velocity of the fixed solid boundary particles interacting with the fluid particles (i.e., $\mathbf{v}_j = -\mathbf{v}_i$ for $i \in \Omega_f = (\Omega_2 \cup \Omega_1)$ and $j \in \Omega_s$). Periodic boundary condition eliminates kernel truncation at the top and bottom boundaries (i.e., at $y/L = 0$ and 1). The particle size of the fluid phase with the greater viscosity (i.e, l_{02}) determines the spatial resolution of the problem by $R = L/l_{02}$. The fluid phase with the smaller viscosity value (i.e, Ω_1) has the higher spatial resolution where the particle size ratio, defined as $q = l_{02}/l_{01}$, is set to 2 and 4. The maximum analytical velocity, U_{max} , occurs at the midpoint of Ω_2 (i.e., at $x/L = 0.75$) and the analytical velocity at the interface (i.e., at $x/L = 0.5$) is denoted as U_0 . The non-dimensional time, T , is given by tU_0/L and equation (8.26) determines the calculation time steps with $C_{CFL}/c_0 = 0.05 \text{ s/m}$, $C_v = 0.25$, and $\eta_2 = 100 \text{ Pa}\cdot\text{s}$. We estimate the normalized root-mean-square-error of the velocity magnitude through $L_2(\|\mathbf{v}\|) = [U_{max}]^{-1} \sqrt{1/N_{tp} \sum_{\forall i \in \Omega_f} [\|\mathbf{v}\|_i - \|\mathbf{v}\|_{analytical}^{at x_i}]^2}$ in which N_{tp} is the total number of

fluid particles. Comparing the analytical solution of the velocity field (represented by Cao et al. [239]) with the results of the single- and multi-resolution simulations, we investigate the numerical accuracy of the model solely related to the shear force operator.

Figure 8.4 illustrates and plots the velocity of the fluid particles for different M and q , at $T = 100$ and with $R = 40$. The single- and multi-resolution simulations predict accurate results as the estimated velocity converges to the analytical velocity profiles. With $q = 4$, small incompatibility between the numerical and analytical results appears at the interface (i.e., at $x/L = 0.5$) and where the maximum velocity occurs (i.e., at $x/L = 0.75$). This discrepancy originates from the adopted assumption that considers the normalization factor (i.e., n_0) to remain valid at the interface (even where $q \neq 1$). Also, the approximation term has no renormalization matrix for ensuring the first-order accuracy of the estimated velocity field.

Next, we perform a particle convergence study of the numerical results compared with the analytical velocity profiles. We estimate and plot $L_2(\|\mathbf{v}\|)$ over the simulation time, $T = 0 - 100$, and with different spatial resolutions (where $R = 8, 10, 16, 20, 40$, and 80) (Figure 8.5). With both single- and multi-resolution simulations, $L_2(\|\mathbf{v}\|)$ reduces as the spatial resolution increases (shown in Figure 8.5-a for $M = 50$). We plot $L_2(\|\mathbf{v}\|)$ against the averaged particle size (i.e., $(l_{01} + l_{02})/2$) in the log-log graphs of Figure 8.5-b; the plots display that the accuracy of results is independent from the viscosity ratio M (e.g., with $q = 2$ and $R = 40$, $L_2(\|\mathbf{v}\|)$ is 1.15, 1.17, and 1.13 %, for $M = 25, 50$, and 100 , respectively). On the other hand, the multi-resolution simulations affect the estimation of velocity profiles and the order of convergence by increasing the numerical errors (e.g., for $M = 100$ and $R = 80$, $L_2(\|\mathbf{v}\|)$ for $q = 1$ increases from 0.5 % to 0.9 and 1.3 % by $q = 2$ and $q = 4$, respectively). However, adopting higher spatial resolutions decreases the errors with an order of convergence greater than one. Considering that the shear force calculation (i.e., $\langle \eta \nabla^2 \mathbf{v} \rangle$) does not benefit from any high-order approximation operators, overall, the errors by the multi-resolution implementations remain in an acceptable range (i.e., $L_2(\|\mathbf{v}\|) \leq 2\%$ for $R \geq 20$).

Hydrostatic pressure

In this 2D benchmark case, two inviscid and immiscible fluids with identical heights fill a steady tank subjected to a constant gravitational force, $\mathbf{g} = (0, -9.81\text{m/s}^2)^t$ [126, 164]. The lighter phase (Ω_1 with the density of $\rho_1 = 1000 \text{ kg}\cdot\text{m}^{-3}$) is on the top of the heavier phase (Ω_2) with the density ratio of $\rho_2/\rho_1 = 2$ (shown in Figure 8.3-b). The total fluid height, H , and the initial particle size of phase 2, l_{02} , determine the spatial resolution as $R = H/l_{02}$.

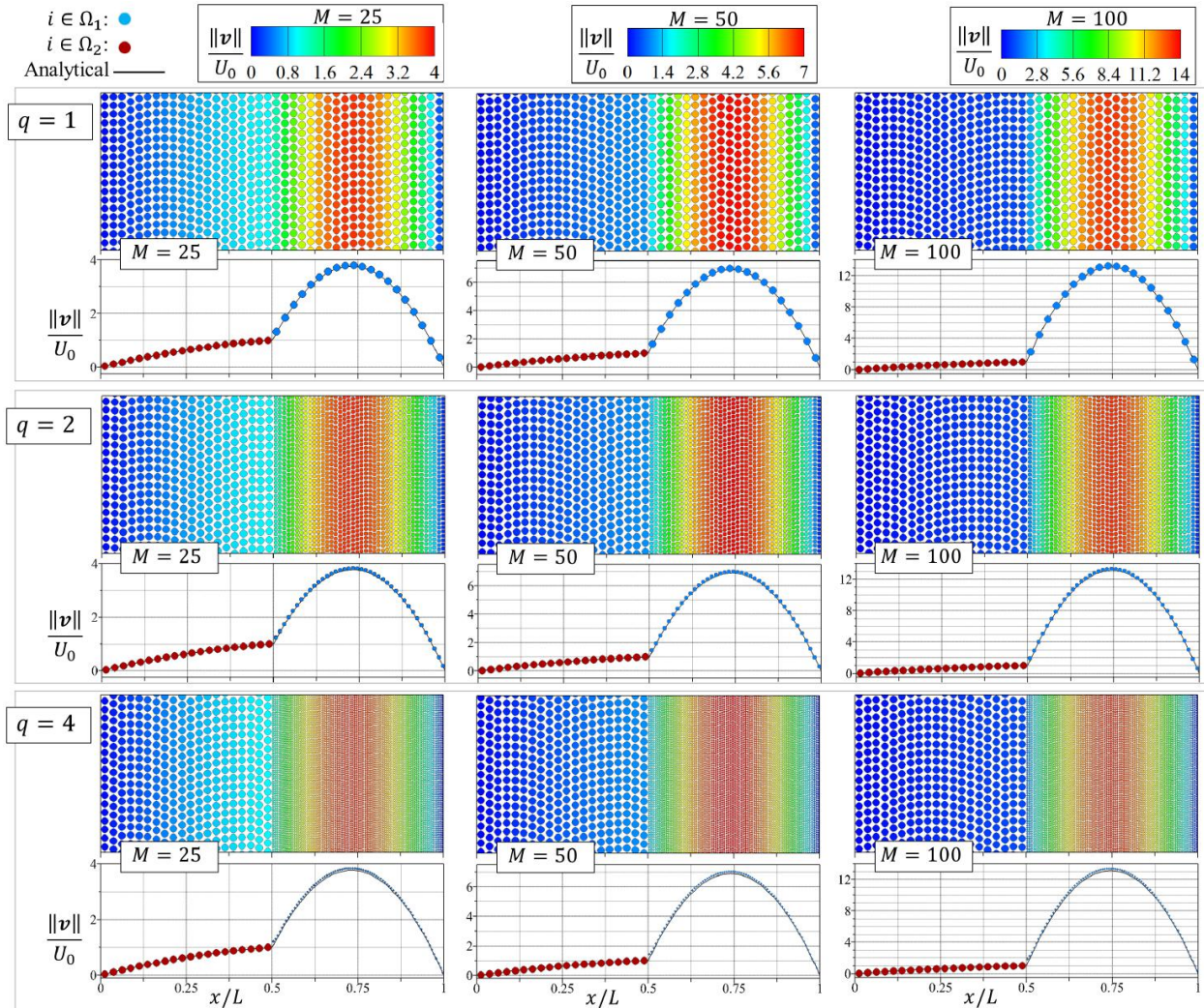


Figure 8.4 Poiseuille flow: velocity of fluid particles ($\forall i \in \Omega_f$) at $T = tU_0/L = 100$ with $M = 25, 50,$ and 100 , simulated by the single-resolution ($q = l_{02}/l_{01} = 1$) and multi-resolution ($q = 2, 4$) MPS models. The spatial resolution of the second fluid phase (Ω_2) is $R = L/l_{02} = 40$. The solid black lines represent the analytical velocity profiles. The magnitude of velocity is normalized by U_0 .

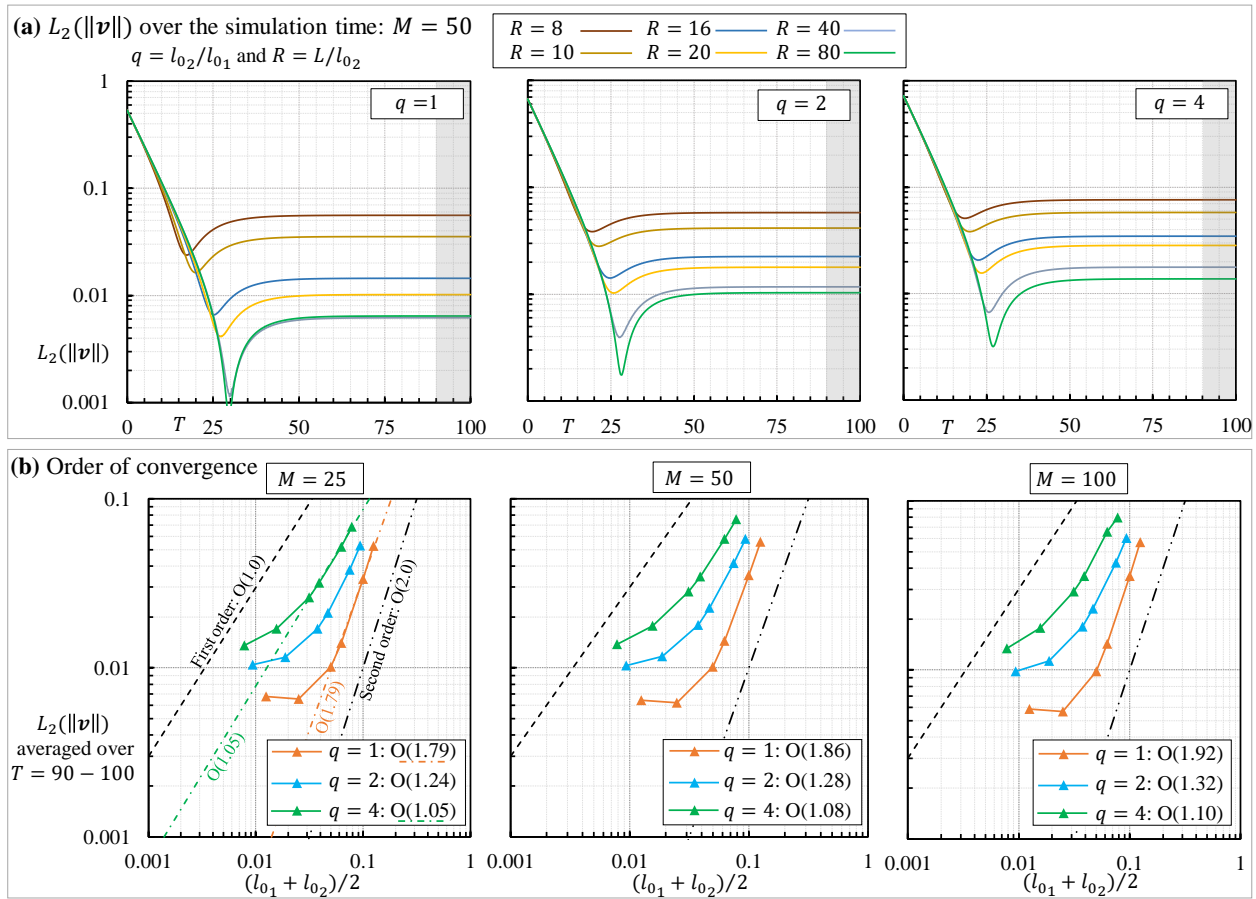


Figure 8.5 Poiseuille flow: (a) $L_2(\|\mathbf{v}\|)$ over the simulation time for $M = 50$ with different spatial resolutions (R), and (b) the numerical errors and order of convergence ($O(\cdot)$) for $M = 25, 50$, and 100 , simulated by the single- and multi-resolution MPS models. In (b), $L_2(\|\mathbf{v}\|)$ is averaged over $T = 90 - 100$ identified as the gray regions in (a).

We set c_0 , ρ_0 , and C_{CFL} to 20 m/s, ρ_1 , and 0.5, respectively. We activate the diffusive term (8.13) with $\delta_{MPS} = 0.2$ while deactivate the DPC technique. The fluid particles ($i \in \Omega_f = \Omega_1 \cup \Omega_2$) are initially located on a Cartesian lattice; the particle distribution of each phase is packed separately before starting the main simulations (similar to the packing algorithm proposed by Colagrossi et al. [228]). The model assigns the initial hydrostatic pressure and the corresponding particle number density to the packed fluid particles [126]. We simulate this test case for 10 seconds where the non-dimensional time, T , is given by $t\sqrt{\|\mathbf{g}\|/H}$. The particle size ratio is denoted by $q = l_{02}/l_{01}$ where $q = 1$ and $q = 2, 4$ refer to the single- and multi-resolution simulations, respectively. To validate the numerical results (compared with the theoretical hydrostatic pressure), we extract the local pressure, p_e , linearly averaged over the fluid particles within an influence radius of $1.5l_{02}$ from the extraction points (e) evenly distributed at $x = 0.05, 0.10, \text{ and } 0.15$ m with $\Delta y_e = 0.005$ m (identified as the delta markers in Figure 8.3-b). The normalized root-mean-square-error of the pressure is calculated by $L_2(p) = [p_{max}]^{-1} \sqrt{1/N_e \sum_e [p_e^{\text{at } y_e} - p_{\text{theoretical}}^{\text{at } y_e}]^2}$ in which N_e is the total number of extraction points. The numerical error is normalized by the maximum theoretical pressure corresponding to each fluid phase, i.e., if $y_e > H/2$ then $p_{max} = 0.5H\rho_1\|\mathbf{g}\|$ and if $y_e < H/2$ then $p_{max} = 0.5H(\rho_1 + \rho_2)\|\mathbf{g}\|$. Through this benchmark case, we investigate the accuracy of the multi-density model in predicting hydrostatic pressure.

Figure 8.6 represents the particle distributions and pressure fields with $R = 100$ and $q = 1, 2, \text{ and } 4$ at $t = 10$ s. Stable and uniform particle distribution exists at the interface of the multi-resolution simulations (where $q = 2, 4$); the implemented diffusive term ensures smooth pressure fields over the entire fluid domain. We plot the local numerical pressures to compare with the hydrostatic pressure profile. The graphs show good agreement between the numerical results and the theoretical pressure for all three cases.

To quantify the accuracy and the convergence order of the results, we calculate the normalized root-mean-square-error of the pressure parameter ($L_2(p)$) for different spatial resolutions (i.e., $R = 20, 50, 100, \text{ and } 200$). The numerical error is normalized by the maximum theoretical pressure corresponding to each fluid phase. The particle rearrangement (due to the assigned pressure field and the initial particle distribution at the interface) oscillates the estimated error at the initial time steps until the simulation reaches a stable condition (for $T > 40$) (Figure 8.7-a). The numerical errors of the single- and multi-resolution simulations reduce as we increase the spatial resolution of each fluid phase. We represent $L_2(p)$ against $(l_{01} + l_{02})/2$ in a log-log plot in Figure 8.7-b. Thanks to the conservative form of the approximation operators (i.e., $\langle \nabla \cdot \mathbf{v} \rangle$ and $\langle \nabla p \rangle$) and the effective diffusive term (8.13), the accuracy of numerical results proves to be independent of q where $R \geq 100$ (noting that $L_2(p)$ becomes negligible, i.e., $L_2(p) \leq 0.5$ %). Moreover, the particle convergence study confirms that

the accuracy of multi-resolution simulations ($q = 2, 4$) improves at the expected rate by increasing R , as the order of convergence remains equal to ~ 1 .

8.5.2 Dam break waves on erodible granular beds

We simulate the water dam break over movable beds as a benchmark case of rapid fluid-driven granular dynamics. First, we specify the main properties of this problem and the numerical model configurations. We conduct a sensitivity analysis concerning the constant material parameters (i.e., μ_2 , a , and b in the post-failure terms of the visco-inertial rheology equation) and the suspension equation (8.23). We validate the results of the proposed multi-resolution MPS model against the available experimental data representing the simulated flow properties and discussing the phenomenology of the sediment erosion. Also, we evaluate the role of multi-scale water-sediment interactions within the continuum-based modeling of such multiphysics problem.

Problem characteristics and configurations

We configure the two-dimensional numerical model based on the experimental setup of [12] (shown in Figure 8.8). In this problem, a column of water collapses under the gravitational force, $\mathbf{g} = (0, -9.81\text{m/s}^2)^t$, on sediment beds fully submerged in water. The non-cohesive sediment material consists of either coarse sand grains or Polyvinyl Chloride (PVC) pellets [12]; table 8.1 represents their reference material properties assigned in the rheology equations (8.20-8.23). The material constants of water are its reference density, $\rho_{0w} = 1000 \text{ kg}\cdot\text{m}^{-3}$, and true viscosity, $\mu_w = 0.001 \text{ Pa}\cdot\text{s}$. The flume's length is $2L = 6.00$. Considering different levels of sediment on the left side of the gate, ΔH_b , different geometrical configurations exist by $\Delta H_b = 0.0, -0.05, \text{ and } 0.10$, identified as cases A, B, and C, respectively. The upstream water level with respect to the downstream sediment level, H , is equal to 0.35 m and identical for all three experimental setups. The gate, located at the middle of the flume, i.e., at $x = 0.0$, is being lowered down with the nominal speed of $\sim 5 \text{ m/s}$ (in the negative y -direction) [12].

In continuum-based modeling of granular material, the particle size/distance must be large enough to represent a sufficient number of grains so that the continuum assumption and hence the constitutive law remain valid [17]. Based on the sensitivity analysis conducted by Jandaghian et al. [126] and Ghāitanellis et al. [114] for the sediment dynamics problems, we fix the initial inter-particle distance of mixture particles, l_{0m} , to 0.005 m and 0.01 m for the sand and PVC bed materials, respectively, which correspond to $\simeq 2.7d_g$ (see Figure 8.8). We define the particle size ratio, q , as the ratio of l_{0m} to the initial inter-particle distance of water particles, l_{0w} , i.e., $q = l_{0m}/l_{0w}$. A packed particle distribution is used for initializing the main

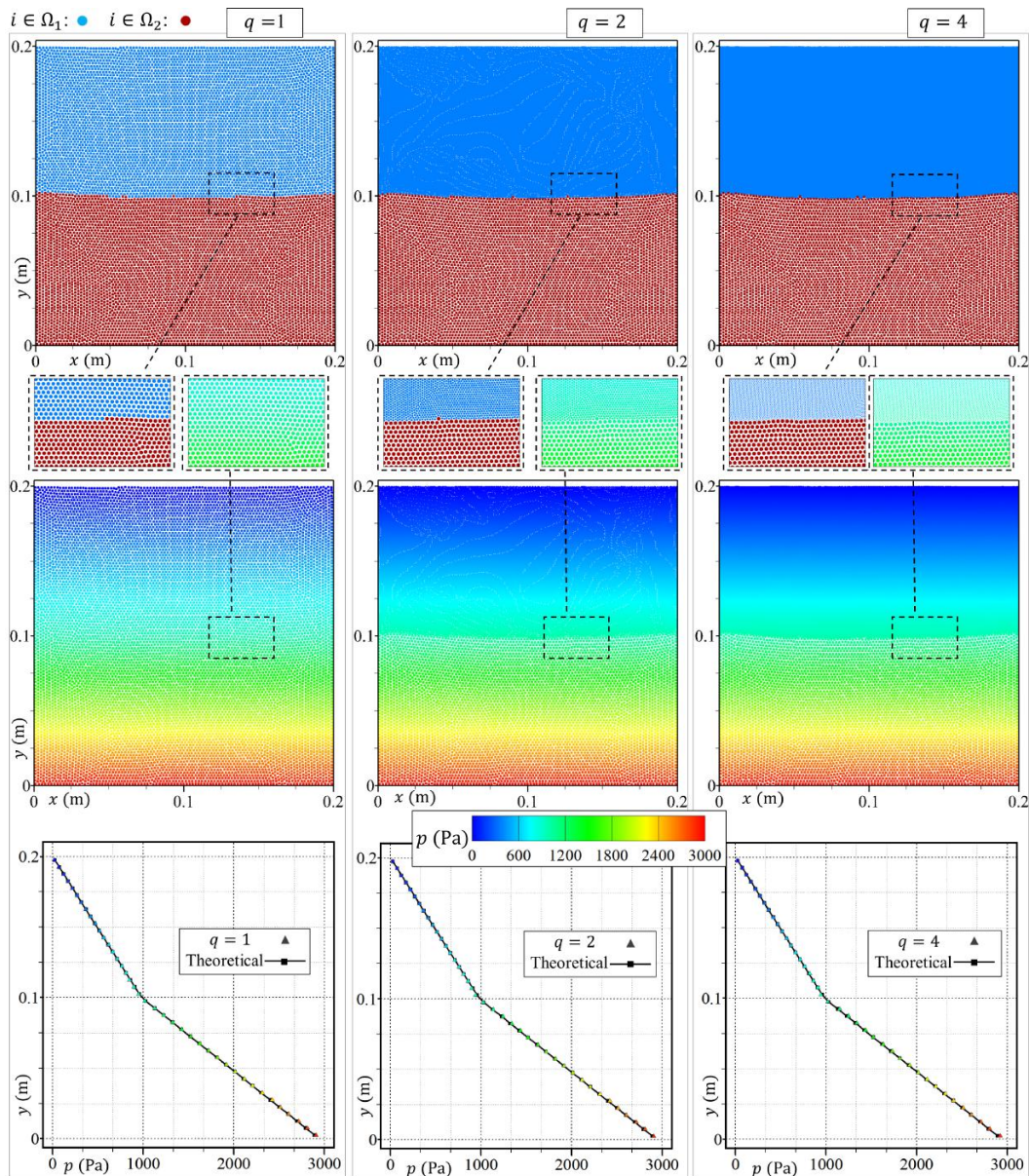


Figure 8.6 Hydrostatic pressure: particle distributions and pressure fields (with $R = H/l_{o_2} = 100$) at $t = 10$ s (represented in the top and the middle rows, respectively). The local pressures extracted at $x = 0.1$ m are plotted against the theoretical hydrostatic pressure (in the bottom row).

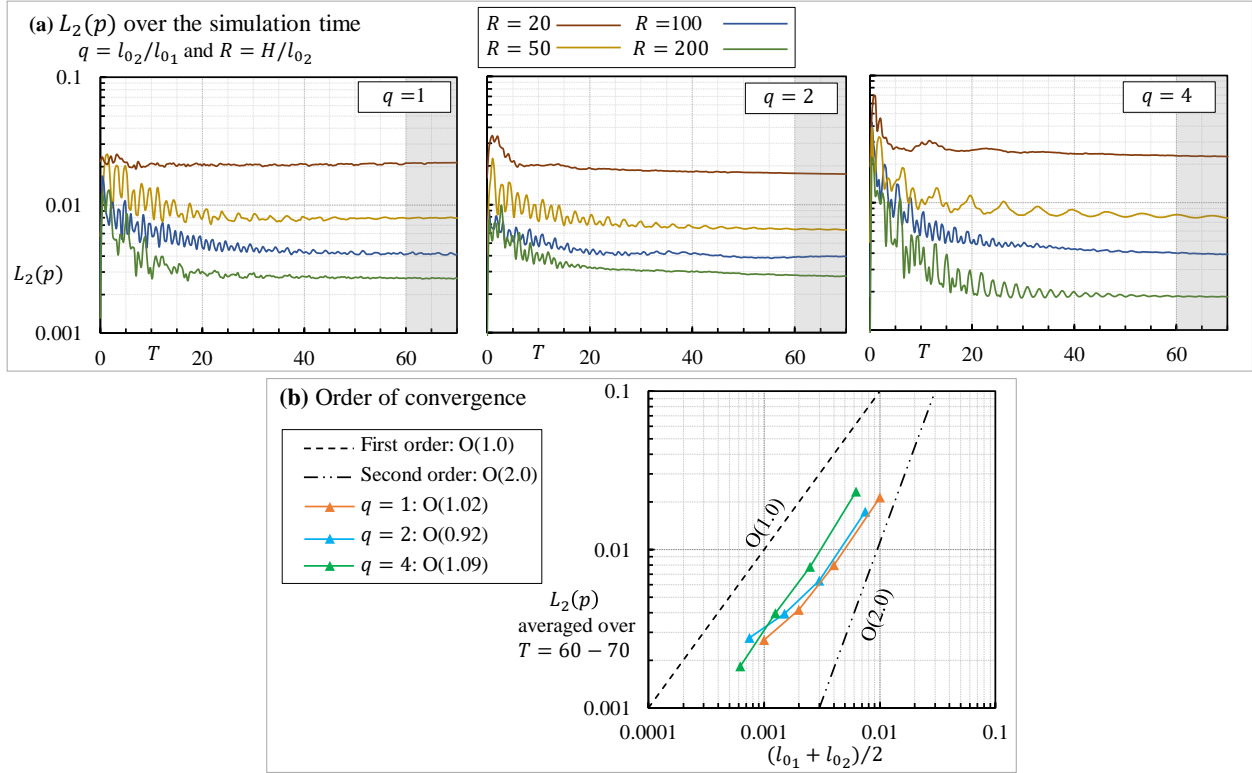


Figure 8.7 Hydrostatic pressure: (a) $L_2(p)$ over the simulation time with different spatial resolutions (R), and (b) the numerical errors and order of convergence, simulated by the single- and multi-resolution MPS models. In (b), $L_2(p)$ is averaged over $T = 60 - 70$ identified as the gray regions in (a). The local numerical pressures are averaged on the extraction points (i.e., at $x = 0.05, 0.10,$ and 0.15 m, shown in Figure 8.3-b).

simulations. Hydrostatic pressure determines the initial density and the effective pressure of the fluid particles at $t = 0$ s [126]. Considering the third-order polynomial spiky kernel of Shakibaeinia and Jin [47] and $k = 3.1$ for the approximation operators, the reference normalization factor $n_0 = 2.2414$ (which is independent of the spatial resolution of each phase). To solve the governing equations, we set C_{CFE} and C_v to 0.5 and 0.125, respectively, and the reference sound speed, c_0 , to 40 m/s. The diffusive term (with $\delta_{MPS} = 0.6$) and the DPC technique are implemented within all the simulations. In this test case, the viscous force is dominant, thus, the maximum viscosity, i.e., η_{max} of the mixture phase, determines the time steps of the calculations through equation (8.26) (which we have set to 4000 and 6000 Pa.s for the sand and PVC cases, respectively). To simulate the physical gate, we implement the virtual gate (VG) technique proposed by Jandaghian et al. [126].

We characterize the dynamics of the immersed granular flow by the interface data (i.e.,

the water free-surface, the dense sediment transport layer, and the bed level), the temporal evolution of the eroded area, A_e , the first moment of the eroded area, $x_c A_e$ (where x_c is the geometric center of A_e), and the wavefront position, x_f (from the experimental data provided by Spinewine and Zech [12] and Spinewine and Capart [13] identified on Figure 8.8-b). We extract the numerical results at time steps identical to the experimental data before the wave reaching the end of the flume (which is at $t = 0.25, 0.5, 0.75, 1.00,$ and 1.25 seconds for the sand case and $t = 0.25, 0.5, 0.75, 1.00, 1.25$ and 1.50 seconds for the PVC case). The non-dimensional time T is given by $t\sqrt{\|\mathbf{g}\|/H}$. We normalize A_e and $x_c A_e$ by their corresponding reference values, i.e., $(A_e)_{exp}^f$ and $(x_c A_e)_{exp}^f$ (which refer to the final data from the experiment at $t = 1.25$ s for sand and at $t = 1.50$ s for PVC), respectively. To detect the simulated eroded area, we employ a velocity threshold (for both water and mixture particles as $\|\mathbf{v}\|_{i \in \Omega_f} \gtrsim 0.25$ [114]) and a minimum volume fraction value (for water particles in the vicinity of the eroded mixture particles as $\langle \phi \rangle_{i \in \Omega_w} / \phi_0 \geq 0.10 - 0.3$ depending on the particle size). Fluid particles that satisfy the two conditions are identified as the eroded particles ($i \in \Omega_{ed}$). Through validating the simulated flow properties, we justify the thresholds set in the detection conditions. The numerical error of the sediment erosion parameters at T is given by $E_r(\cdot) = [(\cdot)_{numerical}^{at T} - (\cdot)_{experimental}^{at T}] / [(\cdot)_{exp}^f \text{ or } L]^{-1}$ normalized by the corresponding reference value. We estimate the global normalized root-mean-square-error, i.e., $L_2(\cdot)$, by $\sqrt{1/N_t \sum_1^{N_t} [E_r(\cdot)]^2}$ where N_t is the number of calculation steps (equal to 5 and 6 for sand and PVC, respectively).

A sensitivity analysis of the rheology parameters

The rheology model dynamically estimates the effective viscosity of the fluid particles as functions of the flow and material properties. Spinewine and Zech [12] reported the reference material parameters of the sand and PVC bed materials (table 8.1); however, the constant parameters in the post-failure terms of the implemented visco-inertial model (i.e., μ_2 , a , and b) remain unknown and should be calibrated. Here, we analysis the sensitivity of the numerical results of case A to the rheology constants (considering the suggested values in [20], [98] and [240]). Also, we quantify the role of the suspension equation (8.23) in the overall

Table 8.1 Material properties of coarse sand grains and PVC pellets.

Sediment	ρ_g (kg.m ⁻³)	θ (degree)	d_g (mm)	ϕ	μ_2	a	b
Sand	2683	30	1.82	0.53	0.84	1.23	0.3
PVC	1580	38	3.9	0.58	1.00	1.23	0.3

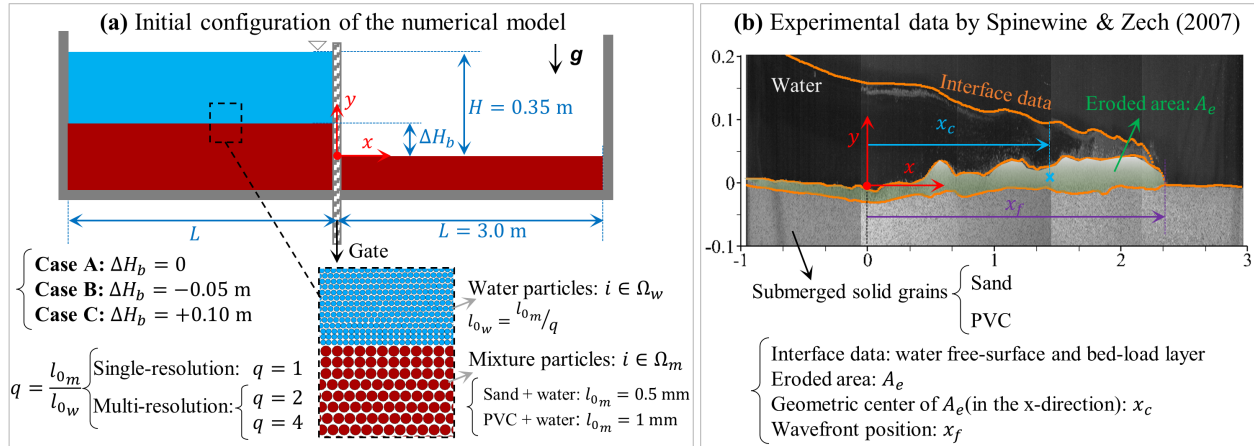


Figure 8.8 Water dam break, under the gravitational force, $\mathbf{g} = (0, -9.81\text{m/s}^2)^t$, on movable beds. (a) The initial configuration of the two-dimensional numerical simulations, and (b) the experimental data by Spinewine and Zech [12]. Considering different levels of sediment on the left side of the gate, ΔH_b , we simulate cases A, B, and C (denoted as (a), (b), and (d) in the experiments, respectively). The fluid particles ($i \in \Omega_f = \Omega_w \cup \Omega_m$) are packed before the initialization of the main simulations.

mechanical behavior of the sediment erosion.

To conduct the sensitivity analysis, we plot the temporal evolution of A_e , $x_c A_e$, and x_f simulated by the single-resolution MPS model ($q = 1$) where μ_2 , a , and b vary as shown in Figures 8.9 and 8.10 (for the sand and PVC cases, respectively). Each parameter changes while the other two parameters are equal to their reference values given in table 8.1. The graphs show that the bed-load evolution with different parameters of the post-failure terms remains almost alike. Table 8.2 and 8.3 represent L_2 of each scenario and compare them with the errors of the reference model (given in the first rows of the tables). For both bed materials, L_2 varies by less than $\sim 3\%$. Thus, the sensitivity analysis confirms that the estimated sediment erosion is almost independent of the variation of the parameters, μ_2 , a , and b in the specified ranges.

Furthermore, we simulate case A-PVC (where $q = 1, 2, 4$) with and without implementing the suspension equation (8.23) in the rheology model. Table 8.4 shows that $L_2(x_f)$ is almost identical for both conditions. Adding the suspension term slightly reduces $L_2(A_e)$ and $L_2(x_c A_e)$ by $\sim 1 - 4\%$, nevertheless, the suspension term does not manipulate the overall sediment dynamics estimated by the single- and multi-resolution models.

The considerable incompatibility between the numerical simulations and the experimental measurements (shown in the graphs of Figures 8.9 and 8.10 and quantified in table 8.4) man-

ifests the incapability of the single-resolution model in capturing accurate flow evolution. The continuum-based numerical model ignores some physical properties of the water-sediment mixing process associated with multi-scale interactions and volume fraction variations. No inter-particle mass exchange occurs in the numerical simulations; therefore, the model neglects the microscopic fluid flow around and between solid grains and the effects of density changes in the rheology model.

Flow properties and interface data

In this section, we present and validate the dam-break waves over erodible beds simulated by the multi-resolution MPS method (where $q = 4$). By reporting the longitudinal and vertical flow properties, we discuss the global flow evolution and the non-linear mechanical behavior of this rapid fluid-driven problem. The velocity magnitude, $\|\mathbf{v}\|$, the effective viscosity (as $\log_{10}(\eta)$), the approximated volume fractions (i.e., $\langle\phi\rangle$ normalized by the reference volume fraction of the mixture phase, ϕ_0), and the mixed number, I_m , of cases A-Sand, A-PVC, B-Sand, and C-Sand (at $t = 0.5$ and $t = 1.0$ seconds) are illustrated in Figures 8.11, 8.12, 8.13, and 8.14, respectively. The figures include snapshots of the experiments and the interface data plotted over the numerical results. Except for the close-up plots/snapshots (i.e., the inset figures with the black dash line boarder), the vertical scale of the images is stretched by a factor of 1.5 to ease visualization of the profiles and flow evolution.

The numerical solution provides in-depth details of the water-sediment dam-break flows. As the top edge of the vertical gate reaches the bed level ($t = 0$ s), the water column collapses on the water-saturated sediment bed driving a thin layer of bed-load toward the downstream. After the sudden vertical collapse, the wave propagates horizontally on the movable bed (considering that the wavefront position advances a distance of $3H$ in the positive x-direction in less than 0.5 seconds). The flow velocity increases uniformly from upstream to downstream;

Table 8.2 The normalized root-mean-square error (L_2) of A_e , $x_c A_e$, and x_f of case A-Sand with values for material properties in the rheology model (a , b , and μ_2) and where $q = 1$.

μ_2	a	b	$L_2(A_e)\%$	$L_2(x_c A_e)\%$	$L_2(x_f)\%$
0.84	1.23	0.3	32.01	25.52	9.88
(0.71, 1.0)	1.23	0.3	(29.99,32.39)	(24.78,25.91)	(10.01,10.20)
0.84	(0.71,0.97)	0.3	(31.54,31.77)	(26.63,26.60)	(9.84,9.85)
0.84	1.23	(0.1, 0.2)	(33.31,31.58)	(26.86,26.62)	(10.04,9.72)

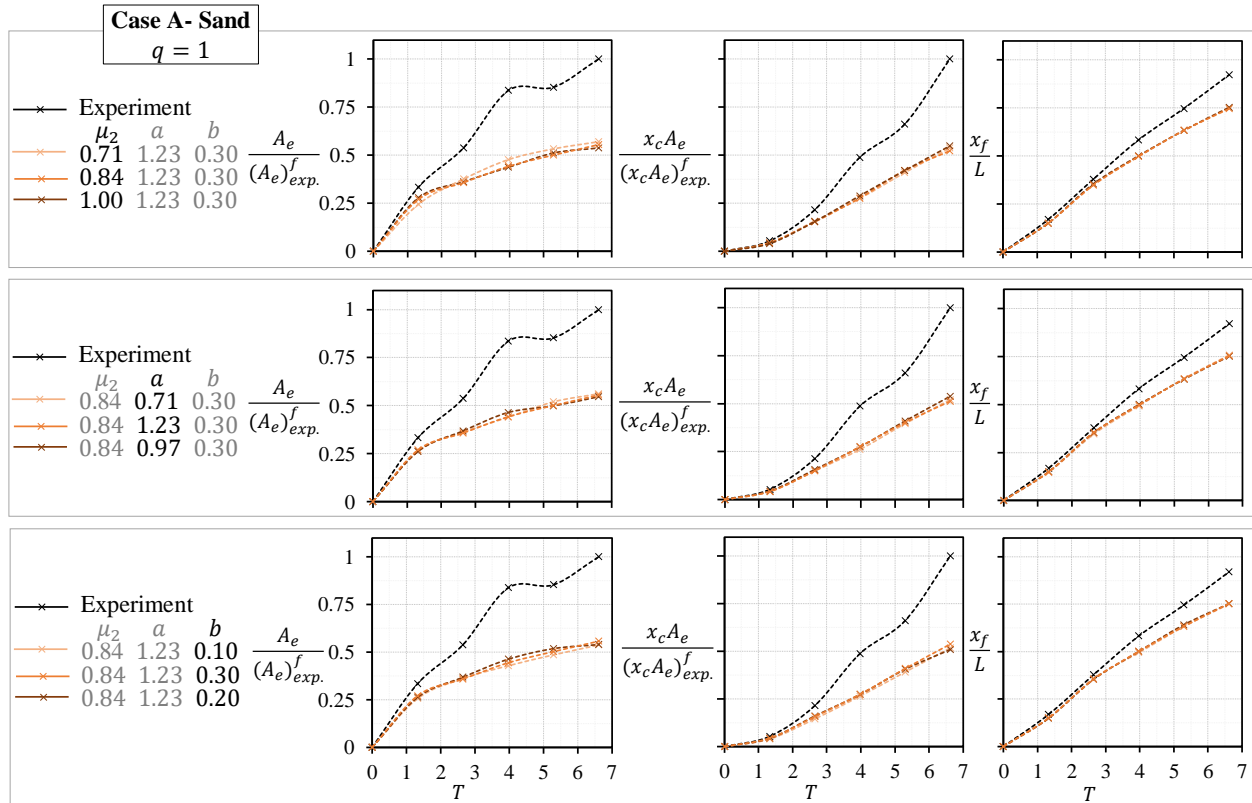


Figure 8.9 Sensitivity analysis of the fluid-driven granular flow (case A-Sand) to the rheology parameters (a , b , and μ_2) through the single-resolution MPS model ($q = 1$). The experimental profiles of the eroded area, A_e , the first moment of the eroded area, $x_c A_e$, and the wavefront position, x_f , are extracted from the interface data by Spinewine and Zech [12].

Table 8.3 The normalized root-mean-square error (L_2) of A_e , $x_c A_e$, and x_f of case A-PVC with different material properties in the rheology model (a , b , and μ_2) and where $q = 1$.

μ_2	a	b	$L_2(A_e)\%$	$L_2(x_c A_e)\%$	$L_2(x_f)\%$
1.00	1.23	0.3	35.41	25.06	5.08
(0.84, 1.39)	1.23	0.3	(33.89, 36.52)	(24.01, 24.88)	(4.67, 4.83)
1.00	(0.71, 0.97)	0.3	(34.18, 35.35)	(23.67, 22.90)	(4.63, 3.99)
1.00	1.23	(0.1, 0.2)	(36.49, 35.02)	(23.95, 23.60)	(4.89, 4.58)

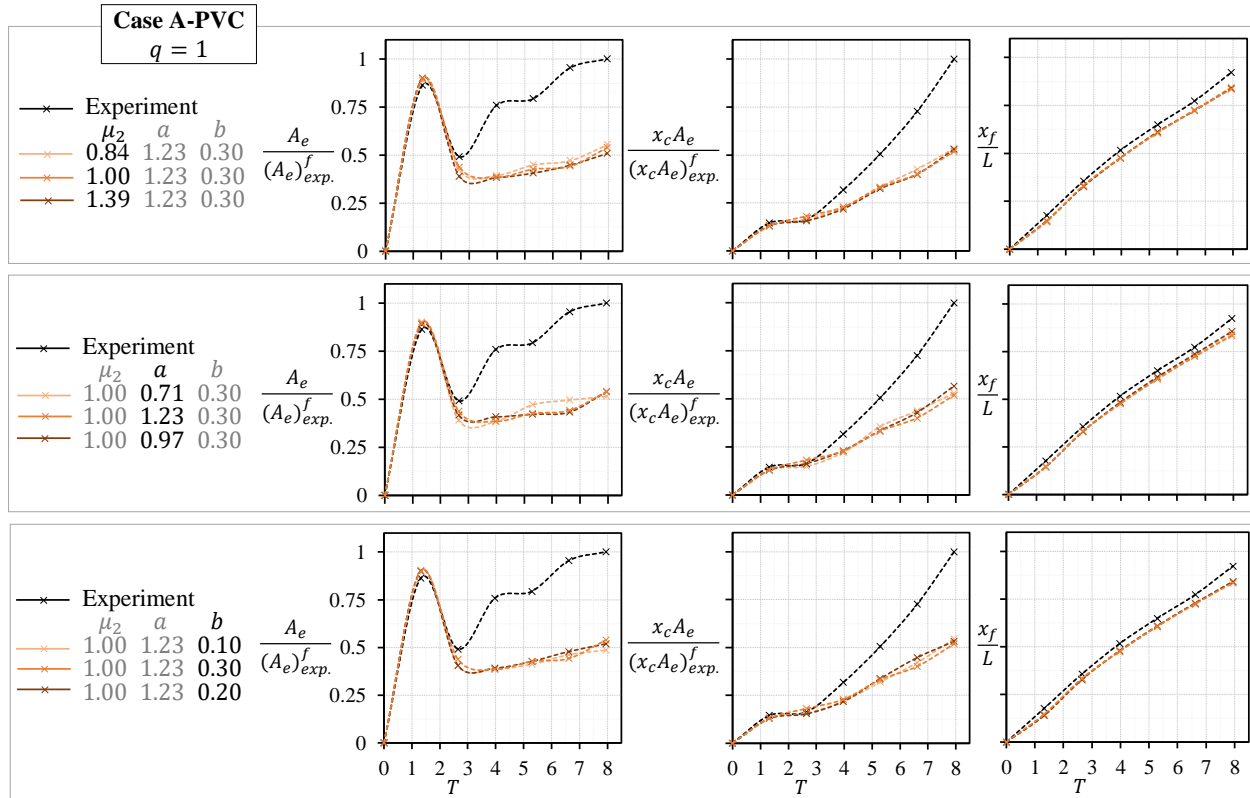


Figure 8.10 Sensitivity analysis of the fluid-driven granular flow (case A-PVC) to the rheology parameters (a , b , and μ_2) through the single-resolution MPS model ($q = 1$). The experimental profiles are extracted from the interface data by Spinewine and Zech [12].

Table 8.4 The normalized root-mean-square-error (L_2) of A_e , $x_c A_e$, and x_f with $q = 1, 2$, and 4 for case A-PVC with and without the suspension equation (8.23).

Case A-PVC	$L_2(A_e)\%$			$L_2(x_c A_e)\%$			$L_2(x_f)\%$		
	1	2	4	1	2	4	1	2	4
q									
With the suspension equation	35.41	30.64	13.77	25.06	14.76	2.23	5.08	1.29	1.39
Without the suspension equation	35.83	32.86	16.05	24.81	18.00	3.24	6.01	2.11	1.38

the dam-break surge exceeds a maximum velocity of 2.5 m/s forming rapid erosional bores at the interface and the head of the wave (as shown in the close-up plots). For all cases the surge celerity develops similarly (independent from the initial configurations and/or the sediment materials). Furthermore, the effective viscosity field (plotted as $\log_{10}(\eta)$) illustrates the yielded and un-yielded regions estimated by the regularized rheology formulation. Inside the bed, high shear forces rapidly reduce the flow velocity towards the bottom of the flume (i.e., in the negative y-direction). The spatial variation of volume fraction at the interface manifests the mixing of water and mixture particles. From upstream to downstream, the longitudinal concentration of mixture particles increases over the bed-load layer; close to the downstream wavefront, the suspended mixture particles fill the entire flow depth (well-observed in case A with the PVC bed material) [13]. In the implemented model, the approximated volume fraction is included in the shear force calculations through the effective viscosity terms. The mixed number of the rheology model, I_m , as a function of the strain rate magnitude and the effective pressure, clearly distinguishes the suspended mixture particles (where $I_m \gtrsim 0.6$) for which the suspension equation (8.23) updates the effective viscosity.

The overall longitudinal flow evolution, including water free-surface, the sediment transport layer thickness, and the bed boundary, are in reasonable agreement with the experimental interface data. In all cases, the high wave velocity, causing highly dynamic sediment erosion, creates irregular free-surface profiles (as rotated S-like shapes which are particularly visible at $t = 0.5$ s). As the wave progresses on the horizontal beds (shown at $t = 1.0$ s), the free-surface curvature reduces and better agreement exists between the numerical and experimental measurements. In the flat-bed cases (A-sand and A-PVC), the sudden vertical surge forms a scour hole at the near-dam region (i.e., the gate's location) partially captured by the numerical simulations. Also, the calculated wavefront positions of these two cases match quite well with the experimental profiles at $t = 0.5$ and 1.0 s. In the case with a forward-facing step of the saturated sediment material (i.e., B-sand where $\Delta H_b = -0.05$ m), the un-yielded bed is comparable with the measured bed profile, even at the near-dam region (at $x = 0$). However, the bed boundary of the case with the backward-facing step (i.e., C-sand where $\Delta H_b = +0.10$ m) does not match with the experimental profile close to the gate's location; this issue also affects the prediction of the water free-surface with stronger curvatures (at $x = \{-0.25, +0.5\}$ m) and underestimates the wavefront position (at $t = 1.00$ s). The observed discrepancies can be attributed to the complex non-linear flow behaviors and turbulence effects at the front of the wave which lead to non-monotonous interface profiles and non-equilibrium sediment transport [18]. The continuum-based particle method struggles to accurately capture the instantaneous and local flow curvatures (especially at $t = 0.5$ s near the wavefront of case B-PVC and the gate's location of case D-sand). We should note that the adopted numerical

formulation is incapable of directly simulating the dilatation and compaction effects on the immersed granular flows. Further, the virtual gates (see [126]) ignore the gate's physical thickness, and therefore, the associated initial disturbance of its movement. Nevertheless, the developed model simulates the overall flow evolution, wave celerity, and sediment erosion processes of the dam break problem comparable with the experimental measurements and snapshots.

Next, we validate the internal flow properties of the numerical simulation of case A-PVC against the available experimental measurements represented by Spinewine and Capart [13] (Figures 8.15 and 8.16). Spinewine and Capart [13] used a particle tracking analysis to measure the vertical velocity profiles, $u_{exp.}$, at 40 cross-sections evenly distributed between $x = -0.95$ and $+2.95$ m with $\Delta x = 0.10$ m. We extract the numerical velocity, $u_{num.}$, by linearly averaging the velocity magnitude of fluid particles at the vicinity of the extraction points with $\Delta y = 0.01$ m on the same vertical cross-sections. Figure 8.15 plots the fluid particles (classified as the eroded and not eroded particles, i.e., $i \in \Omega_{ed}$ and $i \notin \Omega_{ed}$, respectively), the extracted numerical velocity as $x + 0.05u_{num.}$, and the experimental velocity as $x + 0.05u_{exp.}$, at $t = 0.6, 1.0,$ and 1.4 seconds. The numerical model simulates the non-linear velocity profiles with smooth variations at the top and base of the sediment transport layer; the velocity profiles in the water layer remain uniform with maximum magnitudes at the free-surface. At $t = 1.4$ s, the model slightly underestimates the velocity near the wavefront ($x \simeq 2.5$). Nevertheless, the estimated velocity matches the experimental profiles quite well over the entire fluid domain. Moreover, we extract and compare the local granular concentration, c , and the sediment transport intensity defined as the product of c and u (i.e., c and cu , respectively). Spinewine and Capart [13] reported the corresponding experimental measurements limited to the granular layer at 13 laser-instrumented vertical cross-sections between $x = 0.05$ and 1.5 m. To estimate $c_{num.}$, we linearly average the approximated volume fraction of the particles, $\langle \phi \rangle_{i \in \Omega_f}$, at the extraction points. One should note that the experimental measurements are missing at $x \geq 1.25$ m and $t = 0.6$ s (unlike the velocity profiles reported by the particle tracking analysis in Figure 8.15). We plot $x + 0.1c$ and $x + 0.15cu$ over the fluid particles in the left and right graphs of Figure 8.16, respectively. The granular concentration keeps its maximum value (ϕ_0) in the granular layer while reducing across the bed-load layer toward the free surface. At the top interface of the transport layer, the granular concentration drops and further vanishes in the absence of the mixture particles. In spite of some minor discrepancies, the estimated numerical profiles are in good agreement with the experimental measurements; the validation confirms that the numerical model can predict the non-linear profiles with smooth variations across the bed-load layer. We should also highlight that the compatibility between the numerical and experimental profiles justifies conditions we have

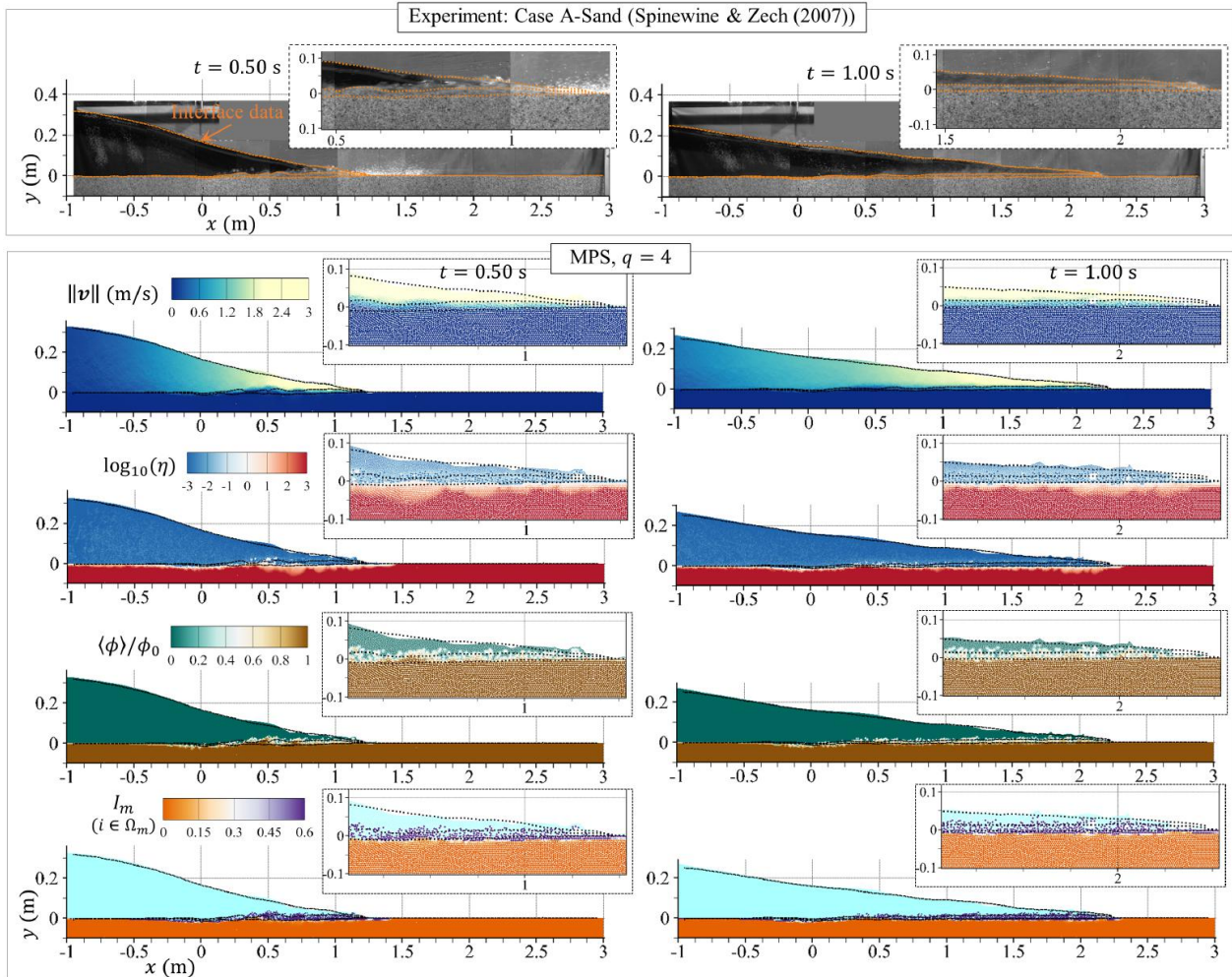


Figure 8.11 Dam break waves over the flat erodible bed (case A-Sand). The first row shows the snapshots and the interface data from the experiments by Spinewine and Zech [12]. The results of the multi-resolution MPS model (with $q = 4$) (i.e., the velocity magnitude, $\|\mathbf{v}\|$, the log of the effective viscosity, $\log_{10}(\eta)$, the approximated volume fraction, $\langle\phi\rangle/\phi_0$, and the mixed number of the rheology model, I_m) are represented at $t = 0.5$ and 1.0 seconds. The experimental interface data (the black squares) are plotted on the numerical results. Except for the close-up plots/snapshots, the vertical scale is stretched by a factor of 1.5.

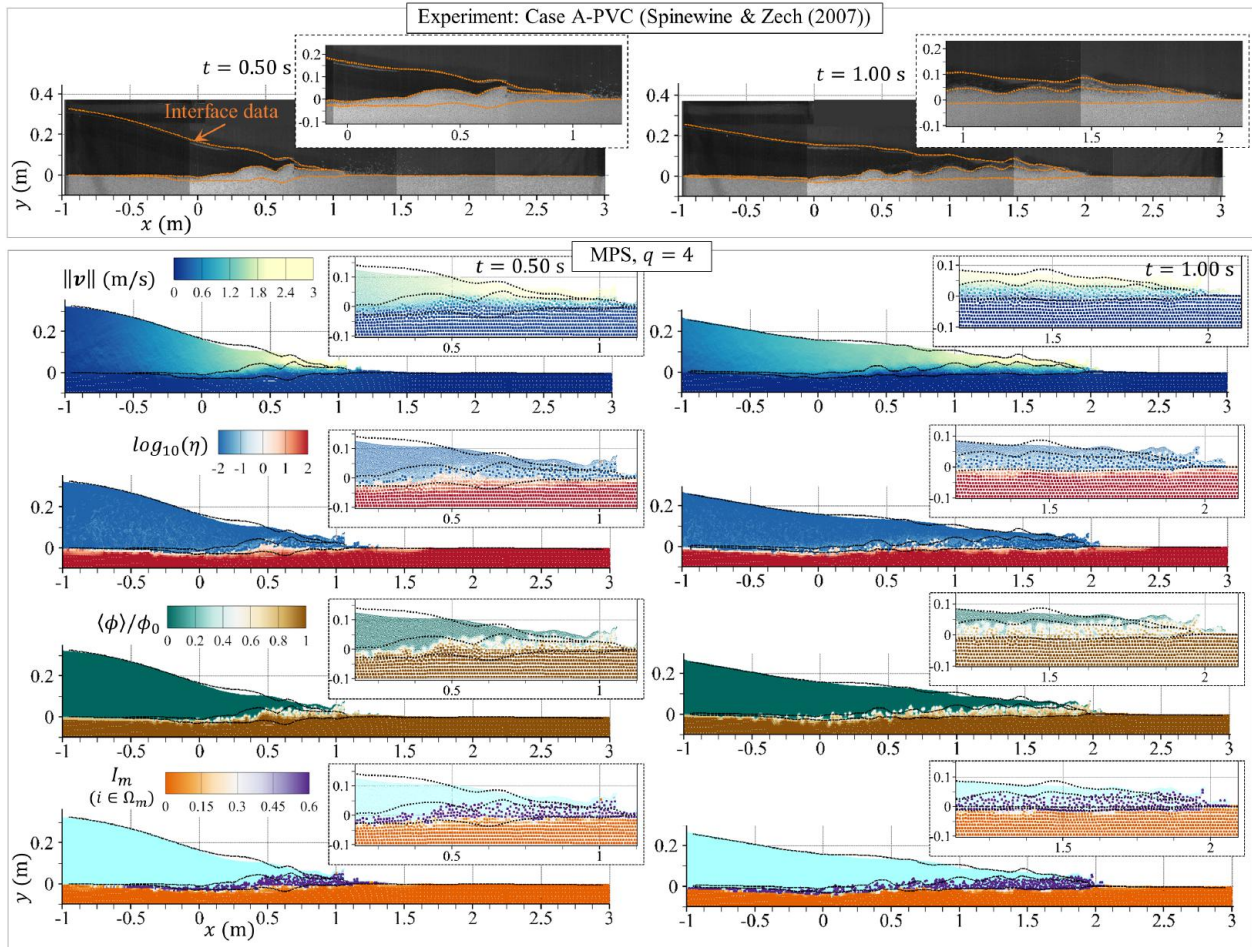


Figure 8.12 Dam break waves over the flat erodible bed (case A-PVC). The first row shows the snapshots and the interface data from the experiments by Spinewine and Zech [12]. The experimental interface data (the black squares) are plotted on the numerical results (where $q = 4$). Except for the close-up plots/snapshots, the vertical scale is stretched by a factor of 1.5.

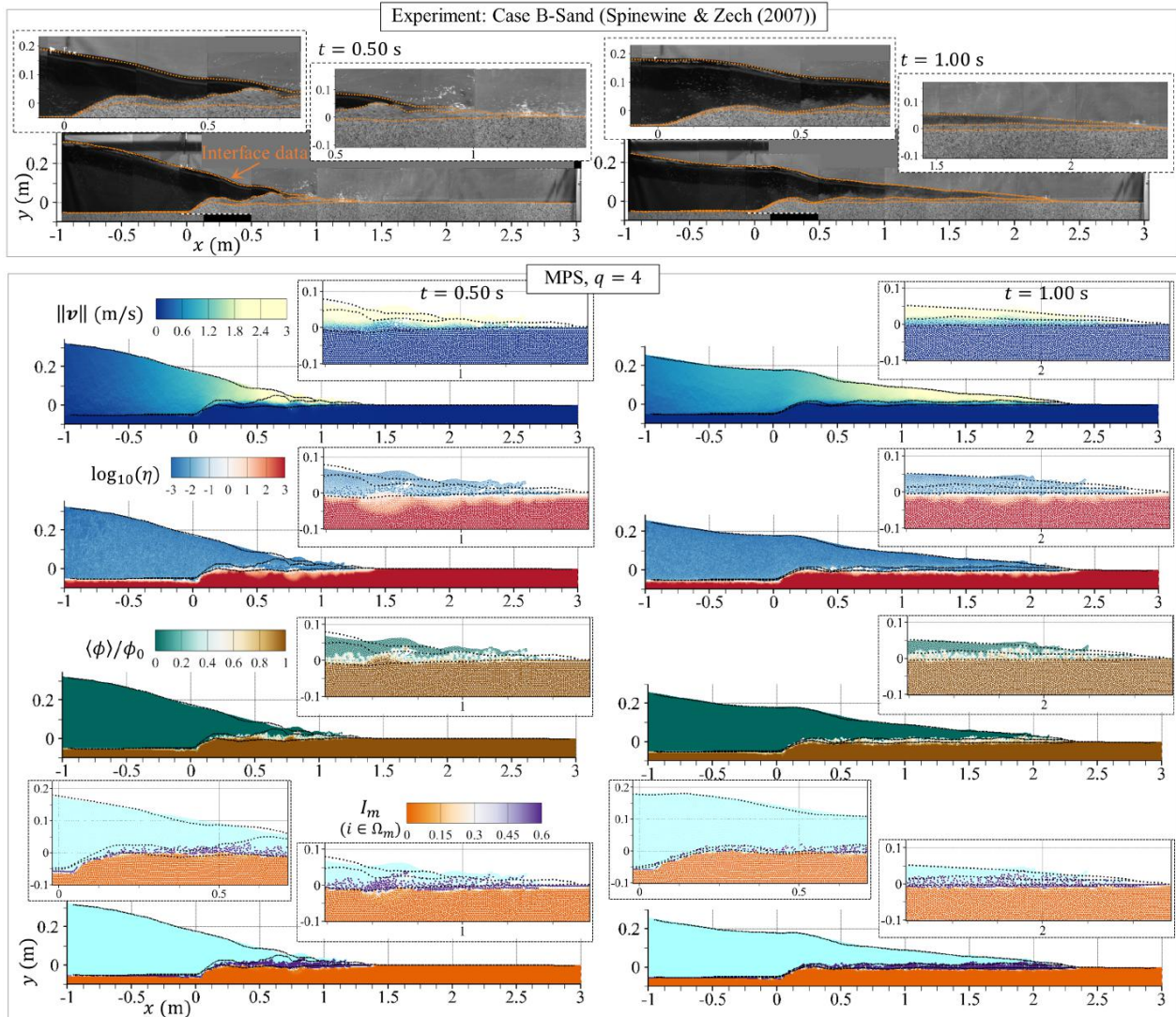


Figure 8.13 Dam break waves over the erodible bed (case B-Sand). The first row shows the snapshots and the interface data from the experiments by Spinewine and Zech [12]. The experimental interface data (the black squares) are plotted on the numerical results (where $q = 4$). Except for the close-up plots/snapshots, the vertical scale is stretched by a factor of 1.5.

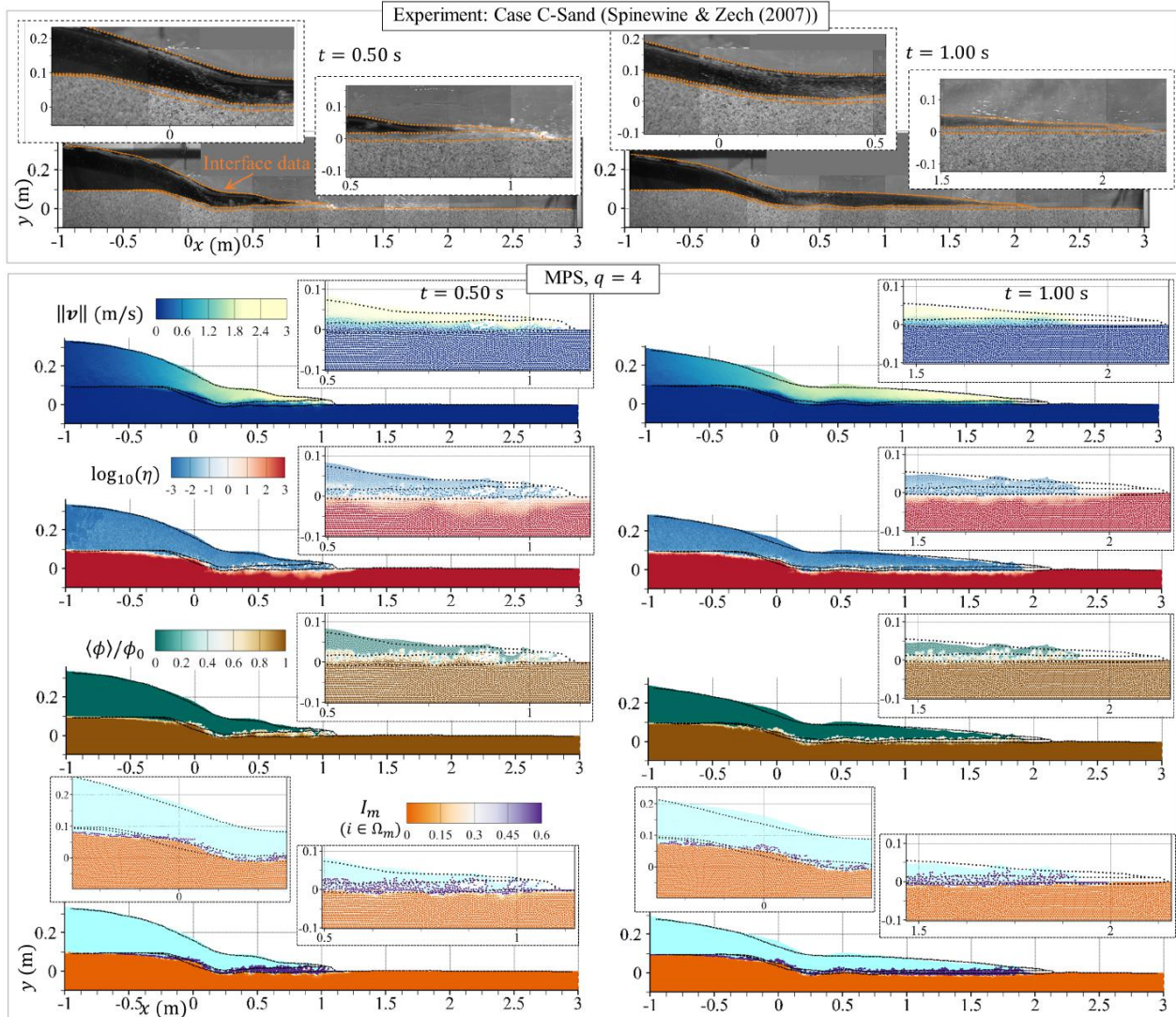


Figure 8.14 Dam break waves over the erodible bed (case C-Sand). The first row shows the snapshots and the interface data from the experiments by Spinewine and Zech [12]. The experimental interface data (the black squares) are plotted on the numerical results. Except for the close-up plots/snapshots, the vertical scale is stretched by a factor of 1.5.

adopted to detect the eroded area (through which we study the phenomenology of sediment erosion and quantify the numerical validations).

Phenomenology of the sediment erosion: A_e , $x_c A_e$, and x_f

To overview the phenomenology of the dam break waves over movable beds, we compare the sediment dynamics of the different configurations. Figure 8.17 shows the wave propagation of cases A-sand, A-PVC, B-sand, and C-sand on the horizontal beds at $t = 1.25$ s. The figure contains experimental snapshots and the interface data of the test cases. Further, we plot the temporal evolution of the global erosion variables, A_e and $x_c A_e$, and the wavefront position, x_f , in Figure 8.18, and represent the associated numerical errors in table 8.5.

Qualitatively, the numerical simulations provide comparable flow evolution and predict the thickness of the transport layer at the center of the wave in all four cases. The base of the transport layer is well-captured; however, near the gate's location, the rapid flow involves complex interface deformations affecting the numerical predictions. As discussed earlier, this incompatibility is more noticeable for case C-sand with the backward-facing step. Comparing case A-PVC with the other configurations illustrates the sensitivity of sediment erosion to the density ratio (i.e., ρ_m/ρ_w). The thickness of the transport layer increases significantly for case A-PVC as the wave can mobilize more mixture particles. On the other hand, with the sand material (i.e., with the heavier grains, but with a smaller friction angle) in cases A, B, and C, the transport layer is thinner; thus, the wave can progress further on the horizontal bed with less sediment erosion toward the downstream [13,18]. While the wavefront position of case A-PVC matches well with the interface data, the numerical simulation slightly underestimates the wave propagation speed of cases with the sand beds (regardless of their initial configuration).

To quantitatively study the sediment dynamics, Figure 8.18 provides an overall overview of the sediment erosion concerning different configurations and bed materials. The graphs of Figure 8.18 show that the multi-resolution MPS model predicts the global behavior of the sediment erosion and wave propagation. Particularly, we observe that $x_c A_e$, and x_f of all four cases are in very good agreement with the experimental data. For the light PVC material, sediment erosion increases significantly as A_e of A-PVC is almost 2.5 times greater than A_e of A-sand (at $t = 1.25$ s). For case C-sand, the wave interaction with the backward-facing step increases the sediment erosion by ~ 30 percents in comparison with cases A-sand and B-sand. With the step-like discontinuity of cases B and C, the results are less satisfactory considering that the numerical model underestimates the sediment erosion at $t = 0.5$ and 0.75 s. Table 8.5 represents the numerical errors of the sediment erosion parameters, L_2 . $L_2(x_f)$

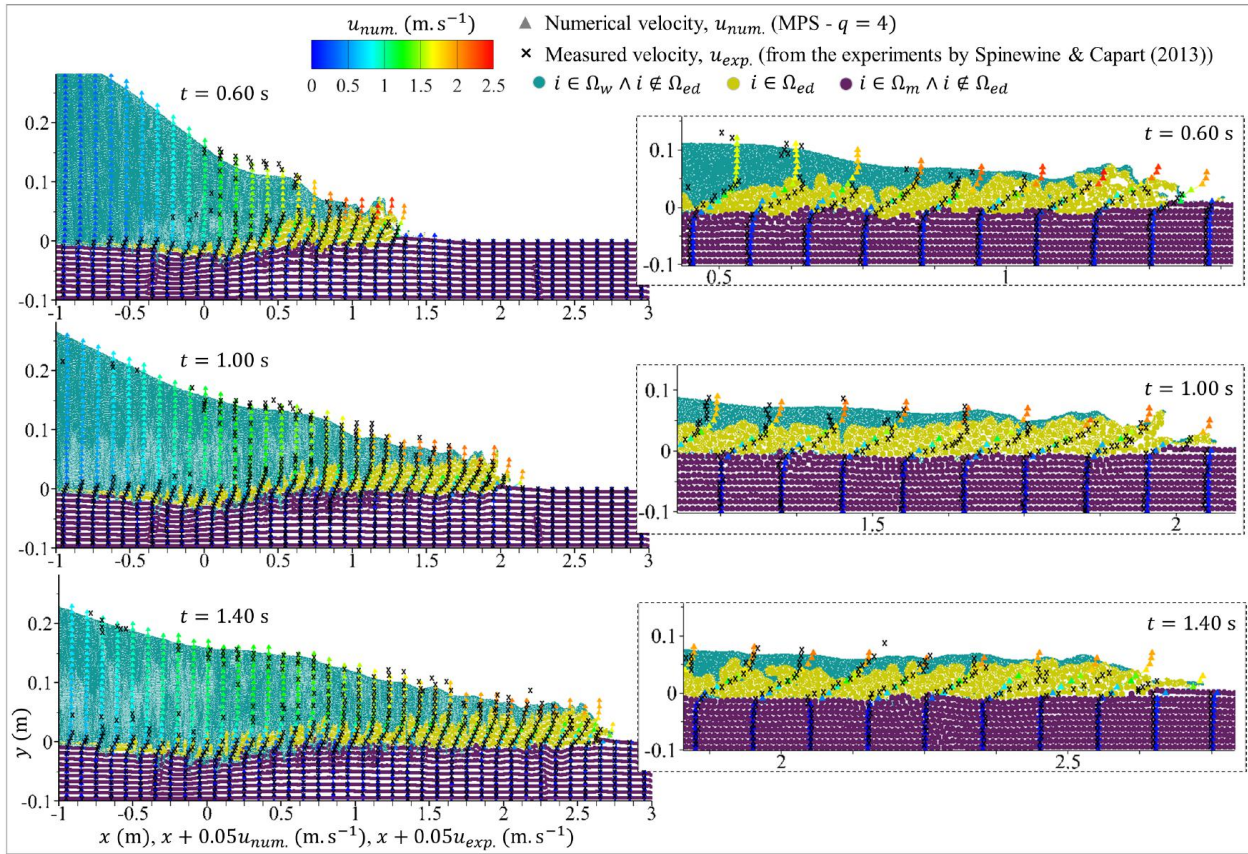


Figure 8.15 Vertical velocity profiles of dam break waves over the flat erodible bed (case A-PVC) in comparison with the experimental data at $t = 0.6$, 1.0 , and 1.4 seconds. The local numerical velocity, $x + 0.05u_{num.}$, is identified by the delta markers and the color map. The experimental data, $x + 0.05u_{exp.}$ (shown as the black x markers) are extracted from the work of Spinewine and Capart [13]. Except for the close-up plots, the vertical scale is stretched by a factor of 4.

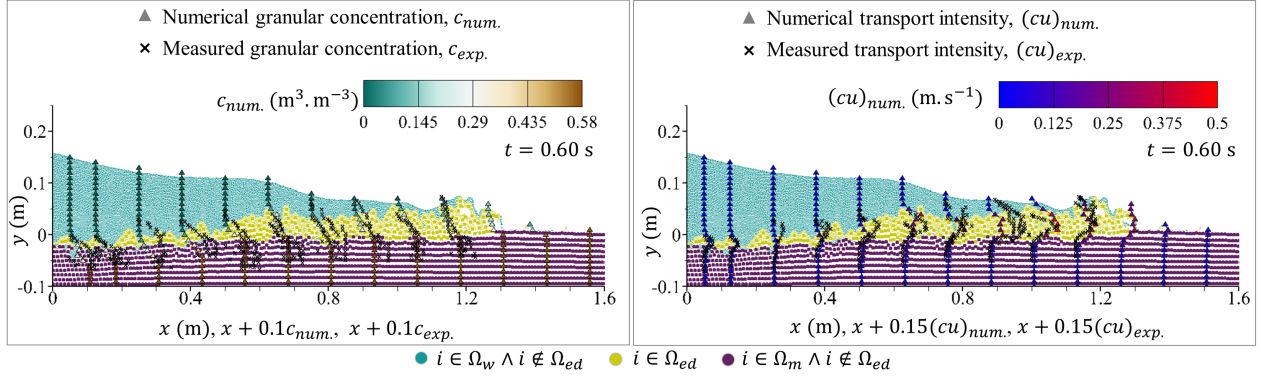


Figure 8.16 Vertical profiles of the granular concentration, c , and sediment transport intensity, cu , of case A-PVC at $t = 0.6$ seconds (on the left and right graphs, respectively). The numerical results of the multi-resolution model ($q = 4$) are compared with the experimental measurements by Spinewine and Capart [13] (plotted as the delta and the black x markers, respectively). The vertical scale is stretched by a factor of 1.5.

and $L_2(x_c A_e)$ remain less than 10 percents manifesting the acceptable accuracy of numerical model in simulating the flow evolution on the movable beds. The results show that with the step-like discontinuities, $L_2(A_e)$ increases by ~ 10 percents (from ~ 8.5 for case A-sand to ~ 19.7 and ~ 14.7 percents). We attribute the numerical errors to the neglected role of granular dilatation and compaction in the adopted single-phase rheology model. This issue indirectly ignores the turbulence suspension effects of the microscopic pore water flow between solid grains within the numerical simulations [13]. Nevertheless, the multi-resolution MPS model proves to be capable of predicting the global behavior of the fluid-driven granular dynamics with reasonable numerical accuracy.

Table 8.5 The normalized root-mean-square error (L_2) of A_e , $x_c A_e$, and x_f of cases A-Sand, A-PVC, B-Sand, and C-Sand simulated by the multi-resolution MPS model ($q = 4$).

Case	$L_2(A_e)\%$	$L_2(x_c A_e)\%$	$L_2(x_f)\%$
A-Sand	8.49	8.20	2.40
A-PVC	13.77	2.23	1.39
B-Sand	19.66	8.09	3.67
C-Sand	14.68	8.54	6.79

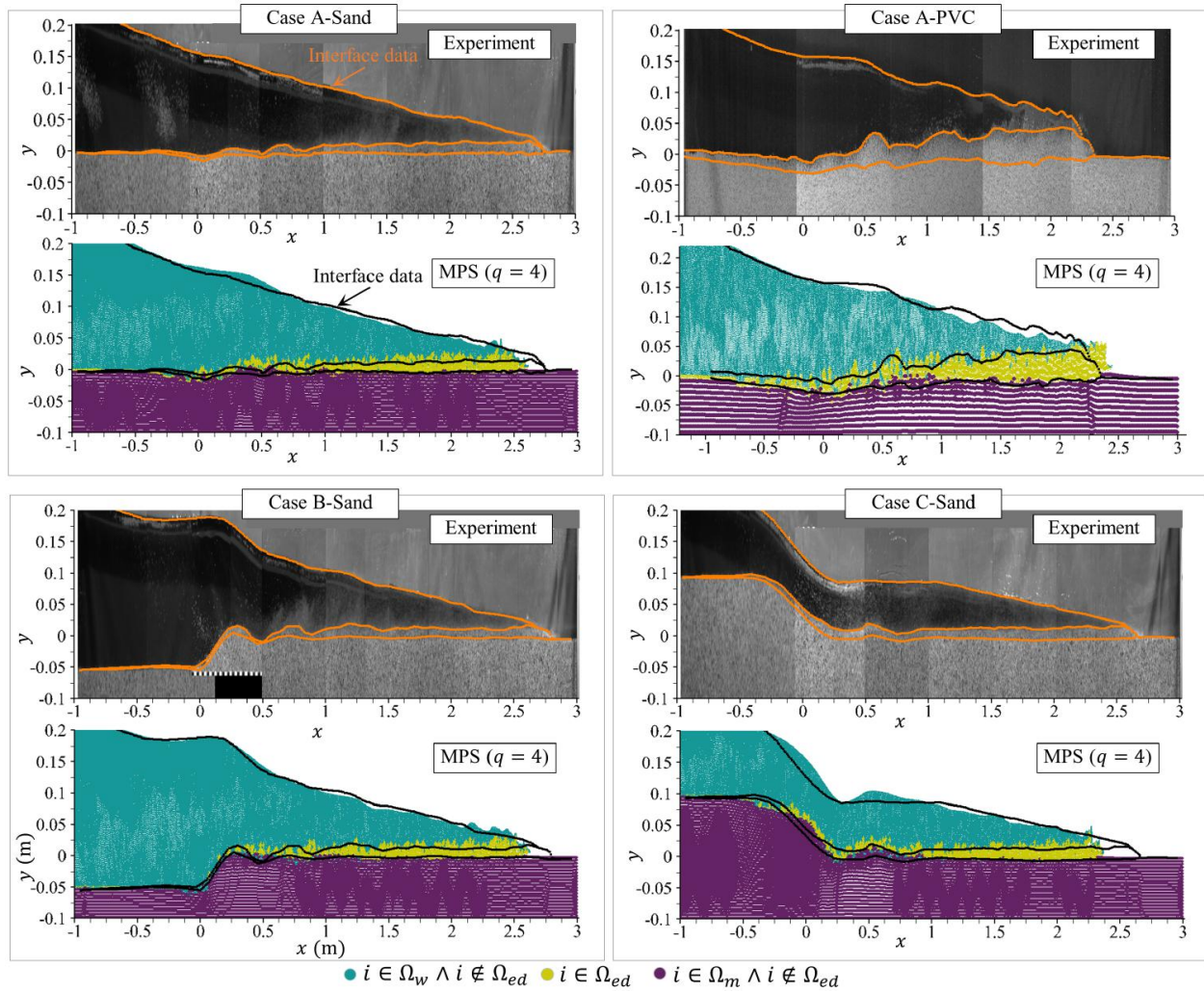


Figure 8.17 Flow evolution and the eroded region, $i \in \Omega_{ed}$, of case A, B, and C, at $t = 1.25$ s, simulated by the multi-resolution MPS model ($q = 4$) compared with the experimental snapshots and interface data (the black squares) from the work of Spinewine and Zech [12]. The vertical scale is stretched by a factor of 5.0.

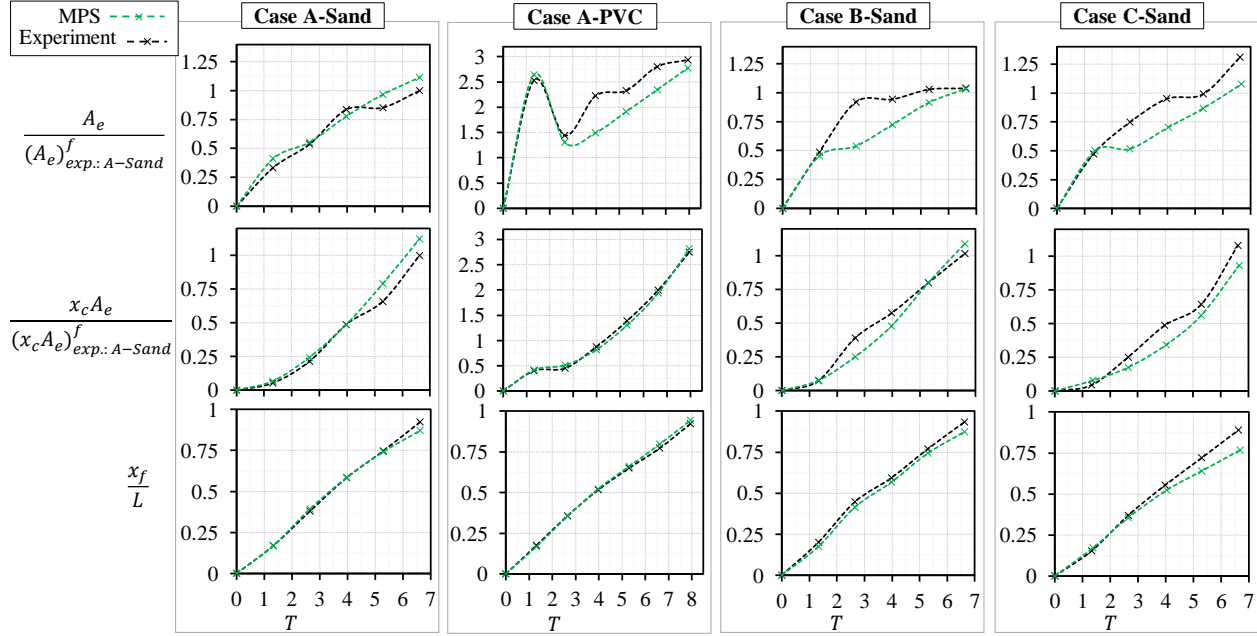


Figure 8.18 Temporal evolution of A_e , $x_c A_e$, and x_f of cases A-Sand, A-PVC, B-Sand, and D-Sand with the multi-resolution MPS model ($q = 4$) compared with the experimental profiles (extracted from the interface data reported by Spinewine and Zech [12]). A_e and $x_c A_e$ are normalized by the corresponding reference values of case A-Sand (denoted as $(A_e)^f_{exp.:A-Sand}$ and $(x_c A_e)^f_{exp.:A-Sand}$, respectively).

Role of multi-scale simulations

Here, we discuss the role of multi-scale interactions in sediment erosion modeling. To do so, we compare the interface data of case A simulated by the single- and multi-resolution models. Figures 8.19 and 8.20 represent the eroded region ($i \in \Omega_{ed}$) of case A with the sand and PVC bed materials, respectively. In these figures, except for the close-up plots, the vertical scale is stretched by a factor of 5.0. Flow evolution of the water and mixture particles (at $t = 0.75$ and 1.25 seconds) shows that the single-resolution model ($q = 1$) underestimates the wavefront position. This discrepancy between the numerical and experimental results is more noticeable for the sand case with a higher density ratio. On the other hand, the multi-resolution models ($q = 2, 4$) predict more flow deformations at the interface, increasing erosion of the mixture particles. Although the continuum-based modeling still misses some physical aspects of sediment erosion (i.e., the pore water flow between the solid grains and the associated changes in the volume fraction of the mixture particles), the multi-resolution particle interactions allow the numerical model to capture more accurate flow evolution related to the multi-scale feature of water-sediment dynamics.

To quantify the numerical validations, we plot the temporal evolution of A_e , $x_c A_e$, and x_f and compare them with the experimental data (Figure 8.21). The profiles manifest improvements in estimating the sediment erosion by the multi-resolution model (with $q = 4$), while the single-resolution model underestimates the granular flow evolution. The remaining incompatibility between the numerical and experimental profiles (especially for the eroded area of case A-PVC at $T \gtrsim 3$) originate from complex water-sediment mixing processes at the interface that the continuum-based particle method is incapable of simulating. Table 8.6 represents the normalized root-mean-square-error, $L_2(\cdot)$ of the sediment erosion parameters. The quantified results show a significant reduction in the numerical errors by the multi-resolution simulations (by a factor of $\sim 2 - 4$) with respect to the single-resolution results. Moreover, to compare the global mechanical behavior of the sediment flow, we plot the global kinetic energy of the mixture particles ($E_k = 0.5 \sum \rho_{0i} l_{0i}^2 \|\mathbf{v}\|_i^2$ for $\forall i \in \Omega_m$) which is independent of the conditions used for detecting the eroded area (Figure 8.22). For case A, E_k of the multi-resolution model (where $q = 4$) is two to three times greater than E_k of the single-resolution model (where $q = 1$) for both bed materials. Overall, we observe that the developed multi-resolution model considerably reduces the errors of the single-resolution simulations by estimating more sediment erosion at the interface.

8.6 Conclusion

We investigated the mechanical behavior of fluid-driven granular dynamics through a consistent multi-resolution particle method. We developed a conservative form of governing equations (based on the enhanced weakly-compressible MPS method) to incorporate multi-scale water-sediment interactions within the continuum-based numerical modeling. Simulating two benchmark cases (i.e., the multi-viscosity Poiseuille flow and the multi-density hydrostatic pressure problems), we studied the accuracy and convergence of the numerical results with the single- and multi-resolution models. As for the fluid-driven granular erosion, we adopted the generalized rheology equation to model the two-dimensional dam-break waves on erodible

Table 8.6 The normalized root-mean-square-error (L_2) of A_e , $x_c A_e$, and x_f with $q = 1, 2$, and 4 for case A with sand and PVC.

Case A	$L_2(A_e)\%$			$L_2(x_c A_e)\%$			$L_2(x_f)\%$			
	q	1	2	4	1	2	4	1	2	4
Sand		32.01	20.10	8.49	25.52	13.47	8.20	9.88	4.33	2.40
PVC		35.41	30.64	13.77	25.06	14.76	2.23	5.08	1.29	1.39

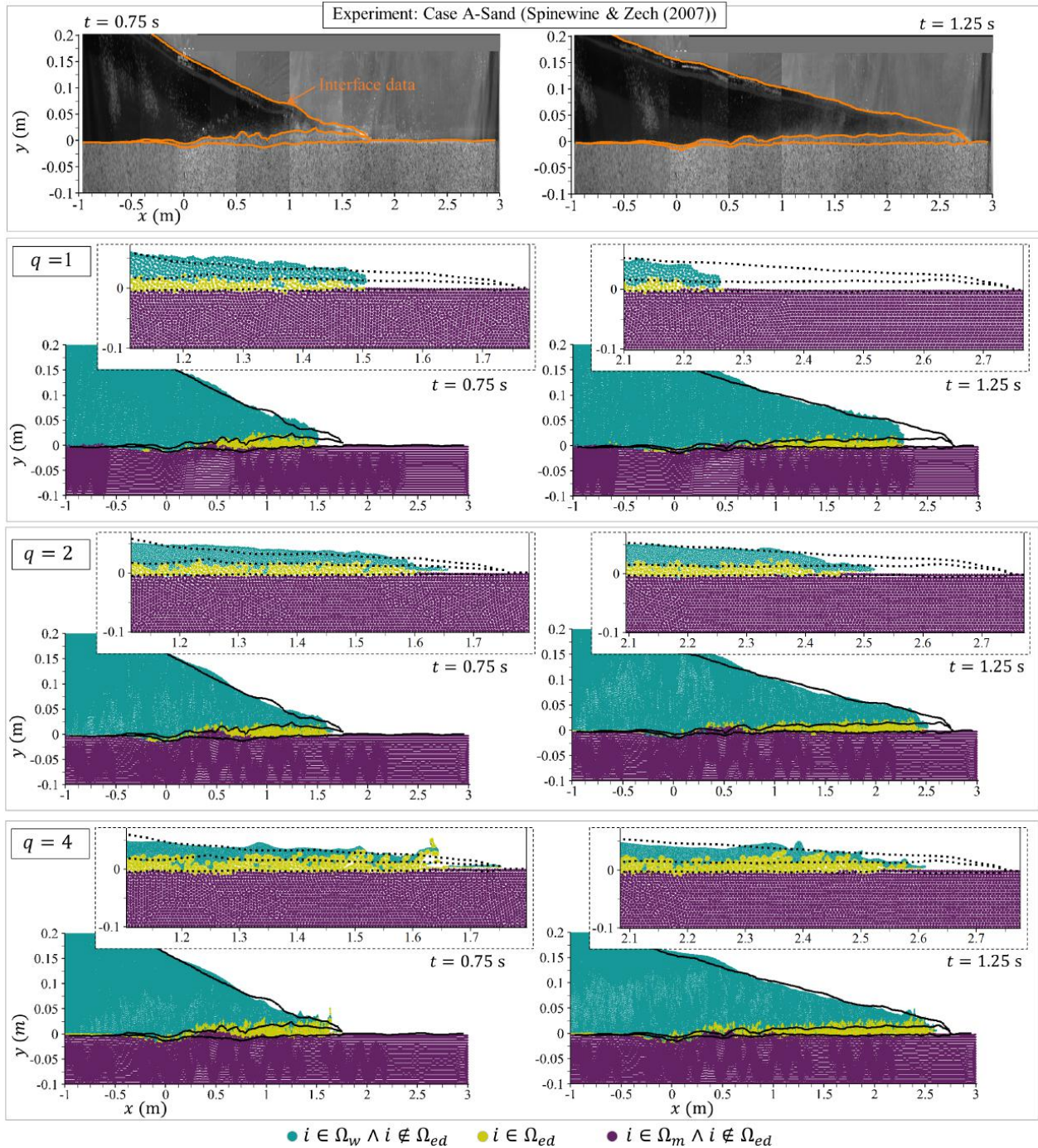


Figure 8.19 Flow evolution and the detected eroded region, $i \in \Omega_{ed}$, for case A-sand with the single-resolution ($q = 1$) and multi-resolution ($q = 2, 4$) MPS models compared with the experimental interface data (the black squares) from [12]. Except for the close-up plots, the vertical scale is stretched by a factor of 5.0.

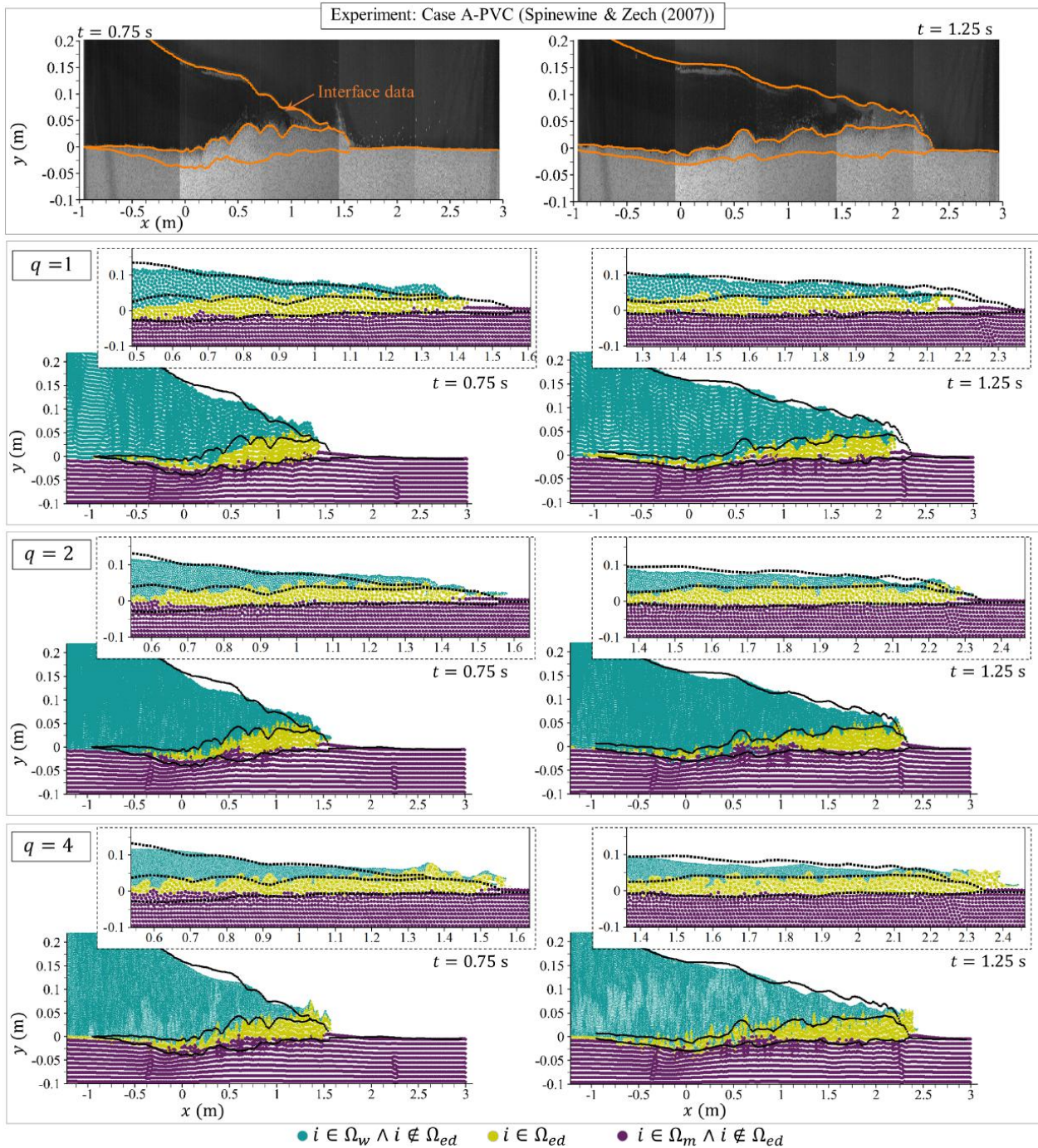


Figure 8.20 Flow evolution and the detected eroded region, $i \in \Omega_{ed}$, for case A-PVC with the single-resolution ($q = 1$) and multi-resolution ($q = 2, 4$) MPS models compared with the experimental interface data (the black squares) from [12]. Except for the close-up plots, the vertical scale is stretched by a factor of 5.0.

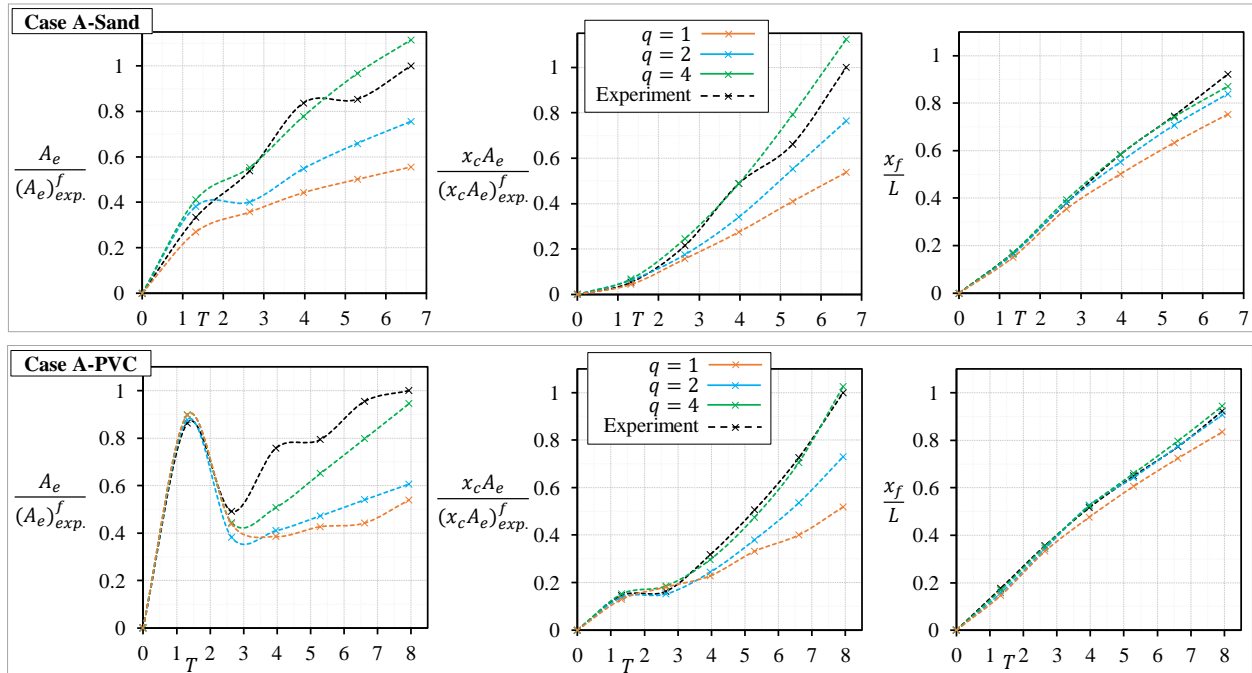


Figure 8.21 Temporal evolution of the eroded area, A_e , the first moment of the eroded area, $x_c A_e$, and the wavefront position, x_f , with the single-resolution ($q = 1$) and multi-resolution ($q = 2, 4$) MPS models for case A with sand and PVC compared with the experimental measurements by Spinewine and Zech [12].

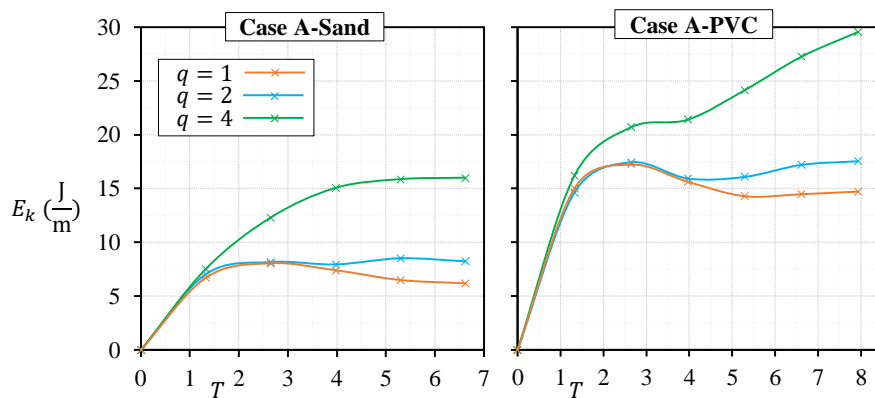


Figure 8.22 The global kinetic energy of the mixture particles ($E_k = 0.5 \sum \rho_{0i} l_{0i}^2 \|\mathbf{v}\|_i^2$ for $\forall i \in \Omega_m$) with the single-resolution ($q = 1$) and multi-resolution ($q = 2, 4$) MPS models for case A with sand and PVC.

sediment beds. We presented and discussed the mechanical behavior of this benchmark case for various configurations (i.e., with the flat-bed and the step-like discontinuities) and bed materials (i.e., the sand and PVC granules). We analyzed the sensitivity of sediment dynamics to the added suspension equation and the constant material parameters of the rheology model. Through comprehensive numerical validations, we studied the flow evolution and mechanical properties of the sediment erosion induced by the rapid water waves. Moreover, we compared the numerical results of the single- and multi-resolution simulations to evaluate the role of multi-scale interactions in capturing the global behavior of this benchmark case.

The particle convergence study on the two numerical benchmark cases confirms that the proposed multi-resolution formulation predicts the analytical results with acceptable accuracy. For the multi-viscosity Poiseuille flow, the multi-resolution shear force respects the convergence behavior of the numerical model and keeps the errors of the velocity profiles to less than 2 %. For the multi-density hydrostatic pressure, the conservative governing equations ensure the accuracy and stability of the results with errors less than 0.5 %. In both cases, increasing the spatial resolution, the numerical results converge to the analytical profiles with the convergence order greater than one.

For the dam break waves on movable beds, the developed numerical model provides in-depth details of the water-sediment mixing processes and the global behavior of sediment dynamics. The nonlinear vertical velocity and granular concentration profiles of the flat-bed with PVC are well estimated. Simulating different geometrical setups with the sand and PVC granules clarifies that the sediment dynamic greatly depends on the mobility of the bed materials, i.e., the density ratio, ρ_m/ρ_w (supporting the theoretical analysis by Spinewine and Capart [13] and Fraccarollo and Capart [18]). In the flat-bed configuration, the eroded sediment and the thickness of the transport layer increase with the light PVC material (by a factor of ~ 2.5) compared with the case with the sand grains. The step-like discontinuities lead to complex bed-load evolution close to the gate's location and slightly increase the mobility of the bed material at the initial stages of erosion. Regardless of the initial configuration, in cases with sand, the wave propagates on the horizontal bed with almost identical bed-load layer thickness and speed. In general, the multi-resolution MPS method proves to be capable of simulating the complex sediment erosion at the interface and the wavefront position. Despite the local discrepancies, the interface data and the flow evolution match well with the experimental measurements. Moreover, we observe that the multi-resolution model captures more interface deformations in comparison with the single-resolution model that underestimates sediment erosion. The results presented highlight the importance of multi-scale multiphase water-sediment interactions in numerical simulations of such a rapid fluid-driven problem.

It is worthwhile to employ the developed particle method for studying complex multi-directional granular flows with applications to industrial and hydro-environmental problems. The proposed multi-resolution formulations can be extended to two-phase mixture models (e.g., [20, 98]) to investigate the effects of dilatation and compaction on the mechanical behavior of immersed granular flows. Furthermore, the multi-resolution MPS method can be further validated to high-density ratio problems and coupled with dynamic particle merging and splitting techniques to simulate violent free-surface flows [124, 164] and fluid-structure interactions [88, 89].

CHAPTER 9 GENERAL DISCUSSION

This research project developed consistent particle methods for simulating violent free-surface and granular flows involved in hydro-environmental and geotechnical problems. Quantitative and qualitative analysis of the numerical results (compared with the analytical solutions and available experimental measurements) proved the effectiveness and efficiency of the proposed enhancements. The new conservative form of the WC-MPS method supplied with several particle stabilization techniques ensures accurate and stable simulations of highly dynamic free-surface flows. Furthermore, the generalized rheology model captures different flow regimes of immersed granular flows driven by gravity and fluid flows. The consistent multi-resolution particle method provided in-depth details and the global evolution of rapid fluid-driven granular dynamics.

We proposed the conservative WC-MPS method by deriving its continuity-based version and the new anti-symmetric approximation operators. We introduced several enhancement techniques to enhance the stability, accuracy and convergence order of the conservative WC-MPS method. In the context of this Enhanced WC-MPS, the density diffusive term plays the key role in eliminating unphysical high-frequency pressure noises. The modified diffusive term (with the convergent and high-order derivatives) resolved the divergent behavior of the standard term at the interfaces. The proposed particle shifting techniques with the special boundary treatments (i.e., the corrected particle shifting technique (CPS+PC) and its consistent form (CPS*+DPC)) effectively improved particle uniformity of the fluid particles. In the proposed CPS*+DPC technique, the diffusive terms of the particle shifting transport-velocity surmount the non-conservative-volume issue of the standard PS methods (including CPS). The dynamic pair-wise particle collision technique (DPC) resolved the particle clustering issue and the associated pressure noises through its dynamic and conservative collision and repulsive terms. Numerical validations of violent free-surface flows confirmed the important role of the particle regularization techniques in assuring numerical stability and capturing the impact events and loads of such problems. In the SPH framework, we re-derived the DPC formulation and implemented the hybrid PS technique (i.e., the cPS method) to study the accuracy and stability of the simulations by the different particle regularization techniques. In both EWC-MPS and WC-SPH, the DPC technique, with dynamic formulations, less energy dissipation, and without boundary treatments, produced more isotropic particle distributions and accurate evolution of the system's global energy. Overall, the proposed stabilization techniques are proven to be essential for the long-term stability of violent free-surface flows involving breaking waves, fluid-fluid and fluid-solid impacts, and

large free-surface deformations.

Furthermore, we developed the multiphase EWC-MPS formulations to simulate and investigate the mechanical behavior of complex immersed granular flows. To model the dense and immersed granular phase as a non-Newtonian mixture, we regularized the visco-inertial rheology equation and proposed a consistent approach for estimating the effective pressure of the mixture phase. Coupling this generalized rheology model with the enhanced particle method, provided us with a robust numerical model for studying the flow evolution and mechanical properties of challenging gravity- and fluid-driven benchmark cases. Thanks to the modified diffusive term the smoothness of pressure field eliminates unphysical mechanical behavior of the mixture flow. The numerical validations against the experimental data showed that the regularized rheology model captures the quasi-static and dense-flow regimes of the rapid granular flows through its dynamic yield and post-failure terms. In addition, the consistent effective pressure (by including the flow dynamics of the mixture in the rheology model) proved to be an essential and efficient formulation for capturing highly deformable and immersed granular flows.

We showed that in the continuum modeling of granular flows, the maximum spatial resolution of the discrete system can be bounded by the continuum assumption of the mixture phase. To resolve this limitation, we introduced a novel multi-resolution particle method for simulating granular flows. In this approach, the particle method adopts a higher spatial resolution for the fluid phase than that of the mixture. The new approximation operators respect the conservative feature of multi-scale particle interactions. The consistent multi-resolution method (including the generalized rheology model and the stabilization techniques) validated the internal flow properties and the mechanical evolution of dam-break waves on movable beds. The multi-resolution simulations highlighted the importance of multi-scale multiphase water-sediment interactions in numerical studies of such a rapid fluid-driven problem.

CHAPTER 10 CONCLUSION AND RECOMMENDATIONS

All in all, this research project has provided consistent particle methods and algorithms for simulating and investigating violent free-surface flows and granular dynamics. The numerical stability, accuracy, and convergence of the enhanced particle methods confirm the efficiency and effectiveness of the developed stabilization techniques and rheology formulations. We conclude that the enhancements of this study are essential for investigating the complex mechanical behavior of rapid free-surface and immersed granular flows involved in various hydro-environmental and engineering problems. Such an understanding of the multiphysics simulations can advance the decision-making processes involved in the related hazard management activities.

The particle methods of this study can be employed and further extended for real-size hydro-environmental and industrial applications. To that end, the numerical model requires further developments and validations to resolve its current limitations. The multiphase governing equations and the proposed diffusive terms are validated for the density ratio corresponding to the immersed granular flows. On the particle regularization techniques, the pair-wise particle collision technique requires special developments and further validations to be capable of resolving the tensile instability issue (e.g., [185]). To simulate internal and free-surface flows with inflow/outflow boundary conditions, the GPU-accelerated model does not include open boundary implementations (e.g., [162]). Also, the solid boundary model still lacks consistent formulations for dealing with surfaces with large curvatures and sharp corners (e.g., [69]). Currently, the initial geometry and parameters of the problem are loaded from an input text file which can be generalized for complex applications. The GPU-accelerated model is developed to execute the simulations on a single GPU device which limits its performance.

10.1 Future research

Future works may include extending and validating the governing equations for high-density ratio multiphase flows (like air-water flows) and fluid-structure interactions (like deformable elements and ice-water dynamics). One can implement the fourth-order time integration schemes (e.g., the Runge-Kutta algorithm [130]) to improve the accuracy of the numerical solutions. Implementing a general solid boundary model (like the polygon models) is essential for simulating problems with large-scale and complex topography. To improve the efficiency of the GPU-accelerated code, one may adopt optimization strategies like the particle sorting algorithms and multi-GPU parallel programming. The multi-resolution MPS

method can be supplied with dynamic splitting and merging techniques (like [77, 84]) for various multiphysics problems (including fluid-structure interactions and floating bodies). Moreover, the multiphase MPS method coupled with the generalized rheology model can be extended to the two-continuum mixture models simulating inter-phase mass exchanges and the mixture's density variations. This would allow us to study the role of granular dilatation and compaction in the mechanical properties of immersed granular flows.

REFERENCES

- [1] G. R. Brooks and D. E. Lawrence, “The drainage of the lake ha!ha! reservoir and downstream geomorphic impacts along ha!ha! river, saguenay area, quebec, canada,” *Geomorphology*, vol. 28, no. 1, pp. 141–167, 1999.
- [2] D. Le Touzé *et al.*, “A critical investigation of smoothed particle hydrodynamics applied to problems with free-surfaces,” *International Journal for Numerical Methods in Fluids*, vol. 73, no. 7, pp. 660–691, 2013.
- [3] P. N. Sun *et al.*, “A consistent approach to particle shifting in the delta-plus-sph model,” *Computer Methods in Applied Mechanics and Engineering*, vol. 348, pp. 912–934, 2019.
- [4] L. Lobovský *et al.*, “Experimental investigation of dynamic pressure loads during dam break,” *Journal of Fluids and Structures*, vol. 48, pp. 407–434, 2014.
- [5] A. Rafiee, F. Pistani, and K. Thiagarajan, “Study of liquid sloshing: numerical and experimental approach,” *Computational Mechanics*, vol. 47, no. 1, pp. 65–75, 2011.
- [6] K. M. T. Kleefsman *et al.*, “A volume-of-fluid based simulation method for wave impact problems,” *Journal of Computational Physics*, vol. 206, no. 1, pp. 363–393, 2005.
- [7] M. Antuono *et al.*, “A measure of spatial disorder in particle methods,” *Computer Physics Communications*, vol. 185, no. 10, pp. 2609–2621, 2014.
- [8] M. Greco, M. Landrini, and O. M. Faltinsen, “Impact flows and loads on ship-deck structures,” *Journal of Fluids and Structures*, vol. 19, no. 3, pp. 251–275, 2004.
- [9] A. Souto-Iglesias, G. Bulian, and E. Botia-Vera, “A set of canonical problems in sloshing. part 2: Influence of tank width on impact pressure statistics in regular forced angular motion,” *Ocean Engineering*, vol. 105, pp. 136–159, 2015.
- [10] M. Pilvar, M. J. Pouraghniaei, and A. Shakibaeinia, “Two-dimensional sub-aerial, submerged, and transitional granular slides,” *Physics of Fluids*, vol. 31, no. 11, p. 113303, 2019.
- [11] J. J. Monaghan and A. Rafiee, “A simple sph algorithm for multi-fluid flow with high density ratios,” *International Journal for Numerical Methods in Fluids*, vol. 71, no. 5, pp. 537–561, 2013.

- [12] B. Spinewine and Y. Zech, “Small-scale laboratory dam-break waves on movable beds,” *Journal of Hydraulic Research*, vol. 45, no. sup1, pp. 73–86, 2007.
- [13] B. Spinewine and H. Capart, “Intense bed-load due to a sudden dam-break,” *Journal of Fluid Mechanics*, vol. 731, pp. 579–614, 2013.
- [14] N/A. (2018, Sep.) Mount polley mine tailing dam breach. [Online]. Available: <https://www2.gov.bc.ca/gov/content/environment/air-land-water/spills-environmental-emergencies/spill-incidents/past-spill-incidents/mt-polley>
- [15] D. Phillips. (2018, Feb.) Canada’s top ten weather stories 2017. [Online]. Available: <https://bulletin.cmos.ca/canadas-top-ten-weather-stories-2017/>
- [16] P. Jop, “Rheological properties of dense granular flows,” *Comptes Rendus Physique*, vol. 16, no. 1, pp. 62–72, 2015.
- [17] E. Guazzelli and O. Pouliquen, “Rheology of dense granular suspensions,” *Journal of Fluid Mechanics*, vol. 852, p. P1, 2018.
- [18] L. Fraccarollo and H. Capart, “Riemann wave description of erosional dam-break flows,” *Journal of Fluid Mechanics*, vol. 461, pp. 183–228, 2002.
- [19] N. J. Balmforth and R. R. Kerswell, “Granular collapse in two dimensions,” *Journal of Fluid Mechanics*, vol. 538, pp. 399–428, 2005.
- [20] A. S. Baumgarten and K. Kamrin, “A general fluid–sediment mixture model and constitutive theory validated in many flow regimes,” *Journal of Fluid Mechanics*, vol. 861, pp. 721–764, 2019.
- [21] P. A. Cundall and O. D. L. Strack, “A discrete numerical model for granular assemblies,” *Geotechnique*, vol. 29, no. 1, pp. 47–65, 1979.
- [22] C. H. Rycroft *et al.*, “Reference map technique for incompressible fluid–structure interaction,” *Journal of Fluid Mechanics*, vol. 898, p. A9, 2020.
- [23] C. Selçuk *et al.*, “A fictitious domain method with distributed lagrange multipliers on adaptive quad/octrees for the direct numerical simulation of particle-laden flows,” *Journal of Computational Physics*, vol. 430, p. 109954, 2021.
- [24] D. Sulsky, Z. Chen, and H. L. Schreyer, “A particle method for history-dependent materials,” *Computer Methods in Applied Mechanics and Engineering*, vol. 118, no. 1, pp. 179–196, 1994.

- [25] S. Koshizuka and Y. Oka, "Moving-particle semi-implicit method for fragmentation of incompressible fluid," *Nuclear science and engineering*, vol. 123, no. 3, pp. 421–434, 1996.
- [26] R. A. Gingold and J. J. Monaghan, "Smoothed particle hydrodynamics: theory and application to non-spherical stars," *Monthly notices of the royal astronomical society*, vol. 181, no. 3, pp. 375–389, 1977.
- [27] M. Luo, A. Khayyer, and P. Lin, "Particle methods in ocean and coastal engineering," *Applied Ocean Research*, vol. 114, p. 102734, 2021.
- [28] R. Feng *et al.*, "Large deformation analysis of granular materials with stabilized and noise-free stress treatment in smoothed particle hydrodynamics (sph)," *Computers and Geotechnics*, vol. 138, p. 104356, 2021.
- [29] A. Shakibaeinia and Y.-C. Jin, "Lagrangian multiphase modeling of sand discharge into still water," *Advances in Water Resources*, vol. 48, pp. 55–67, 2012.
- [30] R. J. LeVeque, *Finite Volume Methods for Hyperbolic Problems*, ser. Cambridge Texts in Applied Mathematics. Cambridge: Cambridge University Press, 2002.
- [31] A. J. Chorin, "A numerical method for solving incompressible viscous flow problems," *Journal of Computational Physics*, vol. 2, no. 1, pp. 12–26, 1967.
- [32] C. W. Hirt and B. D. Nichols, "Volume of fluid (vof) method for the dynamics of free boundaries," *Journal of Computational Physics*, vol. 39, no. 1, pp. 201–225, 1981.
- [33] X. Yan, A. Mohammadian, and C. D. Rennie, "Numerical modeling of local scour due to submerged wall jets using a strict vertex-based, terrain conformal, moving-mesh technique in openfoam," *International Journal of Sediment Research*, vol. 35, no. 3, pp. 237–248, 2020.
- [34] S. Koshizuka *et al.*, *Moving Particle Semi-implicit Method: A Meshfree Particle Method for Fluid Dynamics*. Academic Press, 2018.
- [35] G. R. Liu and M. B. Liu, *Smoothed Particle Hydrodynamics*. World Scientific, 2003.
- [36] A. Colagrossi and M. Landrini, "Numerical simulation of interfacial flows by smoothed particle hydrodynamics," *Journal of Computational Physics*, vol. 191, no. 2, pp. 448–475, 2003.

- [37] H. Gotoh, T. Shibahara, and T. Sakai, “Sub-particle-scale turbulence model for the mps method - lagrangian flow model for hydraulic engineering,” *Advanced Methods for Computational Fluid Dynamics*, vol. 9-4, pp. 339–347, 2001.
- [38] A. Gotoh, Hitoshi; Khayyer, “On the state-of-the-art of particle methods for coastal and ocean engineering,” *Coastal Engineering Journal*, vol. 60, no. 1, pp. 79–103, 2018.
- [39] G. Li *et al.*, “A review on mps method developments and applications in nuclear engineering,” *Computer Methods in Applied Mechanics and Engineering*, vol. 367, p. 113166, 2020.
- [40] M. S. Shadloo, G. Oger, and D. Le Touzé, “Smoothed particle hydrodynamics method for fluid flows, towards industrial applications: Motivations, current state, and challenges,” *Computers and Fluids*, vol. 136, pp. 11–34, 2016.
- [41] X. Y. Hu and N. A. Adams, “A multi-phase sph method for macroscopic and mesoscopic flows,” *Journal of Computational Physics*, vol. 213, no. 2, pp. 844–861, 2006.
- [42] J. J. Monaghan, “Smoothed particle hydrodynamics,” *Reports on Progress in Physics*, vol. 68, no. 8, pp. 1703–1759, 2005.
- [43] A. Souto-Iglesias *et al.*, “On the consistency of mps,” *Computer Physics Communications*, vol. 184, no. 3, pp. 732–745, 2013.
- [44] J. J. Monaghan, “Sph without a tensile instability,” *Journal of Computational Physics*, vol. 159, no. 2, pp. 290–311, 2000.
- [45] J. W. Swegle, D. L. Hicks, and S. W. Attaway, “Smoothed particle hydrodynamics stability analysis,” *Journal of Computational Physics*, vol. 116, no. 1, pp. 123–134, 1995.
- [46] S. Koshizuka, A. Nobe, and Y. Oka, “Numerical analysis of breaking waves using the moving particle semi-implicit method,” *International Journal for Numerical Methods in Fluids*, vol. 26, no. 7, pp. 751–769, 1998.
- [47] A. Shakibaeinia and Y. Jin, “A weakly compressible mps method for modeling of open-boundary free-surface flow,” *International journal for numerical methods in fluids*, vol. 63, no. 10, pp. 1208–1232, 2010.
- [48] J. Bonet and T.-S. Lok, “Variational and momentum preservation aspects of smooth particle hydrodynamic formulations,” *Computer Methods in applied mechanics and engineering*, vol. 180, no. 1-2, pp. 97–115, 1999.

- [49] D. J. Price, “Smoothed particle hydrodynamics and magnetohydrodynamics,” *Journal of Computational Physics*, vol. 231, no. 3, pp. 759–794, 2012.
- [50] S. J. Lind *et al.*, “Incompressible smoothed particle hydrodynamics for free-surface flows: A generalised diffusion-based algorithm for stability and validations for impulsive flows and propagating waves,” *Journal of Computational Physics*, vol. 231, no. 4, pp. 1499–1523, 2012.
- [51] A. Khayyer and H. Gotoh, “A higher order laplacian model for enhancement and stabilization of pressure calculation by the mps method,” *Applied Ocean Research*, vol. 32, no. 1, pp. 124–131, 2010.
- [52] G. Oger *et al.*, “An improved sph method: Towards higher order convergence,” *Journal of Computational Physics*, vol. 225, no. 2, pp. 1472–1492, 2007.
- [53] J. J. Monaghan, “Simulating free surface flows with sph,” *Journal of Computational Physics*, vol. 110, no. 2, pp. 399–406, 1994.
- [54] D. Molteni and A. Colagrossi, “A simple procedure to improve the pressure evaluation in hydrodynamic context using the sph,” *Computer Physics Communications*, vol. 180, no. 6, pp. 861–872, 2009.
- [55] R. Xu, P. Stansby, and D. Laurence, “Accuracy and stability in incompressible sph (isph) based on the projection method and a new approach,” *Journal of Computational Physics*, vol. 228, no. 18, pp. 6703–6725, 2009.
- [56] B.-H. Lee *et al.*, “Step-by-step improvement of mps method in simulating violent free-surface motions and impact-loads,” *Computer Methods in Applied Mechanics and Engineering*, vol. 200, no. 9, pp. 1113–1125, 2011.
- [57] A. Khayyer and H. Gotoh, “Enhancement of stability and accuracy of the moving particle semi-implicit method,” *Journal of Computational Physics*, vol. 230, no. 8, pp. 3093–3118, 2011.
- [58] G. Duan *et al.*, “The truncation and stabilization error in multiphase moving particle semi-implicit method based on corrective matrix: Which is dominant?” *Computers and Fluids*, vol. 190, pp. 254–273, 2019.
- [59] H. Gotoh and A. Khayyer, “Current achievements and future perspectives for projection-based particle methods with applications in ocean engineering,” *Journal of Ocean Engineering and Marine Energy*, vol. 2, no. 3, pp. 251–278, 2016.

- [60] G. Duan *et al.*, “An accurate and stable multiphase moving particle semi-implicit method based on a corrective matrix for all particle interaction models,” *International Journal for Numerical Methods in Engineering*, vol. 115, no. 10, pp. 1287–1314, 2018.
- [61] J. J. Monaghan and R. A. Gingold, “Shock simulation by the particle method sph,” *Journal of Computational Physics*, vol. 52, no. 2, pp. 374–389, 1983.
- [62] S. Marrone *et al.*, “Delta-sph model for simulating violent impact flows,” *Computer Methods in Applied Mechanics and Engineering*, vol. 200, no. 13, pp. 1526–1542, 2011.
- [63] M. Khanpour *et al.*, “Numerical modeling of free surface flow in hydraulic structures using smoothed particle hydrodynamics,” *Applied Mathematical Modelling*, vol. 40, no. 23, pp. 9821–9834, 2016.
- [64] A. Krimi, M. Jandaghian, and A. Shakibaeinia, “A wcsph particle shifting strategy for simulating violent free surface flows,” *Water*, vol. 12, no. 11, p. 3189, 2020.
- [65] M. Antuono, A. Colagrossi, and S. Marrone, “Numerical diffusive terms in weakly-compressible sph schemes,” *Computer Physics Communications*, vol. 183, no. 12, pp. 2570–2580, 2012.
- [66] M. Antuono *et al.*, “Free-surface flows solved by means of sph schemes with numerical diffusive terms,” *Computer Physics Communications*, vol. 181, no. 3, pp. 532–549, 2010.
- [67] A. J. C. Crespo *et al.*, “Dualsphysics: Open-source parallel cfd solver based on smoothed particle hydrodynamics (sph),” *Computer Physics Communications*, vol. 187, pp. 204–216, 2015.
- [68] D. D. Meringolo *et al.*, “Energy balance during generation, propagation and absorption of gravity waves through the δ -les-sph model,” *Coastal Engineering*, vol. 140, pp. 355–370, 2018.
- [69] G. Fourtakas *et al.*, “Local uniform stencil (lust) boundary condition for arbitrary 3-d boundaries in parallel smoothed particle hydrodynamics (sph) models,” *Computers and Fluids*, vol. 190, pp. 346–361, 2019.
- [70] P. N. Sun, D. Le Touzé, and A. M. Zhang, “Study of a complex fluid-structure dam-breaking benchmark problem using a multi-phase sph method with apr,” *Engineering Analysis with Boundary Elements*, vol. 104, pp. 240–258, 2019.

- [71] I. Hammani *et al.*, “Detailed study on the extension of the δ -sph model to multi-phase flow,” *Computer Methods in Applied Mechanics and Engineering*, vol. 368, p. 113189, 2020.
- [72] B. X. Zheng and Z. Chen, “A multiphase smoothed particle hydrodynamics model with lower numerical diffusion,” *Journal of Computational Physics*, vol. 382, pp. 177–201, 2019.
- [73] A. Skillen *et al.*, “Incompressible smoothed particle hydrodynamics (sph) with reduced temporal noise and generalised fickian smoothing applied to body–water slam and efficient wave–body interaction,” *Computer Methods in Applied Mechanics and Engineering*, vol. 265, pp. 163–173, 2013.
- [74] A. Khayyer, H. Gotoh, and Y. Shimizu, “Comparative study on accuracy and conservation properties of two particle regularization schemes and proposal of an optimized particle shifting scheme in isph context,” *Journal of Computational Physics*, vol. 332, pp. 236–256, 2017.
- [75] A. Shakibaeinia and Y.-C. Jin, “Mps mesh-free particle method for multiphase flows,” *Computer Methods in Applied Mechanics and Engineering*, vol. 229-232, pp. 13–26, 2012.
- [76] X. Liu and S. Zhang, “Development of adaptive multi-resolution mps method for multiphase flow simulation,” *Computer Methods in Applied Mechanics and Engineering*, vol. 387, p. 114184, 2021.
- [77] M. Tanaka, R. Cardoso, and H. Bahai, “Multi-resolution mps method,” *Journal of Computational Physics*, vol. 359, pp. 106–136, 2018.
- [78] R. Vacondio *et al.*, “Variable resolution for sph: A dynamic particle coalescing and splitting scheme,” *Computer Methods in Applied Mechanics and Engineering*, vol. 256, pp. 132–148, 2013.
- [79] X. Yang *et al.*, “Smoothed particle hydrodynamics with adaptive spatial resolution (sph-asr) for free surface flows,” *Journal of Computational Physics*, vol. 443, p. 110539, 2021.
- [80] L. Chiron *et al.*, “Analysis and improvements of adaptive particle refinement (apr) through cpu time, accuracy and robustness considerations,” *Journal of Computational Physics*, vol. 354, pp. 552–575, 2018.

- [81] D. A. Barcarolo *et al.*, “Adaptive particle refinement and derefinement applied to the smoothed particle hydrodynamics method,” *Journal of Computational Physics*, vol. 273, pp. 640–657, 2014.
- [82] D. Yamada *et al.*, “Application of improved multiresolution technique for the mps method to fluid lubrication,” *Computational Particle Mechanics*, 2021.
- [83] K. Shibata *et al.*, “The overlapping particle technique for multi-resolution simulation of particle methods,” *Computer Methods in Applied Mechanics and Engineering*, vol. 325, pp. 434–462, 2017.
- [84] P. N. Sun *et al.*, “An accurate sph volume adaptive scheme for modeling strongly-compressible multiphase flows. part 1: Numerical scheme and validations with basic 1d and 2d benchmarks,” *Journal of Computational Physics*, p. 109937, 2020.
- [85] —, “Multi-resolution delta-plus-sph with tensile instability control: Towards high reynolds number flows,” *Computer Physics Communications*, vol. 224, pp. 63–80, 2018.
- [86] P. Omidvar, P. K. Stansby, and B. D. Rogers, “Sph for 3d floating bodies using variable mass particle distribution,” *International Journal for Numerical Methods in Fluids*, vol. 72, no. 4, pp. 427–452, 2013.
- [87] A. Khayyer *et al.*, “Multi-resolution isph-sph for accurate and efficient simulation of hydroelastic fluid-structure interactions in ocean engineering,” *Ocean Engineering*, p. 108652, 2021.
- [88] —, “Multi-resolution mps for incompressible fluid-elastic structure interactions in ocean engineering,” *Applied Ocean Research*, vol. 82, pp. 397–414, 2019.
- [89] C. Zhang, M. Rezavand, and X. Hu, “A multi-resolution sph method for fluid-structure interactions,” *Journal of Computational Physics*, p. 110028, 2020.
- [90] A. Bougouin and L. Lacaze, “Granular collapse in a fluid: Different flow regimes for an initially dense-packing,” *Physical Review Fluids*, vol. 3, no. 6, p. 064305, 2018.
- [91] L. Rondon, O. Pouliquen, and P. Aussillous, “Granular collapse in a fluid: Role of the initial volume fraction,” *Physics of Fluids*, vol. 23, no. 7, p. 073301, 2011.
- [92] J. J. Stickel and R. L. Powell, “Fluid mechanics and rheology of dense suspensions,” *Annual Review of Fluid Mechanics*, vol. 37, no. 1, pp. 129–149, 2005.

- [93] C. Cassar, M. Nicolas, and O. Pouliquen, “Submarine granular flows down inclined planes,” *Physics of Fluids*, vol. 17, no. 10, p. 103301, 2005.
- [94] M. Robbe-Saule *et al.*, “Experimental investigation of tsunami waves generated by granular collapse into water,” *Journal of Fluid Mechanics*, vol. 907, p. A11, 2021.
- [95] M. Pailha and O. Pouliquen, “A two-phase flow description of the initiation of underwater granular avalanches,” *Journal of Fluid Mechanics*, vol. 633, pp. 115–135, 2009.
- [96] L. Lacaze *et al.*, “Immersed granular collapse: from viscous to free-fall unsteady granular flows,” *Journal of Fluid Mechanics*, vol. 912, p. A15, 2021.
- [97] F. Dorai *et al.*, “Fully resolved simulations of the flow through a packed bed of cylinders: Effect of size distribution,” *Chemical Engineering Science*, vol. 129, pp. 180–192, 2015.
- [98] H. Shi *et al.*, “A two-phase sph model for massive sediment motion in free surface flows,” *Advances in Water Resources*, vol. 129, pp. 80–98, 2019.
- [99] P. Jop, Y. Forterre, and O. Pouliquen, “A constitutive law for dense granular flows,” *Nature*, vol. 441, p. 727, 2006.
- [100] L. Amarsid *et al.*, “Viscoinertial regime of immersed granular flows,” *Physical Review E*, vol. 96, no. 1, p. 012901, 2017.
- [101] F. Boyer, E. Guazzelli, and O. Pouliquen, “Unifying suspension and granular rheology,” *Physical Review Letters*, vol. 107, no. 18, p. 188301, 2011.
- [102] Y. Forterre and O. Pouliquen, “Flows of dense granular media,” *Annual Review of Fluid Mechanics*, vol. 40, no. 1, pp. 1–24, 2008.
- [103] M. Rauter, “The compressible granular collapse in a fluid as a continuum: validity of a navier–stokes model with $\mu(j)$, $\phi(j)$ -rheology,” *Journal of Fluid Mechanics*, vol. 915, p. A87, 2021.
- [104] J. Chauchat and M. Médale, “A three-dimensional numerical model for dense granular flows based on the $\mu(i)$ rheology,” *Journal of Computational Physics*, vol. 256, pp. 696–712, 2014.
- [105] A. Nabian Mohammad and L. Farhadi, “Multiphase mesh-free particle method for simulating granular flows and sediment transport,” *Journal of Hydraulic Engineering*, vol. 143, no. 4, p. 04016102, 2017.

- [106] M. Khanpour *et al.*, “Mesh-free sph modeling of sediment scouring and flushing,” *Computers and Fluids*, vol. 129, pp. 67–78, 2016.
- [107] M. X. Rodriguez-Paz and J. Bonet, “A corrected smooth particle hydrodynamics method for the simulation of debris flows,” *Numerical Methods for Partial Differential Equations*, vol. 20, no. 1, pp. 140–163, 2004.
- [108] A. Shakibaeinia and Y.-C. Jin, “A mesh-free particle model for simulation of mobile-bed dam break,” *Advances in Water Resources*, vol. 34, no. 6, pp. 794–807, 2011.
- [109] G. Fourtakas and B. D. Rogers, “Modelling multi-phase liquid-sediment scour and resuspension induced by rapid flows using smoothed particle hydrodynamics (sph) accelerated with a graphics processing unit (gpu),” *Advances in Water Resources*, vol. 92, pp. 186–199, 2016.
- [110] Y. Qi *et al.*, “An improved multi-phase weakly-compressible sph model for modeling various landslides,” *Powder Technology*, vol. 397, p. 117120, 2022.
- [111] M. Jandaghian and A. Shakibaeinia, “A moving particle semi-implicit numerical method for modelling sediment dynamic,” in *Proceedings of the 38th IAHR World Congress*, 2019, Conference Proceedings, pp. 3764–3772.
- [112] M. Tajnesaie, A. Shakibaeinia, and K. Hosseini, “Meshfree particle numerical modelling of sub-aerial and submerged landslides,” *Computers and Fluids*, vol. 172, pp. 109–121, 2018.
- [113] E. Jafari-Nodoushan, A. Shakibaeinia, and K. Hosseini, “A multiphase meshfree particle method for continuum-based modeling of dry and submerged granular flows,” *Powder Technology*, vol. 335, pp. 258–274, 2018.
- [114] A. Ghaitanellis *et al.*, “A sph elastic-viscoplastic model for granular flows and bed-load transport,” *Advances in Water Resources*, vol. 111, pp. 156–173, 2018.
- [115] E. H. Zubeldia *et al.*, “Multi-phase sph model for simulation of erosion and scouring by means of the shields and drucker–prager criteria,” *Advances in Water Resources*, vol. 117, pp. 98–114, 2018.
- [116] S. Manenti *et al.*, “Sph simulation of sediment flushing induced by a rapid water flow,” *Journal of Hydraulic Engineering*, vol. 138, no. 3, pp. 272–284, 2012.
- [117] C.-l. Chen and C.-H. Ling, “Granular-flow rheology: role of shear-rate number in transition regime,” *Journal of engineering mechanics*, vol. 122, no. 5, pp. 469–480, 1996.

- [118] E. J. Nodoushan and A. Shakibaeinia, “Multiphase mesh-free particle modeling of local sediment scouring with meu(i) rheology,” *Journal of Hydroinformatics*, vol. 21, no. 2, pp. 279–294, 2018.
- [119] L. Ke *et al.*, “Investigating the physical characteristics of dense granular flows by coupling the weakly compressible moving particle semi-implicit method with the rheological model,” *Acta Geotechnica*, 2020.
- [120] H. H. Bui and R. Fukagawa, “An improved sph method for saturated soils and its application to investigate the mechanisms of embankment failure: Case of hydrostatic pore-water pressure,” *International Journal for Numerical and Analytical Methods in Geomechanics*, vol. 37, no. 1, pp. 31–50, 2013.
- [121] C. H. Rycroft, K. Kamrin, and M. Z. Bazant, “Assessing continuum postulates in simulations of granular flow,” *Journal of the Mechanics and Physics of Solids*, vol. 57, no. 5, pp. 828–839, 2009.
- [122] P. Baveye and G. Sposito, “The operational significance of the continuum hypothesis in the theory of water movement through soils and aquifers,” *Water Resources Research*, vol. 20, no. 5, pp. 521–530, 1984.
- [123] M. Jandaghian and A. Shakibaeinia, “An enhanced weakly-compressible mps method for free-surface flows,” *Computer Methods in Applied Mechanics and Engineering*, vol. 360, p. 112771, 2020.
- [124] M. Jandaghian *et al.*, “Enhanced weakly-compressible mps method for violent free-surface flows: Role of particle regularization techniques,” *Journal of Computational Physics*, vol. 434, p. 110202, 2021.
- [125] M. Jandaghian, H. M. Siaben, and A. Shakibaeinia, “Stability and accuracy of the weakly compressible sph with particle regularization techniques,” *arXiv preprint arXiv:2110.10076*, 2022.
- [126] M. Jandaghian, A. Krimi, and A. Shakibaeinia, “Enhanced weakly-compressible mps method for immersed granular flows,” *Advances in Water Resources*, vol. 152, p. 103908, 2021.
- [127] M. Jandaghian and A. Shakibaeinia, “Fluid-driven granular dynamics through a consistent multi-resolution particle method,” *arXiv preprint arXiv:2202.13950*, 2022.

- [128] M. Jandaghian *et al.*, “Dynamic particle collision technique for free-surface flows in sph,” in *Proceedings of the 15th International SPHERIC 2021 Workshop*, 2021, Conference Proceedings, pp. 289–296.
- [129] A. Khayyer, H. Gotoh, and Y. Shimizu, “A projection-based particle method with optimized particle shifting for multiphase flows with large density ratios and discontinuous density fields,” *Computers & Fluids*, 2018.
- [130] P. N. Sun *et al.*, “The delta-plus-sph model: simple procedures for a further improvement of the sph scheme,” *Computer Methods in Applied Mechanics and Engineering*, vol. 315, pp. 25–49, 2017.
- [131] C. Zhang *et al.*, “A weakly compressible sph method with weno reconstruction,” *Journal of Computational Physics*, vol. 392, pp. 1–18, 2019.
- [132] N. Tsuruta, A. Khayyer, and H. Gotoh, “A short note on dynamic stabilization of moving particle semi-implicit method,” *Computers and Fluids*, vol. 82, pp. 158–164, 2013.
- [133] G. Duan *et al.*, “A multiphase mps solver for modeling multi-fluid interaction with free surface and its application in oil spill,” *Computer Methods in Applied Mechanics and Engineering*, vol. 320, pp. 133–161, 2017.
- [134] A. Krimi *et al.*, “Multiphase smoothed particle hydrodynamics approach for modeling soil–water interactions,” *Advances in Water Resources*, vol. 121, pp. 189–205, 2018.
- [135] K. Hosseini *et al.*, “Smoothed particle hydrodynamics for the interaction of newtonian and non-newtonian fluids using the meu(i) model,” *Powder Technology*, 2019.
- [136] G. Duan, A. Yamaji, and S. Koshizuka, “A novel multiphase mps algorithm for modeling crust formation by highly viscous fluid for simulating corium spreading,” *Nuclear Engineering and Design*, vol. 343, pp. 218–231, 2019.
- [137] A. Khayyer and H. Gotoh, “A 3d higher order laplacian model for enhancement and stabilization of pressure calculation in 3d mps-based simulations,” *Applied Ocean Research*, vol. 37, pp. 120–126, 2012.
- [138] X. Liu, K. Morita, and S. Zhang, “An advanced moving particle semi-implicit method for accurate and stable simulation of incompressible flows,” *Computer Methods in Applied Mechanics and Engineering*, vol. 339, pp. 467–487, 2018.

- [139] A. Khayyer and H. Gotoh, “Modified moving particle semi-implicit methods for the prediction of 2d wave impact pressure,” *Coastal Engineering*, vol. 56, no. 4, pp. 419–440, 2009.
- [140] J. Sanchez-Mondragon, “On the stabilization of unphysical pressure oscillations in mps method simulations,” *International Journal for Numerical Methods in Fluids*, vol. 82, no. 8, pp. 471–492, 2016.
- [141] Y. Suzuki, S. Koshizuka, and Y. Oka, “Hamiltonian moving-particle semi-implicit (hmps) method for incompressible fluid flows,” *Computer Methods in Applied Mechanics and Engineering*, vol. 196, no. 29, pp. 2876–2894, 2007.
- [142] D. D. Meringolo *et al.*, “A dynamic delta-sph model: how to get rid of diffusive parameter tuning,” *Computers and Fluids*, 2018.
- [143] J. J. Monaghan, “On the problem of penetration in particle methods,” *Journal of Computational Physics*, vol. 82, no. 1, pp. 1–15, 1989.
- [144] S. Adami, X. Hu, and N. A. Adams, “A transport-velocity formulation for smoothed particle hydrodynamics,” *Journal of Computational Physics*, vol. 241, pp. 292–307, 2013.
- [145] X. Xu and P. Yu, “A technique to remove the tensile instability in weakly compressible sph,” *Computational Mechanics*, pp. 1–28, 2018.
- [146] T. Xu and Y.-C. Jin, “Improvements for accuracy and stability in a weakly-compressible particle method,” *Computers and Fluids*, vol. 137, pp. 1–14, 2016.
- [147] T. Pöschel and T. Schwager, *Computational granular dynamics : models and algorithms*. Berlin ; New York: Springer-Verlag, 2005.
- [148] E. Y.M. Lo and S. Shao, “Simulation of near-shore solitary wave mechanics by an incompressible sph method,” *Applied Ocean Research*, vol. 24, no. 5, pp. 275–286, 2002.
- [149] S. Marrone *et al.*, “Fast free-surface detection and level-set function definition in sph solvers,” *Journal of Computational Physics*, vol. 229, no. 10, pp. 3652–3663, 2010.
- [150] S. Tavakkol, A. R. Zarrati, and M. Khanpour, “Curvilinear smoothed particle hydrodynamics,” *International Journal for Numerical Methods in Fluids*, vol. 83, no. 2, pp. 115–131, 2017.

- [151] T. Tamai and S. Koshizuka, “Least squares moving particle semi-implicit method,” *Computational Particle Mechanics*, vol. 1, no. 3, pp. 277–305, 2014.
- [152] M. B. Liu and G. R. Liu, “Smoothed particle hydrodynamics (sph): an overview and recent developments,” *Archives of Computational Methods in Engineering*, vol. 17, no. 1, pp. 25–76, 2010.
- [153] J. J. Monaghan, “Smoothed particle hydrodynamics,” *Annual Review of Astronomy and Astrophysics*, vol. 30, pp. 543–574, 1992.
- [154] P. W. Randles and L. D. Libersky, “Smoothed particle hydrodynamics: Some recent improvements and applications,” *Computer Methods in Applied Mechanics and Engineering*, vol. 139, no. 1, pp. 375–408, 1996.
- [155] G. Oger *et al.*, “Sph accuracy improvement through the combination of a quasi-lagrangian shifting transport velocity and consistent ale formalisms,” *Journal of Computational Physics*, vol. 313, pp. 76–98, 2016.
- [156] A. Colagrossi, “A meshless lagrangian method for free-surface and interface flows with fragmentation,” Thesis, Universit’a di Roma La Sapienza, 2005.
- [157] A. Khayyer and H. Gotoh, “Enhancement of performance and stability of mps mesh-free particle method for multiphase flows characterized by high density ratios,” *Journal of Computational Physics*, vol. 242, pp. 211–233, 2013.
- [158] A. Krimi *et al.*, “Smoothed particle hydrodynamics: A consistent model for interfacial multiphase fluid flow simulations,” *Journal of Computational Physics*, vol. 358, pp. 53–87, 2018.
- [159] R. A. Amaro Junior, L.-Y. Cheng, and P. H. S. Osello, “An improvement of rigid bodies contact for particle-based non-smooth walls modeling,” *Computational Particle Mechanics*, 2019.
- [160] M. Antuono *et al.*, “Energy balance in the delta-sph scheme,” *Computer Methods in Applied Mechanics and Engineering*, vol. 289, pp. 209–226, 2015.
- [161] P.-P. Wang *et al.*, “Improved particle shifting technology and optimized free-surface detection method for free-surface flows in smoothed particle hydrodynamics,” *Computer Methods in Applied Mechanics and Engineering*, vol. 357, p. 112580, 2019.

- [162] A. Shakibaeinia and Y.-C. Jin, “Mps-based mesh-free particle method for modeling open-channel flows,” *Journal of Hydraulic Engineering*, vol. 137, no. 11, pp. 1375–1384, 2011.
- [163] C. Zhang, X. Y. Hu, and N. A. Adams, “A generalized transport-velocity formulation for smoothed particle hydrodynamics,” *Journal of Computational Physics*, vol. 337, pp. 216–232, 2017.
- [164] M. Rezavand, C. Zhang, and X. Hu, “A weakly compressible sph method for violent multi-phase flows with high density ratio,” *Journal of Computational Physics*, vol. 402, p. 109092, 2020.
- [165] M. S. Shadloo *et al.*, “Improved incompressible smoothed particle hydrodynamics method for simulating flow around bluff bodies,” *Computer Methods in Applied Mechanics and Engineering*, vol. 200, no. 9, pp. 1008–1020, 2011.
- [166] A. Zainali *et al.*, “Numerical investigation of newtonian and non-newtonian multiphase flows using isph method,” *Computer Methods in Applied Mechanics and Engineering*, vol. 254, pp. 99–113, 2013.
- [167] A. Mokos, B. D. Rogers, and P. K. Stansby, “A multi-phase particle shifting algorithm for sph simulations of violent hydrodynamics with a large number of particles,” *Journal of Hydraulic Research*, vol. 55, no. 2, pp. 143–162, 2017.
- [168] C. Zhang, M. Rezavand, and X. Hu, “Dual-criteria time stepping for weakly compressible smoothed particle hydrodynamics,” *Journal of Computational Physics*, p. 109135, 2019.
- [169] R. Panton, *Incompressible Flow*. Wiley, 2013.
- [170] A. Khayyer, H. Gotoh, and S. D. Shao, “Corrected incompressible sph method for accurate water-surface tracking in breaking waves,” *Coastal Engineering*, vol. 55, no. 3, pp. 236–250, 2008.
- [171] P. N. Sun *et al.*, “Extension of the delta-plus-sph model for simulating vortex-induced-vibration problems,” *Journal of Fluids and Structures*, vol. 90, pp. 19–42, 2019.
- [172] S. Adami, X. Hu, and N. Adams, “A generalized wall boundary condition for smoothed particle hydrodynamics,” *Journal of Computational Physics*, vol. 231, no. 21, pp. 7057–7075, 2012.

- [173] S. Marrone *et al.*, “Prediction of energy losses in water impacts using incompressible and weakly compressible models,” *Journal of Fluids and Structures*, vol. 54, pp. 802–822, 2015.
- [174] G. Duan *et al.*, “Imposing accurate wall boundary conditions in corrective-matrix-based moving particle semi-implicit method for free surface flow,” *International Journal for Numerical Methods in Fluids*, vol. 93, no. 1, pp. 148–175, 2021.
- [175] S. Marrone *et al.*, “Prediction of energy losses in water impacts using incompressible and weakly compressible models,” *Journal of Fluids and Structures*, vol. 54, pp. 802–822, 2015.
- [176] P. Sun, F. Ming, and A. Zhang, “Numerical simulation of interactions between free surface and rigid body using a robust sph method,” *Ocean Engineering*, vol. 98, pp. 32–49, 2015.
- [177] X. Chen and D. Wan, “Gpu accelerated mps method for large-scale 3-d violent free surface flows,” *Ocean Engineering*, vol. 171, pp. 677–694, 2019.
- [178] R. A. Amaro, L.-Y. Cheng, and S. K. Buruchenko, “A comparison between weakly-compressible smoothed particle hydrodynamics (wcsph) and moving particle semi-implicit (mps) methods for 3d dam-break flows,” *International Journal of Computational Methods*, 2020.
- [179] J. M. Domínguez *et al.*, “Dualsphysics: from fluid dynamics to multiphysics problems,” *Computational Particle Mechanics*, 2021.
- [180] G. Duan and B. Chen, “Large eddy simulation by particle method coupled with sub-particle-scale model and application to mixing layer flow,” *Applied Mathematical Modelling*, vol. 39, no. 10, pp. 3135–3149, 2015.
- [181] T. Zhang *et al.*, “Enhancement of stabilization of mps to arbitrary geometries with a generic wall boundary condition,” *Computers and Fluids*, 2018.
- [182] H.-G. Lyu and P.-N. Sun, “Further enhancement of the particle shifting technique: towards better volume conservation and particle distribution in sph simulations of violent free-surface flows,” *Applied Mathematical Modelling*, 2021.
- [183] M. Antuono *et al.*, “The delta-ale-sph model: an arbitrary lagrangian-eulerian framework for the delta-sph model with particle shifting technique,” *Computers and Fluids*, p. 104806, 2020.

- [184] ———, “Smoothed particle hydrodynamics method from a large eddy simulation perspective. generalization to a quasi-lagrangian model,” *Physics of Fluids*, vol. 33, no. 1, p. 015102, 2021.
- [185] H.-G. Lyu *et al.*, “On removing the numerical instability induced by negative pressures in sph simulations of typical fluid–structure interaction problems in ocean engineering,” *Applied Ocean Research*, vol. 117, p. 102938, 2021.
- [186] S. Marrone *et al.*, “Numerical study on the dissipation mechanisms in sloshing flows induced by violent and high-frequency accelerations. i. theoretical formulation and numerical investigation,” *Physical Review Fluids*, vol. 6, no. 11, p. 114801, 2021.
- [187] Z. L. Zhang *et al.*, “Improved element-particle coupling strategy with delta-sph and particle shifting for modeling sloshing with rigid or deformable structures,” *Applied Ocean Research*, vol. 114, p. 102774, 2021.
- [188] X. Yang *et al.*, “Simulating multi-phase sloshing flows with the sph method,” *Applied Ocean Research*, vol. 118, p. 102989, 2022.
- [189] K. Sato *et al.*, “Validation of the applicability of the particle-based open-source software dualsphysics to violent flow fields,” *Coastal Engineering Journal*, vol. 63, no. 4, pp. 545–572, 2021.
- [190] X. Wen, W. Zhao, and D. Wan, “An improved moving particle semi-implicit method for interfacial flows,” *Applied Ocean Research*, vol. 117, p. 102963, 2021.
- [191] R. A. Dalrymple and B. D. Rogers, “Numerical modeling of water waves with the sph method,” *Coastal Engineering*, vol. 53, no. 2, pp. 141–147, 2006.
- [192] A. English *et al.*, “Modified dynamic boundary conditions (mdbc) for general-purpose smoothed particle hydrodynamics (sph): application to tank sloshing, dam break and fish pass problems,” *Computational Particle Mechanics*, 2021.
- [193] E. S. Lee *et al.*, “Comparisons of weakly compressible and truly incompressible algorithms for the sph mesh free particle method,” *Journal of Computational Physics*, vol. 227, no. 18, pp. 8417–8436, 2008.
- [194] L.-Y. Cheng, R. Augusto Amaro Junior, and E. Henrique Favero, “Improving stability of moving particle semi-implicit method by source terms based on time-scale correction of particle-level impulses,” *Engineering Analysis with Boundary Elements*, vol. 131, pp. 118–145, 2021.

- [195] A. Souto-Iglesias *et al.*, “A set of canonical problems in sloshing. part 0: Experimental setup and data processing,” *Ocean Engineering*, vol. 38, no. 16, pp. 1823–1830, 2011.
- [196] Y. You *et al.*, “Enhancement of delta-sph for ocean engineering applications through incorporation of a background mesh scheme,” *Applied Ocean Research*, p. 102508, 2021.
- [197] G. Duan *et al.*, “Stable multiphase moving particle semi-implicit method for incompressible interfacial flow,” *Computer Methods in Applied Mechanics and Engineering*, vol. 318, pp. 636–666, 2017.
- [198] A. Mahdi, A. Shakibaeinia, and Y. Dibike, “Numerical modelling of oil-sands tailings dam breach runout and overland flow,” *Science of The Total Environment*, p. 134568, 2019.
- [199] H. M. Fritz, F. Mohammed, and J. Yoo, *Lituya Bay Landslide Impact Generated Mega-Tsunami 50th Anniversary*. Basel: Birkhäuser Basel, 2009, pp. 153–175.
- [200] H. Tan and S. Chen, “A hybrid dem-sph model for deformable landslide and its generated surge waves,” *Advances in Water Resources*, vol. 108, pp. 256–276, 2017.
- [201] R. B. Canelas *et al.*, “Sph-dcdem model for arbitrary geometries in free surface solid–fluid flows,” *Computer Physics Communications*, vol. 202, pp. 131–140, 2016.
- [202] E. Harada *et al.*, “Numerical simulation for sediment transport using mps-dem coupling model,” *Advances in Water Resources*, 2017.
- [203] L. Li, E. Marteau, and J. E. Andrade, “Capturing the inter-particle force distribution in granular material using ls-dem,” *Granular Matter*, vol. 21, no. 3, p. 43, 2019.
- [204] E. Kazemi *et al.*, “Sph modelling of turbulent open channel flow over and within natural gravel beds with rough interfacial boundaries,” *Advances in Water Resources*, p. 103557, 2020.
- [205] W.-J. Xu *et al.*, “Study on landslide-induced wave disasters using a 3d coupled sph-dem method,” *Bulletin of Engineering Geology and the Environment*, vol. 79, no. 1, pp. 467–483, 2020.
- [206] B. E. Snelling *et al.*, “Improvements to a smooth particle hydrodynamics simulator for investigating submarine landslide generated waves,” *International Journal for Numerical Methods in Fluids*, vol. n/a, no. n/a, 2020.

- [207] D. M. Robb, S. J. Gaskin, and J.-C. Marongiu, “Sph-dem model for free-surface flows containing solids applied to river ice jams,” *Journal of Hydraulic Research*, vol. 54, no. 1, pp. 27–40, 2016.
- [208] Z. Wang *et al.*, “Numerical modeling of floating bodies transport for flooding analysis in nuclear reactor building,” *Nuclear Engineering and Design*, vol. 341, pp. 390–405, 2019.
- [209] Y. Ye, T. Xu, and D. Z. Zhu, “Numerical analysis of dam-break waves propagating over dry and wet beds by the mesh-free method,” *Ocean Engineering*, vol. 217, p. 107969, 2020.
- [210] Z. Zheng *et al.*, “A novel ghost cell boundary model for the explicit moving particle simulation method in two dimensions,” *Computational Mechanics*, 2020.
- [211] T. Xu *et al.*, “Simulation of velocity and shear stress distributions in granular column collapses by a mesh-free method,” *Journal of Non-Newtonian Fluid Mechanics*, vol. 247, pp. 146–164, 2017.
- [212] L. Fu and Y.-C. Jin, “Investigation of non-deformable and deformable landslides using meshfree method,” *Ocean Engineering*, vol. 109, pp. 192–206, 2015.
- [213] G. D. R. MiDi, “On dense granular flows,” *The European Physical Journal E*, vol. 14, no. 4, pp. 341–365, 2004.
- [214] S. M. Hosseini, M. T. Manzari, and S. K. Hannani, “A fully explicit three-step sph algorithm for simulation of non-newtonian fluid flow,” *International Journal of Numerical Methods for Heat and Fluid Flow*, vol. 17, no. 7, pp. 715–735, 2007.
- [215] G. Pahar and A. Dhar, “Coupled incompressible smoothed particle hydrodynamics model for continuum-based modelling sediment transport,” *Advances in Water Resources*, vol. 102, pp. 84–98, 2017.
- [216] H. H. Bui and G. D. Nguyen, “A coupled fluid-solid sph approach to modelling flow through deformable porous media,” *International Journal of Solids and Structures*, vol. 125, pp. 244–264, 2017.
- [217] C. Chang and R. L. Powell, “Effect of particle size distributions on the rheology of concentrated bimodal suspensions,” *Journal of Rheology*, vol. 38, no. 1, pp. 85–98, 1994.

- [218] M. Bercovier and M. Engelman, “A finite-element method for incompressible non-newtonian flows,” *Journal of Computational Physics*, vol. 36, no. 3, pp. 313–326, 1980.
- [219] I. A. Frigaard and C. Nouar, “On the usage of viscosity regularisation methods for visco-plastic fluid flow computation,” *Journal of Non-Newtonian Fluid Mechanics*, vol. 127, no. 1, pp. 1–26, 2005.
- [220] A. Amicarelli *et al.*, “A 3d smoothed particle hydrodynamics model for erosional dam-break floods,” *International Journal of Computational Fluid Dynamics*, vol. 31, no. 10, pp. 413–434, 2017.
- [221] S. Bandara and K. Soga, “Coupling of soil deformation and pore fluid flow using material point method,” *Computers and Geotechnics*, vol. 63, pp. 199–214, 2015.
- [222] S. T. Grilli *et al.*, “Modeling coastal tsunami hazard from submarine mass failures: effect of slide rheology, experimental validation, and case studies off the us east coast,” *Natural Hazards*, vol. 86, no. 1, pp. 353–391, 2017.
- [223] D. Violeau and A. Leroy, “On the maximum time step in weakly compressible sph,” *Journal of Computational Physics*, vol. 256, pp. 388–415, 2014.
- [224] C. Wang *et al.*, “Dilatancy and compaction effects on the submerged granular column collapse,” *Physics of Fluids*, vol. 29, no. 10, p. 103307, 2017.
- [225] S. B. Savage, M. H. Babaei, and T. Dabros, “Modeling gravitational collapse of rectangular granular piles in air and water,” *Mechanics Research Communications*, vol. 56, pp. 1–10, 2014.
- [226] C. Wang *et al.*, “Two-fluid smoothed particle hydrodynamics simulation of submerged granular column collapse,” *Mechanics Research Communications*, vol. 79, pp. 15–23, 2017.
- [227] C.-H. Lee and Z. Huang, “A two-phase flow model for submarine granular flows: With an application to collapse of deeply-submerged granular columns,” *Advances in Water Resources*, vol. 115, pp. 286–300, 2018.
- [228] A. Colagrossi *et al.*, “Particle packing algorithm for sph schemes,” *Computer Physics Communications*, vol. 183, no. 8, pp. 1641–1653, 2012.
- [229] L.-A. Couston, C. Mei, and M.-R. Alam, “Landslide tsunamis in lakes,” *Journal of Fluid Mechanics*, vol. 772, pp. 784–804, 2015.

- [230] G.-B. Kim *et al.*, “Three dimensional landslide generated tsunamis: Numerical and physical model comparisons,” *Landslides*, 2019.
- [231] M.-L. Yu and C.-H. Lee, “Multi-phase-flow modeling of underwater landslides on an inclined plane and consequently generated waves,” *Advances in Water Resources*, vol. 133, p. 103421, 2019.
- [232] G. S. Miller *et al.*, “Tsunamis generated by long and thin granular landslides in a large flume,” *Journal of Geophysical Research: Oceans*, vol. 122, no. 1, pp. 653–668, 2017.
- [233] T. Capone, A. Panizzo, and J. J. Monaghan, “Sph modelling of water waves generated by submarine landslides,” *Journal of Hydraulic Research*, vol. 48, no. sup1, pp. 80–84, 2010.
- [234] S. Manenti, A. Amicarelli, and S. Todeschini, “Wcsph with limiting viscosity for modeling landslide hazard at the slopes of artificial reservoir,” *Water*, vol. 10, no. 4, 2018.
- [235] K. Kamrin, “Non-locality in granular flow: Phenomenology and modeling approaches,” *Frontiers in Physics*, vol. 7, no. 116, 2019.
- [236] A. E. Lobkovsky *et al.*, “Erosion of a granular bed driven by laminar fluid flow,” *Journal of Fluid Mechanics*, vol. 605, pp. 47–58, 2008.
- [237] V. Vand, “Viscosity of solutions and suspensions. i. theory,” *The Journal of Physical and Colloid Chemistry*, vol. 52, no. 2, pp. 277–299, 1948.
- [238] G. Duan, S. Koshizuka, and B. Chen, “A contoured continuum surface force model for particle methods,” *Journal of Computational Physics*, vol. 298, pp. 280–304, 2015.
- [239] Q. Cao, K. Sarkar, and A. K. Prasad, “Direct numerical simulations of two-layer viscosity-stratified flow,” *International Journal of Multiphase Flow*, vol. 30, no. 12, pp. 1485–1508, 2004.
- [240] C.-H. Lee, Y. M. Low, and Y.-M. Chiew, “Multi-dimensional rheology-based two-phase model for sediment transport and applications to sheet flow and pipeline scour,” *Physics of Fluids*, vol. 28, no. 5, p. 053305, 2016.